

AD-A238 799



DTIC

UNCLASSIFIED

JUL 22 1991

A MULTIPLE MODEL ADAPTIVE ESTIMATOR
USING FIRST AND SECOND-ORDER
ACCELERATION MODELS FOR USE IN
A FORWARD-LOOKING-INFRARED TRACKER

THESIS

Barbara J. Niblett
Captain, USAF

AFIT/GE/ENG/91J-03

DISTRIBUTION STATEMENT A

Approved for public release
Distribution Unlimited

DEPARTMENT OF THE AIR FORCE
AIR UNIVERSITY

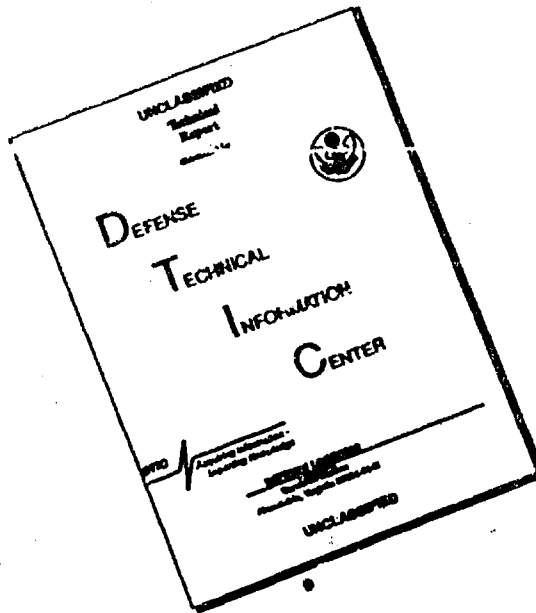
AIR FORCE INSTITUTE OF TECHNOLOGY

Wright-Patterson Air Force Base, Ohio

91 7 19 1 54

91-05716

DISCLAIMER NOTICE



THIS DOCUMENT IS BEST
QUALITY AVAILABLE. THE COPY
FURNISHED TO DTIC CONTAINED
A SIGNIFICANT NUMBER OF
PAGES WHICH DO NOT
REPRODUCE LEGIBLY.

AFIT/GE/ENG/91J-03

13

DTIC
ELECTE
JUL 22 1991
S D

A MULTIPLE MODEL ADAPTIVE ESTIMATOR
USING FIRST AND SECOND-ORDER
ACCELERATION MODELS FOR USE IN
A FORWARD-LOOKING-INFRARED TRACKER

THESIS

Barbara J. Niblett
Captain, USAF

AFIT/GE/ENG/91J-03

Accession For	
NTIS CRA&I	<input checked="" type="checkbox"/>
DTIC TAB	<input type="checkbox"/>
Unannounced	<input type="checkbox"/>
Justification	
By	
Distribution /	
Availability Codes	
Dist	Avail and/or Special
A-1	

DISTRIBUTION STATEMENT A
Approved for public release;
Distribution Unlimited

Approved for public release; distribution unlimited

91-05716



REPORT DOCUMENTATION PAGE			Form Approved OMB No. 0704-0188	
Public reporting burden for this collection of information is estimated to average 1 hour per response, including the time for reviewing instructions, searching existing data sources, gathering and maintaining the data needed, and completing and reviewing the collection of information. Send comments regarding this burden estimate or any other aspect of this collection of information, including suggestions for reducing this burden, to Washington Headquarters Services, Directorate for Information Operations and Reports, 1215 Jefferson Davis Highway, Suite 1204 Arlington, VA 22202-4302, and to the Office of Management and Budget, Paperwork Reduction Project (0704-0188), Washington, DC 20503.				
1. AGENCY USE ONLY (Leave blank)	2. REPORT DATE June 1991	3. REPORT TYPE AND DATES COVERED Thesis		
4. TITLE AND SUBTITLE A Multiple Model Adaptive Estimator using First and Second-Order Acceleration Models for use in a Forward-Looking-Infrared Tracker		5. FUNDING NUMBERS		
6. AUTHOR(S) Barbara J. Niblett, Capt, USAF				
7. PERFORMING ORGANIZATION NAME(S) AND ADDRESS(ES) Air Force Institute of Technology, WPAFB OH 45433-6583		8. PERFORMING ORGANIZATION REPORT NUMBER AFIT/GE/ENG/91J-03		
9. SPONSORING / MONITORING AGENCY NAME(S) AND ADDRESS(ES)		10. SPONSORING / MONITORING AGENCY REPORT NUMBER		
11. SUPPLEMENTARY NOTES				
12a. DISTRIBUTION / AVAILABILITY STATEMENT Approved for Public Release; Distribution Unlimited		12b. DISTRIBUTION CODE		
13. ABSTRACT (Maximum 200 words) <p>→ The performance of a multiple model adaptive estimator (MMAE) for an enhanced correlator/forward-looking-infrared tracker for airborne targets is analyzed in order to improve its performance. Performance evaluation is based on elemental filter selection and MMAE estimation error sizes and trends. The elemental filters are based on either first or second-order acceleration models. Improved filter selection is achieved by using acceleration models that separate the frequency content of acceleration power spectral densities into non-overlapping regions with second-order models versus the more traditional overlapping regions with first-order models. A revised tuning method is presented. The maximum a posteriori (MAP) versus the Bayesian MMAE is investigated. The calculation of the hypothesis probability calculation is altered to see how performance is affected. The impact of the ad hoc selection of a lower bound on the elemental filter probability calculation to prevent filter lockout is evaluated. Parameter space discretization is investigated.</p> <p>Comparable performance is achieved from the MMAEs based on either first or second-order acceleration models. The MAP and Bayesian options give comparable performance. A lower bound of 0.001 gives best results. The traditional probability calculation allows better filter selection by the MMAE for this application.</p>				
14. SUBJECT TERMS MMAE, Second-order Models, FLIR Tracker			15. NUMBER OF PAGES 386	
			16. PRICE CODE	
17. SECURITY CLASSIFICATION OF REPORT Unclassified	18. SECURITY CLASSIFICATION OF THIS PAGE Unclassified	19. SECURITY CLASSIFICATION OF ABSTRACT Unclassified	20. LIMITATION OF ABSTRACT UL	

GENERAL INSTRUCTIONS FOR COMPLETING SF 298

The Report Documentation Page (RDP) is used in announcing and cataloging reports. It is important that this information be consistent with the rest of the report, particularly the cover and title page. Instructions for filling in each block of the form follow. It is important to stay within the lines to meet optical scanning requirements.

Block 1. Agency Use Only (Leave blank).

Block 2. Report Date. Full publication date including day, month, and year, if available (e.g. 1 Jan 88). Must cite at least the year.

Block 3. Type of Report and Dates Covered. State whether report is interim, final, etc. If applicable, enter inclusive report dates (e.g. 10 Jun 87 - 30 Jun 88).

Block 4. Title and Subtitle. A title is taken from the part of the report that provides the most meaningful and complete information. When a report is prepared in more than one volume, repeat the primary title, add volume number, and include subtitle for the specific volume. On classified documents enter the title classification in parentheses.

Block 5. Funding Numbers. To include contract and grant numbers; may include program element number(s), project number(s), task number(s), and work unit number(s). Use the following labels:

C - Contract	PR - Project
G - Grant	TA - Task
PE - Program Element	WU - Work Unit Accession No.

Block 6. Author(s). Name(s) of person(s) responsible for writing the report, performing the research, or credited with the content of the report. If editor or compiler, this should follow the name(s).

Block 7. Performing Organization Name(s) and Address(es). Self-explanatory.

Block 8. Performing Organization Report Number. Enter the unique alphanumeric report number(s) assigned by the organization performing the report.

Block 9. Sponsoring/Monitoring Agency Name(s) and Address(es). Self-explanatory.

Block 10. Sponsoring/Monitoring Agency Report Number. (If known)

Block 11. Supplementary Notes. Enter information not included elsewhere such as. Prepared in cooperation with..., Trans. of., To be published in.... When a report is revised, include a statement whether the new report supersedes or supplements the older report.

Block 12a. Distribution/Availability Statement. Denotes public availability or limitations. Cite any availability to the public. Enter additional limitations or special markings in all capitals (e.g. NOFORN, REL, ITAR).

DOD - See DoDD 5230.24, "Distribution Statements on Technical Documents."

DOE - See authorities.

NASA - See Handbook NHB 2200.2.

NTIS - Leave blank.

Block 12b. Distribution Code.

DOD - Leave blank.

DOE - Enter DOE distribution categories from the Standard Distribution for Unclassified Scientific and Technical Reports.

NASA - Leave blank.

NTIS - Leave blank.

Block 13. Abstract. Include a brief (Maximum 200 words) factual summary of the most significant information contained in the report.

Block 14. Subject Terms. Keywords or phrases identifying major subjects in the report.

Block 15. Number of Pages. Enter the total number of pages.

Block 16. Price Code. Enter appropriate price code (NTIS only).

Blocks 17. - 19. Security Classifications. Self-explanatory. Enter U.S. Security Classification in accordance with U.S. Security Regulations (i.e., UNCLASSIFIED). If form contains classified information, stamp classification on the top and bottom of the page.

Block 20. Limitation of Abstract. This block must be completed to assign a limitation to the abstract. Enter either UL (unlimited) or SAR (same as report). An entry in this block is necessary if the abstract is to be limited. If blank, the abstract is assumed to be unlimited.

AFIT/GE/ENG/91J-03

A MULTIPLE MODEL ADAPTIVE ESTIMATOR USING FIRST AND
SECOND-ORDER ACCELERATION MODELS FOR USE IN A
FORWARD-LOOKING-INFRARED TRACKER

THESIS

Presented to the Faculty of the School of Engineering
of the Air Force Institute of Technology
Air University
In Partial Fulfillment of the
Requirements for the Degree of
Master of Science in Electrical Engineering

Barbara J. Niblett,
Captain, USAF

June, 1991

Approved for public release; distribution unlimited

Acknowledgments

I would like to share the accomplishment of this research with my thesis advisor, Dr. Peter Maybeck, and my G&C classmates.

Dr. Maybeck, you helped make this possible by giving of your time, patience, and knowledge of stochastics and life.

Guys, you helped make this AFIT experience bearable.

Bobbie

Table of Contents

	Page
Acknowledgments	ii
Table of Contents	iii
List of Figures	vii
List of Tables	xix
List of Symbols	xxv
Abstract	xxix
I. Introduction	1-1
1.1 Background	1-1
1.2 Summary of Previous AFIT Research	1-1
1.3 Objectives	1-5
1.3.1 Second-Order Gauss-Markov Acceleration Models.	1-7
1.3.2 Bayesian versus MAP MMAE.	1-7
1.3.3 Alter the p_k Calculation.	1-7
1.3.4 Vary Lower Bound on p_k	1-10
1.4 Text Overview	1-10
II. Theory	2-1
2.1 Introduction	2-1
2.2 The Multiple Model Adaptive Estimator	2-1
2.3 Summary	2-5

	Page
III. Truth Model	3-1
3.1 Introduction	3-1
3.2 Deterministic Target Motion Model	3-1
3.2.1 Trajectories in the Inertial Frame.	3-2
3.2.2 Translate to the α - β - γ Frame.	3-3
3.3 Atmospheric Disturbance Model	3-7
3.4 Augmented Discrete-time Model	3-10
3.5 Measurement Model	3-11
3.6 Summary	3-15
IV. Filter Models	4-1
4.1 Introduction	4-1
4.2 Enhanced Correlator	4-1
4.3 Update Equations	4-4
4.4 Propagation Equations	4-4
4.5 Dynamics Models	4-5
4.5.1 Filter Atmospheric Models.	4-5
4.5.2 Acceleration Models.	4-6
4.5.3 Second-Order Gauss-Markov Acceleration Model. . .	4-12
4.6 Template Generation	4-16
4.7 Summary	4-17
V. Performance Evaluation	5-1
5.1 Introduction	5-1
5.2 Monte Carlo Study	5-1
5.3 Initial Look at Real-Pole MMAE	5-4
5.4 Initial Look at Notch Filters	5-11
5.5 Alternative Approach to Tuning	5-14

	Page
5.6 A Second Notch MMAE	5-20
5.7 Tracking a Target in an Evasive Maneuver.	5-23
5.8 Examining the Hypothesis Probability Calculation	5-27
5.8.1 PC Check on MMAE-1R.	5-28
5.8.2 PC Check on MMAE-2R.	5-33
5.9 MAP MMAE	5-39
5.10 Varying the Lower Bound of the Probability Calculation . . .	5-43
5.11 Summary	5-46
VI. MMAE Based on First-Order Models	6-1
6.1 Introduction	6-1
6.2 First-Order MMAE with Revised Tuning	6-1
6.3 First-Order MMAE with Ad Hoc Tuning	6-7
6.4 Proximity Check for Filters	6-16
6.4.1 Proximity of Notch and First-Order Filters.	6-17
6.4.2 Proximity of Notch Filters.	6-20
6.5 Summary	6-24
VII. Conclusions and Recommendations	7-1
7.1 Introduction	7-1
7.2 Conclusions of Current Investigation	7-2
7.3 Recommendations for Further Investigation	7-3
Appendix A. Parameters of the MMAEs and Trajectories Designed	A-1
Appendix B. Probability Plots for each of the 10 Runs	B-1
Appendix C. Error plots for Real-Pole MMAE	C-1
Appendix D. Error Plots for Notch MMAE-1	D-1

	Page
Appendix E. Error Plots for Notch MMAE-2	E-1
Appendix F. Error Plots for First-Order MMAE	F-1
Bibliography	BIB-1
Vita	VITA-1

List of Figures

Figure	Page
1.1. PSDs of Various Acceleration Models for an MMAE	1-6
1.2. The MMAE Structure	1-8
3.1. The Inertial Frame	3-2
3.2. The Alpha-Beta Plane	3-4
3.3. Mathematical Model for Atmospheric Jitter	3-7
3.4. Simulated Target	3-11
3.5. Correlation Coefficients for Pixel 28	3-14
4.1. Enhanced Correlator and Linear Kalman Filter	4-3
4.2. PSD Plot for the Output of a First-Order Gauss-Markov Filter	4-11
4.3. PSD Plot for the Output of a Real-Pole Filter	4-16
4.4. PSD Plot for the Output of a Complex Pole Filter	4-17
5.1. PSD Plot; Real-Pole MMAE-O	5-7
5.2. Target Position; Detector Plane; Sinusoidal Trajectories with Various Frequencies.	5-8
5.3. Probability Plots; Real-Pole MMAE-O; PC is 1; Basic Trajectories . .	5-10
5.4. PSD Plot; Notch MMAE-1O	5-12
5.5. Probability Plots; Notch MMAE-1O; Basic Trajectories	5-13
5.6. $\mathbf{r}_k^T(t_i)\mathbf{r}_k(t_i)$ and $\mathbf{r}_k^T(t_i)\mathbf{A}_k^{-1}(t_i)\mathbf{r}_k(t_i)$ for the Harsh Notch Filter Tracking the Harsh Trajectory	5-15
5.7. PSD Plots; Real-Pole MMAE-R and Notch MMAE-1R	5-16
5.8. Probability Plots; Real-Pole MMAE-R; PC is 1; Basic Trajectories . .	5-18
5.9. Probability Plots; Notch MMAE-1R; PC is 1; Basic Trajectories . . .	5-19
5.10. Intermediate Model at $\omega = 1.32$	5-21
5.11. Probability Plots; Notch MMAE-2R; PC is 1; Basic Trajectories . . .	5-22

Figure	Page
5.12. Target Position; Detector Plane; Jinking Trajectory	5-24
5.13. Probability Plots; Notch MMAE-1R and Notch MMAE-2R; PC is 1; Jinking Trajectory	5-25
5.14. Probability Plots; Notch MMAE-1R; PC is 2; Basic Trajectories . . .	5-29
5.15. Probability Plots; Notch MMAE-1R; PC is 3; Basic Trajectories . . .	5-30
5.16. Probability Plots; Notch MMAE-1R; PC is 4; Basic Trajectories . . .	5-31
5.17. Probability Plots; Notch MMAE-2R; PC is 2; Basic Trajectories . . .	5-34
5.18. Probability Plots; Notch MMAE-2R; PC is 3; Basic Trajectories . . .	5-35
5.19. Probability Plots; Notch MMAE-2R; PC is 4; Basic Trajectories . . .	5-36
5.20. Probability Plots; Notch MMAE-2R; PC varies; Jinking Trajectory . .	5-38
5.21. Probability Plots; Notch MMAE-2RM; PC is 1; Basic Trajectories . .	5-40
5.22. Probability Plots; Notch MMAE-2RM; PC is 4; Basic Trajectories . .	5-41
5.23. Probability Plots; Notch MMAE-2RM; PC is varied; Jinking Trajectory	5-42
5.24. Probability Plots; Notch MMAE-2R; PC is 1; LB is Varied; Jinking Trajectory	5-45
6.1. PSD Plot; First-Order MMAE-R	6-2
6.2. Probability Plots; First-Order MMAE-R; PC is 1; Basic Trajectories .	6-3
6.3. Probability Plots; First-Order MMAE-R; PC is 4; Basic Trajectories .	6-4
6.4. Probability Plots; First-Order MMAE-R; PC is Varied; Jinking Trajectory	6-6
6.5. PSD Plots; First-Order MMAE with Ad Hoc Tuning	6-8
6.6. Probability Plots; First-Order MMAE-FL; PC is 1; Basic Trajectories	6-10
6.7. Probability Plots; First-Order MMAE-FH; PC is 1; Basic Trajectories	6-11
6.8. Probability Plots; First-Order MMAE-F; PC is 1; Jinking Trajectory	6-12
6.9. PSD Plots; Notch MMAE-2 with Ad Hoc Tuning	6-14
6.10. Probability Plots; Notch MMAE-2F; PC is 1; Jinking Trajectory . . .	6-15
6.11. Probability Plots; Various Notch MMAEs; PC is 1; Intermediate Trajectories	6-18

Figure	Page
6.12. Probability Plots; Special Notch MMAE; PC is 1; Harsh Trajectory .	6-19
6.13. Probability Plots; Notch MMAE-2R; PC is 1; Various Trajectories . .	6-21
6.14. Probability Plots; Notch MMAE-3R; PC is 1; Various Trajectories . .	6-22
6.15. Probability Plots; Notch MMAE-4R; PC is 1; Various Trajectories . .	6-23
B.1. Complete Probability Plots; Notch MMAE-2R; PC is 1; LB is 0.0005; Jinking Trajectory	B-2
B.2. Complete Probability Plots; Notch MMAE-2R; PC is 1; LB is 0.001; Jinking Trajectory	B-3
B.3. Complete Probability Plots; Notch MMAE-2R; PC is 1; LB is 0.005; Jinking Trajectory	B-4
B.4. Complete Probability Plots; Notch MMAE-2R; PC is 1; LB is 0.01; Jinking Trajectory	B-5
C.1. RMS Error Plots; Real-Pole MMAE-O; PC is 1; Trajectory with $\omega = .01$	C-2
C.2. X-Error Plots; Real-Pole MMAE-O; PC is 1; Trajectory with $\omega = .01$	C-3
C.3. Y-Error Plots; Real-Pole MMAE-O; PC is 1; Trajectory with $\omega = .01$	C-4
C.4. RMS Error Plots; Real-Pole MMAE-O; PC is 1; Trajectory with $\omega = .62$	C-5
C.5. X-Error Plots; Real-Pole MMAE-O; PC is 1; Trajectory with $\omega = .62$	C-6
C.6. Y-Error Plots; Real-Pole MMAE-O; PC is 1; Trajectory with $\omega = .62$	C-7
C.7. RMS Error Plots; Real-Pole MMAE-O; PC is 1; Trajectory with $\omega = 2.8$	C-8
C.8. X-Error Plots; Real-Pole MMAE-O; PC is 1; Trajectory with $\omega = 2.8$	C-9
C.9. Y-Error Plots; Real-Pole MMAE-O; PC is 1; Trajectory with $\omega = 2.8$	C-10
C.10. RMS Error Plots; Real-Pole MMAE-R; PC is 1; Trajectory with $\omega = .01$	C-11
C.11. X-Error Plots; Real-Pole MMAE-R; PC is 1; Trajectory with $\omega = .01$	C-12
C.12. Y-Error Plots; Real-Pole MMAE-R; PC is 1; Trajectory with $\omega = .01$	C-13
C.13. RMS Error Plots; Real-Pole MMAE-R; PC is 1; Trajectory with $\omega = .62$	C-14
C.14. X-Error Plots; Real-Pole MMAE-R; PC is 1; Trajectory with $\omega = .62$	C-15
C.15. Y-Error Plots; Real-Pole MMAE-R; PC is 1; Trajectory with $\omega = .62$	C-16

Figure	Page
C.16. RMS Error Plots; Real-Pole MMAE-R; PC is 1; Trajectory with $\omega = 2.8$	C-17
C.17. X-Error Plots; Real-Pole MMAE-R; PC is 1; Trajectory with $\omega = 2.8$	C-18
C.18. Y-Error Plots; Real-Pole MMAE-R; PC is 1; Trajectory with $\omega = 2.8$	C-19
D.1. RMS Error Plots; Notch MMAE-1O; PC is 1; Trajectory with $\omega = .01$	D-2
D.2. X-Error Plots; Notch MMAE-1O; PC is 1; Trajectory with $\omega = .01$	D-3
D.3. Y-Error Plots; Notch MMAE-1O; PC is 1; Trajectory with $\omega = .01$	D-4
D.4. RMS Error Plots; Notch MMAE-1O; PC is 1; Trajectory with $\omega = .62$	D-5
D.5. X-Error Plots; Notch MMAE-1O; PC is 1; Trajectory with $\omega = .62$	D-6
D.6. Y-Error Plots; Notch MMAE-1O; PC is 1; Trajectory with $\omega = .62$	D-7
D.7. RMS Error Plots; Notch MMAE-1O; PC is 1; Trajectory with $\omega = 2.8$	D-8
D.8. X-Error Plots; Notch MMAE-1O; PC is 1; Trajectory with $\omega = 2.8$	D-9
D.9. Y-Error Plots; Notch MMAE-1O; PC is 1; Trajectory with $\omega = 2.8$	D-10
D.10. RMS Error Plots; Notch MMAE-1R; PC is 1; Trajectory with $\omega = .01$	D-11
D.11. X-Error Plots; Notch MMAE-1R; PC is 1; Trajectory with $\omega = .01$	D-12
D.12. Y-Error Plots; Notch MMAE-1R; PC is 1; Trajectory with $\omega = .01$	D-13
D.13. RMS Error Plots; Notch MMAE-1R; PC is 1; Trajectory with $\omega = .62$	D-14
D.14. X-Error Plots; Notch MMAE-1R; PC is 1; Trajectory with $\omega = .62$	D-15
D.15. Y-Error Plots; Notch MMAE-1R; PC is 1; Trajectory with $\omega = .62$	D-16
D.16. RMS Error Plots; Notch MMAE-1R; PC is 1; Trajectory with $\omega = 2.8$	D-17
D.17. X-Error Plots; Notch MMAE-1R; PC is 1; Trajectory with $\omega = 2.8$	D-18
D.18. Y-Error Plots; Notch MMAE-1R; PC is 1; Trajectory with $\omega = 2.8$	D-19
D.19. RMS Error Plots; Notch MMAE-1R; PC is 2; Trajectory with $\omega = .01$	D-20
D.20. X-Error Plots; Notch MMAE-1R; PC is 2; Trajectory with $\omega = .01$	D-21
D.21. Y-Error Plots; Notch MMAE-1R; PC is 2; Trajectory with $\omega = .01$	D-22
D.22. RMS Error Plots; Notch MMAE-1R; PC is 2; Trajectory with $\omega = .62$	D-23
D.23. X-Error Plots; Notch MMAE-1R; PC is 2; Trajectory with $\omega = .62$	D-24
D.24. Y-Error Plots; Notch MMAE-1R; PC is 2; Trajectory with $\omega = .62$	D-25

Figure	Page
D.25. RMS Error Plots; Notch MMAE-1R; PC is 2; Trajectory with $\omega = 2.8$	D-26
D.26. X-Error Plots; Notch MMAE-1R; PC is 2; Trajectory with $\omega = 2.8$	D-27
D.27. Y-Error Plots; Notch MMAE-1R; PC is 2; Trajectory with $\omega = 2.8$	D-28
D.28. RMS Error Plots; Notch MMAE-1R; PC is 3; Trajectory with $\omega = .01$	D-29
D.29. X-Error Plots; Notch MMAE-1R; PC is 3; Trajectory with $\omega = .01$	D-30
D.30. Y-Error Plots; Notch MMAE-1R; PC is 3; Trajectory with $\omega = .01$	D-31
D.31. RMS Error Plots; Notch MMAE-1R; PC is 3; Trajectory with $\omega = .62$	D-32
D.32. X-Error Plots; Notch MMAE-1R; PC is 3; Trajectory with $\omega = .62$	D-33
D.33. Y-Error Plots; Notch MMAE-1R; PC is 3; Trajectory with $\omega = .62$	D-34
D.34. RMS Error Plots; Notch MMAE-1R; PC is 3; Trajectory with $\omega = 2.8$	D-35
D.35. X-Error Plots; Notch MMAE-1R; PC is 3; Trajectory with $\omega = 2.8$	D-36
D.36. Y-Error Plots; Notch MMAE-1R; PC is 3; Trajectory with $\omega = 2.8$	D-37
D.37. RMS Error Plots; Notch MMAE-1R; PC is 4; Trajectory with $\omega = .01$	D-38
D.38. X-Error Plots; Notch MMAE-1R; PC is 4; Trajectory with $\omega = .01$	D-39
D.39. Y-Error Plots; Notch MMAE-1R; PC is 4; Trajectory with $\omega = .01$	D-40
D.40. RMS Error Plots; Notch MMAE-1R; PC is 4; Trajectory with $\omega = .62$	D-41
D.41. X-Error Plots; Notch MMAE-1R; PC is 4; Trajectory with $\omega = .62$	D-42
D.42. Y-Error Plots; Notch MMAE-1R; PC is 4; Trajectory with $\omega = .62$	D-43
D.43. RMS Error Plots; Notch MMAE-1R; PC is 4; Trajectory with $\omega = 2.8$	D-44
D.44. X-Error Plots; Notch MMAE-1R; PC is 4; Trajectory with $\omega = 2.8$	D-45
D.45. Y-Error Plots; Notch MMAE-1R; PC is 4; Trajectory with $\omega = 2.8$	D-46
D.46. RMS Error Plots; Notch MMAE-1R; PC is 1; Jinking Trajectory . . .	D-47
D.47. X-Error Plots; Notch MMAE-1R; PC is 1; Jinking Trajectory	D-48
D.48. Y-Error Plots; Notch MMAE-1R; PC is 1; Jinking Trajectory	D-49
D.49. Probability Calculation Plots; Notch MMAE-1R; PC is 1; Jinking Trajectory	D-50
E.1. RMS Error Plots; Notch MMAE-2R; PC is 1; Trajectory with $\omega = .01$	E-2

Figure	Page
E.2. X-Error Plots; Notch MMAE-2R; PC is 1; Trajectory with $\omega = .01$.	E-3
E.3. Y-Error Plots; Notch MMAE-2R; PC is 1; Trajectory with $\omega = .01$.	E-4
E.4. RMS Error Plots; Notch MMAE-2R; PC is 1; Trajectory with $\omega = 1.32$	E-5
E.5. X-Error Plots; Notch MMAE-2R; PC is 1; Trajectory with $\omega = 1.32$.	E-6
E.6. Y-Error Plots; Notch MMAE-2R; PC is 1; Trajectory with $\omega = 1.32$.	E-7
E.7. RMS Error Plots; Notch MMAE-2R; PC is 1; Trajectory with $\omega = 2.8$	E-8
E.8. X-Error Plots; Notch MMAE-2R; PC is 1; Trajectory with $\omega = 2.8$.	E-9
E.9. Y-Error Plots; Notch MMAE-2R; PC is 1; Trajectory with $\omega = 2.8$; .	E-10
E.10. RMS Error Plots; Notch MMAE-2R; PC is 2; Trajectory with $\omega = .01$	E-11
E.11. X-Error Plots; Notch MMAE-2R; PC is 2; Trajectory with $\omega = .01$.	E-12
E.12. Y-Error Plots; Notch MMAE-2R; PC is 2; Trajectory with $\omega = .01$.	E-13
E.13. RMS Error Plots; Notch MMAE-2R; PC is 2; Trajectory with $\omega = 1.32$	E-14
E.14. X-Error Plots; Notch MMAE-2R; PC is 2; Trajectory with $\omega = 1.32$.	E-15
E.15. Y-Error Plots; Notch MMAE-2R; PC is 2; Trajectory with $\omega = 1.32$.	E-16
E.16. RMS Error Plots; Notch MMAE-2R; PC is 2; Trajectory with $\omega = 2.8$	E-17
E.17. X-Error Plots; Notch MMAE-2R; PC is 2; Trajectory with $\omega = 2.8$.	E-18
E.18. Y-Error Plots; Notch MMAE-2R; PC is 2; Trajectory with $\omega = 2.8$.	E-19
E.19. RMS Error Plots; Notch MMAE-2R; PC is 3; Trajectory with $\omega = .01$	E-20
E.20. X-Error Plots; Notch MMAE-2R; PC is 3; Trajectory with $\omega = .01$.	E-21
E.21. Y-Error Plots; Notch MMAE-2R; PC is 3; Trajectory with $\omega = .01$.	E-22
E.22. RMS Error Plots; Notch MMAE-2R; PC is 3; Trajectory with $\omega = 1.32$	E-23
E.23. X-Error Plots; Notch MMAE-2R; PC is 3; Trajectory with $\omega = 1.32$.	E-24
E.24. Y-Error Plots; Notch MMAE-2R; PC is 3; Trajectory with $\omega = 1.32$.	E-25
E.25. RMS Error Plots; Notch MMAE-2R; PC is 3; Trajectory with $\omega = 2.8$	E-26
E.26. X-Error Plots; Notch MMAE-2R; PC is 3; Trajectory with $\omega = 2.8$.	E-27
E.27. Y-Error Plots; Notch MMAE-2R; PC is 3; Trajectory with $\omega = 2.8$.	E-28
E.28. RMS Error Plots; Notch MMAE-2R; PC is 4; Trajectory with $\omega = .01$	E-29

Figure	Page
E.29. X-Error Plots; Notch MMAE-2R; PC is 4; Trajectory with $\omega = .01$.	E-30
E.30. Y-Error Plots; Notch MMAE-2R; PC is 4; Trajectory with $\omega = .01$.	E-31
E.31. RMS Error Plots; Notch MMAE-2R; PC is 4; Trajectory with $\omega = 1.32$	E-32
E.32. X-Error Plots; Notch MMAE-2R; PC is 4; Trajectory with $\omega = 1.32$.	E-33
E.33. Y-Error Plots; Notch MMAE-2R; PC is 4; Trajectory with $\omega = 1.32$.	E-34
E.34. RMS Error Plots; Notch MMAE-2R; PC is 4; Trajectory with $\omega = 2.8$	E-35
E.35. X-Error Plots; Notch MMAE-2R; PC is 4; Trajectory with $\omega = 2.8$.	E-36
E.36. Y-Error Plots; Notch MMAE-2R; PC is 4; Trajectory with $\omega = 2.8$.	E-37
E.37. RMS Error Plots; Notch MMAE-2R; PC is 1; Jinking Trajectory . . .	E-38
E.38. X-Error Plots; Notch MMAE-2R; PC is 1; Jinking Trajectory	E-39
E.39. Y-Error Plots; Notch MMAE-2R; PC is 1; Jinking Trajectory	E-40
E.40. Probability Calculation Plots; Notch MMAE-2R; PC is 1; Jinking Trajectory	E-41
E.41. RMS Error Plots; Notch MMAE-2R; PC is 2; Jinking Trajectory . . .	E-42
E.42. X-Error Plots; Notch MMAE-2R; PC is 2; Jinking Trajectory	E-43
E.43. Y-Error Plots; Notch MMAE-2R; PC is 2; Jinking Trajectory	E-44
E.44. Probability Calculation Plots; Notch MMAE-2R; PC is 2; Jinking Trajectory	E-45
E.45. RMS Error Plots; Notch MMAE-2R; PC is 3; Jinking Trajectory . . .	E-46
E.46. X-Error Plots; Notch MMAE-2R; PC is 3; Jinking Trajectory	E-47
E.47. Y-Error Plots; Notch MMAE-2R; PC is 3; Jinking Trajectory	E-48
E.48. Probability Calculation Plots; Notch MMAE-2R; PC is 3; Jinking Trajectory	E-49
E.49. RMS Error Plots; Notch MMAE-2R; PC is 4; Jinking Trajectory . . .	E-50
E.50. X-Error Plots; Notch MMAE-2R; PC is 4; Jinking Trajectory	E-51
E.51. Y-Error Plots; Notch MMAE-2R; PC is 4; Jinking Trajectory	E-52
E.52. Probability Calculation Plots; Notch MMAE-2R; PC is 4; Jinking Trajectory	E-53

Figure	Page
E.53. RMS Error Plots; Notch MMAE-2RM; PC is 1; Trajectory with $\omega = .01$	E-54
E.54. X-Error Plots; Notch MMAE-2RM; PC is 1; Trajectory with $\omega = .01$	E-55
E.55. Y-Error Plots; Notch MMAE-2RM; PC is 1; Trajectory with $\omega = .01$	E-56
E.56. RMS Error Plots; Notch MMAE-2RM; PC is 1; Trajectory with $\omega = 1.32$	E-57
E.57. X-Error Plots; Notch MMAE-2RM; PC is 1; Trajectory with $\omega = 1.32$	E-58
E.58. Y-Error Plots; Notch MMAE-2RM; PC is 1; Trajectory with $\omega = 1.32$	E-59
E.59. RMS Error Plots; Notch MMAE-2RM; PC is 1; Trajectory with $\omega = 2.8$	E-60
E.60. X-Error Plots; Notch MMAE-2RM; PC is 1; Trajectory with $\omega = 2.8$	E-61
E.61. Y-Error Plots; Notch MMAE-2RM; PC is 1; Trajectory with $\omega = 2.8$;	E-62
E.62. RMS Error Plots; Notch MMAE-2RM; PC is 4; Trajectory with $\omega = .01$	E-63
E.63. X-Error Plots; Notch MMAE-2RM; PC is 4; Trajectory with $\omega = .01$	E-64
E.64. Y-Error Plots; Notch MMAE-2RM; PC is 4; Trajectory with $\omega = .01$	E-65
E.65. RMS Error Plots; Notch MMAE-2RM; PC is 4; Trajectory with $\omega = 1.32$	E-66
E.66. X-Error Plots; Notch MMAE-2RM; PC is 4; Trajectory with $\omega = 1.32$	E-67
E.67. Y-Error Plots; Notch MMAE-2RM; PC is 4; Trajectory with $\omega = 1.32$	E-68
E.68. RMS Error Plots; Notch MMAE-2RM; PC is 4; Trajectory with $\omega = 2.8$	E-69
E.69. X-Error Plots; Notch MMAE-2RM; PC is 4; Trajectory with $\omega = 2.8$	E-70
E.70. Y-Error Plots; Notch MMAE-2RM; PC is 4; Trajectory with $\omega = 2.8$	E-71
E.71. RMS Error Plots; Notch MMAE-2RM; PC is 1; Jinking Trajectory . .	E-72
E.72. X-Error Plots; Notch MMAE-2RM; PC is 1; Jinking Trajectory . . .	E-73
E.73. Y-Error Plots; Notch MMAE-2RM; PC is 1; Jinking Trajectory . . .	E-74
E.74. Probability Calculation Plots; Notch MMAE-2RM; PC is 1; Jinking Trajectory	E-75
E.75. RMS Error Plots; Notch MMAE-2RM; PC is 4; Jinking Trajectory . .	E-76
E.76. X-Error Plots; Notch MMAE-2RM; PC is 4; Jinking Trajectory . . .	E-77
E.77. Y-Error Plots; Notch MMAE-2RM; PC is 4; Jinking Trajectory . . .	E-78
E.78. Probability Calculation Plots; Notch MMAE-2RM; PC is 4; Jinking Trajectory	E-79

Figure	Page
E.79. RMS Error Plots; Notch MMAE-2R; PC is 1; LB is .0005; Jinking Trajectory	E-80
E.80. X-Error Plots; Notch MMAE-2R; PC is 1; LB is .0005; Jinking Trajectory	E-81
E.81. Y-Error Plots; Notch MMAE-2R; PC is 1; LB is .0005; Jinking Trajectory	E-82
E.82. Probability Calculation Plots; Notch MMAE-2R; PC is 1; LB is .0005; Jinking Trajectory	E-83
E.83. RMS Error Plots; Notch MMAE-2R; PC is 1; LB is .005; Jinking Trajectory	E-84
E.84. X-Error Plots; Notch MMAE-2R; PC is 1; LB is .005; Jinking Trajectory	E-85
E.85. Y-Error Plots; Notch MMAE-2R; PC is 1; LB is .005; Jinking Trajectory	E-86
E.86. Probability Calculation Plots; Notch MMAE-2R; PC is 1; LB is .005; Jinking Trajectory	E-87
E.87. RMS Error Plots; Notch MMAE-2R; PC is 1; LB is .01; Jinking Trajectory	E-88
E.88. X-Error Plots; Notch MMAE-2R; PC is 1; LB is .01; Jinking Trajectory	E-89
E.89. Y-Error Plots; Notch MMAE-2R; PC is 1; LB is .01; Jinking Trajectory	E-90
E.90. Probability Calculation Plots; Notch MMAE-2R; PC is 1; LB is .01; Jinking Trajectory	E-91
E.91. RMS Error Plots; Notch MMAE-2FB; PC is 1; Jinking Trajectory . .	E-92
E.92. X-Error Plots; Notch MMAE-2FB; PC is 1; Jinking Trajectory	E-93
E.93. Y-Error Plots; Notch MMAE-2FB; PC is 1; Jinking Trajectory	E-94
E.94. Probability Calculation Plots; Notch MMAE-2FB; PC is 1; Jinking Trajectory	E-95
E.95. RMS Error Plots; Notch MMAE-2FH; PC is 1; Jinking Trajectory . .	E-96
E.96. X-Error Plots; Notch MMAE-2FH; PC is 1; Jinking Trajectory	E-97
E.97. Y-Error Plots; Notch MMAE-2FH; PC is 1; Jinking Trajectory	E-98
E.98. Probability Calculation Plots; Notch MMAE-2FH; PC is 1; Jinking Trajectory	E-99
F.1. RMS Error Plots; First-Order MMAE-R; PC is 1; Trajectory with $\omega = .01$	F-2

Figure	Page
F.2. X-Error Plots; First-Order MMAE-R; PC is 1; Trajectory with $\omega = .01$	F-3
F.3. Y-Error Plots; First-Order MMAE-R; PC is 1; Trajectory with $\omega = .01$	F-4
F.4. RMS Error Plots; First-Order MMAE-R; PC is 1; Trajectory with $\omega = 1.32$	F-5
F.5. X-Error Plots; First-Order MMAE-R; PC is 1; Trajectory with $\omega = 1.32$	F-6
F.6. Y-Error Plots; First-Order MMAE-R; PC is 1; Trajectory with $\omega = 1.32$	F-7
F.7. RMS Error Plots; First-Order MMAE-R; PC is 1; Trajectory with $\omega = 2.8$	F-8
F.8. X-Error Plots; First-Order MMAE-R; PC is 1; Trajectory with $\omega = 2.8$	F-9
F.9. Y-Error Plots; First-Order MMAE-R; PC is 1; Trajectory with $\omega = 2.8$	F-10
F.10. RMS Error Plots; First-Order MMAE-R; PC is 4; Trajectory with $\omega = .01$	F-11
F.11. X-Error Plots; First-Order MMAE-R; PC is 4; Trajectory with $\omega = .01$	F-12
F.12. Y-Error Plots; First-Order MMAE-R; PC is 4; Trajectory with $\omega = .01$	F-13
F.13. RMS Error Plots; First-Order MMAE-R; PC is 4; Trajectory with $\omega = 1.32$	F-14
F.14. X-Error Plots; First-Order MMAE-R; PC is 4; Trajectory with $\omega = 1.32$	F-15
F.15. Y-Error Plots; First-Order MMAE-R; PC is 4; Trajectory with $\omega = 1.32$	F-16
F.16. RMS Error Plots; First-Order MMAE-R; PC is 4; Trajectory with $\omega = 2.8$	F-17
F.17. X-Error Plots; First-Order MMAE-R; PC is 4; Trajectory with $\omega = 2.8$	F-18
F.18. Y-Error Plots; First-Order MMAE-R; PC is 4; Trajectory with $\omega = 2.8$	F-19
F.19. RMS Error Plots; First-Order MMAE-R; PC is 1; Jinking Trajectory	F-20
F.20. X-Error Plots; First-Order MMAE-R; PC is 1; Jinking Trajectory . .	F-21
F.21. Y-Error Plots; First-Order MMAE-R; PC is 1; Jinking Trajectory . .	F-22
F.22. Probability Calculation Plots; First-Order MMAE-R; PC is 1; Jinking Trajectory	F-23
F.23. RMS Error Plots; First-Order MMAE-R; PC is 4; Jinking Trajectory	F-24
F.24. X-Error Plots; First-Order MMAE-R; PC is 4; Jinking Trajectory . .	F-25
F.25. Y-Error Plots; First-Order MMAE-R; PC is 4; Jinking Trajectory . .	F-26

Figure	Page
F.26. Probability Calculation Plots; First-Order MMAE-R; PC is 4; Jinking Trajectory	F-27
F.27. RMS Error Plots; First-Order MMAE-FB; PC is 1; Trajectory with $\omega = .01$	F-28
F.28. X-Error Plots; First-Order MMAE-FB; PC is 1; Trajectory with $\omega = .01$	F-29
F.29. Y-Error Plots; First-Order MMAE-FB; PC is 1; Trajectory with $\omega = .01$	F-30
F.30. RMS Error Plots; First-Order MMAE-FB; PC is 1; Trajectory with $\omega = 1.32$	F-31
F.31. X-Error Plots; First-Order MMAE-FB; PC is 1; Trajectory with $\omega = 1.32$	F-32
F.32. Y-Error Plots; First-Order MMAE-FB; PC is 1; Trajectory with $\omega = 1.32$	F-33
F.33. RMS Error Plots; First-Order MMAE-FB; PC is 1; Trajectory with $\omega = 2.8$	F-34
F.34. X-Error Plots; First-Order MMAE-FB; PC is 1; Trajectory with $\omega = 2.8$	F-35
F.35. Y-Error Plots; First-Order MMAE-FB; PC is 1; Trajectory with $\omega = 2.8$	F-36
F.36. RMS Error Plots; First-Order MMAE-FH; PC is 1; Trajectory with $\omega = .01$	F-37
F.37. X-Error Plots; First-Order MMAE-FH; PC is 1; Trajectory with $\omega = .01$	F-38
F.38. Y-Error Plots; First-Order MMAE-FH; PC is 1; Trajectory with $\omega = .01$	F-39
F.39. RMS Error Plots; First-Order MMAE-FH; PC is 1; Trajectory with $\omega = 1.32$	F-40
F.40. X-Error Plots; First-Order MMAE-FH; PC is 1; Trajectory with $\omega = 1.32$	F-41
F.41. Y-Error Plots; First-Order MMAE-FH; PC is 1; Trajectory with $\omega = 1.32$	F-42
F.42. RMS Error Plots; First-Order MMAE-FH; PC is 1; Trajectory with $\omega = 2.8$	F-43
F.43. X-Error Plots; First-Order MMAE-FH; PC is 1; Trajectory with $\omega = 2.8$	F-44
F.44. Y-Error Plots; First-Order MMAE-FH; PC is 1; Trajectory with $\omega = 2.8$	F-45
F.45. RMS Error Plots; First-Order MMAE-FB; PC is 1; Jinking Trajectory	F-46
F.46. X-Error Plots; First-Order MMAE-FB; PC is 1; Jinking Trajectory .	F-47
F.47. Y-Error Plots; First-Order MMAE-FB; PC is 1; Jinking Trajectory .	F-48

Figure	Page
F.48. Probability Calculation Plots; First-Order MMAE-FB; PC is 1; Jinking Trajectory	F-49
F.49. RMS Error Plots; First-Order MMAE-FH; PC is 1; Jinking Trajectory	F-50
F.50. X-Error Plots; First-Order MMAE-FH; PC is 1; Jinking Trajectory .	F-51
F.51. Y-Error Plots; First-Order MMAE-FH; PC is 1; Jinking Trajectory .	F-52
F.52. Probability Calculation Plots; First-Order MMAE-FH; PC is 1; Jinking Trajectory	F-53

List of Tables

Table	Page
5.1. Errors Kept by the Simulation Software	5-2
5.2. Trajectories Used to Evaluate the Real-Pole MMAE	5-6
5.3. Average Position Errors for Real-Pole and Notch-1 MMAEs with -O and -R Options	5-17
5.4. Position Error Statistics for Notch MMAE-1R and -2R with Jinking Trajectory	5-24
5.5. Average Position Errors for Notch MMAE-1R with Basic Trajectories and all PC Options	5-28
5.6. Average Position Errors for Notch MMAE-2R with all Trajectories and PC Options	5-33
5.7. Appropriate Compilation for Comparing Position Error Statistics in Bayesian and MAP Options with Notch MMAE-2R	5-39
5.8. Average Errors for Notch MMAE-2R with Various Lower Bounds . .	5-44
6.1. Average Position Errors for First-Order-R and Notch-2R MMAEs with PC = 1 and 4 Options	6-5
6.2. The Tuning Values used for the First-Order Models	6-9
6.3. Average Position Errors for First-Order and Notch-2 MMAEs with -FB, -FH, and -R Tuning Options, PC = 1	6-13
6.4. The Tuning Values used for the Notch-2 Models	6-16
6.5. Summary Comparing Best First-Order and Notch MMAEs; PC is 1 .	6-25
A.1. Real-Pole Noise Strengths	A-1
A.2. Notch Filter Model Parameters	A-2
A.3. First-Order Filter Model Parameters	A-2
A.4. Trajectory Parameters and Associated Accelerations	A-3
A.5. Parameters Needed for the Simulation Software	A-4

Table	Page
C.1. Temporal Average and Residuals; Real-Pole MMAE-O; PC is 1; Trajectory with $\omega = .01$	C-2
C.2. Temporal Average and Residuals; Real-Pole MMAE-O; PC is 1; Trajectory with $\omega = .62$	C-5
C.3. Temporal Average and Residuals; Real-Pole MMAE-O; PC is 1; Trajectory with $\omega = 2.8$	C-8
C.4. Temporal Average and Residuals; Real-Pole MMAE-R; PC is 1; Trajectory with $\omega = .01$	C-11
C.5. Temporal Average and Residuals; Real-Pole MMAE-R; PC is 1; Trajectory with $\omega = .62$	C-14
C.6. Temporal Average and Residuals; Real-Pole MMAE-R; PC is 1; Trajectory with $\omega = 2.8$	C-17
D.1. Temporal Averages and Residuals; Notch MMAE-1O; PC is 1; Trajectory with $\omega = .01$	D-2
D.2. Temporal Averages and Residuals; Notch MMAE-1O; PC is 1; Trajectory with $\omega = .62$	D-5
D.3. Temporal Averages and Residuals; Notch MMAE-1O; PC is 1; Trajectory with $\omega = 2.8$	D-8
D.4. Temporal Averages and Residuals; Notch MMAE-1R; PC is 1; Trajectory with $\omega = .01$	D-11
D.5. Temporal Averages and Residuals; Notch MMAE-1R; PC is 1; Trajectory with $\omega = .62$	D-14
D.6. Temporal Averages and Residuals; Notch MMAE-1R; PC is 1; Trajectory with $\omega = 2.8$	D-17
D.7. Temporal Averages and Residuals; Notch MMAE-1R; PC is 2; Trajectory with $\omega = .01$	D-20
D.8. Temporal Averages and Residuals; Notch MMAE-1R; PC is 2; Trajectory with $\omega = .62$	D-23
D.9. Temporal Averages and Residuals; Notch MMAE-1R; PC is 2; Trajectory with $\omega = 2.8$	D-26

Table	Page
D.10. Temporal Averages and Residuals; Notch MMAE-1R; PC is 3; Trajectory with $\omega = .01$	D-29
D.11. Temporal Averages and Residuals; Notch MMAE-1R; PC is 3; Trajectory with $\omega = .62$	D-32
D.12. Temporal Averages and Residuals; Notch MMAE-1R; PC is 3; Trajectory with $\omega = 2.8$	D-35
D.13. Temporal Averages and Residuals; Notch MMAE-1R; PC is 4; Trajectory with $\omega = .01$	D-38
D.14. Temporal Averages and Residuals; Notch MMAE-1R; PC is 4; Trajectory with $\omega = .62$	D-41
D.15. Temporal Averages and Residuals; Notch MMAE-1R; PC is 4; Trajectory with $\omega = 2.8$	D-44
D.16. Temporal Averages; Notch MMAE-1R; PC is 1; Jinking Trajectory	D-47
E.1. Temporal Averages and Residuals; Notch MMAE-2R; PC is 1; Trajectory with $\omega = .01$	E-2
E.2. Temporal Averages and Residuals; Notch MMAE-2R; PC is 1; Trajectory with $\omega = 1.32$	E-5
E.3. Temporal Averages and Residuals; Notch MMAE-2R; PC is 1; Trajectory with $\omega = 2.8$	E-8
E.4. Temporal Averages and Residuals; Notch MMAE-2R; PC is 2; Trajectory with $\omega = .01$	E-11
E.5. Temporal Averages and Residuals; Notch MMAE-2R; PC is 2; Trajectory with $\omega = 1.32$	E-14
E.6. Temporal Averages and Residuals; Notch MMAE-2R; PC is 2; Trajectory with $\omega = 2.8$	E-17
E.7. Temporal Averages and Residuals; Notch MMAE-2R; PC is 3; Trajectory with $\omega = .01$	E-20
E.8. Temporal Averages and Residuals; Notch MMAE-2R; PC is 3; Trajectory with $\omega = 1.32$	E-23

Table	Page
E.9. Temporal Averages and Residuals; Notch MMAE-2R; PC is 3; Trajectory with $\omega = 2.8$	E-26
E.10. Temporal Averages and Residuals; Notch MMAE-2R; PC is 4; Trajectory with $\omega = .01$	E-29
E.11. Temporal Averages and Residuals; Notch MMAE-2R; PC is 4; Trajectory with $\omega = 1.32$	E-32
E.12. Temporal Averages and Residuals; Notch MMAE-2R; PC is 4; Trajectory with $\omega = 2.8$	E-35
E.13. Temporal Averages; Notch MMAE-2R; PC is 1; Jinking Trajectory . .	E-38
E.14. Temporal Averages; Notch MMAE-2R; PC is 2; Jinking Trajectory . .	E-42
E.15. Temporal Averages; Notch MMAE-2R; PC is 3; Jinking Trajectory . .	E-46
E.16. Temporal Averages; Notch MMAE-2R; PC is 4; Jinking Trajectory . .	E-50
E.17. Temporal Averages and Residuals; Notch MMAE-2RM; PC is 1; Trajectory with $\omega = .01$	E-54
E.18. Temporal Averages and Residuals; Notch MMAE-2RM; PC is 1; Trajectory with $\omega = 1.32$	E-57
E.19. Temporal Averages and Residuals; Notch MMAE-2RM; PC is 1; Trajectory with $\omega = 2.8$	E-60
E.20. Temporal Averages and Residuals; Notch MMAE-2RM; PC is 4; Trajectory with $\omega = .01$	E-63
E.21. Temporal Averages and Residuals; Notch MMAE-2RM; PC is 4; Trajectory with $\omega = 1.32$	E-66
E.22. Temporal Averages and Residuals; Notch MMAE-2RM; PC is 4; Trajectory with $\omega = 2.8$	E-69
E.23. Temporal Averages; Notch MMAE-2RM; PC is 1; Jinking Trajectory	E-72
E.24. Temporal Averages; Notch MMAE-2RM; PC is 4; Jinking Trajectory	E-76
E.25. Temporal Averages; Notch MMAE-2R; PC is 1; LB is .0005; Jinking Trajectory	E-80
E.26. Temporal Averages; Notch MMAE-2R; PC is 1; LB is .005; Jinking Trajectory	E-84

Table	Page
E.27. Temporal Averages; Notch MMAE-2R; PC is 1; LB is .01; Jinking Trajectory	E-88
E.28. Temporal Averages; Notch MMAE-2FB; PC is 1; Jinking Trajectory .	E-92
E.29. Temporal Averages; Notch MMAE-2FH; PC is 1; Jinking Trajectory .	E-96
F.1. Temporal Averages and Residuals; First-Order MMAE-R; PC is 1; Trajectory with $\omega = .01$	F-2
F.2. Temporal Averages and Residuals; First-Order MMAE-R; PC is 1; Trajectory with $\omega = 1.32$	F-5
F.3. Temporal Averages and Residuals; First-Order MMAE-R; PC is 1; Trajectory with $\omega = 2.8$	F-8
F.4. Temporal Averages and Residuals; First-Order MMAE-R; PC is 4; Trajectory with $\omega = .01$	F-11
F.5. Temporal Averages and Residuals; First-Order MMAE-R; PC is 4; Trajectory with $\omega = 1.32$	F-14
F.6. Temporal Averages and Residuals; First-Order MMAE-R; PC is 4; Trajectory with $\omega = 2.8$	F-17
F.7. Temporal Averages and Residuals; First-Order MMAE-R; PC is 1; Jinking Trajectory	F-20
F.8. Temporal Averages and Residuals; First-Order MMAE-R; PC is 4; Jinking Trajectory	F-24
F.9. Temporal Averages and Residuals; First-Order MMAE-FB; PC is 1; Trajectory with $\omega = .01$	F-28
F.10. Temporal Averages and Residuals; First-Order MMAE-FB; PC is 1; Trajectory with $\omega = 1.32$	F-31
F.11. Temporal Averages and Residuals; First-Order MMAE-FB; PC is 1; Trajectory with $\omega = 2.8$	F-34
F.12. Temporal Averages and Residuals; First-Order MMAE-FH; PC is 1; Trajectory with $\omega = .01$	F-37
F.13. Temporal Averages and Residuals; First-Order MMAE-FH; PC is 1; Trajectory with $\omega = 1.32$	F-40

Table	Page
F.14. Temporal Averages and Residuals; First-Order MMAE-FH; PC is 1; Trajectory with $\omega = 2.8$	F-43
F.15. Temporal Averages and Residuals; First-Order MMAE-FB; PC is 1; Jinking Trajectory	F-46
F.16. Temporal Averages and Residuals; First-Order MMAE-FH; PC is 1; Jinking Trajectory	F-50

List of Symbols

Symbol	Page
\mathbf{A} - filter-computed residual covariance	2-3
A - amplitude of the y-axis inertial velocity	3-3
AR - aspect ratio of the target	3-12
\mathbf{a} - parameter vector	2-1
a - acceleration	3-3
a - subscript denoting atmospheric	3-7
α_s - exponential smoothing constant	4-17
α - β - γ - spherical coordinate system	3-3
\mathbf{B} - input distribution matrix	2-1
B - bias of the y-axis inertial velocity	3-3
b - first state of the two-state acceleration model	4-13
b - subscript denoting the benign filter	5-8
c - second state of the two-state acceleration model	4-13
D - current data array, pixel output	4-1
D - subscript denoting detector plane	3-5
d - subscript denoting discrete-time	3-7
\bar{E} - the average error over the Monte Carlo study	5-2
EKF - extended Kalman filter	1-2
$e(t_i)$ - the error at one time sample averaged over N runs	5-2
e_{Bx}, e_{By}, e_{Bz} - the target body frame	3-10
e_{Dx}, e_{Dy} - the detector frame	3-5
e_{Ix}, e_{Iy}, e_{Iz} - the inertial frame	3-2
\mathbf{F} - dynamics matrix	2-1
-FB - tuned for flat PSD plot at the benign model height	6-7
-FH - tuned for flat PSD plot at the harsh model height	6-7

Symbol	Page
FLIR - forward looking infrared	1-1
FOV - field of view	1-1
f - subscript denoting filter model	4-2
G - noise distribution matrix	2-1
$G(s)$ - transfer function	5-5
g 's - meters per second ² divided by 9.8 meters per second ²	5-22
H - output distribution vector	2-3
h - subscript denoting the harsh filter	5-8
I - subscript denoting inertial frame	3-2
I_{\max} - maximum intensity of the IR signature	3-12
IR - infrared	3-1
i - subscript denoting the intermediate filter	5-8
K - Kalman filter gain	2-3
K_{ta} - gain for the atmospheric jitter model	3-7
KF - Kalman filter	2-1
k - constant for the notch filter	5-11
L - pixel proportionality constant	3-5
LB - the lower bound value	5-42
LOS - line of sight vector	3-3
MAP - maximum a posteriori	1-3
MMAE - multiple model adaptive estimator	1-1
m - subscript denoting motion dynamics in the truth model	3-6
N - number of runs in the Monte Carlo study	5-2
O - an MMAE tuned in the original manner	5-8
P - covariance matrix for the state vector estimate	2-2
PC - method of calculating the probability	5-27
PSD - power spectral density	1-5

Symbol	Page
p - position	3-3
p_k - probability calculated for the k th elemental filter	1-9
$\Phi(t_{i+1}, t_i)$ - state transition matrix	2-2
ϕ - phase of the y-axis inertial velocity	3-3
Q - covariance of the dynamics driving noise	2-1
R - covariance of the measurement noise	2-3
R - array of correlation numbers from enhanced correlator	4-1
R - an MMAE tuned in the revised manner	5-15
RMS - root mean squared	1-3
r - residual	2-3
r - range to the target	3-5
r_h - horizontal range to the target	3-4
S - smoothed template array	4-1
SNR - signal-to-noise ratio	3-12
σ - standard deviation	3-7
σ^2 - variance	4-5
T - correlation time of a first-order model	4-5
t - subscript denoting truth model	3-6
u - deterministic input vector	2-1
v - measurement noise vector	2-3
v - velocity	3-3
w - dynamics driving noise vector	2-1
ω - frequency for trajectory and notch filter	3-3
x - truth model state vector	2-1
\hat{x} - conditional mean to estimate the state vector	2-2
x_{cen}, y_{cen} - center of the IR intensity profile	3-12
x_{peak}, y_{peak} - center of the R array, input to linear KF	4-2

Symbol	Page
y - output vector	3-9
z - measurement vector	2-3
ζ - damping ratio for the notch filter	5-11
-1 - the notch MMAE with intermediate filter at $\omega = 0.62$ radians per second	5-11
-2 - the notch MMAE with intermediate filter at $\omega = 1.32$ radians per second	5-20
-3 - the notch MMAE with intermediate filter at $\omega = 1.92$ radians per second	6-17
-4 - the notch MMAE with intermediate filter at $\omega = 2.32$ radians per second	6-17

Abstract

The performance of a multiple model adaptive estimator (MMAE) for an enhanced correlator/forward-looking-infrared tracker for airborne targets is analyzed in order to improve its performance. Performance evaluation is based on elemental filter selection and MMAE estimation error sizes and trends. The elemental filters are based on either first or second-order acceleration models. Improved filter selection is achieved by using acceleration models that separate the frequency content of acceleration power spectral densities into non-overlapping regions with second-order models versus the more traditional overlapping regions with first-order models. A revised tuning method is presented. The maximum a posteriori (MAP) versus the Bayesian MMAE is investigated. The calculation of the hypothesis probability calculation is altered to see how performance is affected. The impact of the ad hoc selection of a lower bound on the elemental filter probability calculation to prevent filter lockout is evaluated. Parameter space discretization is investigated.

Comparable performance is achieved from the MMAEs based on either first or second-order acceleration models. The MAP and Bayesian options give comparable performance. A lower bound of 0.001 gives best results. The traditional probability calculation allows better filter selection by the MMAE for this application.

A MULTIPLE MODEL ADAPTIVE ESTIMATOR USING FIRST AND SECOND-ORDER ACCELERATION MODELS FOR USE IN A FORWARD-LOOKING-INFRARED TRACKER

I. Introduction

1.1 Background

The Department of Defense has placed great emphasis on the potential of a high energy laser as a weapon against airborne targets. Current laser technology requires extremely tight specifications for the pointing and tracking systems supporting these laser weapons. The Phillips Laboratory at Kirtland AFB, New Mexico, maintains ongoing research efforts in this area and is supporting AFIT's continued research emphasis in tracking as well as other aspects of the potential weapon system. The AFIT effort in tracking was started in 1978 [11]. An understanding of the direction that effort has taken will aid this current thesis [11, 3, 17, 1, 16, 4, 12, 19, 6, 14, 20, 5: chronologically].

The purpose of this thesis is to enhance the multiple model adaptive estimator's (MMAE) ability to select the most appropriate elemental filter as system dynamics vary rapidly. The MMAE used in this investigation is one developed for the Forward Looking Infrared (FLIR)/correlator tracker that will be used in a high energy laser weapon system [10, 11, 19, 20].

1.2 Summary of Previous AFIT Research

The tracking of airborne targets is currently done with a conventional correlator. This correlator tracker has several limitations contributing to tracking errors. Two important ones are:

1. There is a time lag due to the time it takes the correlator algorithm to correlate the current frame of FLIR outputs to the previous frame and for the the actual pointing gimbals to point the FLIR sensor in the next appropriate direction to keep

the target in the center of the field of view (FOV). The FOV is the number of pixels the correlator and, later, the Kalman filter will use in estimating target position. The FLIR sensor is 300-by-500 pixels. Normally, 24-by-24 pixels is the maximum sized tracking "window" used in the algorithm.

2. Apparent target motion results from physical phenomena like atmospheric jitter and bending and vibration of the tracker optics. The correlator does not distinguish true target motion from this erroneous apparent motion.

Mercier [11] conducted the initial feasibility study of adding a Kalman filter to the tracker to overcome these two limitations. Using the statistical characteristics of atmospheric jitter and measurement errors, and the model of anticipated target motion, the filter predicts an estimated target position one sample period (1/30 second) into the future. The prediction allows the correlator to anticipate target position so tracking error due to time delay is reduced. The tracking algorithm was a single extended Kalman filter (EKF), with a first-order Gauss-Markov model for target position, resulting in enhanced performance an order of magnitude better than tracking with the correlator tracker in benign scenarios. The EKF was required because the measurement model for the FLIR detector is nonlinear. The target was assumed distant and so is considered to be a point source. The intensity pattern on the detector array was analytically expressed as a two-dimensional Gaussian function, and the "measurements" represented the average intensity over each of 64 pixels in an 8-by-8 pixel array on the FLIR image plane.

Most airborne targets of interest are not always in benign trajectories. So Jensen and Harnly [3] incorporated velocity and acceleration estimates to allow tracking of more maneuverable targets. They used a first-order Gauss-Markov process model for the target acceleration. For performance evaluation of such a tracker, realistic target trajectory paths were generated in three-dimensional inertial space and projected onto the FLIR image plane. They also conducted the statistical analysis of the temporal and spatial correlation of the background noise that will corrupt the IR image from the target.

Singletery [17] first applied digital signal processing techniques to the FLIR data to determine the underlying shape of the target image, assuming the target could have

multiple hotspots. Rogers [16] completed this, considering both an extended Kalman filter to process the 64 intensity measurements directly and an alternative design that inserted an enhanced correlator into the "front end" of the tracker and processed the enhanced correlator outputs with a linear Kalman filter. His enhanced correlator algorithm compared the current FLIR image with a template instead of the image from the previous time frame. The template estimated the target shape by averaging the centered image over the previous 10 time frames. The "measurement" given to the Kalman filter is the offset of the image from the center of the FOV, as produced by the enhanced correlator. The resulting linear Kalman filter reduced computational loading and gave comparable performance to the EKF. He used the same four-state state dynamics model as Mercier had used in both the EKF and the linear Kalman filter when he compared their performance.

Flynn [1] continued the work of Jensen and Harnly and compared two other models for target acceleration, a Brownian motion acceleration model and a constant turn-rate one, as compared to their first-order Gauss-Markov acceleration model. He also implemented a multiple model filter with less than satisfactory results.

Kozemchak [4] and Millner [12] continued comparing the EKF and the linear filter/correlator with highly maneuverable targets. They incorporated Flynn's nonlinear constant turn-rate model for the target dynamics and compared performance with the first-order Gauss-Markov acceleration model. Performance was good for more benign targets.

To overcome the problem of losing harshly maneuvering targets, Suizu [19] successfully applied the MMAE. He used two elemental filters, one for benign and one for harshly maneuvering targets. The benign filter used a narrow FOV (8-by-8 pixels) and the other filter used a wider FOV (24-by-24 pixels). Two MMAEs were evaluated, one with EKF elemental filters and one with linear Kalman filters with enhanced correlator measurements. Each MMAE gave comparable RMS errors, although the EKF had larger mean errors but smaller standard deviations [19:VI-2].

Loving [6] added a third elemental filter to the Bayesian MMAE based on intermediate target dynamics. This showed significant improvement in tracking performance.

A maximum a posteriori (MAP) algorithm was also developed. It used the same bank of filters. However, it produced an estimate based only on the elemental filter with the highest probability of being correct. The Bayesian MMAE outputs an estimate that is the probabilistically weighted average of all elemental filter estimates. The MAP showed no significant performance improvement.

Netzer [14] continued work with the three-elemental-filter Bayesian MMAE with the linear filter/correlator algorithm to investigate some unresolved biases and ramps in previous results. He also looked at putting a time lag in the control applied by the system to keep the FOV pointed at the target. He concluded that the errors resulting from nonideal controller dynamics are small and interpreted as jitter error.

Tobin [20] then expanded the results of Loving's Bayesian MMAE with the linear filter/correlator algorithm. He used separate elemental filters that were tuned for harsh maneuvers in either the x or y directions. This allows the tracker to expand the FOV only in the direction of the maneuver while maintaining maximum resolution in the other direction. Also, he considered the constant turn-rate dynamics model for target motion used by Kozemchak and Flynn as well as the first-order Gauss-Markov acceleration model.

More recently, Leeny [5] applied the MMAE algorithm based on Gauss-Markov acceleration models to a truth model that included bending and vibrational effects of a large space structure. Even though the MMAE was not modified to include any bending or vibration information or states, the filter was able to track a harshly maneuvering target. Leeny also investigated the use of a rotating rectangular (24-by-8 pixel) FOV in which the elongated side of the FOV would be aligned with the estimated acceleration direction. This could hopefully replace the two rectangular FOV elemental filters of Tobin with one filter.

Norton [15] implemented the rotating rectangular FOV. He also considered the effect of filter dynamics driving noise strength versus FOV size on filter performance. The results showed that choosing a larger dynamics driving noise strength in the direction of maneuver was more important than increasing the FOV. This variable driving noise is easily implemented in a MMAE.

1.3. Objectives

This thesis investigates modifying the filter dynamics models to produce elemental filters with nonoverlapping acceleration power spectral densities (PSDs). A first-order Gauss-Markov model is the basis of a low-pass filter driven by white Gaussian noise, as shown in Figure 4.2 (page 4-11). The corresponding acceleration PSDs are overlapped by the one whose acceleration model has the highest break frequency, as depicted in plot (a) of Figure 1.1. In contrast, second-order Gauss-Markov models are used in bandpass filters as seen in Figure 4.3 (page 4-16) and Figure 4.4 (page 4-17). Model parameters can be selected so that the PSDs have minimal overlap, as in plots (b) and (c) of Figure 1.1. The residual monitoring done by the conditional probability computation should then quickly select the elemental filter with the most benign dynamics model when a target vehicle transitions from harsh maneuvering to a benign trajectory, so the estimation will be the most precise. In previous investigations, the MMAE had little trouble moving from an elemental filter tuned for benign target trajectories to one tuned for harsher trajectories when the target initiates a jinking maneuver. The problem comes when the target *returns* to a more benign trajectory. The MMAE takes longer to return to the elemental filter tuned for the more benign trajectory. It has been conjectured that part of this problem is due to the fact that, with acceleration PSDs that overlap in the low-frequency region, all models are able to represent such behavior. On the other hand, when the target vehicle truly exhibits harsh maneuvering, only those models with nonzero acceleration PSD values over the higher frequencies can be deemed adequate [10].

The system dynamics are modeled as a second-order Gauss-Markov acceleration process. The linear filter with enhanced correlator measurement model is used, as investigated by Rogers and others [5, 6, 14, 15, 16, 19, 20]. The FOV remains constant for each elemental filter and the bending effects modeled in the truth model are removed. A parallel investigation uses filters based on first-order Gauss-Markov acceleration processes. The PSD of the acceleration models in the MMAE are overlapping in the low frequency end as in plot (a) of Figure 1.1. The second-order models can have almost no overlap or some overlap as in plots (b) and (c). Plots (b) through (e) are possible MMAE configurations. The break frequency of the PSD is driven by how fast the target can change its velocity

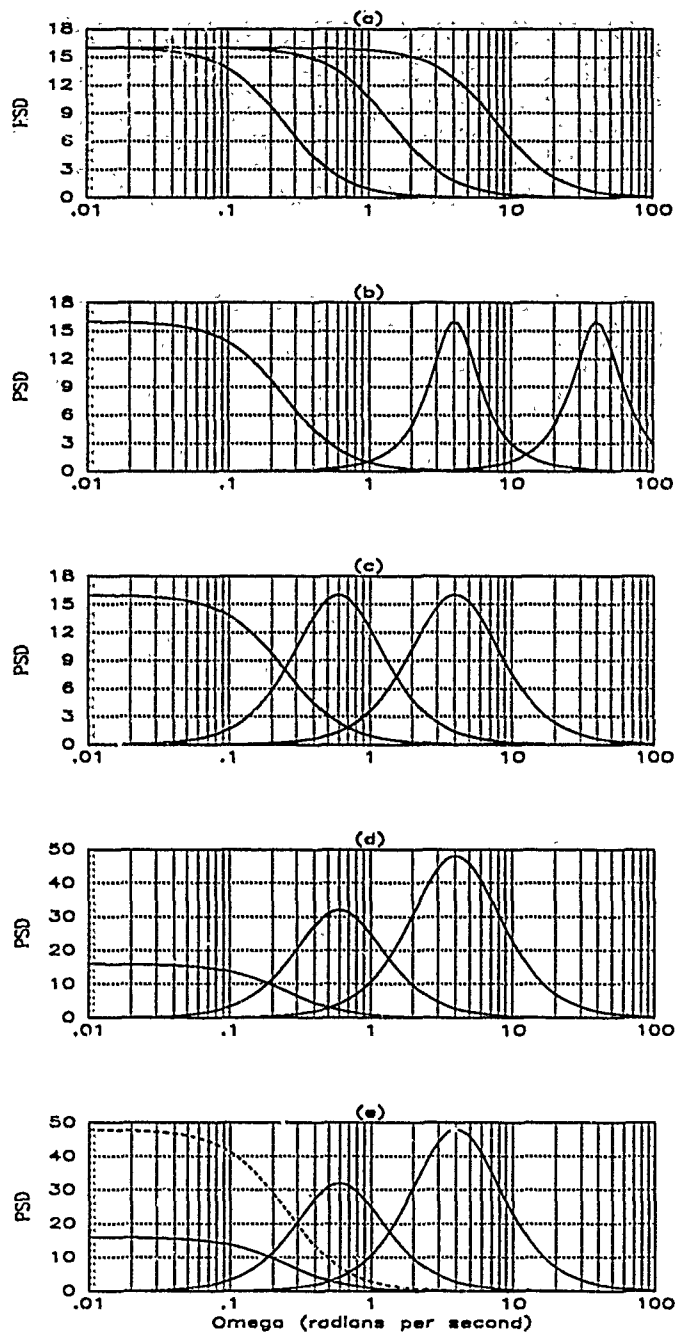


Figure 1.1. PSDs of Various Acceleration Models for an MMAE

vector. The height of the PSD plot represents the acceleration magnitude that the target is exhibiting. The increased height of the PSDs in plots (d) and (e) acknowledge that the target capable of showing high frequency acceleration power is capable of pulling greater acceleration magnitude as well. This should be allowed in the low frequency model, too, as portrayed by plot (e), in which two low frequency acceleration models with the same break frequency but different magnitudes are each considered as the basis for an elemental filter design. Specific objectives are as follows:

1.3.1 Second-Order Gauss-Markov Acceleration Models. The poles and zeros of the second-order Gauss-Markov shaping filters describing expected target accelerations will be selected for each elemental filter so that the PSDs of the filters have minimally overlapping frequency content. This can be accomplished with filters having two real poles or a complex pair of poles. The expected dynamic range of airborne targets to be tracked is up to 2.5 Hz.

Several sensitivity studies are accomplished:

1. The location and number of cutoff frequencies of the PSDs for the elemental shaping filters are varied.
2. The height of the PSD curves as determined by the dynamic driving noise are varied.
3. The accuracy of the measurements from the FLIR are varied as much as an order of magnitude up and down.

1.3.2 Bayesian versus MAP MMAE. After a reasonable set of elemental filters is selected, a comparison between Bayesian and MAP MMAE application is done. Previous studies [6] cause one to anticipate that performance will be very comparable between Bayesian and MAP forms, but this is explored to ensure the trend is not altered by the introduction of different dynamics models.

1.3.3 Alter the p_k Calculation. The probabilistically weighted average used in the Bayesian MMAE is investigated. As shown in Figure 1.2, the elemental filters are tied together with a hypothesis conditional probability computation that monitors the residuals

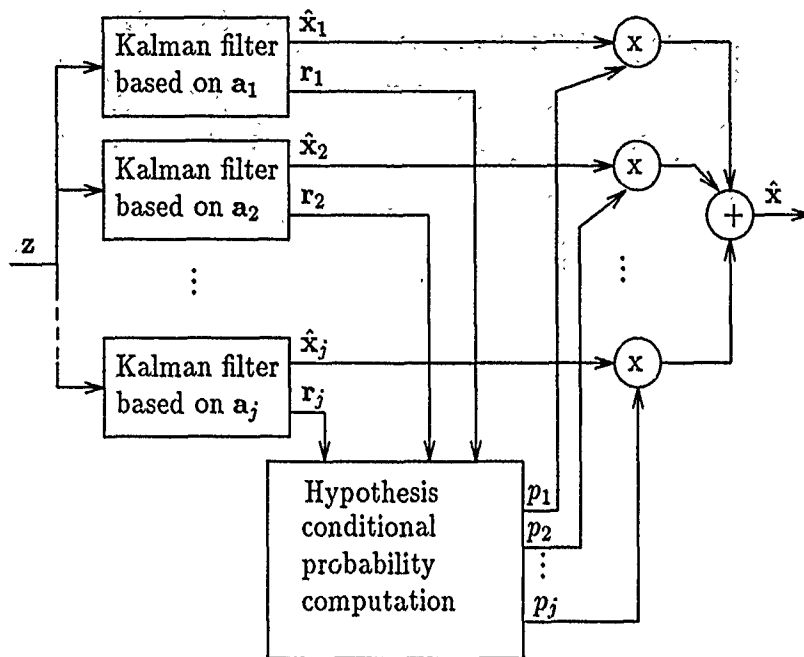


Figure 1.2. The MMAE Structure. [8:132]

of each elemental filter. Each elemental filter is tracking the target and producing residuals, r_k , from the common measurement input, z . The residuals are used to compute hypothesis conditional probabilities, p_1, p_2, \dots, p_j , in order to make a probabilistically weighted average of all the elemental estimates such that they all contribute to the single estimate of the MMAE. However, if each is properly tuned and the parameter space is appropriately discretized, only one elemental filter should be the major contributor at each sample period; hopefully, it will be the one with the smallest magnitude residuals.

The probability calculation is discussed in Chapter II. It is presented here to emphasize the purpose of this thesis. The probability calculation for the k th filter is:

$$p_k(t_i) = \frac{\frac{1}{(2\pi)^{\frac{m}{2}} |A_k(t_i)|^{\frac{1}{2}}} \exp \left\{ -\frac{1}{2} r_k^T(t_i) A_k^{-1}(t_i) r_k(t_i) \right\} p_k(t_{i-1})}{\sum_{g=1}^j \left[\frac{1}{(2\pi)^{\frac{m}{2}} |A_g(t_i)|^{\frac{1}{2}}} \exp \left\{ -\frac{1}{2} r_g^T(t_i) A_g^{-1}(t_i) r_g(t_i) \right\} p_g(t_{i-1}) \right]} \quad (1.1)$$

where $A_k(t_i)$ is the k th filter's computed residual covariance:

$$A_k(t_i) = H_k(t_i)P_k(t_i^-)H_k^T(t_i) + R_k(t_i) \quad (1.2)$$

The magnitude of the residuals squared comes into the p_k calculation in the exponential term. However, the residual covariance, $A_k(t_i)$, enters into the exponential *and* the leading coefficient, potentially resulting in a larger p_k for the elemental filter that does not have the smallest magnitude residuals. For example, a filter tuned to expect harsh trajectories normally has larger dynamics noise strength. This makes the corresponding denominator $|A_k|$ tend to be of larger magnitude, while also making the term within the exponential a smaller magnitude negative number. The exponential terms thus make the probability calculation tend to favor the filter tuned for harsher trajectories when the residuals from several filters are of similar magnitude. However, the leading coefficient will be smaller for the larger $|A_k|$ and should counter the exponential. This particular trait of the probability calculation is suspect when the "wrong" elemental filter is selected in a particular application [8, 9, 18] and various "fixes" can be used. For example, Stevens [9, 18] suggested removing the leading coefficient on the calculation of the conditional probability density that goes into the computation of the hypothesis conditional probability, p_k , via Equation (1.1) for a problem that caused the MMAE to show an artificial bias towards elemental filters with small $|A_k|$. This suggestion may not be useful since, in the class of problems of interest in this research, one would like to enhance a bias toward elemental filters with small $|A_k|$. The presence of the determinant in the leading coefficient would tend to counter the empirically observed sluggishness of the MMAE in returning to a benign-model elemental filter when a target vehicle stops maneuvering. However, an associated concept, called "maximum entropy" design, alters both the leading term and the exponential term by setting A_k to I in all filters (due to lack of confidence in the filter computed A_k values, the impact of A_k is thereby removed). This may, in fact, prove useful in reducing the sluggishness of returning high probability to a benign-model elemental filter when a target stops maneuvering. Removal or nonremoval of the coefficient, and maximum entropy design, combined with use of elemental filters with nonoverlapping acceleration PSDs, should provide sufficient design freedom to improve tracking.

1.3.4 *Vary Lower Bound on p_k .* A particular problem of MMAE application is that when the p_k of the k th elemental filter gets very small, it can get locked onto zero (or essentially zero) even if the real world situation becomes such that this p_k value should increase. Since the p_k of the previous time frame is used iteratively in Equation (1.1) to calculate the p_k of the current time, once it becomes zero, that elemental filter is essentially off-line for all time. This has been remedied by placing an artificial lower bound on the p_k . The lower bound is varied or even eliminated, and the sensitivity of performance to lower bound values is portrayed. Muravez [13] suggests a semi-Markov probability propagation as an alternative to the lower bound. In the thesis, the probability is calculated after measurement update, at t_i^+ . The same probability is used at t_{i+1}^- . In the current thesis, the probability is calculated after measurement update at t_i^+ . The same probability is used at t_{i+1}^- . In the Muravez presentation of the adaptive learning theory of Moose and Wang, the probability at t_{i+1}^- is calculated as $p_k(t_{i+1}^-) = [T_{k=k} - T_{k \neq k}]p_k(t_i^+) + T_{k \neq k}$ where $T_{k=k}$ is the transition probability of true system dynamic parameters *not* changing during sample time interval and is determined empirically. The $T_{k \neq k}$ is the transition probability of true system dynamic parameters changing during sample time interval and is $[1 - T_{k=k}/(j - 1)]$ with j being the number of elemental filters in the MMAE. This is investigated.

1.4 Text Overview

The structure of an MMAE is described in Chapter II. Chapter III describes the truth model needed to generate the true values of the states to compare to the filter-estimated values. The calculations required to simulate the output of the FLIR detector that will be the input to the tracker algorithm used are also outlined. Chapter IV discusses the tracker algorithm which is composed of the enhanced correlator and linear filter algorithms. The correlator manipulates the input data from the truth model so that linear filter models can be used to process the correlator outputs. Chapter V details what filters are used in the various MMAEs. Tuning techniques are discussed and final results are also presented. Chapter VI gives the results of the similar studies conducted with a MMAE with elemental filters that are all first order. Finally, Chapter VII presents the final conclusions and recommendations for further study into this fruitful area.

II. Theory

2.1 Introduction

This chapter reviews the basic structure of the MMAE. Features pertinent to this investigation are highlighted. Full mathematical development of these concepts is found in Maybeck [8:130].

2.2 The Multiple Model Adaptive Estimator

The Kalman filter (KF) is a predictor/corrector algorithm. In the predictor function a model that describes the true system dynamics is propagated through one time increment producing an estimate of states of interest of the true system. In this thesis the true system dynamics are those displayed by the airborne target being tracked. The states of interest are the target's position, velocity, and acceleration and the apparent motion of the target due to atmospheric jitter. Certainly in this application many parameters describing the dynamics of motion of the target are unknown or can change over time. The target or its potential dynamics will not be known exactly a priori. However, there is a physical limit on the range of the dynamics a tracker can be expected to see. This range of possible dynamics is described by a parameter vector \mathbf{a} . This vector is discretized over its continuous space into j distinct models. Each of these j parameter vector values is embedded into the predictor portion of an individual KF called an elemental filter. That is, the vector $\mathbf{a}_k; k = 1, 2, \dots, j$; determines the coefficients of the differential or equivalent discrete-time difference equation upon which the KF is based:

$$\dot{\mathbf{x}}(t) = \mathbf{F}(t)\mathbf{x}(t) + \mathbf{B}(t)\mathbf{u}(t) + \mathbf{G}(t)\mathbf{w}(t) \quad (2.1)$$

$\mathbf{F}(t)$, $\mathbf{B}(t)$, and $\mathbf{G}(t)$ are the dynamics, input distribution, and noise distribution matrices, respectively, where the coefficients will be placed. $\mathbf{x}(t)$ is the system state vector and $\mathbf{u}(t)$ is the deterministic control input vector. The zero-mean white Gaussian noise, $\mathbf{w}(t)$, has strength $E\{\mathbf{w}(t)\mathbf{w}^T(t')\} = \mathbf{Q}\delta(t - t')$. Since this investigation is done with simulations on

a digital computer, the equivalent discrete-time difference equation is used:

$$\mathbf{x}(t_{i+1}) = \Phi(t_{i+1}, t_i)\mathbf{x}(t_i) + \mathbf{B}_d(t_i)\mathbf{u}(t_i) + \mathbf{w}_d(t_i) \quad (2.2)$$

where $\Phi(t_{i+1}, t_i)$ is the state transition matrix and $\mathbf{B}_d(t_i) = \int_{t_i}^{t_{i+1}} \Phi(t_{i+1}, \tau)\mathbf{B}(\tau) d\tau$. The input vector, $\mathbf{u}(t_i)$, is piecewise constant: $\mathbf{u}(t_i)$ is computed and held constant over the ensuing sample period. The vector, $\mathbf{w}_d(t_i)$ is a zero-mean white Gaussian noise process with covariance kernel $E\{\mathbf{w}_d(t_i)\mathbf{w}_d^T(t_j)\} = \mathbf{Q}_d(t_i)\delta_{ij}$ where:

$$\mathbf{Q}_d(t_i) = \int_{t_i}^{t_{i+1}} \Phi(t_{i+1}, \tau)\mathbf{G}(\tau)\mathbf{Q}(\tau)\mathbf{G}^T(\tau)\Phi^T(t_{i+1}, \tau) d\tau \quad (2.3)$$

The elements of the equivalent discrete-time difference equation are placed in the KF equations for the conditional mean state estimate and error covariance [7:275]:

$$\hat{\mathbf{x}}(t_i^-) = \Phi(t_i, t_{i-1})\hat{\mathbf{x}}(t_{i-1}^+) + \mathbf{B}_d(t_{i-1})\mathbf{u}(t_{i-1}) \quad (2.4)$$

$$\mathbf{P}(t_i^-) = \Phi(t_i, t_{i-1})\mathbf{P}(t_{i-1}^+)\Phi^T(t_i, t_{i-1}) + \mathbf{Q}_d(t_{i-1}) \quad (2.5)$$

where the minus sign in the superscript denotes propagation up to time t_i , but before the measurement update that will happen at time t_i . There will be an elemental KF for each equivalent discrete-time difference equation model. A different model results from each discrete parameter vector chosen. The conditional mean used to estimate the state is $\hat{\mathbf{x}}(t_i^-)$. The conditional covariance of the state (and the error in using the conditional mean to estimate that state) is $\mathbf{P}(t_i^-)$. The initial conditions are [7:207,209]:

$$\hat{\mathbf{x}}(t_0) = E\{\mathbf{x}(t_0)\} = \hat{\mathbf{x}}_0 \quad (2.6)$$

$$\mathbf{P}(t_0) = E\{[\mathbf{x}(t_0) - \hat{\mathbf{x}}_0][\mathbf{x}(t_0) - \hat{\mathbf{x}}_0]^T\} = \mathbf{P}_0 \quad (2.7)$$

Each of the elemental filters is corrected at time t_i with the same update equations that are based on a simulated discrete-time measurement process. The model of the measurement is:

$$\mathbf{z}(t_i) = \mathbf{H}(t_i)\mathbf{x}(t_i) + \mathbf{v}(t_i) \quad (2.8)$$

where $z(t_i)$ is the m -dimensional measurement vector, $H(t_i)$ is the output matrix, and $v(t_i)$ is a zero-mean white Gaussian noise process, independent from w_d , and with covariance kernel $E\{v(t_i)v^T(t_j)\} = R(t_i)\delta_{ij}$. The estimate of the state vector is updated by defining the KF gain $K(t_i)$ and using it to find the new mean and covariance [7:217]:

$$\hat{x}(t_i^+) = \hat{x}(t_i^-) + K(t_i) [z - H\hat{x}(t_i^-)] \quad (2.9)$$

$$P(t_i^+) = P(t_i^-) - K(t_i)HP(t_i^-) \quad (2.10)$$

$$K(t_i) = P(t_i^-)H^T [HP(t_i^-)H^T + R]^{-1} \quad (2.11)$$

where the plus sign in the superscript means after the measurement update.

In this investigation, the uncertain parameters are allowed to affect Φ and Q_d . In the simulation, the measurements are created by the truth model portion that will be covered in Chapter III. The elemental filter models are discussed in Chapter IV

The elemental filters are tied together in a MMAE as in Figure 1.2. In this configuration each of the j elemental filters propagates one time increment, producing an estimate of the states, $\hat{x}_k(t_i^-)$ for each $k = 1, 2, \dots, j$. Then the measurement update is performed with the single measurement, $z(t_i)$, and a residual, $r_k(t_i)$, is calculated for each:

$$r_k(t_i) \triangleq z(t_i) - H_k(t_i)\hat{x}_k(t_i^-) \quad (2.12)$$

Now the MMAE can make an adaptive estimate of the state based on the characteristics of these residuals. A hypothesis conditional probability is calculated for each elemental filter, producing $p_k(t_i)$:

$$p_k(t_i) = \frac{\frac{1}{(2\pi)^{\frac{m}{2}} |A_k(t_i)|^{\frac{1}{2}}} \exp \left\{ -\frac{1}{2} r_k^T(t_i) A_k^{-1}(t_i) r_k(t_i) \right\} p_k(t_{i-1})}{\sum_{g=1}^j \left[\frac{1}{(2\pi)^{\frac{m}{2}} |A_g(t_i)|^{\frac{1}{2}}} \exp \left\{ -\frac{1}{2} r_g^T(t_i) A_g^{-1}(t_i) r_g(t_i) \right\} p_g(t_{i-1}) \right]} \quad (2.13)$$

where $A_k(t_i)$ is the k th filter's computed residual covariance:

$$A_k(t_i) = H_k(t_i)P_k(t_i^-)H_k^T(t_i) + R_k(t_i) \quad (2.14)$$

is the k th filter-computed residual covariance, and m is the number of measurements. For this thesis, m is two, and the "measurements" are x and y position offsets in the FLIR image plane computed by the enhanced correlator. The sum of the probabilities is 1, $\sum_{g=1}^j p_g = 1$, because of the divisor in Equation (2.13). The probability calculation is recursive. Since the current probability calculation includes the previous value, if the probability for any filter, p_k , goes to zero at one sample time, that probability will remain zero for all subsequent time increments. Tactics to prevent this lockout of a filter are varied [8:130][13:18]. The one used by previous AFIT theses [5, 6, 14, 15, 19, 20] is the lower bound mentioned in Chapter I. Each p_k is set to the lower bound if its calculated value is below that bound. Then the denominator in Equation (2.13) is recalculated so the sum of probabilities will still be one.

The state estimate for the MMAE after measurement update is then:

$$\hat{\mathbf{x}}(t_i^+) = \sum_{k=1}^j p_k(t_i) \hat{\mathbf{x}}_k(t_i^+) \quad (2.15)$$

and similarly for the estimate at t_i^- . This is called a Bayesian estimate.

A variation on this is the maximum a posterior (MAP) estimate. In this case, the probabilities are calculated as in Equation (2.13) and the MMAE estimate is set equal to the $\hat{\mathbf{x}}_k(t_i)$ corresponding to the largest computed probability, $p_k(t_i)$.

The MMAE makes the adaptive estimate of the state based on the characteristics of the residuals. It is important that there be significant differences between residuals from the elemental filter designed for a specific trajectory and the other elemental filters. Therefore, the correct elemental filter will be selected, that is, have the largest $p_k(t_i)$. Two things contribute to distinctive residuals among the elemental filters. First, the model upon which the filter is based must be specific for an expected trajectory. This is key to this thesis using second-order filters. Each elemental filter is designed for a trajectory displaying a specific range of acceleration frequency content. For example, how fast the plane responds to stick input will contribute to the frequency content of the resulting trajectory, as in the trajectory an air superiority aircraft versus that of a cargo plane. Second, the filter must be tuned specifically for the expected trajectory. If pseudonoise

is added, as in conservative tuning practices with nonadaptive filters [7:339], it can blur the distinction between residuals of competing filters in the MMAE structure, and thereby incapacitate the adaptive mechanism of the MMAE algorithm [8:133].

2.3 Summary

This chapter discussed the basic function of the MMAE with emphasis on the parts that are investigated.

III. Truth Model

3.1 Introduction

The truth model is an accurate representation of the real world. Complete or not, it must include all aspects the researcher deems necessary for what is to be investigated. In this research the truth model must do two things:

1. Determine the true position of the target image in the FLIR detector. The FLIR detector is the array of 8-by-8 infrared (IR) sensors used to look at the IR signature of the airborne target. The true position is used to determine how well the tracking algorithm works. The model to generate this true position is outlined in Section 3.2.
2. Provide the measurements for the tracking algorithm to use as input. The measurements are the average intensity of IR radiation seen by each of the 64 pixels. To generate this, the apparent location of the target is found. The apparent location is the sum of the true target position and the apparent position jitter due to atmospheric distortion of the IR wavefront. Section 3.3 discusses the model of atmospheric distortion that causes apparent target motion. Section 3.4 shows the augmented model. Generation of the measurement model is outlined in Section 3.5.

3.2 Deterministic Target Motion Model

The position of the image in the detector plane is due to:

1. true motion of the target
2. the "jitter" caused by distortion of the IR wavefront as it travels from the target to the detector plane.

The target is maneuvering in an earth-centered-earth-fixed frame that has been traditionally called an inertial frame. The origin can be defined at the FLIR detector. The trajectories used in the investigation are *created* in this frame. The velocity vector must then be transferred from the inertial frame to a velocity of the image in the FLIR detector. As discussed later in the chapter, the truth model must generate the simulated target IR

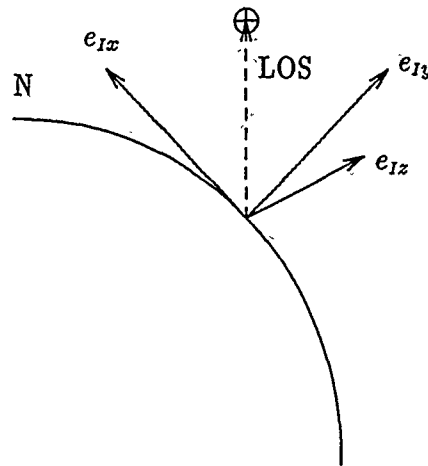


Figure 3.1. The Inertial Frame.

intensity pattern. To this end, the hotspot locations in the body frame of the target craft are projected into the detector plane, as well.

3.2.1 Trajectories in the Inertial Frame. Several trajectories are used in this investigation. They are created in an inertial frame, (e_{Ix}, e_{Iy}, e_{Iz}) where I means inertial frame and the x , y , or z denotes one of the directions. The origin is at the center of the FLIR detector, as in Figure 3.1. The e_{Ix} axis is due north in a plane tangent to the earth's surface at the FLIR detector. The e_{Iy} axis is perpendicular up from that plane. The e_{Iz} axis is the third of the right hand set and so points east. The trajectories are created by giving a starting position and an initial velocity. The trajectory is propagated as a position vector in the inertial frame, \mathbf{p}_I whose value is:

$$\mathbf{p}_I(t_i) = \mathbf{p}_I(t_{i-1}) + \mathbf{v}_I \Delta t \quad (3.1)$$

The following values are common to all trajectories finally used:

$$\begin{aligned}
 p_{Ix}(t_0) &= 3000 \text{ meters} \\
 v_{Ix}(t_0) &= -1000 \text{ meters per second} \\
 a_{Ix}(t_0) &= 0 \text{ meters per second}^2 \\
 p_{Iy}(t_0) &= 0 \text{ meters} \\
 v_{Iy}(t_0) &= A\omega \cos(\phi) + B \text{ meters per second} \\
 a_{Iy}(t_0) &= [v_{Iy}(t_0 + \Delta t) - v_{Iy}(t_0)] / \Delta t \text{ meters per second}^2 \\
 p_{Iz}(t_0) &= 20000 \text{ meters} \\
 v_{Iz}(t_0) &= 0 \text{ meters per second} \\
 a_{Iz}(t_0) &= 0 \text{ meters per second}^2
 \end{aligned}$$

where p , v , and a are the position, velocity, and acceleration of the target. The airborne target stays at a constant altitude with constant velocity in the negative x direction throughout the 6 second simulation. The motion dynamics are introduced in the y -direction via:

$$v_{Iy}(t) = A\omega \cos(\omega t + \phi) + B \text{ meters per second} \quad (3.2)$$

The amplitude of the cosine wave, A , would vary, limited by the maximum acceleration the manned target would pull. This acceleration due to the sinusoidal velocity can also be written:

$$a_{Iy}(t) = A\omega^2 \sin(\omega t + \phi) \text{ meters per second}^2 \quad (3.3)$$

The bias (B) and phase (ϕ) variables are used in more elaborate trajectory construction, for example, creating a target pulling a jinking maneuver in the velocity domain so that it will not have discontinuities in acceleration.

3.2.2 Translate to the α - β - γ Frame. The velocity vector in the inertial frame must be projected onto the FLIR detector plane. To do this, an α - β - γ frame is introduced as in Figure 3.2. The line of sight (LOS) vector from the detector to the target coincides with the positive e_γ axis, α is the azimuth angle measured east from e_{Ix} to the projection of the LOS vector onto the e_{Ix} - e_{Iz} plane, and β is the angle down to the e_{Ix} - e_{Iz} plane from

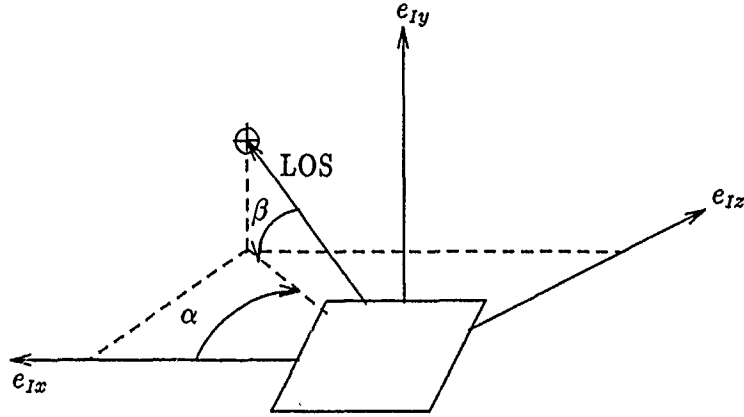


Figure 3.2. The Alpha-Beta Plane. This perspective is from the back of the detector.

the e_γ axis. From this definition and Figure 3.2, α is [3:32]:

$$\alpha(t) = \arctan\left(\frac{p_{Iz}(t)}{p_{Ix}(t)}\right) \quad (3.4)$$

The velocity comes from a simple derivative:

$$\dot{\alpha}(t) = \frac{1}{1 + [p_{Iz}(t)/p_{Ix}(t)]^2} \left[\frac{\dot{p}_{Iz}(t)p_{Ix}(t) - p_{Iz}(t)\dot{p}_{Ix}(t)}{p_{Ix}^2(t)} \right] \quad (3.5)$$

$$= \frac{v_{Iz}(t)p_{Ix}(t) - v_{Ix}(t)p_{Iz}(t)}{r_h^2(t)} \quad (3.6)$$

where r_h , the horizontal range to the target, is the length of the projection of the *LOS* vector onto the horizontal plane of e_{Ix} and e_{Iz} :

$$r_h(t) = \sqrt{p_{Ix}^2(t) + p_{Iz}^2(t)} \quad (3.7)$$

Similarly for β [3:33]:

$$\beta(t) = \arctan\left(\frac{p_{Iy}(t)}{r_h(t)}\right) \quad (3.8)$$

$$(3.9)$$

$$\dot{\beta}(t) = \frac{1}{1 + [p_{Iy}(t)/r_h(t)]^2} \left[\frac{\dot{p}_{Iy}(t)r_h(t) - p_{Iy}(t)\dot{r}_h(t)}{r_h^2(t)} \right] \quad (3.10)$$

$$= \frac{v_{Iy}(t)r_h(t) - \dot{r}_h(t)p_{Iy}(t)}{r^2(t)} \quad (3.11)$$

where r is the range to the target and is given by:

$$r(t) = \sqrt{p_{Ix}^2(t) + p_{Iz}^2(t) + p_{Iy}^2(t)} \quad (3.12)$$

and:

$$\dot{r}_h(t) = \frac{1}{2} [p_{Ix}^2(t) + p_{Iz}^2(t)]^{-\frac{1}{2}} [2\dot{p}_{Ix}(t)p_{Ix}(t) + 2\dot{p}_{Iz}(t)p_{Iz}(t)] \quad (3.13)$$

$$= \frac{v_{Ix}(t)p_{Ix}(t) + v_{Iz}(t)p_{Iz}(t)}{r_h(t)} \quad (3.14)$$

At time t_i^+ , the center of mass of the target is at a position defined by $\alpha(t_i^+)$ and $\beta(t_i^+)$. The superscript plus means just after the measurement update of the KF. This shows up as an image at the center of the detector, $(p_{Dx}(t_i^+), p_{Dy}(t_i^+))$, where the subscript D denotes the detector plane. The detector is two dimensional, with the (e_{Dx}, e_{Dy}) frame origin at the center, positive e_{Dx} pointing to the right from behind the detector, and positive e_{Dy} pointing down. During this time increment, $\Delta t = t_{i+1}^- - t_i^+$, the target will move to a new position in inertial space and the image will translate across the detector. The new position of the image is defined as $p_{Dx}(t_{i+1}^-), p_{Dy}(t_{i+1}^-)$. It is found by converting the velocity in the α - β - γ frame to a velocity in the detector frame with the pixel proportionality constant, L , the detector is designed to have. The constant used in this research is 20 microradians per pixel. For example:

$$(p_{Dx}(t_{i+1}^-) - p_{Dx}(t_i^+)) = (\alpha(t_{i+1}^-) - \alpha(t_i^+)) / L \quad (3.15)$$

$$\frac{p_{Dx}(t_{i+1}^-) - p_{Dx}(t_i^+)}{\Delta t} = \frac{1}{L} \left[\frac{\alpha(t_{i+1}^-) - \alpha(t_i^+)}{\Delta t} \right] \quad (3.16)$$

$$p_{Dx}(t_{i+1}^-) = \Delta t [\dot{\alpha}(t_i)/L] + p_{Dx}(t_i^+) \quad (3.17)$$

A similar relationship exists for p_{Dy} and β . The angular velocities, scaled by the pixel proportionality constant, become the velocity control inputs for the truth model propagation.

This purely deterministic model for true target dynamics is put into state space form based on tradition (Mercier started with a first-order Gauss-Markov model for target dynamics in the truth model [11:9,11]), to allow for possible future addition of a stochastic term to this deterministic model, and to allow augmentation to the already stochastic atmospheric state space model. The state space form of the mathematical model for the true target motion is:

$$\dot{\mathbf{x}}_{tm}(t) = \mathbf{B}_{tm} \mathbf{u}_{tm}(t) \quad (3.18)$$

$$\begin{bmatrix} \dot{x}_{tmx}(t) \\ \dot{x}_{tmy}(t) \end{bmatrix} = \begin{bmatrix} u_{tmx}(t) \\ u_{tmy}(t) \end{bmatrix} = \begin{bmatrix} \dot{\alpha}(t)/L \\ \dot{\beta}(t)/L \end{bmatrix} \quad (3.19)$$

from the initial condition, $\mathbf{x}_{tm}(t_0) = \mathbf{x}_0$. The variables x_{tmx} and x_{tmy} are the truth model states representing the position of the target centroid in the detector plane due to the true motion of the target in its trajectory. The subscript t denotes the truth model state. The subscript m means due to actual motion of the target. The initial conditions are arbitrarily chosen to be 3 pixels in each the x and y direction in the detector plane. The input matrix is \mathbf{B}_{tm} and is $\mathbf{I}_{2 \times 2}$. The system dynamic matrix, \mathbf{F}_{tm} , is $\mathbf{0}$, making the state transition matrix, $\Phi_{tm}(t, t_0)$, equal to $\mathbf{I}_{2 \times 2}$. The continuous-time solution is [7:40,42]:

$$\mathbf{x}_{tm}(t) = \Phi_{tm}(t, t_0) \mathbf{x}_{tm}(t_0) + \int_{t_0}^t \Phi_{tm}(t, \tau) \mathbf{B}(\tau) \mathbf{u}_{tm}(\tau) d\tau \quad (3.20)$$

Since this will be simulated on a computer, the equivalent discrete-time system model of this continuous-time model is needed. The deterministic input is made a piecewise constant function. Then, using [7:171]:

$$\mathbf{B}_{dtm} = \int_{t_i}^{t_{i+1}} \Phi_{tm}(t_{i+1}, \tau) \mathbf{B}_{tm}(\tau) d\tau \quad (3.21)$$

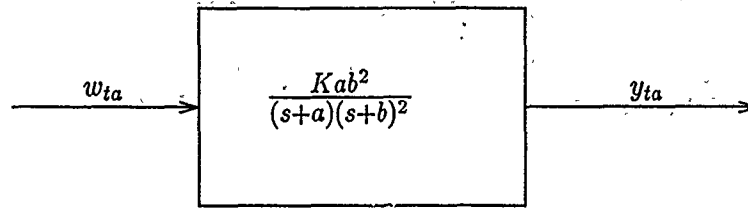


Figure 3.3. Mathematical Model for Atmospheric Jitter. [11:12]

the difference equation is:

$$\mathbf{x}_{tm}(t_{i+1}) = \Phi_{tm}(t_{i+1}, t_i) \mathbf{x}_{tm}(t_i) + \mathbf{B}_{dtm} \mathbf{u}_{dtm}(t_i) \quad (3.22)$$

$$\begin{bmatrix} x_{tmx}(t_{i+1}) \\ x_{tmy}(t_{i+1}) \end{bmatrix} = \begin{bmatrix} x_{tmx}(t_i) \\ x_{tmy}(t_i) \end{bmatrix} + \begin{bmatrix} \Delta t & 0 \\ 0 & \Delta t \end{bmatrix} \begin{bmatrix} \dot{\alpha}(t_i)/L \\ \dot{\beta}(t_i)/L \end{bmatrix} \quad (3.23)$$

The subscript d denotes the equivalent discrete-time model. The initial conditions are defined as in the continuous-time case.

3.3 Atmospheric Disturbance Model

The image of the target in the detector frame will undergo apparent motion due to the IR wavefront propagating through the atmosphere. The model used for this was developed by The Analytical Sciences Corporation and was first discussed by Mercier [11:10]. As with the true target dynamics above, a mathematical model is devised. It is transformed to state space form as a differential equation, but stochastic this time. The equation is solved so the equivalent discrete-time form is written for implementation in the simulation.

The mathematical model for atmospheric jitter is a three-state linear shaping filter driven by unit-strength, zero-mean, white Gaussian noise as in Figure 3.3. The poles and

other important parameters are:

$$a_{ta} = 14.14 \text{ radians per second}$$

$$b_{ta} = 659.5 \text{ radians per second}$$

$$K_{ta} = 0.382109544 \sigma_{ta}$$

$$\sigma_{ta} = 0.447$$

The variable, σ_{ta} , is the standard deviation of the output, y_{ta} . The subscript a refers to the atmospheric model. Mercier calculated the gain K_{ta} [11:76]. He developed the Jordan canonical form of the state differential equation used in the following equations [11:73].

The jitter effect is assumed independent of the direction of interest in the detector plane, so the state-space model is developed independently in each e_{Dx} and e_{Dy} direction. The stochastic differential equation (in the less rigorous white noise notation [7:163,204]) for the x direction is:

$$\dot{\mathbf{x}}_{tax}(t) = \mathbf{F}_{tax}\mathbf{x}_{tax}(t) + \mathbf{G}_{tax}w_{tax}(t) \quad (3.24)$$

$$\begin{bmatrix} \dot{x}_{ta1}(t) \\ \dot{x}_{ta2}(t) \\ \dot{x}_{ta3}(t) \end{bmatrix} = \begin{bmatrix} -a & 0 & 0 \\ 0 & -b & 1 \\ 0 & 0 & -b \end{bmatrix} \begin{bmatrix} x_{ta1}(t) \\ x_{ta2}(t) \\ x_{ta3}(t) \end{bmatrix} + \begin{bmatrix} Kab^2/(a-b)^2 \\ -Kab^2/(a-b)^2 \\ Kab^2/(a-b) \end{bmatrix} w_{tax}(t) \quad (3.25)$$

with an output equation of:

$$y_{tax}(t) = \mathbf{H}_{tax}\mathbf{x}_{tax}(t) = \begin{bmatrix} 1 & 1 & 0 \end{bmatrix} \begin{bmatrix} x_{ta1}(t) \\ x_{ta2}(t) \\ x_{ta3}(t) \end{bmatrix} \quad (3.26)$$

Subscripts 1, 2, and 3, refer to the states related to the poles, a and the repeated b .

Since the \mathbf{F}_{tax} is time invariant, $\Phi_{tax}(t_{i+1}, t_i)$ depends only on the time increment, Δt . The solution is the inverse Laplace transform of the resolvent matrix [7:42] and is:

$$\Phi_{tax}(\Delta t) = \begin{bmatrix} \exp(-a\Delta t) & 0 & 0 \\ 0 & \exp(-b\Delta t) & \Delta t \exp(-b\Delta t) \\ 0 & 0 & \exp(-b\Delta t) \end{bmatrix} \quad (3.27)$$

A similar development is done for the detector y-axis. The resulting matrices, \mathbf{F}_{tay} , \mathbf{G}_{tay} , \mathbf{H}_{tay} , and $\Phi_{tay}(\Delta t)$ are all equal to and augmented to their x-axis counterparts:

$$\dot{\mathbf{x}}_{ta}(t) = \mathbf{F}_{ta}\mathbf{x}_{ta}(t) + \mathbf{G}_{ta}\mathbf{w}_{ta}(t) \quad (3.28)$$

$$\begin{bmatrix} \dot{\mathbf{x}}_{tax}(t) \\ \dot{\mathbf{x}}_{tay}(t) \end{bmatrix} = \begin{bmatrix} \mathbf{F}_{tax} & \mathbf{0}_{3 \times 3} \\ \mathbf{0}_{3 \times 3} & \mathbf{F}_{tay} \end{bmatrix} \begin{bmatrix} \mathbf{x}_{tax}(t) \\ \mathbf{x}_{tay}(t) \end{bmatrix} + \begin{bmatrix} \mathbf{G}_{tax} & \mathbf{0}_{3 \times 3} \\ \mathbf{0}_{3 \times 3} & \mathbf{G}_{tay} \end{bmatrix} \begin{bmatrix} \mathbf{w}_{tax}(t) \\ \mathbf{w}_{tay}(t) \end{bmatrix} \quad (3.29)$$

The white noise process for the y-axis has the same statistics as that for the x-axis described above. The output vector, \mathbf{y}_{ta} , is given by:

$$\mathbf{y}_{ta}(t) = \begin{bmatrix} y_{tax}(t) \\ y_{tay}(t) \end{bmatrix} = \begin{bmatrix} \mathbf{H}_{tax} & \mathbf{0}_{1 \times 3} \\ \mathbf{0}_{1 \times 3} & \mathbf{H}_{tay} \end{bmatrix} \begin{bmatrix} \mathbf{x}_{tax}(t) \\ \mathbf{x}_{tay}(t) \end{bmatrix} \quad (3.30)$$

The augmented state transition matrix is:

$$\Phi_{ta}(\Delta t) = \begin{bmatrix} \Phi_{tax}(\Delta t) & \mathbf{0}_{3 \times 3} \\ \mathbf{0}_{3 \times 3} & \Phi_{tay}(\Delta t) \end{bmatrix} \quad (3.31)$$

Using the state transition matrix, the equivalent difference equation is written:

$$\mathbf{x}_{ta}(t_{i+1}) = \Phi_{ta}(\Delta t)\mathbf{x}_{ta}(t_i) + \mathbf{w}_{dtaq}(t_i) \quad (3.32)$$

where the white Gaussian discrete-time stochastic noise process is a vector of dimension six with mean and covariance given by:

$$E\{\mathbf{w}_{dtaq}(t_i)\} = \mathbf{0} \quad (3.33)$$

$$E\{\mathbf{w}_{dtaq}(t_i)\mathbf{w}_{dtaq}^T(t_j)\} = \mathbf{Q}_{dta}(t_i)\delta_{ij} \quad (3.34)$$

where the covariance depicting the strength of the discrete-time noise is:

$$\mathbf{Q}_{dta}(t_i) = \int_{t_i}^{t_{i+1}} \Phi_{ta}(t_{i+1} - \tau) \mathbf{G}_{ta}(\tau) \mathbf{Q}_{ta}(\tau) \mathbf{G}_{ta}^T(\tau) \Phi_{ta}^T(t_{i+1} - \tau) d\tau \quad (3.35)$$

The computation of the elements of the 6-by-6 covariance matrix is outlined by Jensen and Harnly [3:Vol. 2, p. 21].

In fact, the simulation is done with unit-strength white noise which is scaled by the Cholesky square root of the covariance matrix found above, $\sqrt[6]{\mathbf{Q}_{dta}(t_i)}$ [7:370]. The discrete-time simulation model is:

$$\mathbf{x}_{ta}(t_{i+1}) = \Phi_{ta}(t_{i+1} - t_i) \mathbf{x}_{ta}(t_i) + \sqrt[6]{\mathbf{Q}_{dta}(t_i)} \mathbf{w}_{dta}(t_i) \quad (3.36)$$

with the output matrix \mathbf{H}_{ta} described above, and \mathbf{w}_{dta} being a readily simulated zero-mean white Gaussian noise of covariance equal to the identity matrix.

3.4 Augmented Discrete-time Model

The deterministic process describing the true target motion is independent of the stochastic process describing the apparent target motion. The two are augmented into an eight-state model:

$$\begin{bmatrix} \mathbf{x}_{tm}(t_{i+1}) \\ \mathbf{x}_{ta}(t_{i+1}) \end{bmatrix} = \begin{bmatrix} \Phi_{tm}(\Delta t) & \mathbf{0}_{2 \times 6} \\ \mathbf{0}_{6 \times 2} & \Phi_{ta}(\Delta t) \end{bmatrix} \begin{bmatrix} \mathbf{x}_{tm}(t_i) \\ \mathbf{x}_{ta}(t_i) \end{bmatrix} + \mathbf{B}_{dtm} \mathbf{u}_{dtm}(t_i) + \begin{bmatrix} \mathbf{0}_{2 \times 2} & \mathbf{0}_{2 \times 6} \\ \mathbf{0}_{6 \times 2} & \sqrt[6]{\mathbf{Q}_{dta}(t_i)} \end{bmatrix} \begin{bmatrix} \mathbf{0}_{2 \times 1} \\ \mathbf{w}_{dta}(t_i) \end{bmatrix} \quad (3.37)$$

with the output equation:

$$\mathbf{y}_t(t) = \begin{bmatrix} y_{tx}(t) \\ y_{ty}(t) \end{bmatrix} = \begin{bmatrix} \mathbf{H}_{tm} & \mathbf{H}_{ta} \end{bmatrix} \begin{bmatrix} \mathbf{x}_{tm}(t) \\ \mathbf{x}_{ta}(t) \end{bmatrix} \quad (3.38)$$

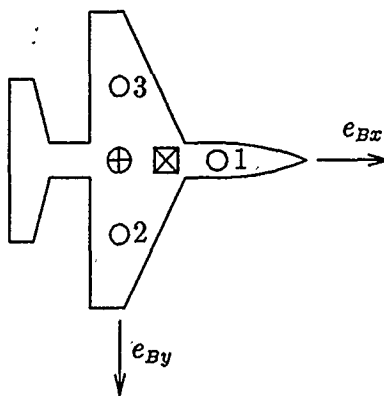


Figure 3.4. Simulated Target. The target body frame is noted; the third axis is into the paper through the center of mass. The center of mass is the cross-haired circle. The hotspots are the empty circles. The approximate position of peak intensity due to the hotspot pattern is marked by the square.

3.5 Measurement Model

The output of the detector is a set of voltage levels that represent the average intensity of the IR radiation impinging on each of the 64 IR sensitive pixels in the detector. The output intensity is simulated by the truth model to be the input for the tracker. This simulation is done in three steps:

1. A target shape must be decided upon.
2. The IR signature of that target is simulated.
3. The image that signature would make on the detector is simulated. This image is calculated at the end of each target motion propagation cycle.

The target is shown in Figure 3.4. The target body frame is (e_{Bx}, e_{By}, e_{Bz}) . The e_{Bx} axis is out the nose of the plane. The sideslip angle and angle-of-attack are assumed zero so that e_{Bx} is also along the velocity vector. The y-axis, e_{By} , is to the right side. The last axis points out the underside of the fuselage. The target center of mass is at the origin.

The target in Figure 3.4 shows the center of intensity not colocated with the center of mass. Chapter IV will show that the MMAE tracks the center of intensity in the FOV. The truth model simulates the true location with the center of mass of the target. As

Tobin points out [20:137], the distance between the centers is 0.333 meters in the body frame. At the range of 20000 meters, this represents a distance of 0.8325 pixels on the detector plane in the e_{Dx} . Since the error is defined as the estimate from the MMAE minus the position from the truth model, this distance should appear as a bias in the x-position error plots as described in Section 5.2.

The IR signature is sufficiently described with the location of the hotspots of the target. These are the spots that produce the greatest amount of IR radiation and are described in the target frame. Three hotspots are assumed and their locations in meters are:

Hotspot	p_{Bx}	p_{By}	p_{Bz}
1	1	0	0
2	0	0.5	0
3	0	-0.5	0

The simulation of the IR radiation from the target on the detector is more complex. Mercier decided the intensity of a single hotspot image on the detector can be represented by a bivariate Gaussian function [11:5-7]. According to Jensen and Harnly [3:6,7], for the range and type of targets in this simulation, this function has elliptical constant-intensity contours, with the semimajor axis along the direction of the velocity vector in the FLIR image plane. According to Rogers [16:36] and Suizu [19:II-21], the intensity function for a target with three hotspots is the sum of the bivariate Gaussian intensities due to each hotspot.

Being a Gaussian function, three things are needed to define the intensity for each hotspot, the center, the maximum magnitude, and the covariance matrix. The center of each intensity function is the hotspot location in the detector frame. The diagonal elements of the covariance matrix represent the spread of the function. The spread determines the image size in the detector plane. The intensity function in the body frame is:

$$I = I_{\max} \exp \left(-\frac{1}{2} \begin{bmatrix} x - x_{\text{cen}} & y - y_{\text{cen}} \end{bmatrix} \begin{bmatrix} \sigma_v^2 & 0 \\ 0 & \sigma_{pv}^2 \end{bmatrix}^{-1} \begin{bmatrix} x - x_{\text{cen}} \\ y - y_{\text{cen}} \end{bmatrix} \right) \quad (3.39)$$

The covariance matrix elements are σ_v^2 and σ_{pv}^2 . One is in the direction of the projection of the inertial velocity vector onto the detector plane (the v subscript). The other is perpendicular to that in the detector plane (the pv subscript). These two values define the aspect ratio (AR) of the target; $AR = \sigma_v / \sigma_{pv}$. The AR is one for the reference target in the inertial frame for these simulations [20:44]. The hotspot location is (x_{cen}, y_{cen}) . The maximum intensity of each hotspot, I_{max} , is given a value of 20 which makes a signal-to-noise ratio (SNR) of 20 [3:62,68,148] [20:77]. The signal to noise ratio is I_{max} over the RMS value of the measurement noise.

The average of this function over the area of each pixel is the output for that pixel due to this single hotspot. Rather than integrate the function, the average is approximated:

1. Divide the pixel into a 5-by-5 array of subpixels;
2. At the center point in each of the 25 divisions calculate the value of the intensity due to each of the three hotspots and sum the three values;
3. Sum the 25 values and divide by 25.

The output vector is then the sequential listing of these average intensities for the 64 pixels.

To make the intensity calculations during each time increment, the current (x_{cen}, y_{cen}) , σ_v^2 , and σ_{pv}^2 are needed. In the case of the covariance elements, a reference value for each, σ_{v0}^2 and σ_{pv0}^2 , is selected for a nominal target hotspot at a given nominal range, r_0 , to the target in the inertial frame. New covariance values are calculated from the reference and the change in range and orientation of the target from the nominal values at each time frame.

The hotspot locations in the target frame are translated to a position in the detector plane using the fact that the target axis, $e_B x$, is in the same direction as v_I and the velocities have already been defined for all frames. This is outlined in Jensen and Harnly [12:37].

The output of the detector is, of course, corrupted by noise. The dominant source is the background radiation that hits the detector with the radiation from the target. Jensen and Harnly investigated the statistical nature of this background noise and concluded that

1:0	2: 0	3: 0	4: 0	5: 0	6: 0	7:0	8:0
9:0	10:0.0591	11:0.1069	12:0.1353	13:0.1069	14:0.0591	15:0	16:0
17:0	18:0.1069	19:0.2431	20:0.3679	21:0.2431	22:0.1069	23:0	24:0
25:0	26:0.1353	27:0.3679	28: 1	29:0.3679	30:0.1353	31:0	32:0
33:0	34:0.1069	35:0.2431	36:0.3679	37:0.2431	38:0.1069	39:0	40:0
41:0	42:0.0591	43:0.1069	44:0.1353	45:0.1069	46:0.0591	47:0	48:0
49:0	50: 0	51: 0	52: 0	53: 0	54: 0	55:0	56:0
57:0	58: 0	59: 0	60: 0	61: 0	62: 0	63:0	64:0

Figure 3.5. Correlation Coefficients for Pixel 28.

it is spatially correlated [3:19]. For the pixel size used, that correlation extends to the second pixel from the one of interest. The pixels are numbered 1 through 64 as shown in Figure 3.5 along with the correlation coefficient pattern of pixel 28. The correlation coefficient between 28 and the rest of the pixels not in Figure 3.5 are 0. This pattern of coefficients will be repeated for every pixel in the detector and gives the elements in the 64-by-64 matrix of coefficients. That is, 1 is in position (28,28) and 0.3679 is in positions (20,28), (28,20), (28,29), (29,28), (28,36), (36,28), (28,27), and (27,28); and so forth. This matrix of coefficients is multiplied by the appropriate variance to make the measurement error covariance matrix, \mathbf{R}_t . As with the noise for the atmospheric distortion process of Section 3.3, the simulation generates a 64-element vector of unit-strength white noise, $\mathbf{v}'_t(t_i)$, that is scaled with $\sqrt{\mathbf{R}_t}$ to make the measurement noise, $\mathbf{v}_t(t_i) = \sqrt{\mathbf{R}_t} \mathbf{v}'_t(t_i)$. The appropriate statistical description is:

$$E\{\mathbf{v}_t(t_i)\} = 0 \quad (3.40)$$

$$E\{\mathbf{v}_t(t_i) \mathbf{v}_t^T(t_j)\} = \mathbf{R}_t(t_i) \delta_{ij} \quad (3.41)$$

The measurement handed off to the tracker, $\mathbf{z}_t(t_i)$, is then the 64-dimensional output intensity vector plus the noise, $\mathbf{v}_t(t_i)$.

3.6 Summary

This chapter has presented several models that will create the real world for the simulation. The target and its trajectory through the atmosphere were described. The measurements from the detector array were simulated. And finally, atmospheric jitter and the spatially correlated background noise and their effects were discussed. The parameters used for the models discussed in this chapter are compiled and presented in Appendix A.

IV. Filter Models

4.1 Introduction

Chapter III presented the truth model, which is the representation of the environment from which the measurement vector, $z(t_i)$, is generated. This vector is a series of intensities, each representing the amount of IR radiation impinging on one pixel. Using this measurement vector directly would require a nonlinear update in the Kalman filter tracking the target. Rogers developed a hybrid enhanced correlator/Kalman filter [16]. A new measurement vector is created such that the measurement update in the Kalman filter is linear. This reduces computational loading [16:52].

First, the enhanced correlator and filter measurement model are discussed. Then the filter models and KF equations are given. Finally, template generation is outlined.

4.2 Enhanced Correlator

The enhanced correlator is an algorithm that correlates the current array of noise-corrupted intensities with a template generated as an average of the past ten centered arrays. It does this to find how much the center of mass of the current intensity has moved from the center of the detector due to the target motion over a sample period, as simulated by the propagation cycle of the truth model. The correlation is done on a 24-by-24 array of input intensities rather than the 8-by-8 FOV to reduce the edge effects, aliasing, and leakage conditions involved in transforming a finite array of numbers [19:III-15]. The outer 8 columns and rows are filled with simulated data calculated at one spot in each pixel (rather than at 25 spots and averaged) plus the spatially correlated noise.

Correlation methods were investigated by Millner, resulting in the correlation being done in the frequency domain [12:96,150][16:53,131]. A Fourier transform is taken of the current data, $D(t_i)$, and the smoothed data in the template, $S(t_{i-1})$. The conjugate of the transformed S is multiplied by the transformed D . Then, the inverse transform is the cross correlation matrix, R ,:

$$R(t_i) = \mathcal{F}^{-1} [\mathcal{F}(S(x, y))^* \mathcal{F}(D(x, y))] \quad (4.1)$$

This matrix, \bar{R} , is an array of numbers, the magnitude of which represents the amount the elements in that same position in D and S resemble each other. Since the inputs were Gaussian, the result, \bar{R} , shows a spatial Gaussian spread in the magnitude of its elements. The offset of D from the template, S , is the offset of the peak of the Gaussian in \bar{R} from the center of the array.

Before the peak location is found, the array is smoothed somewhat by a thresholding step. The threshold level was investigated by both Rogers [16:111] and Millner [12:78,96]. Millner's value of 0.3 is selected. The maximum magnitude of the 24-by-24 elements is found. Then each element that is not at least 30% of that magnitude is set to zero. This is to smooth out the array so local smaller peaks due to noise won't corrupt finding the location of the peak that is due to the actual target intensity. The peak location is estimated with a centroid summation rather than a peak detector [12:82]. The form of this is [16:62]:

$$x_{peak} = \frac{\sum_{i=1}^{24} i A_i}{\sum_{i=1}^{24} A_i} \quad (4.2)$$

where i is the horizontal coordinate of each of the array elements and A_i is the magnitude of the correlation in that position. Similarly, y_{peak} is found. These values, (x_{peak}, y_{peak}) , are the measurements for the update cycle of the elemental Kalman filter. These measurements are given as:

$$z_f = \begin{bmatrix} x_{peak} \\ y_{peak} \end{bmatrix} = H_f x_f + v_f \quad (4.3)$$

The new measurement vector is z_f , H_f is the output distribution matrix, and x_f is the state vector. The subscript f denotes a model for the KF equations. The additive measurement noise is v_f . This noise is white zero-mean, Gaussian and has strength R_f . The description of H_f and x_f will be given as the dynamics models are discussed in the next section. The two directions are assumed independent so the R_f matrix is diagonal. The values for this thesis are 0.00436 and 0.00598 pixels² as used by Tobin [20:65]. A block diagram representation of the enhanced correlator and linear Kalman filter is in Figure 4.1. Note that the controller points the center of the FOV at the predicted centroid location using $\hat{x}(t_{i+1}^-)$.

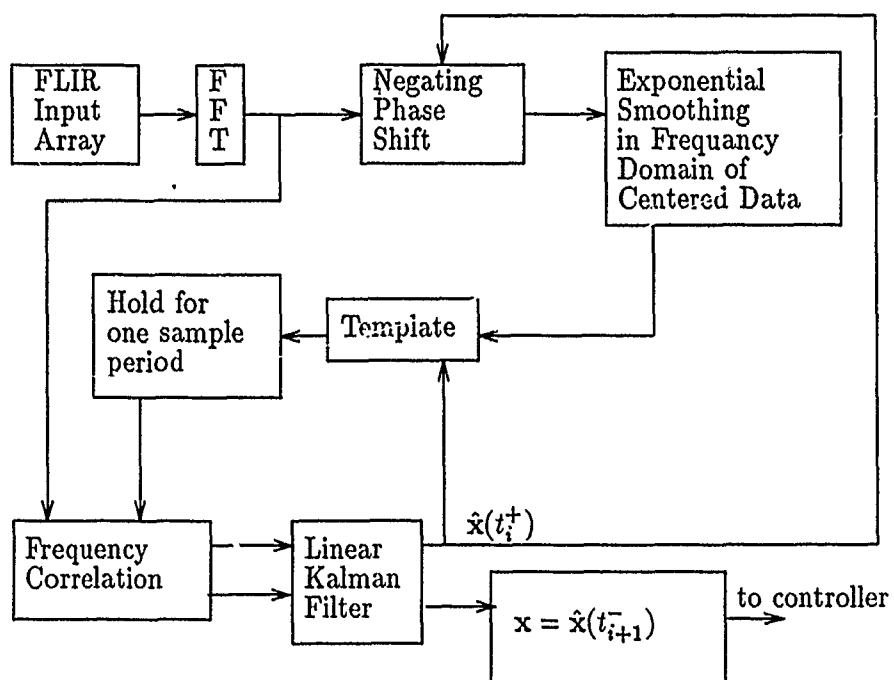


Figure 4.1. Enhanced Correlator and Linear Kalman Filter

4.3 Update Equations

Now that the measurements are the offset position in the detector plane, a linear update can be done. The update equations for each elemental Kalman filter are:

$$\hat{\mathbf{x}}(t_i^+) = \hat{\mathbf{x}}(t_i^-) + \mathbf{K}(t_i) [\mathbf{z}_f - \mathbf{H}_f \hat{\mathbf{x}}(t_i^-)] \quad (4.4)$$

$$\mathbf{P}(t_i^+) = \mathbf{P}(t_i^-) - \mathbf{K}(t_i) \mathbf{H}_f \mathbf{P}(t_i^-) \quad (4.5)$$

$$\mathbf{K}(t_i) = \mathbf{P}(t_i^-) \mathbf{H}_f^T [\mathbf{H}_f \mathbf{P}(t_i^-) \mathbf{H}_f^T + \mathbf{R}_f]^{-1} \quad (4.6)$$

where the matrices are described in Chapter II. The \mathbf{R}_f is described just above, and \mathbf{H}_f will be presented when the filter models are established in Section 4.5.

4.4 Propagation Equations

The Kalman filter consists of update equations and propagation equations. The propagation equations predict the position of the target in the detector plane at the end of the next 1/30 second sample period. The propagation equations based on an equivalent discrete-time model are:

$$\hat{\mathbf{x}}(t_{i+1}^-) = \Phi_f(t_{i+1}, t_i) \hat{\mathbf{x}}(t_i^+) \quad (4.7)$$

$$\mathbf{P}(t_{i+1}^-) = \Phi_f(t_{i+1}, t_i) \mathbf{P}(t_i^+) \Phi_f^T(t_{i+1}, t_i) + \mathbf{Q}_{df}(t_i) \quad (4.8)$$

where the state transition matrix, $\Phi_f(t_{i+1}, t_i)$, will be presented with the filter models in Section 4.5.

It is during the propagation cycle that control is applied. The detector is pointed so the center of the FOV points toward the estimated target intensity location. This is done at each sample time by redefining the upper left corner of the FOV to a value that puts the estimated target position, $(\hat{p}_{mx}, \hat{p}_{my})$, at the middle of the screen. The subscript m denotes true target motion. It is assumed that the controller can accomplish such pointing perfectly in 1/30 second.

Appropriate models for the target dynamics are developed now to find the matrices needed by the KF equations, $\Phi_f(t_{i+1}, t_i)$, $\mathbf{Q}_{df}(t_i)$, and \mathbf{H}_f .

4.5 Dynamics Models

Models are developed to describe the atmospheric jitter and the target acceleration process. From these models, the appropriate matrices for the KF equations are generated. The models are described in the continuous-time domain, then the equivalent discrete-time version is found.

4.5.1 Filter Atmospheric Models. The atmospheric jitter for the filter equations is modeled as a stationary first-order Gauss-Markov process. This is the output of a first-order lag driven by white Gaussian noise of strength q [7:184]. The differential equation for the first-order lag model is $\dot{x}(t) = (-1/T)x(t) + w(t)$ with noise described with $E\{w(t)\} = 0$ and $E\{w(t)w(t+\tau)\} = q\delta(\tau)$ where $q = 2\sigma^2/T$. The correlation time is T and the mean squared value of the output is σ^2 .

The first-order lag model is used as the atmospheric model independently in each direction in the detector plane. The state vector is:

$$\mathbf{x}_{fa}(t) = \begin{bmatrix} p_{fax}(t) \\ p_{fay}(t) \end{bmatrix} \quad (4.9)$$

where the variable p is jitter position in the detector plane. The subscripts f and a denote the model is for the KF equations and is modeling the apparent motion that is due to the atmospheric distortion. Of course, x and y are the directions in the detector plane. The time-invariant \mathbf{F}_{fa} matrix is:

$$\mathbf{F}_{fa} = \begin{bmatrix} -1/T_{fa} & 0 \\ 0 & -1/T_{fa} \end{bmatrix} \quad (4.10)$$

The noise input matrix, \mathbf{G}_{fa} , is $\mathbf{I}_{2 \times 2}$, and the covariance matrix for the vector of white Gaussian zero-mean noise is:

$$\mathbf{Q}_{fa} = \begin{bmatrix} 2\sigma_{fa}^2/T_{fa} & 0 \\ 0 & 2\sigma_{fa}^2/T_{fa} \end{bmatrix} \quad (4.11)$$

The difference equation for the model of atmospheric jitter is:

$$\mathbf{x}_{fa}(t_{i+1}) = \Phi_{fa}(\Delta t)\mathbf{x}_{fa}(t_i) + \mathbf{w}_{dfa}(t_i) \quad (4.12)$$

The state transition matrix is:

$$\Phi_{fa}(\Delta t) = \begin{bmatrix} \exp\{\frac{-\Delta t}{T_{fa}}\} & 0 \\ 0 & \exp\{\frac{-\Delta t}{T_{fa}}\} \end{bmatrix} \quad (4.13)$$

The discrete-time noise, $\mathbf{w}_{dfa}(t_i)$ is zero-mean Gaussian and has covariance \mathbf{Q}_{dfa} where the subscript d denotes discrete-time. The covariance is found as:

$$\mathbf{Q}_{dfa}(t_i) = \int_{t_i}^{t_{i+1}} \Phi_{fa}(t_{i+1} - \tau) \mathbf{G}_f(\tau) \mathbf{Q}_{fa}(\tau) \mathbf{G}_{fa}^T(\tau) \Phi_{fa}^T(t_{i+1} - \tau) d\tau \quad (4.14)$$

This gives:

$$\mathbf{Q}_{dfa} = \begin{bmatrix} \sigma_{fa}^2 \left[1 - \exp\{\frac{-2\Delta t}{T_{fa}}\}\right] & 0 \\ 0 & \sigma_{fa}^2 \left[1 - \exp\{\frac{-2\Delta t}{T_{fa}}\}\right] \end{bmatrix} \quad (4.15)$$

The appropriate values are $T_{fa} = 0.0707$ seconds and $\sigma_{fa}^2 = 0.2$ pixels² in each direction on the detector plane.

Recall the jitter is created in the truth model with three states. In the interest of keeping the number of states down, the filter tracks only the dominant single pole at $1/T_{fa}$ or 14.14 radians per second. Note the output jitter variance is the same for both models.

4.5.2 Acceleration Models. Two kinds of acceleration models are developed. The acceleration can be modeled as a first-order Gauss-Markov process, leading to three filter states for each axis in the detector plane. This acceleration model has been implemented many times before [6, 20, 5]. Or the target acceleration can be modeled as a second-order Gauss-Markov process, resulting in four filter states per axis.

4.5.2.1 First-Order Gauss-Markov Acceleration Process Model. The first-order Gauss-Markov model is described for the atmospheric model above. The development is similar for the acceleration process except that two additional states are needed for the

velocity and position. Now the model looks like:

$$\begin{aligned}\dot{p}(t) &= v(t) \\ \dot{v}(t) &= a(t) \\ \dot{a}(t) &= (-1/T)a(t) + w(t)\end{aligned}\tag{4.16}$$

where the noise is zero-mean with strength of $q = 2\sigma^2/T$. The state space form of the differential equation is:

$$\begin{bmatrix} \dot{p}(t) \\ \dot{v}(t) \\ \dot{a}(t) \end{bmatrix} = \begin{bmatrix} 0 & 1 & 0 \\ 0 & 0 & 1 \\ 0 & 0 & -1/T \end{bmatrix} \begin{bmatrix} p(t) \\ v(t) \\ a(t) \end{bmatrix} + \begin{bmatrix} 0 \\ 0 \\ 1 \end{bmatrix} w(t)\tag{4.17}$$

The state transition matrix derived from the time-invariant **F** matrix is:

$$\Phi(\Delta t) = \begin{bmatrix} 1 & \Delta t & T^2 \left[\frac{\Delta t}{T} - 1 + \exp\left\{-\frac{\Delta t}{T}\right\} \right] \\ 0 & 1 & T \left[1 + \exp\left\{-\frac{\Delta t}{T}\right\} \right] \\ 0 & 0 & \exp\left\{-\frac{\Delta t}{T}\right\} \end{bmatrix}\tag{4.18}$$

This model is used for both the x and y directions in the detector plane. The filter states modeling the motion of the target are:

$$\mathbf{x}_{fm} = \begin{bmatrix} p_{fmx} \\ p_{fmy} \\ v_{fmx} \\ v_{fmy} \\ a_{fmx} \\ a_{fmy} \end{bmatrix}\tag{4.19}$$

where the variables, p , v , and a , are position, velocity, and acceleration. The subscripts, f , m , x , and y show filter model, actual target motion (versus apparent motion due to atmospheric jitter, with subscript a), the x direction in the detector plane, and the y

direction, respectively. The G_{fm} matrix is:

$$G_{fm} = \begin{bmatrix} 0 & 0 \\ 0 & 0 \\ 0 & 0 \\ 0 & 0 \\ 1 & 0 \\ 0 & 1 \end{bmatrix} \quad (4.20)$$

The dynamic driving noise is a vector with the covariance matrix:

$$Q_{fm} = \begin{bmatrix} 2\sigma_{fm}^2/T_{fm} & 0 \\ 0 & 2\sigma_{fm}^2/T_{fm} \end{bmatrix} \quad (4.21)$$

The discrete-time difference equation is written:

$$x_{fm}(t_{i+1}) = \Phi_{fm}(\Delta t)x_{fm}(t_i) + w_{dfm}(t_i) \quad (4.22)$$

The appropriate state transition matrix is:

$$\Phi_{fm}(\Delta t) = \begin{bmatrix} 1 & 0 & \Delta t & 0 & T_{fm}^2 \left[\frac{\Delta t}{T_{fm}} - 1 + \exp\left\{\frac{-\Delta t}{T_{fm}}\right\} \right] & 0 \\ 0 & 1 & 0 & \Delta t & 0 & T_{fm}^2 \left[\frac{\Delta t}{T_{fm}} - 1 + \exp\left\{\frac{-\Delta t}{T_{fm}}\right\} \right] \\ 0 & 0 & 1 & 0 & T_{fm} \left[1 + \exp\left\{\frac{-\Delta t}{T_{fm}}\right\} \right] & 0 \\ 0 & 0 & 0 & 1 & 0 & T_{fm} \left[1 + \exp\left\{\frac{-\Delta t}{T_{fm}}\right\} \right] \\ 0 & 0 & 0 & 0 & \exp\left\{\frac{-\Delta t}{T_{fm}}\right\} & 0 \\ 0 & 0 & 0 & 0 & 0 & \exp\left\{\frac{-\Delta t}{T_{fm}}\right\} \end{bmatrix} \quad (4.23)$$

The discrete-time noise strength is found with:

$$Q_{dfm}(t_i) = \int_{t_i}^{t_{i+1}} \Phi_{fm}(t_{i+1} - \tau) G_{fm}(\tau) Q_{fm}(\tau) G_{fm}^T(\tau) \Phi_{fm}^T(t_{i+1} - \tau) d\tau \quad (4.24)$$

yielding:

$$\begin{bmatrix} Q_{dfm}(1) & 0 & Q_{dfm}(2) & 0 & Q_{dfm}(3) & 0 \\ 0 & Q_{dfm}(1) & 0 & Q_{dfm}(2) & 0 & Q_{dfm}(3) \\ Q_{dfm}(4) & 0 & Q_{dfm}(5) & 0 & Q_{dfm}(6) & 0 \\ 0 & Q_{dfm}(4) & 0 & Q_{dfm}(5) & 0 & Q_{dfm}(6) \\ Q_{dfm}(7) & 0 & Q_{dfm}(8) & 0 & Q_{dfm}(9) & 0 \\ 0 & Q_{dfm}(7) & 0 & Q_{dfm}(8) & 0 & Q_{dfm}(9) \end{bmatrix}$$

These values are [12:57, 164]:

$$Q_{dfm}(1) = \sigma_{fm}^2 T_{fm} \times \quad (4.25)$$

$$\left[\frac{2\Delta t^3}{3} - 2T_{fm}\Delta t^2 - 4T_{fm}^2\Delta t \exp\left(\frac{-\Delta t}{T_{fm}}\right) + 2T_{fm}^2\Delta t - T_{fm}^3 \exp\left(\frac{-2\Delta t}{T_{fm}}\right) + T_{fm}^3 \right]$$

$$Q_{df}(2) = \sigma_{fm}^2 T_{fm} \times \quad (4.26)$$

$$\left[\Delta t^2 + 2T_{fm}\Delta t \exp\left(\frac{-\Delta t}{T_{fm}}\right) + T_{fm}^2 - 2T_{fm}^2 \exp\left(\frac{-\Delta t}{T_{fm}}\right) - 2T_{fm}\Delta t + T_{fm}^2 \exp\left(\frac{-2\Delta t}{T_{fm}}\right) \right]$$

$$Q_{df}(3) = \sigma_{fm}^2 T_{fm} [-2\Delta t \exp(-\Delta t/T_{fm}) + T_{fm} - T_{fm} \exp(-2\Delta t/T_{fm})] \quad (4.27)$$

$$Q_{df}(4) = Q_{df}(2) \quad (4.28)$$

$$Q_{df}(5) = \sigma_{fm}^2 T_{fm} \left[2\Delta t - 3T_{fm} + 4T_{fm} \exp\left(\frac{-\Delta t}{T_{fm}}\right) - T_{fm} \exp\left(\frac{-2\Delta t}{T_{fm}}\right) \right] \quad (4.29)$$

$$Q_{df}(6) = \sigma_{fm}^2 T_{fm} [1 - 2 \exp(-\Delta t/T_{fm}) + \exp(-2\Delta t/T_{fm})] \quad (4.30)$$

$$Q_{df}(7) = Q_{df}(3) \quad (4.31)$$

$$Q_{df}(8) = Q_{df}(6) \quad (4.32)$$

$$Q_{df}(9) = \sigma_{fm}^2 [1 - \exp(-2\Delta t/T_{fm})] \quad (4.33)$$

The 8-by-8 Φ_f matrix is block diagonal, with diagonal blocks of Φ_{fm} and Φ_{fa} . Similarly, the 8-by-8 Q_{df} matrix is block diagonal with Q_{dfm} and Q_{dfa} as diagonal blocks. Since the estimated position of the target (due to actual motion and apparent motion from the jitter effect) in the detector plane is the desired output, given the filter state description, the appropriate H_f matrix is $[I_{2 \times 2} \ 0_{2 \times 4} \ I_{2 \times 2}]$. Thus are the elements of the KF equations defined. The variables T_{fm} and σ_{fm} are what distinguish the various elemental filters in the MMAE and will be described as the MMAE is used in Chapter V.

The KF algorithm must start from some initial conditions. Based on these models placed into the KF equations, the initial condition for the state estimate is:

$$\hat{x}_f(t_0) = \begin{bmatrix} 3 \\ 3 \\ u_{tx}(t_0) \\ u_{ty}(t_0) \\ (1/\Delta t)[u_{tx}(t_1) - u_{tx}(t_0)] \\ (1/\Delta t)[u_{ty}(t_1) - u_{ty}(t_0)] \\ 0 \\ 0 \end{bmatrix} \quad (4.34)$$

The estimated position is the same as the starting position of the truth model in the detector plane. The initial velocity and acceleration use the actual control velocity input. These "artificial" initial conditions allow the filter to avoid harsh initial acquisition problems. Initial acquisition has been investigated before [20:9,130,145] and is not germane to

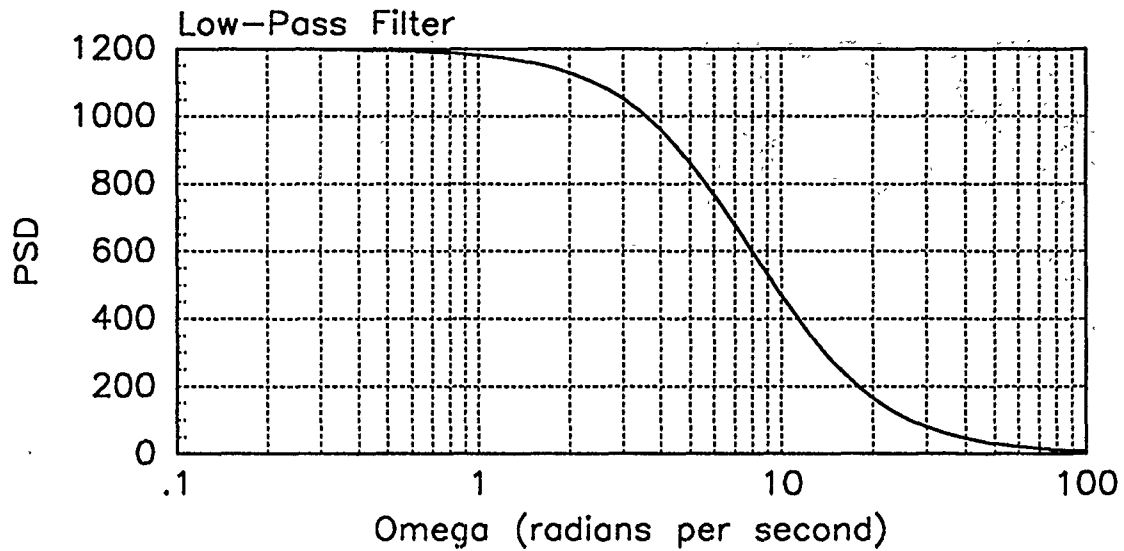


Figure 4.2. PSD Plot for the Output of a First-Order Gauss-Markov Filter. The parameters are $\sigma_f^2 = 4800 \text{ pixels}^2$ and $T_f = 0.125 \text{ seconds}$

this thesis. The initial covariance matrix is a diagonal matrix. The diagonal elements are:

$$\begin{bmatrix} P_{11} \\ P_{22} \\ P_{33} \\ P_{44} \\ P_{55} \\ P_{66} \\ P_{77} \\ P_{88} \end{bmatrix} = \begin{bmatrix} 10 \text{ pixels}^2 \\ 10 \text{ pixels}^2 \\ 2000 (\text{pixels/second})^2 \\ 2000 (\text{pixels/second})^2 \\ \sigma_{fm}^2 \\ \sigma_{fm}^2 \\ \sigma_{fa}^2 \\ \sigma_{fa}^2 \end{bmatrix} \quad (4.35)$$

The initial values for states 4 through 8 are the expected steady state values. The steady state covariance values are the variance associated with that first-order process model. The other four states are given reasonable numbers since they do not have steady state values [20:78] .

The first-order Gauss-Markov acceleration model is a low-pass filter driven by white noise as shown by the PSD plot. An example of this is given in Figure 4.2 for the case of $\sigma_f^2 = 4800 \text{ pixels}^2$ and $T_f = 0.125 \text{ seconds}$.

4.5.3 *Second-Order Gauss-Markov Acceleration Model.* The acceleration process can be modeled as a second-order process by driving a transfer function having two poles with unit-strength zero-mean white noise [7:185]. Four states for each direction are required to model the motion. A closed form solution in terms of variable Δt for $\Phi(\Delta t)$ is cumbersome so the actual numerical elements of $\Phi(\Delta t)$ for fixed Δt are evaluated via Matrix_x [2] from the transfer function and placed in the simulation software. A two-pole transfer function is selected that will model an acceleration process with an appropriate PSD selected by the researcher. This transfer function can have two real poles or a complex pair. Matrix_x is used to find a state space form with a dynamic driving matrix, $F_{2 \times 2}$, an input matrix, $G_{2 \times 1}$, and an output matrix, $H_{1 \times 2}$ from the transfer function. The 2-by-1 input matrix indicates a scalar zero-mean noise input. The strength of this noise is q . The two-state acceleration model is augmented with the position and velocity model and the model is applied to both axes yielding the eight-state state vector:

$$\mathbf{x}_{fm} = \begin{bmatrix} p_{fmx} \\ p_{fmy} \\ v_{fmx} \\ v_{fmy} \\ b_{fmx} \\ b_{fmy} \\ c_{fmx} \\ c_{fmy} \end{bmatrix} \quad (4.36)$$

where the variables b and c are the two states that together generate a scalar acceleration output. The $F_{8 \times 8}$ is:

$$F_{8 \times 8} = \begin{bmatrix} 0 & 1 & 0 & 0 & 0 & 0 & 0 & 0 \\ 0 & 0 & 0 & 1 & 0 & 0 & 0 & 0 \\ 0 & 0 & 0 & 0 & H_{11} & 0 & H_{12} & 0 \\ 0 & 0 & 0 & 0 & 0 & H_{11} & 0 & H_{12} \\ 0 & 0 & 0 & 0 & F_{11} & 0 & F_{12} & 0 \\ 0 & 0 & 0 & 0 & 0 & F_{11} & 0 & F_{12} \\ 0 & 0 & 0 & 0 & F_{21} & 0 & F_{22} & 0 \\ 0 & 0 & 0 & 0 & 0 & F_{21} & 0 & F_{22} \end{bmatrix} \quad (4.37)$$

where the subscript count is the matrix position, row and column, of $F_{2 \times 2}$ and $H_{1 \times 2}$. Then $\Phi(\Delta t) = \exp\{(1/\Delta t)F\}$ is used to find the state transition matrix. The $G_{8 \times 2}$ is made from the elements of $G_{2 \times 1}$ as:

$$G_{8 \times 2} = \begin{bmatrix} 0_{4 \times 2} \\ G_{11} & 0 \\ 0 & G_{11} \\ G_{21} & 0 \\ 0 & G_{21} \end{bmatrix} \quad (4.38)$$

The dynamics driving noise is now a vector with the covariance matrix, $Q_{2 \times 2}$. The acceleration process is modeled independently on each axis so this matrix is diagonal. The diagonal terms, one for each the x and y direction, are input from the researcher for each simulation. This matrix is given as:

$$Q_{2 \times 2} = \begin{bmatrix} q_x & 0 \\ 0 & q_y \end{bmatrix} \quad (4.39)$$

Rather than perform the integral to find the discrete-time noise strength matrix, $Q_{d8 \times 8}$, an approximation is used [7:359]:

$$Q_d \simeq \frac{1}{2} \left[\Phi(\Delta t) G Q_f G^T \Phi^T(\Delta t) + G Q G^T \right] \Delta t \quad (4.40)$$

Augmentation with the atmospheric states is done for Φ_f and Q_{df} . The proper H_f matrix is $[I_{2 \times 2} \ 0_{2 \times 6} \ I_{2 \times 2}]$. Thus, all the elements of the KF equations are given.

The initial estimate of the state vector is:

$$\hat{x}_f = \begin{bmatrix} 3 \\ 3 \\ u_{tx}(t_0) \\ u_{ty}(t_0) \\ \hat{b}_{fmx0} \\ \hat{b}_{fmy0} \\ \hat{c}_{fmx0} \\ \hat{c}_{fmy0} \\ 0 \\ 0 \end{bmatrix} \quad (4.41)$$

$$\hat{b}_{fmx0} = [H_{11} / (H_{11}^2 + H_{12}^2)] (1/\Delta t) [u_{tx}(t_1) - u_{tx}(t_0)] \quad (4.42)$$

$$\hat{b}_{fmy0} = [H_{11} / (H_{11}^2 + H_{12}^2)] (1/\Delta t) [u_{ty}(t_1) - u_{ty}(t_0)] \quad (4.43)$$

$$\hat{c}_{fmx0} = [H_{12} / (H_{11}^2 + H_{12}^2)] (1/\Delta t) [u_{tx}(t_1) - u_{tx}(t_0)] \quad (4.44)$$

$$\hat{c}_{fmy0} = [H_{12} / (H_{11}^2 + H_{12}^2)] (1/\Delta t) [u_{ty}(t_1) - u_{ty}(t_0)] \quad (4.45)$$

where the H terms are the elements of the $H_{1 \times 2}$ determined by the matrix analysis package from the transfer function model for the acceleration. The initial x-direction acceleration, $a_{fmx0} = (1/\Delta t) [u_{tx}(t_1) - u_{tx}(t_0)]$, is the same as described in Equation (4.34) and similarly for a_{fmy0} . The states b and c together with the output matrix $H_{1 \times 2}$ generate the scalar acceleration output. For example, for the x-axis:

$$a_{fmx} = H_{11} \hat{b}_{fmx} + H_{12} \hat{c}_{fmx} \quad (4.46)$$

$$= H_{11} [H_{11} / (H_{11}^2 + H_{12}^2)] a_{fmx} + H_{12} [H_{12} / (H_{11}^2 + H_{12}^2)] a_{fmx} \quad (4.47)$$

$$= a_{fmx} \quad (4.48)$$

and similarly for the y-axis. The initial covariance is block diagonal. The diagonal elements are:

$$\begin{bmatrix} P_{11} \\ P_{22} \\ P_{33} \\ P_{44} \\ P_{55} & P_{56} & P_{57} & P_{58} \\ P_{65} & P_{66} & P_{67} & P_{68} \\ P_{75} & P_{76} & P_{77} & P_{78} \\ P_{85} & P_{86} & P_{87} & P_{88} \\ P_{99} \\ P_{00} \end{bmatrix} = \begin{bmatrix} 10 \\ 10 \\ 2000 \\ 2000 \\ P_{bbx} & 0 & P_{bcx} & 0 \\ 0 & P_{bby} & 0 & P_{bcy} \\ P_{bcx} & 0 & P_{ccx} & 0 \\ 0 & P_{bcy} & 0 & P_{ccy} \\ \sigma_{fa}^2 \\ \sigma_{fa}^2 \end{bmatrix} \quad (4.49)$$

where:

$$P_{bcx} = \frac{[-2F_{11}F_{22}G_{11}G_{21} + F_{22}F_{21}q_x^2 + F_{11}F_{12}q_xG_{21}^2]}{[-2F_{21}F_{12}F_{22} + F_{11}^2F_{22} + F_{22}^2F_{11} - F_{11}F_{12}F_{21}]} \quad (4.50)$$

$$P_{bbx} = [1/F_{11}] [q_xG_{11}^2 - 2F_{12}P_{bcx}] \quad (4.51)$$

$$P_{ccx} = [1/(2F_{22})] [-q_xG_{21}^2F_{21}P_{bcx}] \quad (4.52)$$

$$P_{bcy} = \frac{[-2F_{11}F_{22}G_{11}G_{21} + F_{22}F_{21}q_y^2 + F_{11}F_{12}q_yG_{21}^2]}{[-2F_{21}F_{12}F_{22} + F_{11}^2F_{22} + F_{22}^2F_{11} - F_{11}F_{12}F_{21}]} \quad (4.53)$$

$$P_{bby} = [1/F_{11}] [q_yG_{11}^2 - 2F_{12}P_{bcy}] \quad (4.54)$$

$$P_{ccy} = [1/(2F_{22})] [-q_yG_{21}^2F_{21}P_{bcy}] \quad (4.55)$$

The initial values for the terms given by Equations (4.50) to (4.55) and P_{99} and P_{00} are the expected steady state values. For the states based on second-order models, the steady state covariance values are found by solving:

$$\dot{P}_{2 \times 2}(t) = F_{2 \times 2}P_{2 \times 2}(t) + P_{2 \times 2}(t)F_{2 \times 2}^T + G_{2 \times 1}Q_{2 \times 2}G_{2 \times 1}^T = 0 \quad (4.56)$$

where the subscript 2x2 denotes calculating for two-state acceleration process only, not the entire $P_{10 \times 10}$ that is calculated in the KF equations.

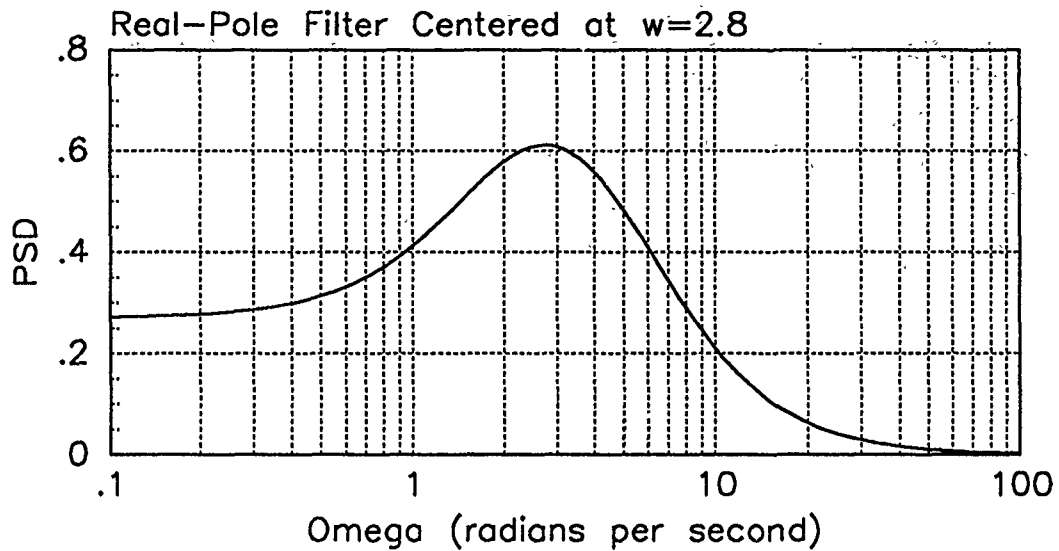


Figure 4.3. PSD Plot for the Output of a Real-Pole Filter. The poles are at 2.0222 and 5.0.

The second-order filter is a bandpass filter as shown by the PSD plot for the output acceleration. An example of this for a filter based on transfer function with two real poles at 2.0222 and 5.0 is given in Figure 4.3. An example of this for a filter based on transfer function with a complex pair of poles at $-.56 \pm j.2743$ is given in Figure 4.4.

4.6 Template Generation

The array, $D(t_i)$, defined in Equation (4.1), is incorporated into the averaging process along with the template $S(t_{i-1})$ to form the new template $S(t_i)$. After the measurement update, the location of the center of the intensity profile in the x direction is the sum of states $\hat{p}_{fmx}(t_i^+)$ and $\hat{p}_{fax}(t_i^+)$, and similarly for the y direction. This sum is used to translate the intensity profile in the $D(t_i)$ array so it is centered in the array and can be incorporated into the template where all previous inputs to the template were centered. The translation is actually accomplished as a phase shift in the Fourier domain [16:151].

The template is used to give the filter a picture of what the intensity profile looks like for this target, in what ever orientation it appears. The data used by the filter is noise corrupted. By averaging several (up to 10) arrays of centered intensity profile data, the random noise that is quickly changing between each time increment will be reduced, while

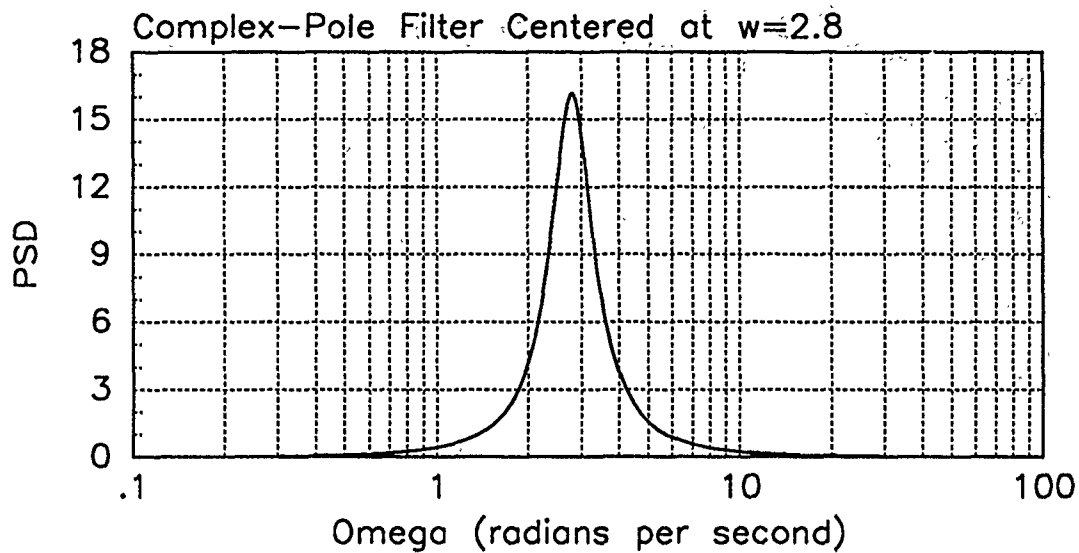


Figure 4.4. PSD Plot for the Output of a Complex Pole Filter. The poles are at $-.56 \pm j.2743$.

the target intensity pattern will not be, assuming the target shape function changes at a slower rate. Instead of storing a number of arrays of data to form a true average of the most recent N sets of intensity profiles, an exponential smoothing algorithm is used. This algorithm is:

$$S(t_i) = \alpha_s D(t_i) + (1 - \alpha_s) S(t_{i-1}) \quad (4.57)$$

The value of the template smoothing coefficient α_s is 1 divided by the time increment, i , $i = 1, 2, 3, \dots$, until α_s reaches 0.1. Thereafter, the algorithm is essentially averaging the previous 10 arrays of data and only the $S(t_{i-1})$ array is stored rather than all 10 previous arrays. Selection of α_s is based on work by Millner [12:101,150].

4.7 Summary

This chapter described the enhanced correlator and how it defines a measurement vector that allows use of a linear update model. The standard linear KF update and propagation equations needed for this simulation were presented. Then the filter models were developed to generate the matrices required in the KF algorithm, including the initial conditions. Finally, the template used in the enhanced correlator was described. The parameters used for the models discussed in this chapter are compiled in Appendix A.

V. Performance Evaluation

5.1 Introduction

The truth model is described in Chapter III. This is the model of the real world that creates the inputs for the MMAE. Chapter IV presents the dynamics models for the acceleration and atmospheric processes that are placed in the estimator. This chapter describes the actual MMAEs tested and how they perform.

Two kinds of MMAEs are of interest here, one with elemental KFs based on first-order Gauss-Markov models for acceleration. This has been investigated in various forms before [6, 14, 20, 5]. The second MMAE has a mix of elemental filters, some based on first-order Gauss-Markov acceleration models, and some based on second-order Gauss-Markov acceleration models. A Monte Carlo analysis is done for each MMAE so comparisons can be made on the performance potential of each.

The Monte Carlo analysis technique is described. Several MMAEs are designed. First, the elemental filters are mixed, that is some are based on first-order acceleration models and others on second-order models. The results of the Monte Carlo study for each MMAE are presented and comparisons are made. Then in Chapter VI, the MMAEs are such that all elemental filters are based on a first-order acceleration model. This provides a basis of comparison, in order to assess the fundamental advantages and disadvantages of second-order versus first-order acceleration models, i.e., of acceleration models with overlapping versus nonoverlapping PSD frequency content, in the elemental filters of a MMAE algorithm.

5.2 Monte Carlo Study

The performance of the MMAEs is evaluated by calculating the errors committed by the filter in estimating the states. The error is the estimate from the MMAE minus the state from the truth model. The model for atmospheric jitter is stochastic. Therefore, the ensemble statistics of that error are needed to evaluate the filter performance. For this thesis, a Monte Carlo study is accomplished to get these values. In a Monte Carlo study, many samples of the error are simulated and the sample statistics are computed [7:329].

An infinite number of samples are required to get the true statistics of the stochastic process model. However, usually a smaller number of samples will converge to a value that is close to the true value. Previous students [11:43][3:28][1:26,33] have investigated what this smaller number should be. They selected 20 as showing convergence. Considering the much longer individual runs required in this thesis (for the jinking trajectory), 10 runs showed acceptable convergence and still allowed reasonable run times.

The mean error is calculated as [19:V-3]:

$$\bar{E}(t_i) = 1/N \sum_{n=1}^N [x_t(t_i) - \hat{x}_f(t_i)] = 1/N \sum_{n=1}^N e(t_i) \quad (5.1)$$

with the variance given by:

$$\sigma^2(t_i) = \frac{1}{N-1} \sum_{n=1}^N e^2(t_i) - \frac{N}{N-1} \bar{E}^2(t_i) \quad (5.2)$$

The number of runs in a Monte Carlo study, N , is 10. The mean error is $\bar{E}(t_i)$ while the error for one run of the Monte Carlo study at one time, t_i , is $e(t_i)$. Possible values of the generic true and filter-computed variables x_t and x_f are shown in Table 5.1. The variables of primary interest are the position of the target and position of the centroid in the detector plane. The velocity and atmospheric data were used to investigate the software. Error statistics are kept at each t_i^- and t_i^+ and for each the x and y directions in the detector plane. The statistics are presented in two forms, a temporal average from 0.5 seconds to the end of the run or a plot of the data versus t_i . The average is started at a half second so the initial transients do not affect the averages. Plots are available for:

Table 5.1. Errors Kept by the Simulation Software.

Error	Calculation
Actual Position of the Target	$p_{fm} - x_{tm}$
Position of the Centroid	$(p_{fm} + p_{fa}) - y_t$
Velocity of the Target	$v_{fm} - u_t$
Apparent Position due to Atmospherics	$p_{fa} - (x_{ta1} + x_{ta2})$

1. True RMS error versus filter-computed RMS error for the actual position of the target. The true RMS error is described above. The filter-computed RMS error is the square root of the appropriate diagonal terms, P_{11} and P_{22} , of the covariance matrix, P , as computed with Equations (4.5) and (4.8). Such plots allow for assessment of how well tuned the filters are.
2. Mean error, \pm one standard deviation, plotted at t_i^- . These include plots of the actual position of the target and the position of the centroid. The data on the actual position represents the tracking performance of the MMAE since it is used for pointing the center of the FOV for the subsequent sample period. The centroid error indicates the effectiveness of the target intensity template identification [20:83].
3. Mean error, \pm one standard deviation, plotted at t_i^+ . This is presented for the actual position of the target only and represents the highest level of precision in target tracking.

Temporal average values are computed for 2 and 3 only. Such temporal averages are useful for sensitivity studies or other comparisons for which entire time histories of statistics would be somewhat unwieldy to use.

The plots are presented in the appendices due to the large number that has resulted from this thesis. Each appendix is devoted to one particular MMAE, as will become evident when the MMAEs are discussed. The temporal averages for the individual studies are presented in tabular form with the respective plots in the appendices. These temporal averages are also tabulated in the main text at points where comparisons between MMAEs are done or sensitivity studies are analyzed.

Also available from each Monte Carlo study is information on the magnitude of $r_k^T(t_i)r_k(t_i)$, $r_k^T(t_i)A_k^{-1}(t_i)r_k(t_i)$, the leading coefficient of the p_k calculation, and the time history of the p_k calculation. Recall from Section 1.3.3 that the relative magnitudes of first three terms determine which elemental filter will have the largest p_k assigned. This probability calculation is one of several characteristics of the MMAE algorithm being investigated in this thesis to determine how best to help the MMAE select the correct elemental filter for tracking a particular target. To aid this investigation, these terms are

presented. The probability time histories are presented as a plot for each study. This plot is for the first run of each 10-run Monte Carlo study rather than a mean plot over the 10 runs as with the error plots. This is discussed in Appendix B and the probability time history plots for all 10 runs in four Monte Carlo studies are presented along with the time history of the mean. The probability plot will appear in the chapter text since there are fewer of them and filter selection is important for this initial look at elemental filters based on second-order models. If the Monte Carlo study is done for a trajectory with nonvarying parameters, a temporal average of each $\mathbf{r}_k^T(t_i)\mathbf{r}_k(t_i)$ and $\mathbf{r}_k^T(t_i)\mathbf{A}_k^{-1}(t_i)\mathbf{r}_k(t_i)$ is calculated and then an average over the 10 runs in the study is determined. These average values for $\mathbf{r}_k^T(t_i)\mathbf{r}_k(t_i)$ and $\mathbf{r}_k^T(t_i)\mathbf{A}_k^{-1}(t_i)\mathbf{r}_k(t_i)$ for each elemental filter in the MMAE is presented in tabular form in the appendix with the appropriate error plots. If the trajectory has varying parameters, time histories of $\mathbf{r}_k^T(t_i)\mathbf{r}_k(t_i)$, $\mathbf{r}_k^T(t_i)\mathbf{A}_k^{-1}(t_i)\mathbf{r}_k(t_i)$, and the leading coefficient for each elemental filter are presented. These time histories are presented in plot form in the appendices with the appropriate error plots. Recall that temporal averages are presented for position errors no matter what the trajectory type. The distinction between trajectory types is not made because position error is based on the estimate from the MMAE, not from the individual elemental filters. The MMAE is not expected to have its position errors increase due to a maneuver during the six second simulation, it just selects another elemental filter and continues tracking. A trajectory with nonvarying parameters is one for which the A and ω of v_y in Equation (3.2) (page 3-3) do not change over the 6 second run. The trajectory with varying parameters is called the jinking trajectory and is created with concatenated 2-second increments of Equation (3.2) to simulate a maneuvering target.

5.3 Initial Look at Real-Pole MMAE

The first second-order filter investigated is the filter based on an acceleration model with two real poles. Manned aircraft will show a range of frequency content for acceleration. A cargo plane traveling straight and level will have an acceleration that shows power in a PSD below a cutoff of 0.25 radians per second ($T_{fm} = 4$ seconds). The subscript, fm , refers to the filter motion dynamics as is used in Equation (4.21). An air superiority craft pulling evasive maneuvers can show power at frequencies greater than a cutoff of 0.6 to 0.8

radians per second. Manned craft should show no power content above a frequency cutoff of about 2.5 radians per second [10]. This readily translates to three elemental filters. One is based on an acceleration model that is a low-pass filter with cutoff at 0.25 radians per seconds. It is referred to as the "benign" filter. This is the same benign filter used by previous investigations [20:69][5:67]. The second, called the "intermediate" filter, is second-order and centered between 0.25 and 0.8 radians per second. The last, the "harsh" filter, is centered between about 0.6 and 2.5 radians per second. Within these rough limits, filters based on acceleration models with two real poles are created. These filters are also referred to as "real-pole" filters.

The transfer function, $G(s)$, describing the acceleration model that is the basis for the intermediate filter is:

$$G(s) = \frac{1.715(s + 0.1768)}{(s + 1.4305)(s + 0.3531)} \quad (5.3)$$

The transfer function describing the acceleration model that is the basis for the harsh filter is:

$$G(s) = \frac{5.2(s + 1.0111)}{(s + 2.0222)(s + 5)} \quad (5.4)$$

The elemental filter is created as detailed in Chapter IV. It now must be tuned.

Calling a filter "tuned" is accomplished based on:

1. the true RMS error versus filter-computed RMS error. A tuned filter for an MMAE should have a plot showing the filter-computed RMS error with the same value as the true RMS error.
2. the mean error plot after update (at t_i^+). The error should be zero-mean and show no signs of the trajectory.
3. filter selection through computed p_k values in the MMAE algorithm. If the dynamics driving noise is too high, model "goodness" can be masked, and an inappropriate filter can "take the job" for which another elemental filter is *more appropriately* designed. Filter selection is one of the criteria for determining a successful model in this initial study of the second-order model based filter.

....

Tuning is accomplished by varying the value of the σ_{fmx} and σ_{fmy} in Equation (4.21) for the first-order models or the q_x and q_y in Equation (4.39) for the second order models. One can also change the measurement noise, but that was not accomplished at this juncture since the measurement precision is assumed well known for this application. The tuning value for both the x and y direction are kept the same so the x and y subscripts are dropped. Allowing the diagonal elements to be different would fill the role of the rectangular FOV that Tobin studied [20:8] or the directionally tuned filters that Norton investigated [15]. Two elemental filters would result, one expecting a maneuver in the x direction, and one expecting the maneuver in the y direction. This is not accomplished in order to keep the number of elemental filters small and so aid understanding the filter selection.

In order to tune these filters *created* with an acceleration model having a particular frequency range in mind, a trajectory showing an acceleration with that frequency is used. The trajectory described in Equation (3.2) is used. The three trajectories used to investigate the real-pole MMAE are shown in Table 5.2. These three trajectories are called basic to this MMAE because they are the frequencies about which the PSDs of the elemental filter models are centered. The PSD plots are in Figure 5.1. A plot of the y-direction of these trajectories in the detector plane is shown in Figure 5.2.

A tuned value of q is selected for each real-pole elemental filter by tracking the appropriate trajectory of Table 5.2 with the appropriate elemental filter only and checking the tuning criteria mentioned above. The benign filter is assumed tuned with the same value for σ that was used by previous studies [20:69][5:67]. Recall that q for the first-order Gauss-Markov filter is $(2\sigma^2)/T$. The elemental filters are called tuned with $\sigma_b^2 = 250$ ($q_b = 125$) for the benign filter, $q_i = 2000$ for the intermediate filter, and $q_h = 29000$ for the harsh filter. The subscripts, b , i , and h , will refer to the benign, intermediate, and harsh

Table 5.2. Trajectories Used to Evaluate the Real-Pole MMAE.

Trajectory	Amplitude	Omega	Bias	ϕ
Benign	9 meters	0.01 radians per second	0 meters	0 degrees
Intermediate	9 meters	0.62 radians per second	0 meters	0 degrees
Harsh	9 meters	2.8 radians per second	0 meters	0 degrees

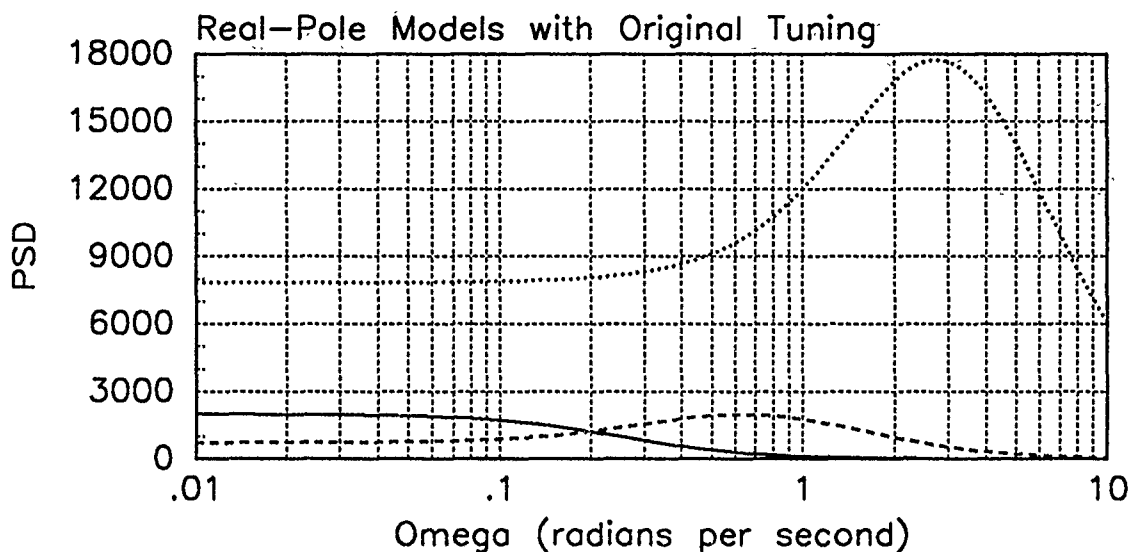


Figure 5.1. PSD Plot; Real-Pole MMAE-O

elemental filters of whatever MMAE is currently being discussed. (Recall the tuning values are the same for both the x and y directions.) The units of the strength of the dynamics driving noise, q , is pixels² per seconds⁵. A PSD plot of the three acceleration models in the tuned, real-pole MMAE is in Figure 5.1. The -O refers to the tuning technique used: original. Note the peak of the PSD for the harsh filter is at 2.8 radians per second which is a little above the 2.5 radians per second desired above.

The MMAE is allowed to track the same three target trajectories one at a time and sort out which elemental filter is best for the job. At this point, the hypothesis probability calculation is done as with Equation (2.13). This is referred to as a probability calculation (PC) type 1. (This will be explained further in Section 5.8.) A plot of the probability assigned to each elemental filter for each of the trajectories is shown in Figure 5.3.

The error plots are in Figures C.1 through C.9. These error plots come in sets of three pages:

1. The two plots of the first page show the filter-computed RMS error and the actual RMS error for the x- and y-directions. The actual RMS error is the solid line. The filter-computed RMS error is the dashed line that appears as a band. The band is due to the increase in error during the propagation cycle and then the drop in magnitude after the measurement update.

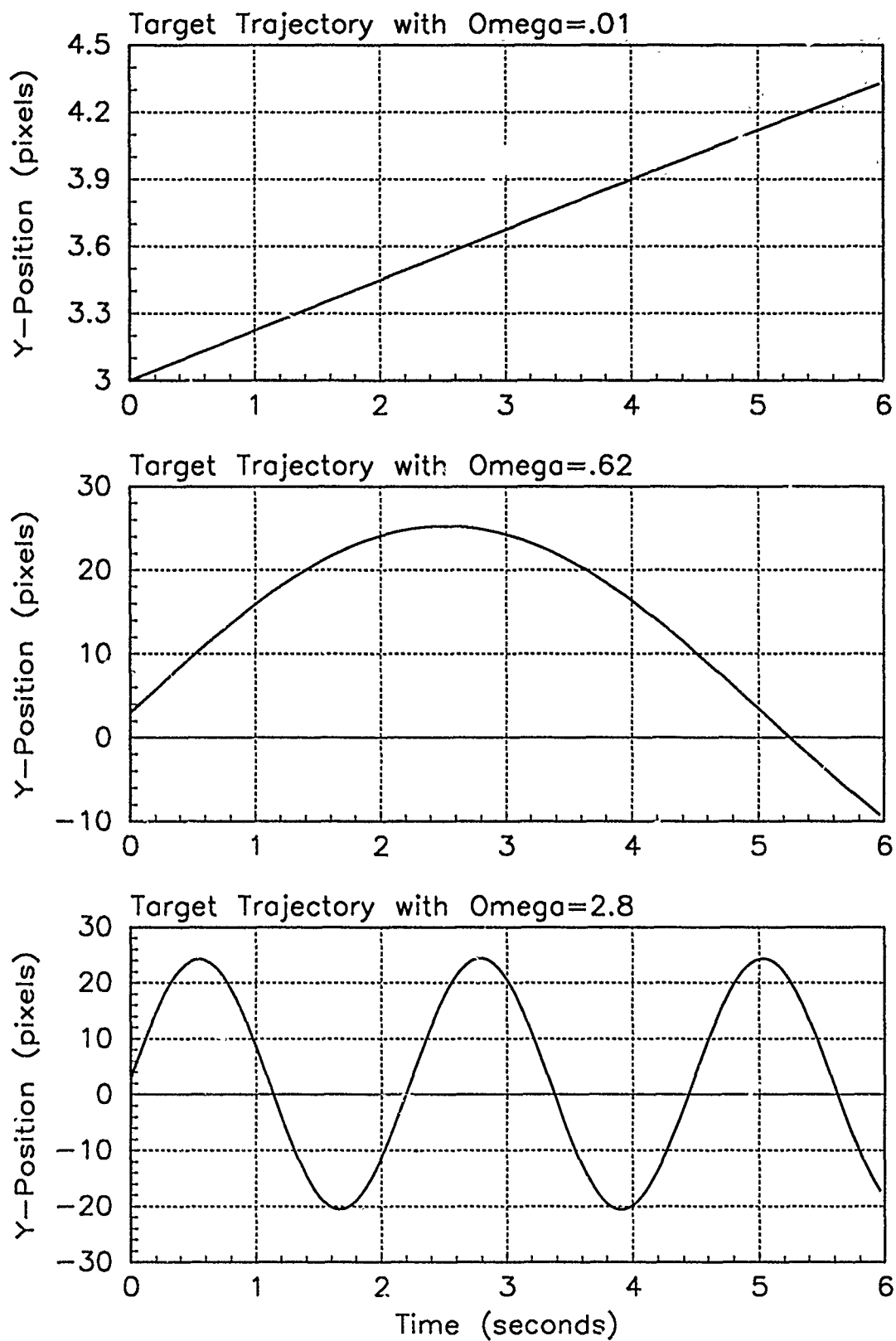


Figure 5.2. Target Position; Detector Plane; Sinusoidal Trajectories with Various Frequencies.

2. The next page has three plots. The first is the x-position error at t_i^- ; the second is x-position error at t_i^+ . The centroid error is presented in the third plot. In each, the mean error is the solid line bounded by the mean $\pm\sigma$ dashed lines.
3. The third page shows the same plots as the second but for errors in the the y direction of the detector plane.

The temporal averages of the information in the plots is presented in Tables C.1 through C.3 appearing on the first page of the appropriate set of plots. Also, the temporal average of $\mathbf{r}_k^T(t_i)\mathbf{r}_k(t_i)$ and $\mathbf{r}_k^T(t_i)\mathbf{A}_k^{-1}(t_i)\mathbf{r}_k(t_i)$ are presented. The MMAE should select the elemental filter with the smallest squared residual value, $\mathbf{r}_k^T(t_i)\mathbf{r}_k(t_i)$. The $\mathbf{r}_k^T(t_i)\mathbf{A}_k^{-1}(t_i)\mathbf{r}_k(t_i)$ is the term in the exponential for the calculation of p_k as in Equation (1.1) (page 1-8). The temporal averages for $\mathbf{r}_k^T(t_i)\mathbf{r}_k(t_i)$ and $\mathbf{r}_k^T(t_i)\mathbf{A}_k^{-1}(t_i)\mathbf{r}_k(t_i)$ are over each run in the Monte Carlo study then averaged over the 10 runs in the study.

From the probability plots in Figure 5.3 we see that the benign filter is selected by the MMAE to track both the benign and intermediate trajectories. Also, the intermediate filter is predominantly selected to track the harsh trajectory. Since the benign filter is the only elemental filter contributing to the MMAE estimate, the RMS error plots for the benign (Figure C.1) and intermediate (Figure C.4) trajectories show the benign filter to be conservatively tuned for both trajectories. The x- (Figure C.2 and Figure C.5) and y-position (Figure C.3 and Figure C.6) error plots show no unacceptable trends or magnitudes. The tracking is deemed adequate, except the "wrong" filter is selected for the intermediate trajectory. Indeed, the elemental filter with the smallest average $\mathbf{r}_k^T(t_i)\mathbf{r}_k(t_i)$ is selected by the MMAE to do most of the tracking. The intermediate and harsh filters have averages very close in magnitude when the MMAE is tracking the harsh trajectory; thus is seen the inability of the MMAE to select one clearly. Note, the harsh filter has the smallest average $\mathbf{r}_k^T(t_i)\mathbf{A}_k^{-1}(t_i)\mathbf{r}_k(t_i)$ no matter the trajectory.

The RMS error plots for the harsh trajectory in Figure C.7 show a filter-computed band at a greater average magnitude than for the benign and intermediate cases due to the increased dynamics noise strength contributed by both the intermediate and harsh filters. The ripple look to the band is due to filter selection almost switching between the interme-

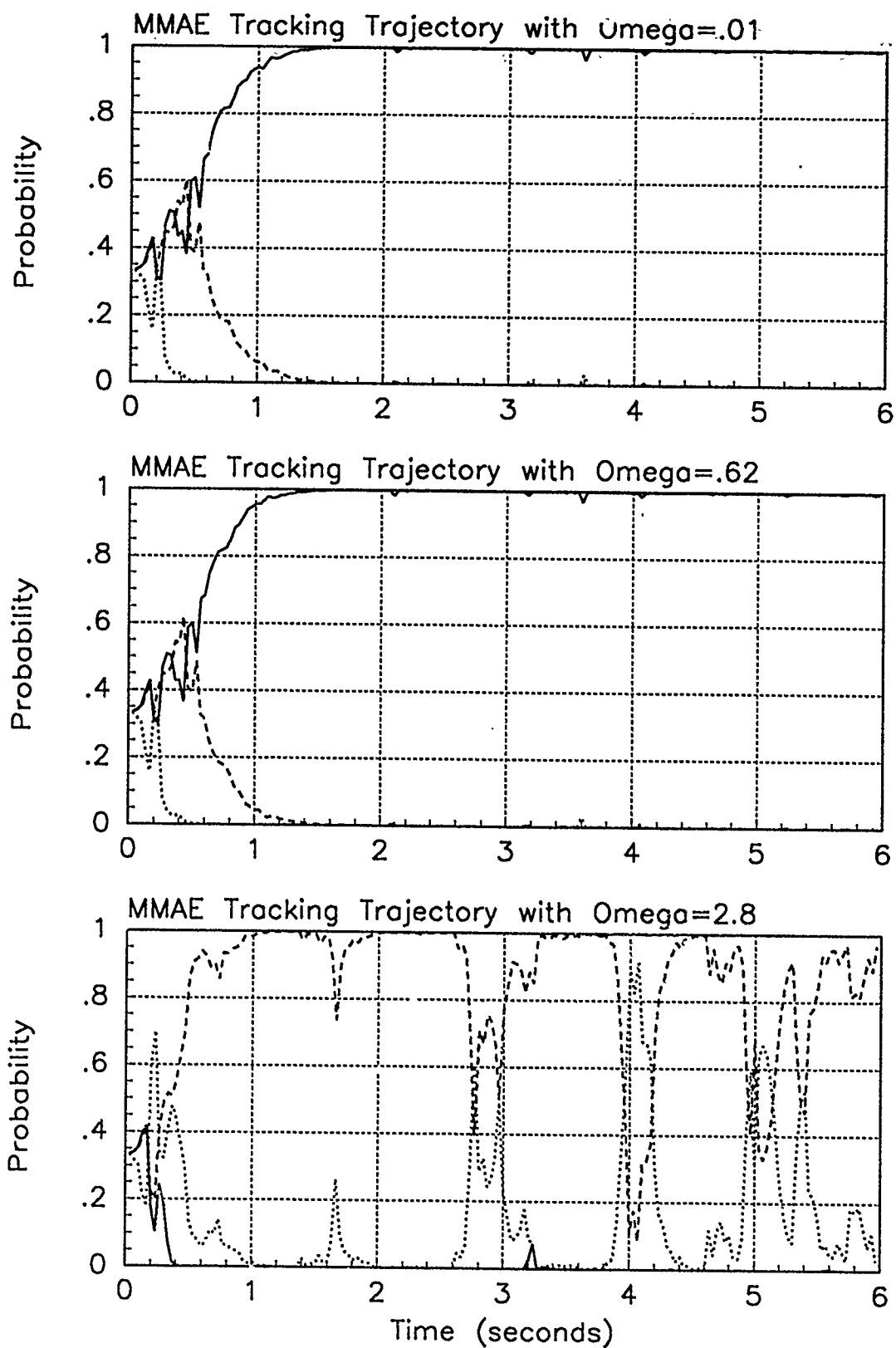


Figure 5.3. Probability Plots; Real-Pole MMAE-O; PC is 1; Basic Trajectories. Benign filter has solid line; intermediate filter has dashed line; harsh filter has dotted line.

diated and harsh filters. Some of the trajectory is still evident in the y-position error plots in Figure C.9. The magnitude of the t_i^- versus t_i^+ plots dramatically demonstrate the effect of the filter update cycle that corrects the estimate. In this case, the intermediate filter is incapable of predicting the harsh trajectory propagation, and the peak error magnitudes are almost 1 pixel in the t_i^- . The measure update brings the errors back down to below 0.5 pixels at t_i^+ . The temporal average statistics remain of small magnitude, 0.03 pixels for x- and 0.02 pixels for y-position error, because the trends in the y-positions errors are sinusoidal about a zero-mean. The slightly larger x-position error should not be due to the expected bias due to the truth model determining position based on the target center of mass and the MMAE tracking the center of intensity. The magnitude is much smaller than the expected 0.8 pixels (page 3-12).

5.4 Initial Look at Notch Filters

Filter selection for the real-pole MMAE was not what was desired. The benign filter tracked targets with the benign *and* intermediate trajectories. The intermediate filter tracked the harsh trajectory. The inappropriate filter selection could be due to the overlapping PSD plots shown in Figure 5.1. The potential for overlap is inherent in a real-pole model when the dynamics driving noise strength is as high as was deemed necessary. Therefore, a notch filter is designed. If dynamics driving noise strengths of these magnitudes are necessary for tracking performance, the notch filter can yield almost no PSD overlap and should help the MMAE sort out the low-frequency end of the filters.

The notch filter is based on an acceleration represented as the output of a white-noise-driven linear model with the transfer function:

$$G(s) = \frac{ks}{s^2 + 2\zeta\omega_t s + \omega_t^2} \quad (5.5)$$

where ζ is 0.2 and ω for the intermediate and harsh filters are 0.62 and 2.8 radians per second, respectively. The value of k is 1 and 4.5 for the intermediate and harsh filters, respectively. The small ζ gives minimal overlap of the PSD plots for the benign and intermediate filters. The ω 's selected center the notch filters at the same frequencies as the

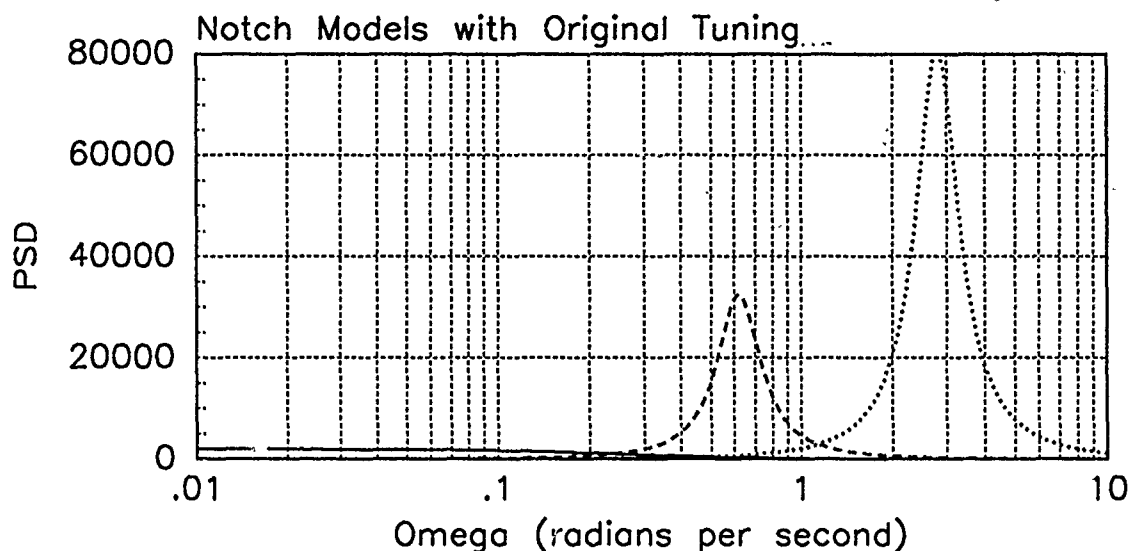


Figure 5.4. PSD Plot; Notch MMAE-10

real pole filters are centered. These are tuned in the same manner as the real-pole filters. Tuning values used are $\sigma_b^2 = 250$ for the benign filter, $q_i = 2000$ for the intermediate filter and $q_h = 5000$ for the harsh filter. The resulting set of PSD plots is in Figure 5.4. The -10 refers to the *first* notch MMAE (with the intermediate filter at $\omega = 0.62$ radians per second) tuned in the *original* manner.

The MMAE with the benign filter and these two notch filters is allowed to track the three trajectories in Table 5.2. The probability plots are in Figure 5.5. The error plots are in Figures D.1 through D.9. The temporal averages of the mean position errors and the averages of $\mathbf{r}_k^T(t_i)\mathbf{r}_k(t_i)$ and $\mathbf{r}_k^T(t_i)\mathbf{A}_k^{-1}(t_i)\mathbf{r}_k(t_i)$ are presented in Tables D.1 through D.3.

As with the real-pole MMAE, the probability time history plots (Figure 5.5) show the benign and intermediate trajectories are tracked by the benign filter. The harsh filter does eventually get the harsh trajectory from the intermediate filter. The time of the transfer, 1.4 seconds, does not correspond to any obvious feature of the trajectory at that point (Figure 5.2). The velocity and acceleration magnitudes are about the same at this time as at 0.3 and 0.8 seconds in this sinusoidal motion. In fact, 0.3 seconds is about when the initial filter selection is sorted out and the *intermediate* one is selected. So velocity or acceleration magnitude does not seem to drive the residuals.

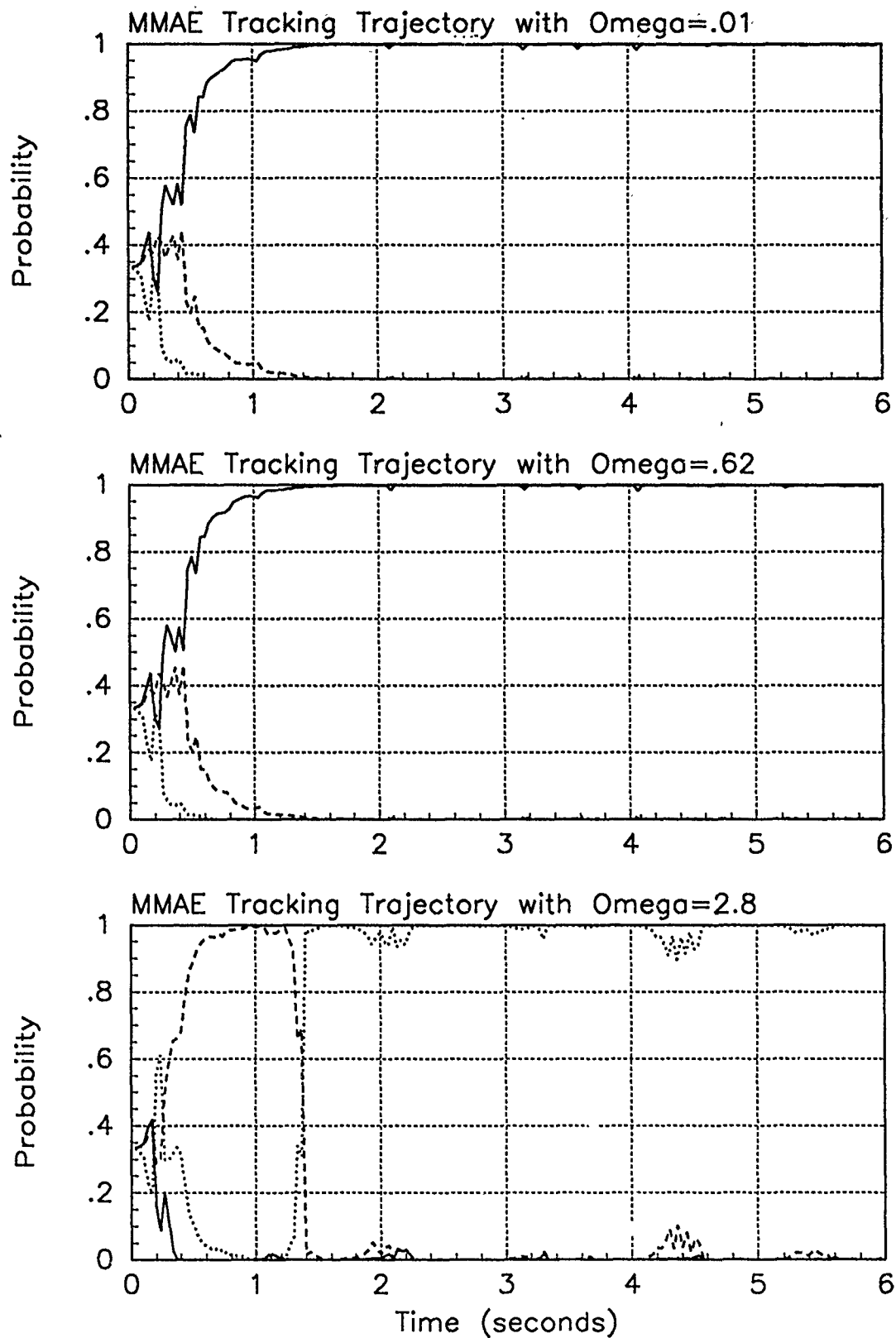


Figure 5.5. Probability Plots; Notch MMAE-10; PC is 1; Basic Trajectories. Benign filter has solid line; intermediate filter has dashed line; harsh filter has dotted line.

The x- and y-position error plots look about the same as the plots from the real-pole MMAE-O, as would be expected since the same elemental filter did the tracking. The filter-computed RMS error plot for the harsh trajectory in Figure D.7 shows less of the ripple, with only one bump at the only filter selection change at 1.4 seconds. The width of the band and its average magnitude are about the same as for the real-pole MMAE-O (Figure F.7). The x-position error plots look very similar. The y-position error plots in Figure D.9 lose the sinusoid of the trajectory after the MMAE selects the harsh filter at 1.4 seconds. This does not result in a reduction in corresponding temporal average. In fact, the average error increased for each y-position error listed in Table C.3 and Table D.3. The standard deviations remain about the same.

5.5 Alternative Approach to Tuning

Again, the filter selection is not what was expected. This time the tuning process is reviewed. The strength of the dynamics driving noise of the filter, q , is changed for each tuning run. This results in a different average value of $\mathbf{r}_k^T(t_i)\mathbf{r}_k(t_i)$ and $\mathbf{r}_k^T(t_i)\mathbf{A}_k^{-1}(t_i)\mathbf{r}_k(t_i)$ for each run. A plot of q versus $\mathbf{r}_k^T(t_i)\mathbf{r}_k(t_i)$ and q versus $\mathbf{r}_k^T(t_i)\mathbf{A}_k^{-1}(t_i)\mathbf{r}_k(t_i)$ is made as in Figure 5.6. This example is for tuning the harsh filter while it is tracking the harsh trajectory. Since it is desired that the MMAE choose the elemental filter with the smallest $\mathbf{r}_k^T(t_i)\mathbf{r}_k(t_i)$ (see Section 1.3.3), a reasonable value to select for q_h is the one with the smallest $\mathbf{r}_k^T(t_i)\mathbf{r}_k(t_i)$, $q_h = 400 \text{ pixels}^2 \text{ per seconds}^5$. This is an order of magnitude smaller than that selected in the ad hoc manner. Similar plots are made for the intermediate filter tracking the intermediate trajectory and the benign filter tracking the benign trajectory. For the real-pole MMAE, the new tuning values are $\sigma_b^2 = 150$, $q_i = 500$, $q_h = 4000$. The new values are $\sigma_b^2 = 150$ ($q_b = 75$), $q_i = 75$, and $q_h = 400$ for the notch MMAE. New PSD plots based on the revised tuning values are in Figure 5.7. The -R signifies the tuning is done with the *revised* method. For the remainder of the thesis, tuning is done with this revised method. For the real-pole models, the amount by which the harsh model overlaps the PSD of the other models is less than that resulting from the original tuning (Figure 5.1). However, the overlap is still significant. Overlap seems essentially nonexistent in the notch filter PSD plots.

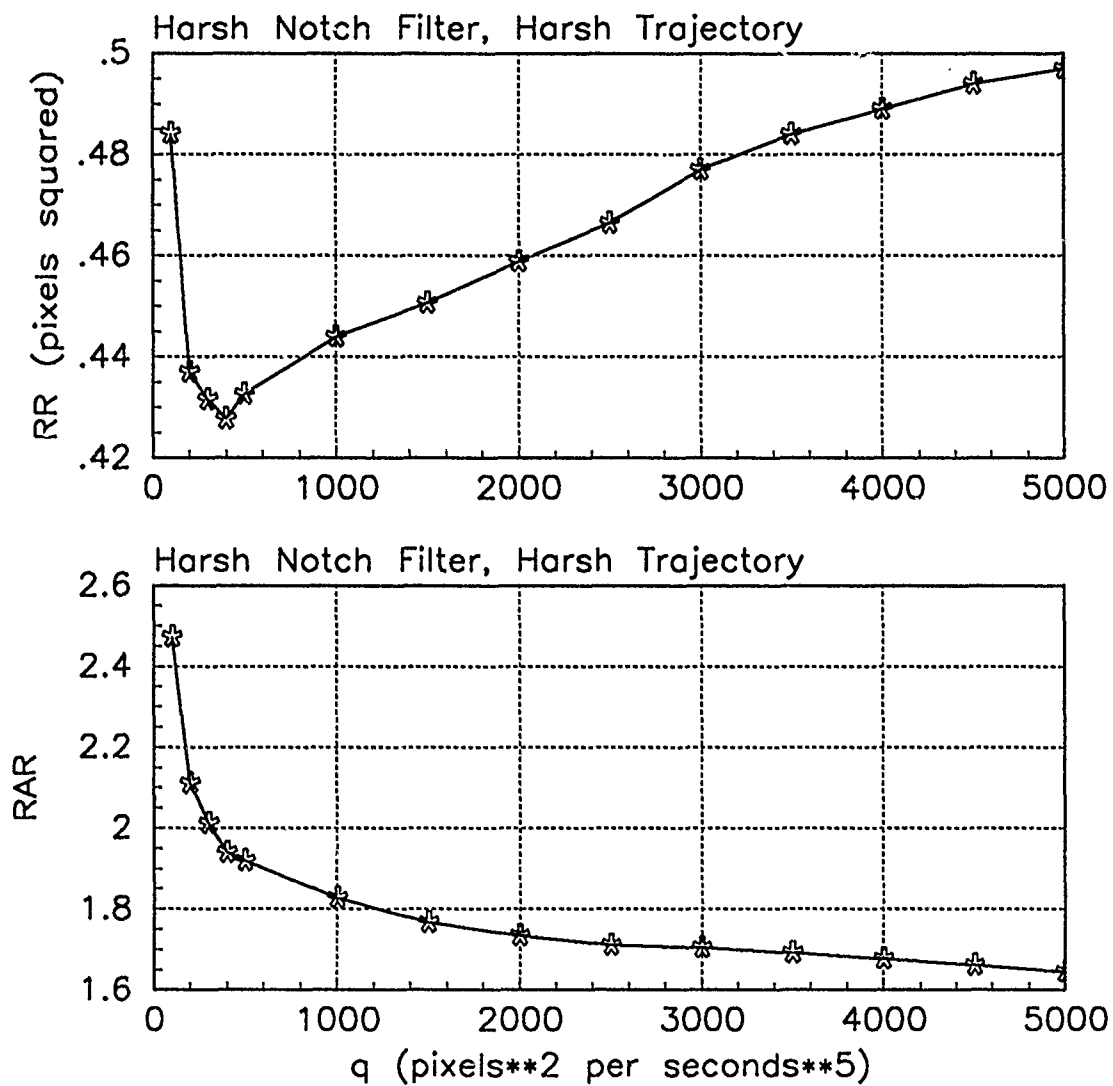


Figure 5.6. $\mathbf{r}_k^T(t_i)\mathbf{r}_k(t_i)$ and $\mathbf{r}_k^T(t_i)\mathbf{A}_k^{-1}(t_i)\mathbf{r}_k(t_i)$ for the Harsh Notch Filter Tracking the Harsh Trajectory

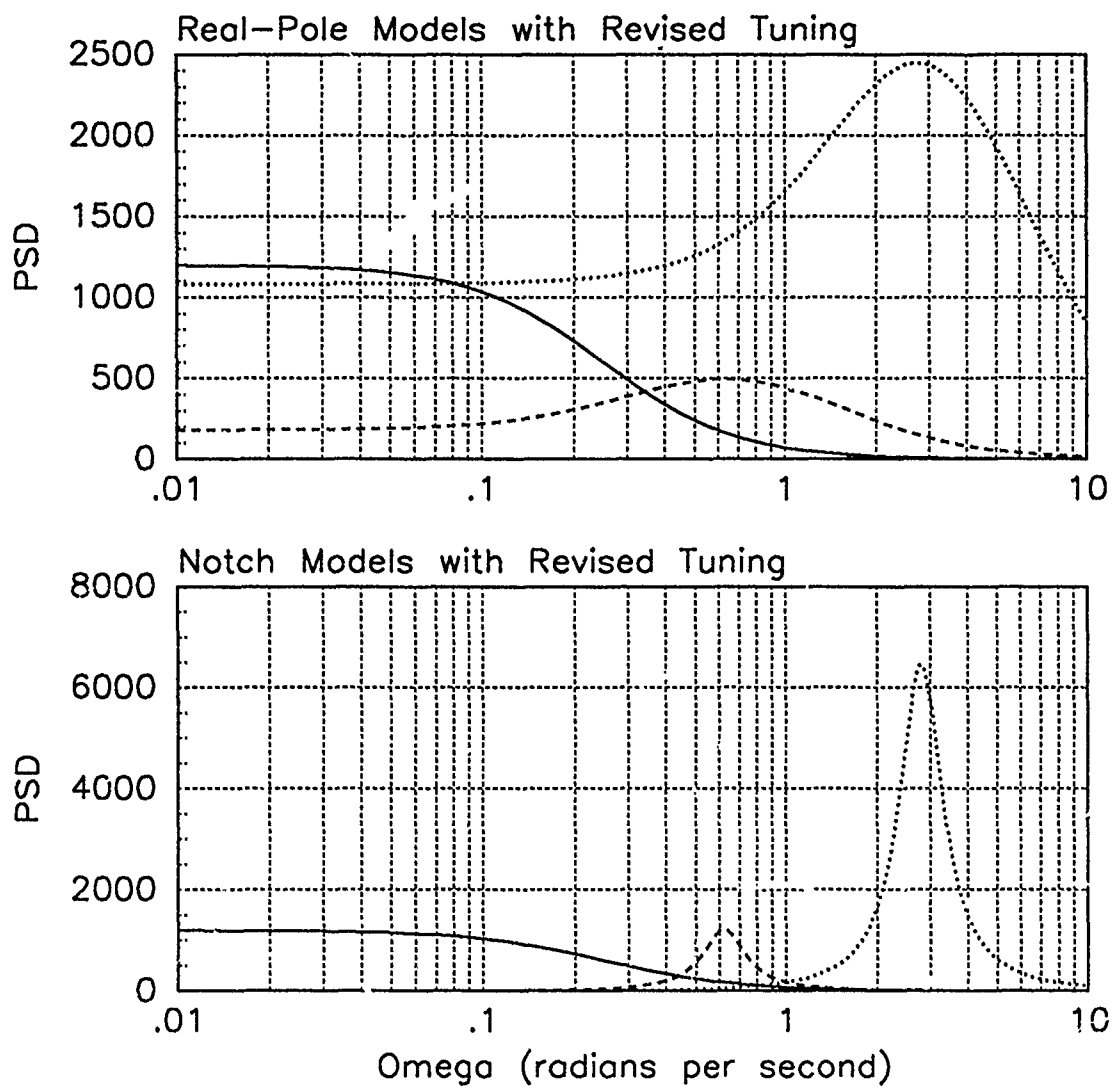


Figure 5.7. PSD Plots; Real-Pole MMAE-R and Notch MMAE-1R

Table 5.3. Average Position Errors for Real-Pole and Notch-1 MMAEs with -O and -R Options.

Traj ω	Error in:						MMAE Specs:
	$p_x(t_i^-)$	$p_x(t_i^+)$	$y_x(t_i^-)$	$p_y(t_i^-)$	$p_y(t_i^+)$	$y_y(t_i^-)$	
.01	.133±.422	.100±.383	.089±.384	-.004±.359	-.003±.322	.001±.370	Real,O
.01	.167±.411	.129±.375	.106±.382	.003±.347	.004±.315	.009±.368	Real,R
.01	.133±.421	.099±.381	.088±.383	-.008±.357	-.006±.320	-.002±.369	Not,1O
.01	.066±.422	.050±.383	.050±.385	-.006±.346	-.005±.313	-.001±.366	Not,1R
.62	.150±.422	.116±.382	.105±.384	.002±.359	.001±.322	.005±.369	Real,O
.62	.162±.412	.124±.375	.101±.382	.009±.344	.124±.375	.101±.382	Real,R
.62	.136±.424	.102±.385	.091±.384	.002±.358	.002±.321	.006±.369	Not,1O
.62	.069±.423	.053±.384	.053±.387	.034±.347	.026±.315	.023±.367	Not,1R
2.8	-.026±.509	-.027±.422	-.014±.421	-.018±.504	-.019±.400	-.016±.426	Real,O
2.8	-.018±.557	-.016±.446	-.004±.446	.011±.493	-.127±.384	.004±.426	Real,R
2.8	-.022±.577	-.009±.446	-.005±.464	-.070±.540	-.065±.399	-.067±.455	Not,1O
2.8	-.100±.510	-.063±.429	-.064±.420	.062±.450	.024±.370	.043±.402	Not,1R

The MMAE is allowed to track each trajectory as before, error plots are made and averages are computed. Table 5.3 shows the average position errors for the four Monte Carlo studies. For the real-pole MMAE-R, the probability plots are in Figures 5.8 and 5.9. Error plots are shown in Figures C.10 through C.18 and the average residuals are tabulated in Tables C.4 through C.6. For the notch MMAE-1R, the error plots are in Figures D.10 through D.18 and the average residuals are tabulated in Tables D.4 through D.6.

From the residual information tables we see that the filter with the smallest average $\mathbf{r}_k^T(t_i)\mathbf{r}_k(t_i)$ value is ultimately selected for all trajectories for both MMAEs. Both MMAEs show excellent response in selecting the harsh filter for the harsh trajectory. Note the harsh filter always has the smallest $\mathbf{r}_k^T(t_i)\mathbf{A}_k^{-1}(t_i)\mathbf{r}_k(t_i)$ value because of its greater dynamics driving noise strength and the similar magnitude of residuals for each elemental filter. There is a trace of the trajectory in the y-position error, but the error magnitude remains less than half a pixel. The average position errors in Table 5.3 are small, in the hundredths of a pixel, because the error plot is sinusoidal. However, the probability plots show almost identical traces for the benign and intermediate trajectories for both MMAEs. The benign filter is selected for the benign and intermediate trajectories with the real-pole MMAE-R. Neither benign nor intermediate are clearly chosen by the notch MMAE-1R.

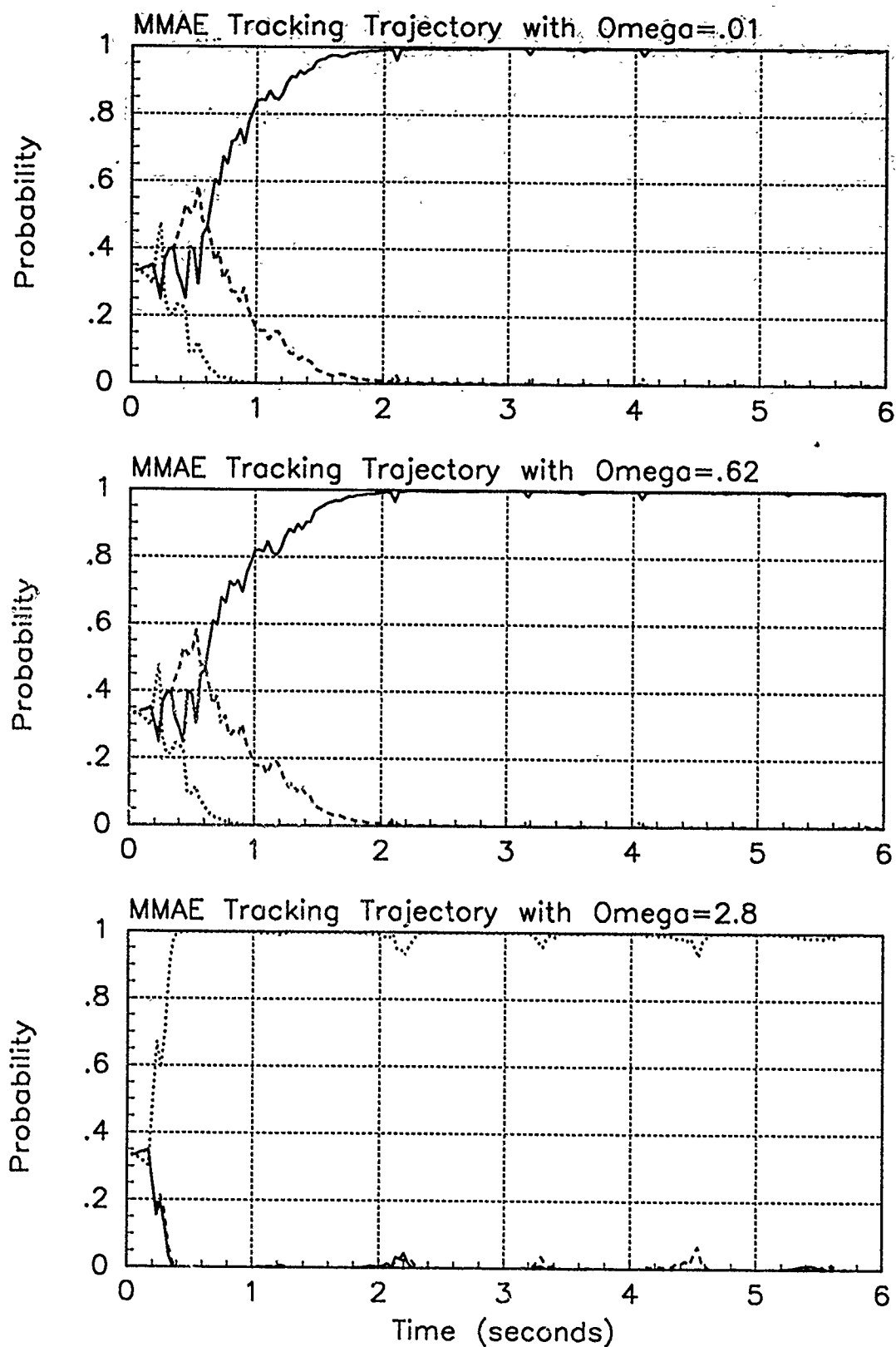


Figure 5.8. Probability Plots; Real-Pole MMAE-R; PC is 1; Basic Trajectories. Benign filter has solid line; intermediate filter has dashed line; harsh filter has dotted line.

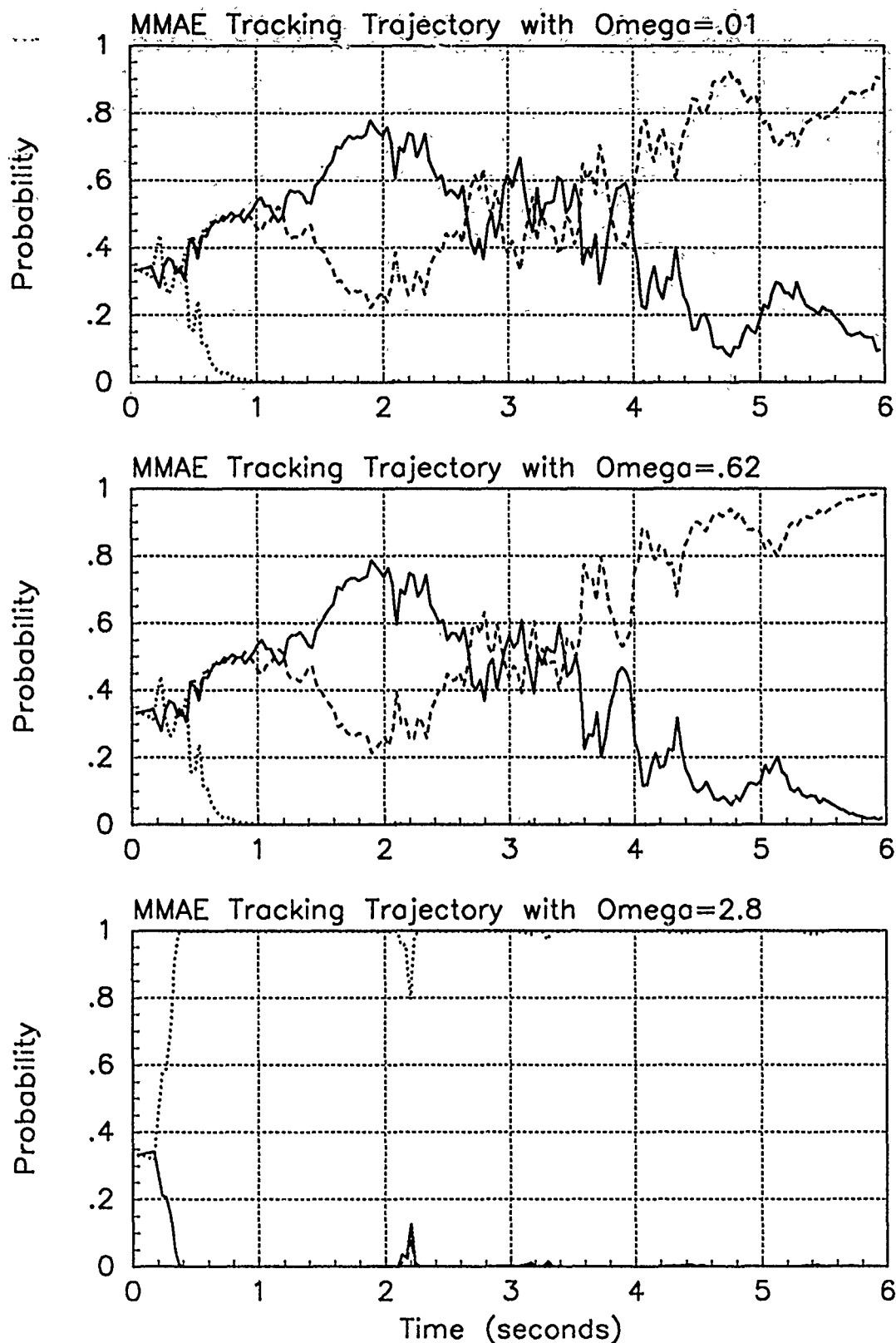


Figure 5.9. Probability Plots; Notch MMAE-1R; PC is 1; Basic Trajectories. Benign filter has solid line; intermediate filter has dashed line; harsh filter has dotted line.

5.6 A Second Notch MMAE

Again we see the probability plots show the "wrong" filter is being selected to track the target. Now, is this a phenomenon, again, of the filter design or perhaps of the hypothesis probability calculation as discussed in Chapter 1? To address the latter, a quick check is done using all variations on the probability calculation that are addressed in Section 1.3.3 for the notch MMAE only and is presented in the first part of Section 5.8.

Section 5.8 points out that alternative probability calculations do not help filter selection for notch MMAE-1R, so filter design is examined in this section. When the *benign* filter is subject to the revised tuning process while tracking the intermediate trajectory, it comes out with almost the same values of $r_k^T(t_i)r_k(t_i)$ that the *intermediate* filter does tracking the intermediate trajectory. So, the intermediate filter with a model designed at $\omega = 0.62$ radians per second *should not* be expected to be definitively selected out of the MMAE to track the intermediate trajectory. The definition of the intermediate filter and trajectory is not different enough from the benign definition, within the parameter space limited as we have to manned airborne targets. A two-filter MMAE can result, or a new intermediate filter and corresponding trajectory can be designed.

To investigate the hypothesis that distinguishability of "benign" and "intermediate" trajectories is the key issue, a new intermediate filter is chosen based on an acceleration model that shows a peak at $\omega = 1.32$ radians per second in a PSD plot. The peak falls between the peaks for the models at 0.62 and 2.8 radians per second (an ad hoc choice based on $1.32 = \exp\{0.5 [\log(2.8) - \log(0.62)] + \log(0.62)\}$). The filter is tuned for a trajectory with $\omega = 1.32$ radians per second and an amplitude of 9 meters. A plot of the resulting y position in the detector plane for this new intermediate trajectory is in Figure 5.10 as well as the PSD plot of the tuned MMAE. Compare this PSD to the second plot in Figure 5.7. The -2R denotes the *second* notch MMAE designed and the *revised* tuning method.

This MMAE is allowed to track targets undergoing accelerations with frequencies of 0.01, 1.32, and 2.8 radians per second (the basic trajectories for which the elemental filters are tuned). The probability plots are in Figure 5.11. The error plots are in Figures E.1 through E.9. The temporal averages are in Tables E.1 through E.3.

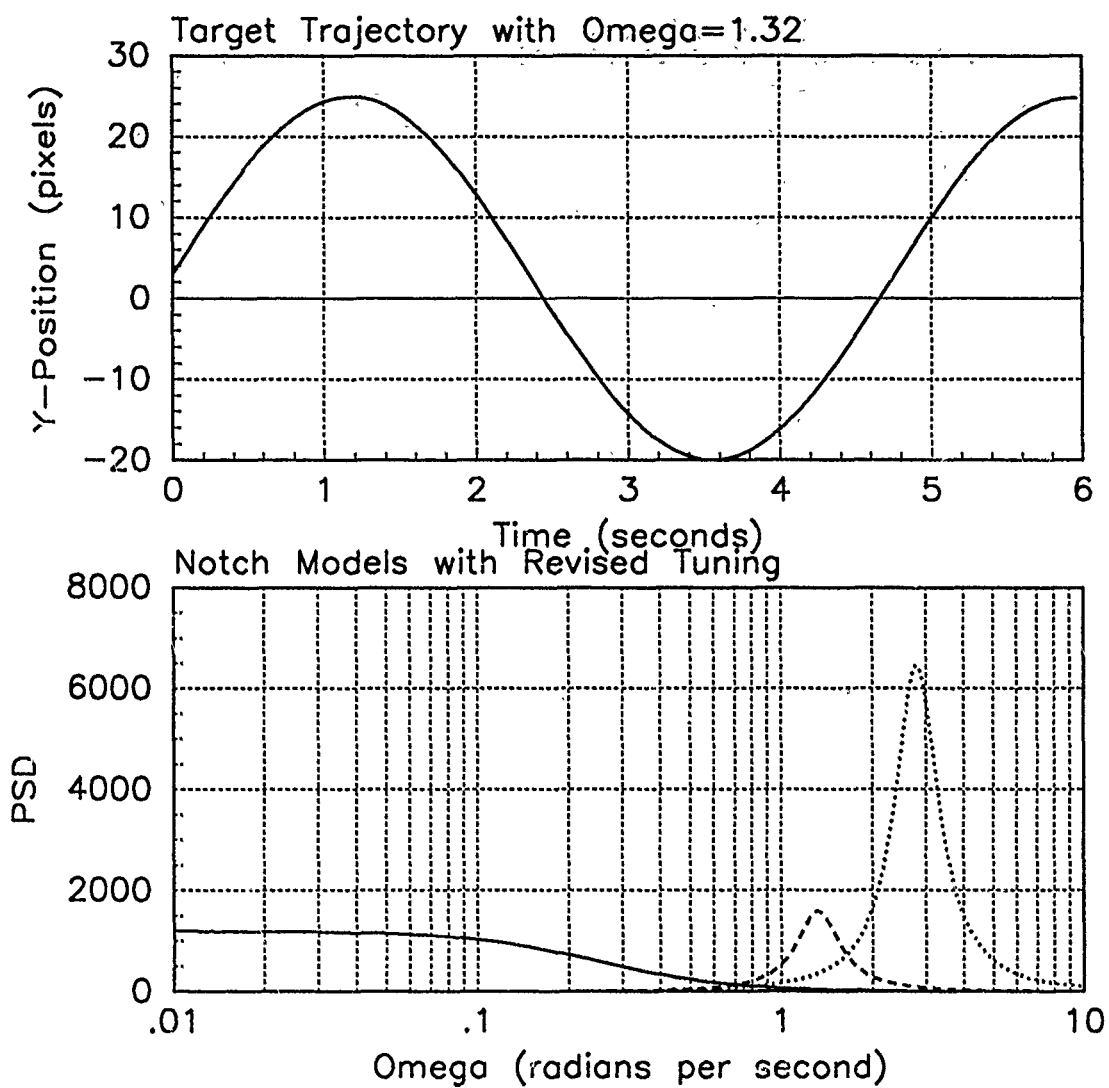


Figure 5.10. Intermediate Model at $\omega = 1.32$ radians per second. The top plot is target position in the detector plane. The bottom plot is the PSD plot for the models for the notch MMAE-2R.

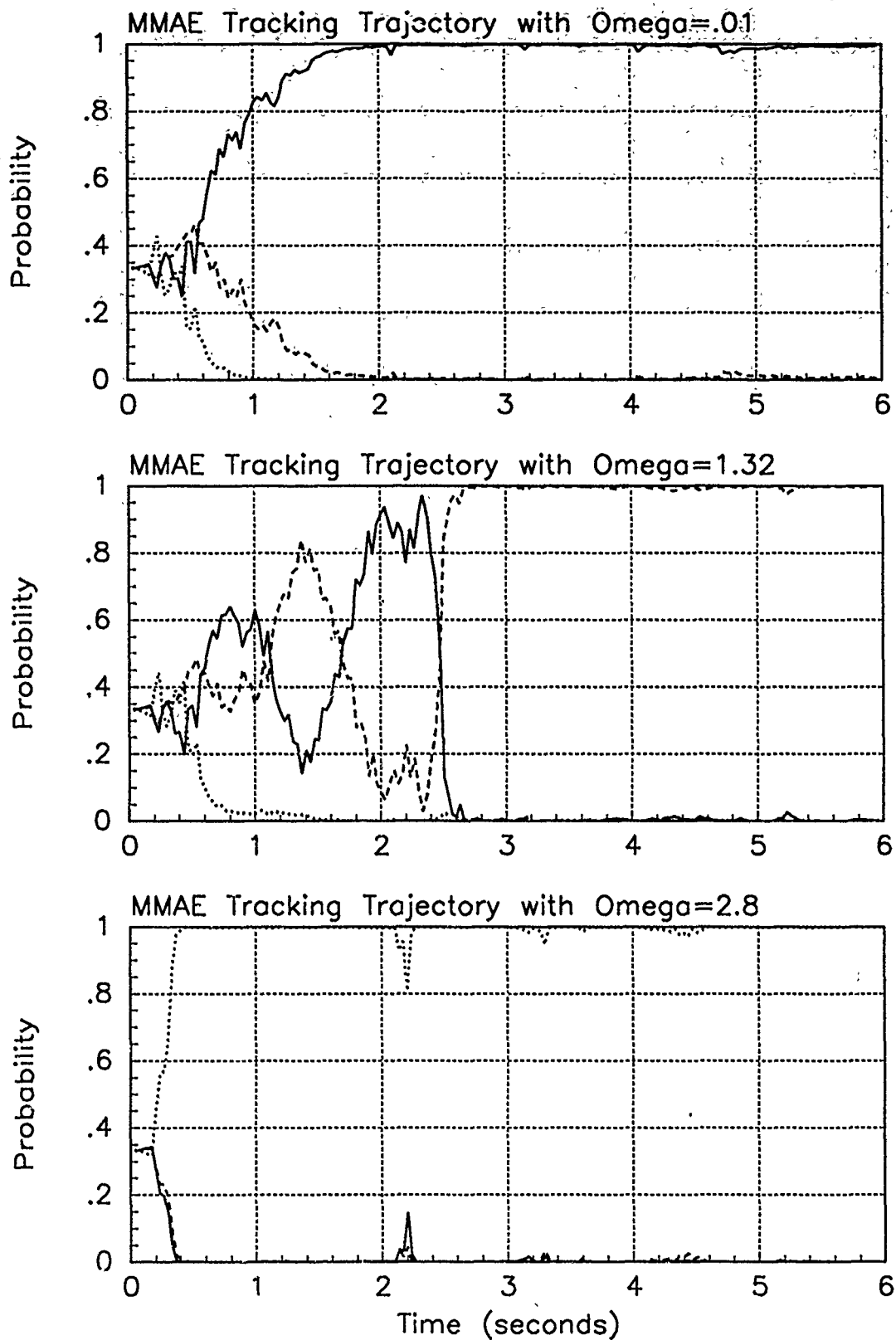


Figure 5.11. Probability Plots; Notch MMAE-2R; PC is 1; Basic Trajectories. Benign filter has solid line; intermediate filter has dashed line; harsh filter has dotted line.

As a result of these efforts, we finally see a difference in elemental filter selection when the MMAE is tracking the benign and the intermediate trajectories. The harsh filter remains uncontested in tracking the harsh trajectory. The benign filter gets the benign trajectory after about 0.6 seconds. There is a lot of switching between the benign and intermediate filters for the intermediate trajectory. The times of switching, 0.6, 1.1, 1.7, and 2.5 seconds, again, are not related to anything obvious in the trajectory acceleration. The average $\mathbf{r}_k^T(t_i)\mathbf{r}_k(t_i)$ is smaller for the intermediate filter (Table E.2) but the leading coefficient in the probability calculation gives the benign filter an advantage due to its smaller magnitude dynamics driving noise strength. It is expected that the y-position RMS error plot of Figure E.4 would show the ripples due to filter switching as noted before (Figure C.7). The ripples are less evident probably because the strength of the dynamics driving noise is not as different between the benign and intermediate filters. There are trajectory trends remaining in the y-position error plots in for both the intermediate (Figure E.6) and harsh (Figure E.9) trajectories, still of a small magnitude, less than half a pixel for the t_i^+ plots.

This seemingly better designed notch MMAE will be used, also, in a probability calculation analysis. The method is presented in Section 5.8 and the results are in Section 5.8.2.

5.7 Tracking a Target in an Evasive Maneuver

The trajectories considered thus far are tied to the elemental filters in the MMAE as we investigate filter selection. In other words, the simulated "real world" is one of the three nominal trajectories for all 6 seconds of the simulation. A trajectory was created to simulate a target in an evasive maneuver by concatenating two seconds of each nominal trajectory type together. As with the basic trajectories used above, the motion dynamics are added only to the y direction. The y position in the detector plane for this jinking motion is shown in the plot in Figure 5.12. In the inertial frame the target experiences about 7.3 g's acceleration in the dive.

The notch MMAEs are allowed to track this trajectory. The error plots for the notch MMAE-1R are in Figures D.46 to D.48. The error statistics are in Table D.16. No average

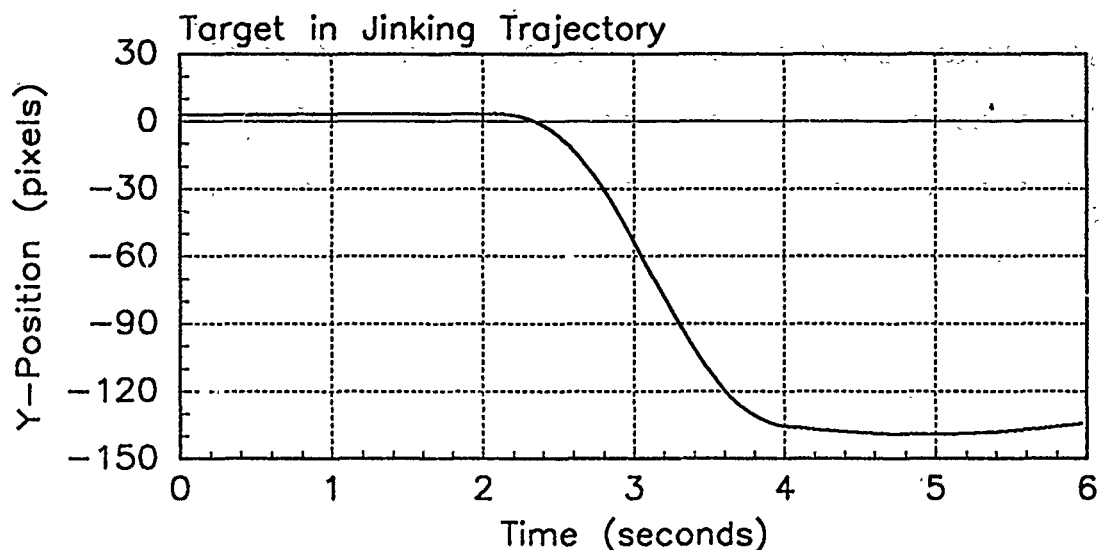


Figure 5.12. Target Position; Detector Plane; Jinking Trajectory

$\mathbf{r}_k^T(t_i)\mathbf{r}_k(t_i)$ or $\mathbf{r}_k^T(t_i)\mathbf{A}_k^{-1}(t_i)\mathbf{r}_k(t_i)$ is presented because it is expected that the magnitudes of the residuals will change for each elemental filter over the course of the changing dynamics. Instead, a series of plots showing $\mathbf{r}_k^T(t_i)\mathbf{r}_k(t_i)$, $\mathbf{r}_k^T(t_i)\mathbf{A}_k^{-1}(t_i)\mathbf{r}_k(t_i)$, and the leading coefficient in the hypothesis probability calculation are presented in Figure D.49. The error plots for the notch MMAE-2R are in Figures E.37 to E.39. The associated error statistics are in Table E.13. A compilation of the error statistics is in Table 5.4. The probability plots for each notch MMAE are in Figure 5.13.

The first part of the trajectory is benign. Thus the probability plots match pretty well the corresponding probability plot for the benign trajectory in Figure 5.9 for the notch MMAE-1R and Figure 5.11 for the notch MMAE-2R. The diving part of the trajectory is a piece of the harsh trajectory from Figure 5.2. Thus, it is expected that the harsh filter would be selected for that part. The harsh trajectory is inserted at 2 seconds but care was

Table 5.4. Position Error Statistics for Notch MMAE-1R and -2R with Jinking Trajectory.

Traj	Error in:						Notch MMAE
	$p_x(t_i^-)$	$p_x(t_i^+)$	$y_x(t_i^-)$	$p_y(t_i^-)$	$p_y(t_i^+)$	$y_y(t_i^-)$	
Jink	-.021±.470	-.013±.409	-.008±.404	.136±.420	.085±.359	.106±.392	-1R
Jink	-.009±.471	-.005±.408	.001±.406	.137±.425	.087±.361	.106±.393	-2R

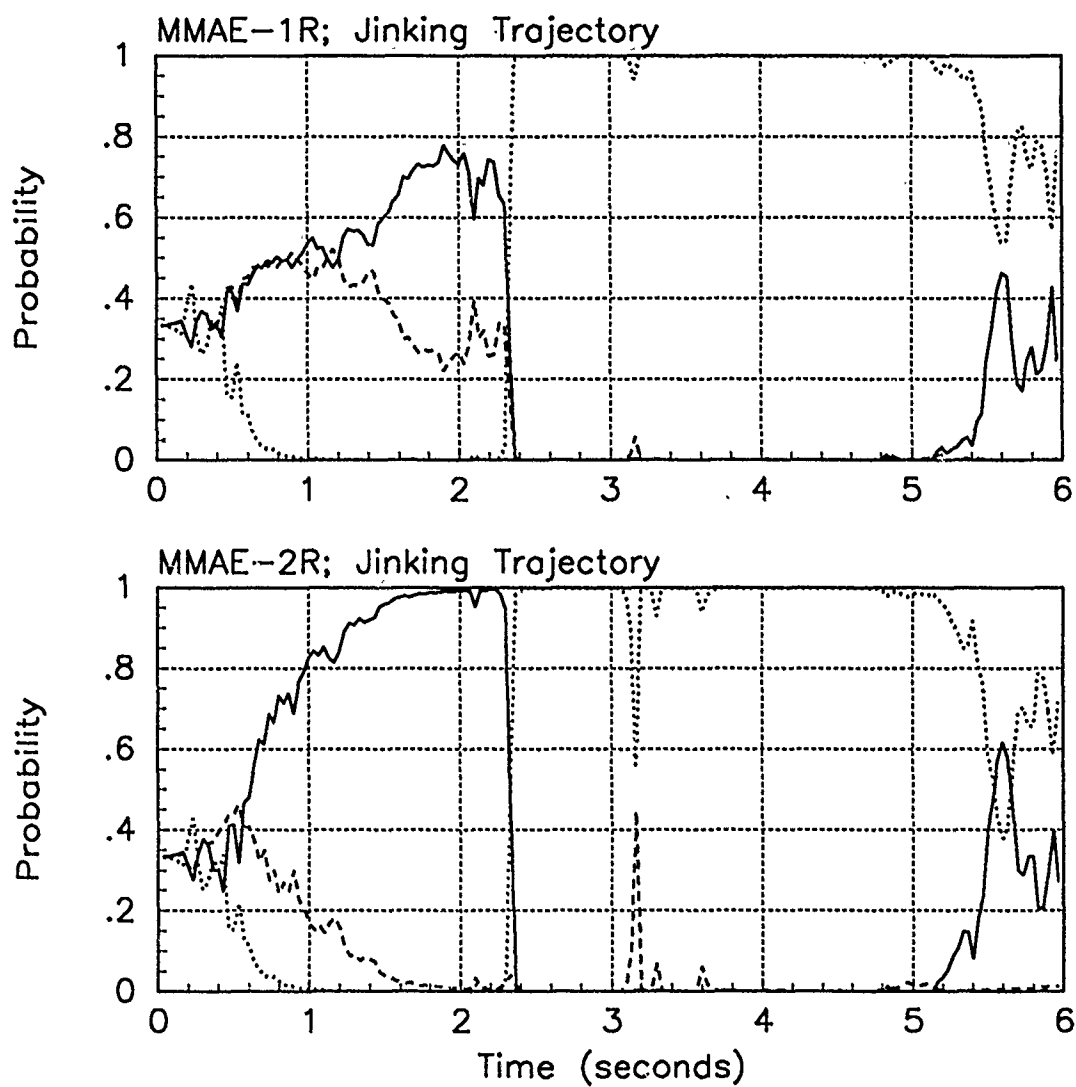


Figure 5.13. Probability Plots; Notch MMAE-1R and Notch MMAE-2R; PC is 1; Jinking Trajectory. Benign filter has solid line; intermediate filter has dashed line; harsh filter has dotted line.

taken by using the phase and bias variables in the velocity equation of Equation (3.3) to ensure no discontinuities in the acceleration or jerk domains. Therefore, the target slowly falls into the dive and filter selection is delayed for about 0.3 seconds. At 4 seconds, the trajectory with $\omega = 0.62$ radians per second is inserted. This is evident in the trajectory plot in Figure 5.12, but filter selection does not begin to change until past 5 seconds for either MMAE. For both, the benign filter is being selected when the simulation ends.

Trends from the trajectory are evident in the y-position error plots for both MMAEs (Figures D.48 and E.39) and the magnitude of the average values in Table 5.4 reflect this. The error trends are in the positive direction, meaning the filter is estimating the position with a positive bias during the dive. The filter-computed RMS bands in Figures D.46 and E.37 each make a step when the harsh filter is selected at 2.3 seconds and the average magnitude of the band starts coming down only at the end when the benign filter comes in.

The plots of $\mathbf{r}_k^T(t_i)\mathbf{r}_k(t_i)$, $\mathbf{r}_k^T(t_i)\mathbf{A}_k^{-1}(t_i)\mathbf{r}_k(t_i)$, and the leading coefficient show the biggest difference between the two intermediate filters designed thus far. In Figure D.49, the dashed lines for the intermediate filter follow the solid line for the benign filter more closely than the corresponding lines for MMAE-2R in Figure E.40. The drop in the leading coefficient for the benign filter at 3.47 seconds is due to the benign filter losing lock and being reset with the proportional values from the intermediate and harsh filters that did not lose lock. At this point, the harsh filter is contributing the most to the MMAE estimate and so contributes the most to the restart of the benign filter. This restart of the benign filter covariance is improper. It could have retained its precomputable steady-state value during the restart of the state estimates [10]. Quite obviously, the harsh filter has the smallest residuals during the dive and so is selected. The advantage given to the benign filter by the leading coefficient is quite obvious when presented in this graphical form.

5.8 Examining the Hypothesis Probability Calculation

As discussed in Chapter I, there are alternatives in the way the hypothesis probability is calculated. The probability calculation for the k th filter in Figure 1.2 is repeated here:

$$p_k(t_i) = \frac{\frac{1}{(2\pi)^{\frac{n}{2}} |A_k(t_i)|^{\frac{1}{2}}} \exp \left\{ -\frac{1}{2} \mathbf{r}_k^T(t_i) \mathbf{A}_k^{-1}(t_i) \mathbf{r}_k(t_i) \right\} p_k(t_{i-1})}{\sum_{g=1}^j \left[\frac{1}{(2\pi)^{\frac{n}{2}} |A_g(t_i)|^{\frac{1}{2}}} \exp \left\{ -\frac{1}{2} \mathbf{r}_g^T(t_i) \mathbf{A}_g^{-1}(t_i) \mathbf{r}_g(t_i) \right\} p_g(t_{i-1}) \right]} \quad (5.6)$$

where $A_k(t_i)$ is the k th filter's computed residual covariance:

$$A_k(t_i) = \mathbf{H}_k(t_i) \mathbf{P}_k(t_i^-) \mathbf{H}_k^T(t_i) + \mathbf{R}_k(t_i) \quad (5.7)$$

It is proposed to set $A_k(t_i)$ equal to $\mathbf{I}_{2 \times 2}$ in the exponential, in the leading coefficient, or in both. This leads to four possibilities:

1. Use the traditional calculation as in Equations (5.6) and (5.7). This is what has been done thus far in the thesis. At issue here is that, when the residuals of each of the elemental filters are of the same magnitude, the leading coefficient will cause the MMAE to select the "more benign" filter because it tends to have the smaller dynamics driving noise. However, the $\mathbf{A}_k^{-1}(t_i)$ in the exponential will cause the calculation to favor the "harsher" elemental filter because it has the greater dynamics driving noise. This investigation will help in deciding if removing one or both of the $A_k(t_i)$ s will aid in tracking.
2. Leave the leading coefficient as it is in the Equation (5.6), but set $A_k(t_i)$ equal to $\mathbf{I}_{2 \times 2}$ in the exponential. This should enhance the ability to return high probability to the benign elemental filter when a target stops maneuvering and returns to a benign flight trajectory.
3. Remove the leading coefficient. Setting $A_k(t_i)$ to $\mathbf{I}_{2 \times 2}$ in the leading coefficient would leave a constant multiplier that is the same for all elemental filters. The multiplier is set to one which will allow the *exponential* term to select the "correct" elemental filter when the residuals from each are about the same magnitude. The MMAE should favor the "harsh" filter.

Table 5.5. Average Position Errors for Notch MMAE-1R with Basic Trajectories and all PC Options.

Traj ω	Error in:						PC=
	$p_x(t_i^-)$	$p_x(t_i^+)$	$y_x(t_i^-)$	$p_y(t_i^-)$	$p_y(t_i^+)$	$y_y(t_i^-)$	
.01	.066±.422	.050±.383	.050±.385	-.006±.346	-.005±.313	-.001±.366	1
.01	.116±.414	.089±.378	.077±.832	-.003±.346	-.002±.314	.002±.367	2
.01	-.050±.496	-.028±.423	-.024±.414	-.004±.433	-.007±.364	-.001±.394	3
.01	.082±.418	.068±.381	.062±.384	-.001±.354	-.0002±.321	.004±.370	4
.62	.069±.423	.053±.384	.053±.387	.034±.347	.026±.315	.023±.367	1
.62	.115±.417	.088±.381	.077±.384	.015±.346	.011±.314	.012±.367	2
.62	-.047±.492	-.025±.420	-.022±.413	.083±.432	.038±.364	.057±.393	3
.62	.080±.422	.065±.385	.058±.386	.026±.350	.020±.316	.020±.368	4
2.8	-.100±.510	-.063±.429	-.064±.420	.062±.450	.024±.370	.043±.402	1
2.8	-.081±.507	-.048±.429	-.047±.417	.106±.457	.056±.375	.072±.407	2
2.8	-.013±.509	-.067±.428	-.068±.418	.061±.450	.023±.370	.041±.402	3
2.8	-.093±.509	-.058±.428	-.058±.420	.084±.451	.043±.371	.063±.402	4

4. Remove the leading coefficient and set $A_k(t_i)$ equal to $I_{2 \times 2}$ in the exponential. This is the maximum entropy application discussed in Chapter I. Only residual magnitudes (absolute magnitudes, not scaled relative to anticipated RMS residual size) will determine filter selection

Each of these probability calculations are referenced with the variable, "PC". The values of the variable are 1 through 4 as enumerated above.

5.8.1 PC Check on MMAE-1R. As shown in Section 5.6, particularly Figure 5.11, MMAE-1R is showing almost no difference between tracking the benign and intermediate trajectories. The trajectories are different to the eye as in Figure 5.2 and the acceleration models are certainly of very different design as shown in the PSD plot of Figure 5.7. It seems reasonable to expect that when the possible effects of dynamics driving noise strength are removed by setting A to $I_{2 \times 2}$, the matched dynamics of the acceleration model and the trajectory would cause the correct filter to be selected.

For the PC check, Table 5.5 shows the average position errors for the Monte Carlo studies for all trajectories and all PC options. The probability plots are in Figures 5.14 through 5.16 and are to be compared to the probability plots in Figure 5.9. The corre-

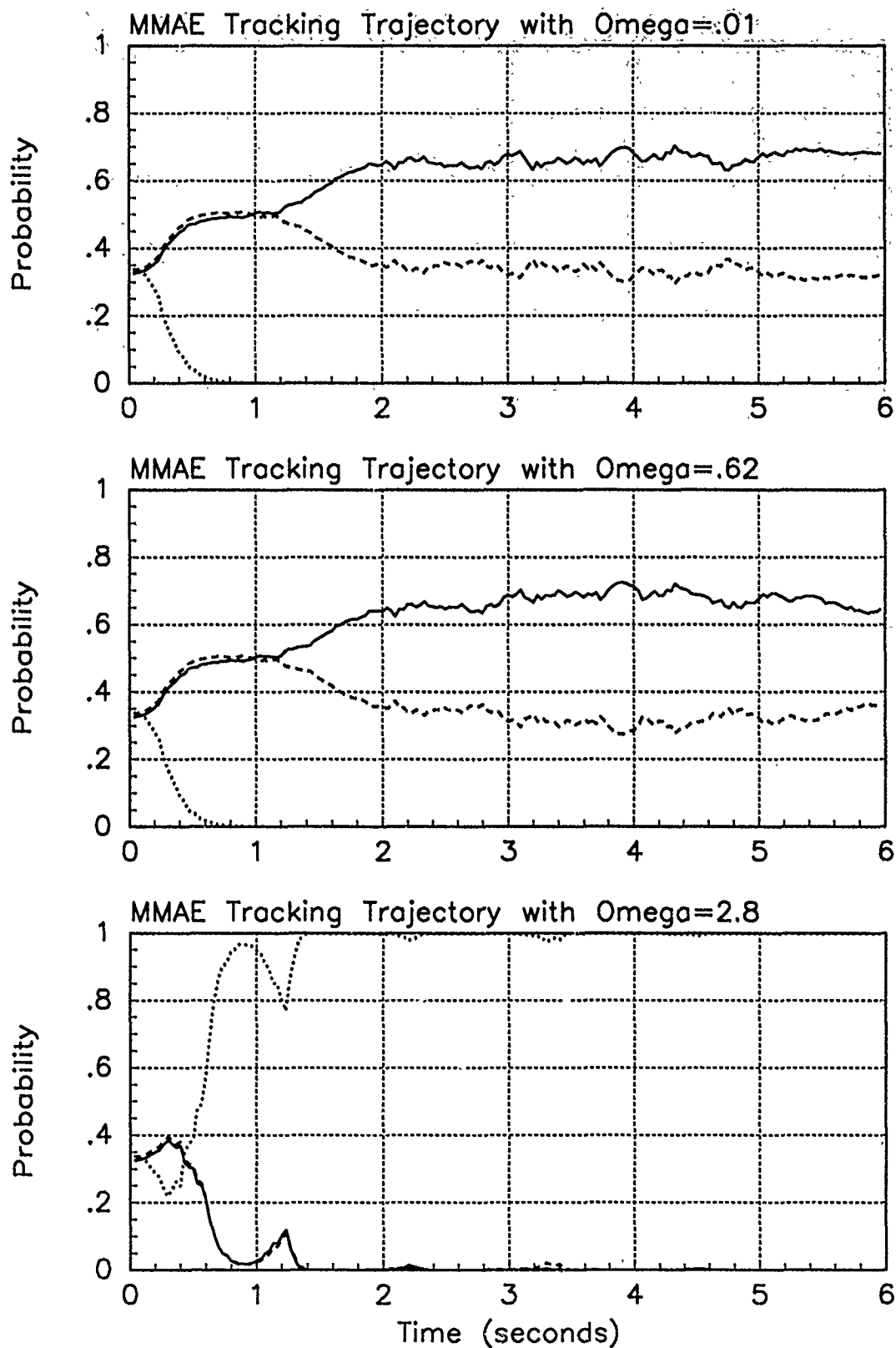


Figure 5.14. Probability Plots; Notch MMAE-1R; PC is 2; Basic Trajectories. Benign filter has solid line; intermediate filter has dashed line; harsh filter has dotted line.

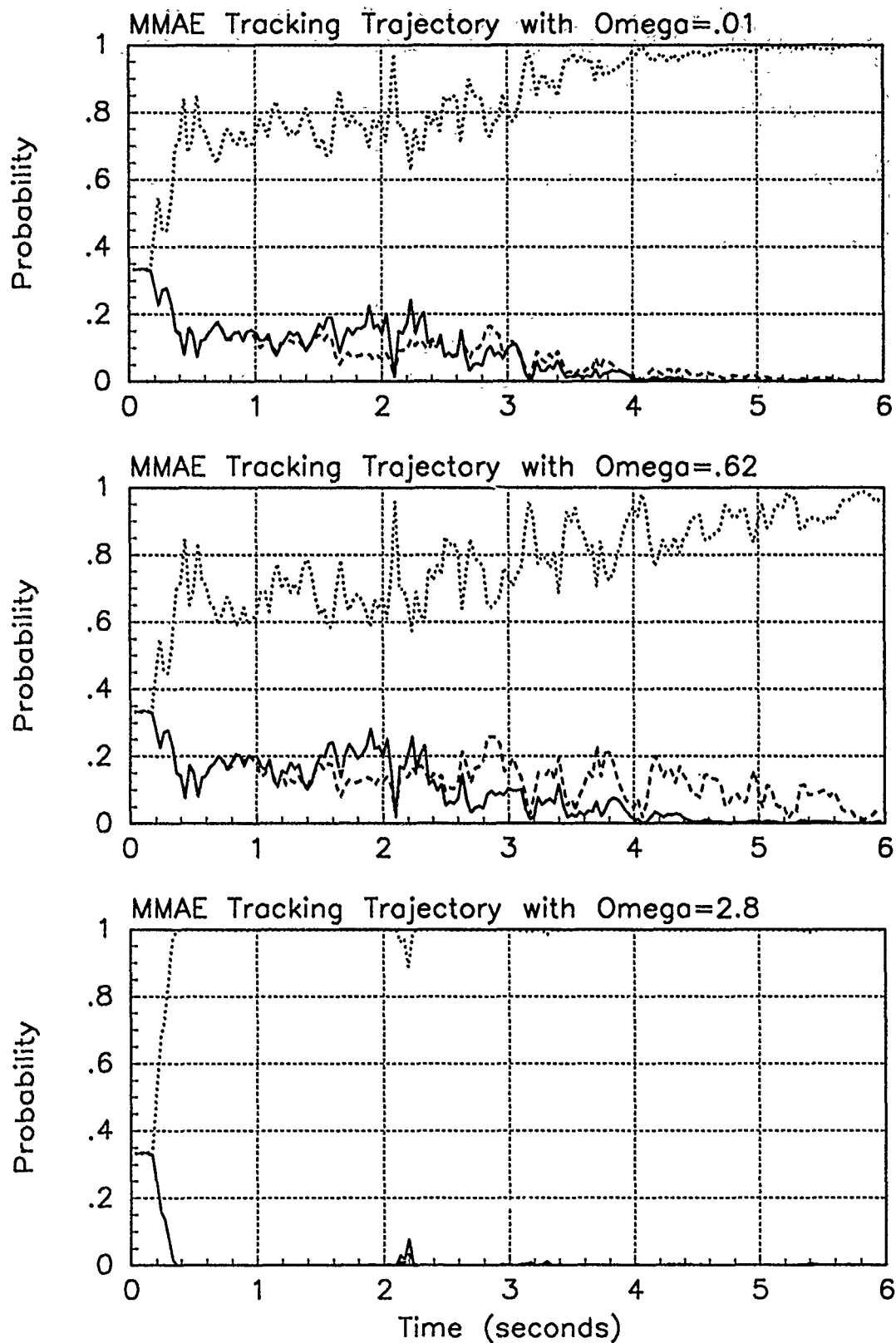


Figure 5.15. Probability Plots; Notch MMAE-1R; PC is 3; Basic Trajectories. Benign filter has solid line; intermediate filter has dashed line; harsh filter has dotted line.

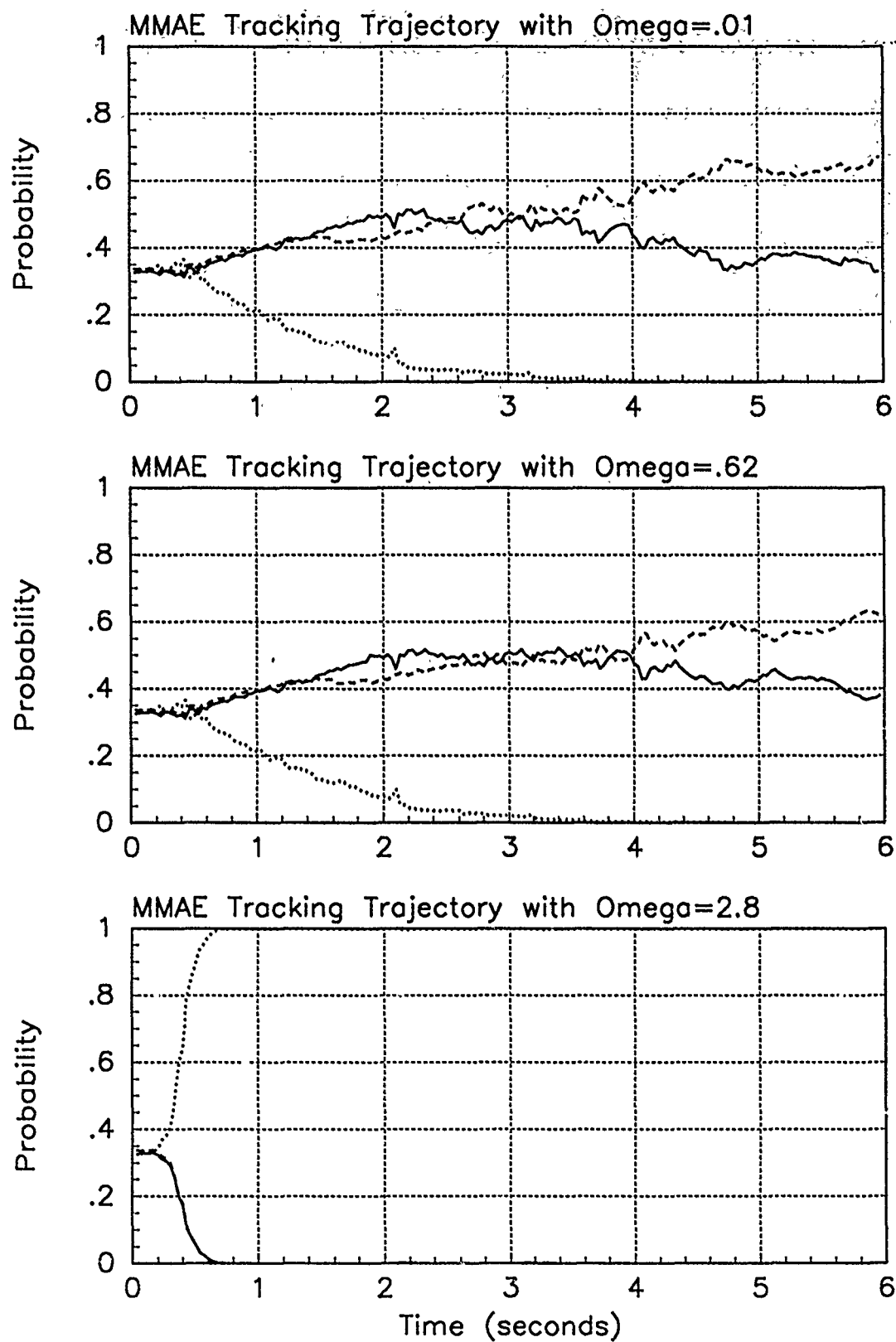


Figure 5.16. Probability Plots; Notch MMAE-1R; PC is 4; Basic Trajectories. Benign filter has solid line; intermediate filter has dashed line; harsh filter has dotted line.

sponding error plots are in Figures D.19 to D.45. These are to be compared to the error plots of Figures D.10 to D.18. The tables of averages are in Tables D.7 and D.15 and are to be compared to the averages in Tables D.4 to D.6.

The probability plot for $PC = 2$ in Figure 5.14 shows the benign filter selected more for the benign and intermediate trajectories. This is expected because the magnitude of the residuals, $\mathbf{r}_k^T(t_i)\mathbf{r}_k(t_i)$, in the exponential is about the same whether tracked by the benign or intermediate filters. The determining factor will then be the leading coefficient. The leading coefficient is greater for the filter with the weakest dynamics driving noise. The harsh trajectory is tracked by the harsh filter because, by far, it gives the smallest magnitude of residuals. The error plot in Figure D.27 shows an increased magnitude for the first 0.5 seconds because of the nontrivial (and inappropriate) contribution of the benign filter.

The probability plots of the Monte Carlo study with $PC = 3$ in Figure 5.15 shows the harsh filter tracking all the trajectories. This is expected since the leading coefficient is removed. The leading coefficient tends to be smallest for the harshest filter (see Figure D.49) while the magnitude of the $\mathbf{r}_k^T(t_i)\mathbf{A}_k^{-1}(t_i)\mathbf{r}_k(t_i)$ that remains in the exponential is smallest for the harsh filter. This makes the probability the largest for the filter with the greater dynamics driving noise strength when the residuals are not very different between elemental filters. Because the harsh filter does all the tracking, the standard deviations of the errors in Table D.10 are greater than the corresponding values in Table D.4.

The probability plots for $PC = 4$ in Figure 5.16 look much like the plots for $PC = 1$ except with a much slower response. The benign and intermediate filters fight for both the benign and intermediate trajectories. Again the plot for the benign trajectory looks very similar to the plot for the intermediate trajectory. The slow response time makes the filter selection smoother which should put less ripple in the band of filter-computed RMS errors, but still the "wrong" filter is selected.

Given these probability plots and these *non-varying* trajectories, a PC of 2 or 4 would be acceptable. There is less switching, the harsh filter does track the harsh trajectory (the hardest job), and either the benign or intermediate filters (or both) show adequate

Table 5.6. Average Position Errors for Notch MMAE-2R with all Trajectories and PC Options.

Traj ω	Error in:						PC=
	$p_x(t_i^-)$	$p_x(t_i^+)$	$y_x(t_i^-)$	$p_y(t_i^-)$	$p_y(t_i^+)$	$y_y(t_i^-)$	
.01	.164±.411	.126±.373	.103±.381	-.004±.347	-.003±.314	.002±.366	1
.01	.167±.408	.127±.372	.104±.380	-.002±.346	-.001±.314	.004±.367	2
.01	-.057±.503	-.031±.427	-.028±.417	-.005±.440	-.031±.427	-.028±.417	3
.01	.098±.427	.081±.387	.065±.388	.004±.362	.004±.326	.008±.372	4
1.32	-.033±.445	-.028±.396	-.016±.392	-.008±.391	-.014±.343	-.016±.374	1
1.32	.161±.411	.122±.376	.099±.381	.016±.348	.0003±.316	.002±.365	2
1.32	-.091±.497	-.058±.421	-.056±.414	.006±.445	-.009±.369	-.0001±.400	3
1.32	-.026±.444	-.017±.396	-.010±.391	-.014±.389	-.023±.343	-.014±.378	4
2.8	-.096±.512	-.060±.431	-.061±.420	.066±.450	.028±.371	.047±.403	1
2.8	-.093±.496	-.062±.422	-.056±.414	.060±.460	.031±.375	.040±.406	2
2.8	-.104±.511	-.068±.430	-.069±.419	.064±.450	.026±.372	.045±.402	3
2.8	-.093±.509	-.058±.429	-.058±.420	.086±.453	.043±.373	.062±.402	4
Jink	-.009±.471	-.005±.408	.001±.406	.137±.425	.087±.361	.106±.393	1
Jink	.009±.459	.007±.401	.011±.402	.199±.425	.137±.360	.138±.395	2
Jink	-.071±.502	-.041±.426	-.038±.417	.103±.451	.060±.379	.079±.402	3
Jink	-.038±.482	-.025±.416	-.015±.411	.151±.435	.095±.370	.110±.396	4

performance tracking either the benign or intermediate trajectories. The slow response time that makes these plots look so smooth would make the PC options unacceptable in tracking an evading target, and so a PC of 1 would be preferred.

Finally, the intermediate filter was not definitively selected. It is appropriate at this time to abandon it for the intermediate filter based on the acceleration model with $\omega = 1.32$ radians per second.

5.8.2 PC Check on MMAE-2R. The notch MMAE-2R is allowed to track its basic trajectories with each of the four hypothesis probability calculations. Table 5.6 is a compilation of the average position errors for the Monte Carlo studies for all trajectories and all PC options. The probability plots are presented in Figures 5.17 to 5.19 and are to be compared to the probability plots in Figure 5.11 (page 5-22). The error plots are in Figures E.10 to E.36. These are to be compared to the error plots of Figures E.1 to E.9. The tables of averages are in Tables E.4 and E.12 and are to be compared to the averages in Tables E.1 to E.3.

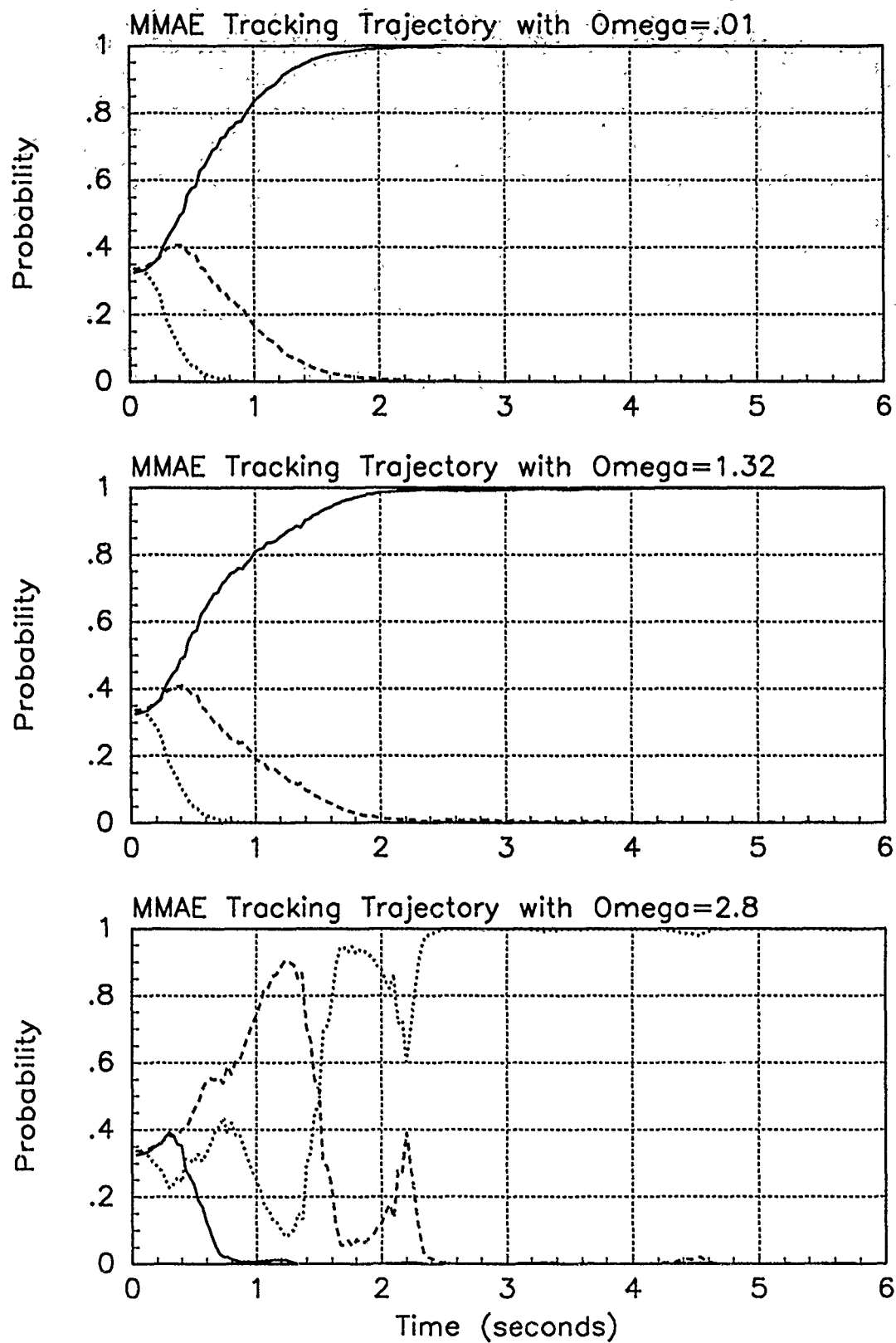


Figure 5.17. Probability Plots; Notch MMAE-2R; PC is 2; Basic Trajectories. Benign filter has solid line; intermediate filter has dashed line; harsh filter has dotted line.

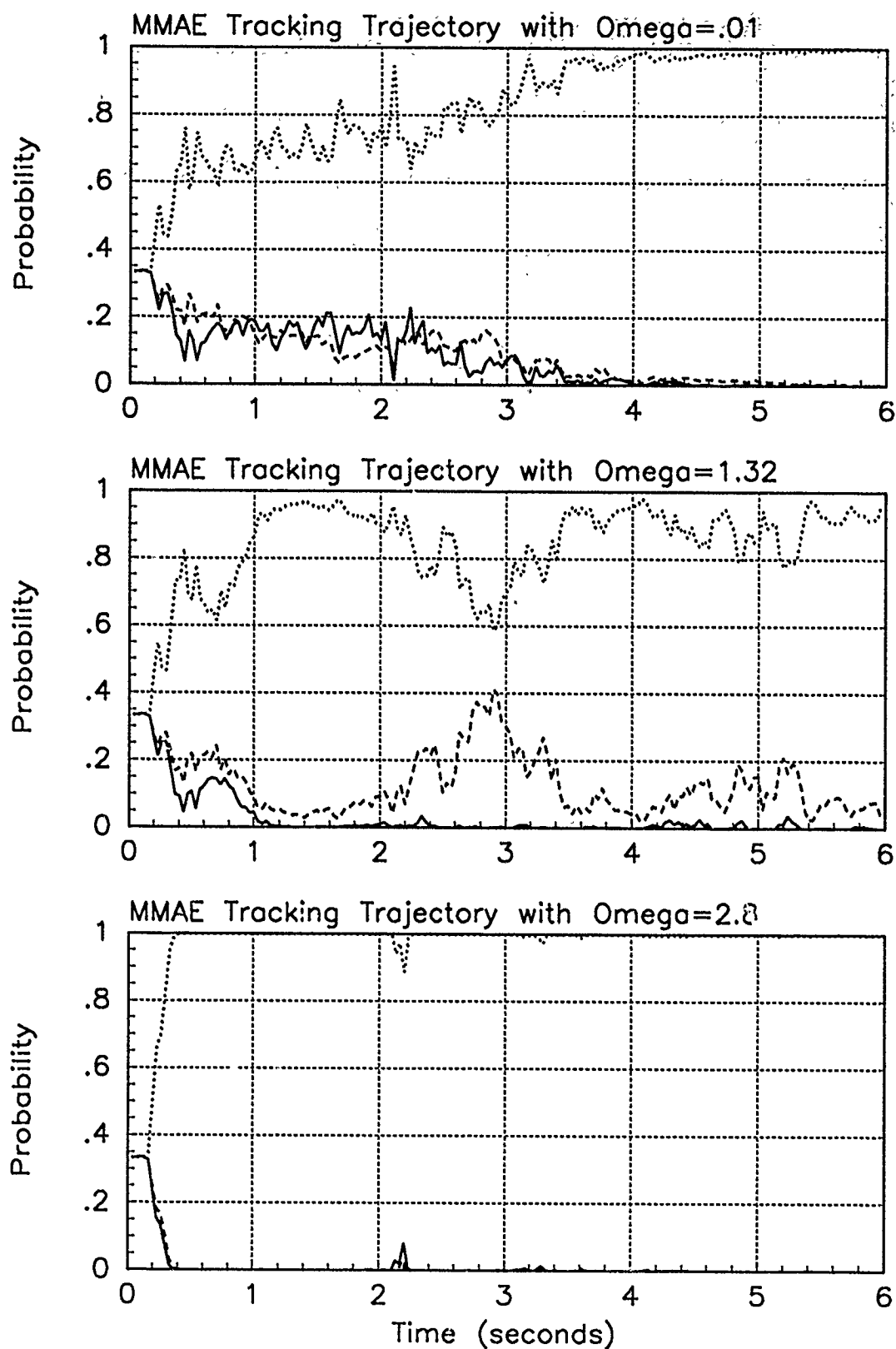


Figure 5.18. Probability Plots; Notch MMAE-2R; PC is 3; Basic Trajectories. Benign filter has solid line, intermediate filter has dashed line, harsh filter has dotted line.

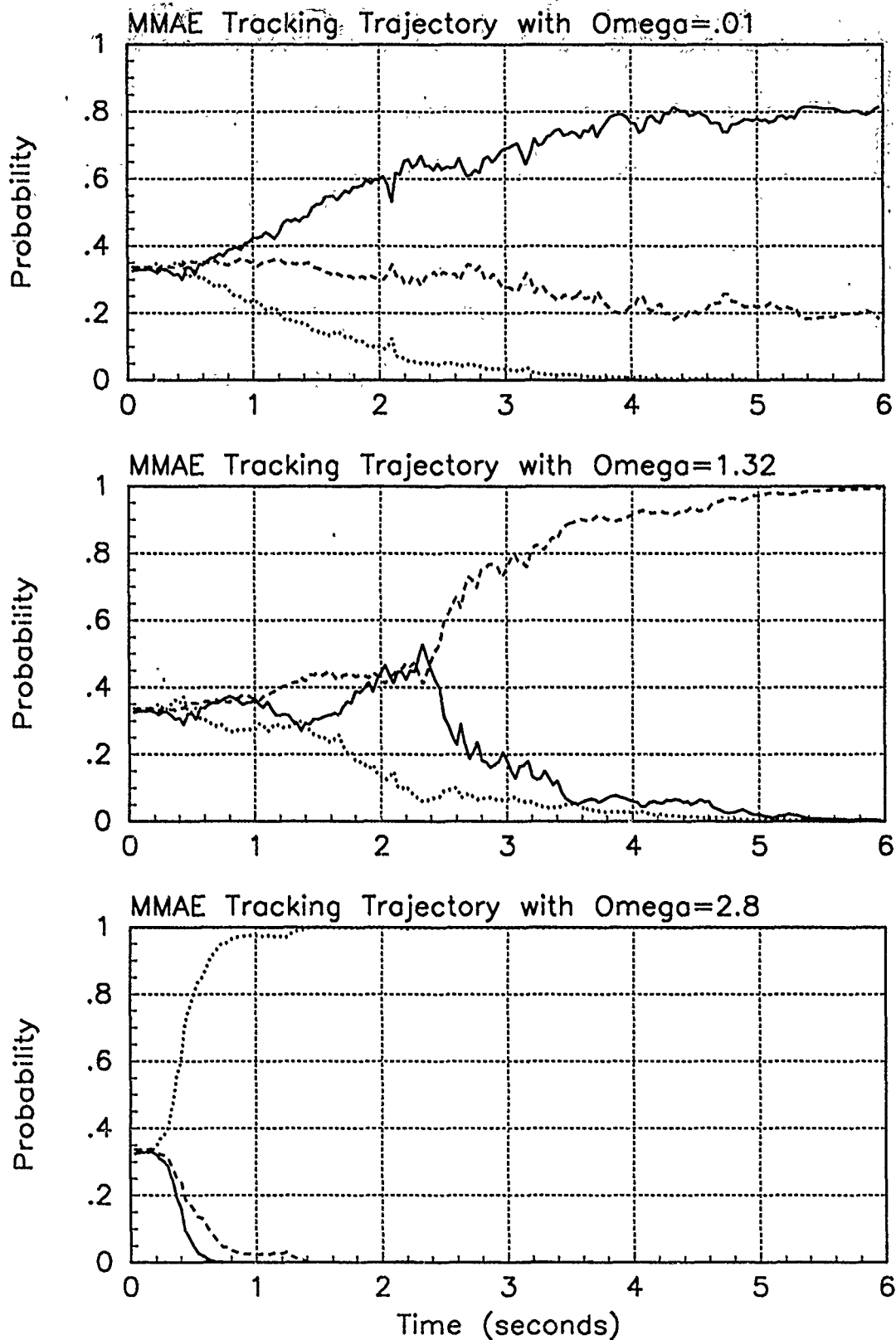


Figure 5.19. Probability Plots; Notch MMAE-2R; PC is 4; Basic Trajectories. Benign filter has solid line, intermediate filter has dashed line, harsh filter has dotted line.

The results of MMAE-2R are similar to that for MMAE-1R. PC = 3 still allows the harsh filter to do all the tracking. The filter selection looks smoother with PC = 4. The more benign filters are selected for PC = 2. For MMAE-2R, the intermediate filter is more able to track the harsh trajectory and so gets some input into the MMAE estimate when it is tracking the harsh trajectory with PC = 2 (Figure 5.17). This leaves PC of 1 or 4 as acceptable options. In fact, if a MAP version of the MMAE is run with MMAE-2R and PC = 4, the "correct" filter will be used for each trajectory through most of the 6 seconds.

The notch MMAE-2R is allowed to track the jinking trajectory using PC options 2, 3, and 4. The probability plots are in Figure 5.20. The error plots are in Figures E.41 to E.51. The error statistics are in Tables E.14 to E.16. Recall, the probability plot for the notch MMAE-2R with PC = 1 tracking the jinking trajectory is in Figure 5.13 (page 5-25). The error plots are in Figures E.37 to E.39. The error averages are in Table E.13. The residual and related plots are in Figure E.40.

With PC = 2, the probability plot looks very similar to the probability plot for PC = 1, except that the switch from the benign to harsh filter after 2 seconds is delayed by almost 0.3 seconds, as is the switch from harsh to benign after 5 seconds. The plot does show the desired improvement in removing high probability from the harsh elemental filter from $t = 4.0$ seconds on, but at the expense of the intermediate one contributing to the MMAE estimate during $t = 2.6$ to 3.6 seconds. The PC = 3 option causes the MMAE to select only the harsh filter. With PC = 4, the switch after 2 seconds is delayed and the one after 5 seconds did not even take place. Using this option appears to disable the MMAE and it cannot make a decision, even a wrong one, quickly. Given these responses, only the PC = 1 option is acceptable.

For *only* this jinking trajectory, a notch MMAE-2R modified as a MAP and using option PC = 2 should give suitable performance based on these plots of filter selection. Recall, however, this combination would not work looking at the basic trajectories as discussed just above. Moreover, PC = 1 would still provide superior performance, even implemented in MAP fashion. Except for the switching after 2 seconds and the lack of switching at the end, the PC = 4 option would give a MAP MMAE reasonably good performance. This will be pursued further in the next section.

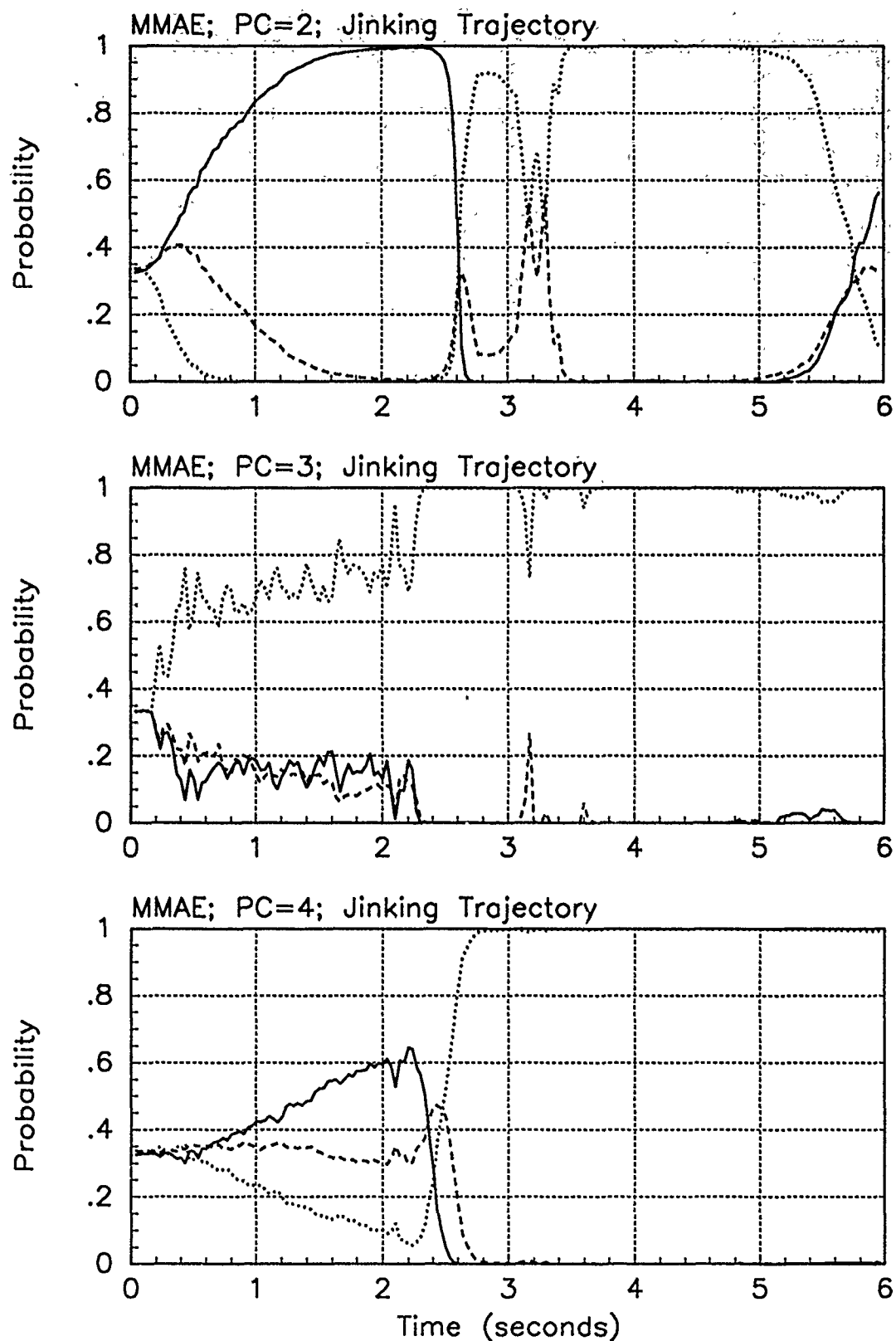


Figure 5.20. Probability Plots; Notch MMAE-2R; PC varies; Jinking Trajectory. Benign filter has solid line, intermediate filter has dashed line, harsh filter has dotted line.

Table 5.7. Appropriate Compilation for Comparing Position Error Statistics in Bayesian and MAP Options with Notch MMAE-2R.

Traj ω	Error in:						Ver, PC=
	$p_x(t_i^-)$	$p_x(t_i^+)$	$y_x(t_i^-)$	$p_y(t_i^-)$	$p_y(t_i^+)$	$y_y(t_i^-)$	
.01	.164±.411	.126±.374	.103±.381	-.004±.347	-.003±.314	.002±.366	B,1
.01	.098±.427	.081±.387	.065±.388	.004±.362	.004±.326	.008±.372	B,4
.01	.159±.403	.118±.367	.094±.380	-.011±.343	-.010±.311	-.005±.366	M,1
.01	.156±.404	.115±.368	.092±.381	-.009±.343	-.008±.311	-.003±.366	M,4
1.32	-.033±.445	-.028±.396	-.016±.392	-.008±.391	-.014±.343	-.016±.374	B,1
1.32	-.026±.444	-.017±.396	-.010±.391	-.014±.389	-.023±.343	-.014±.378	B,4
1.32	-.036±.446	-.033±.394	-.020±.394	-.007±.402	-.011±.350	-.013±.382	M,1
1.32	-.058±.445	-.052±.393	-.039±.400	.002±.398	-.005±.347	-.006±.380	M,4
2.8	-.096±.512	-.060±.431	-.061±.420	.066±.450	.028±.371	.047±.403	B,1
2.8	-.093±.509	-.058±.429	-.058±.420	.086±.453	.043±.373	.062±.402	B,4
2.8	-.103±.509	-.066±.428	-.067±.419	.048±.450	.010±.371	.029±.402	M,1
2.8	-.107±.507	-.070±.425	-.071±.419	.054±.450	.016±.371	.035±.402	M,4
Jink	-.009±.471	-.005±.408	.001±.406	.137±.425	.087±.361	.106±.393	B,1
Jink	-.038±.482	-.025±.416	-.015±.411	.151±.435	.095±.370	.11±.396	B,4
Jink	-.013±.470	-.013±.405	-.005±.406	.123±.421	.075±.358	.093±.393	M,1
Jink	-.016±.468	-.017±.405	-.007±.406	.144±.424	.089±.360	.105±.393	M,4

5.9 MAP MMAE

The maximum a posteriori (MAP) MMAE is described in Chapter I. In the MAP version of the MMAE, the estimate is the output of the elemental filter that has the highest probability, that is, no weighted average is used to calculate the MMAE estimate. This MAP MMAE can be used with any PC option. However, as discussed in Section 5.8, only PC options 1 and 4 are investigated. The MMAE-2R is used to track the nominal trajectories basic to it and to track a target in the jinking trajectory. A compilation of the position error statistics is in Table 5.7. The probability plots are in Figures 5.21 to 5.23. The error plots are in Figures E.53 to E.77. The average errors and average $\mathbf{r}_k^T(t_i)\mathbf{r}_k(t_i)$ and $\mathbf{r}_k^T(t_i)\mathbf{A}_k^{-1}(t_i)\mathbf{r}_k(t_i)$ are in Tables E.17 to E.24 where applicable. The runs that simulate tracking a target during an evasive maneuver have plots of $\mathbf{r}_k^T(t_i)\mathbf{r}_k(t_i)$, $\mathbf{r}_k^T(t_i)\mathbf{A}_k^{-1}(t_i)\mathbf{r}_k(t_i)$, and the leading coefficient that goes into the probability calculation and do not have average residual values presented in tabular form. These sets of plots are in Figure E.74 and E.78.

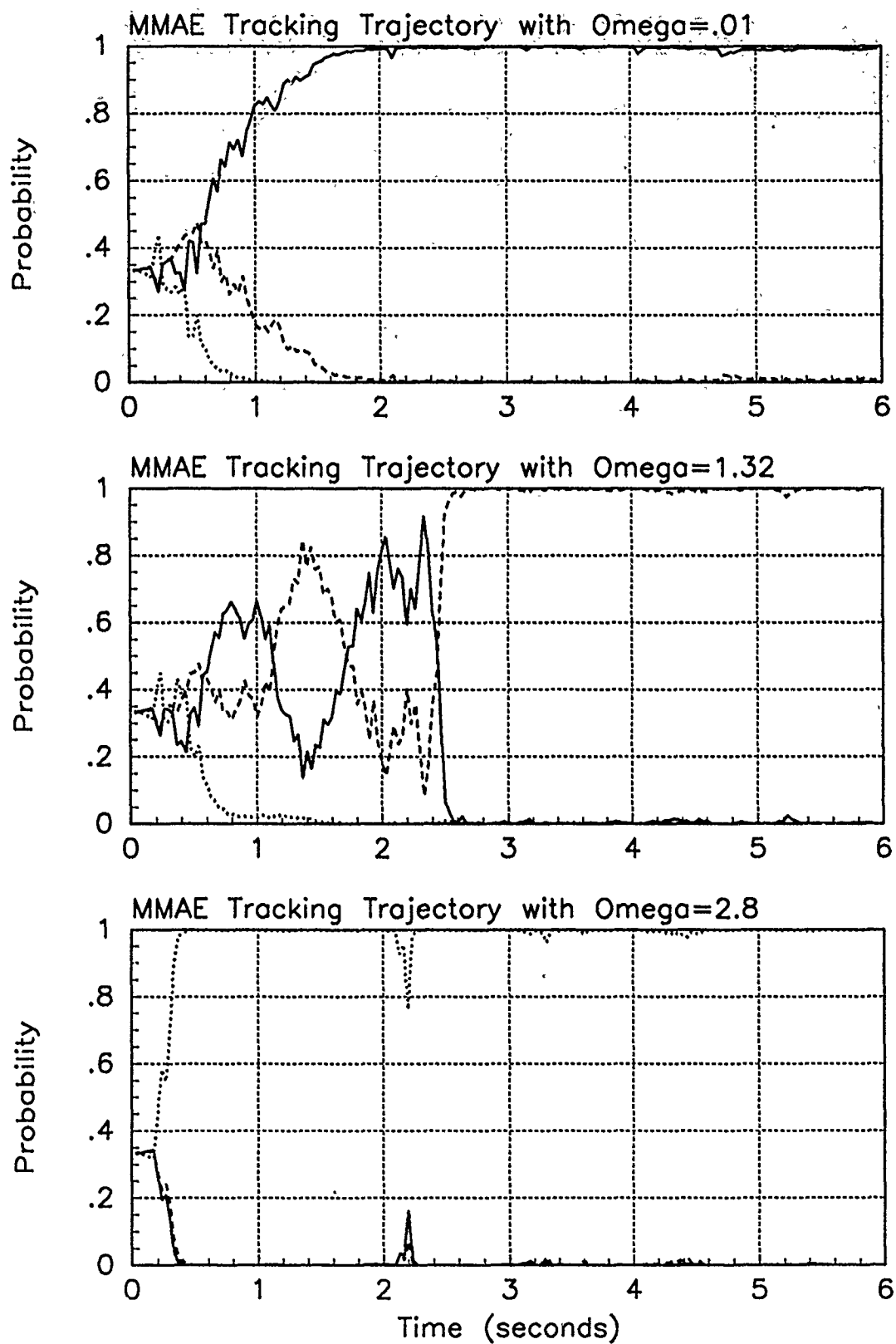


Figure 5.21. Probability Plots; Notch MMAE-2RM; PC is 1; Basic Trajectories. Benign filter has solid line, intermediate filter has dashed line, harsh filter has dotted line.

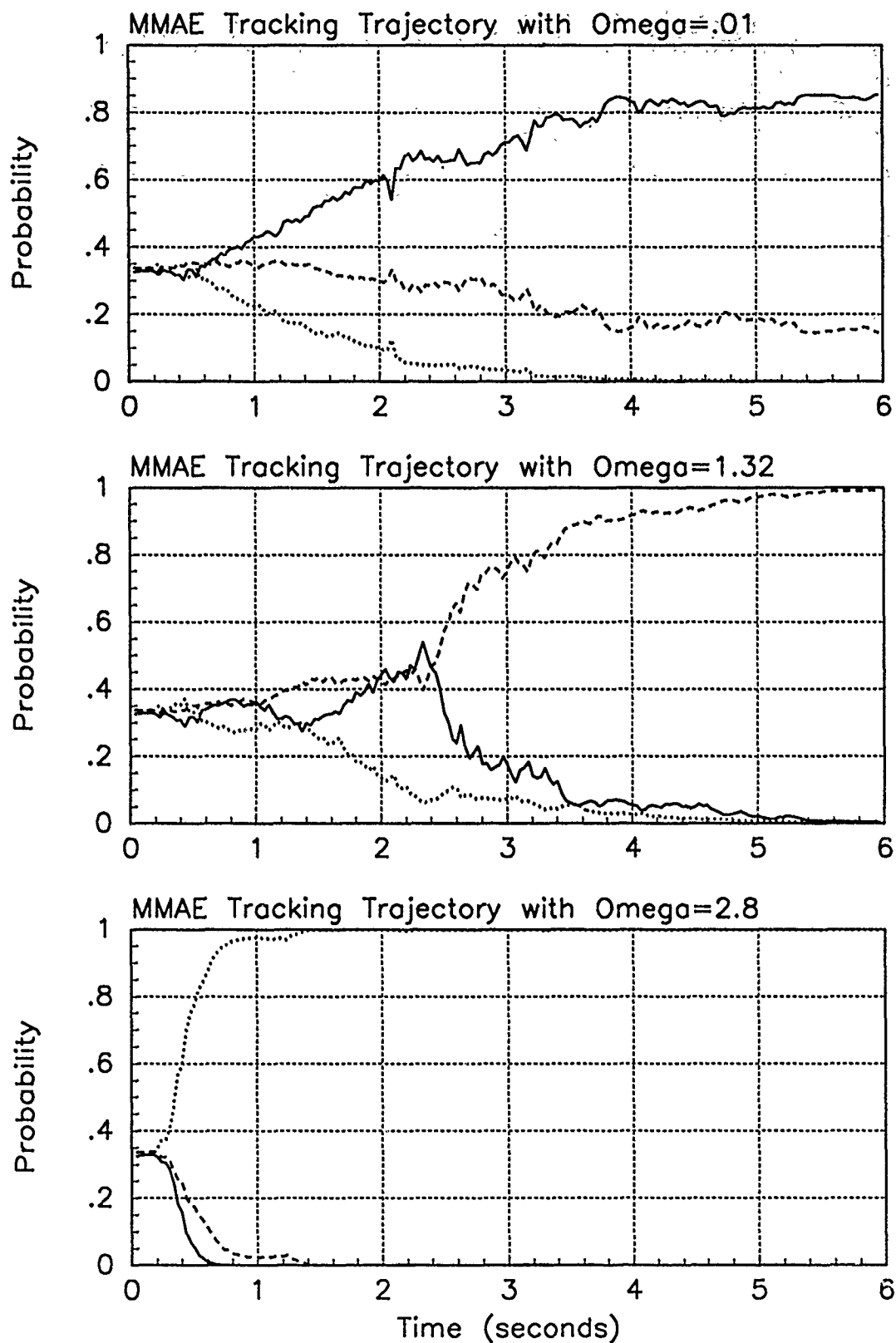


Figure 5.22. Probability Plots; Notch MMAE-2RM; PC is 4; Basic Trajectories. Benign filter has solid line, intermediate filter has dashed line, harsh filter has dotted line.

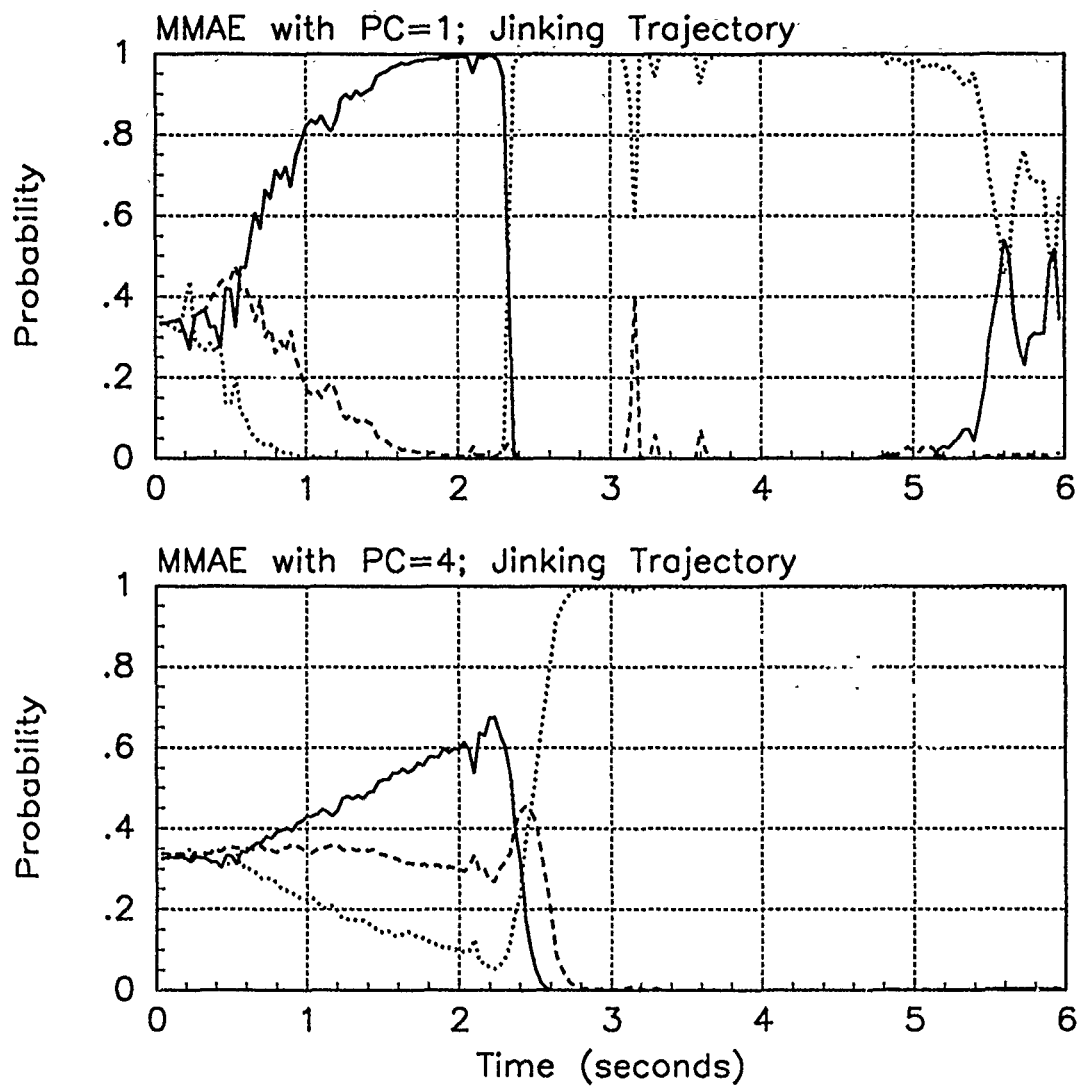


Figure 5.23. Probability Plots; Notch MMAE-2RM; PC is 1; Jinking Trajectory. Benign filter has solid line, intermediate filter has dashed line, harsh filter has dotted line.

The probability plots look very similar to the non-MAP counterparts as would be expected. (Compare Figure 5.21 to Figure 5.11, Figure 5.22 to Figure 5.19, the top plot of Figure 5.23 to the top plot of Figure 5.13, and the bottom plot of Figure 5.23 to the bottom plot of Figure 5.20.) In these cases, when filters are competing, the decision is between the benign and intermediate. The contribution to the estimate by the "wrong" filter would not be much. So, when that contribution is removed in the MAP option, the estimates and thus the residuals will not be that different.

The error plots, again, are very similar. The error statistics should tell of any benefit reaped from the MAP option. The results of that comparison is, for the benign trajectory for either PC option, the mean errors are about the same and the standard deviations are slightly smaller for the MAP version. For the intermediate trajectory, the mean errors are comparable and the standard deviations are slightly larger. For the harsh trajectory, the errors are about the same and the standard deviations are slightly smaller. For the jinking trajectory, both the mean errors and standard deviations are smaller for the MAP version, but not smaller than the errors for the Bayesian notch MMAE-2R with $PC = 1$.

5.10 Varying the Lower Bound of the Probability Calculation

A lower bound is used to prevent elemental filter lock out for this thesis, as discussed in Section 1.3.4. The magnitude of this lower bound will impact both the estimate made by the MMAE and filter selection. If the lower bound is too large, all elemental filters, even those that are based on very inappropriate models and so have poor estimates, will contribute a larger amount to every estimate of the MMAE. However, if the lower bound is too small, filter switching when appropriate may be slowed because of the recursive nature of the probability calculation. More sample times must pass before the now smaller magnitude residuals of the correct elemental filter can pull the probability calculated for that elemental filter off a value "too close" to zero.

For this analysis, the lower bound is varied while MMAE-2R, using $PC = 1$, is tracking the target as it undergoes an evasive maneuver. The lower bound is referred to as "LB" and the values used are 0.0005, 0.005, and 0.01. The respective plots and tables are in this order here and in Appendix E. Table 5.8 shows the average errors

Table 5.8. Average Errors for Notch MMAE-2R with Various Lower Bounds.

Traj	Error in:						LB=
	$p_x(t_i^-)$	$p_x(t_i^+)$	$y_x(t_i^-)$	$p_y(t_i^-)$	$p_y(t_i^+)$	$y_y(t_i^-)$	
Jink	-.013±.472	-.009±.408	-.002±.407	.133±.425	.083±.361	.101±.393	0.0005
Jink	-.009±.471	-.005±.408	.001±.406	.137±.425	.087±.361	.106±.393	0.001
Jink	-.004±.467	.003±.406	.004±.404	.134±.421	.086±.357	.105±.392	0.005
Jink	-.007±.468	.001±.407	.001±.404	.130±.425	.083±.360	.101±.393	0.01

for the Monte Carlo studies. The probability plots are in Figure 5.24. These are to be compared to the bottom plot in Figure 5.13 where the lower bound is the traditional 0.001. (The probability time history for all 10 runs of each of these four Monte Carlo studies is presented in Appendix B along with a discussion of why only run one is presented in the chapter. Recall the discussion in Section 5.2.) The error plots are in Figures E.79 to E.81, Figures E.83 to E.85, and Figures E.87 to E.89. The list of error statistics are in Tables E.25 to E.27. The plots of $\mathbf{r}_k^T(t_i)\mathbf{r}_k(t_i)$, $\mathbf{r}_k^T(t_i)\mathbf{A}_k^{-1}(t_i)\mathbf{r}_k(t_i)$, and leading coefficient used in the probability calculation are in Figures E.82, E.86, and E.90.

Consider Figure 5.24. As the lower bound increases, the MMAE is quicker at removing high probability from the harsh filter after the maneuver stops at 4 seconds. Also, the noisy looking spikes at 2.1 seconds and between 3 and 4 seconds get larger due to the quicker response time of the MMAE.

The filter-computed RMS error plot shows more rippling of the band as the lower bound increases, due to the increased filter switching. The error plots do not seem to be affected by the lower bound. The error statistics show the standard deviation values the lowest at $LB = 0.005$. The x-position mean errors are so much smaller than the y-position mean errors that only the trends in the latter are of importance. That trend seems to show *slightly* smaller errors when tracking with $LB = 0.01$. Since all of these differences are in third decimal place, no real benefit of change in the lower bound can be reported based on these error statistics.

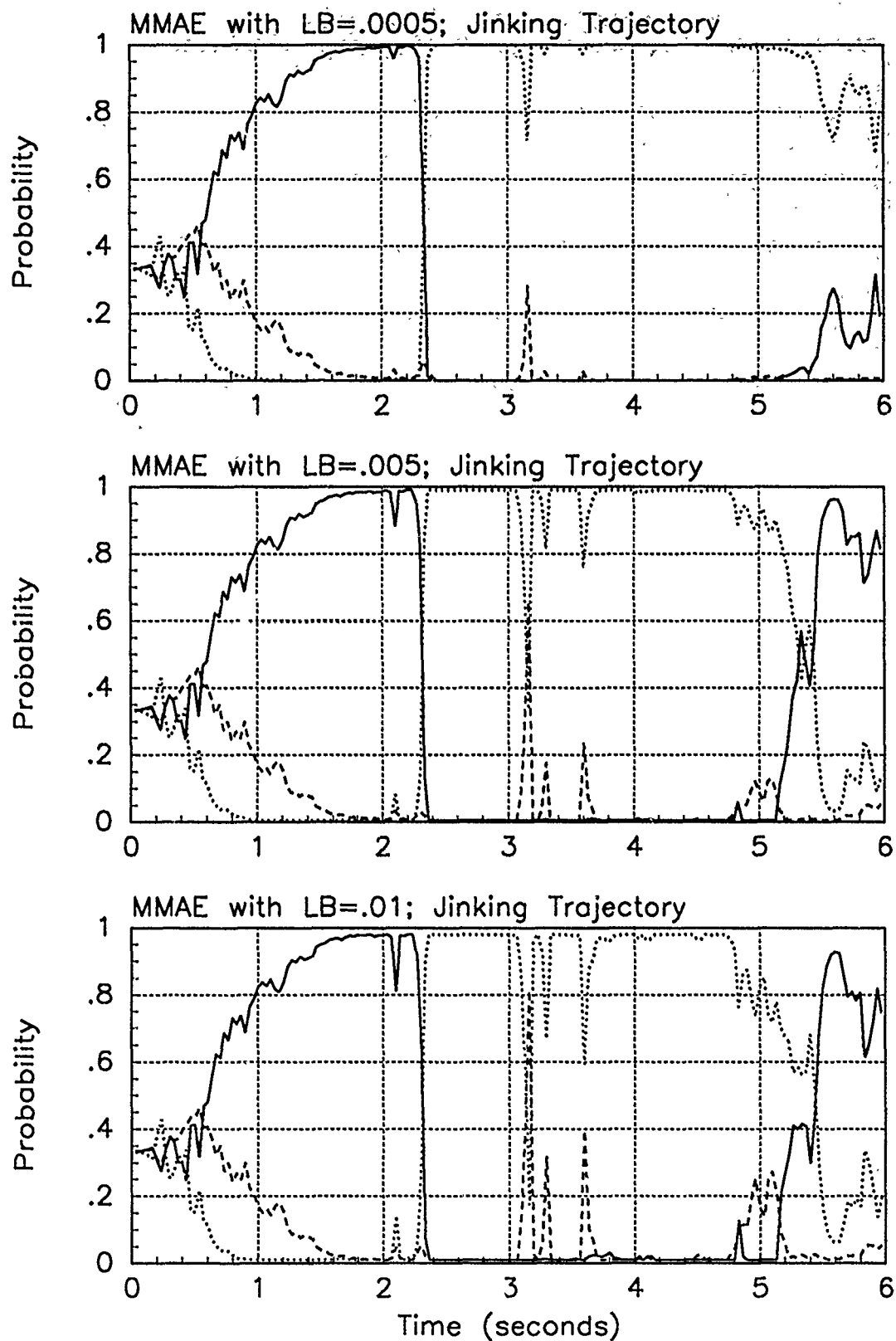


Figure 5.24. Probability Plots; Notch MMAE-2R; PC is 1; LB is Varied; Jinking Trajectory. Benign filter has solid line, intermediate filter has dashed line, harsh filter has dotted line.

5.11 Summary

This chapter discussed only the MMAEs with one first-order filter and two second-order filters. The analysis started out with second-order filters based on acceleration models with two real poles. This was quickly abandoned when the similarly designed notch MMAE gave comparable performance and elemental filter redesign was required.

The parameter space was coarsely discretized into three models based on aircraft type; the cargo plane in level flight, the air-superiority aircraft in a maneuver, and the generic "other" aircraft that occupies the frequency range in the middle. Revised tuning (Section 5.5) and changing the probability calculation did not help this discretization choice and a second notch MMAE was designed so as to embody better frequency separation of acceleration PSDs. This notch MMAE-2R was used in a second probability calculation investigation to ensure the previous results were not corrupted by the improper MMAE design. The notch MMAE-2R was then used in the MAP versus Bayesian, and the lower bound investigations.

In the PC study on the notch MMAE-2R, the basic probability calculation ($PC = 1$) gave the best probability time history with regard to correct elemental filter selection and the speed with which the MMAE would assign maximum probability to the appropriate filter. The maximum entropy option ($PC = 4$) gives the same filter selection with regard to which elemental filter is assigned the largest probability. But maximum probability (probability greater than 0.9) is not assigned quickly and the MMAE is especially sluggish in returning any probability to the more benign filter when the target stops maneuvering.

The MAP MMAE did not give clear advantage in either the error magnitude mean value or standard deviation. The lower bound check gave more interesting results. The greater the lower bound, the more easily the MMAE can assign greater probability to another elemental filter either appropriately (as when the target starts or stops maneuvering) or unexpectedly (as in apparant response to noise). The tradeoff of fast probability response versus noise susceptibility may not be crucial as it affects only the filter-computed RMS error: the mean error and standard deviation are about the same for all LB values. Based on the time history plots (Figure 5.24), a lower bound of 0.001 is selected.

VI. MMAE Based on First-Order Models

6.1 Introduction

Since previous theses have used first-order acceleration models, a comparison must be made to determine which MMAE tracks better, one with all elemental filters based on first-order acceleration models or the MMAEs with some of the elemental filters based on second-order models. One "first-order" MMAE is designed. The elemental filters have the correlation times of 4, 0.5, and 0.125 seconds for the benign, intermediate, and harsh filters, respectively. These values do not correspond to previous theses, but place the break frequency for the intermediate filter between the peaks for the intermediate and harsh notch models. The break frequency for the harsh filter is slightly above the peak of the harsh notch model. The lower bound for the probability calculation is held at 0.001. The MMAE is used to track the basic trajectories, those with ω 's of 0.01, 1.32, and 2.8 radians per second, and the jinking trajectory.

6.2 First-Order MMAE with Revised Tuning

The elemental filters are tuned with the revised method (-R) yielding $\sigma_b^2 = 150$, $\sigma_i^2 = 400$, and $\sigma_h^2 = 10000$ each in units of pixels². These mean squared acceleration values require the respective first-order acceleration model be driven by a white noise of strength $q_b = 75$, $q_i = 1600$, and $q_h = 160000$, each with units of pixels² per seconds⁵. The acceleration PSD plot of these is in Figure 6.1. The height of the curves may be misleading, especially for the PSD of the model for the benign and intermediate filters. It is the area under the PSD curve that is related to the magnitude of the acceleration the resulting filter is designed to track. The area under these curves is increasing and comparable to the respective PSD plots for the notch filter models. This is discussed in Appendix A. Only the PC options 1 and 4 are used (as described in Section 5.8). First the basic trajectories are discussed. The probability plots are in Figures 6.2 and 6.3. The error plots are in Figures F.1 to F.18. The respective error statistics and average $\mathbf{r}_k^T(t_i)\mathbf{r}_k(t_i)$ and $\mathbf{r}_k^T(t_i)\mathbf{A}_k^{-1}(t_i)\mathbf{r}_k(t_i)$ are in Tables F.1 to F.6.

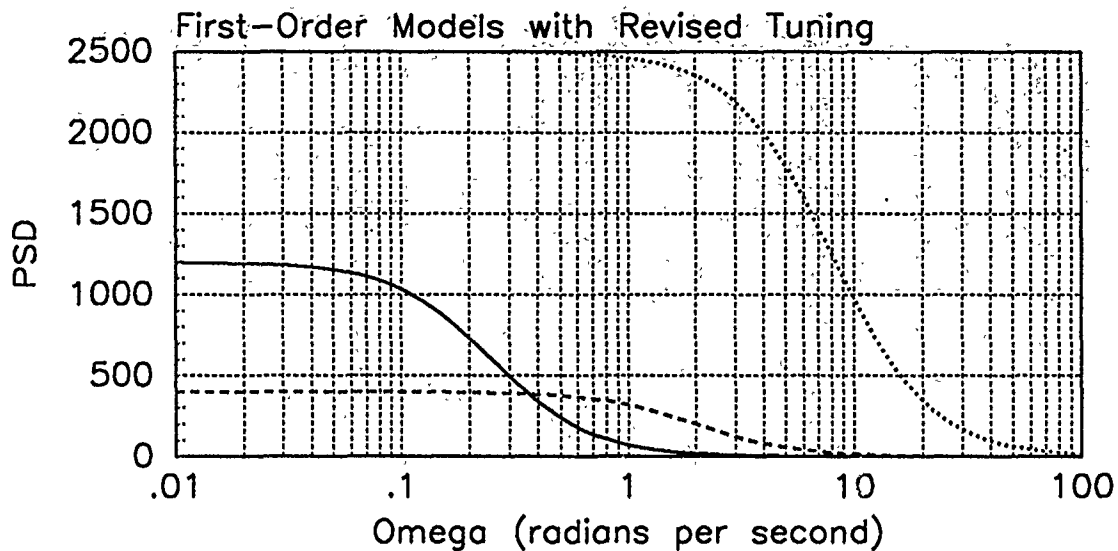


Figure 6.1. PSD Plot; First-Order MMAE-R

The performance of this MMAE must be compared to that of the notch MMAE-2R. The probability plots are in Figures 5.11 for $PC = 1$ (page 5-22) and 5.19 for $PC = 4$ (page 5-36). The error plots are in Figures E.1 to E.9 for $PC = 1$ and in Figures E.28 to E.36 for $PC = 4$. The error statistics are in Tables E.1 to E.3 and Tables E.10 to E.12. A compilation of the position error statistics is in Table 6.1.

The probability plots for the first-order MMAE-R are almost identical to that of the notch MMAE-2R for either PC option. (Certainly a suitable set of first-order acceleration models has been selected for the comparison.) Again, the MMAE does not clearly select the intermediate filter for the intermediate trajectory until after 2.5 seconds of switching between the benign and intermediate filters. The probability given to the benign filter between 2 and 2.5 seconds by the first-order MMAE-R is not as great (0.7) as what the notch MMAE-2R gives (0.9), but it is still interesting that the final switch has no further ripples of indecision. $PC = 4$ yields the same filter selection pattern as with $PC = 1$, but the MMAE takes longer to make the selection clearly; in fact, the benign filter never gets probability greater than 0.9 for the benign trajectory.

Given the magnitude of the standard deviations in the position error tables, there is no appreciable difference in the mean error magnitudes between the two kinds of MMAE or the two PC options. It is good to see the how close the mean errors and standard deviations are for the MMAEs each tracking the benign trajectory since they both have

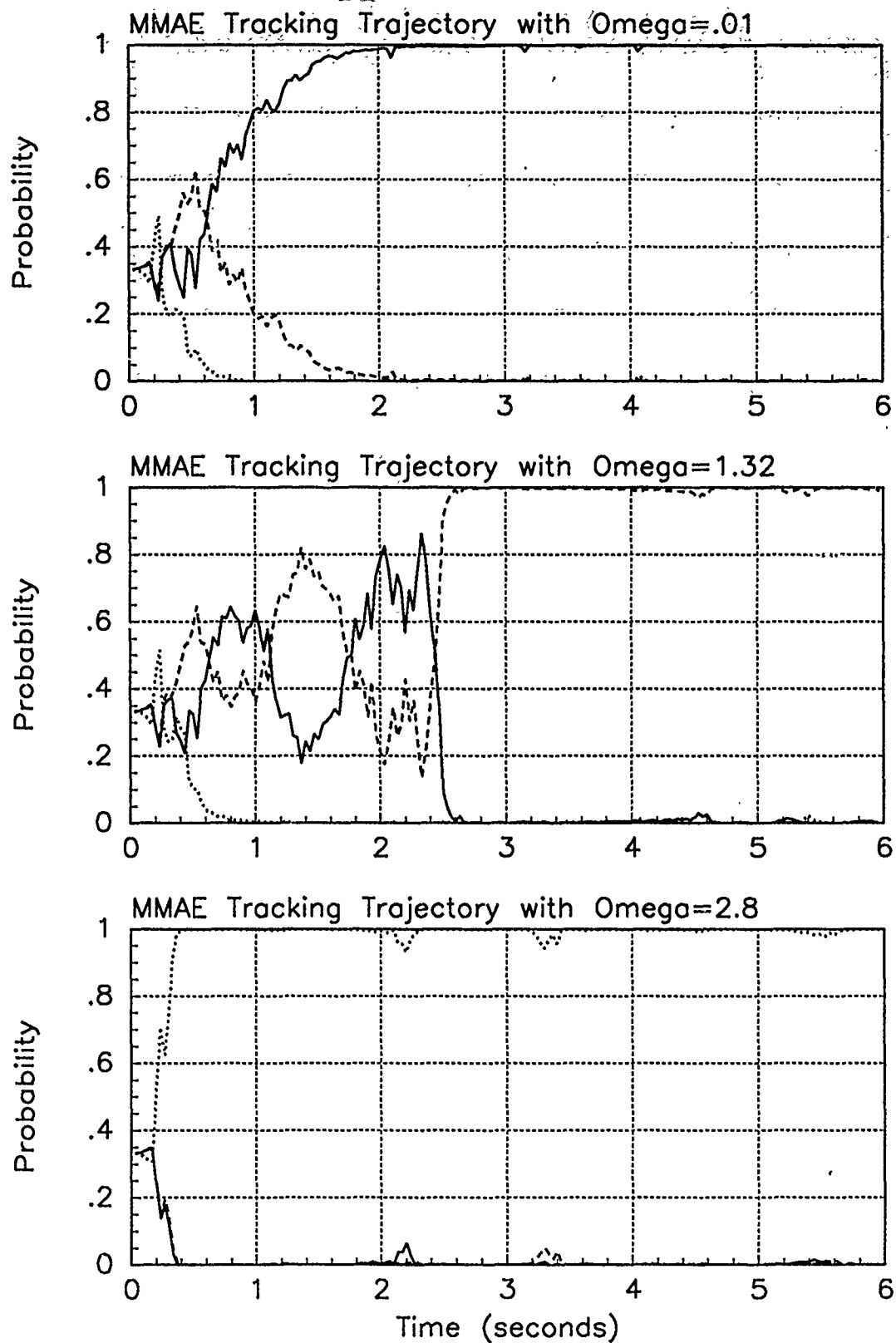


Figure 6.2. Probability Plots; First-Order MMAE-R; PC is 1; Basic Trajectories. Benign filter has solid line, intermediate filter has dashed line, harsh filter has dotted line.

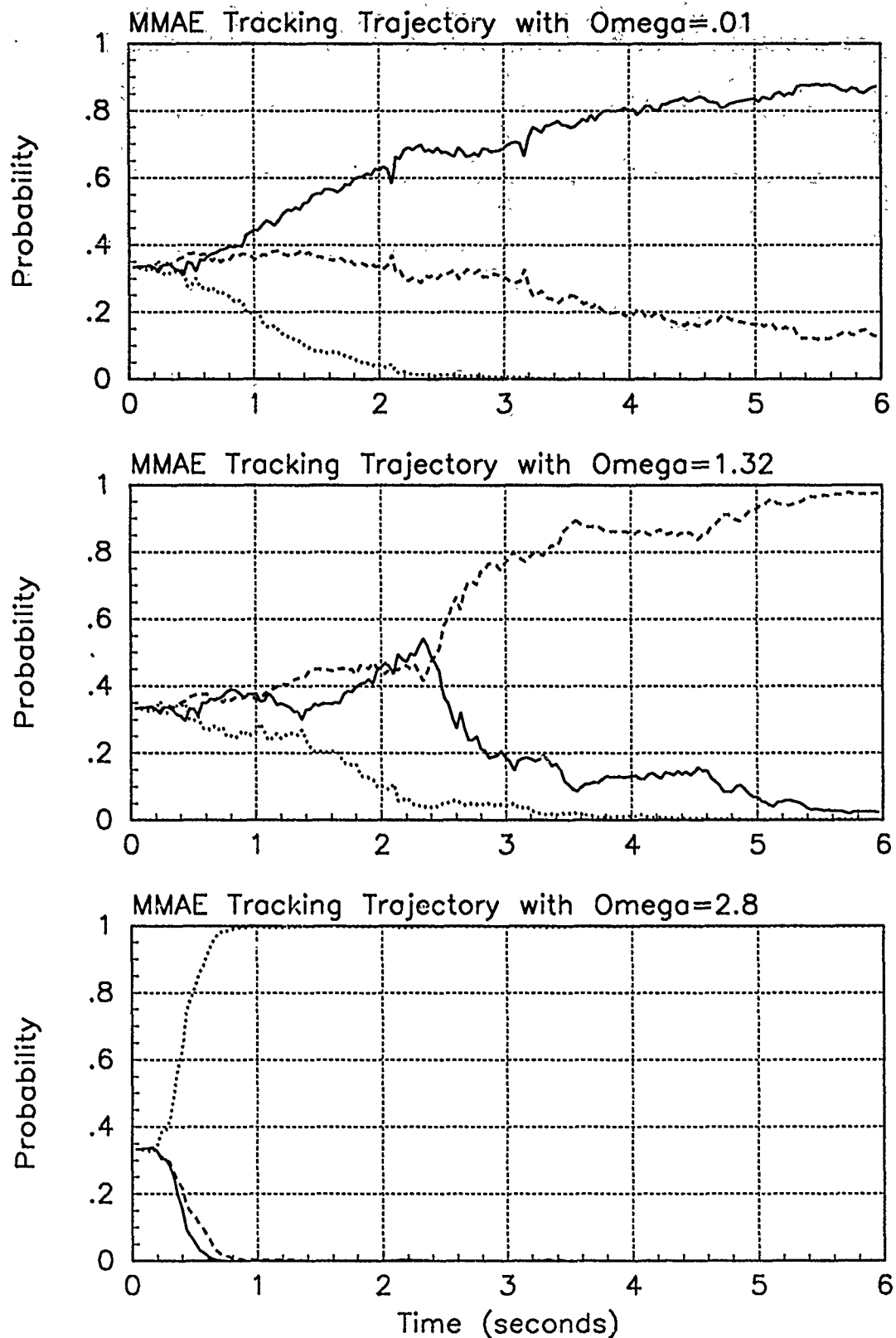


Figure 6.3. Probability Plots; First-Order MMAE-R; PC is 4; Basic Trajectories. Benign filter has solid line, intermediate filter has dashed line, harsh filter has dotted line.

Table 6.1. Average Position Errors for First-Order-R and Notch-2R MMAEs with PC = 1 and 4 Options.

Traj ω	Error in:						MMAE, PC
	$p_x(t_i^-)$	$p_x(t_i^+)$	$y_x(t_i^-)$	$p_y(t_i^-)$	$p_y(t_i^+)$	$y_y(t_i^-)$	
.01	.159±.408	.121±.371	.098±.381	.005±.347	.006±.315	.011±.366	FO,1
.01	.114±.422	.086±.381	.071±.385	.003±.361	.003±.325	.008±.370	FO,4
.01	.164±.411	.126±.373	.103±.381	-.004±.347	-.003±.314	.002±.366	N2,1
.01	.098±.427	.081±.387	.065±.388	.004±.362	.004±.326	.008±.372	N2,4
1.32	.058±.447	.034±.398	.043±.395	-.002±.408	-.007±.361	-.008±.383	FO,1
1.32	.063±.443	.040±.394	.046±.392	-.026±.401	-.029±.355	-.021±.380	FO,4
1.32	-.033±.445	-.028±.396	-.016±.392	-.008±.391	-.014±.343	-.016±.374	N2,1
1.32	-.026±.444	-.017±.396	-.010±.391	-.014±.389	-.023±.343	-.014±.378	N2,4
2.8	-.023±.559	-.024±.446	-.010±.446	.013±.498	-.003±.386	.008±.429	FO,1
2.8	-.016±.560	-.018±.447	-.003±.446	.027±.501	.007±.389	.019±.429	FO,4
2.8	-.096±.512	-.060±.431	-.061±.420	.066±.450	.028±.371	.047±.403	N2,1
2.8	-.093±.509	-.058±.429	-.058±.420	.086±.453	.043±.373	.062±.402	N2,4
Jink	.035±.497	.018±.412	.031±.419	.025±.459	.017±.376	.021±.409	FO,1
Jink	.003±.509	-.007±.420	.012±.425	.063±.473	.012±.385	.041±.415	FO,4
Jink	-.009±.471	-.005±.408	.001±.406	.137±.425	.087±.361	.106±.393	N2,1
Jink	-.038±.482	-.025±.416	-.015±.411	.151±.435	.095±.370	.110±.396	N2,4

the same benign filter with which to do it. As with the notch MMAE-2R errors, the magnitude of the mean x-position error and standard deviation for the benign trajectory is larger than that for the y-position error. This does not seem correct. The acceleration in the x direction is zero while the acceleration in the y direction for the benign trajectory is not zero but remains less than 0.00006 meters per second². One would expect a similar magnitude error for either the x- or y-position error for the benign trajectory. As the dynamics in the y-axis get more harsh ($\omega = 1.32$, then 2.8), the magnitude of the x-position errors decreases while its standard deviation increases because the dynamics in the y-axis forces the MMAE to select a harsher filter that has greater dynamics noise strength. The shapes of the error plots for the first-order MMAE-R are slightly different but the magnitudes are about the same as the plots for the notch MMAE-2R.

A target in the jinking trajectory is tracked with PC options 1 and 4. The resulting probability plots are in Figure 6.4. The error plots are in Figures F.19 to F.21 and Figures F.23 to F.25. The error statistics are in Tables F.7 and F.8. The plots of the probability calculation elements are in Figures F.22 and F.26.

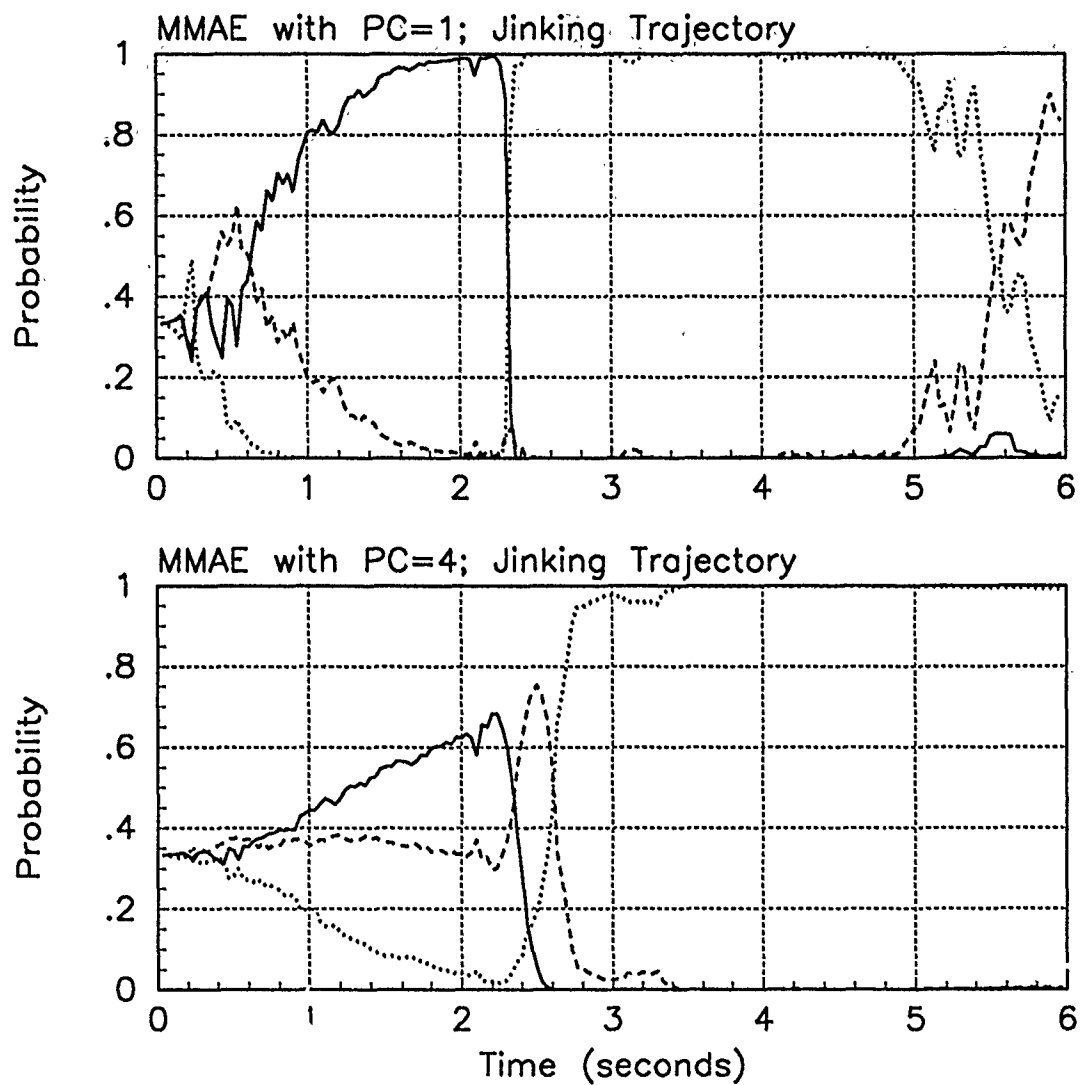


Figure 6.4. Probability Plots; First-Order MMAE-R; PC is Varied; Jinking Trajectory. Benign filter has solid line, intermediate filter has dashed line, harsh filter has dotted line.

The probability plots compare favorably to the plots for the notch MMAE-2R tracking the jinking trajectory. For $PC = 1$, the probability plot for the notch MMAE-2R is the bottom one in Figure 5.13 (page 5-25). For $PC = 4$, the appropriate plot is the bottom one in Figure 5.20 (page 5-38). The trace for the intermediate filter is slightly different for both PC options. The first-order MMAE-R selects the intermediate filter to track the target after it pulls out of the dive when $PC = 1$. Based on the way the trajectory is made, either the benign or the intermediate filter could be the one that is selected at the end of the jinking trajectory. (The last two-second segment has $\omega = 0.62$.) In the probability plot for $PC = 4$, the first-order MMAE-R starts to choose the intermediate filter to track the target after it dives, but then quickly switches to the more correct harsh filter. The same slow filter selection response is seen in the plot for $PC = 4$ as has been noted before. Again, $PC = 1$ appears to be the better option.

The error statistics are compared with the statistics for the notch MMAE-2R in Tables E.13 and E.16 for $PC = 1$ and 4, respectively. The first-order MMAE-R has smaller position errors for y-position but not x-position.

Table 6.1 shows a compilation of the average position errors for the four Monte Carlo studies. The key comparison is for $PC = 1$ since that option yields an MMAE that gives the best performance with regard to filter selection. For the intermediate trajectory, the notch MMAE has smaller mean errors. For the harsh trajectory, the first-order MMAE has smaller mean errors but slightly larger standard deviations. Neither the first-order MMAE-R nor the notch MMAE-2R outperforms the other based on the criteria used for the evaluation.

6.3 First-Order MMAE with Ad Hoc Tuning

Ad hoc tuning is applied to the first-order MMAE as shown in Figure 6.5. The acceleration model dynamics noise strengths are selected such that the PSD plots of the acceleration models are all of the same height. The height of the benign filter in Figure 6.1 is selected for the first MMAE. This MMAE is referred to as first-order MMAE-FB for the flat PSD plot at a *benign* height. The tuning values are $\sigma_b^2 = 150$, $\sigma_i^2 = 1200$, and $\sigma_h^2 = 4800$. The second MMAE, called first-order MMAE-FH, has elemental filters each tuned such

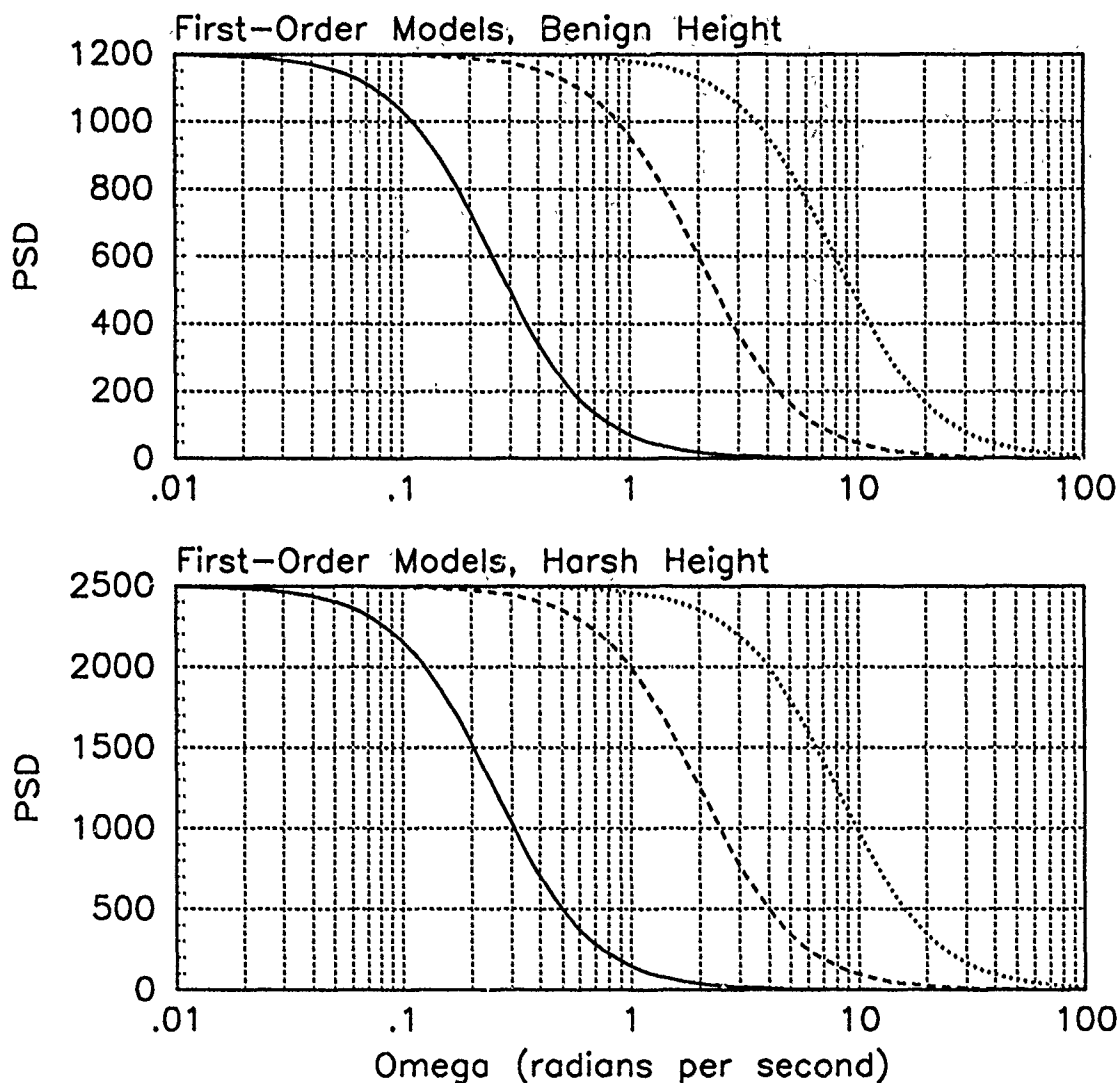


Figure 6.5. PSD Plots; First-Order MMAE with Ad Hoc Tuning. The top plot shows each model tuned so the height of the PSD curve is the same as that of the benign filter's acceleration model with revised tuning. The bottom plot shows the models tuned for the height of the harsh filter's acceleration model.

Table 6.2. The Tuning Values used for the First-Order Models.

Tuning:	σ_b^2	q_b	σ_i^2	q_i	σ_h^2	q_h
-R	150	75	400	1600	10000	160000
-FB	150	75	1200	4800	4800	76800
-FB	313	156	2500	10000	10000	160000

that the PSD of their acceleration models are the height of the *harsh* acceleration model in Figure 6.1. Tuning values for this are $\sigma_b^2 = 312.5$, $\sigma_i^2 = 2500$, and $\sigma_h^2 = 10000$. The tuning values for these options and the revised values are in Table 6.2. Note, the strength of the dynamics driving noise is increased for the intermediate filter for both the -FB and -FH options. These two MMAEs are allowed to track targets in the basic trajectories and the results are compared to tracking with the first-order MMAE-R of the previous section. The mean errors are compiled (with the results of studies still to be discussed) in Table 6.3 on Page 6-13. The probability plots are in Figures 6.6 and 6.7. The error plots are in Figures F.27 to F.44. The error statistics and average residuals for the individual studies are in Tables F.9 to F.14.

The probability plots for the first-order MMAE-FB are very similar to those for the first-order MMAE-R. The intermediate filter contributes a little more to tracking the harsh trajectory due to the increased noise strength of the filter. There do not appear to be any trends in the average position errors as tabulated in Table 6.3 because different filters are selected for the different trajectories. One exception is that the standard deviation is increased when the filter tracking the trajectory has an increased dynamics driving noise strength. There is a larger trace of the harsh trajectory left in the error plot for the -FB option.

The probability plots for -FH look much like the probability plots of the MMAEs tuned in the original manner. The intermediate and benign filters have unacceptably high strength of dynamics driving noise. As discussed before, this disables the MMAE adaptation. The first-order MMAE-FH selects the benign filter to track the intermediate trajectory and cannot clearly select the harsh filter for the harsh trajectory for most of the simulation time.

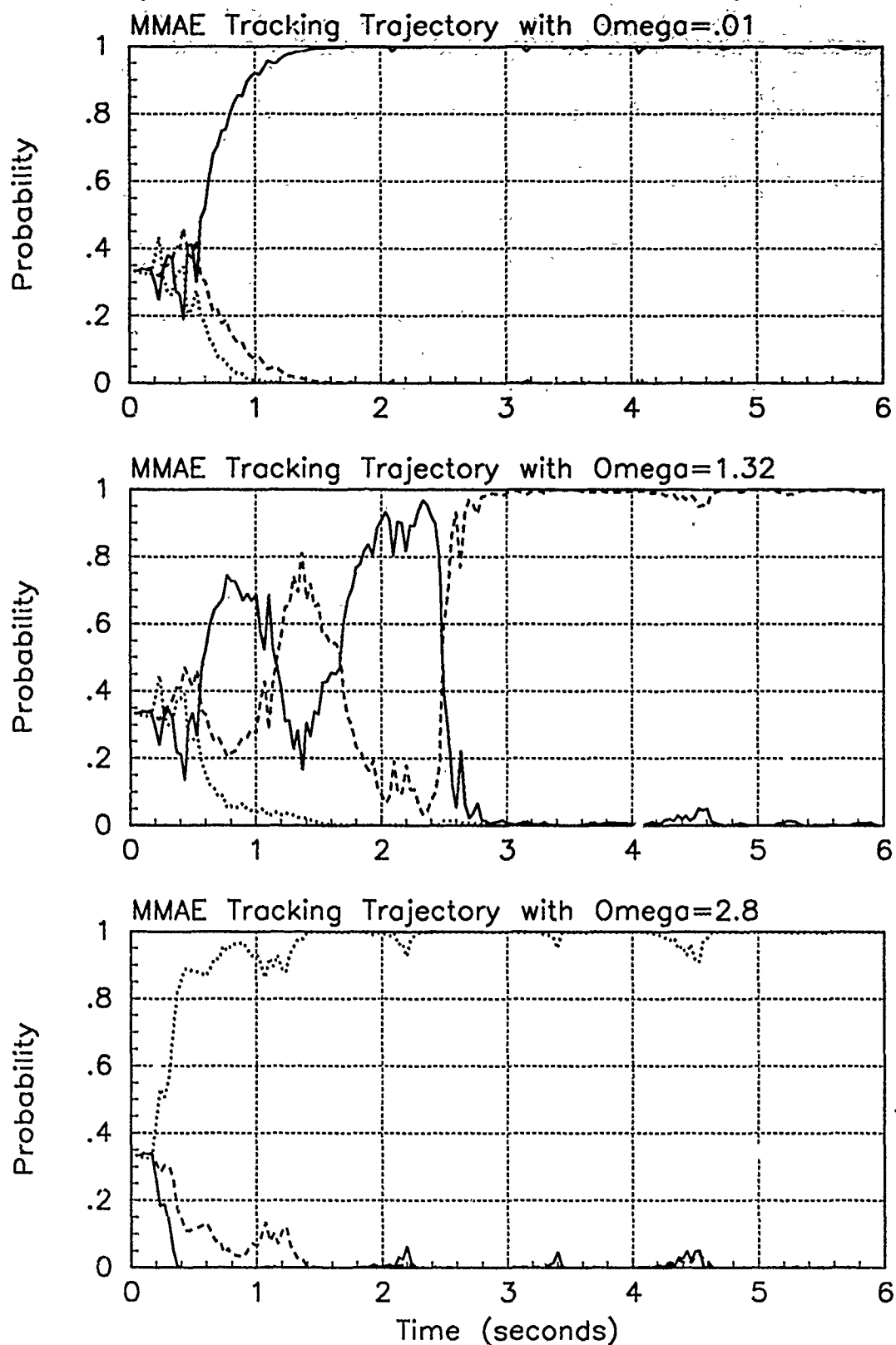


Figure 6.6. Probability Plots; First-Order MMAE-FB; PC is 1; Basic Trajectories. Benign filter has solid line, intermediate filter has dashed line, harsh filter has dotted line.

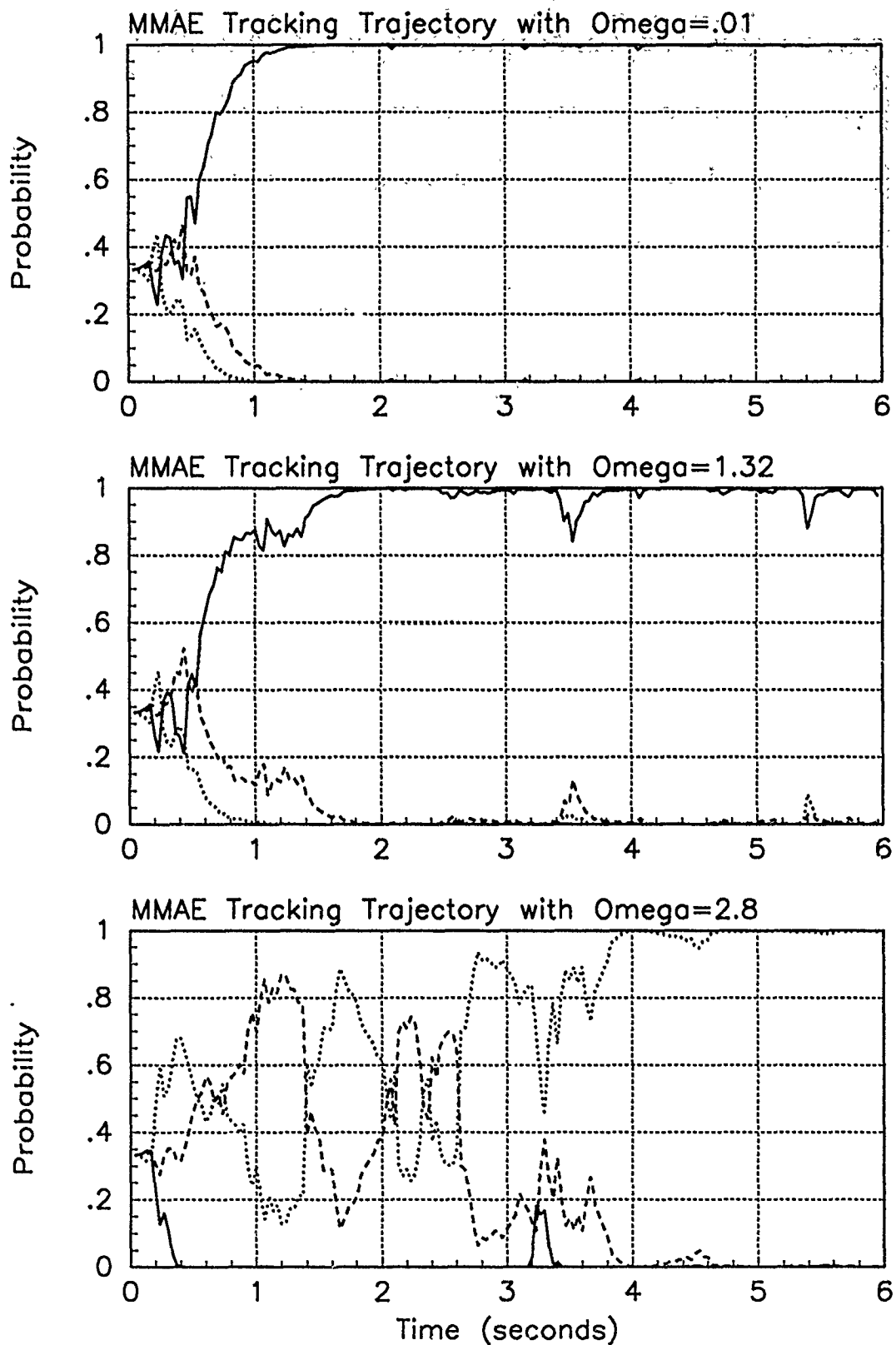


Figure 6.7. Probability Plots; First-Order MMAE-FH; PC is 1; Basic Trajectories. Benign filter has solid line, intermediate filter has dashed line, harsh filter has dotted line.

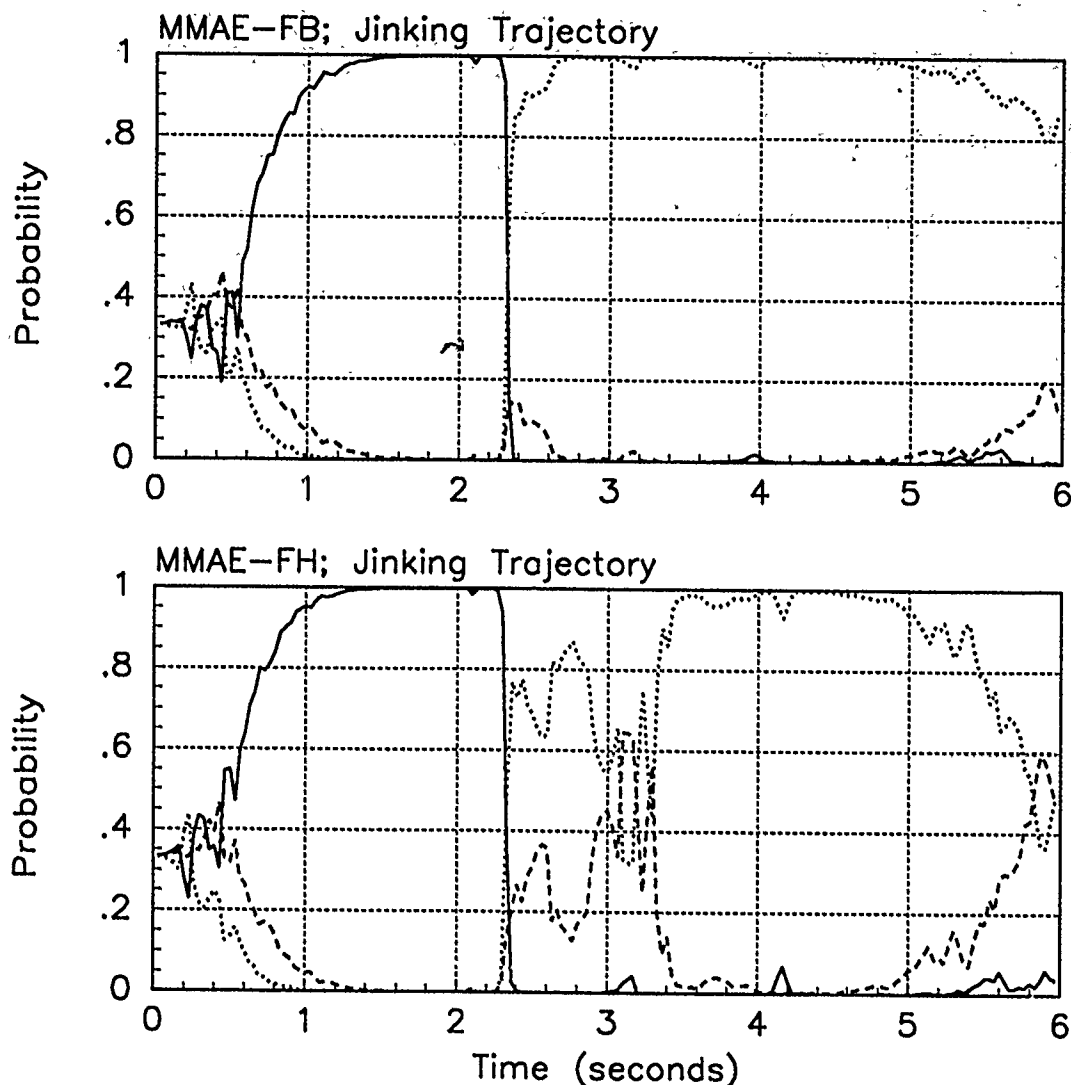


Figure 6.8. Probability Plots; First-Order MMAE-F; PC is 1; Jinking Trajectory. Benign filter has solid line, intermediate filter has dashed line, harsh filter has dotted line.

The MMAEs are also allowed to track the jinking trajectory. The probability plots are in Figure 6.8. The error plots are in Figures F.45 to F.51. The error statistics are in Tables F.15 and F.16. The probability calculation related plots are in Figures F.48 and F.52.

Again, from the probability plot, the -FH option is unacceptable since the intermediate filter is allowed to help track the harsh trajectory, driving the average y-position error up. The standard deviation is increased as mentioned above. The error plots and statistics need to be compared to the performance of the first-order MMAE-R as presented in

Table 6.3. Average Position Errors for First-Order and Notch-2 MMAEs with -FB, -FH, and -R Tuning Options, PC = 1.

Traj ω	Error in:						MMAE, Tune
	$p_x(t_i^-)$	$p_x(t_i^+)$	$y_x(t_i^-)$	$p_y(t_i^-)$	$p_y(t_i^+)$	$y_y(t_i^-)$	
.01	.165±.406	.126±.370	.102±.380	-.003±.348	-.002±.316	.003±.367	FO,FB
.01	.116±.424	.085±.382	.078±.382	-.003±.366	-.002±.328	.003±.371	FO,FH
.01	.159±.408	.121±.371	.098±.381	.051±.347	.006±.315	.011±.366	FO,R
.01	.164±.411	.126±.373	.103±.381	-.004±.347	-.003±.314	.002±.366	N2,R
1.32	.046±.463	.026±.404	.037±.401	-.021±.426	-.022±.365	-.022±.386	FO,FB
1.32	.089±.436	.059±.393	.053±.390	-.009±.383	-.020±.341	-.014±.373	FO,FH
1.32	.058±.447	.034±.398	.043±.395	-.002±.408	-.007±.361	-.008±.383	FO,R
1.32	-.033±.445	-.028±.396	-.016±.392	-.008±.391	-.014±.343	-.016±.374	N2,R
2.8	-.006±.528	-.009±.435	.006±.430	.056±.470	.035±.379	.045±.411	FO,FB
2.8	-.018±.546	-.021±.436	-.006±.440	-.015±.494	-.025±.385	-.019±.428	FO,FH
2.8	-.023±.559	-.024±.446	-.010±.446	.013±.498	-.003±.386	.008±.429	FO,R
2.8	-.096±.512	-.060±.431	-.061±.420	.066±.450	.028±.371	.047±.403	N2,R
Jink	.043±.481	.022±.407	.039±.412	.009±.444	.004±.370	.006±.401	FO,FB
Jink	.003±.509	-.007±.420	.012±.425	.063±.473	.042±.385	.041±.415	FO,FH
Jink	.035±.497	.018±.412	.031±.419	.025±.459	.017±.376	.021±.409	FO,R
Jink	-.067±.437	-.045±.391	-.033±.391	.241±.415	.193±.359	.168±.392	N2,FB
Jink	-.022±.477	-.015±.411	-.007±.406	.088±.461	.057±.380	.066±.410	N2,FH
Jink	-.009±.471	-.005±.408	.001±.406	.137±.425	.087±.361	.106±.393	N2,R

Figures F.19 to F.21 and Table F.7. For the -FB option, the error statistics and the plots are only slightly different from the results using the second-order acceleration models. The mean errors in the x position are less, while in the y position they are more by the same amount.

Table 6.3 is a compilation of the average position errors for the Monte Carlo studies performed for the two MMAEs tuned in the ad hoc manner and revised manner. This table includes the notch-MMAE-R that is covered below.

For completeness, this same ad hoc tuning, -FB and -FH, is applied to the notch MMAE-2R. The PSD plots of these are in Figure 6.9. Tuning values for the -FB option are all $q = 75$. For the -FB option, the benign filter needs $\sigma_b^2 = 800$ so $q = 400$ for each filter. These values are listed in Table 6.4. The MMAE is allowed to track only the jinking trajectory with PC = 1. The probability plots are in Figure 6.10 and are to be compared to the bottom plot in Figure 5.13 (page 5-25) for the notch MMAE-2R. The error plots

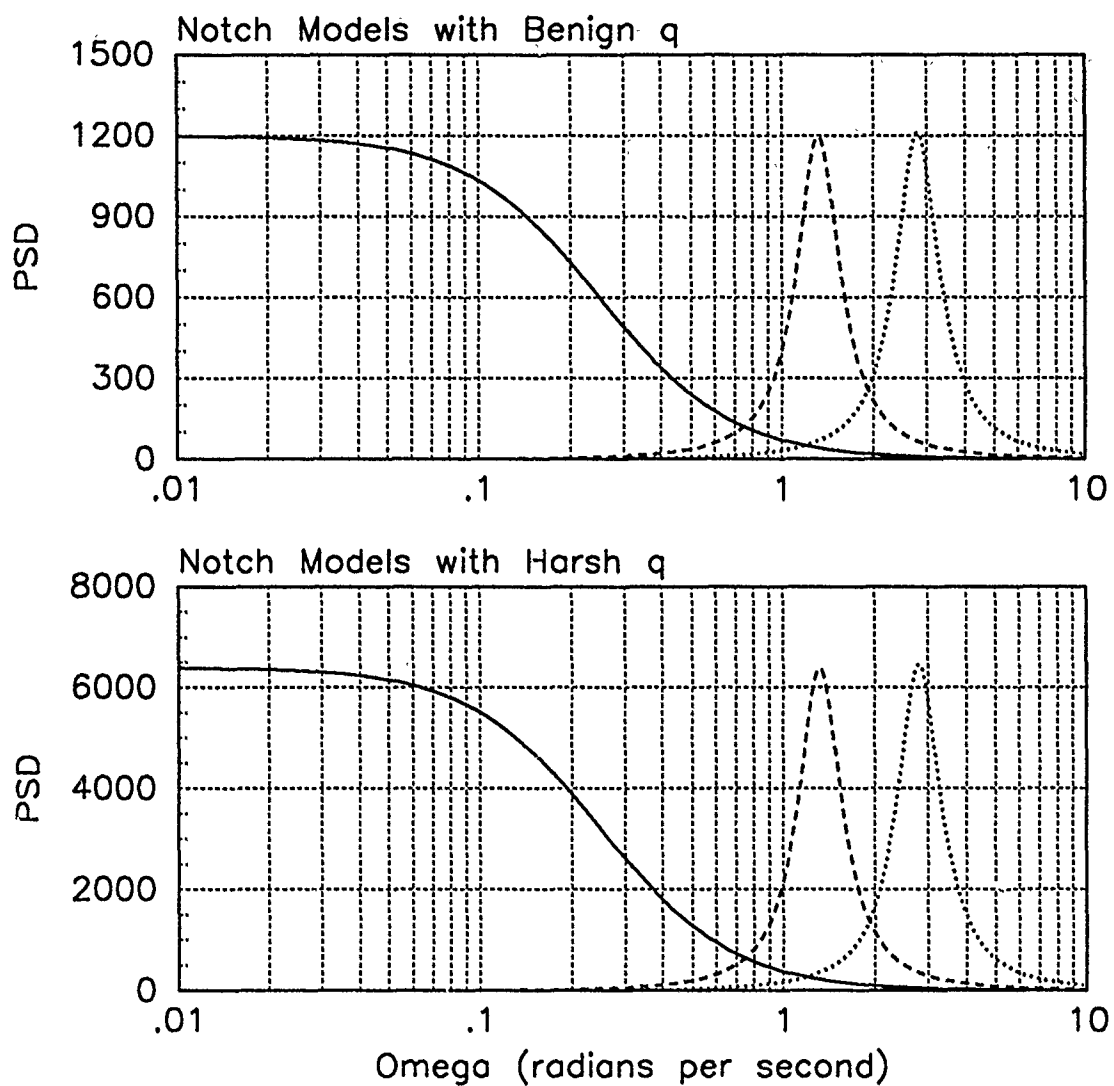


Figure 5.9. PSD Plots; Notch MMAE-2 with Ad Hoc Tuning. The top plot shows each model tuned so the height of the PSD curve is the same as that of the benign filter's acceleration model with revised tuning. The bottom plot shows the models tuned for the height of the harsh filter's acceleration model.

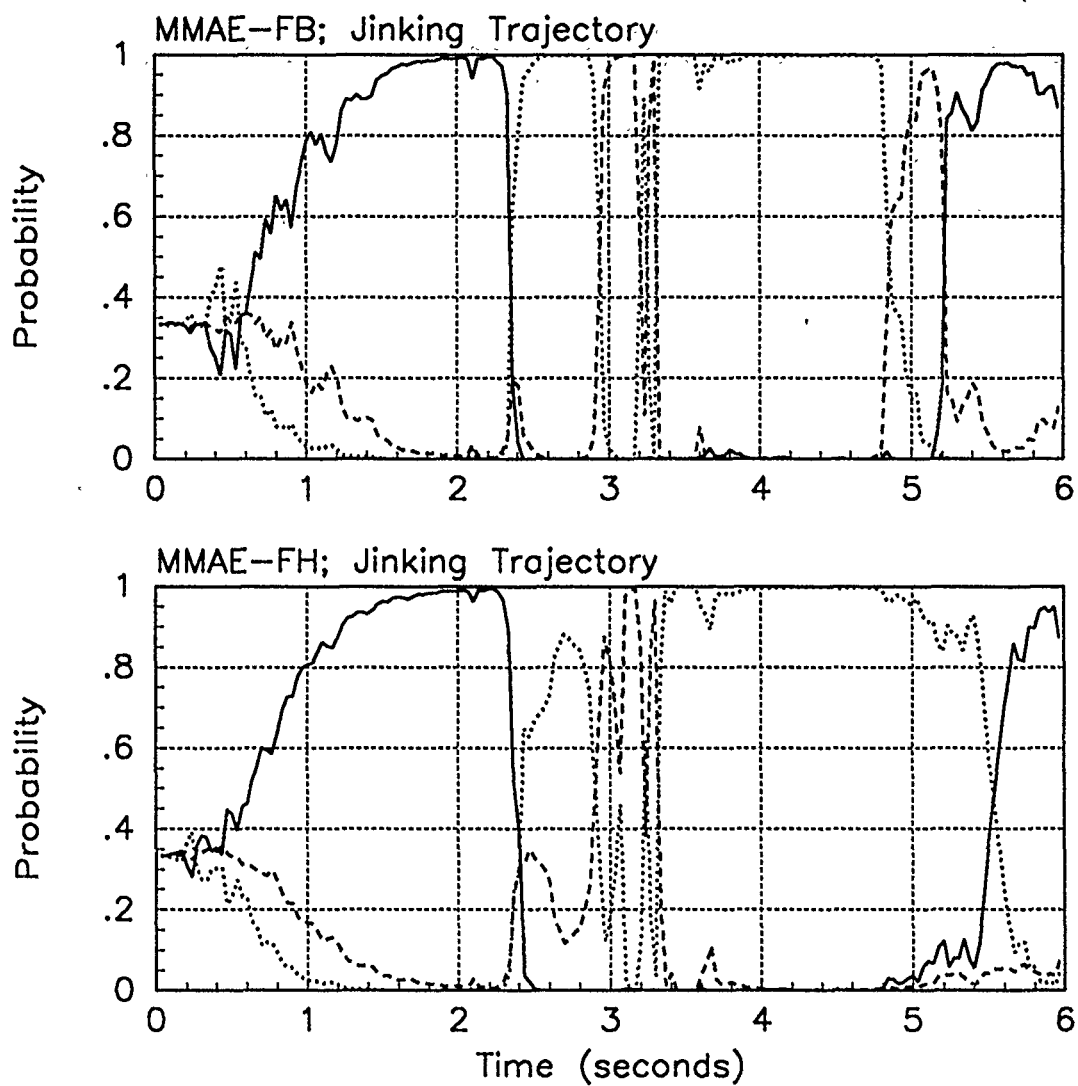


Figure 6.10. Probability Plots; Notch MMAE-2F; PC is 1; Jinking Trajectory. Benign filter has solid line, intermediate filter has dashed line, harsh filter has dotted line.

Table 6.4. The Tuning Values used for the Notch-2 Models.

Tuning:	σ_b^2	q_b	q_i	q_h
-R	150	75	100	400
-FB	150	75	75	75
-FB	800	400	400	400

are in Figures E.91 to E.97 and are to be compared to Figures E.37 to E.39. The error statistics are in Tables E.28 and E.29 and are to be compared to Table E.13.

The probability plot for the -FB option shows the quickest response after the dive is stopped for a less harsh filter to be selected. The y-position RMS error plots have large spikes during the time the target is diving. The spikes show up with both the -FB and -FH options and are due to the input of the intermediate filter during the time when the harsh filter should be selected. The mean errors on the -FH option are all less than 0.09 pixels. These are smaller than the mean errors for the notch MMAE-2R of Table E.13. The standard deviations are all increased by one or more in the second decimal place. The error plots look very similar to those of the notch MMAE-2R in Figure E.39. Thus, except for the unusual looking probability plot, this option *may* be acceptable as a tuning method. The magnitude of the y-position error plots for the -FB option as shown in Figure E.93 make this an unacceptable option.

6.4 Proximity Check for Filters

There is some difficulty defining an intermediate filter that will allow the MMAE to select the "correct" elemental filter for a particular trajectory. The elemental filters were initially defined by what is known about how major classes of manned aircraft perform. This proved inappropriate despite the various modifications applied to the MMAE in this thesis. These difficulties motivate a proximity check to determine how practically the parameter space could be divided for a three-filter MMAE. The issue is, how much acceleration PSD overlap is permissible before elemental filter selection becomes inappropriate or ambiguous? In other words, how much separation between notched PSD regions should be maintained in order to generate unambiguous and correct filter selections?

6.4.1 Proximity of Notch and First-Order Filters. The first difficulty encountered was the MMAE selecting the benign filter to track what was "designed" to be the intermediate trajectory. This benign filter is needed in the MMAE because any airborne target is capable of presenting a trajectory with acceleration power in the low frequency range, a level flyby. Therefore, the benign filter will be held constant and the intermediate notch filter is moved to higher frequencies. The *two-filter* MMAE is then allowed to track the corresponding intermediate trajectory.

Two more intermediate filters are defined. Again, the distance on the PSD plot between the current intermediate model and the harsh model is split by the new intermediate model. This results in a MMAE-3R with $\omega_{i3} = 1.92$ radians per second and $q_{i3} = 200$. The distance is split again so MMAE-4R has $\omega_{i4} = 2.32$ radians per second and $q_{i4} = 400$. For the check, only the benign and intermediate filters are allowed to contribute to the MMAE while it tracks a target with the respective newly defined intermediate trajectory. Only the probability plots are presented, and these are in Figure 6.11. Because these are two-filter MMAEs, the probability plots start from 0.5 and the numeral 2 is appended to the familiar MMAE notation. The plot for notch MMAE-2R2 looks as expected based on the three-filter performance. This is unacceptable if filter selection is the goal, however the notch MMAE-2R2 gave good performance tracking its intermediate trajectory based on error magnitudes and trends. If clear filter selection is a primary goal, then MMAE-3R2 or MMAE-4R2 should be selected.

Does this proximity hold at the high frequency end? The harsh notch filter is held constant and the time constant of the first-order filter model is reduced. Of course the new filter is tuned at each step and the resulting two-filter MMAE is allowed to track the harsh trajectory. Always the notch filter is selected by the MMAE. This is demonstrated here by placing the harsh first-order filter ($T_h = 0.125$, $\sigma_h^2 = 10000$, $q_h = 160000$) and the harsh notch filter ($\omega_h = 2.8$, $q_h = 400$) in the MMAE. The probability plot labeled (a) of Figure 6.12 results. The harsh notch filter is selected over the harsh first-order filter. PSD plots without the log scale on the x-axis show that the approximate area under the curve for either harsh model is about the same magnitude (10000), so either *should* be able to track the same. (The area under the PSD plots is discussed in Appendix A.) When

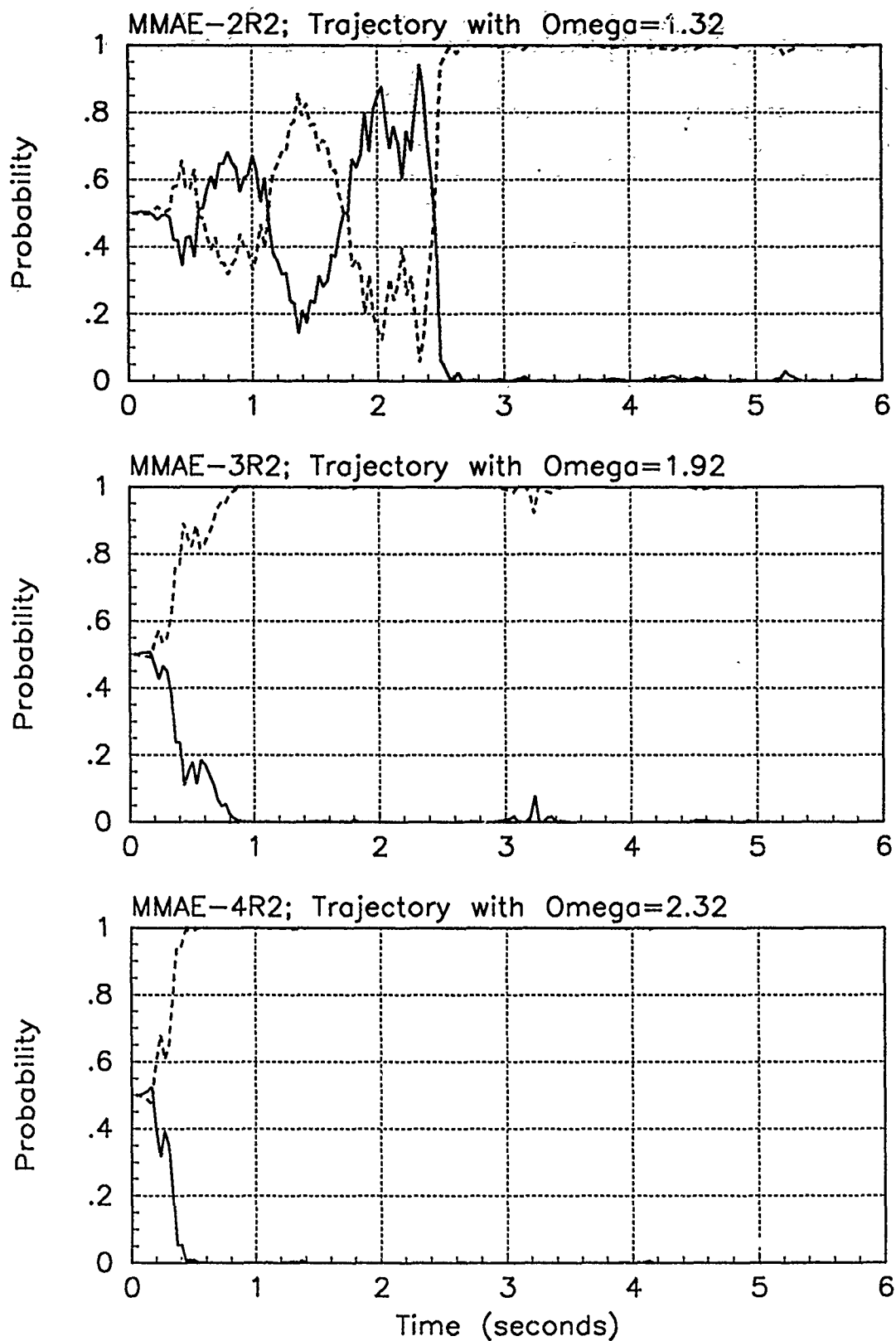


Figure 6.11. Probability Plots; Various Notch MMAEs; PC is 1; Intermediate Trajectories. Benign filter has solid line, intermediate filter has dashed line.

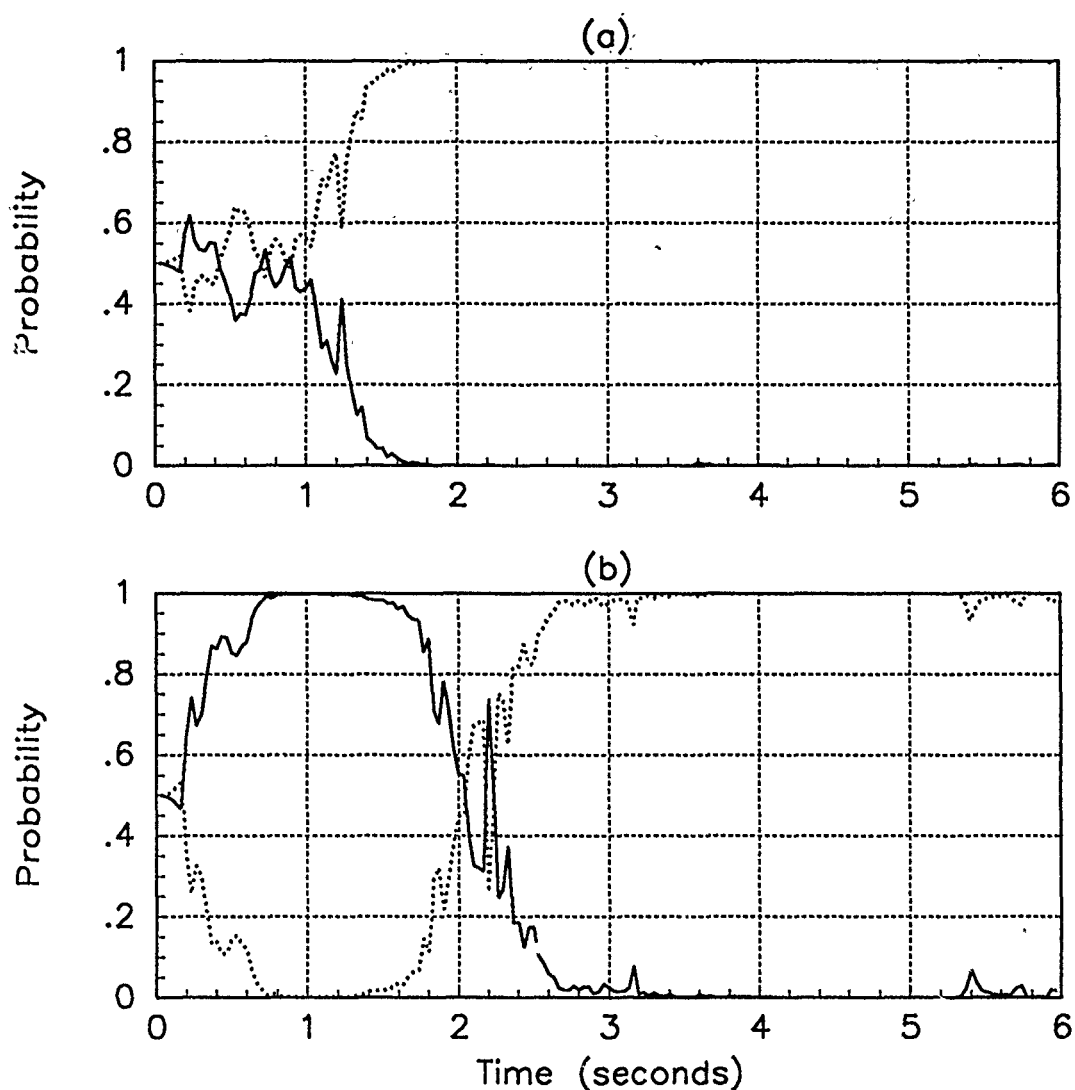


Figure 6.12. Probability Plots; Special Notch MMAE; PC is 1; Harsh Trajectory. The harsh first-order and notch filters are used. For plot (a), the tuning values are $\sigma_h^2 = 10000$ and $q_h = 400$. For plot (b), the tuning values are $\sigma_h^2 = 10000$ and $q_h = 156$. First-order filter has solid line, notch filter has dotted line.

the q_h of the notch model is reduced ($q_h = 156$) so that the height of its PSD curve is the same height as the first-order model (a purely ad hoc choice), the resulting filters take turns tracking the target as in plot (b) of Figure 6.12. Thus, area under the PSD curve is either an inconclusive way to compare two different filter models or an inappropriate area estimation method was selected. Each harsh filter is designed and tuned to track the same trajectory. It is expected that each should contribute to the MMAE estimate. Plot (a) indicates that the second-order model based filter must be disabled by reduced tuning to let the first-order filter have a chance. The second-order filter is apparently more able to handle the harsh dynamics.

6.4.2 Proximity of Notch Filters. An obvious remaining point to investigate is, how "close" can the intermediate and harsh notch filter models get in their PSD representation and still track the intermediate and harsh trajectories? To this end, MMAEs 2R, 3R, and 4R are allowed to track their respective intermediate trajectory, the harsh trajectory, and a sinusoidal trajectory with an ω between the PSD representation of the filter models, called the middle trajectory. Again, only the probability plots are presented. These are in Figures 6.13 to 6.15.

In both the notch MMAE-2R and the notch MMAE-3R, the harsh filter is selected to track the harsh trajectory and not the intermediate trajectory. In the notch MMAE-2R, the middle trajectory is tracked by both notch elemental filters; neither is more "correct". In contrast, the notch MMAE-3R and the notch MMAE-4R each select the intermediate filter to track their respective middle trajectories and the latter MMAE selects the intermediate filter to track even the harsh trajectory. This latter MMAE has the intermediate and harsh elemental filter models designed too closely in the parameter space. Notch MMAE-3R gives better performance for filter selection.

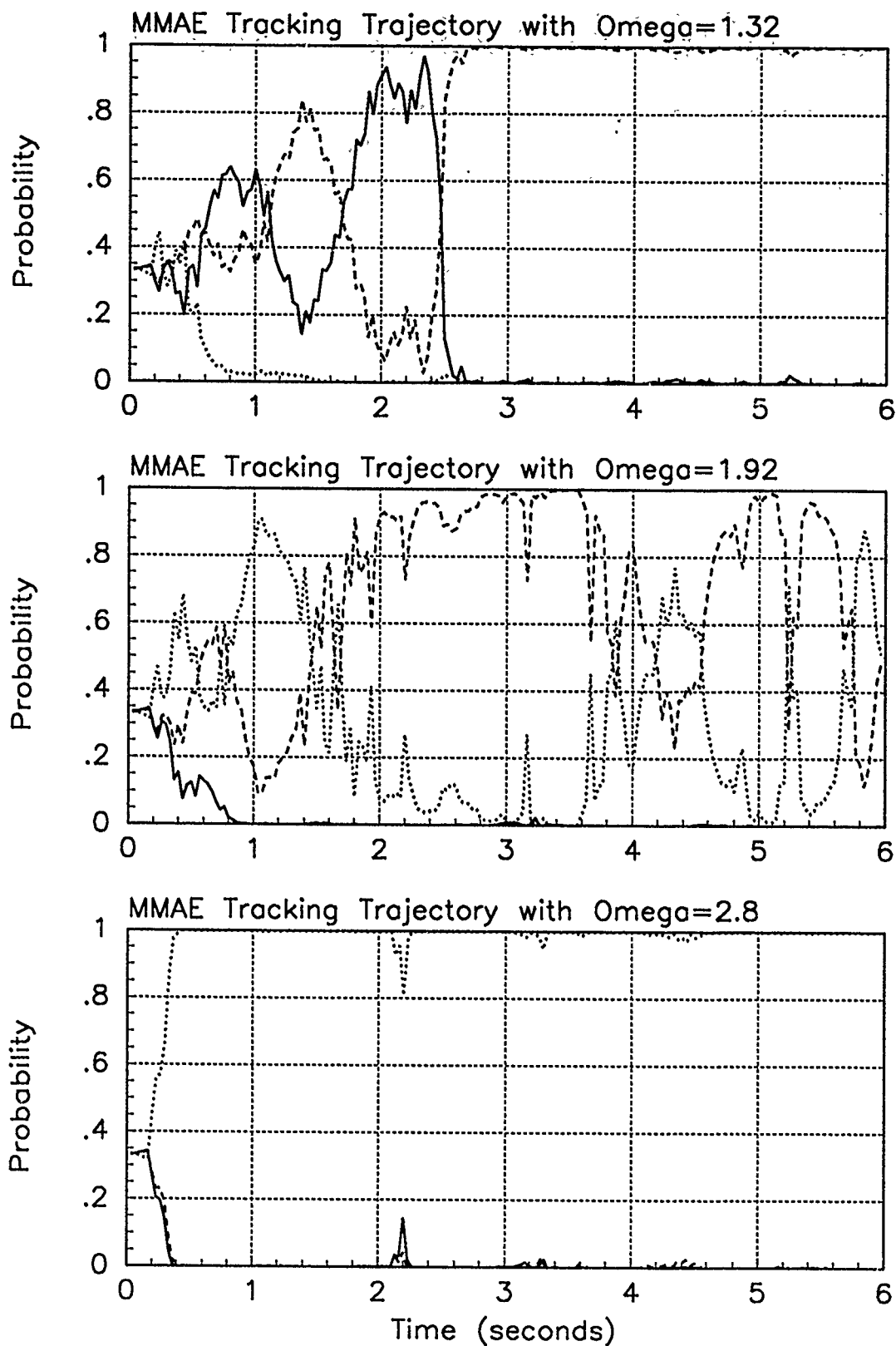


Figure 6.13. Probability Plots; Notch MMAE-2R; PC is 1; Various Trajectories. The trajectories are intermediate, middle, and harsh, respectively. Benign filter has solid line, intermediate filter has dashed line, harsh filter has dotted line.

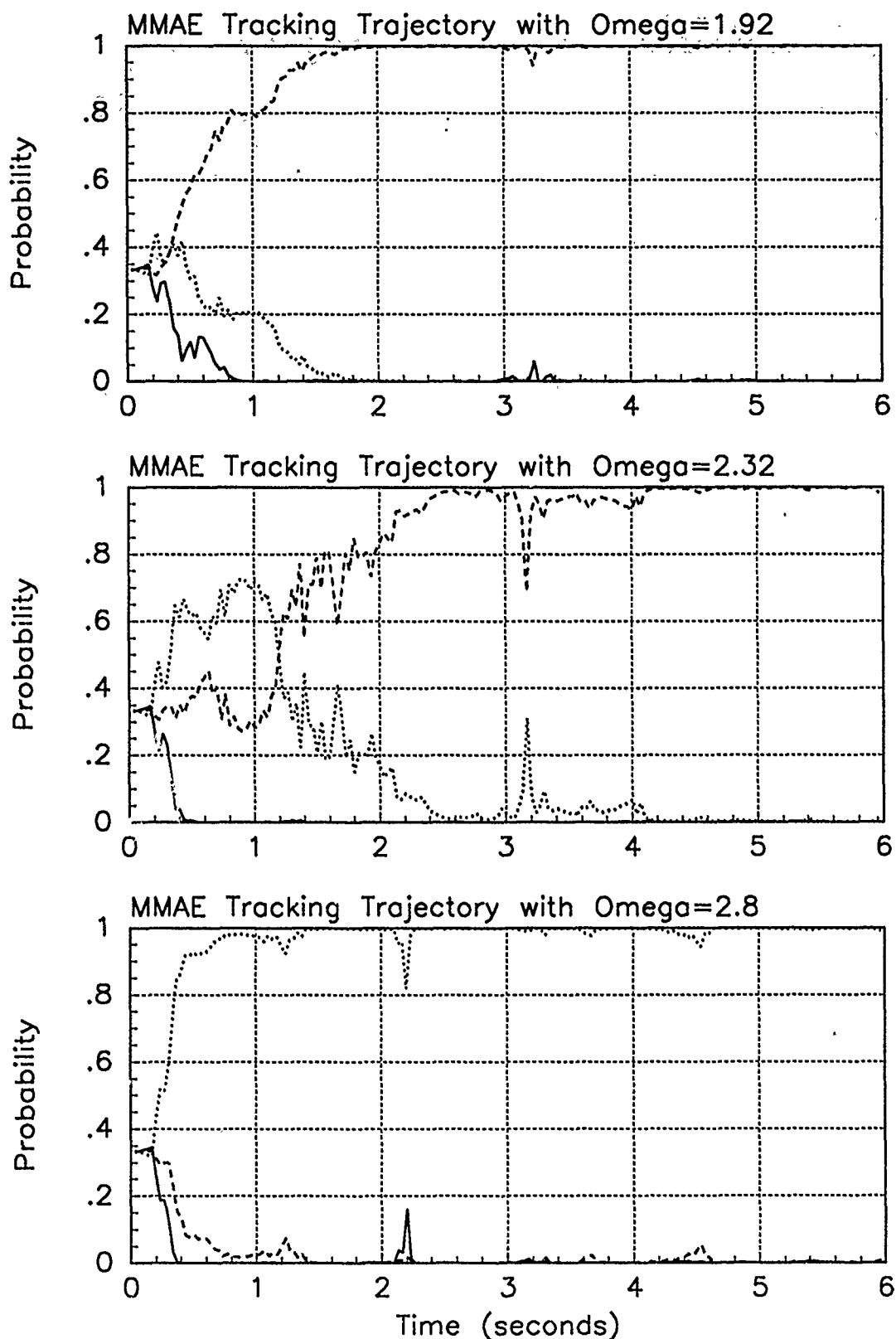


Figure 6.14. Probability Plots; Notch MMAE-3R; PC is 1; Various Trajectories. The trajectories are intermediate, middle, and harsh, respectively. Benign filter has solid line, intermediate filter has dashed line, harsh filter has dotted line.

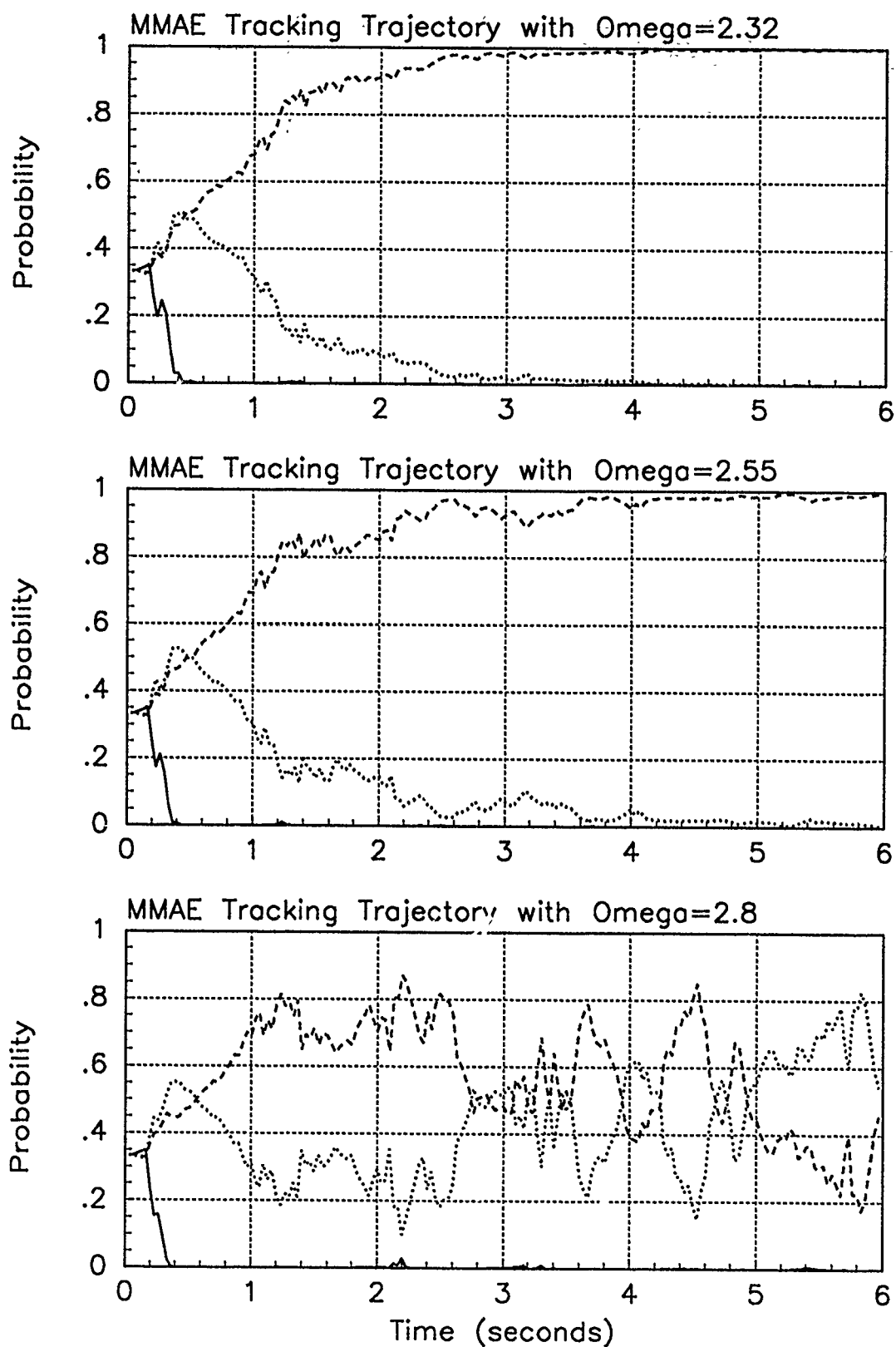


Figure 6.15. Probability Plots; Notch MMAE-4R PC is 1; Various Trajectories. The trajectories are intermediate, middle, and harsh, respectively. Benign filter has solid line, intermediate filter has dashed line, harsh filter has dotted line.

6.5 Summary

Elemental filter design is a trial and error process. The time histories of the probabilities assigned to the elemental filters is essential for deciding if the parameter space has been divided between the filters appropriately. For this thesis, the parameter space is the range of frequencies in which nonzero acceleration PSD content is expected for manned airborne targets. Three elemental filters appear to cover the space adequately, especially when the benign filter is based on a first-order model. The first-order benign model does not allow a second filter model, notch or first-order, to get very close in the frequency domain without causing ambiguities in the p_k calculations. The parameters used to describe each elemental filter used, first- or second-order, are compiled in Appendix A for convenience.

The ad hoc tuning method is inadequate based on the results from the two attempts, -FB or -FH. Other attempts are felt unnecessary since any acceleration model resulting in a flat PSD plot will require increased dynamics driving noise strength on the intermediate filter model as it is defined for this thesis. That disables the MMAE. If the dynamics driving noise strength for the harsh filter model is reduced, the filter does not track the harsh trajectory as well, as shown by the increased magnitude of the mean y-position error plots.

Many of the options run on the notch MMAEs are not accomplished on the first-order MMAE because the results for the notch MMAEs showed the options to be unnecessary or even unacceptable. Best performance is achieved with a basic MMAE; i.e., Bayesian, $PC = 1$, tuned with the revised method, and the lower bound set at 0.001. Table 6.5 gives the average position errors and standard deviations for the first-order MMAE-R and the notch MMAE-2R with $PC = 1$. The notch MMAE-2R consistently gives smaller standard deviations than the first-order MMAE-R. Either performs well with regard to filter selection. Neither performs consistently better than the other with regard to mean error magnitudes. The first-order MMAE-R has as small or smaller average error magnitudes for the y-position errors. That is where the dynamics are entered, but the x-position is as important for determining target location. Unfortunately, neither shows consistently better results for the x-position errors magnitudes.

Table 6.5. Summary Comparing Best First-Order and Notch MMAEs; PC is 1.

Traj ω	Error in:						MMAE, PC
	$p_x(t_i^-)$	$p_x(t_i^+)$	$y_x(t_i^-)$	$p_y(t_i^-)$	$p_y(t_i^+)$	$y_y(t_i^-)$	
.01	.159±.408	.121±.371	.098±.381	.005±.347	.006±.315	.011±.366	FO,1
.01	.164±.411	.126±.373	.103±.381	-.004±.347	-.003±.314	-.002±.366	N2,1
1.32	.058±.447	.034±.398	.043±.395	-.002±.408	-.007±.361	-.008±.383	FO,1
1.32	-.033±.445	-.028±.396	-.016±.392	-.008±.391	-.014±.343	-.016±.374	N2,1
2.8	-.023±.559	-.024±.446	-.010±.446	.013±.498	-.003±.386	.008±.429	FO,1
2.8	-.096±.512	-.060±.431	-.061±.420	.066±.450	.028±.371	.047±.403	N2,1
Jink	.035±.497	.018±.412	.031±.419	.025±.459	.017±.376	.021±.409	FO,1
Jink	-.009±.471	-.005±.408	.001±.406	.137±.425	.087±.361	.106±.393	N2,1

The greatest motivation for trying the second-order filter models (and looking at the acceleration models in the frequency domain of the PSD plot) was to get an MMAE that would assign greater probability to a filter based on a less harsh model more quickly after a target stops maneuvering. To this end, a target in a jinking maneuver was simulated and many MMAEs were allowed to track it. Of these, based only on their respective probability time histories, the following list of viable filters is compiled:

1. Notch MMAE-2R; PC=1; LB=0.001; Figure 5.13, bottom plot, Page 5-25
2. Notch MMAE-2R; PC=1; LB=0.005; Figure 5.24, bottom plot, Page 5-45
3. Notch MMAE-2R; PC=2; LB=0.001; Figure 5.20, top plot, Page 5-38
4. First-order MMAE-R; PC=1; LB=0.001; Figure 6.4, top plot, Page 6-6

The notch MMAE-R with PC = 2 has increased mean error magnitude but the same standard deviation as tracking with the same MMAE with PC = 1. The notch MMAE-R with PC = 1 and the increased lower bound of 0.005 makes the MMAE filter selection susceptible to noise, as shown by the increased sized spikes in the probability time history between 2.5 and 4.5 seconds. These spikes also show up with the notch MMAE-R with PC = 1 and LB = 0.001, except smaller. These spikes may be acceptable since performance is still adequate. The first-order MMAE-R with PC = 1 and LB = 0.001 shows almost none of these spikes but, as mentioned above, has increased standard deviation of the position errors and no real improvement in error magnitudes.

VII. *Conclusions and Recommendations*

7.1 *Introduction*

This thesis is the initial investigation into the possibility (and perhaps necessity) of using second-order acceleration models, rather than first-order models, in the elemental filters of the MMAE used in the enhanced correlator/FLIR tracker. This is motivated by the shape of the acceleration PSD of the model. That is, the frequency range expected target accelerations can exhibit is divided up by the acceleration models with minimal overlap. The minimal overlap should help the MMAE select the proper filter quickly even when the target motion changes from harsh to more benign dynamics, a problem that has plagued MMAE algorithms in the past.

First, a suitable MMAE is designed with emphasis on:

1. Discretizing the parameter space appropriately for the three elemental filters. That is, vary the location of the low pass and bandpass filter models in the frequency domain of the PSD and see what filter selection the resulting MMAE makes. This is referred to as the proximity check.
2. Selecting proper tuning values for the dynamics driving noise to allow the MMAE to select the proper filter based on residual magnitudes. The tuning changes the height of the PSD curve and is done in both ad hoc and revised manners. The measurement noise matrix, $R_{2 \times 2}$, for the "measurements" from the enhanced correlator is not investigated in this thesis since other matters took precedence in the limited time available, and because there is much greater uncertainty associated with current target trajectory characteristics than with precision of measuring devices [10].

Then, the MMAE itself is investigated in three areas:

1. Bayesian versus MAP elemental filter probability assignment.
2. Setting the residual covariance, $A_k(t_i)$ equal to $I_{2 \times 2}$ in one or both of the locations where it appears in the hypothesis probability calculation so that four possible probability computation implementations are considered. These are numbered PC = 1 through 4.

3. Changing the lower bound value that prevents elemental filter lockout. The Markov probability propagation suggested by Muravez [13] is not investigated.

Finally, based on the results for the second-order models, first-order models are designed and the benchmark performance of the resulting MMAE is compared to the performance of the MMAE based on second-order models.

7.2 *Conclusions of Current Investigation*

1. The parameter space is suitably discretized with the "notch" MMAE-2 or the notch MMAE-3. These are three-elemental-filter MMAEs each with a "benign" filter based on a first-order acceleration model ($T = 4$ seconds) and a "harsh" filter based on a notch acceleration model ($\omega = 2.8$ radians per second). The "intermediate" filter is based on a notch model with $\omega = 1.32$ radians per second for notch MMAE-2 or $\omega = 1.92$ radians per second for notch MMAE-3. The "first-order" MMAE is designed with break frequencies (T is 4, 0.5, and 0.125 seconds for the three elemental filters) close to the roll-off frequencies of the notch MMAE-2 and the resulting models also represent a suitable discretization. The suitability of the discretization can be corrupted by improper tuning.
2. The revised tuning method does produce a magnitude for the dynamics driving noise strength that allows the MMAE to make proper filter selection.
3. The MAP option did not show any reduction in tracking error. The Bayesian approach is sufficient.
4. The probability calculation option that gives acceptable results with regard to both filter selection and error magnitudes is 1 (the "basic" hypothesis probability calculation). The maximum entropy option allows the MMAE to take too long to select an elemental filter clearly. The errors increase for this option with the harsher trajectories because the more benign filters are allowed to affect the MMAE estimate too much.
5. The probability lower bound of 0.001 is the most suitable choice of those investigated, based on filter selection from the probability plots. The error magnitudes did not

change appreciably between the Monte Carlo studies accomplished with the various lower bound values.

6. The MMAE based on the first-order acceleration models performs basically the same as the MMAE based on the second-order models. The standard deviation of the position errors are smaller for the notch MMAE but the magnitudes of the mean errors are about the same for each MMAE over all the trajectories tested.
7. The greatest motivation for trying the second-order filter models (and looking at the acceleration models in the frequency domain of the PSD plot) was to get an MMAE that would assign greater probability to a filter based on a less harsh model more quickly after a target stops maneuvering. The first-order MMAE appears to do this the best and still have reasonable error magnitudes and an acceptable probability time history through the whole simulation.

7.3 Recommendations for Further Investigation

1. Return to the first-order filter models but use the break frequencies used in this thesis. This thesis did not demonstrate any improvement from the second-order filters that warrants the additional filter complexity. Filter run-times are inconclusive. It is impossible to separate out the time required for the truth model simulation that is common to both and get a percentage increase in filter algorithm run-time for the MMAE based on the second-order models.
2. If second-order filters are investigated further, vary the ζ of the notch models. Don't bother with the real-pole models, since the notch ones work the same and are much easier to make and place precisely in the frequency domain of the PSD. Perhaps a two-filter MMAE will be sufficient; the typical benign filter with lag time at $T = 4$ seconds with a notch at about 2.2 radians and a ζ of about 0.5.
3. Create the deterministic target trajectory for the truth model in the acceleration domain to ease creation of realistic target motion without the discontinuities in the acceleration domain. Discontinuities are a product of the simulation only and corrupt the filter evaluation.

4. A four-filter MMAE can be designed that will have two elemental filters, each based on a first-order acceleration model with the correlation time, $T = 4$ seconds, but with differing dynamics driving noise strength (see Section 1.3). In the frequency domain of a PSD plot (Figure 1.1), this recognizes that a target for which the direction of the velocity vector cannot change rapidly can still exhibit large acceleration magnitudes. The inclusion of this elemental filter into either the notch or first-order MMAE must be investigated.
5. A bias was expected in the x-position error due to an idiosyncrasy of the simulation software (see Section 3.5). This was not found in this thesis nor was a correction in the software noted. This discrepancy must be resolved.

Appendix A. *Parameters of the MMAEs and Trajectories Designed*

Several different kinds of MMAEs are used in this thesis:

1. MMAEs with all first-order elemental filter models.
2. MMAEs with a first-order elemental filter model (the benign filter) and two second-order elemental filter models.
 - (a) MMAEs with the second-order filter models having real poles.
 - (b) MMAEs with the second-order filter models having complex poles (notch-filter models).

This appendix presents the parameter specifications for all elemental filters used in Chapters V and VI. It also presents models required in the truth model simulation.

There are two real-pole second-order models, five notch second-order models, and three first-order models. The real-pole models are best presented as the transfer functions. These are in Equations (5.3) and (5.4) and are repeated here for first what is used in the intermediate filter and then what is in the harsh filter:

$$G(s) = \frac{1.715s + 0.3032}{(s + 1.4305)(s + 0.3531)} \quad (\text{A.1})$$

$$G(s) = \frac{5.2(s + 1.0111)}{(s + 2.0222)(s + 5)} \quad (\text{A.2})$$

The strengths of the dynamics driving noise that were tried are in Table A.1.

The notch-filter models are described by the transfer function given in Equation (5.5), which is repeated here:

$$G(s) = \frac{ks}{s^2 + 2\zeta\omega_t s + \omega_t^2} \quad (\text{A.3})$$

Table A.1. Real-Pole Noise Strengths.

Tuning	q_i	q_h
Original	2000	29000
Revised	500	4000

Table A.2. Notch Filter Model Parameters.

ω	k	ζ	Tuning	q	Area
0.62	1	0.2	Original	2000	nc
0.62	1	0.2	Revised	75	430
1.32	2.11	0.2	Revised	100	1200
1.92	3.07	0.2	Revised	200	3500
2.32	3.71	0.2	Revised	400	10000
2.8	4.5	0.2	Original	5000	nc
2.8	4.5	0.2	Revised	400	10300

Table A.2 shows the parameters used for the various elemental filters used and value of q for the tuned filter. The entry, nc, denotes a value that was not calculated because the filter model was not deemed inappropriate. The area noted in the table is the area under the PSD curve for the acceleration model when generated with the given white noise strength. The PSD curve is not on a log scale for the calculation. The area is an estimate; the height times the width at one third the height.

The first-order models are described by:

$$G(s) = \frac{1/T}{s + (1/T)} \quad (\text{A.4})$$

The correlation time, T , and the value of σ^2 associated with the acceleration and the strength, q , of the dynamics driving noise are in Table A.3.

Table A.3. First-Order Filter Model Parameters.

T	Tuning	σ^2	q	Area
4	Original	250	125	nc
4	Revised	150	75	420
0.5	Revised	400	1600	1380
0.125	Revised	10000	160000	11300

Table A.4. Trajectory Parameters and Associated Accelerations.

ω	A	Max Accel
(rad/sec)	(meters)	(g's)
0.01	9	0
0.62	9	0.35
1.32	9	1.6
1.92	9	3.4
2.32	9	5.0
2.55	9	6.0
2.8	9	7.3
Jinking Trajectory		7.3

The area under the PSD curve of the acceleration model from which an estimator is made is related to the maximum acceleration the estimator can track. The trajectories used in this thesis are listed in Table A.4 along with the maximum acceleration, $A\omega^2$, shown by the trajectory. The trajectory is created with no acceleration in the x-axis. The dynamics are entered in the y-axis in the velocity domain with the sinusoidal equation of Equation (3.3). The acceleration is given by Equation (3.4) and is repeated here:

$$a_{iy}(t) = A\omega^2 \sin(\omega t + \phi) \text{ meters per second}^2 \quad (\text{A.5})$$

Recall that A is an amplitude, ϕ is a phase option added to help the researcher simulate evasive maneuvers, and the subscript i denotes the inertial frame that is described in Chapter III.

The parameters of the filter models have been given in the tables above. Following is a compilation of the remaining parameters necessary for the simulation. Many of these are discussed briefly in Chapters III and IV. In Table A.5, a – denotes a parameter for which no variable was assigned. The initial probability assigned to each of the elemental filters is 1/3 when three filters are used. The initial values are 1/2 when two elemental filters are used. The lower bound is generally 0.001 except where discussed in the Chapter V.

Table A.5. Parameters Needed for the Simulation Software.

-	180 time steps	number of time steps in one run, 6 sec \times 30 steps/sec
-	10 runs	number of runs per Monte Carlo study
σ_{ta}	0.447 radians/second	standard deviation for true atmospheric model
T_{fa}	0.0707 seconds	correlation time for filter atmospheric model
σ_{fa}^2	0.2 pixels ²	variance for filter atmospheric model
L	0.000020 radians/pixel	pixel proportionality constant
AR	1	aspect ratio of the target
-	1.4142 meters	reference length of the target semimajor axis
R_f	0.00436 pixels ²	term (1,1) in the measurement noise strength matrix
	0.00598 pixels ²	term (2,2) in the measurement noise strength matrix
-	(1,0,0) meters	position of hotspot one, body frame
-	(0,0.5,0) meters	position of hotspot two, body frame
-	(0,-0.5,0) meters	position of hotspot three, body frame
I_{max}	20	maximum intensity of each hotspot
α_s	0.1	smoothing constant for template generation
-	0.3	correlator threshold
-	1	designating an FFT correlation rather than phase
$p_{Ix}(t_0)$	3000	initial conditions on true target trajectory p (meters), v (meters/second), a (meters/second ²)
$v_{Ix}(t_0)$	-1000	
$a_{Ix}(t_0)$	0	
$p_{Iy}(t_0)$	0	
$v_{Iy}(t_0)$	$A\omega \cos(\phi) + B$	
$a_{Iy}(t_0)$	$[v_{Iy}(t_0 + \Delta t) - v_{Iy}(t_0)] / \Delta t$	
$p_{Iz}(t_0)$	20000	
$v_{Iz}(t_0)$	0	
$a_{Iz}(t_0)$	0	

Appendix B. *Probability Plots for each of the 10 Runs*

One of the tools that is used for evaluating the performance of each of the MMAEs tested is the probability time history as discussed in Chapter V. The time history plots presented in Chapters V and VI are the time histories for run 1 of each of the 10-run Monte Carlo studies accomplished. Legitimate question can be raised whether this accurately represents the MMAE performance. To address this question, a series of plots (the probability time history for each of the 10 runs and for the mean over the 10 runs) are generated for several Monte Carlo runs. These are shown in Figures B.1 through B.4. These Monte Carlo studies are the notch MMAE-2R with $PC = 1$ and varying lower bound as discussed in Section 5.10 and corresponding to Figure 5.24. The plot of the mean probability time history is a misleading one to present because the noise has been averaged out. If the tracker is used, the expected response will be noisy, as shown by the other plots. Some of the samples are noisier than others. The most dramatic difference though is in the time history plots between 4 and 6 seconds. In some samples, the harsh filter does not lose its high probability, in others, it does. The plot for run 1 of 10 is an "average looking" plot for the group of 10 for each of the four Monte Carlo studies presented. The same ten sets of noise samples are used for each Monte Carlo study in the thesis. The probability time history for run one is presented for the simulations in Chapters V and VI.

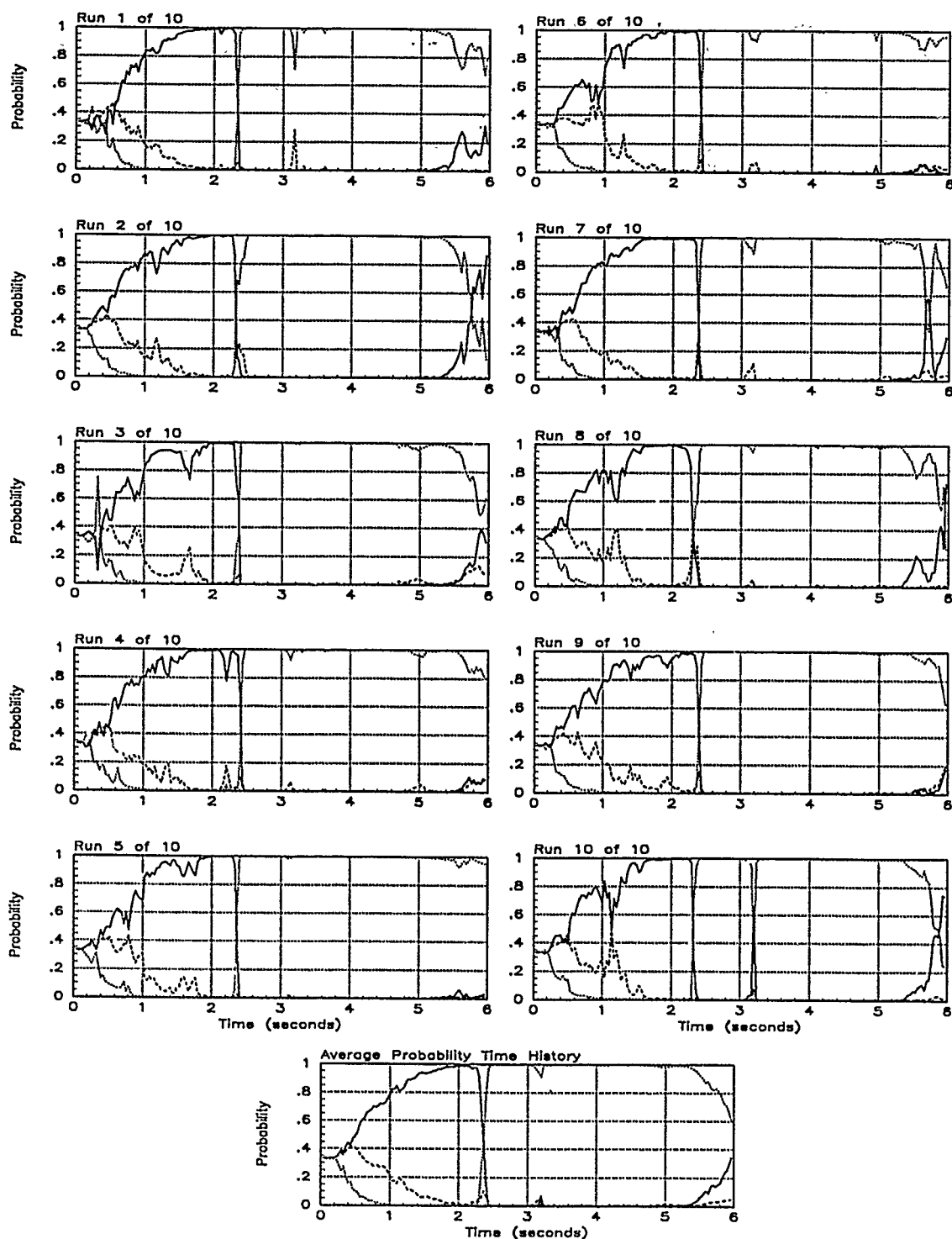


Figure B.1. Complete Probability Plots; Notch MMAE-2R; PC is 1; LB is 0.0005; Jinking Trajectory. Benign filter has solid line; intermediate filter has dashed line; harsh filter has dotted line.

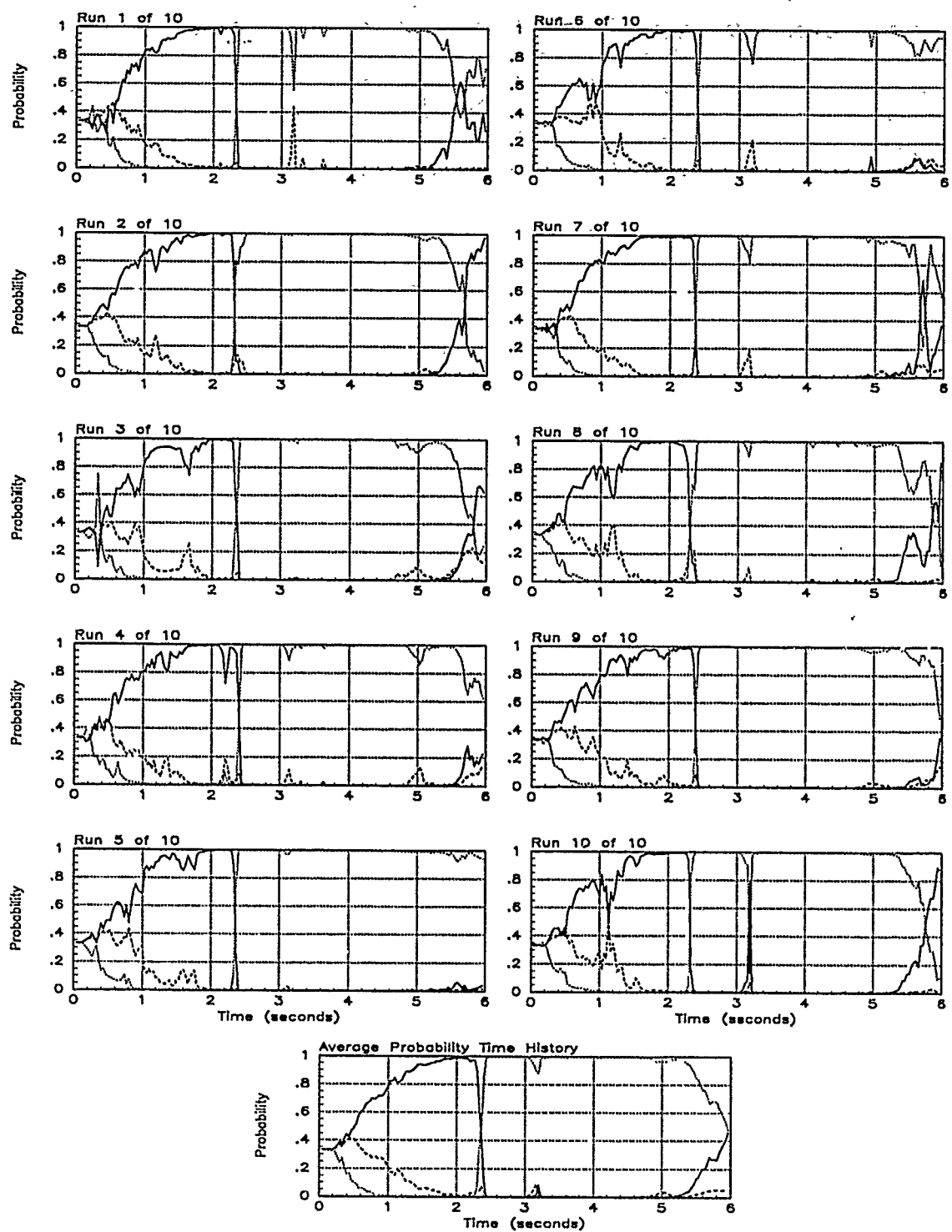


Figure B.2. Complete Probability Plots; Notch MMAE-2R; PC is 1; LB is 0.001; Jinking Trajectory. Benign filter has solid line; intermediate filter has dashed line; harsh filter has dotted line.

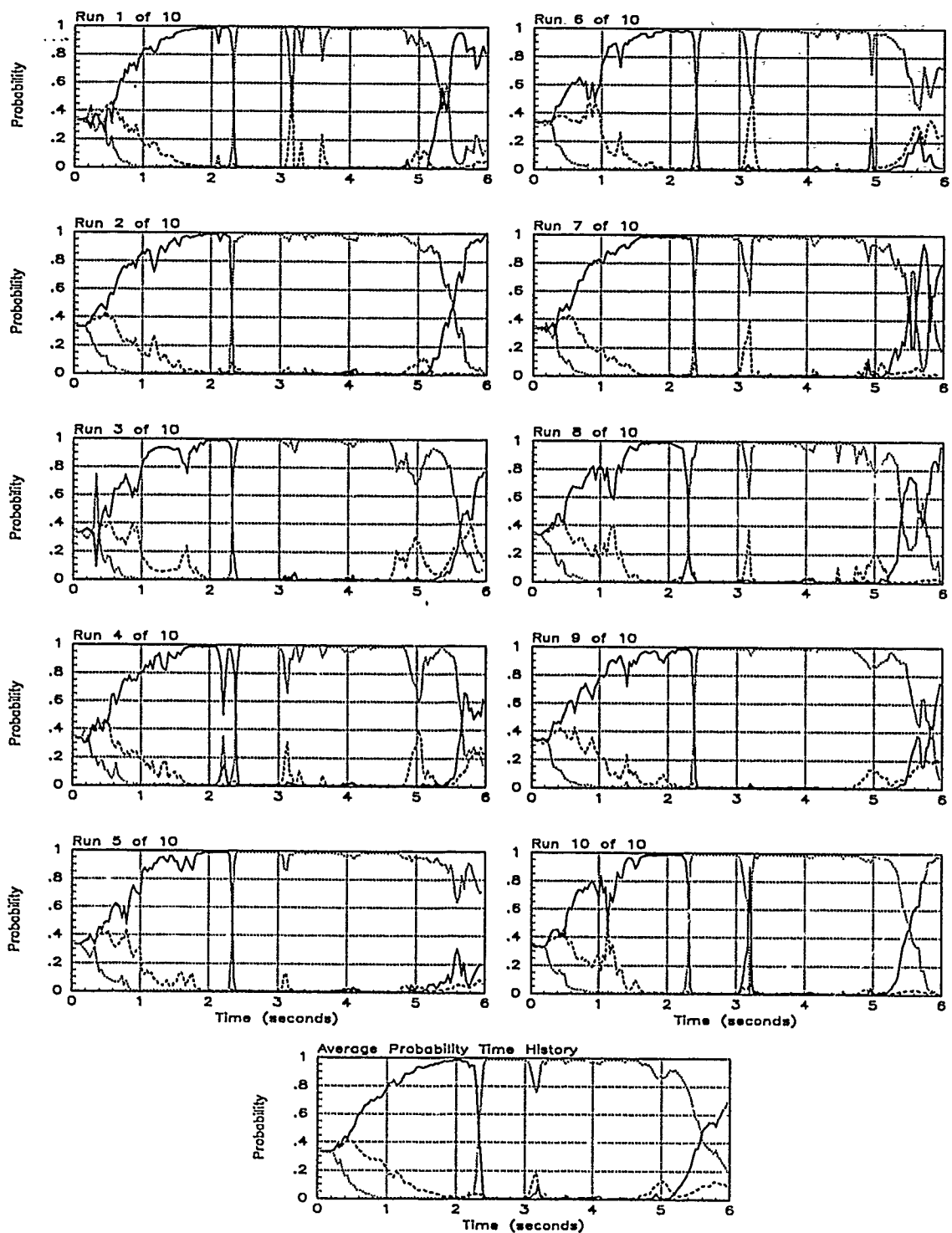


Figure B.3. Complete Probability Plots; Notch MMAE-2R; PC is 1; LB is 0.005; Jinking Trajectory. Benign filter has solid line; intermediate filter has dashed line; harsh filter has dotted line.

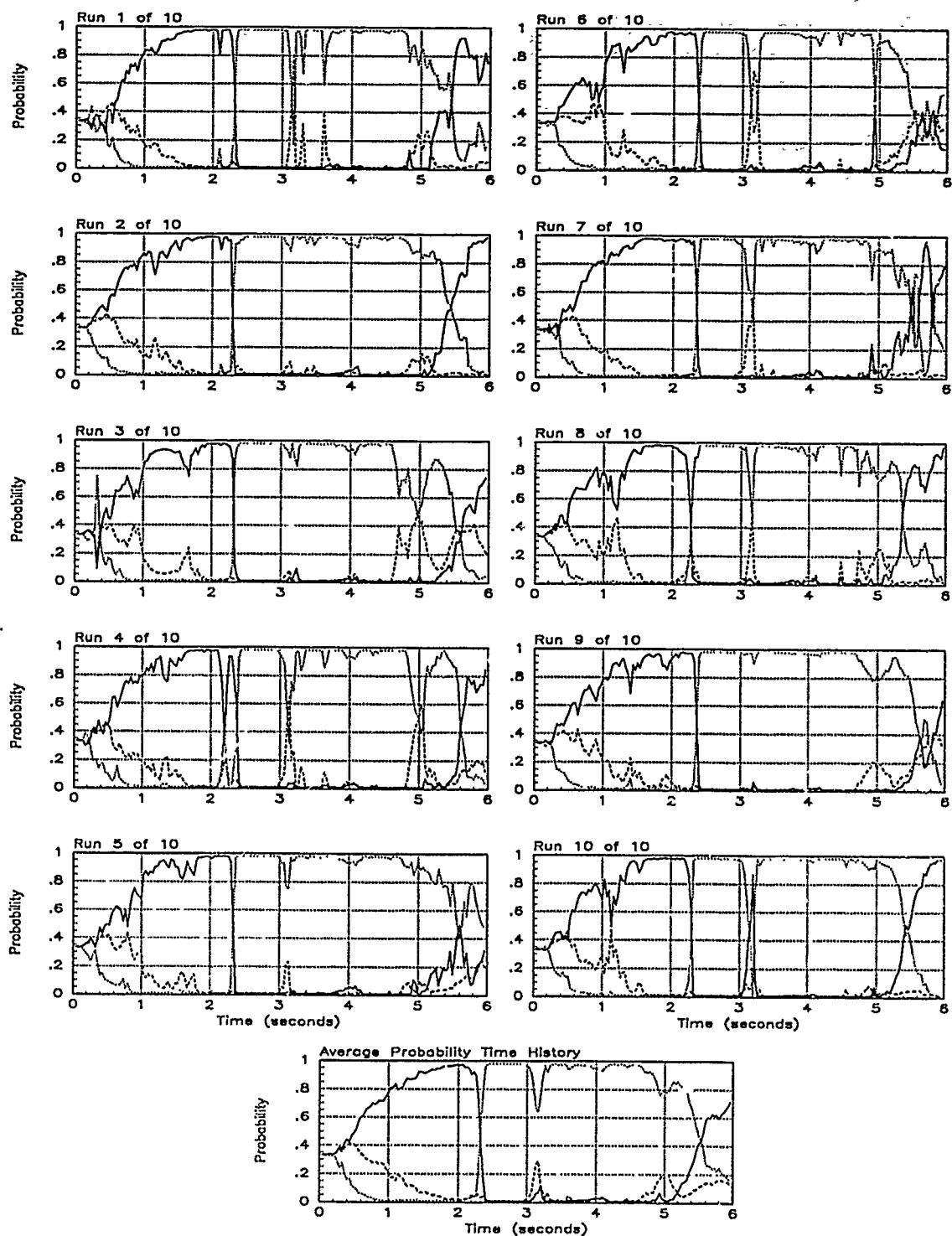


Figure B.4. Complete Probability Plots; Notch MMAE-2R; PC is 1; LB is 0.01; Jinking Trajectory. Benign filter has solid line; intermediate filter has dashed line; harsh filter has dotted line.

Appendix C. *Error plots for Real-Pole MMAE*

This appendix contains the complete set of error plots for the runs discussed in Chapter V for the real-pole MMAE. The first part is results for the MMAE as originally tuned. The latter part is from the MMAE as retuned.

The results for one Monte Carlo study consist of a set of three pages. The first page shows the RMS error plots for each of the x- and y-positions. The band is the dashed line for the filter-computed RMS error. The solid line is the actual RMS error calculated over the Monte Carlo study. These plots give an indication of adequacy of filter tuning. Below these plots are two tables. The table on the left lists the temporal average of the position errors. This temporal average is from .5 seconds to the end of each of the 10 runs in the Monte Carlo study as described in Section 5.2. The table on the right is the list of the average $\mathbf{r}_k^T(t_i)\mathbf{r}_k(t_i)$ and $\mathbf{r}_k^T(t_i)\mathbf{A}_k^{-1}(t_i)\mathbf{r}_k(t_i)$ over the 10 runs for the entire run, not just the last 5.5 seconds. The lack of time notation (rather than the traditional overbar) in the table signifies the temporal average. These values are presented because, depending on what hypothesis probability calculation is used, the relative magnitudes of $\mathbf{r}_k^T(t_i)\mathbf{r}_k(t_i)$ or $\mathbf{r}_k^T(t_i)\mathbf{A}_k^{-1}(t_i)\mathbf{r}_k(t_i)$ will determine what filter is selected. The average $\mathbf{r}_k^T(t_i)\mathbf{r}_k(t_i)$ and $\mathbf{r}_k^T(t_i)\mathbf{A}_k^{-1}(t_i)\mathbf{r}_k(t_i)$ are presented only for nonvarying trajectories. If the average value of $\mathbf{r}_k^T(t_i)\mathbf{r}_k(t_i)$ is small for one elemental filter, that filter should be selected for the entire 6 second run. If it was not, other influences need to be determined. The next page of each set shows the mean \pm one standard deviation error plots for the x-position at time t_i^- and t_i^+ and the mean x-centroid position error at time t_i^- . The final page shows similar plots for the mean y-position errors. The solid line denotes the mean error while the dashed line is the mean $\pm \sigma$.

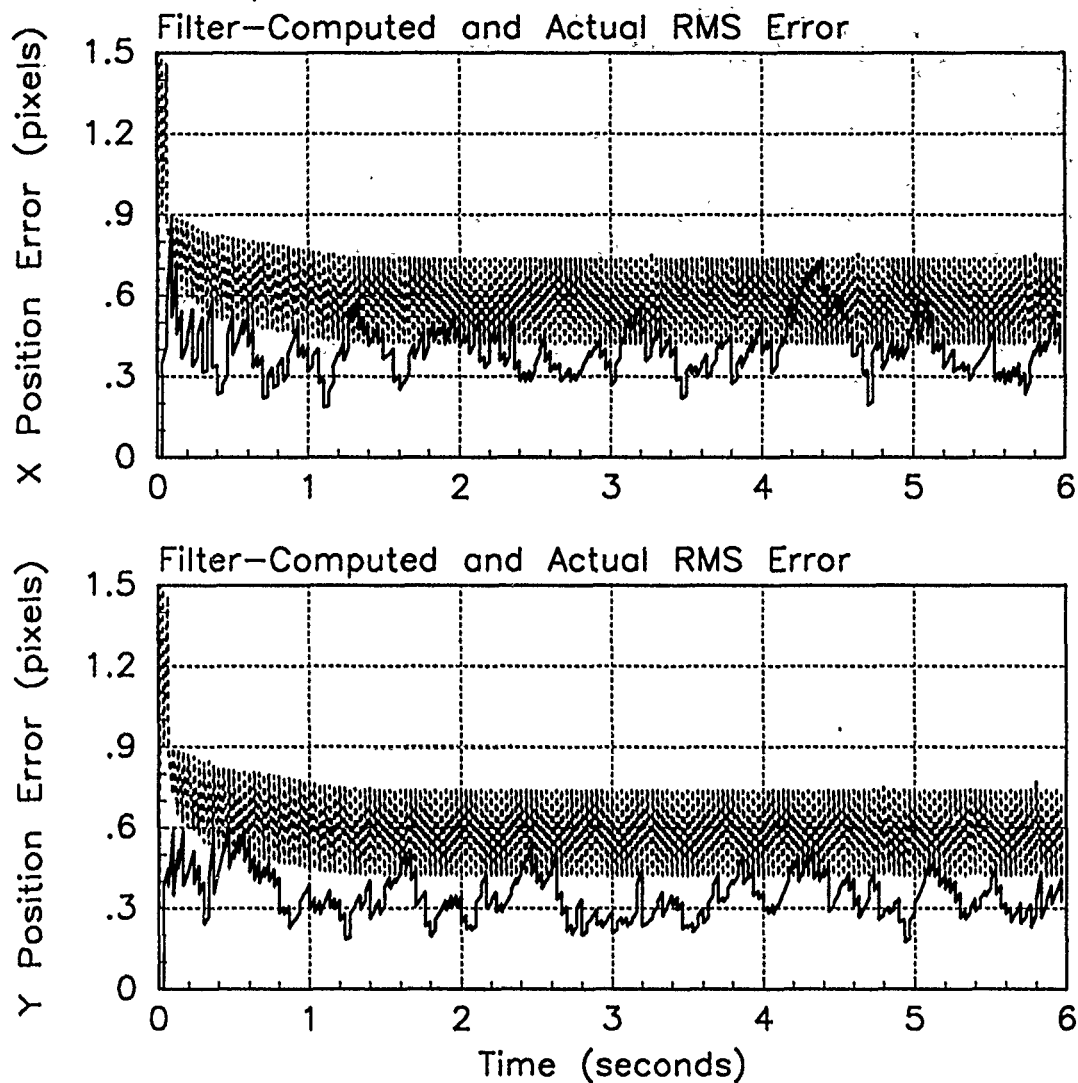


Figure C.1. RMS Error Plots; Real-Pole MMAE-O; PC is 1; Trajectory with $\omega = .01$

Table C.1. Temporal Average and Residuals; Real-Pole MMAE-O; PC is 1; Trajectory with $\omega = .01$.

Error in:	Mean	σ
$p_x(t_i^-)$	0.13389	0.42208
$p_x(t_i^+)$	0.10040	0.38270
$y_x(t_i^-)$	0.089433	0.38411
$p_y(t_i^-)$	-0.0043953	0.35911
$p_y(t_i^+)$	-0.0031046	0.32245
$y_y(t_i^-)$	0.0013646	0.36994

Filter	$\mathbf{r}_k^T \mathbf{r}_k$	$\mathbf{r}_k^T \mathbf{A}_k^{-1} \mathbf{r}_k$
Benign	0.31486	1.81639
Intermediate	0.35553	1.68579
Harsh	0.53661	1.40270

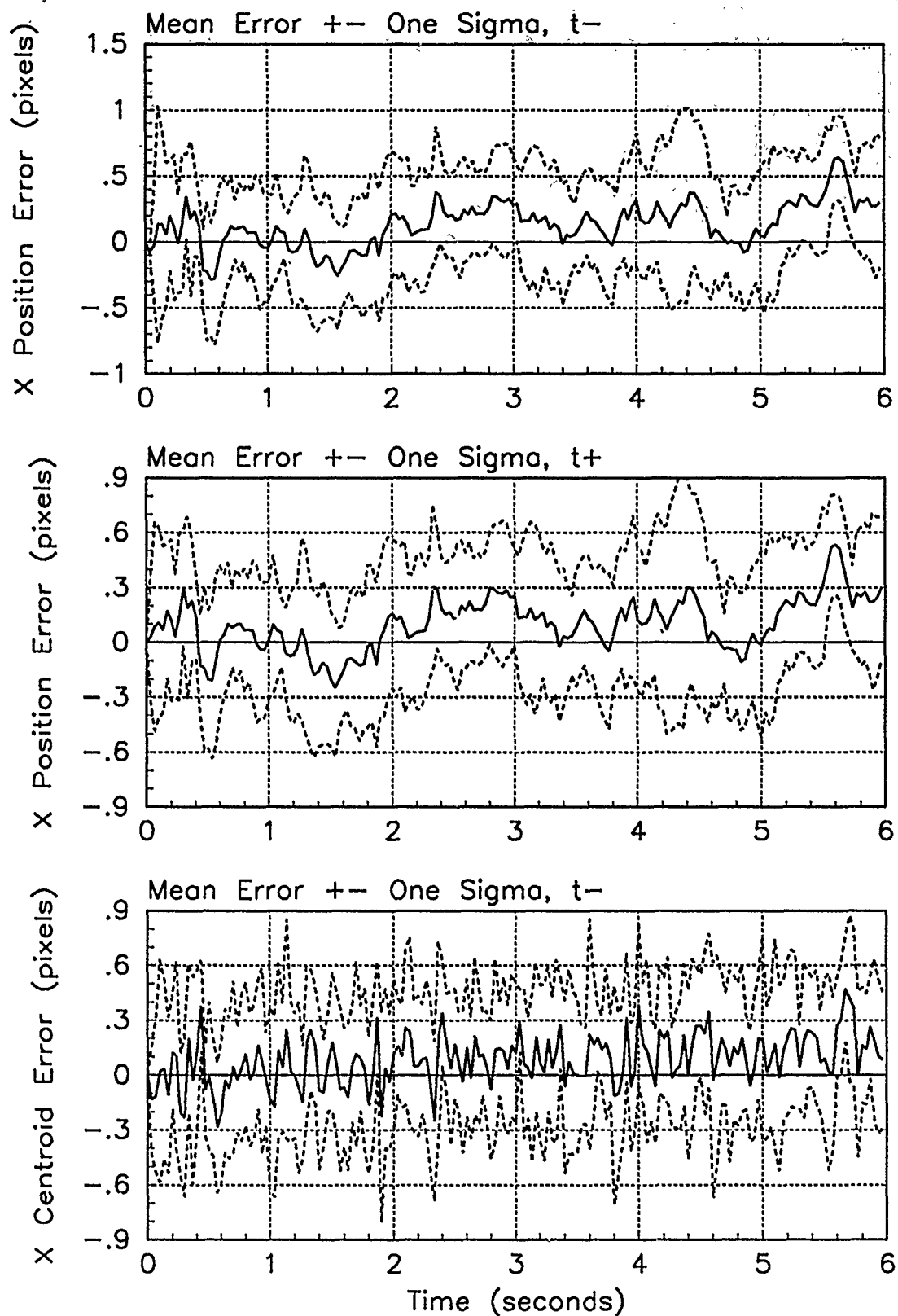


Figure C.2. X-Error Plots; Real-Pole MMAE-O; PC is 1; Trajectory with $\omega = .01$

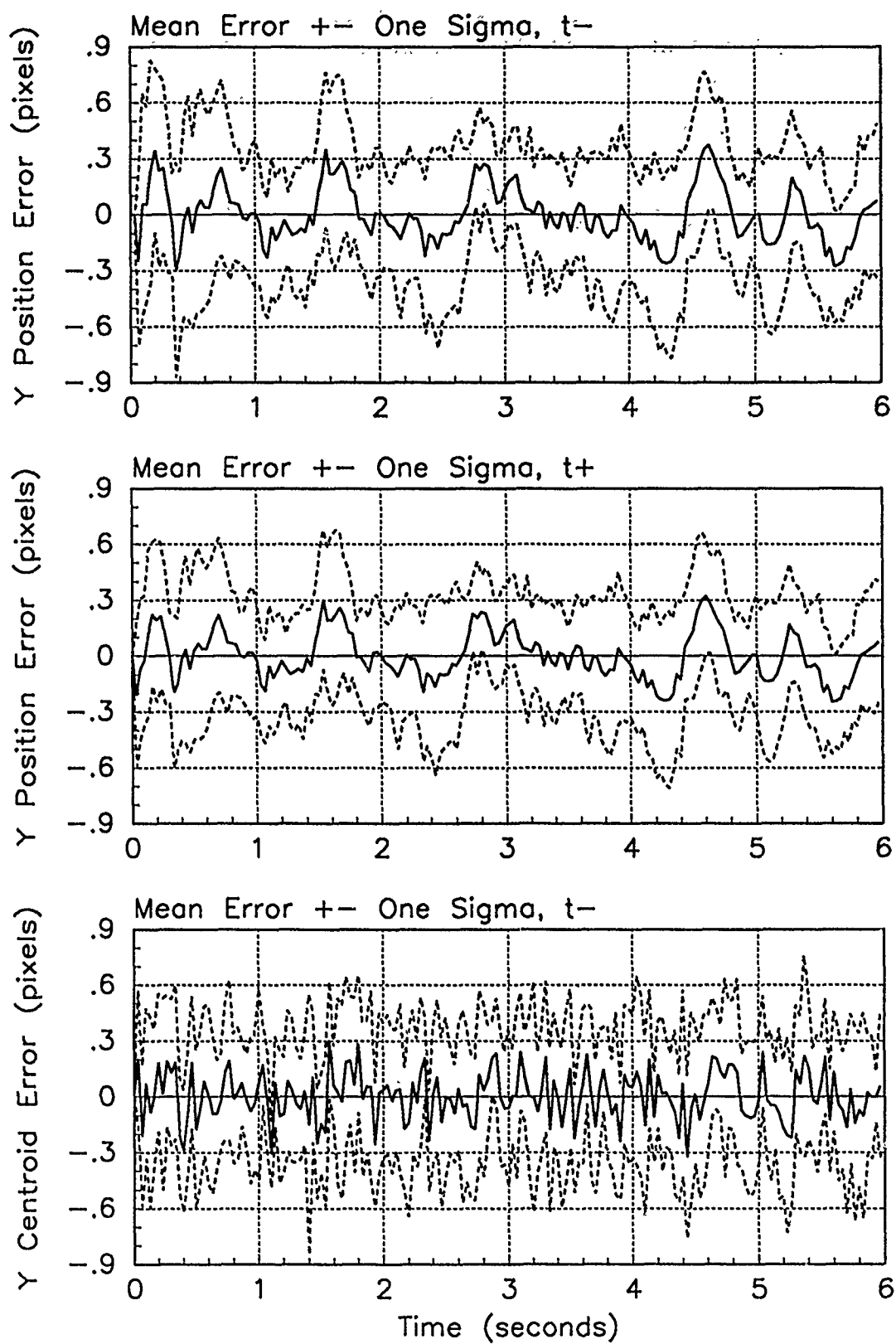


Figure C.3. Y-Error Plots; Real-Pole MMAE-O; PC is 1; Trajectory with $\omega = .01$

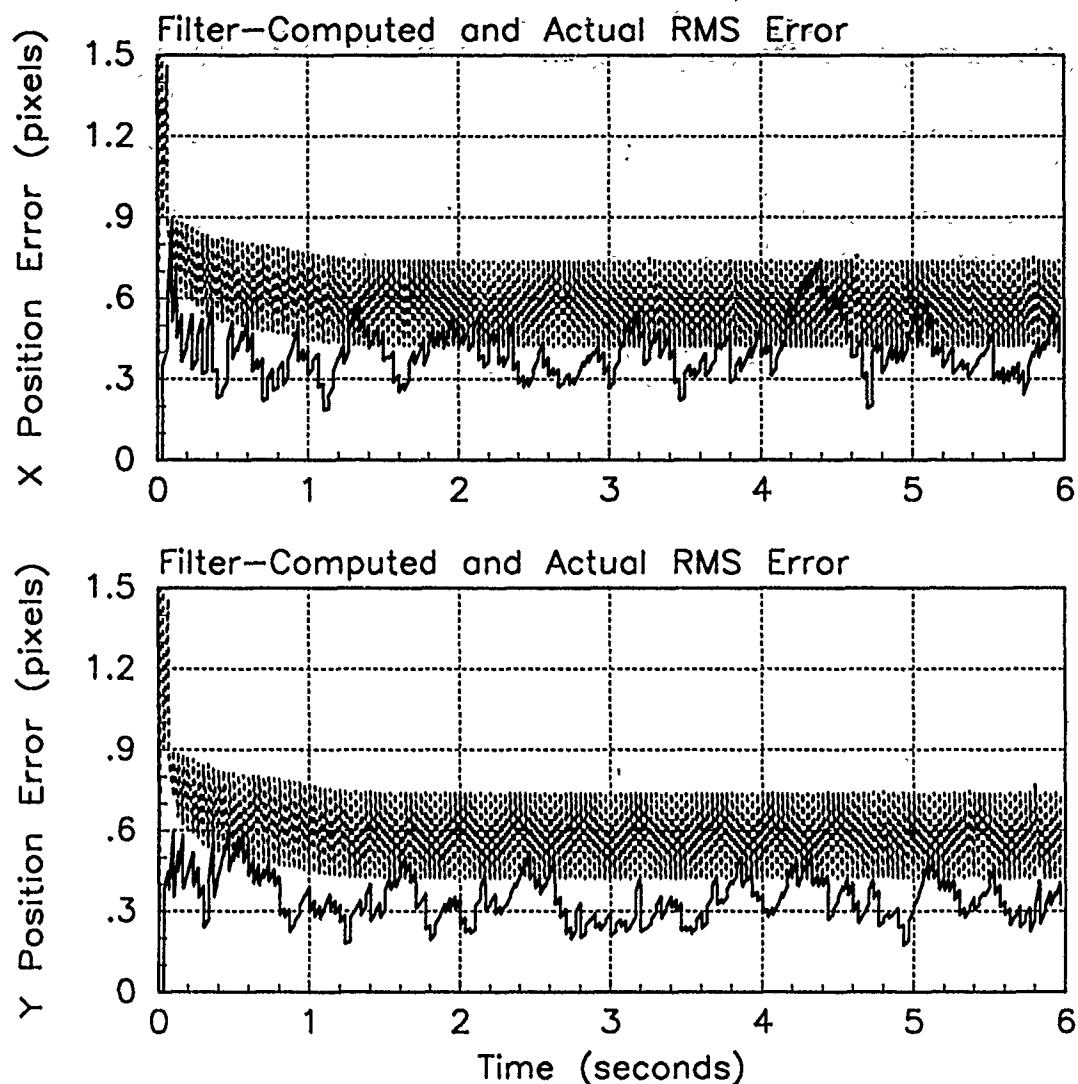


Figure C.4. RMS Error Plots; Real-Pole MMAE-O; PC is 1; Trajectory with $\omega = .62$

Table C.2. Temporal Average and Residuals; Real-Pole MMAE-O; PC is 1; Trajectory with $\omega = .62$.

Error in:	Mean	σ
$p_x(t_i^-)$	0.14914	0.42189
$p_x(t_i^+)$	0.11576	0.38228
$y_x(t_i^-)$	0.10470	0.38396
$p_y(t_i^-)$	0.0016695	0.35867
$p_y(t_i^+)$	0.0012898	0.32162
$y_y(t_i^-)$	0.0046943	0.36945

Filter	$\mathbf{r}_k^T \mathbf{r}_k$	$\mathbf{r}_k^T \mathbf{A}_k^{-1} \mathbf{r}_k$
Benign	0.31511	1.81768
Intermediate	0.35663	1.69112
Harsh	0.53743	1.40485

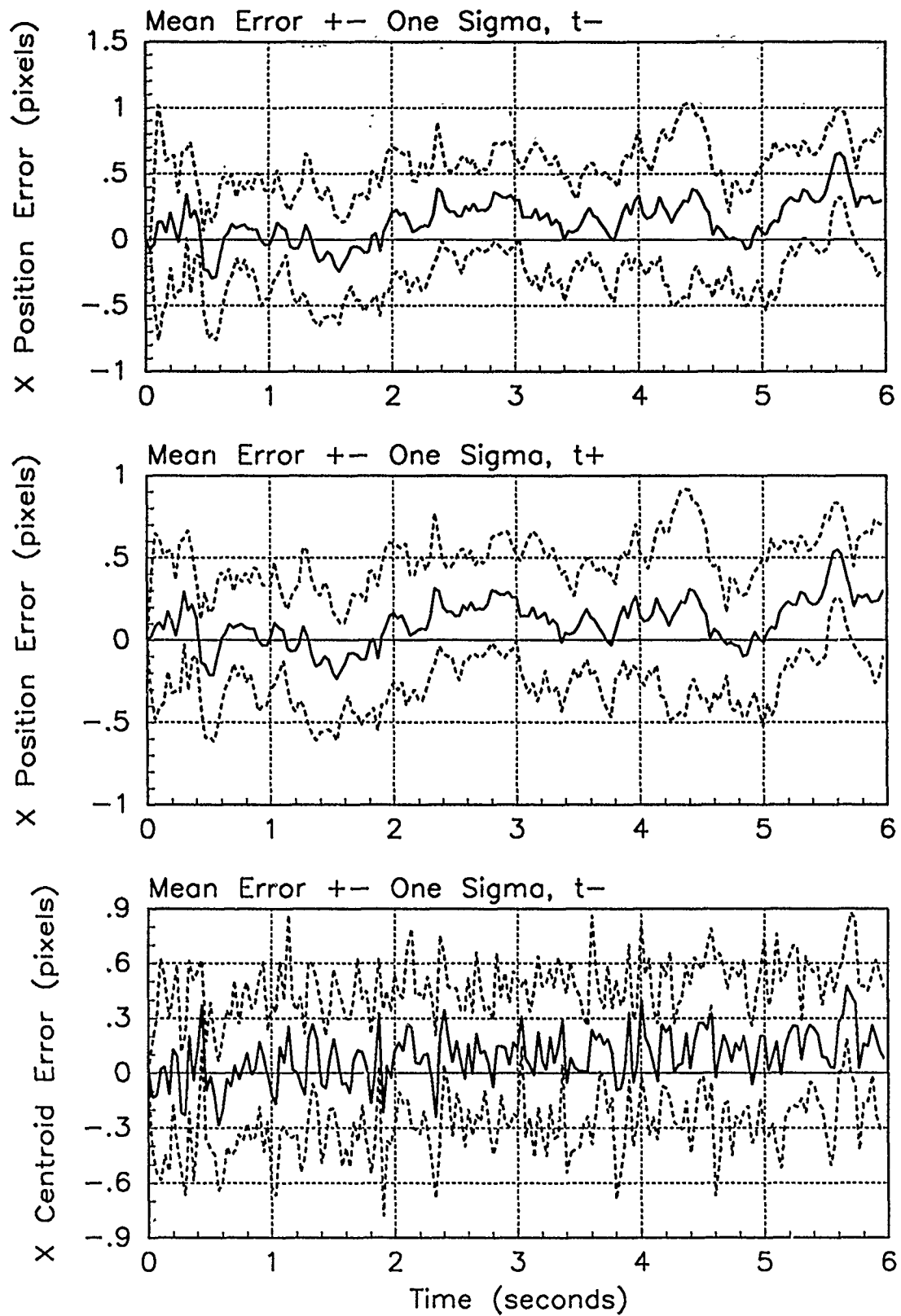


Figure C.5. X-Error Plots; Real-Pole MMAE-O; PC is 1; Trajectory with $\omega = .62$

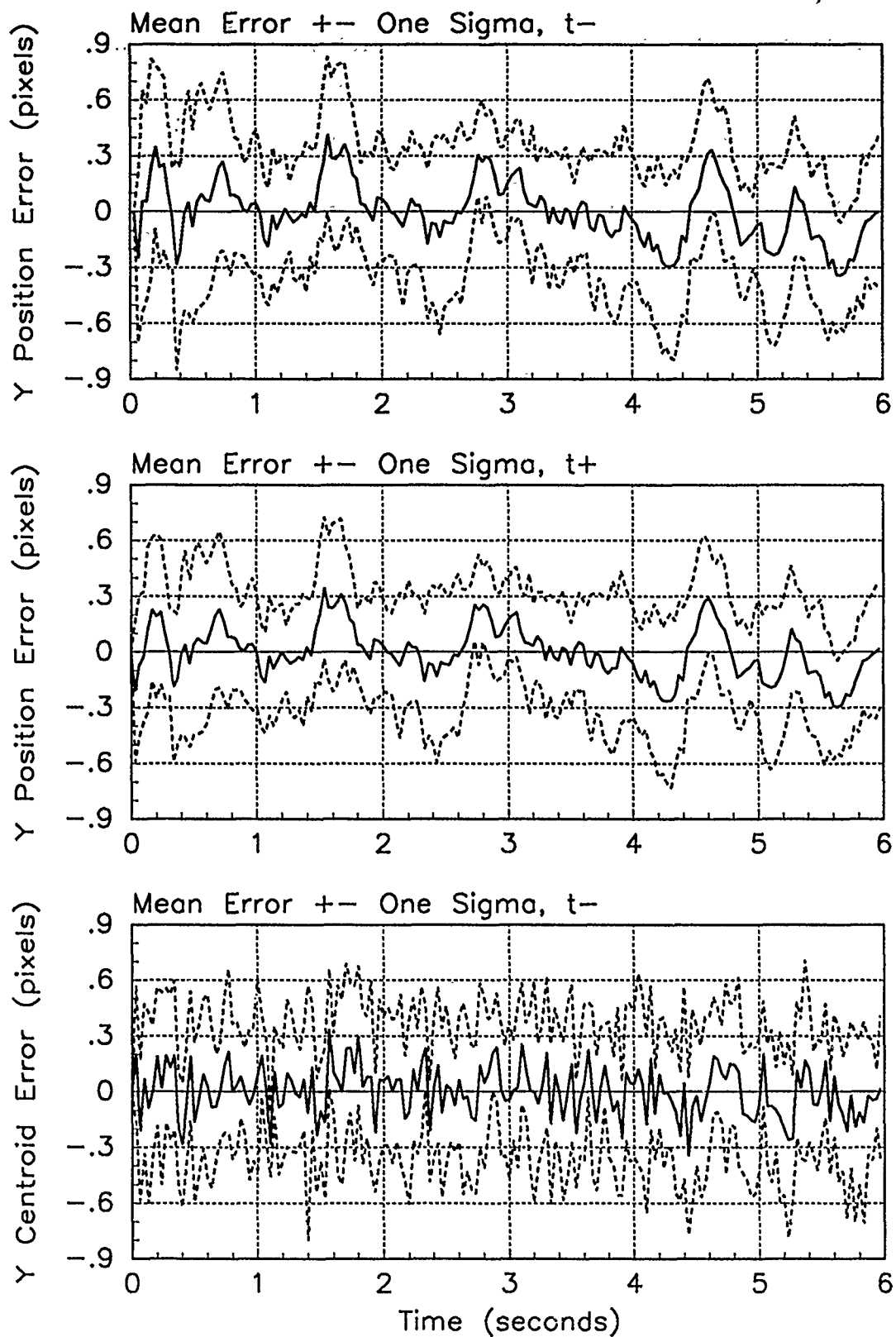


Figure C.6. Y-Error Plots; Real-Pole MMAE-O; PC is 1; Trajectory with $\omega = .62$

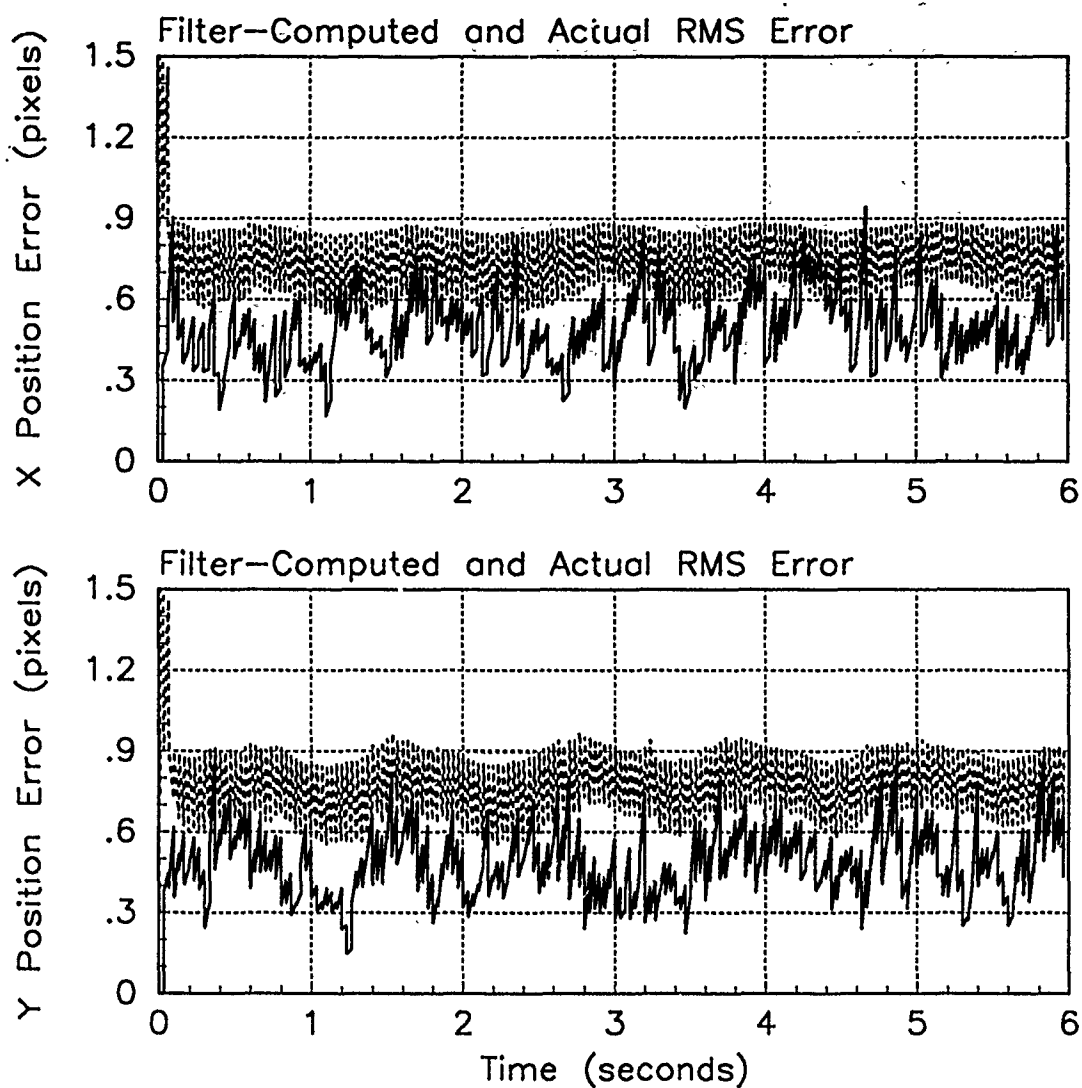


Figure C.7. RMS Error Plots; Real-Pole MMAE-O; PC is 1; Trajectory with $\omega = 2.8$

Table C.3. Temporal Average and Residuals; Real-Pole MMAE-O; PC is 1; Trajectory with $\omega = 2.8$.

Error in:	Mean	σ
$p_x(t_i^-)$	-0.026393	0.50948
$p_x(t_i^+)$	-0.027495	0.42177
$y_x(t_i^-)$	-0.014240	0.42098
$p_y(t_i^-)$	-0.017667	0.50444
$p_y(t_i^+)$	-0.019032	0.40048
$y_y(t_i^-)$	-0.016266	0.42632

Filter	$\mathbf{r}_k^T \mathbf{r}_k$	$\mathbf{r}_k^T \mathbf{A}_k^{-1} \mathbf{r}_k$
Benign	3.80063	22.23022
Intermediate	0.52535	2.49601
Harsh	0.53827	1.40698

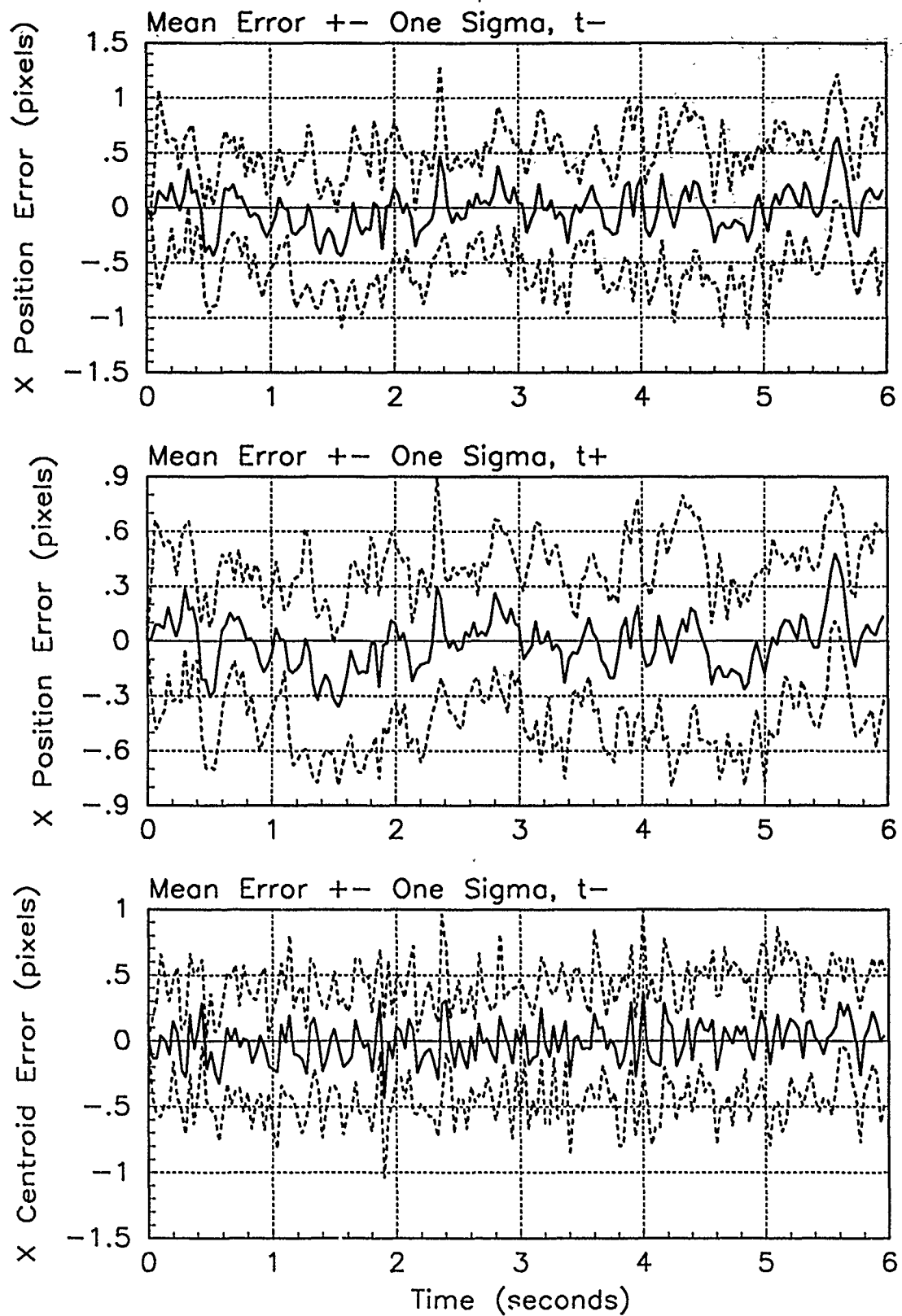


Figure C.8. X-Error Plots; Real-Pole MMAE-O; PC is 1; Trajectory with $\omega = 2.8$

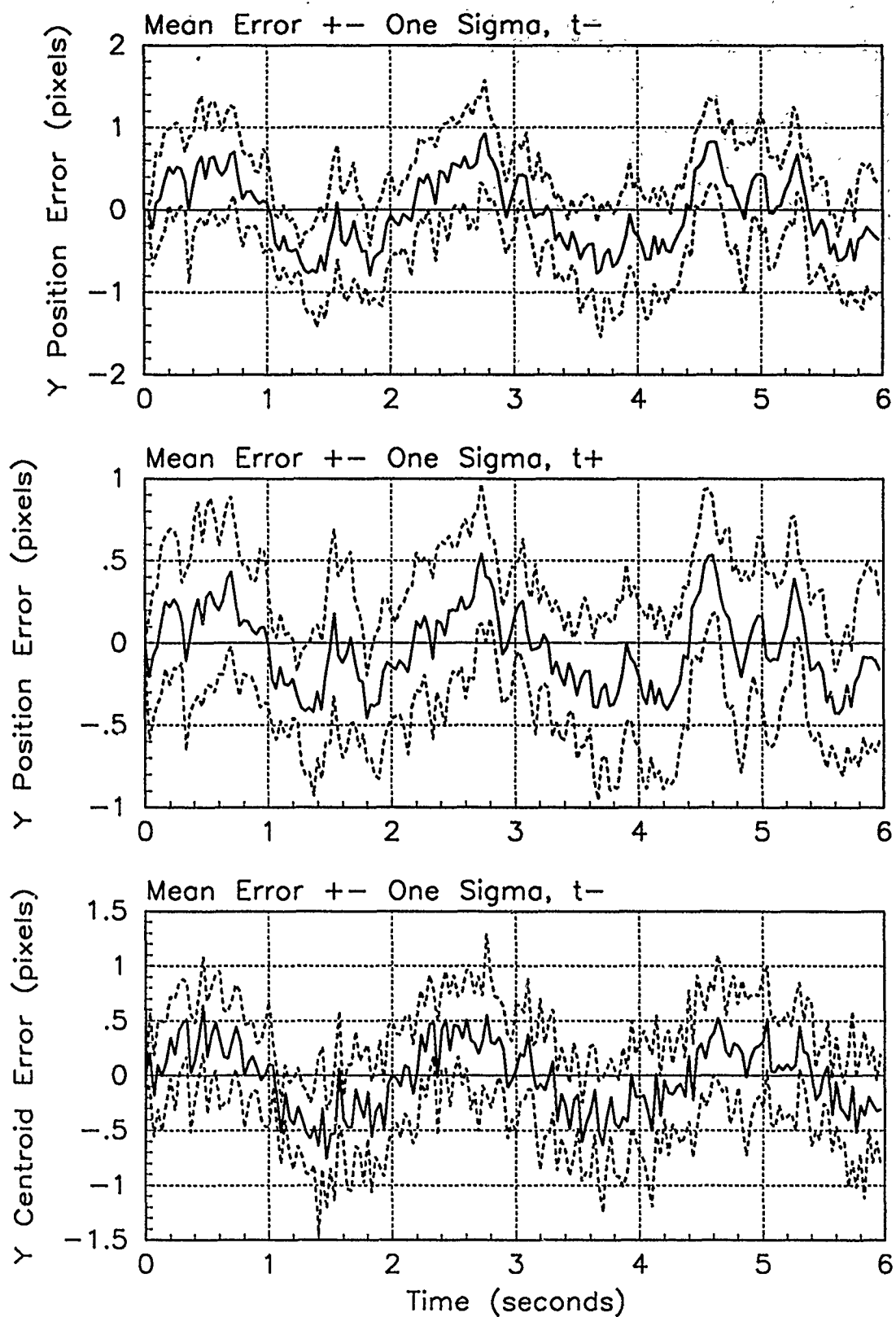


Figure C.9. Y-Error Plots; Real-Pole MMAE-O; PC is 1; Trajectory with $\omega = \pi/8$

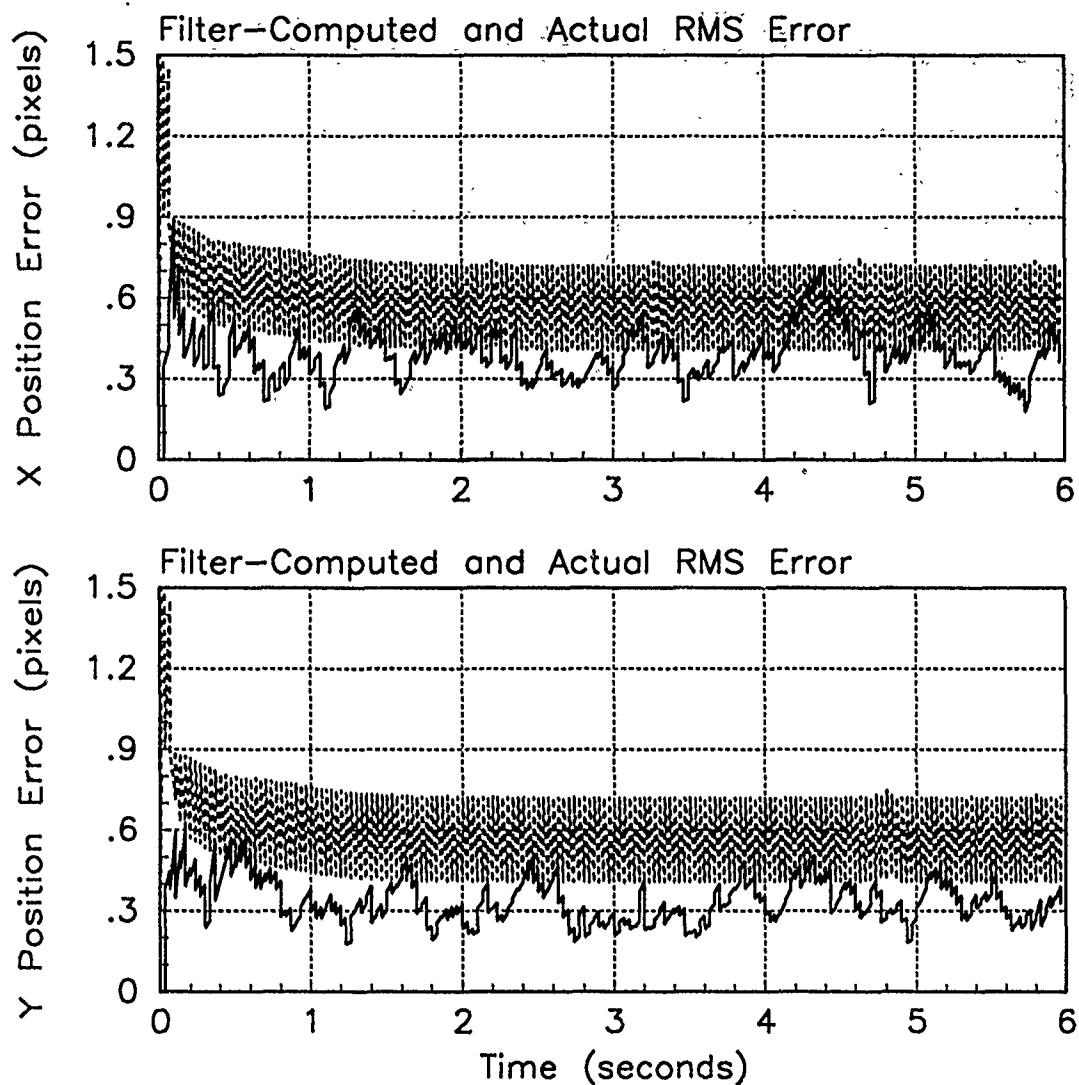


Figure C.10. RMS Error Plots; Real-Pole MMAE-R; PC is 1; Trajectory with $\omega = .01$

Table C.4. Temporal Average and Residuals; Real-Pole MMAE-R; PC is 1; Trajectory with $\omega = .01$.

Error in:	Mean	σ
$p_x(t_i^-)$	0.16729	0.41147
$p_x(t_i^+)$	0.12927	0.37482
$y_x(t_i^-)$	0.10607	0.38161
$p_y(t_i^-)$	0.0025636	0.34717
$p_y(t_i^+)$	0.0039588	0.31505
$y_y(t_i^-)$	0.0085098	0.36838

Filter	$\mathbf{r}_k^T \mathbf{r}_k$	$\mathbf{r}_k^T \mathbf{A}_k^{-1} \mathbf{r}_k$
Benign	0.31347	1.84759
Intermediate	0.33138	1.74876
Harsh	0.41194	1.56997

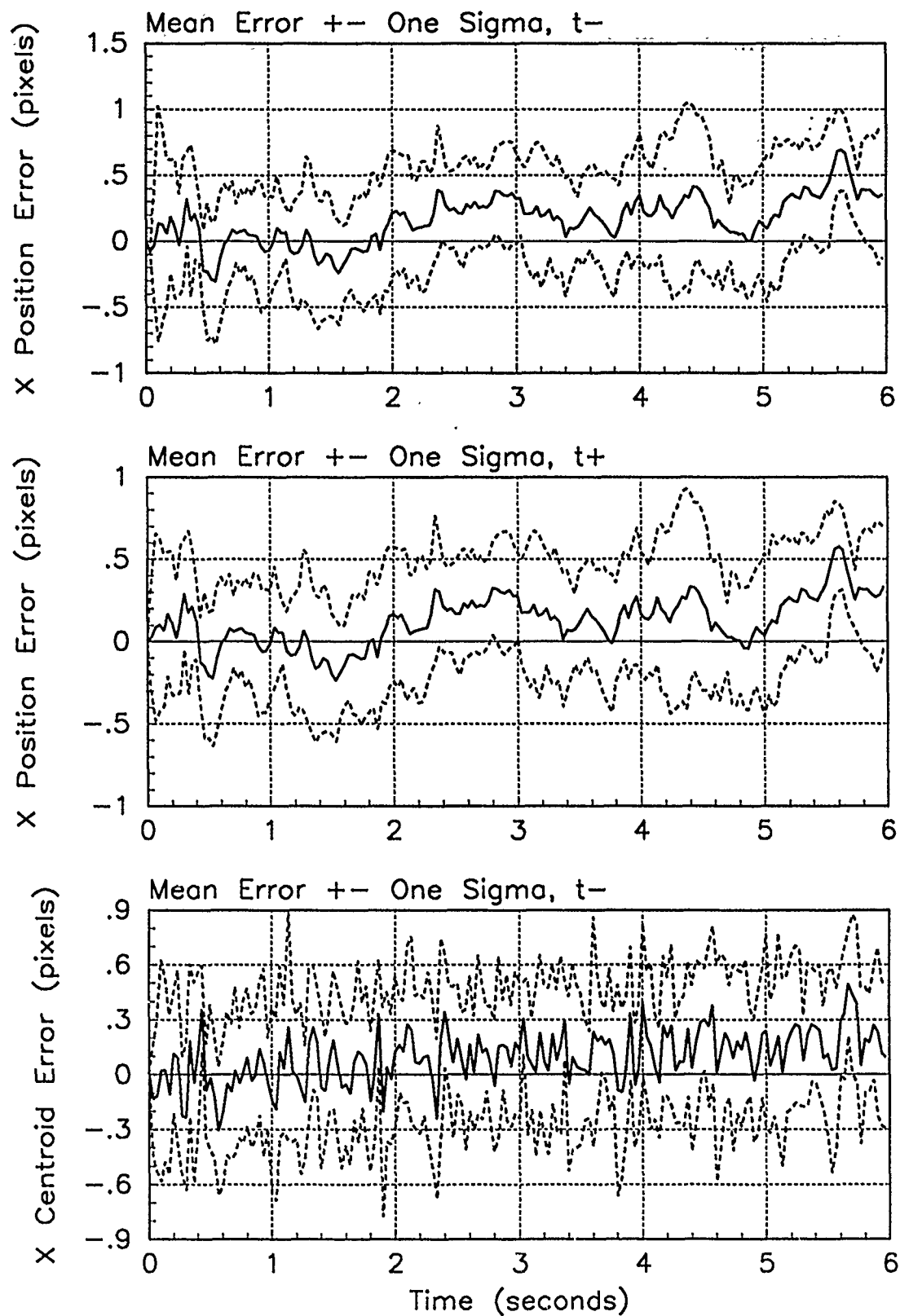


Figure C.11. X-Error Plots; Real-Pole MMAE-R; PC is 1; Trajectory with $\omega = .01$

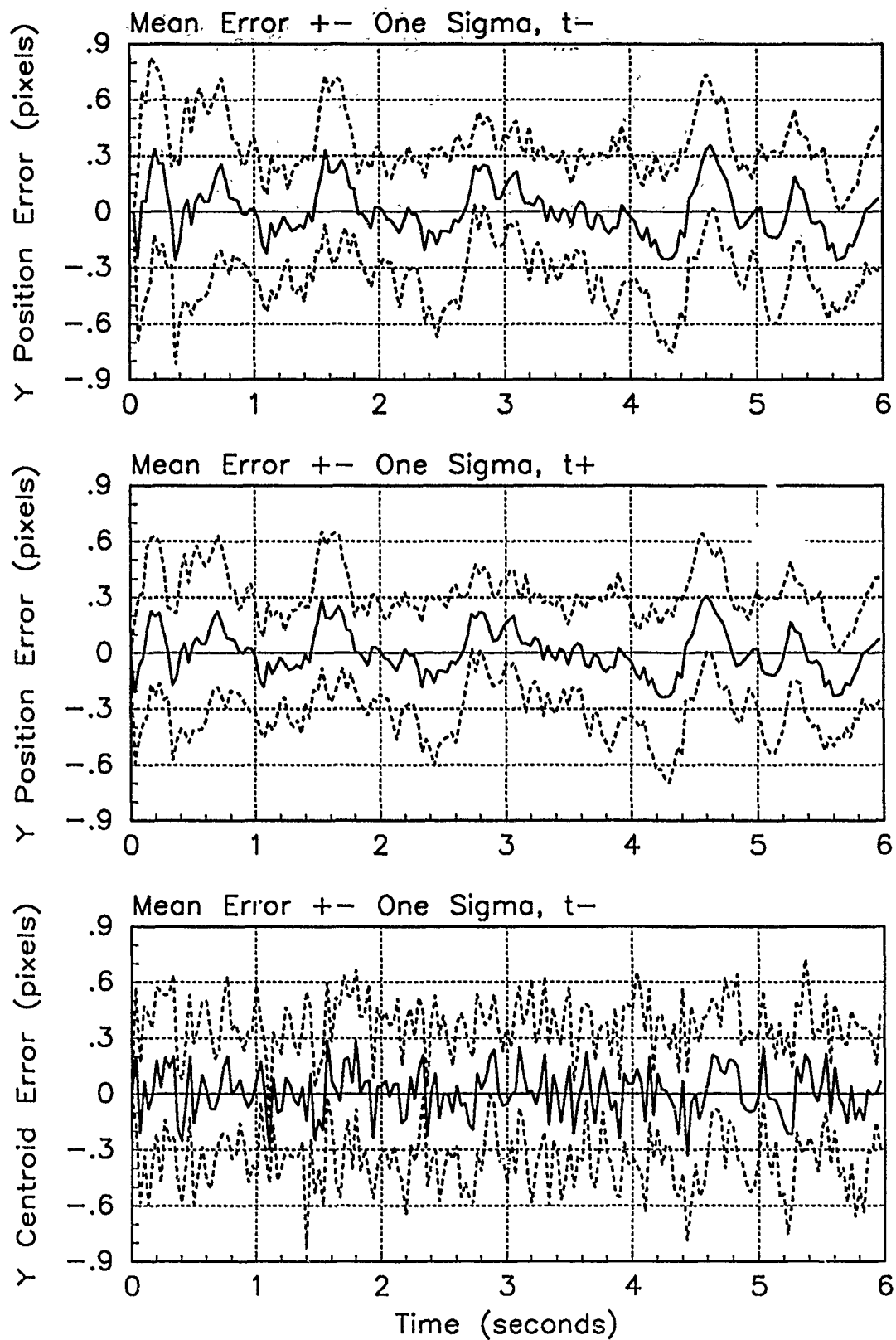


Figure C.12. Y-Error Plots; Real-Pole MMAE-R; PC is 1; Trajectory with $\omega = .01$

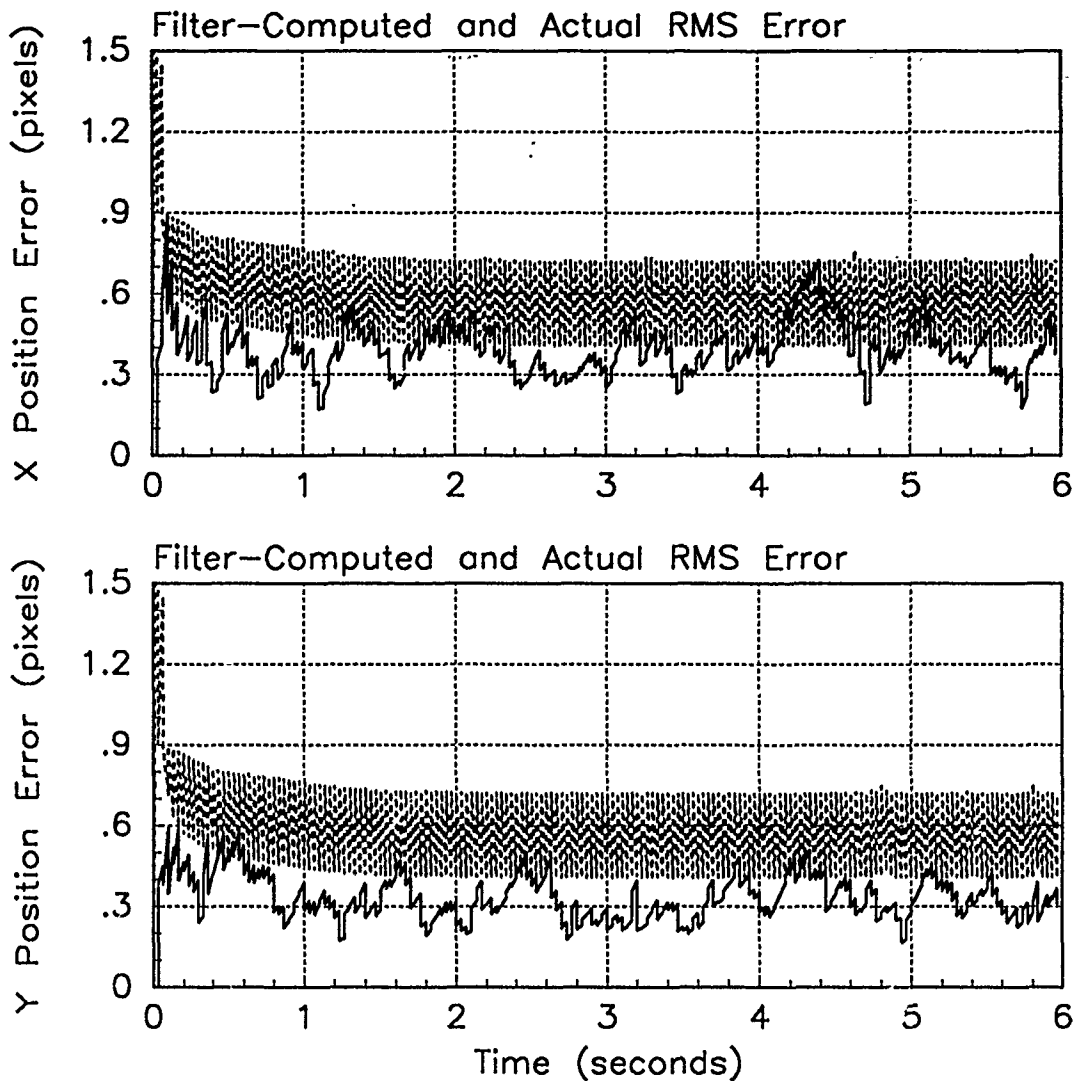


Figure C.13. RMS Error Plots; Real-Pole MMAE-R; PC is 1; Trajectory with $\omega = .62$

Table C.5. Temporal Average and Residuals; Real-Pole MMAE-R; PC is 1; Trajectory with $\omega = .62$.

Error in:	Mean	σ
$p_x(t_i^-)$	0.16224	0.41166
$p_x(t_i^+)$	0.12445	0.37512
$y_x(t_i^-)$	0.10131	0.38216
$p_y(t_i^-)$	0.0093033	0.34414
$p_y(t_i^+)$	0.0084065	0.31142
$y_y(t_i^-)$	0.011496	0.36649

Filter	$\mathbf{r}_k^T \mathbf{r}_k$	$\mathbf{r}_k^T \mathbf{A}_k^{-1} \mathbf{r}_k$
Benign	0.31397	1.85046
Intermediate	0.33211	1.75272
Harsul	0.41180	1.56946

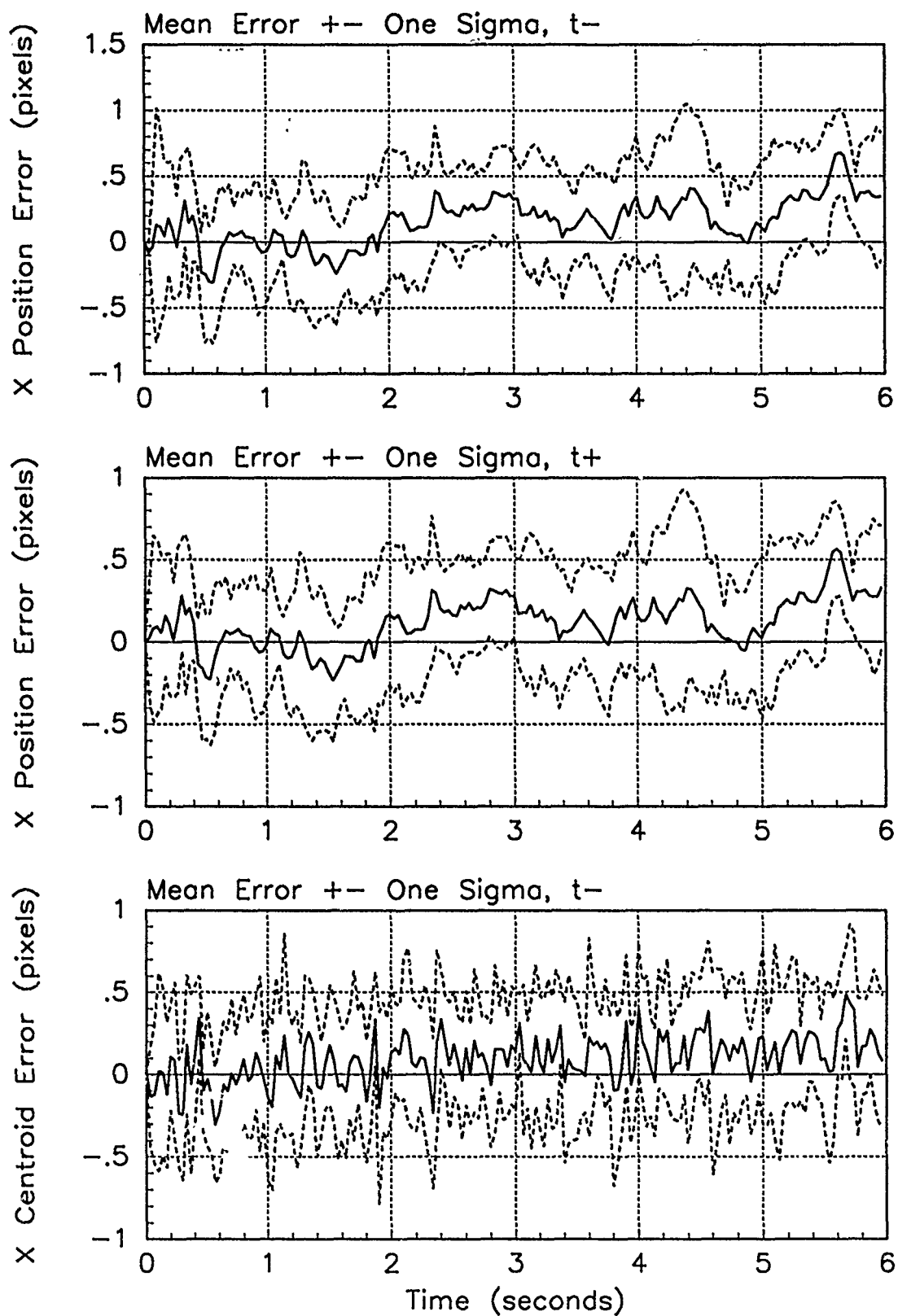


Figure C.1.1. X-Error Plots; Real-Pole MMAE-R; PC is 1; Trajectory with $\omega = .62$

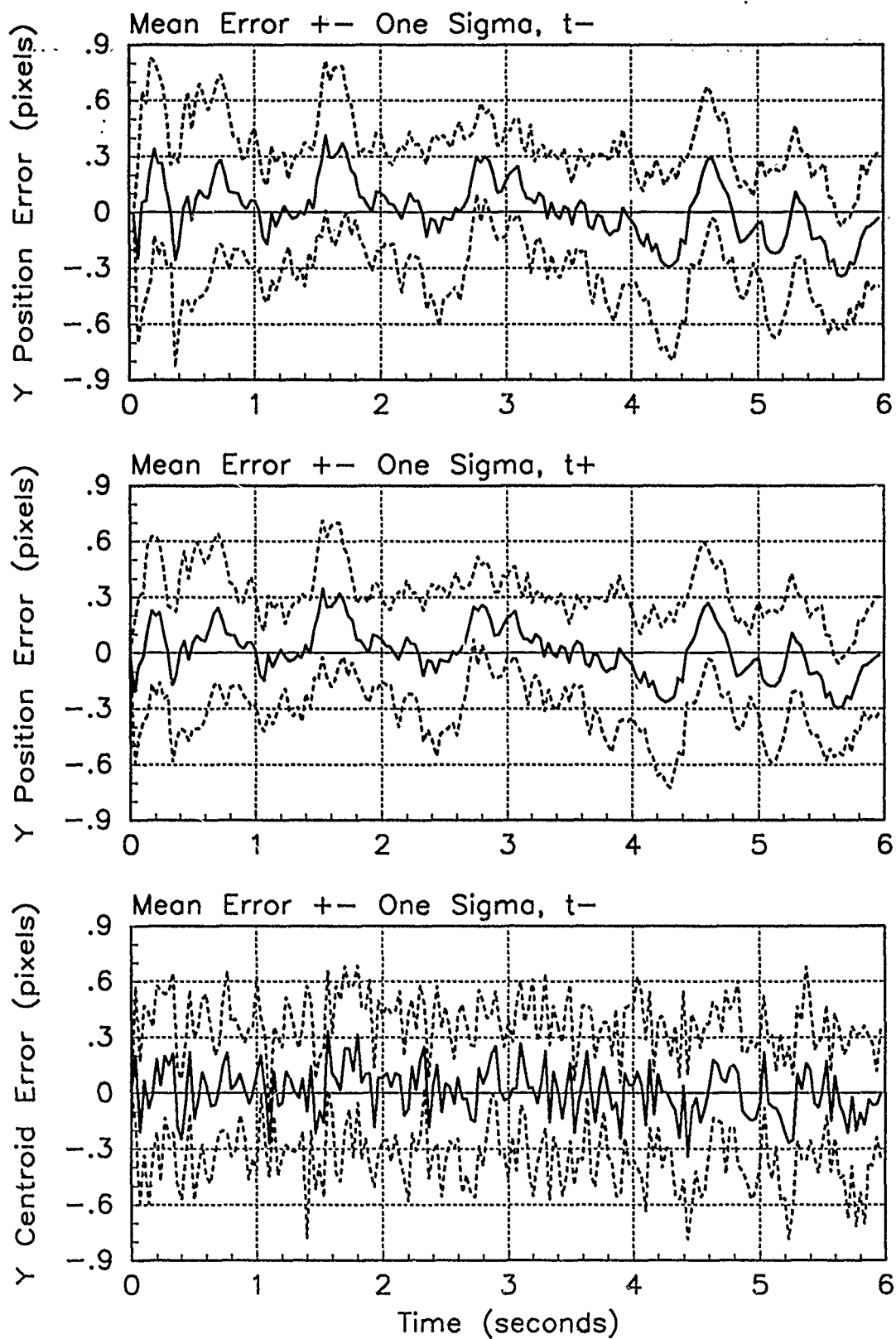


Figure C.15. Y-Error Plots; Real-Pole MMAE-R; PC is 1; Trajectory with $\omega = .62$

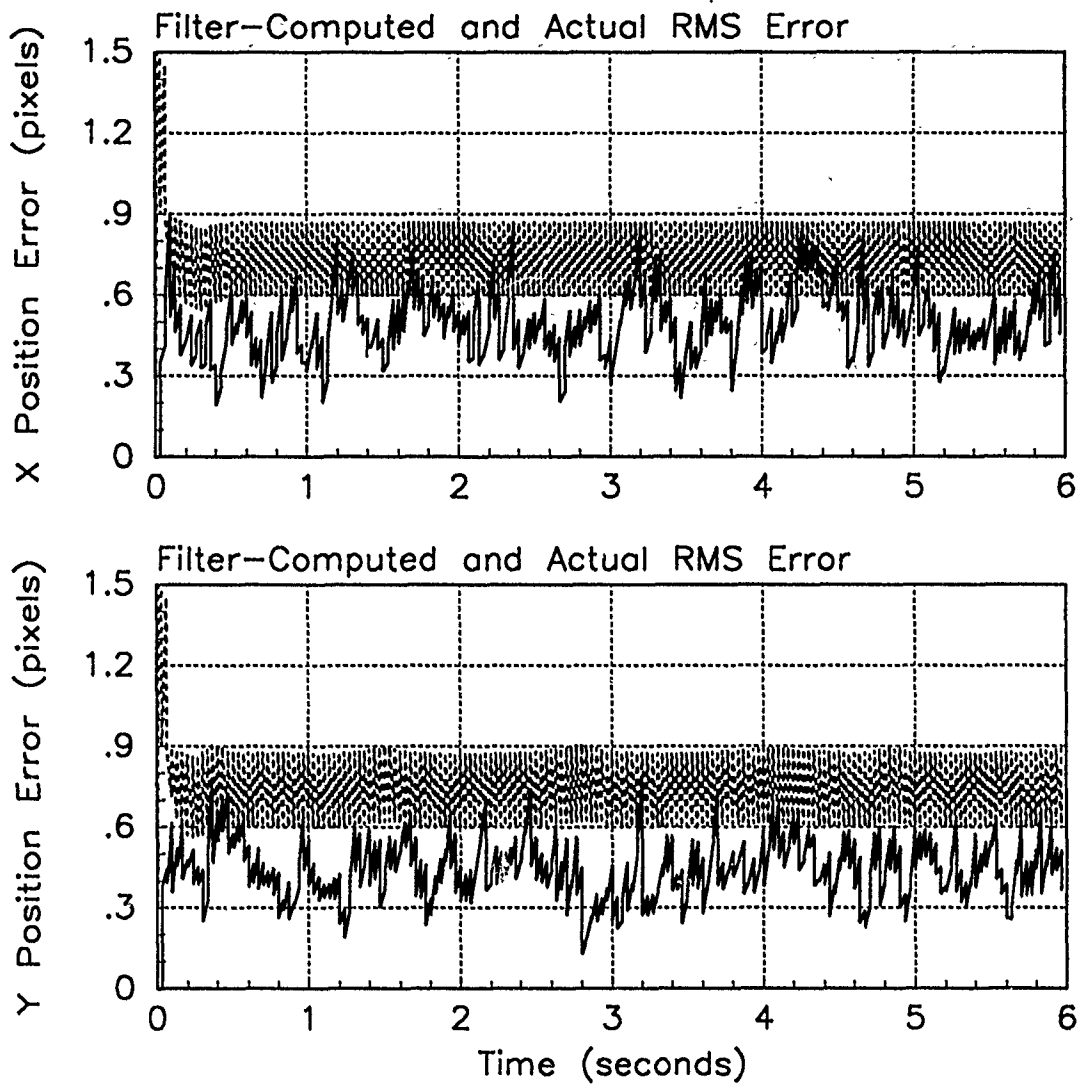


Figure C.16. RMS Error Plots; Real-Pole MMAE-R; PC is 1; Trajectory with $\omega = 2.8$

Table C.6. Temporal Average and Residuals; Real-Pole MMAE-R; PC is 1; Trajectory with $\omega = 2.8$.

Error in:	Mean	σ
$p_x(t_i^-)$	-0.018441	0.55672
$p_x(t_i^+)$	-0.016016	0.44602
$y_x(t_i^-)$	-0.0040403	0.44564
$p_y(t_i^-)$	0.011116	0.49278
$p_y(t_i^+)$	-0.012656	0.38439
$y_y(t_i^-)$	0.0035426	0.42634

Filter	$\mathbf{r}_k^T \mathbf{r}_k$	$\mathbf{r}_k^T \mathbf{A}_k^{-1} \mathbf{r}_k$
Benign	2.62178	15.29063
Intermediate	0.93188	4.94933
Harsh	0.46173	1.76017

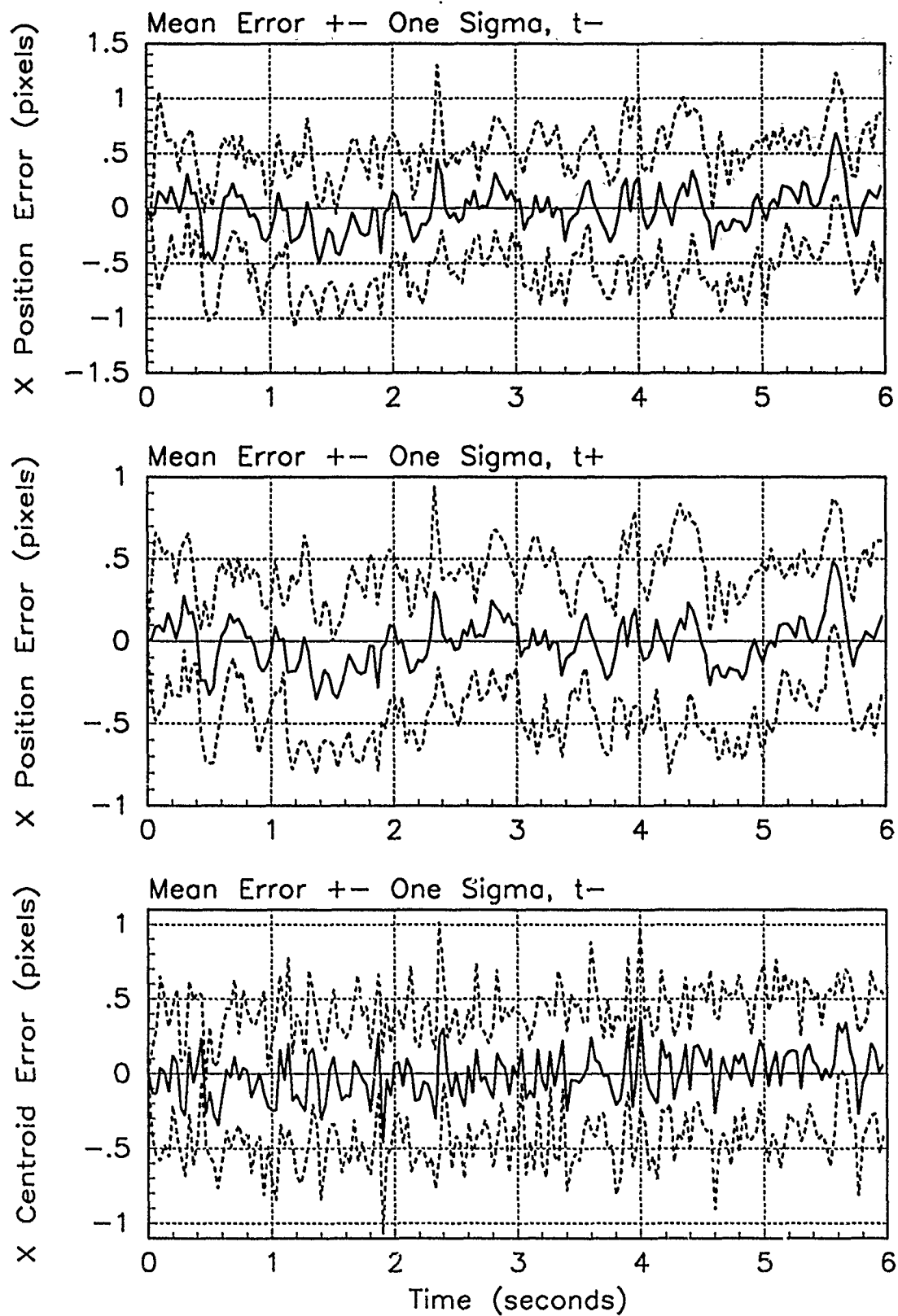


Figure C.17. X-Error Plots; Real-Pole MMAE-R; PC is 1; Trajectory with $\omega = 2.8$

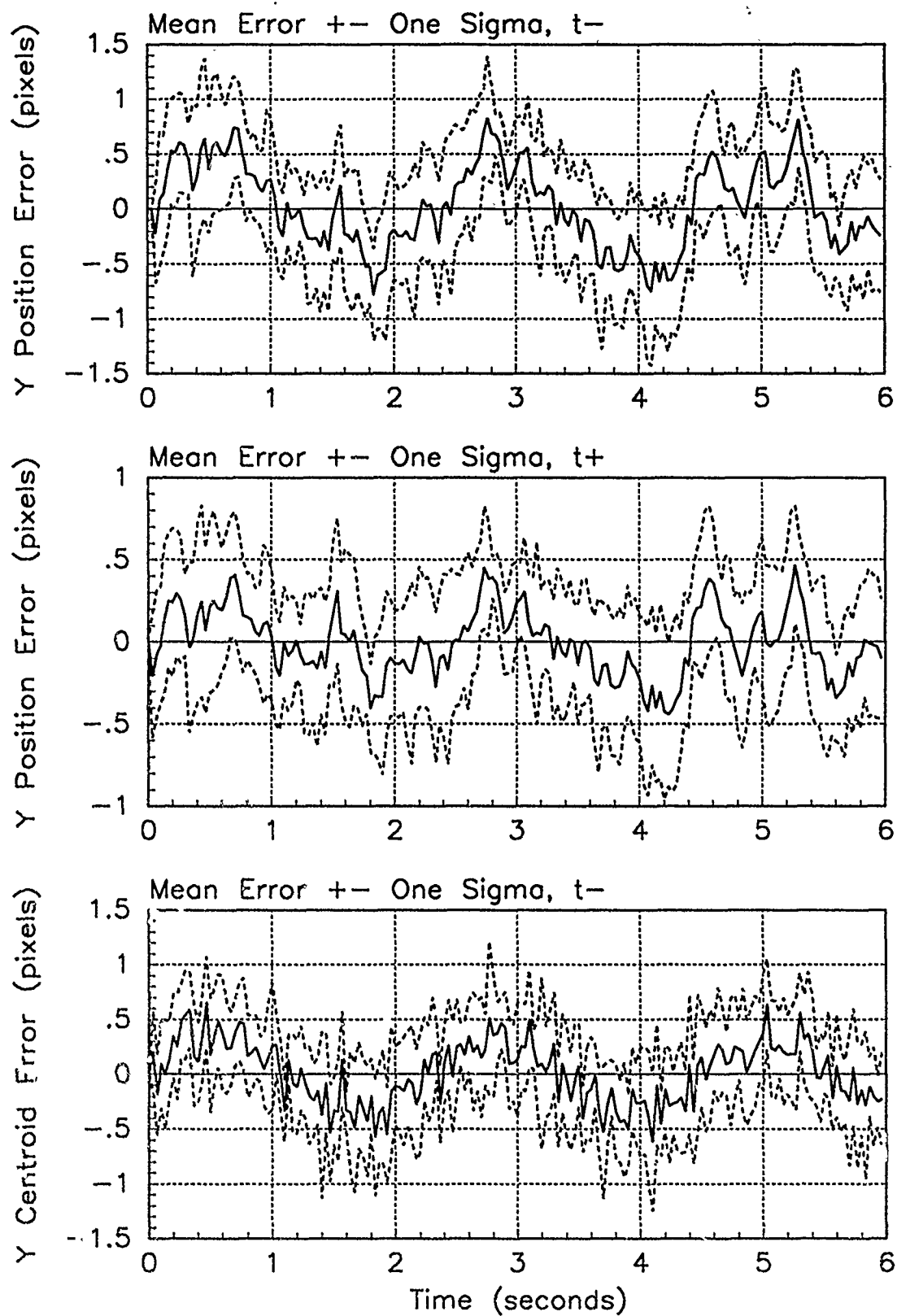


Figure C.18. Y-Error Plots; Real-Pole MMAE-R; PC is 1; Trajectory with $\omega = 2.8$

Appendix D. *Error Plots for Notch MMAE-1*

This appendix shows the error plots for the notch MMAE with the intermediate filter at $\omega = .62$ radians per second as discussed in Chapter V. This is referred to as MMAE-1. The first part is results for the MMAE as originally tuned. The latter part is from the MMAE as retuned.

The results for one Monte Carlo study consists of a set of three pages. The first page shows the RMS error plots for each of the x- and y-positions. The band is the dashed line for the filter-computed RMS error. The solid line is the actual RMS error calculated over the Monte Carlo study. Below these plots are two tables. The table on the left lists the temporal average of the position errors. This temporal average is from .5 seconds to the end of each of the 10 runs in the Monte Carlo study as described in Section 5.2. The table on the right is the list of the average $\mathbf{r}_k^T(t_i)\mathbf{r}_k(t_i)$ and $\mathbf{r}_k^T(t_i)\mathbf{A}_k^{-1}(t_i)\mathbf{r}_k(t_i)$ over the 10 runs for the entire run, not just the last 5.5 seconds due only to ease of programing. The lack of time notation (rather than the traditional overbar) in the table signifies the temporal average. The next page of each set shows the mean ± 1 standard deviation error plots for the x-position at time t_i^- and t_i^+ and the mean x-centroid position error at time t_i^- . The final page shows similar plots for the mean y-position errors. The solid line denotes the mean error while the dashed line is the mean $\pm \sigma$.

When the MMAE is tracking the target in a jinking maneuver, there is no table on the first page for the average $\mathbf{r}_k^T(t_i)\mathbf{r}_k(t_i)$ and $\mathbf{r}_k^T(t_i)\mathbf{A}_k^{-1}(t_i)\mathbf{r}_k(t_i)$. Instead, plots of the $\mathbf{r}_k^T(t_i)\mathbf{r}_k(t_i)$, $\mathbf{r}_k^T(t_i)\mathbf{A}_k^{-1}(t_i)\mathbf{r}_k(t_i)$, and leading coefficient needed in the hypothesis probability calculation are presented to help determine why one filter is selected over the others.

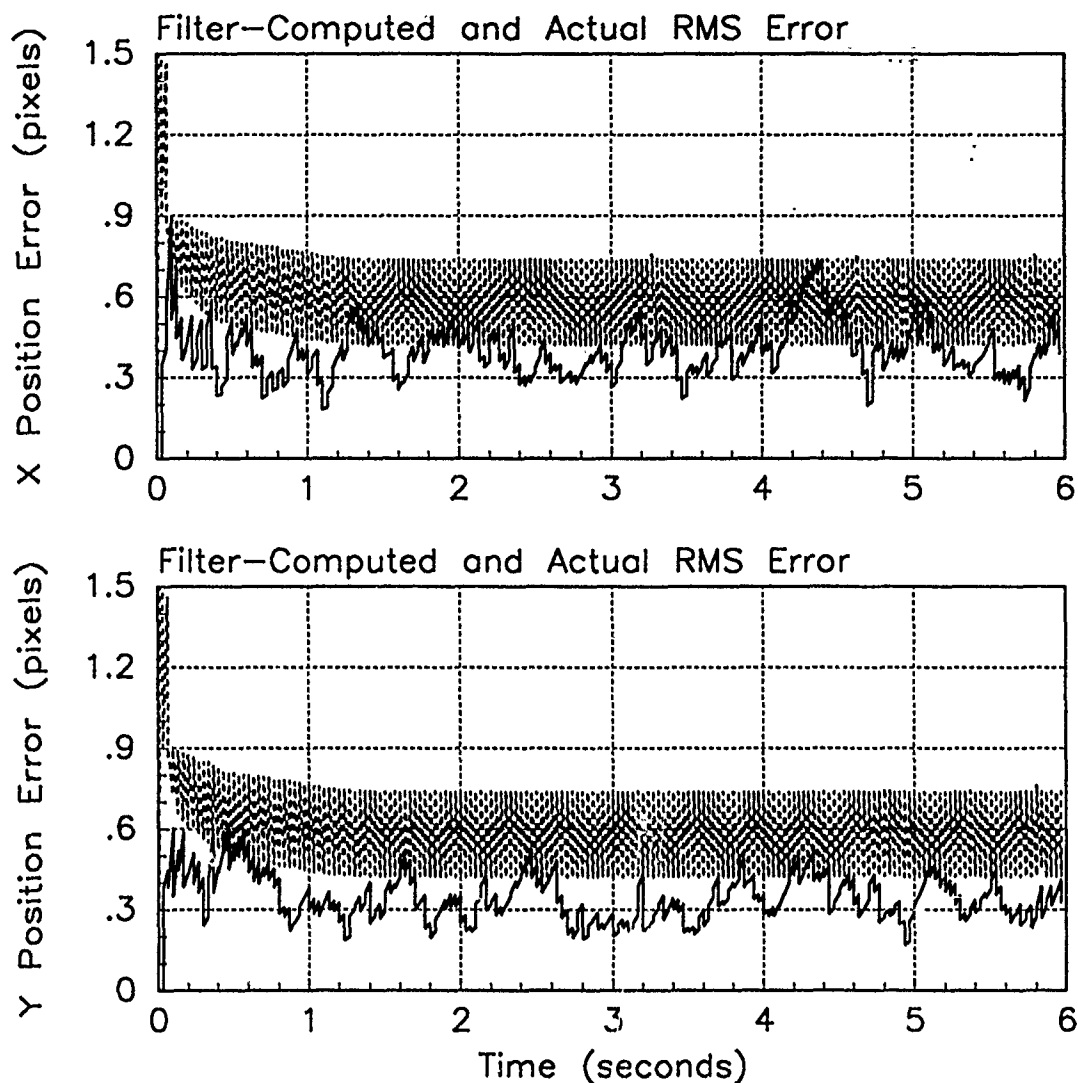


Figure D.1. RMS Error Plots; Notch MMAE-10; PC is 1; Trajectory with $\omega = .01$

Table D.1. Temporal Averages and Residuals; Notch MMAE-10; PC is 1; Trajectory with $\omega = .01$.

Error in:	Mean	σ
$p_x(t_i^-)$	0.13314	0.42082
$p_x(t_i^+)$	0.098728	0.38137
$y_x(t_i^-)$	0.087985	0.38305
$p_y(t_i^-)$	-0.0079997	0.35707
$p_y(t_i^+)$	-0.0064396	0.32042
$y_y(t_i^-)$	-0.0020653	0.36901

Filter	$r_k^T r_k$	$r_k^T A_k^{-1} r_k$
Benign	0.31409	1.81240
Intermediate	0.35060	1.71287
Harsh	0.46834	1.55518

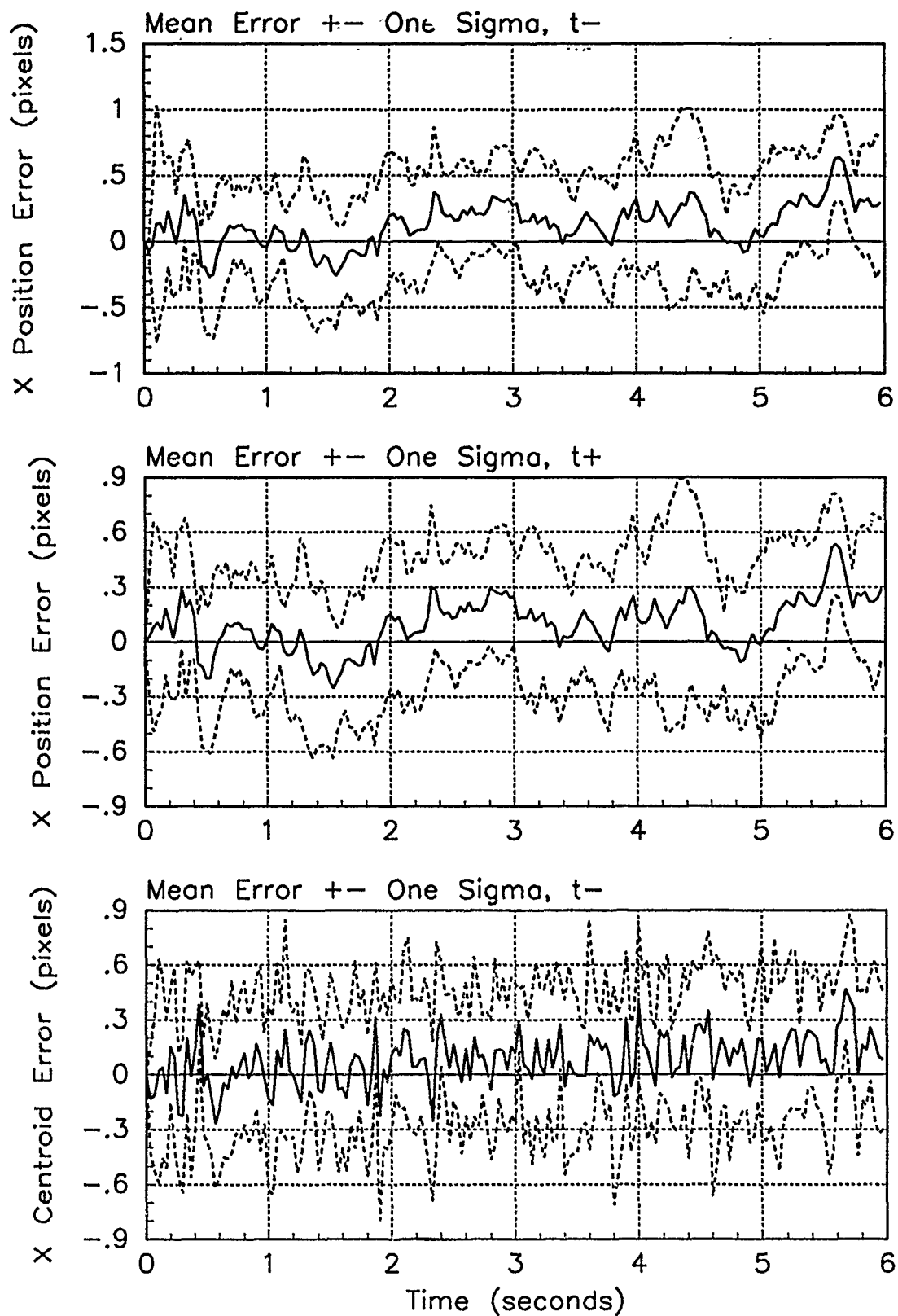


Figure D.2. X-Error Plots; Notch MMAE-10; PC is 1; Trajectory with $\omega = .01$

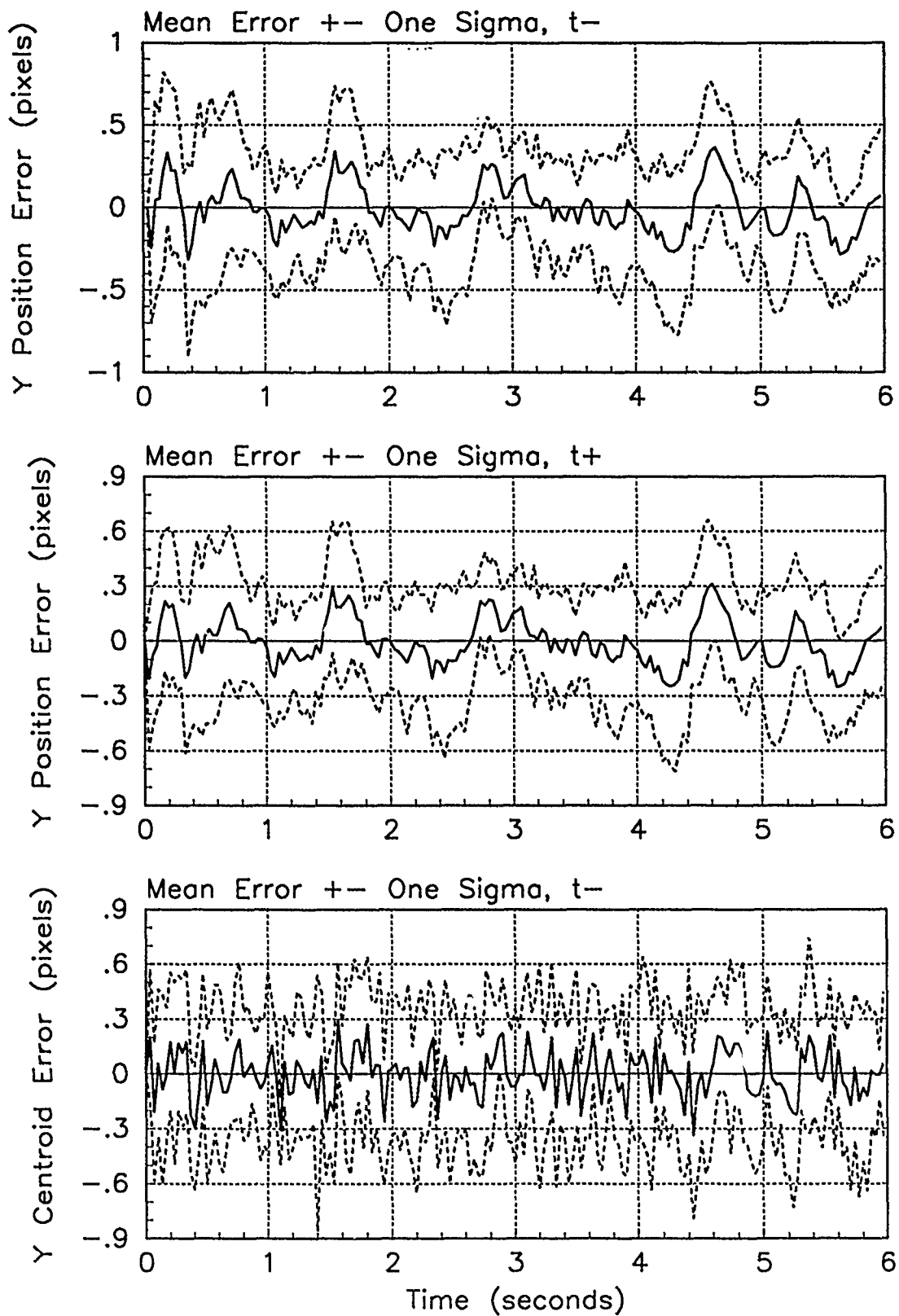


Figure D.3. Y-Error Plots; Notch MMAE-10; PC is 1; Trajectory with $\omega = .01$

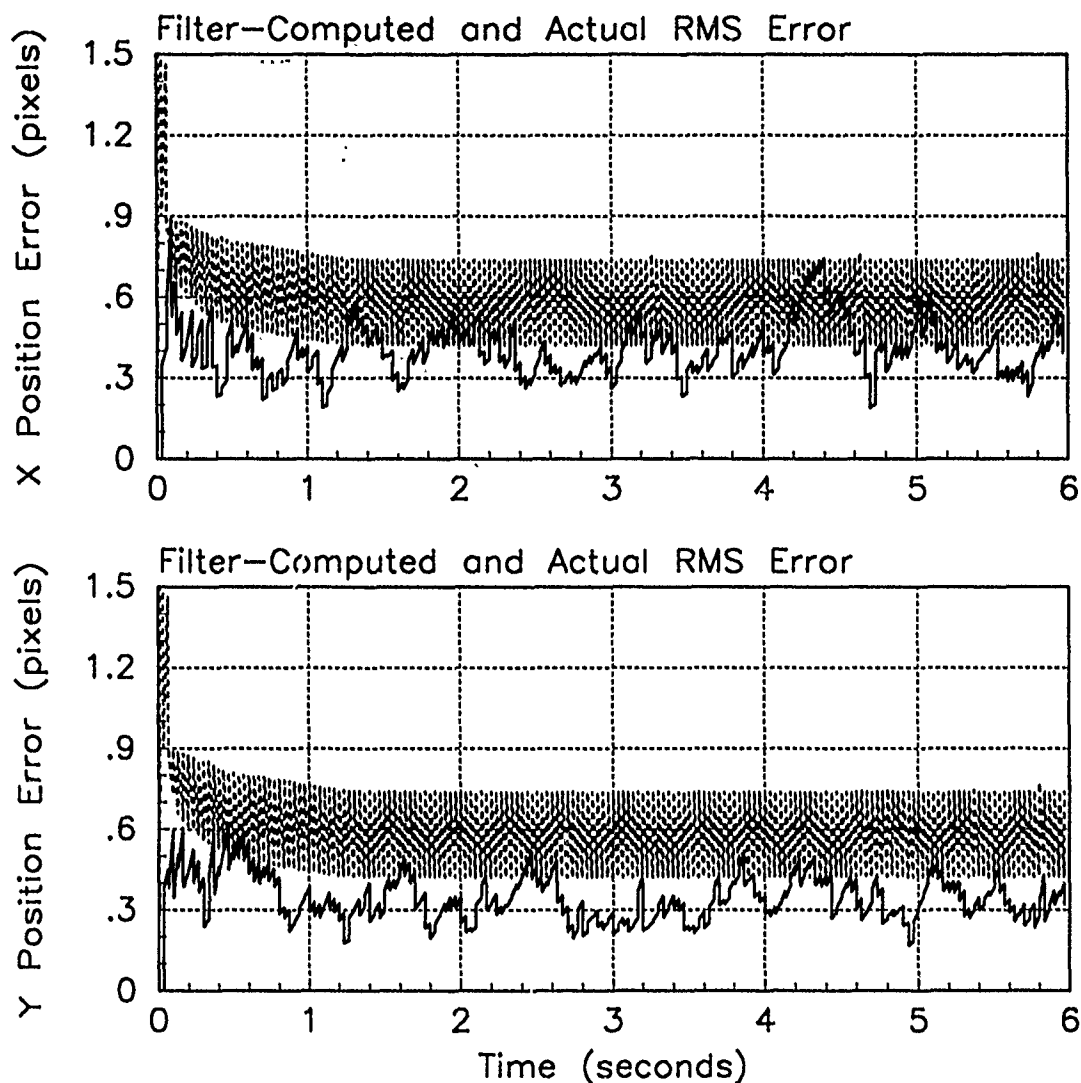


Figure D.4. RMS Error Plots; Notch MMAE-10; PC is 1; Trajectory with $\omega = .62$

Table D.2. Temporal Averages and Residuals; Notch MMAE-10; PC is 1; Trajectory with $\omega = .62$.

Error in:	Mean	σ
$p_x(t_i^-)$	0.13628	0.42397
$p_x(t_i^+)$	0.10193	0.38462
$y_x(t_i^-)$	0.091146	0.38427
$p_y(t_i^-)$	0.0024705	0.35754
$p_y(t_i^+)$	0.0022286	0.32053
$y_y(t_i^-)$	0.0055900	0.36884

Filter	$\mathbf{r}_k^T \mathbf{r}_k$	$\mathbf{r}_k^T \mathbf{A}_k^{-1} \mathbf{r}_k$
Benign	0.31506	1.81781
Intermediate	0.35186	1.71896
Harsh	0.47046	1.56216

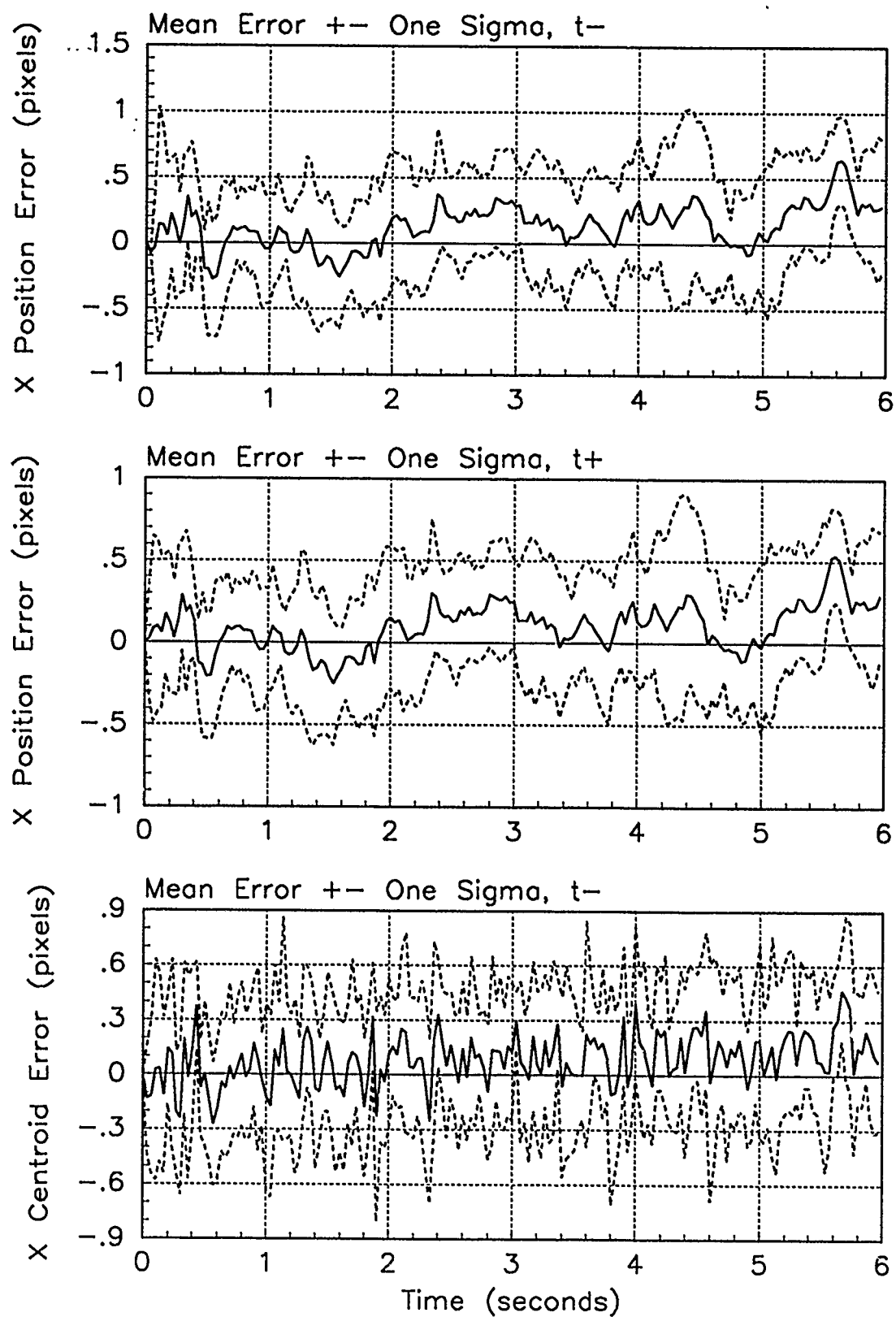


Figure D.5. X-Error Plots; Notch MMAE-10; PC is 1; Trajectory with $\omega = .62$

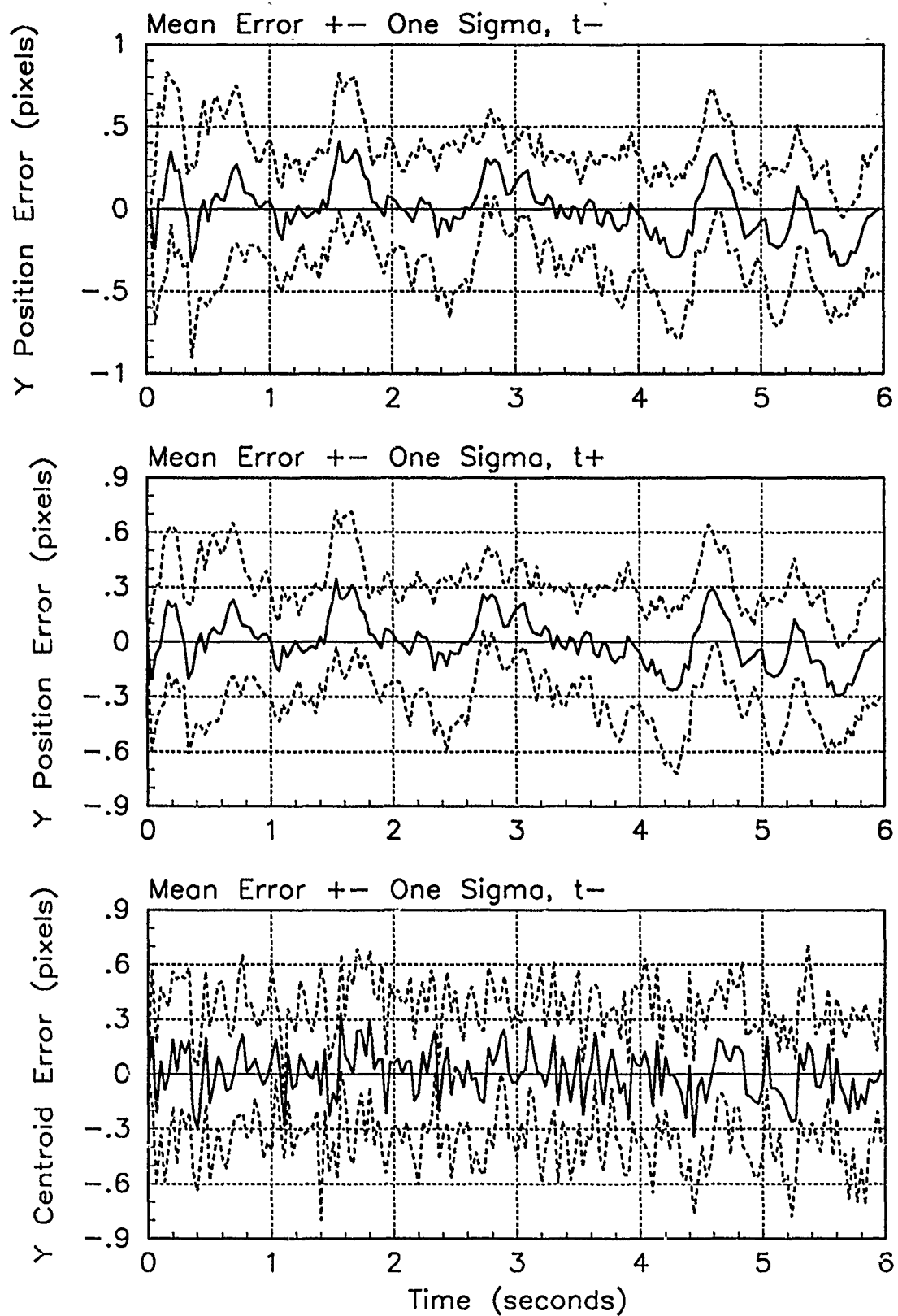


Figure D.6. Y-Error Plots; Notch MMAE-10; PC is 1; Trajectory with $\omega = .62$

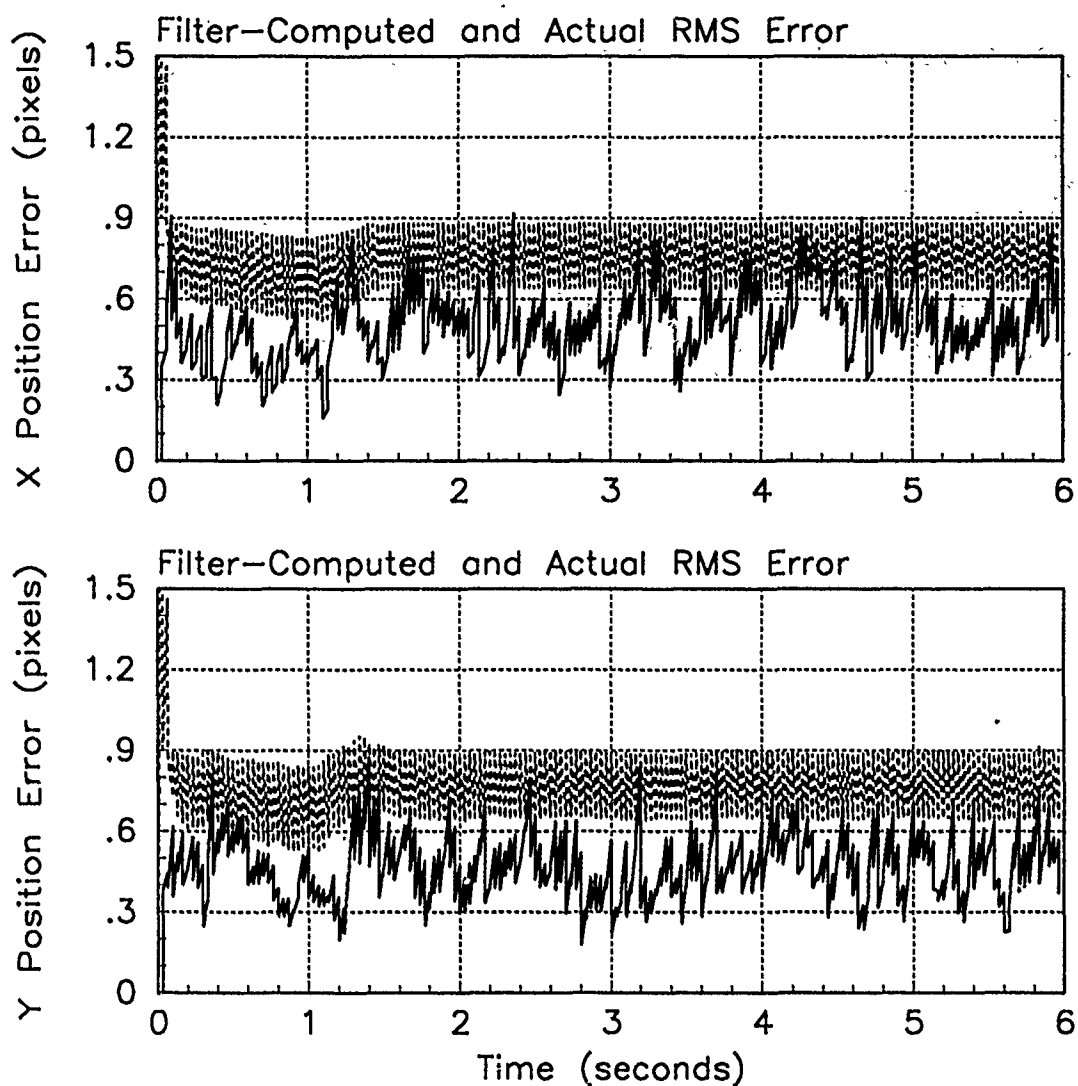


Figure D.7. RMS Error Plots; Notch MMAE-10; PC is 1; Trajectory with $\omega = 2.8$

Table D.3. Temporal Averages and Residuals; Notch MMAE-10; PC is 1; Trajectory with $\omega = 2.8$.

Error in:	Mean	σ
$p_x(t_i^-)$	-0.022058	0.57723
$p_x(t_i^+)$	-0.0092969	0.44565
$y_x(t_i^-)$	-0.0049930	0.46382
$p_y(t_i^-)$	-0.069637	0.54025
$p_y(t_i^+)$	-0.065185	0.39927
$y_y(t_i^-)$	-0.066540	0.45485

Filter	$\mathbf{r}_k^T \mathbf{r}_k$	$\mathbf{r}_k^T \mathbf{A}_k^{-1} \mathbf{r}_k$
Benign	2.47745	14.24848
Intermediate	0.67420	3.31920
Harsh	0.45968	1.52569

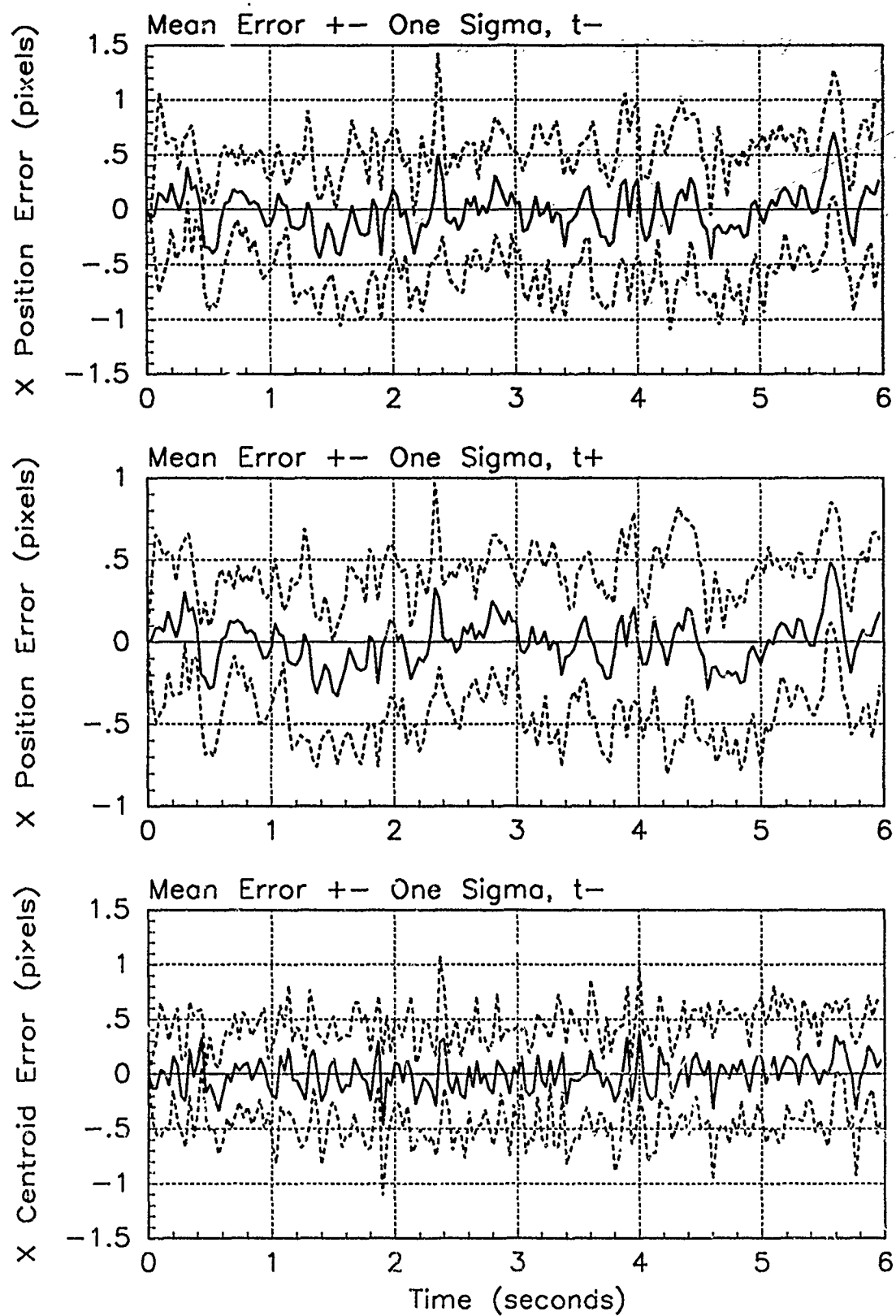


Figure D.8. X-Error Plots; Notch MMAE-10; PC is 1; Trajectory with $\omega = 2.8$

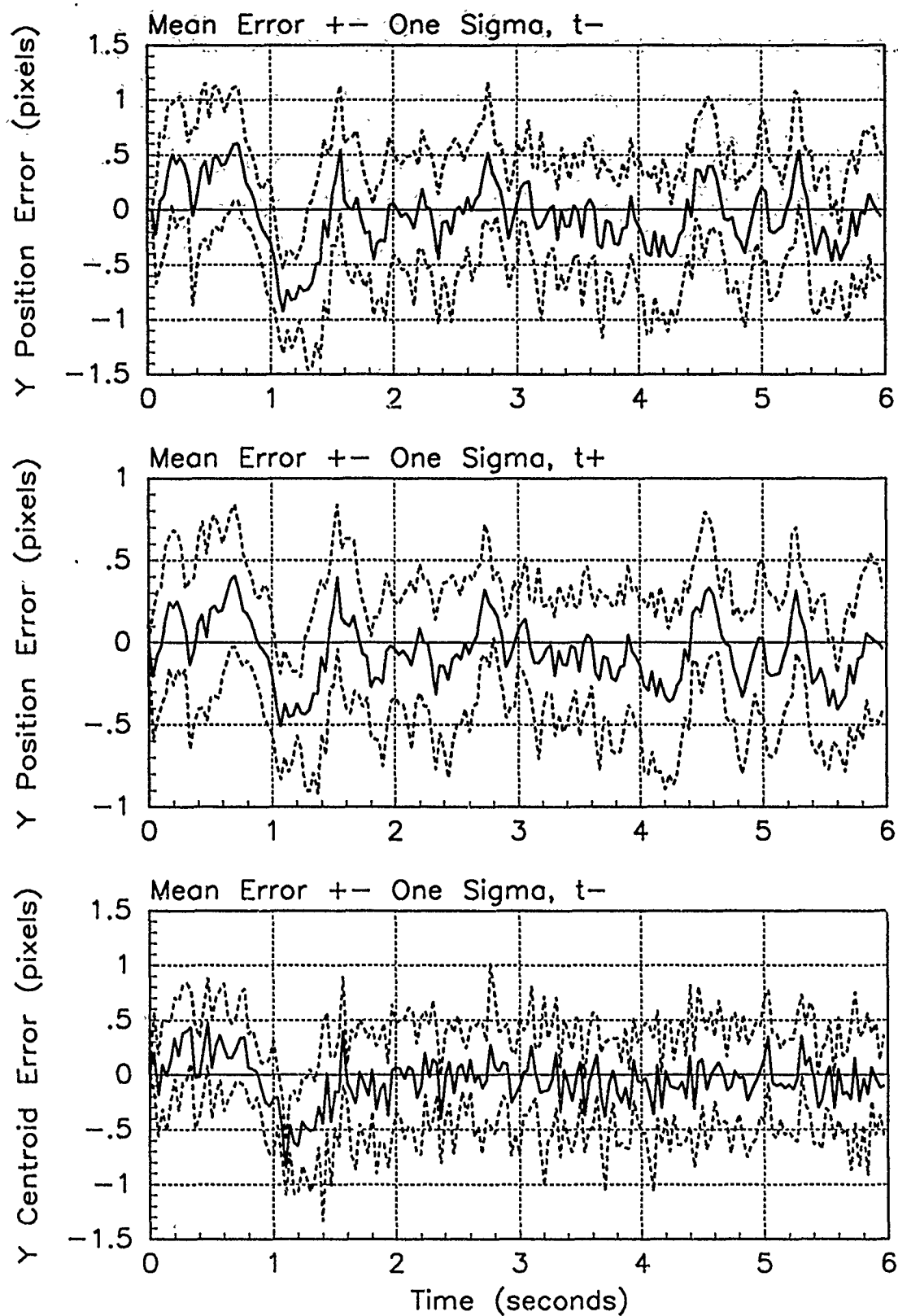


Figure D.9. Y-Error Plots; Notch MMAE-10; PC is 1; Trajectory with $\omega = 2.8$

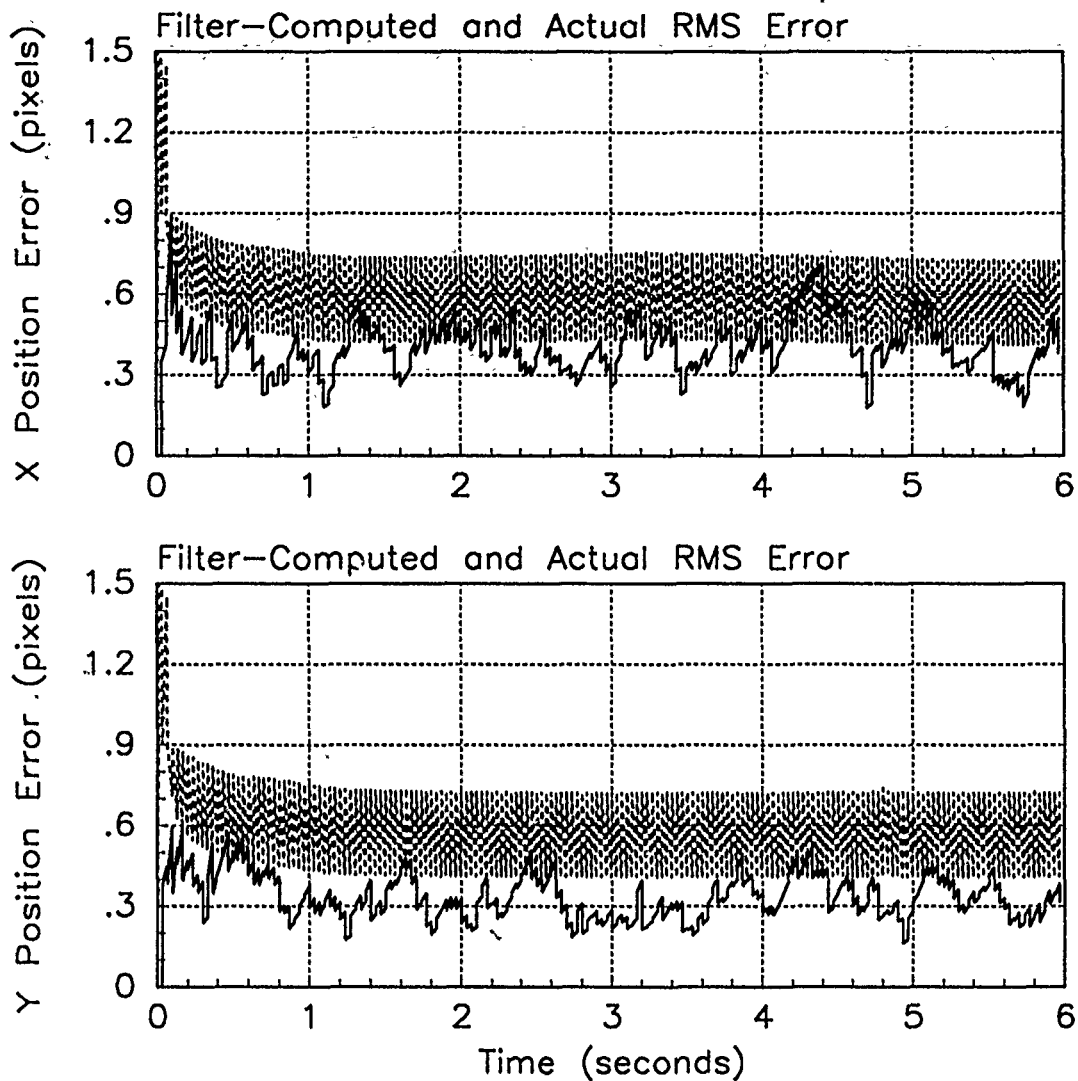


Figure D.10. RMS Error Plots; Notch MMAE-1R; PC is 1; Trajectory with $\omega = .01$

Table D.4. Temporal Averages and Residuals; Notch MMAE-1R; PC is 1; Trajectory with $\omega = .01$.

Error in:	Mean	σ
$p_x(t_i^-)$	0.066378	0.42229
$p_x(t_i^+)$	0.050430	0.38346
$y_x(t_i^-)$	0.049527	0.38468
$p_y(t_i^-)$	-0.0060739	0.34624
$p_y(t_i^+)$	-0.0052504	0.31336
$y_y(t_i^-)$	-0.0012147	0.36622

Filter	$r_k^T r_k$	$r_k^T A_k^{-1} r_k$
Benign	0.31313	1.84578
Intermediate	0.30794	1.80083
Harsh	0.38003	1.73025

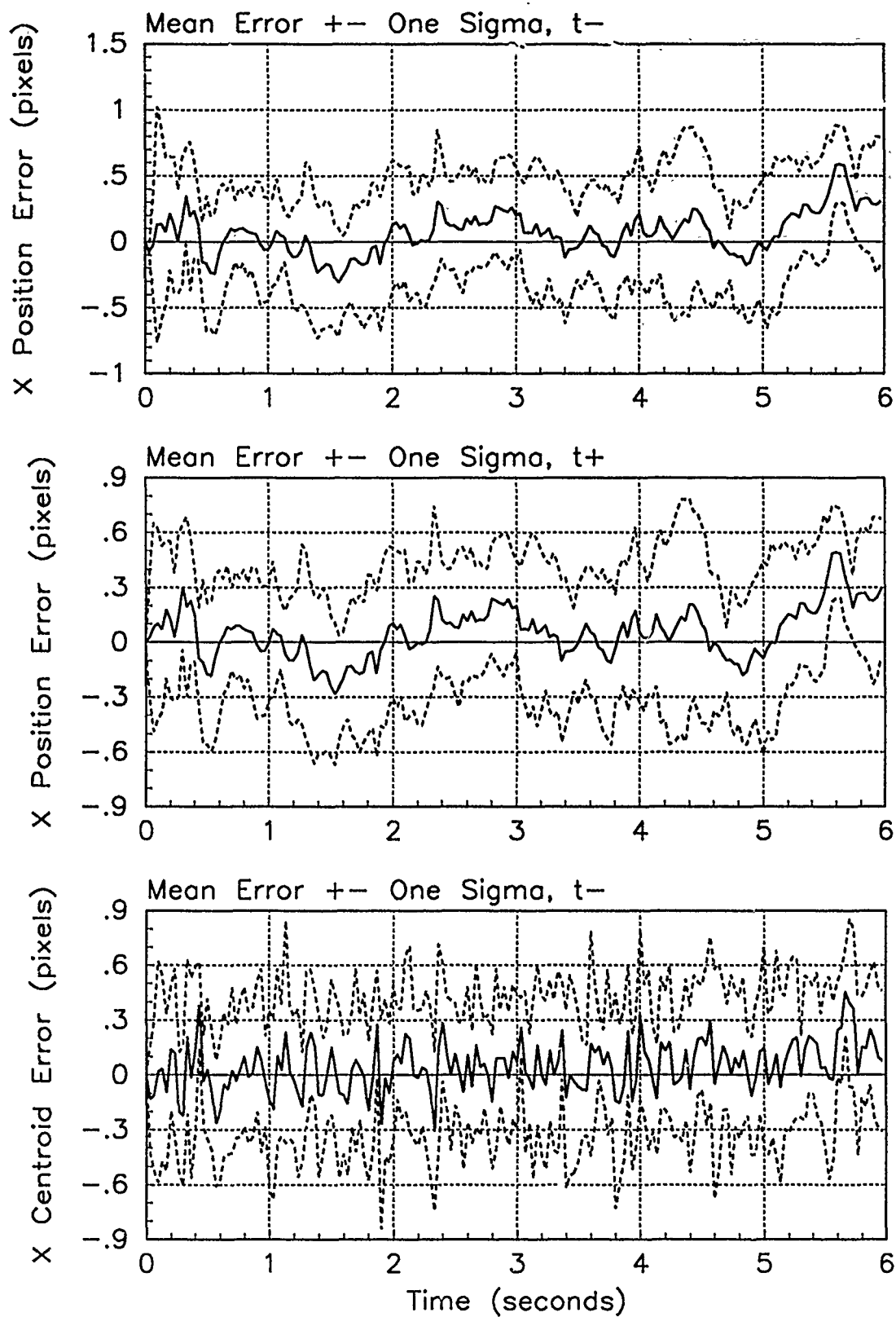


Figure D.11. X-Error Plots; Notch MMAE-1R; PC is 1; Trajectory with $\omega = .01$

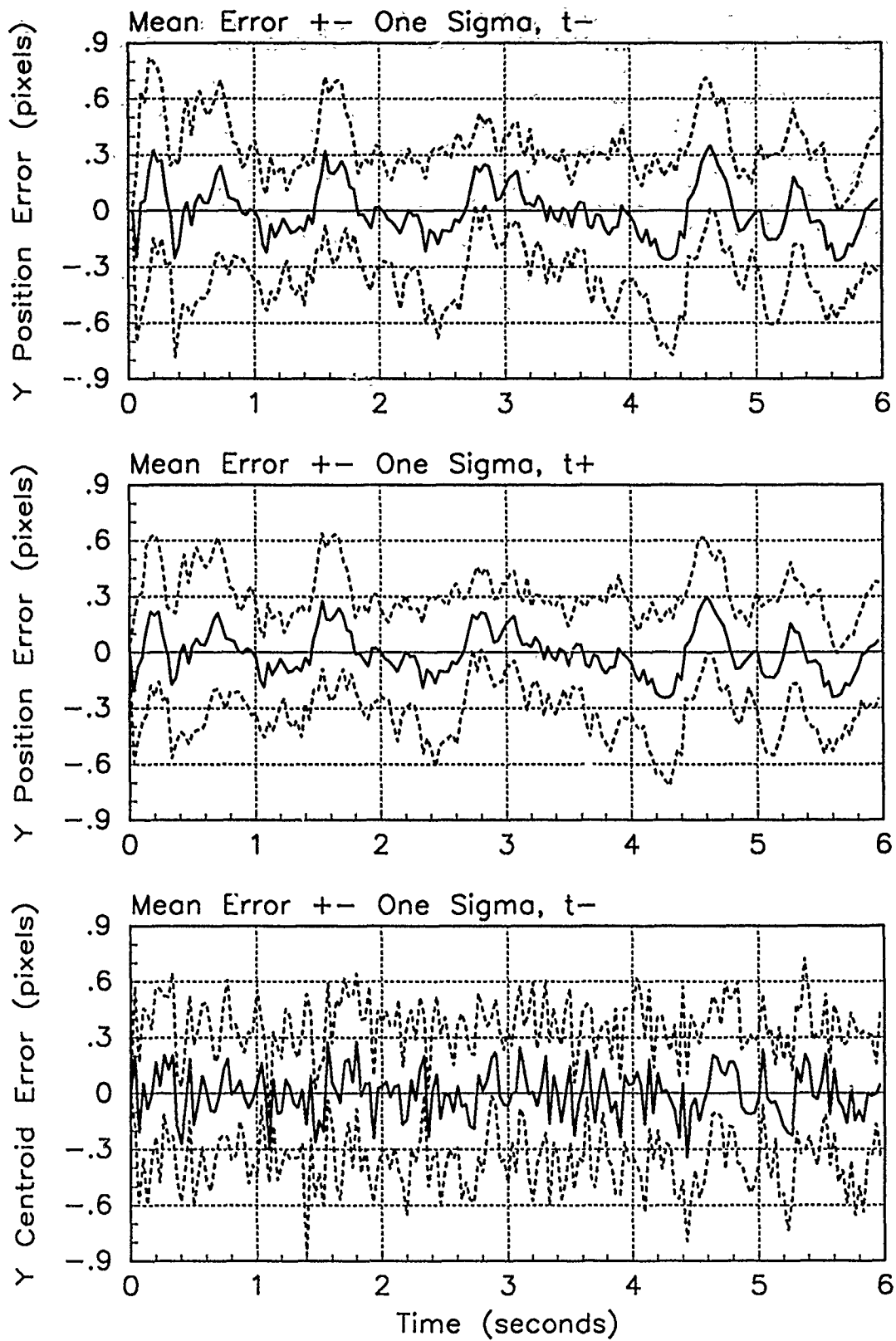


Figure D.12. Y-Error Plots; Notch MMAE-1R; PC is 1; Trajectory with $\omega = .01$

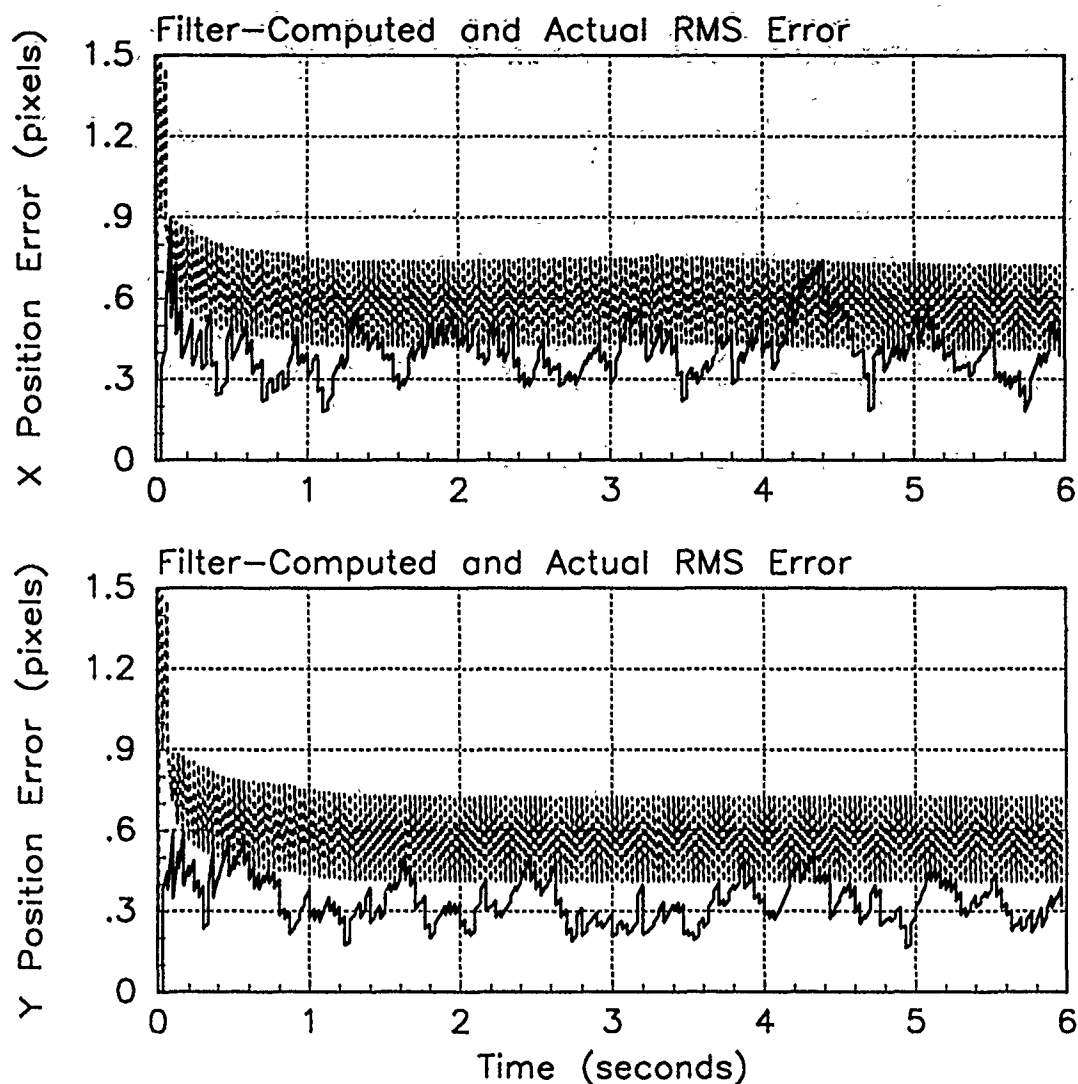


Figure D.13. RMS Error Plots; Notch MMAE-1R; PC is 1; Trajectory with $\omega = .62$

Table D.5. Temporal Averages and Residuals; Notch MMAE-1R; PC is 1; Trajectory with $\omega = .62$.

Error in:	Mean	σ
$p_x(t_i^-)$	0.068746	0.42274
$p_x(t_i^+)$	0.053178	0.38391
$y_x(t_i^-)$	0.052772	0.38689
$p_y(t_i^-)$	0.033674	0.34746
$p_y(t_i^+)$	0.025586	0.31473
$y_y(t_i^-)$	0.023106	0.36711

Filter	$\mathbf{r}_k^T \mathbf{r}_k$	$\mathbf{r}_k^T \mathbf{A}_k^{-1} \mathbf{r}_k$
Benign	0.31484	1.85585
Intermediate	0.30817	1.80175
Harsh	0.38557	1.75574

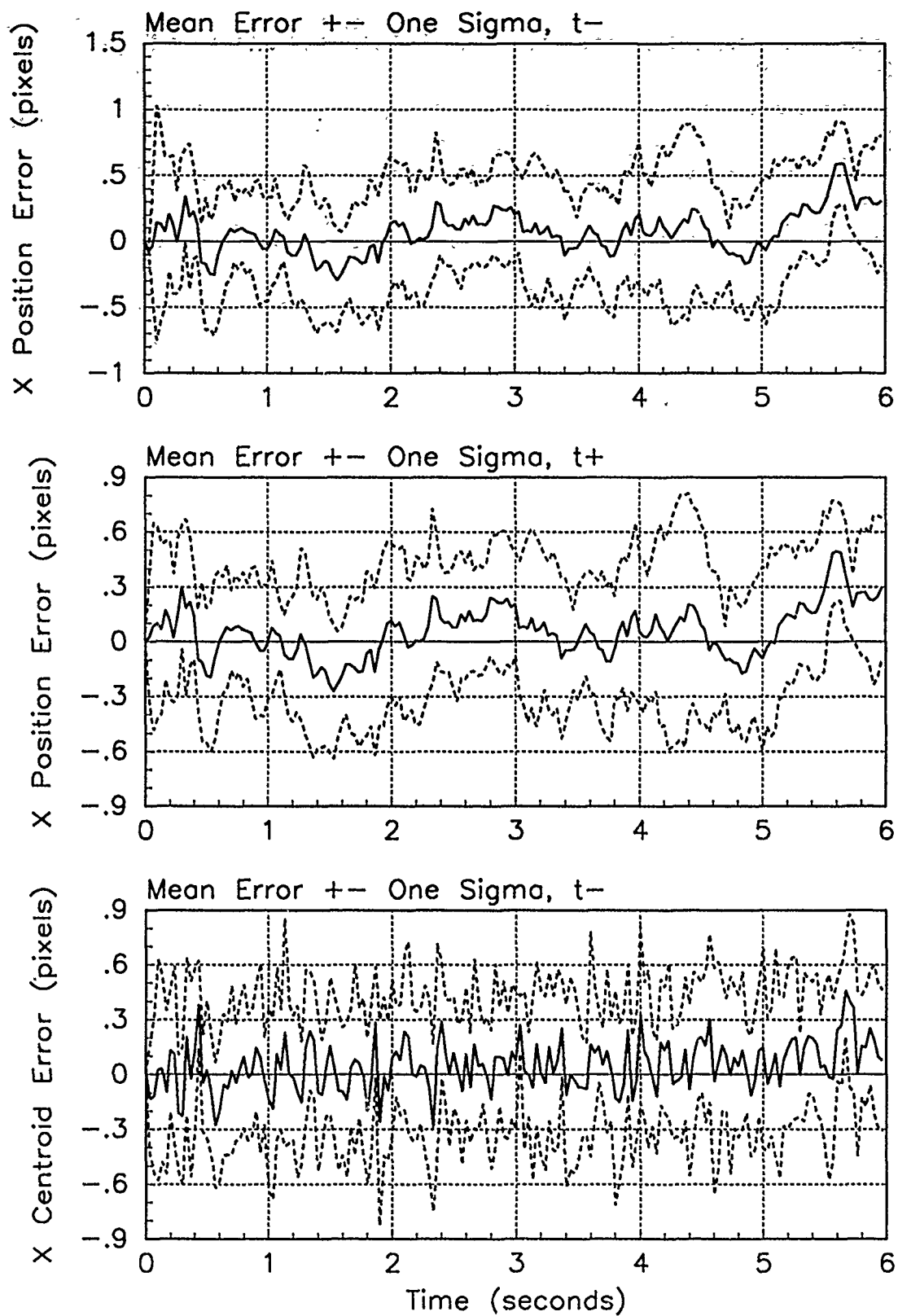


Figure D.14. X-Error Plots; Notch MMAE-1R; PC is 1, Trajectory with $\omega = .62$

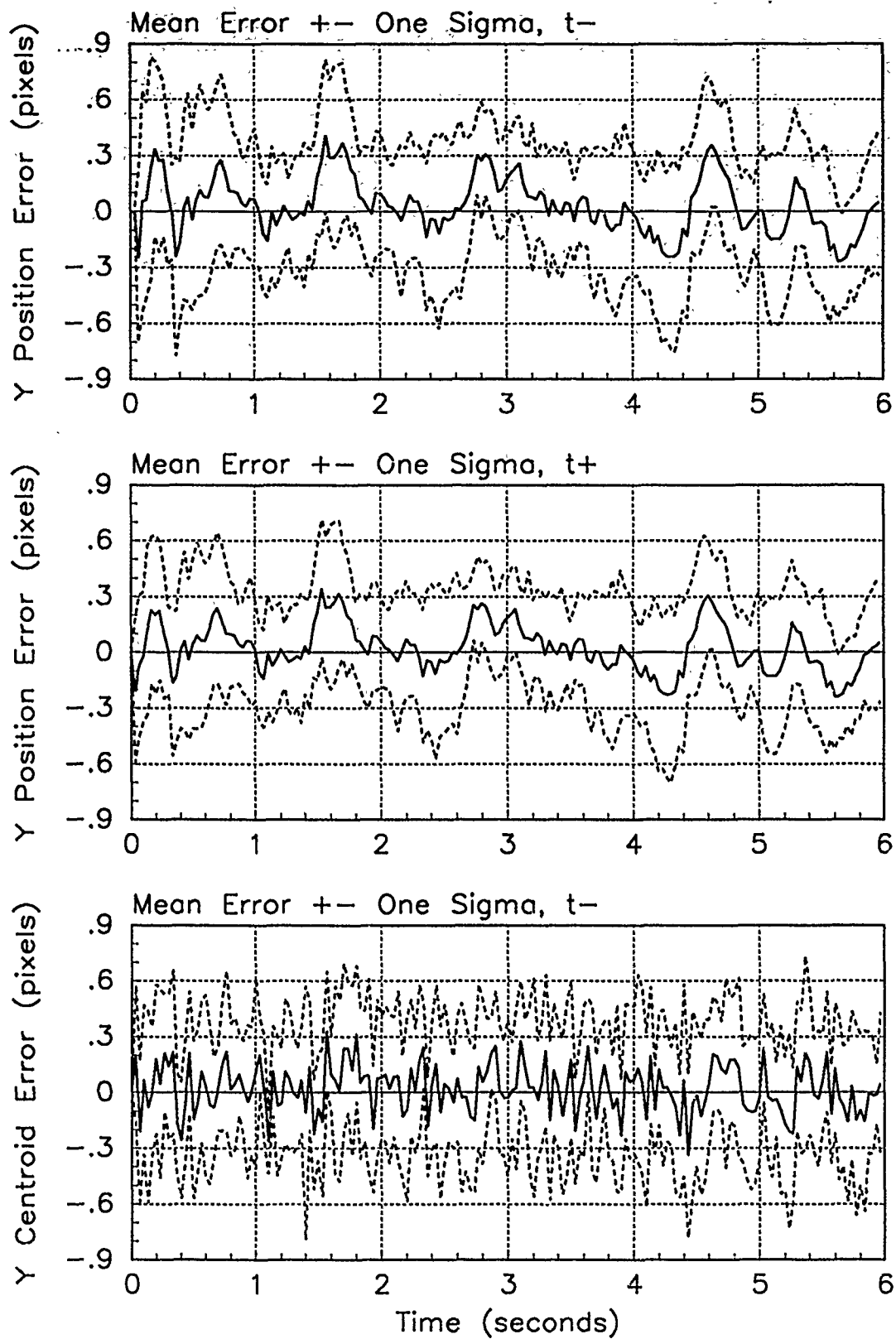


Figure D.15. Y-Error Plots; Notch MMAE-1R; PC is 1; Trajectory with $\omega = .62$

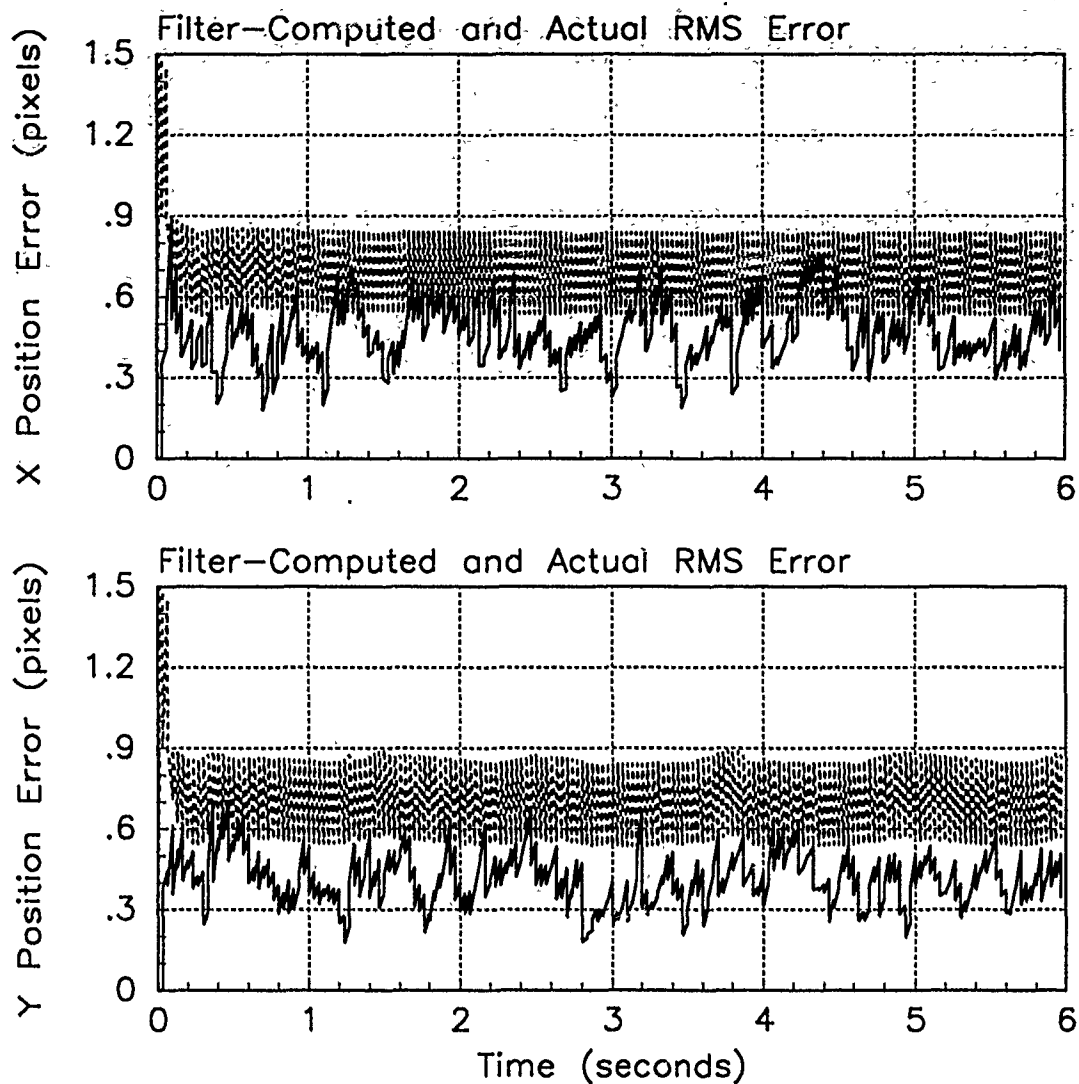


Figure D.16. RMS Error Plots; Notch MMAE-1R; PC is 1; Trajectory with $\omega = 2.8$

Table D.6. Temporal Averages and Residuals; Notch MMAE-1R; PC is 1; Trajectory with $\omega = 2.8$.

Error in:	Mean	σ
$p_x(t_i^-)$	-0.099560	0.50994
$p_x(t_i^+)$	-0.063166	0.42876
$y_x(t_i^-)$	-0.064370	0.41940
$p_y(t_i^-)$	0.061973	0.44972
$p_y(t_i^+)$	0.023998	0.37022
$y_y(t_i^-)$	0.042546	0.40173

Filter	$\mathbf{r}_k^T \mathbf{r}_k$	$\mathbf{r}_k^T \mathbf{A}_k^{-1} \mathbf{r}_k$
Benign	2.19094	12.78353
Intermediate	2.72419	16.09295
Harsh	0.40112	1.82285

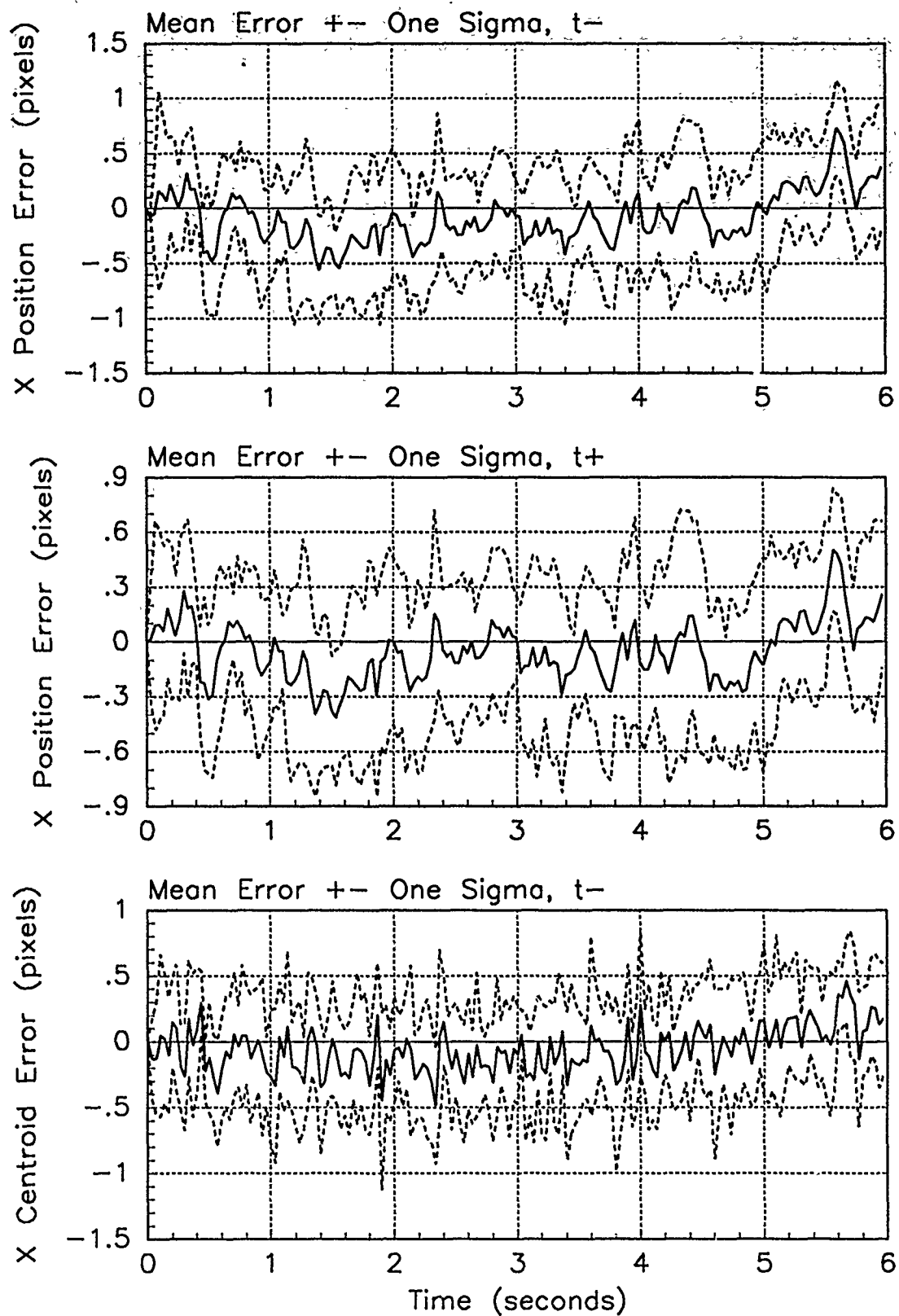


Figure D.17. X-Error Plots; Notch MMAE 1R; PC is 1; Trajectory with $\omega = 2.8$

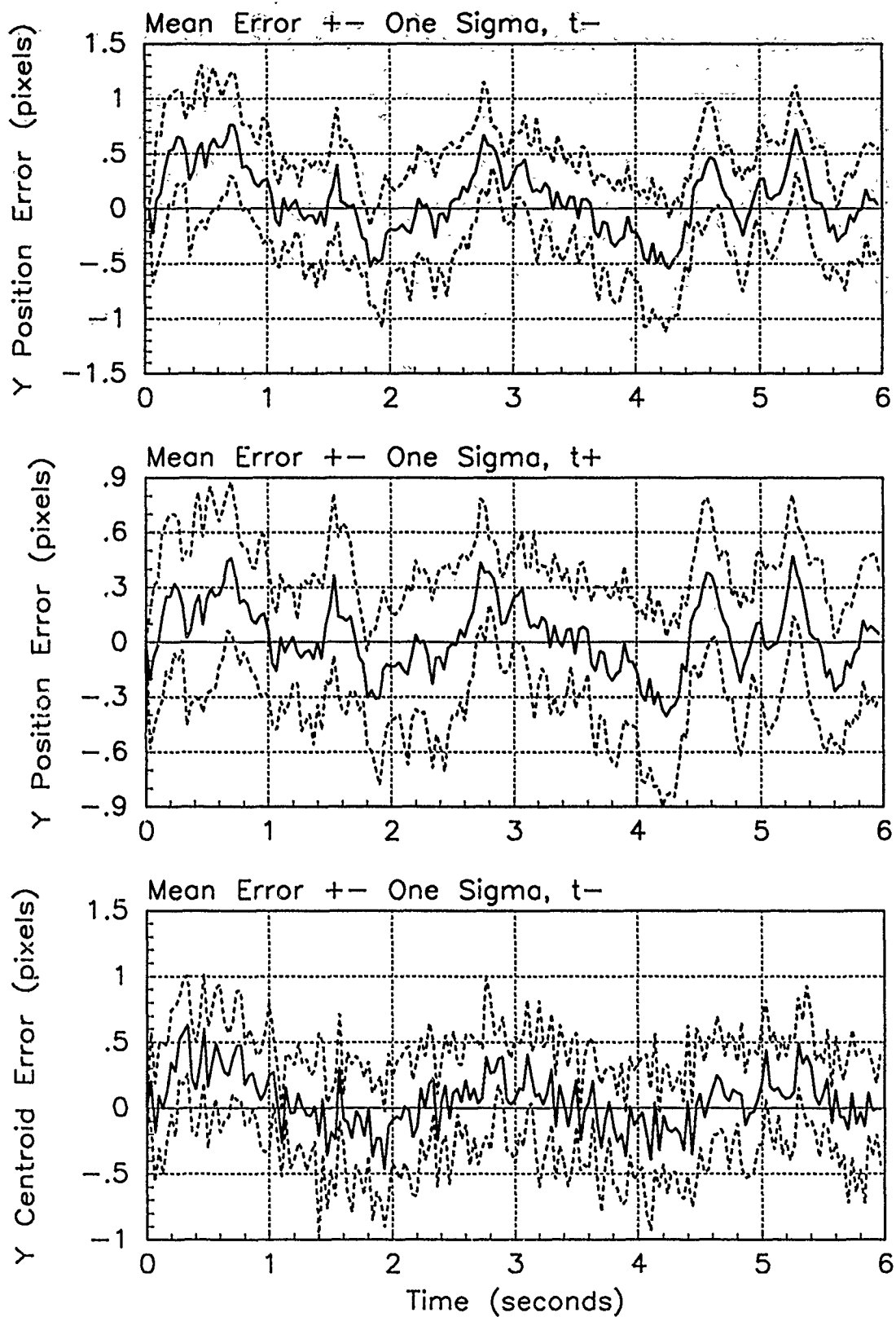


Figure D.18. Y-Error Plots; Notch MMAE-1R; PC is 1; Trajectory with $\omega = 2.8$

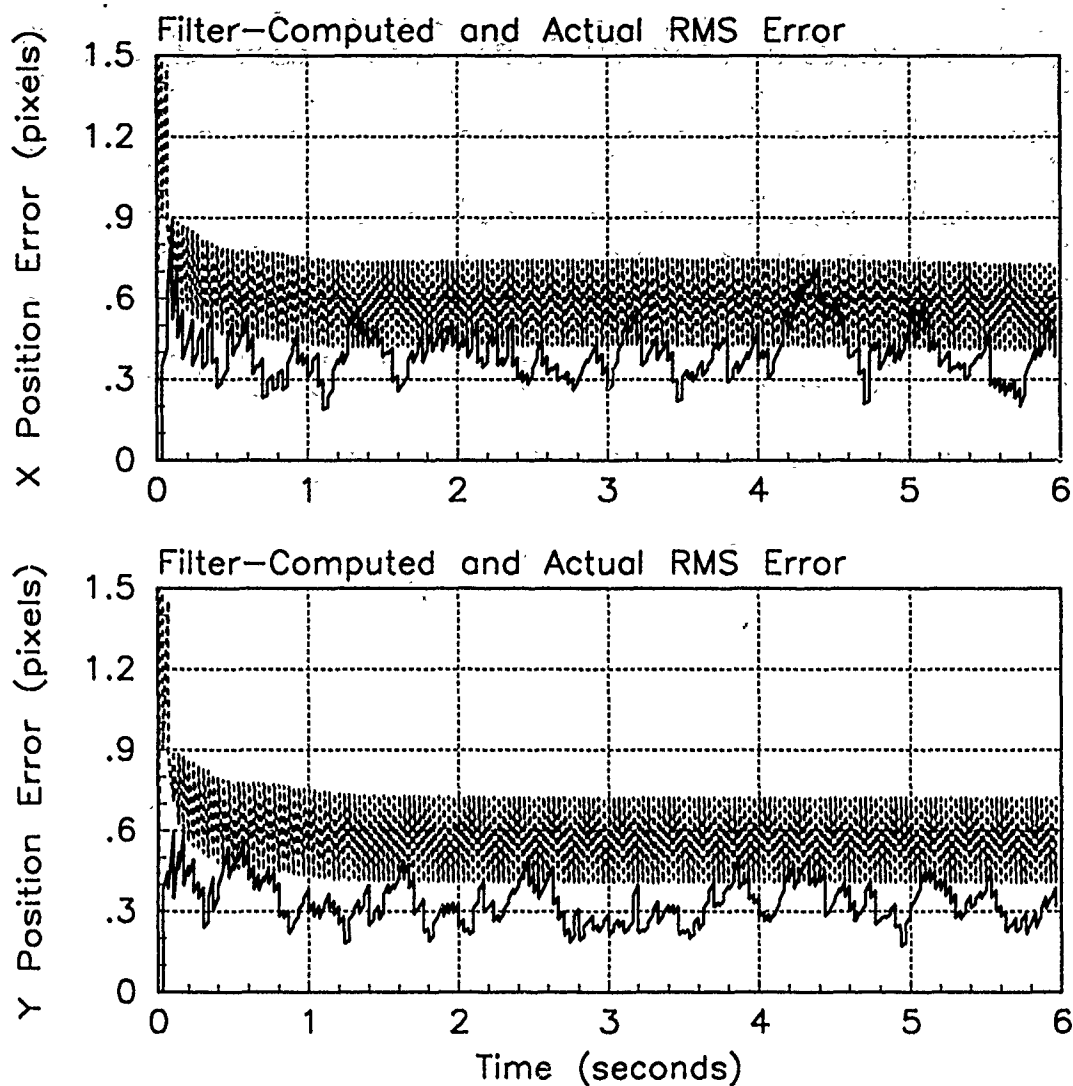


Figure D.19. RMS Error Plots; Notch MMAE-1R; PC is 2; Trajectory with $\omega = .01$

Table D.7. Temporal Averages and Residuals; Notch MMAE-1R; PC is 2; Trajectory with $\omega = .01$.

Error in:	Mean	σ
$p_x(t_i^-)$	0.11581	0.41398
$p_x(t_i^+)$	0.088775	0.37784
$y_x(t_i^-)$	0.077106	0.38203
$p_y(t_i^-)$	-0.0030749	0.34571
$p_y(t_i^+)$	-0.0019485	0.31354
$y_y(t_i^-)$	0.0022142	0.36685

Filter	$r_k^T r_k$	$r_k^T A_k^{-1} r_k$
Benign	0.31419	1.85222
Intermediate	0.30907	1.80760
Harsh	0.38000	1.73004

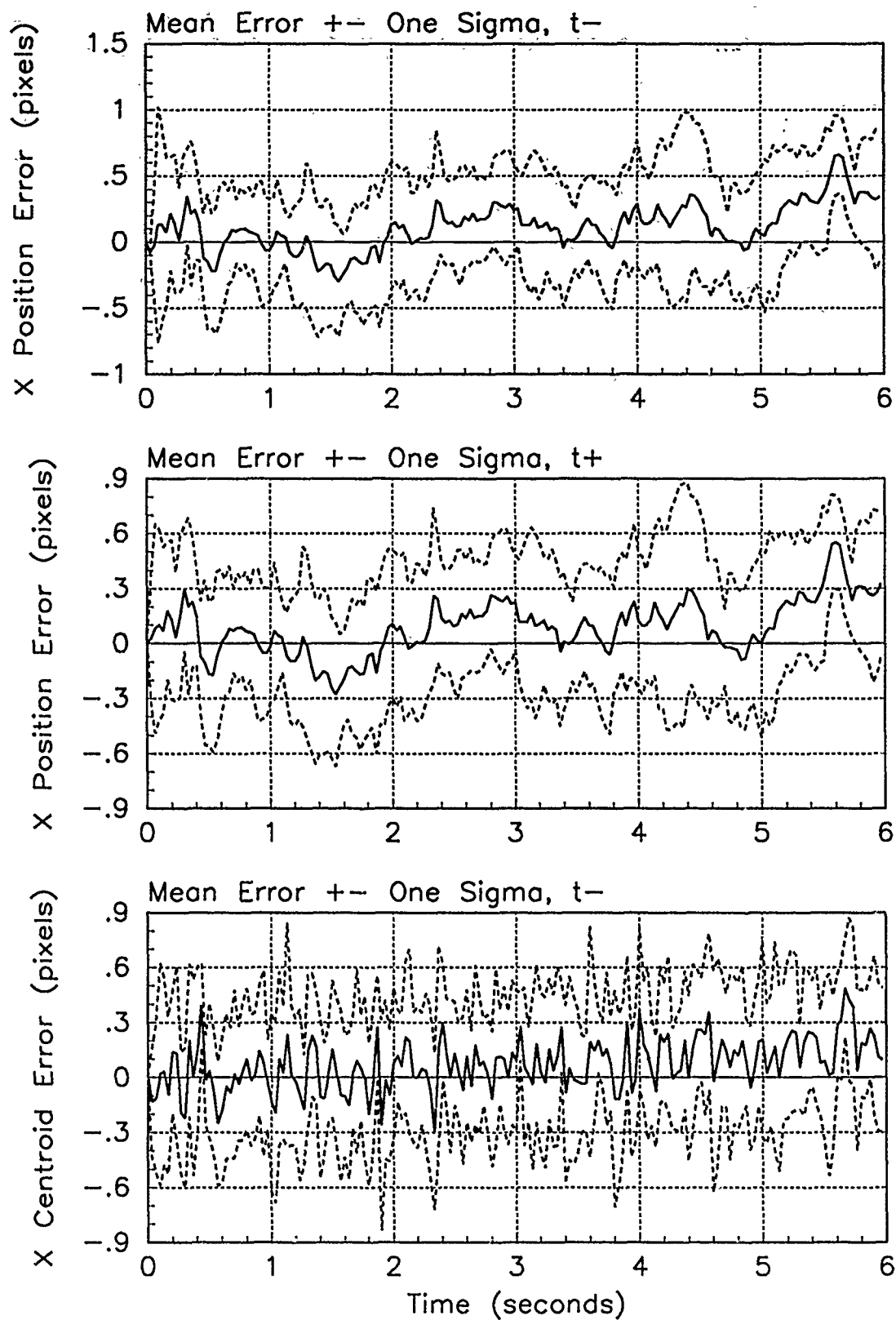


Figure D.20. X-Error Plots; Notch MMAE-1R; PC is 2; Trajectory with $\omega = .01$

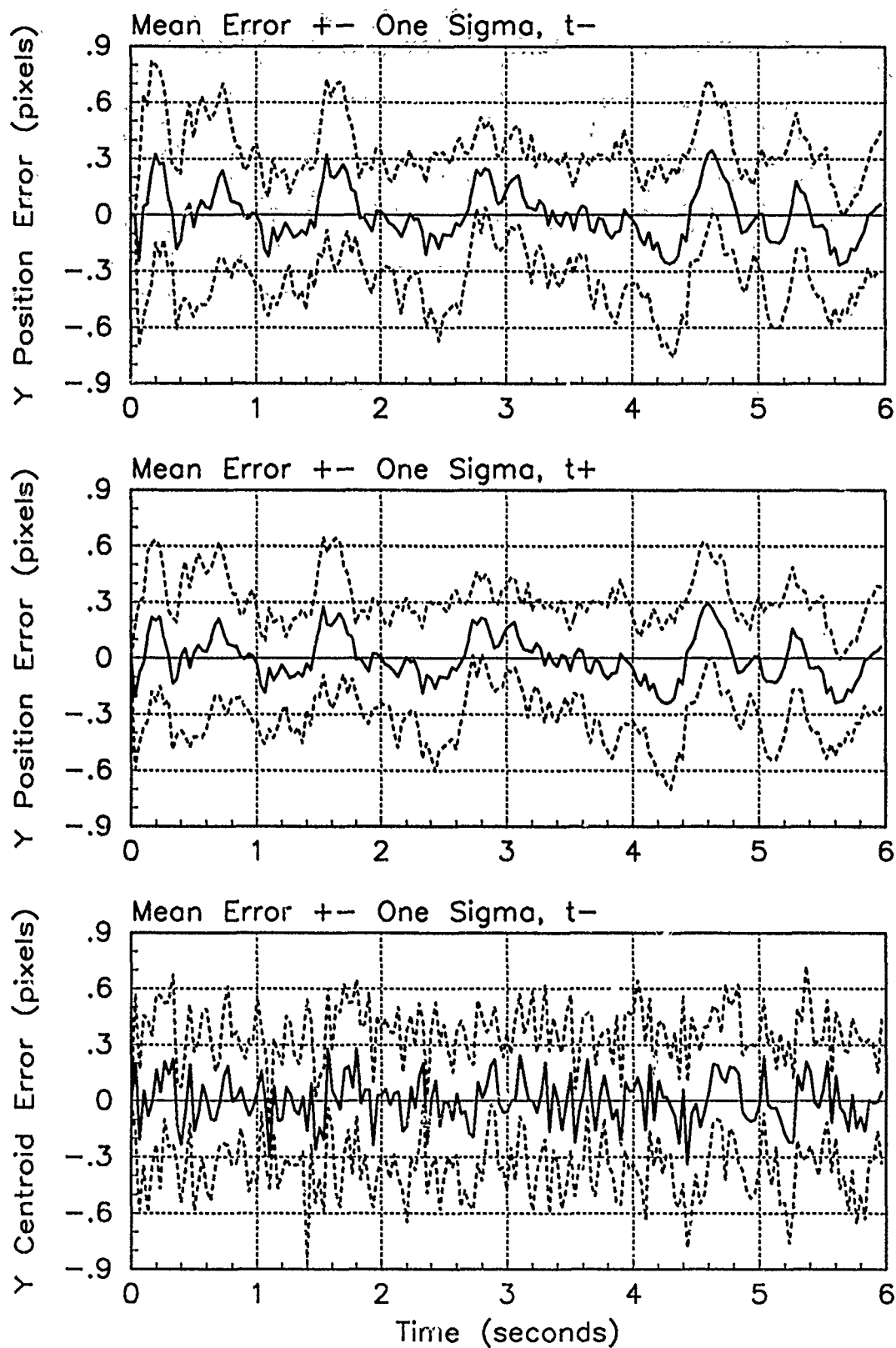


Figure D.21. Y-Error Plots; Notch MMAE-1R; PC is 2; Trajectory with $\omega = .01$

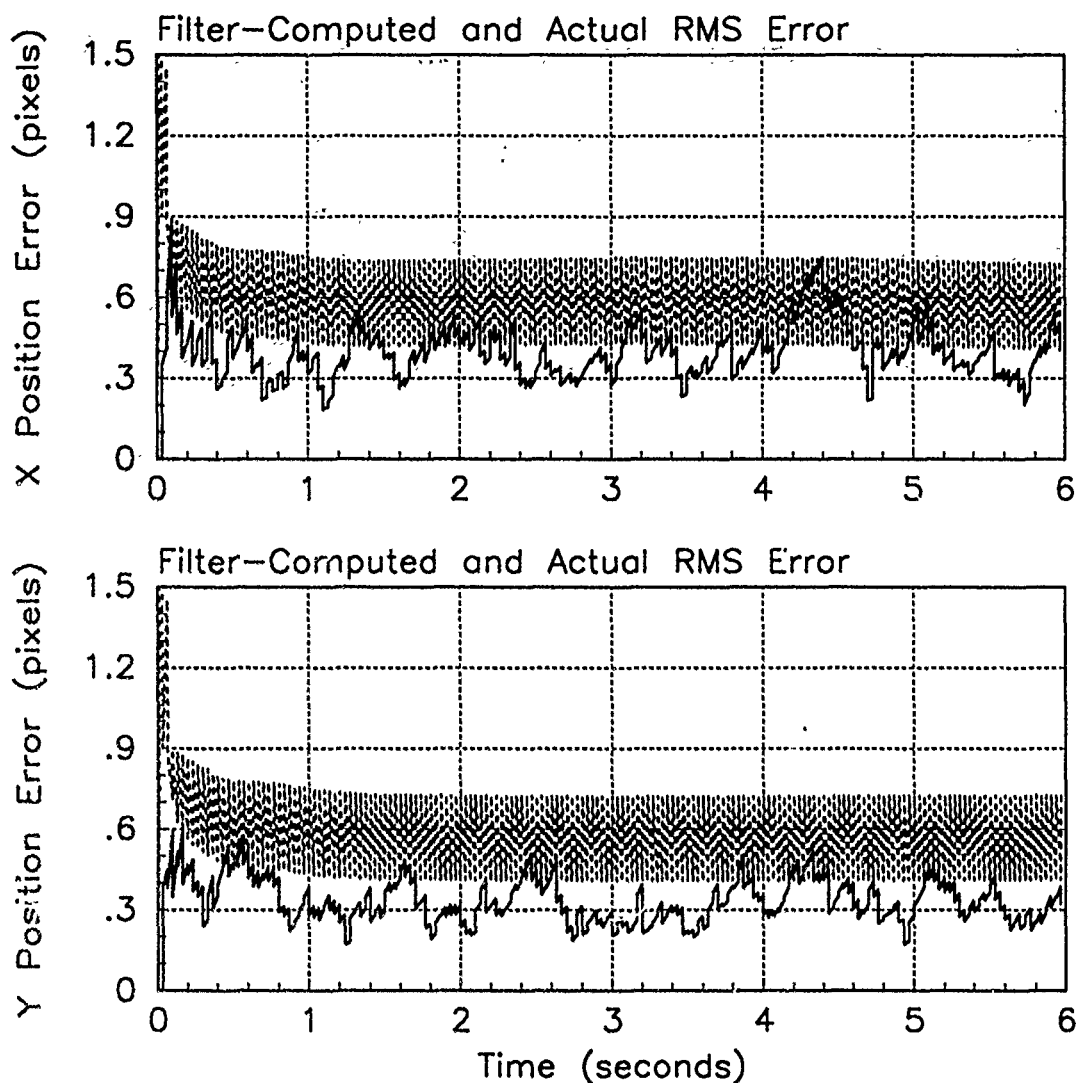


Figure D.22. RMS Error Plots; Notch MMAE-1R; PC is 2; Trajectory with $\omega = .62$

Table D.8. Temporal Averages and Residuals; Notch MMAE-1R; PC is 2; Trajectory with $\omega = .62$.

Error in:	Mean	σ
$p_x(t_i^-)$	0.11523	0.41719
$p_x(t_i^+)$	0.88291	0.38139
$y_x(t_i^-)$	0.076764	0.38411
$p_y(t_i^-)$	0.014898	0.34589
$p_y(t_i^+)$	0.011082	0.31380
$y_y(t_i^-)$	0.011787	0.36650

Filter	$\mathbf{r}_k^T \mathbf{r}_k$	$\mathbf{r}_k^T \mathbf{A}_k^{-1} \mathbf{r}_k$
Benign	0.31542	1.85918
Intermediate	0.30953	1.80396
Harsh	0.38552	1.75528

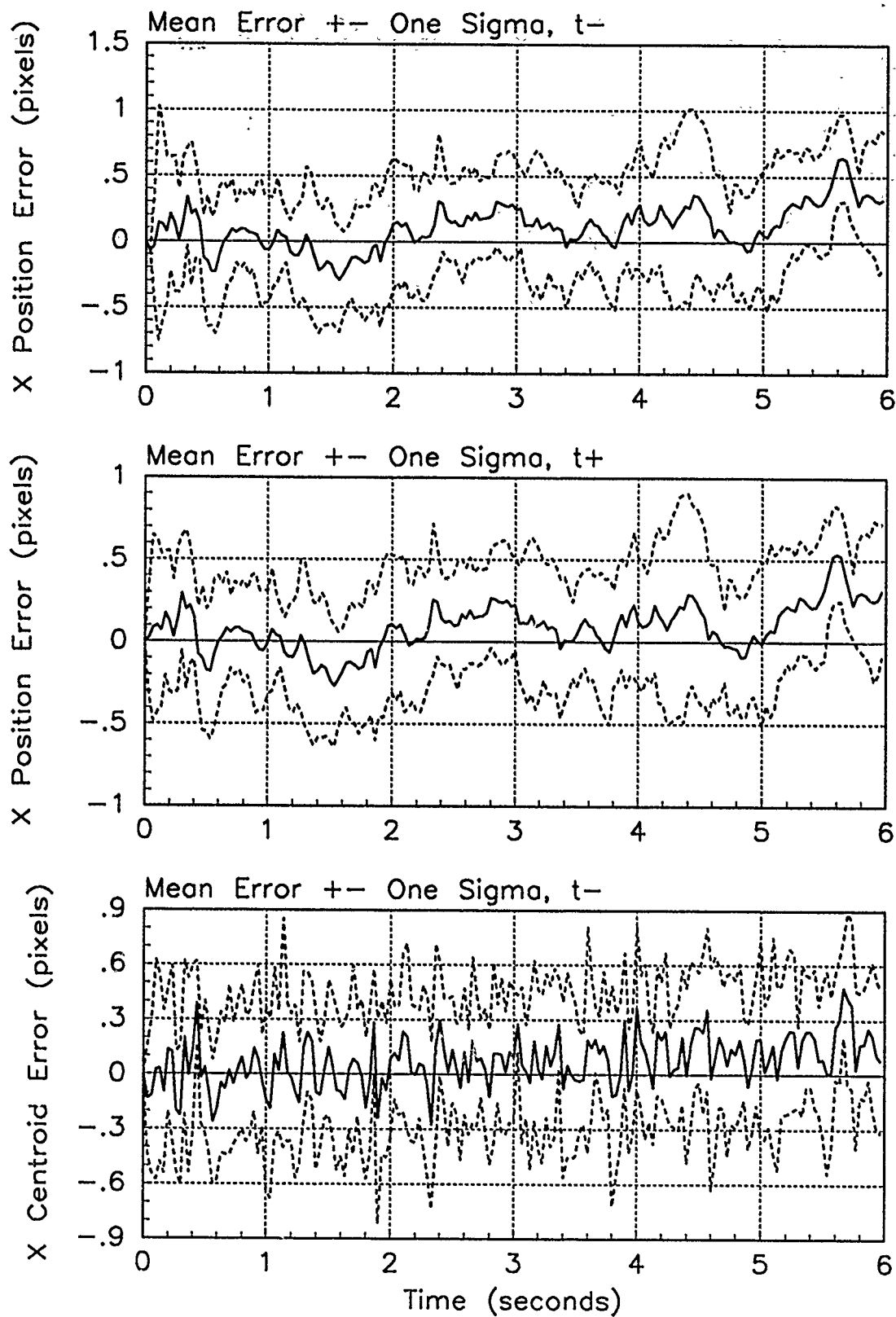


Figure D.23. X-Error Plots; Notch MMAE-1R; PC is 2; Trajectory with $\omega = .62$

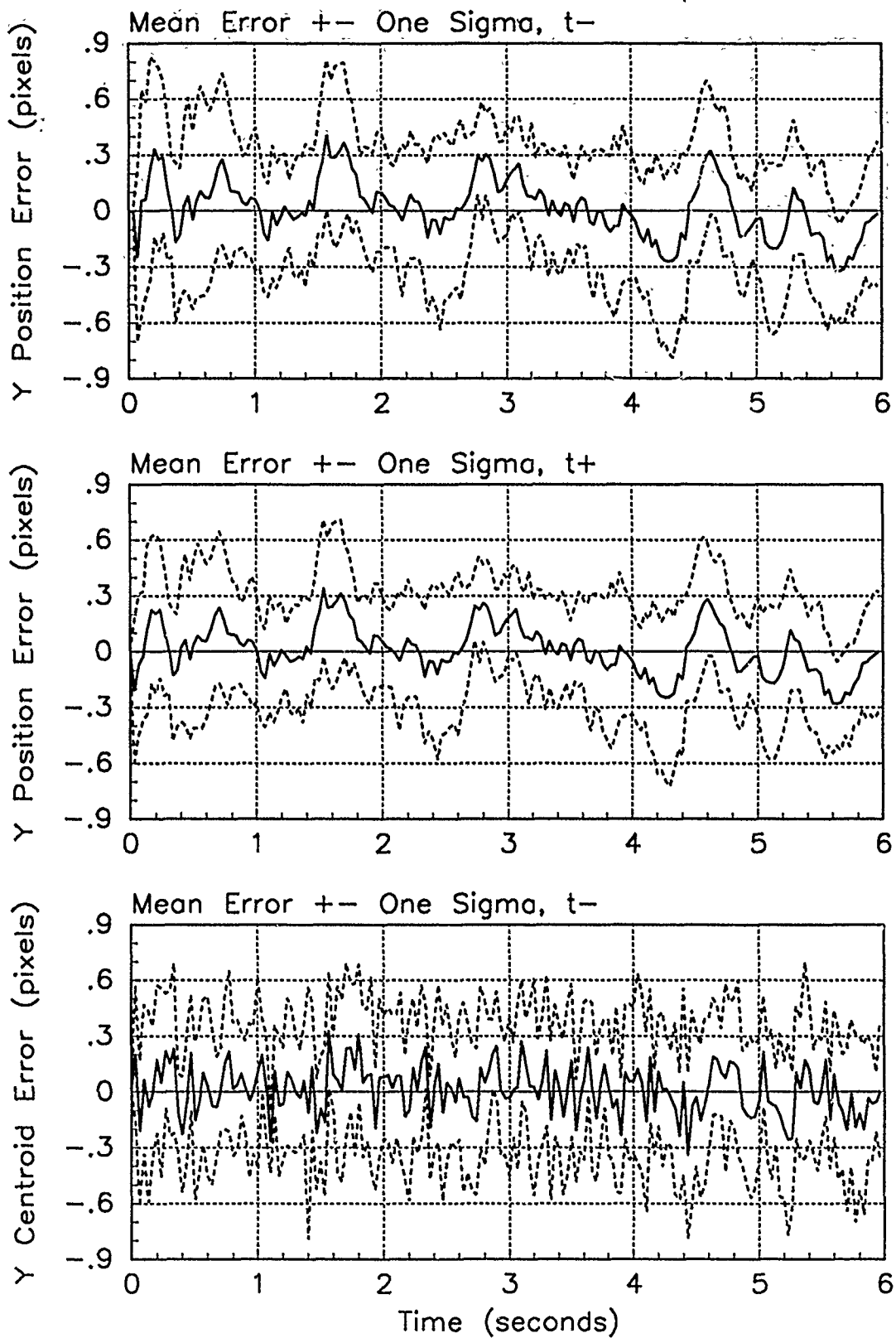


Figure D.24. Y-Error Plots; Notch MMAE-1R; PC is 2; Trajectory with $\omega = .62$

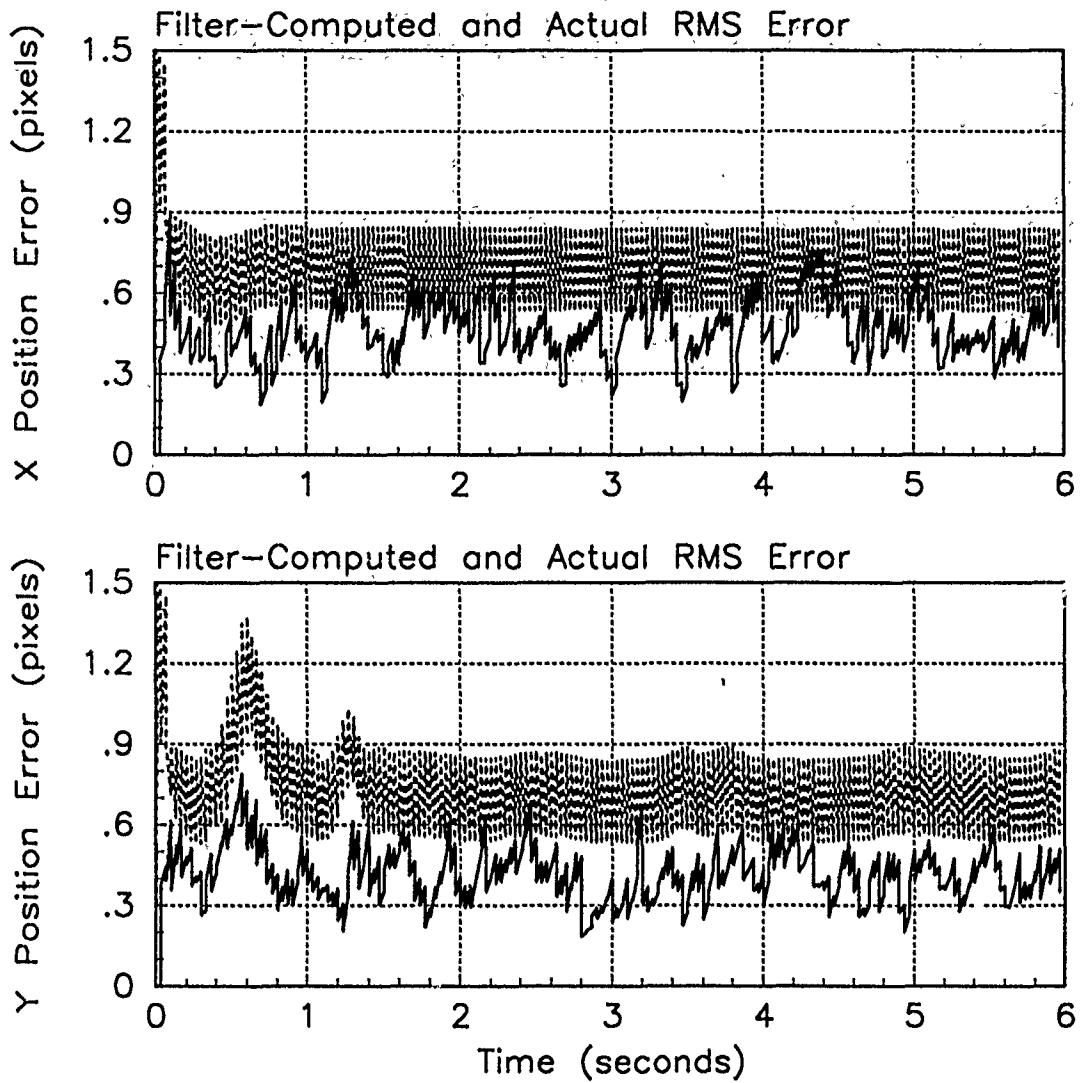


Figure D.25. RMS Error Plots; Notch MMAE-1R; PC is 2; Trajectory with $\omega = 2.8$

Table D.9. Temporal Averages and Residuals; Notch MMAE-1R; PC is 2; Trajectory with $\omega = 2.8$.

Error in:	Mean	σ
$p_x(t_i^-)$	-0.081160	0.50749
$p_x(t_i^+)$	-0.047907	0.42873
$y_x(t_i^-)$	-0.047496	0.41749
$p_y(t_i^-)$	0.10597	0.45741
$p_y(t_i^+)$	0.055791	0.37485
$y_y(t_i^-)$	0.071927	0.40658

Filter	$\mathbf{r}_k^T \mathbf{r}_k$	$\mathbf{r}_k^T \mathbf{A}_k^{-1} \mathbf{r}_k$
Benign	2.22412	12.97866
Intermediate	2.70873	16.00030
Harsh	0.40205	1.82690

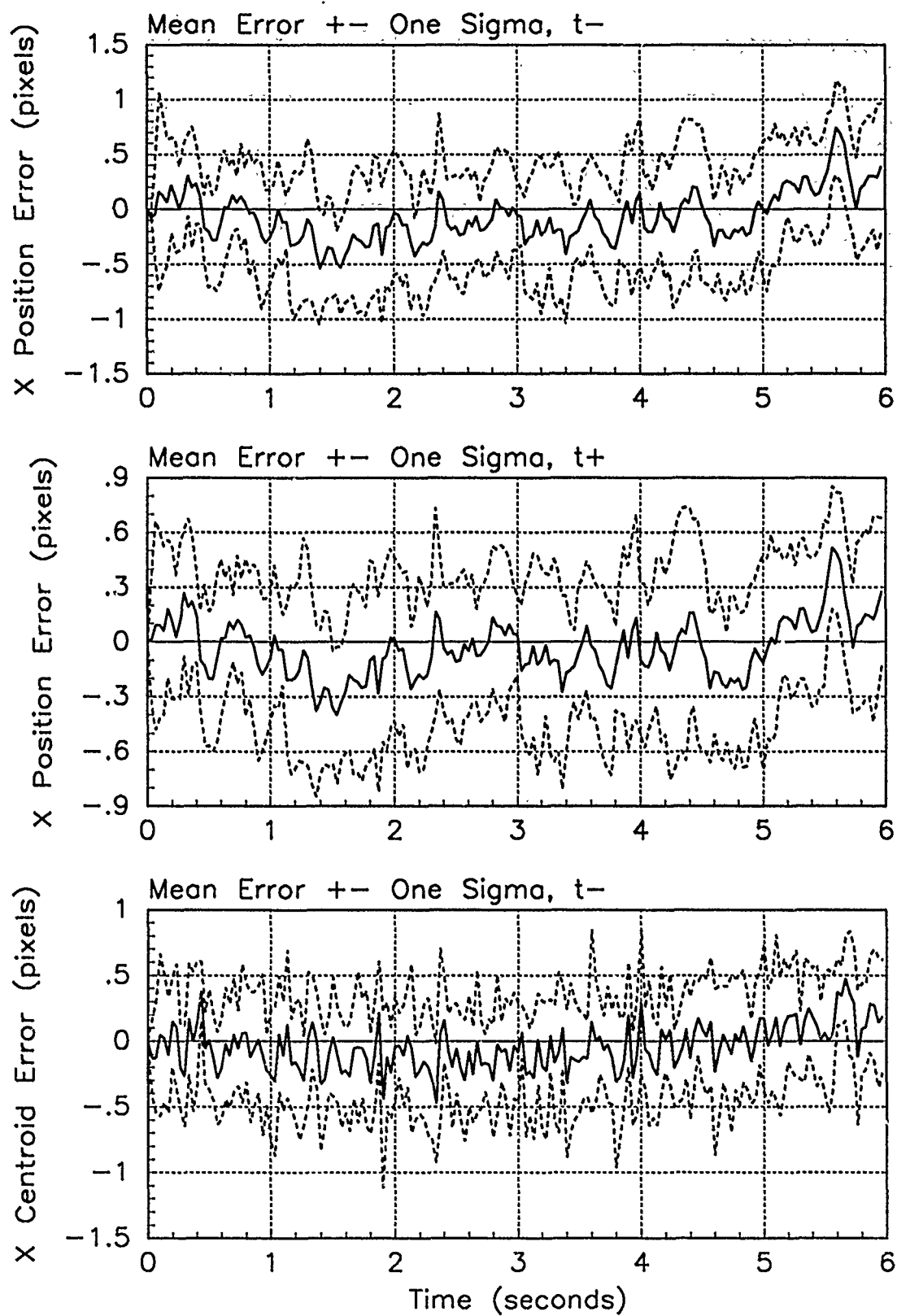


Figure D.26. X-Error Plots; Notch MMAE-1R; PC is 2; Trajectory with $\omega = 2.8$

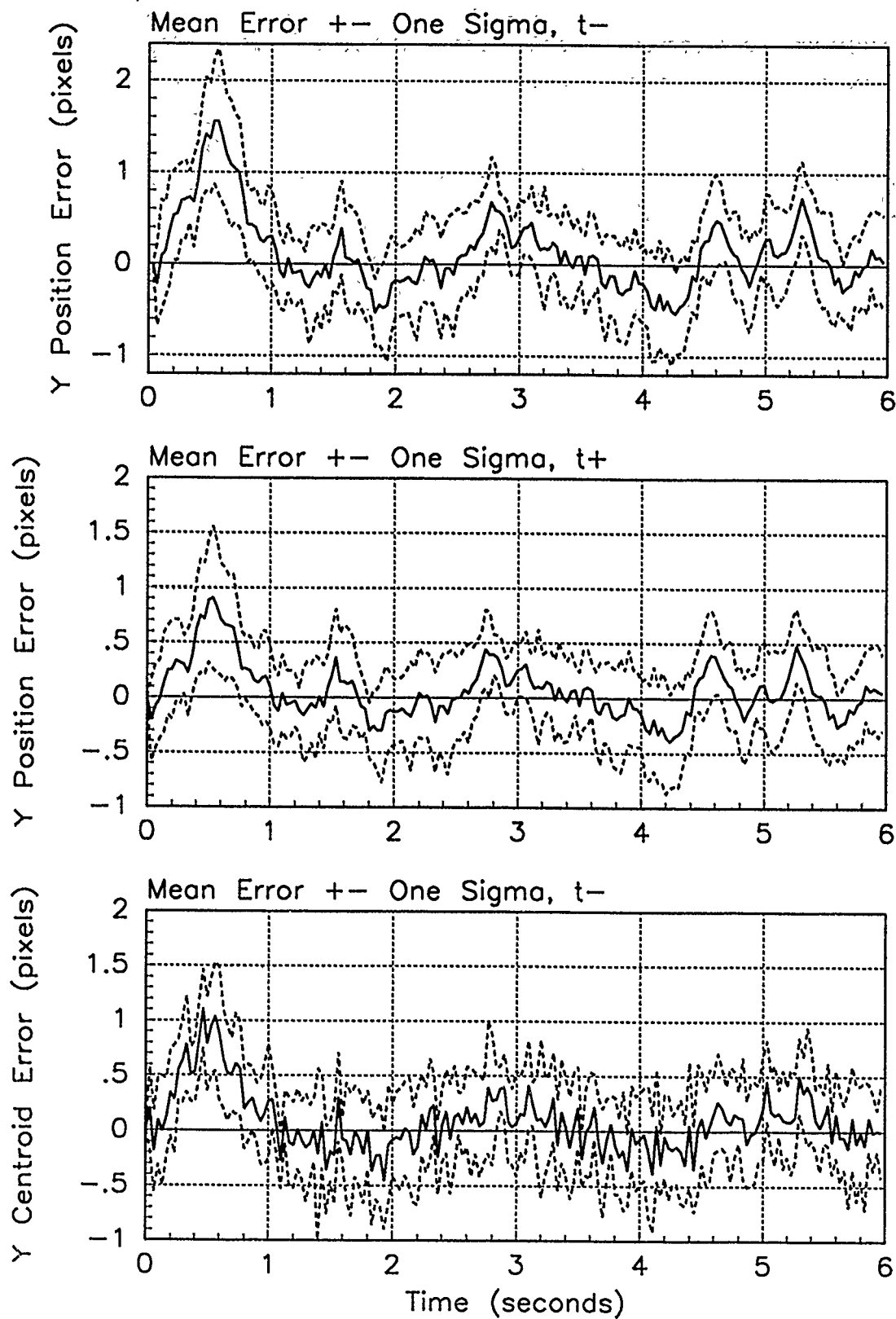


Figure D.27. Y-Error Plots; Notch MMAE-1R; PC is 2; Trajectory with $\omega = 2.8$

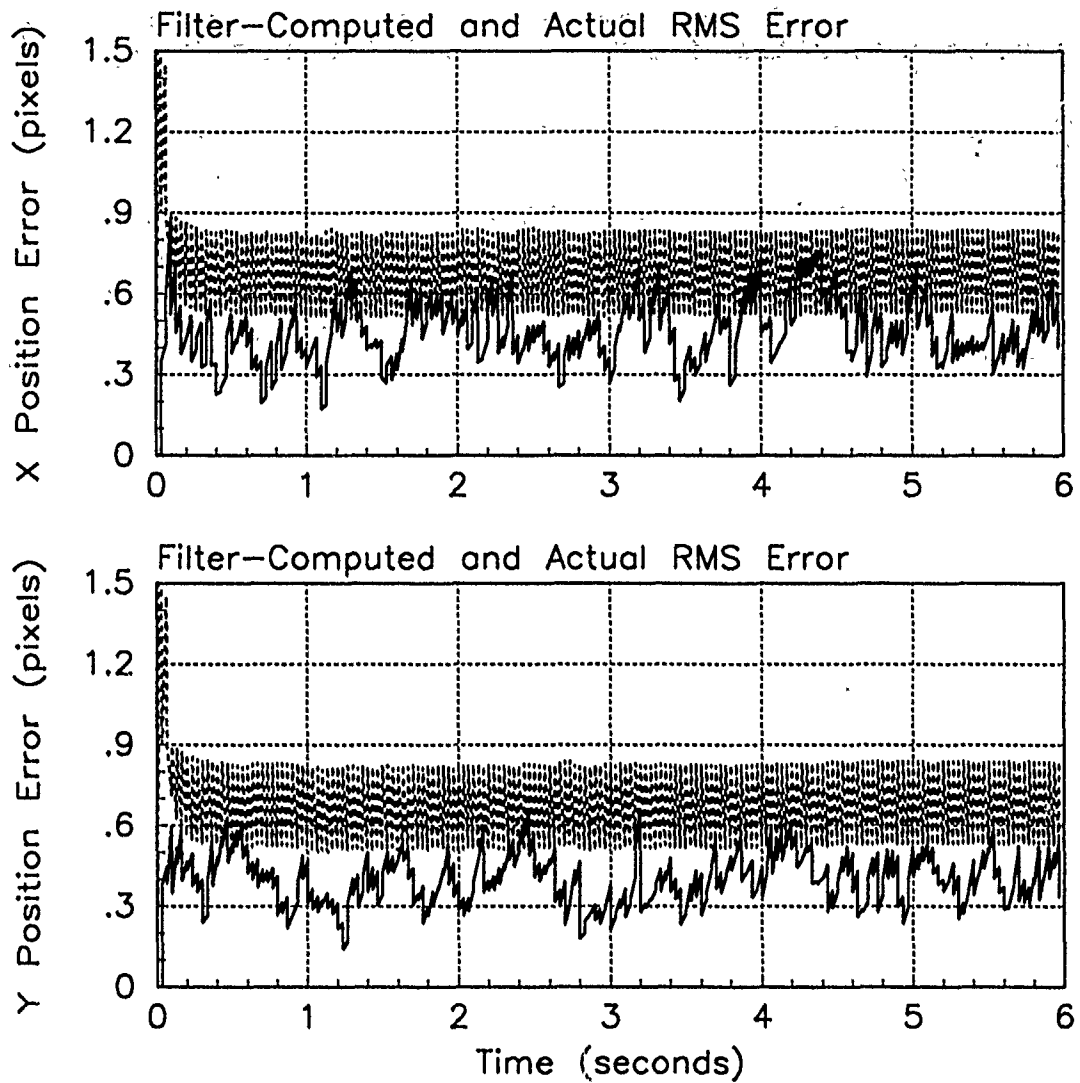


Figure D.28. RMS Error Plots; Notch MMAE-1R; PC is 3; Trajectory with $\omega = .01$

Table D.10. Temporal Averages and Residuals; Notch MMAE-1R; PC is 3; Trajectory with $\omega = .01$.

Error in:	Mean	σ
$p_x(t_i^-)$	-0.050487	0.49598
$p_x(t_i^+)$	-0.027731	0.42257
$y_x(t_i^-)$	-0.023628	0.41439
$p_y(t_i^-)$	-0.0038789	0.43262
$p_y(t_i^+)$	-0.0065926	0.36371
$y_y(t_i^-)$	-0.0013384	0.39367

Filter	$\mathbf{r}_k^T \mathbf{r}_k$	$\mathbf{r}_k^T \mathbf{A}_k^{-1} \mathbf{r}_k$
Benign	0.31079	1.83162
Intermediate	0.30487	1.78230
Harsh	0.37680	1.71529

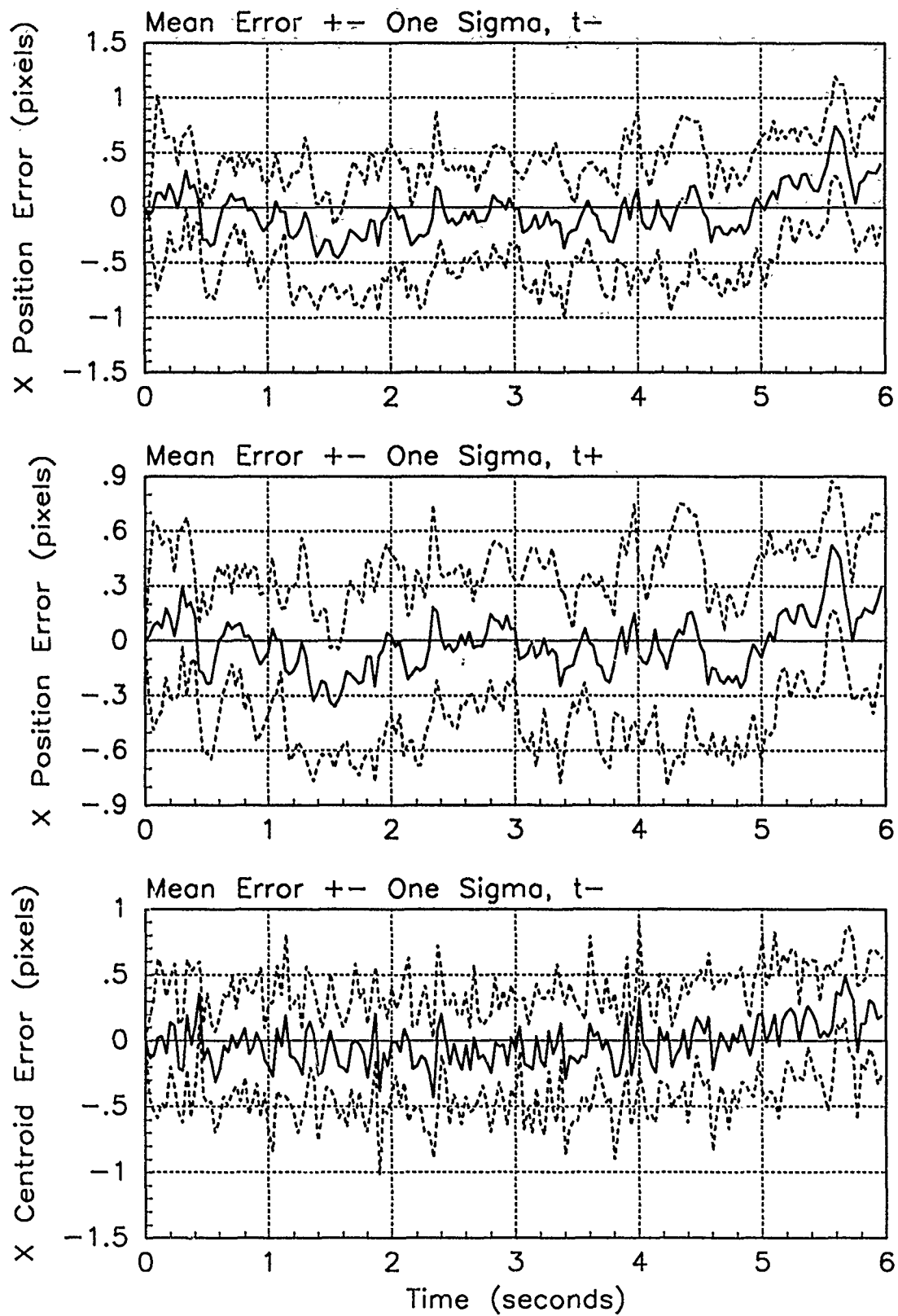


Figure D.29. X-Error Plots; Notch MMAE-1R; PC is 3; Trajectory with $\omega = .01$

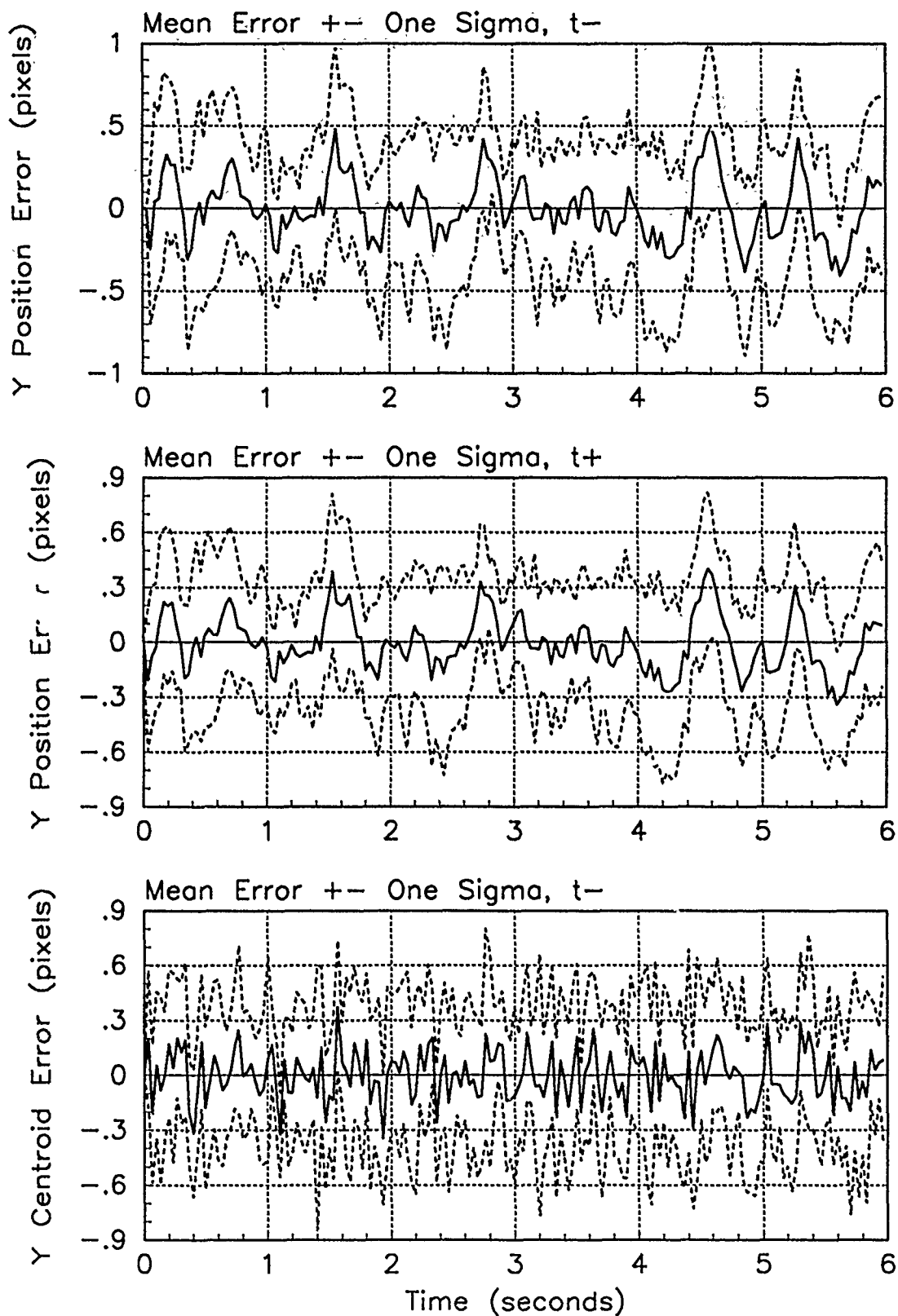


Figure D.30. Y-Error Plots; Notch MMAE-1R; PC is 3; Trajectory with $\omega = .01$

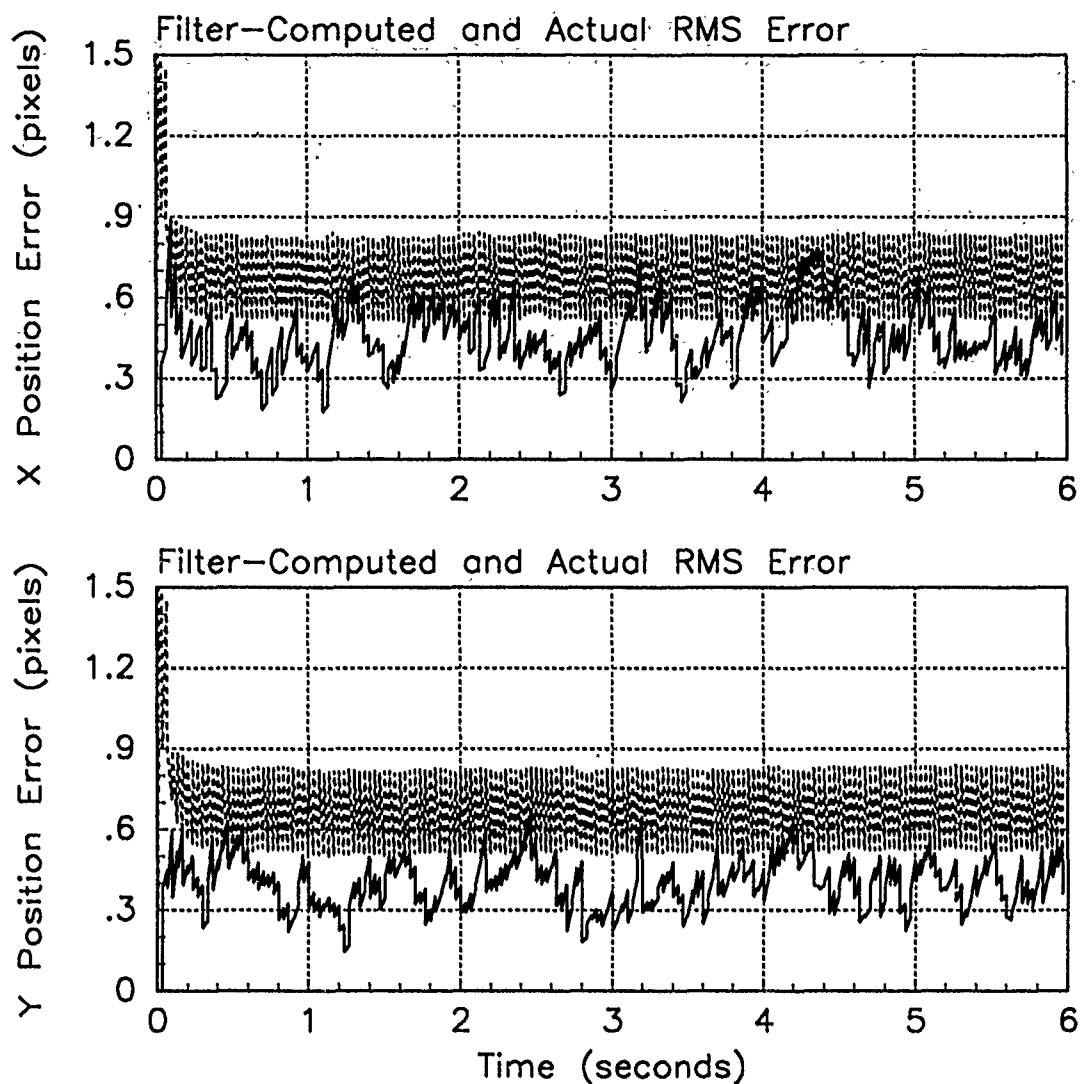


Figure D.31. RMS Error Plots; Notch MMAE-1R; PC is 3; Trajectory with $\omega = .62$

Table D.11. Temporal Averages and Residuals; Notch MMAE-1R; PC is 3; Trajectory with $\omega = .62$.

Error in:	Mean	σ
$p_x(t_i^-)$	-0.047181	0.49152
$p_x(t_i^+)$	-0.024761	0.42006
$y_x(t_i^-)$	-0.021591	0.41321
$p_y(t_i^-)$	0.082595	0.43193
$p_y(t_i^+)$	0.038382	0.36413
$y_y(t_i^-)$	0.056653	0.39264

Filter	$r_k^T r_k$	$r_k^T A_k^{-1} r_k$
Benign	0.31174	1.83688
Intermediate	0.30684	1.79374
Harsh	0.38349	1.74601

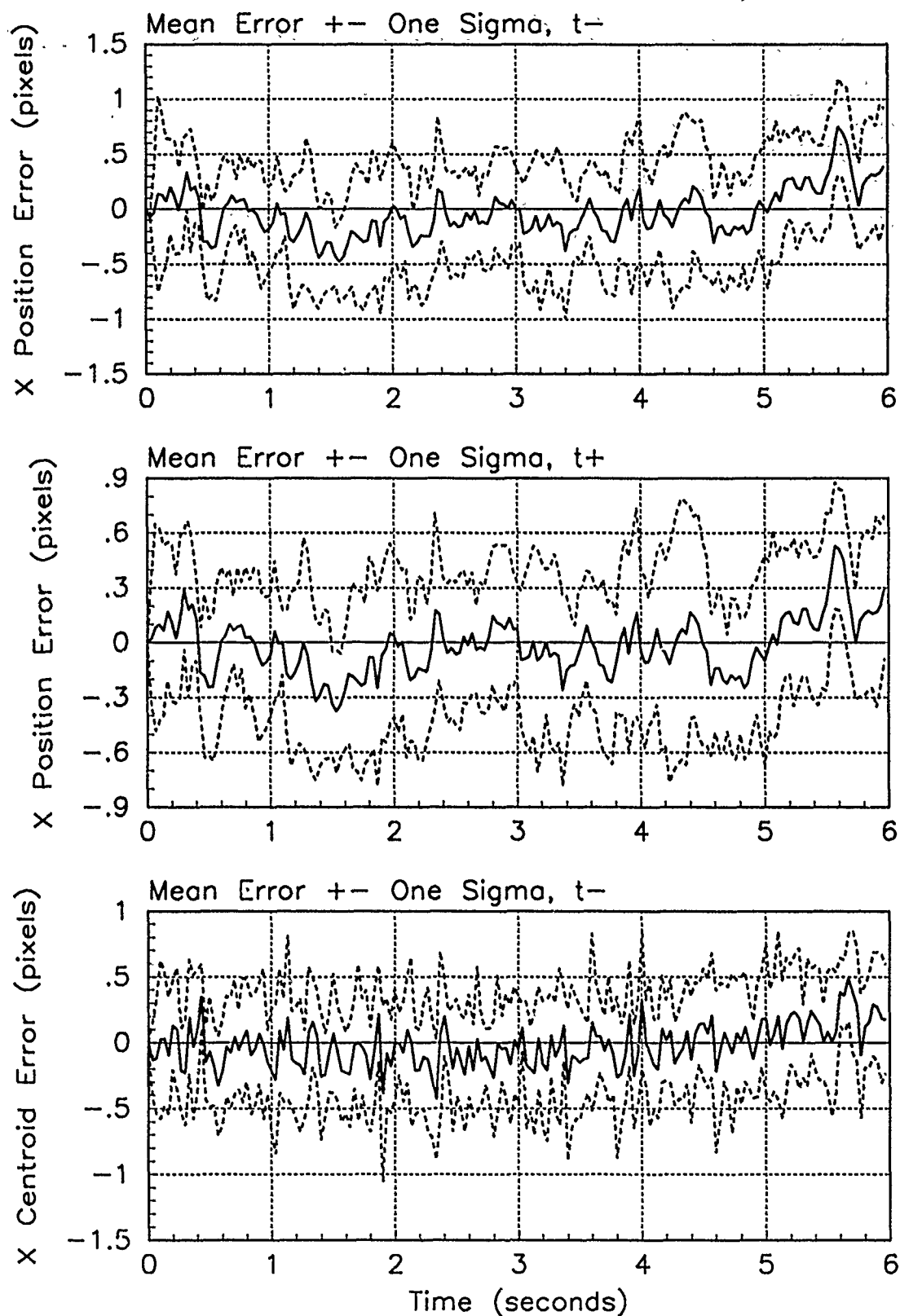


Figure D.32. X-Error Plots; Notch MMAE-1R; PC is 3; Trajectory with $\omega = .62$

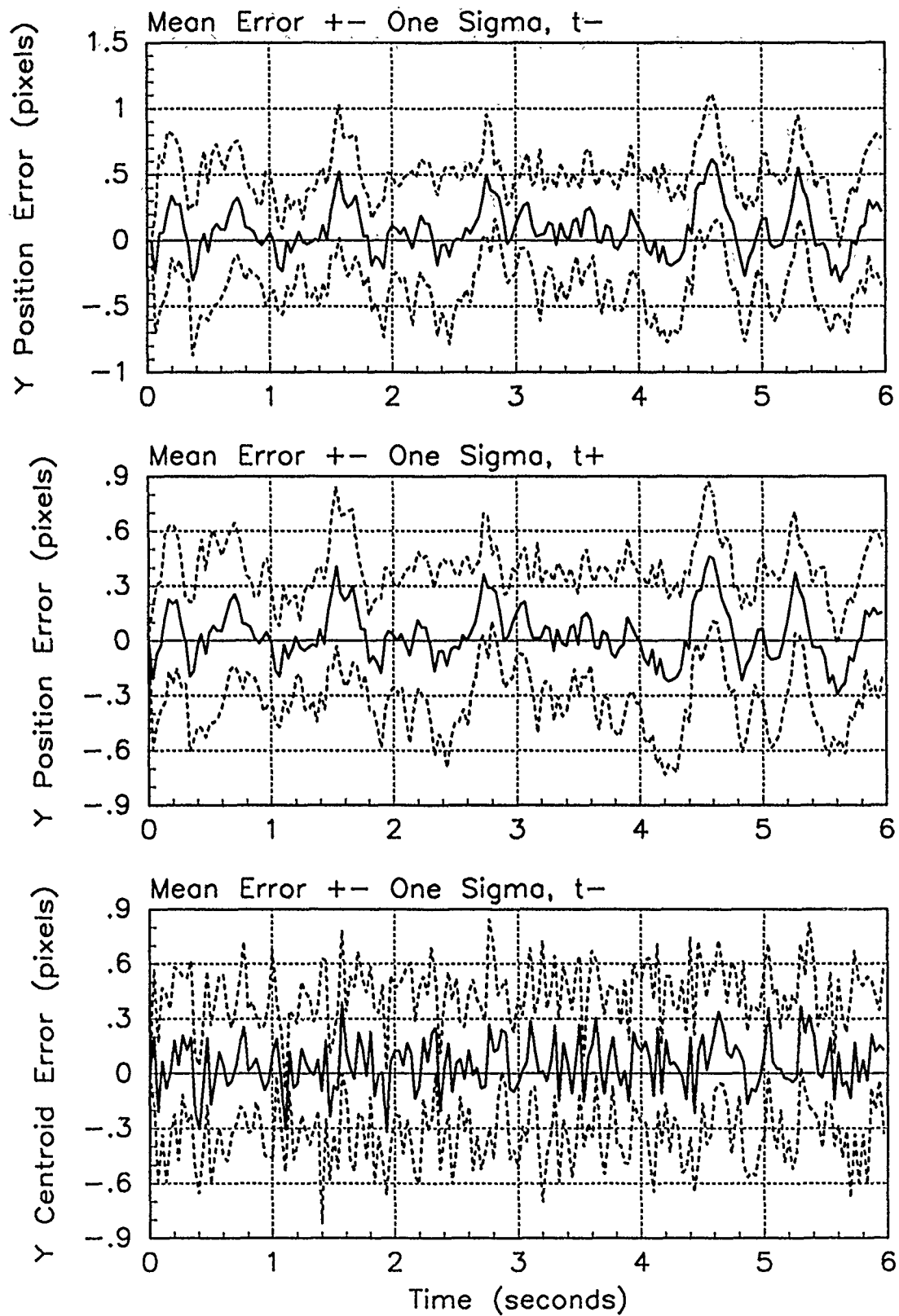


Figure D.33. Y-Error Plots; Notch MMAE-1R; PC is 3; Trajectory with $\omega = .62$

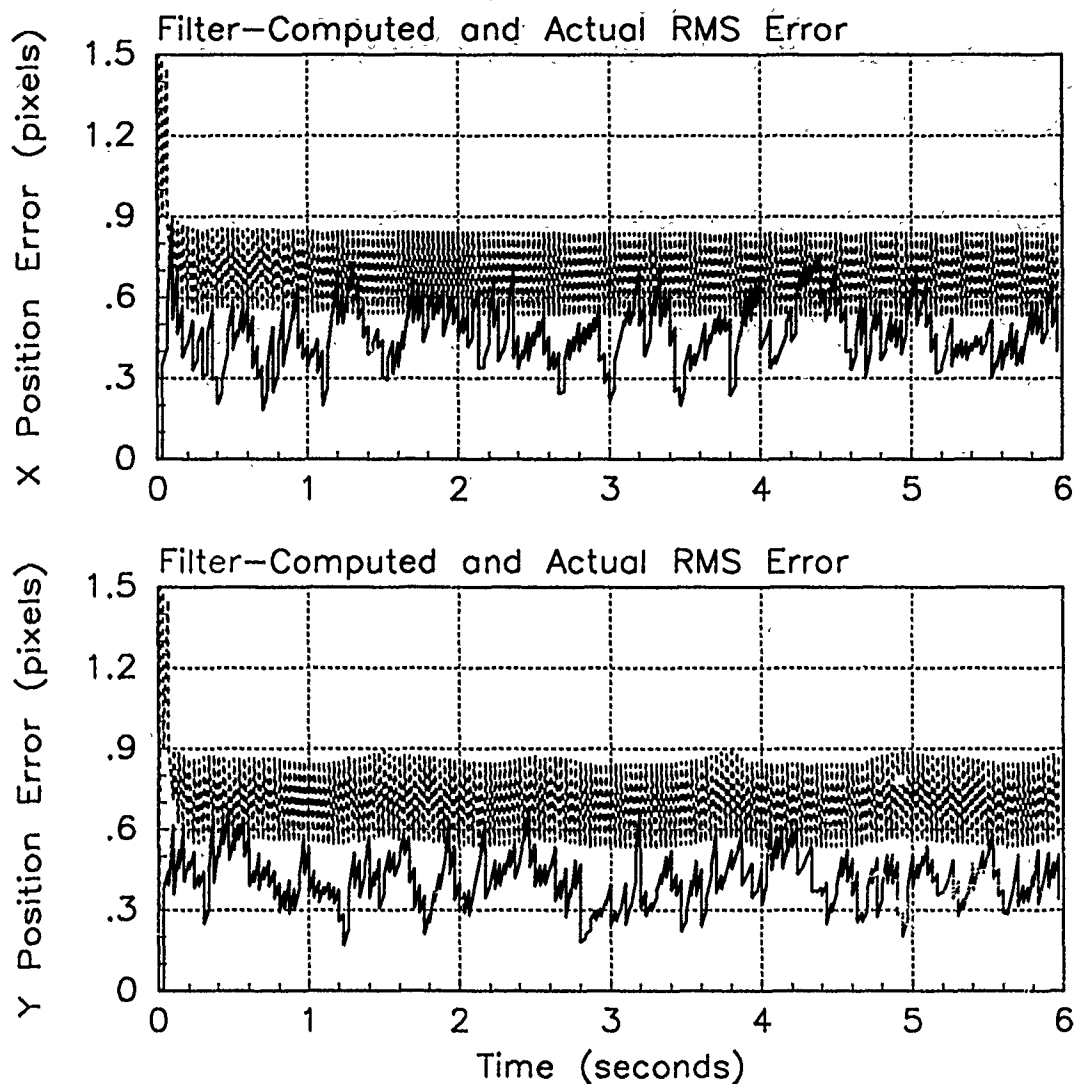


Figure D.34. RMS Error Plots; Notch MMAE-1R; PC is 3; Trajectory with $\omega = 2.8$

Table D.12. Temporal Averages and Residuals; Notch MMAE-1R; PC is 3; Trajectory with $\omega = 2.8$.

Error in:	Mean	σ
$p_x(t_i^-)$	-0.10336	0.50942
$p_x(t_i^+)$	-0.066899	0.42816
$y_x(t_i^-)$	-0.068122	0.41849
$p_y(t_i^-)$	0.060898	0.44930
$p_y(t_i^+)$	0.022934	0.37038
$y_y(t_i^-)$	0.041416	0.40205

Filter	$\mathbf{r}_k^T \mathbf{r}_k$	$\mathbf{r}_k^T \mathbf{A}_k^{-1} \mathbf{r}_k$
Benign	2.21391	12.91533
Intermediate	2.72299	16.08609
Harsh	0.40008	1.81825

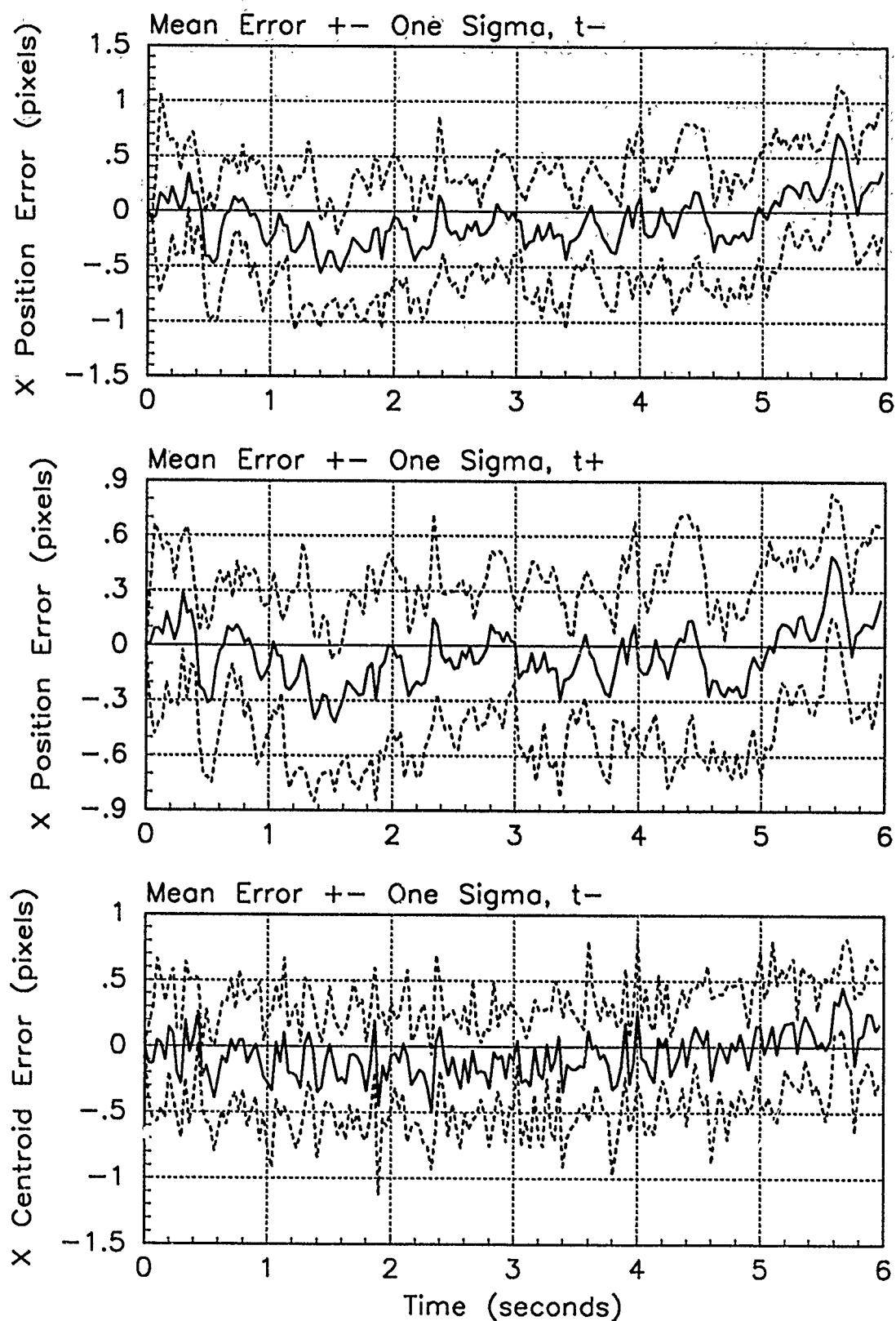


Figure D.35. X-Error Plots; Notch MMAE-1R; PC is 3; Trajectory with $\omega = 2.8$

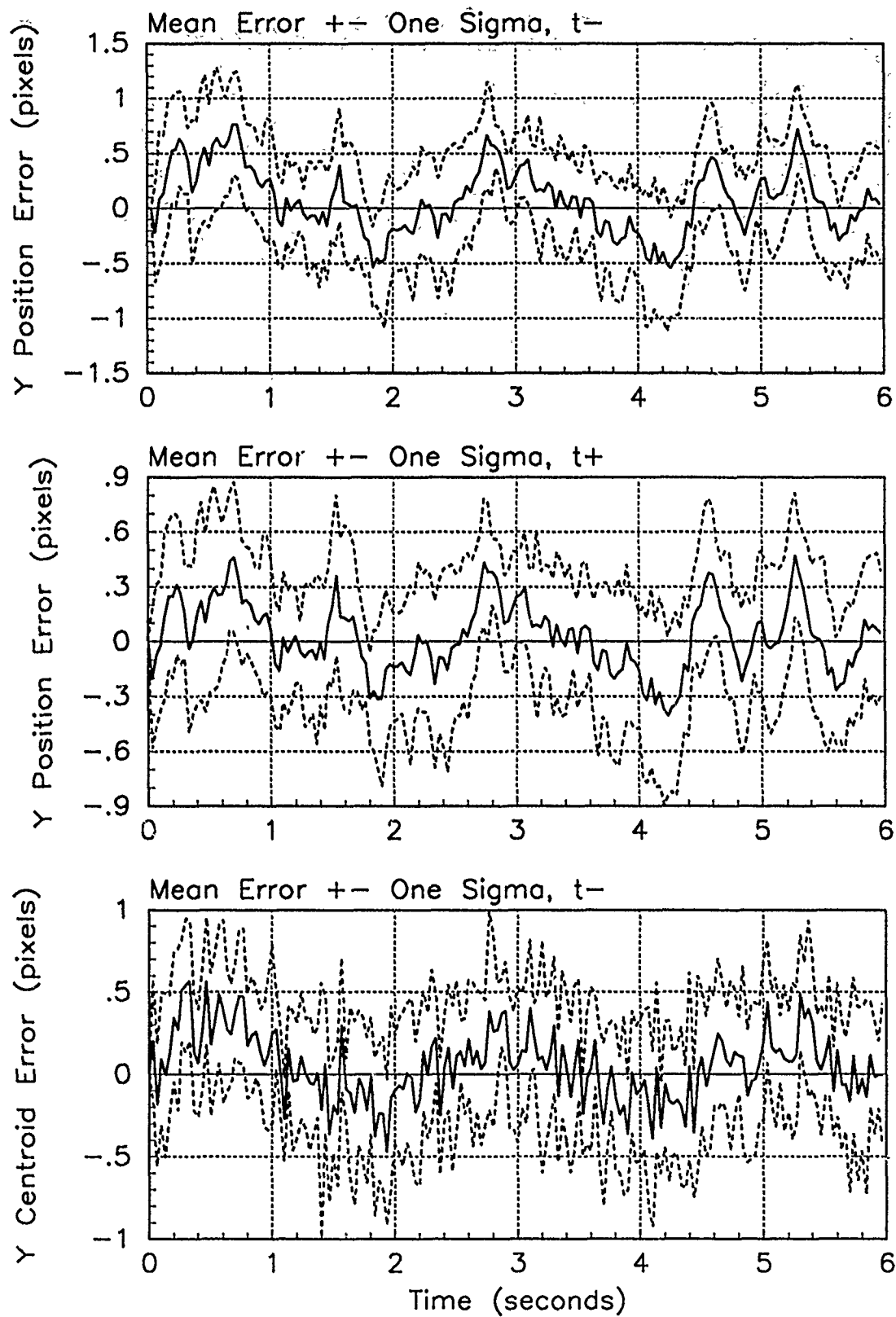


Figure D.36. Y-Error Plots; Notch MMAE-1R; PC is 3; Trajectory with $\omega = 2.8$

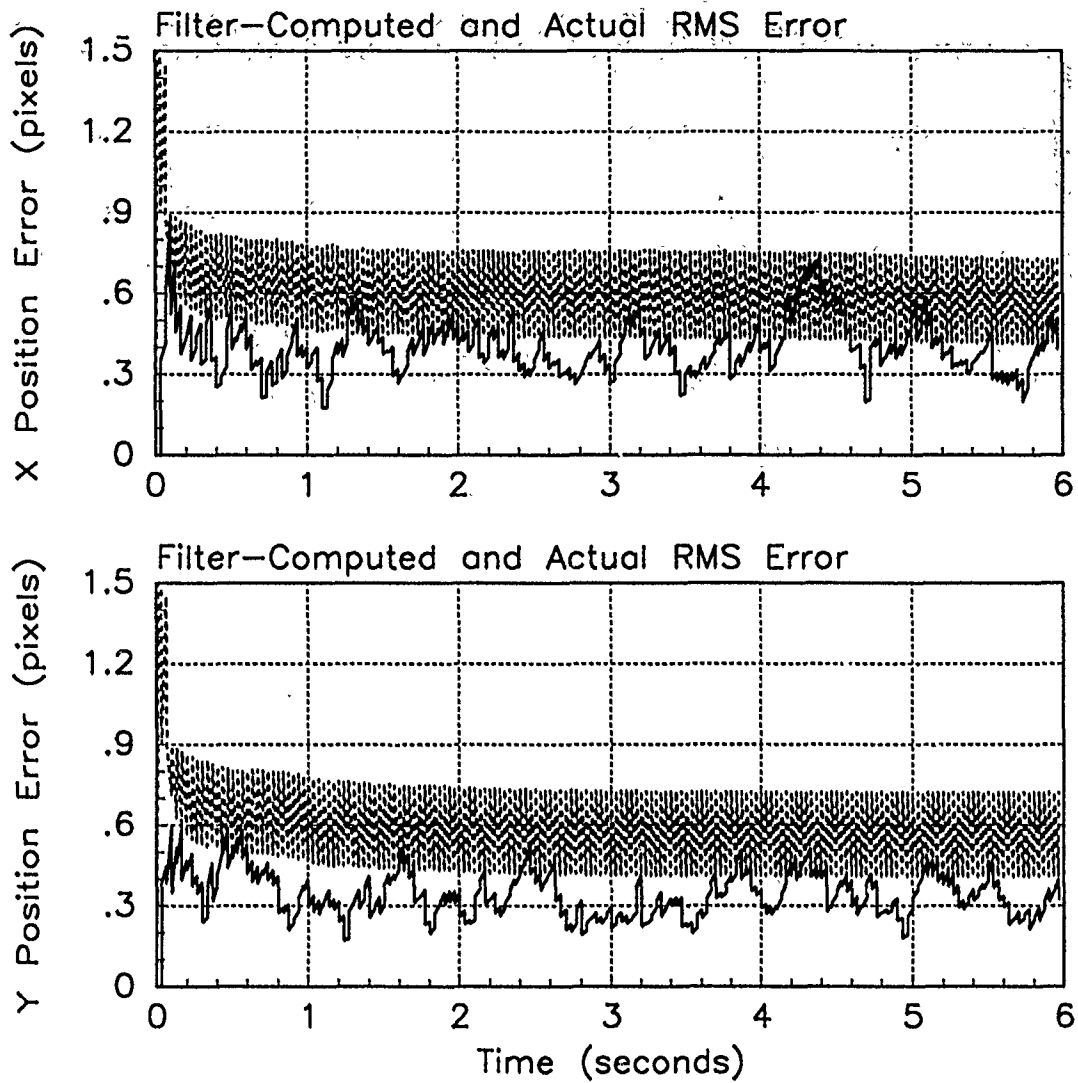


Figure D.37. RMS Error Plots; Notch MMAE-1R; PC is 4; Trajectory with $\omega = .01$

Table D.13. Temporal Averages and Residuals; Notch MMAE-1R; PC is 4; Trajectory with $\omega = .01$.

Error in:	Mean	σ
$p_x(t_i^-)$	0.082393	0.41841
$p_x(t_i^+)$	0.068079	0.38066
$y_x(t_i^-)$	0.061653	0.38355
$p_y(t_i^-)$	-0.00058354	0.35407
$p_y(t_i^+)$	-0.00026798	0.32088
$y_y(t_i^-)$	0.0040345	0.36966

Filter	$r_k^T r_k$	$r_k^T A_k^{-1} r_k$
Benign	0.31492	1.85673
Intermediate	0.30830	1.80297
Harsh	0.38061	1.73296

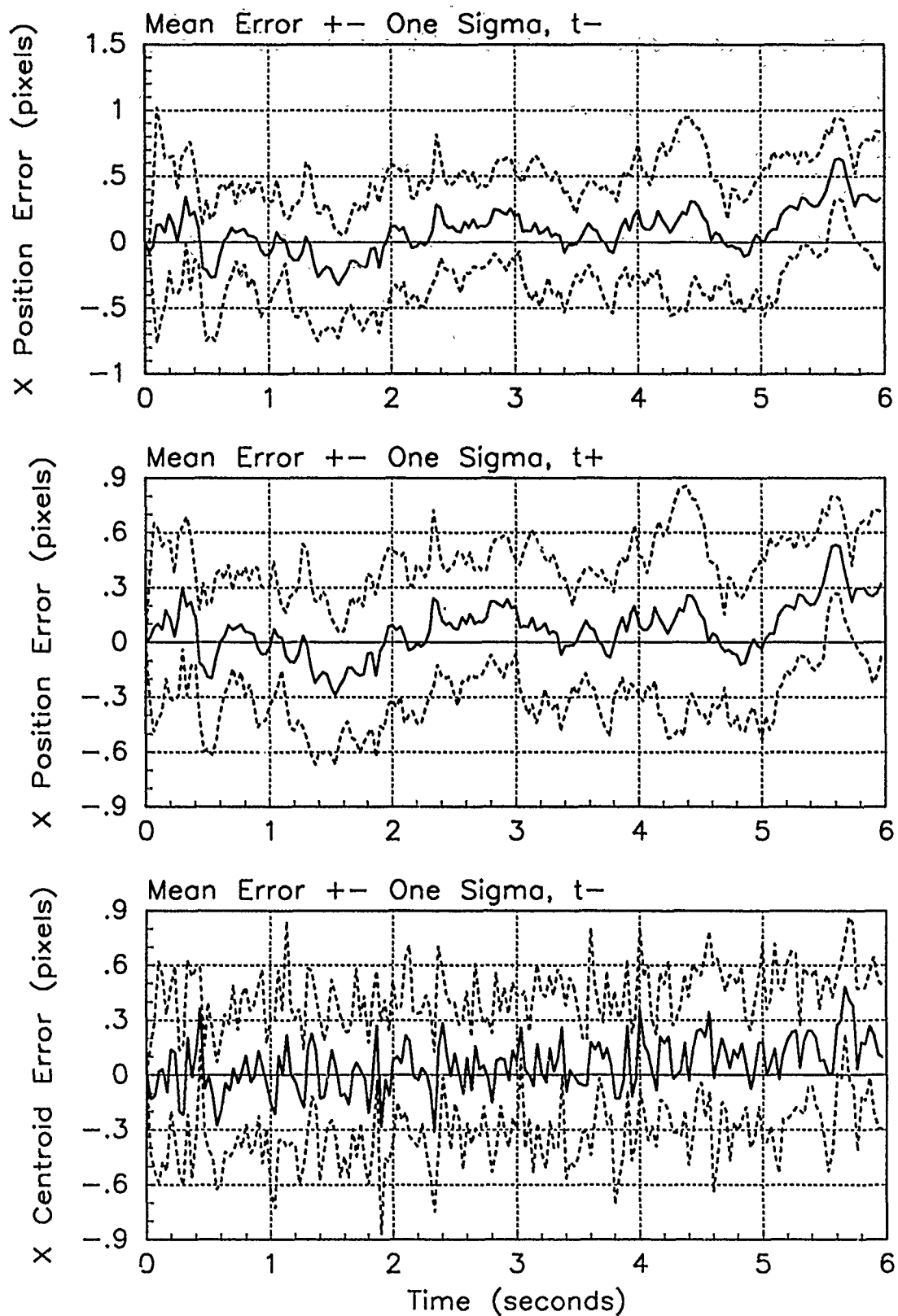


Figure D.38. X-Error Plots; Notch MMAE-1R; PC is 4; Trajectory with $\omega = .01$

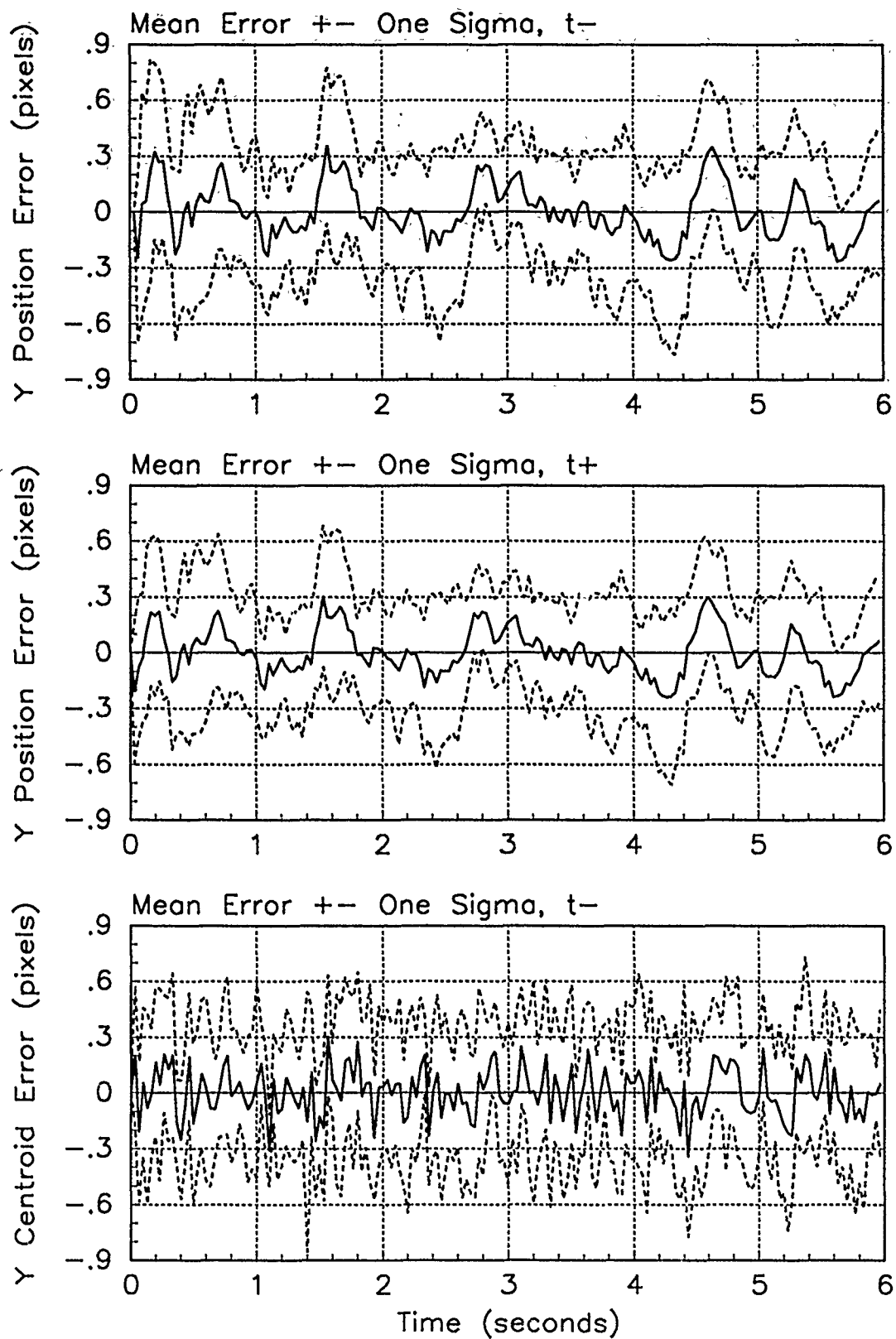


Figure D.39. Y-Error Plots; Notch MMAE-1R; PC is 4; Trajectory with $\omega = .01$

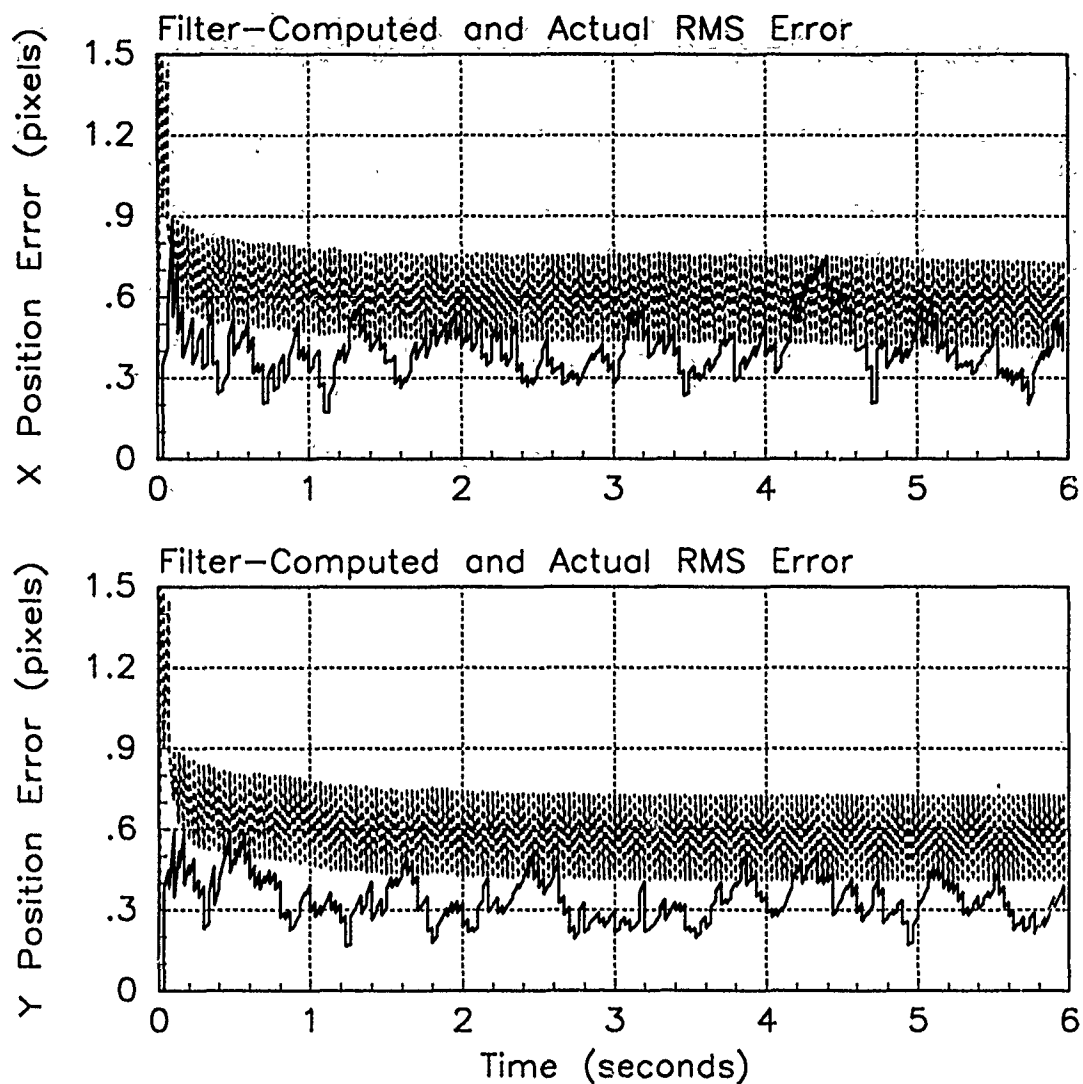


Figure D.40. RMS Error Plots; Notch MMAE-1R; PC is 4; Trajectory with $\omega = .62$

Table D.14. Temporal Averages and Residuals; Notch MMAE-1R; PC is 4; Trajectory with $\omega = .62$.

Error in:	Mean	σ
$p_x(t_i^-)$	0.080174	0.42232
$p_x(t_i^+)$	0.065309	0.38483
$y_x(t_i^-)$	0.058459	0.38644
$p_y(t_i^-)$	0.026384	0.34956
$p_y(t_i^+)$	0.019793	0.31601
$y_y(t_i^-)$	0.020130	0.36826

Filter	$\mathbf{r}_k^T \mathbf{r}_k$	$\mathbf{r}_k^T \mathbf{A}_k^{-1} \mathbf{r}_k$
Benign	0.31548	1.85949
Intermediate	0.30918	1.80763
Harsh	0.38565	1.75591

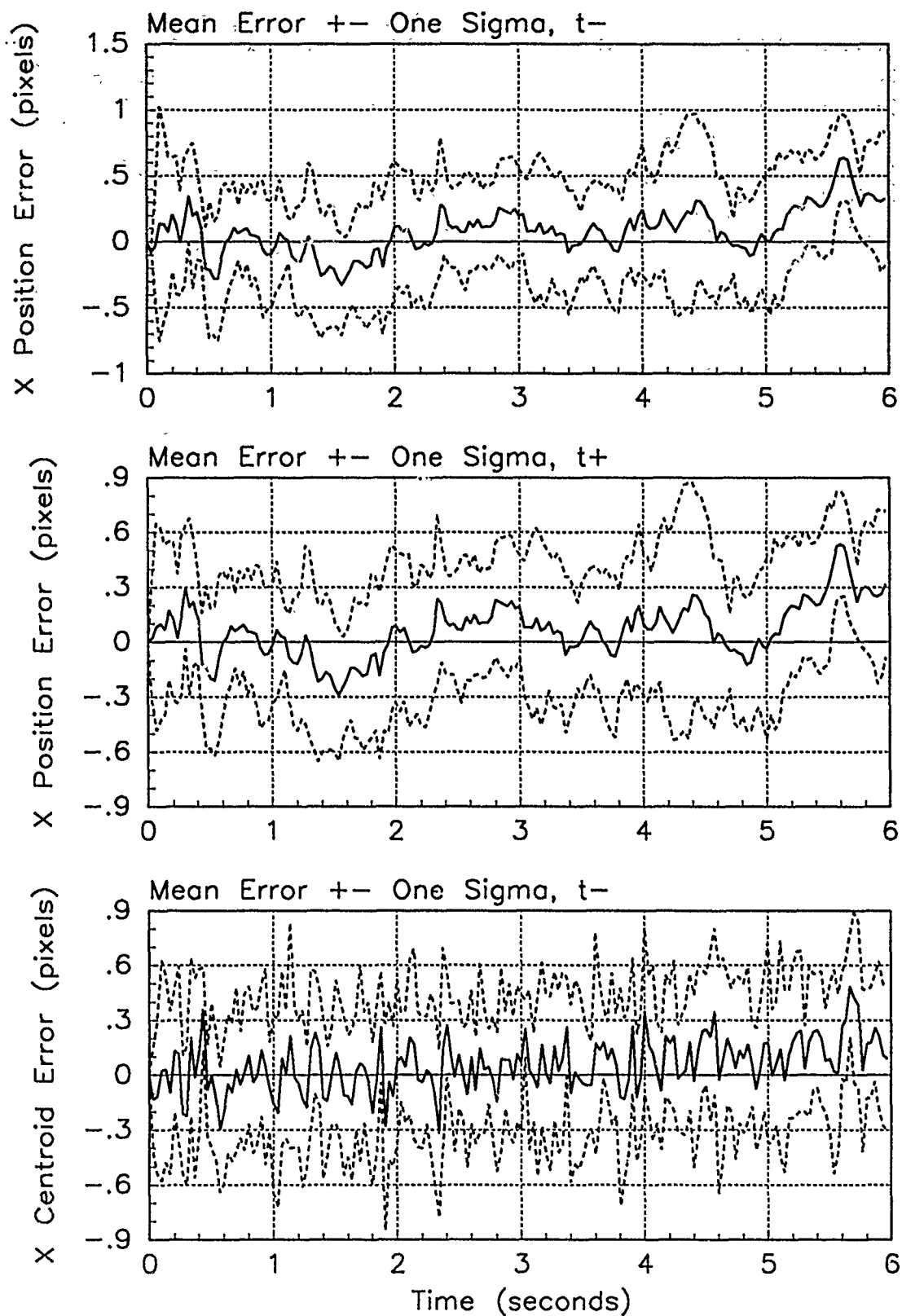


Figure D.41. X-Error Plots; Notch MMAE-1R; PC is 4; Trajectory with $\omega = .62$

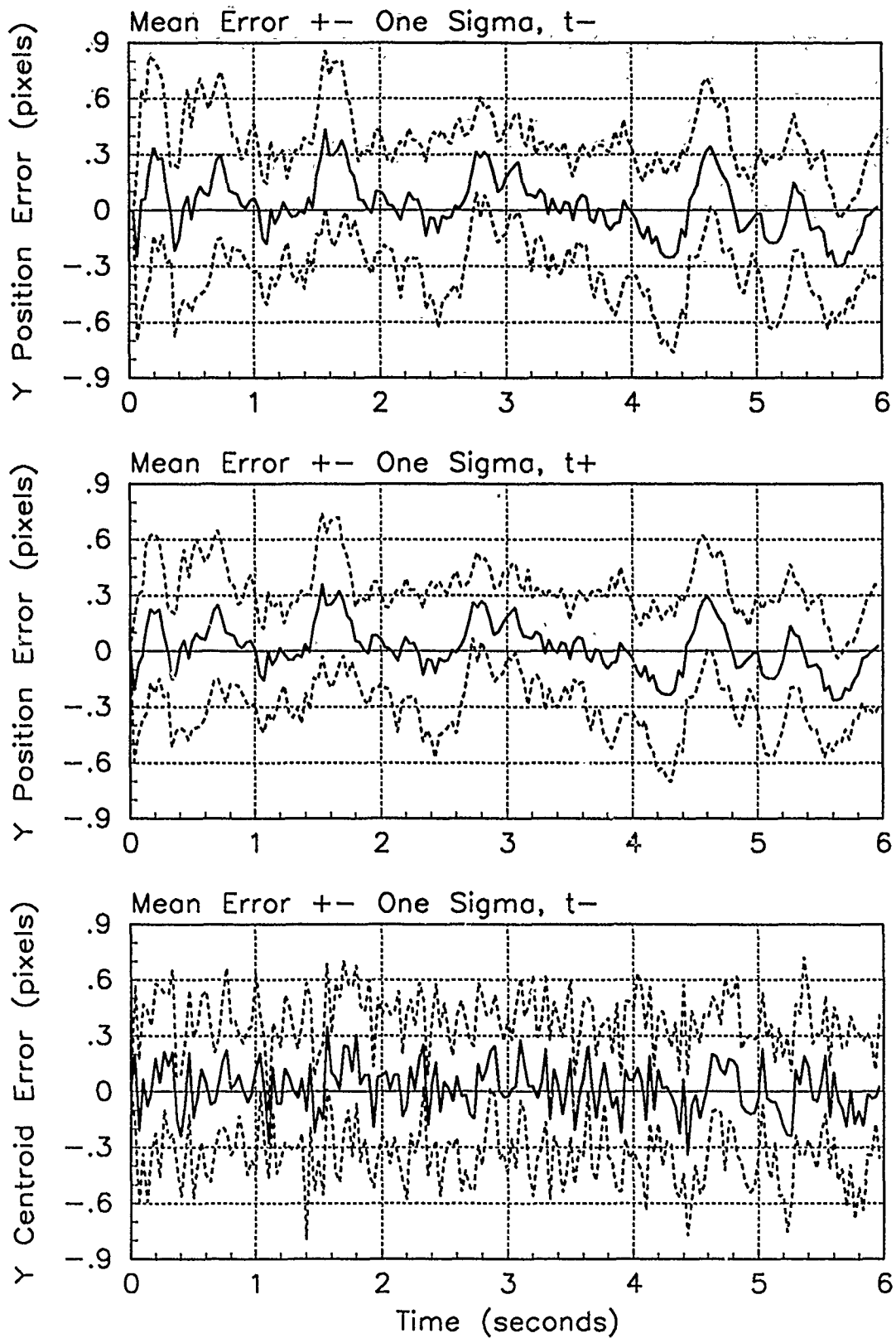


Figure D.42. Y-Error Plots; Notch MMAE-1R; PC is 4; Trajectory with $\omega = .62$

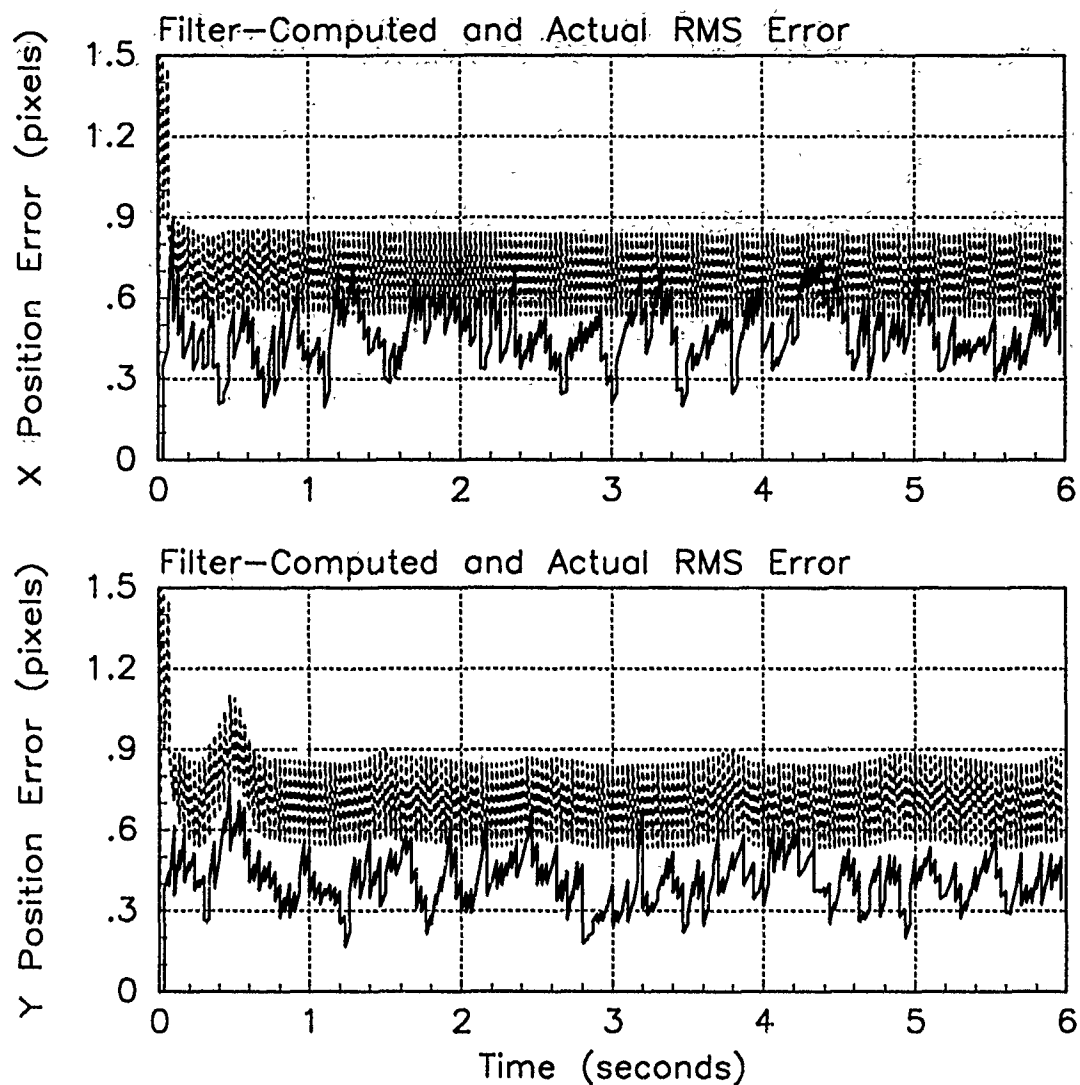


Figure D.43. RMS Error Plots; Notch MMAE-1R; PC is 4; Trajectory with $\omega = 2.8$

Table D.15. Temporal Averages and Residuals; Notch MMAE-1R; PC is 4; Trajectory with $\omega = 2.8$.

Error in:	Mean	σ
$p_x(t_i^-)$	-0.093248	0.50884
$p_x(t_i^+)$	-0.057815	0.42845
$y_x(t_i^-)$	-0.058479	0.41982
$p_y(t_i^-)$	0.085308	0.45102
$p_y(t_i^+)$	0.042720	0.37132
$y_y(t_i^-)$	0.062680	0.40167

Filter	$\mathbf{r}_k^T \mathbf{r}_k$	$\mathbf{r}_k^T \mathbf{A}_k^{-1} \mathbf{r}_k$
Benign	2.23683	13.05215
Intermediate	2.72495	16.09862
Harsh	0.40132	1.82378

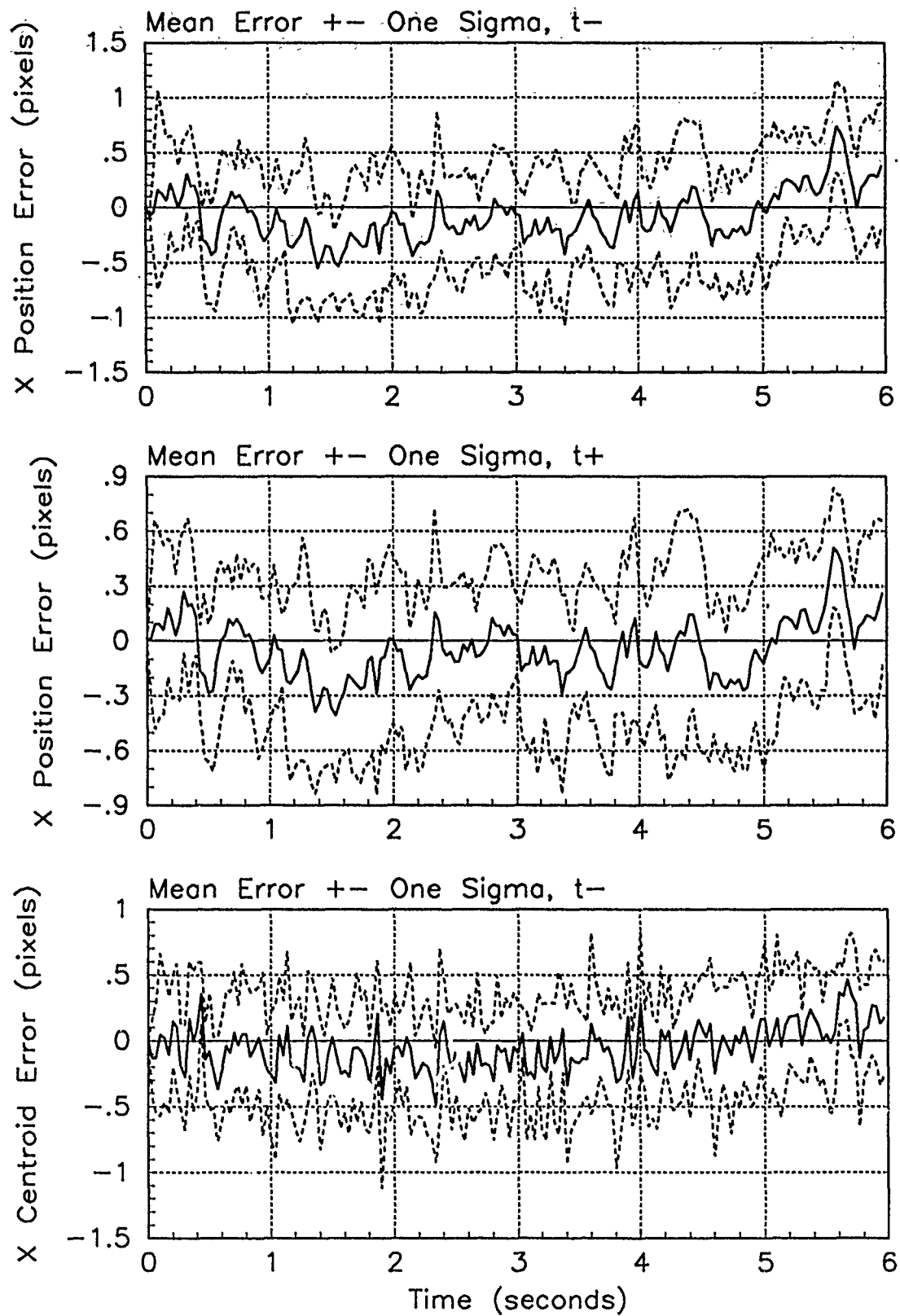


Figure D.44. X-Error Plots; Notch MMAE-1R; PC is 4; Trajectory with $\omega = 2.8$

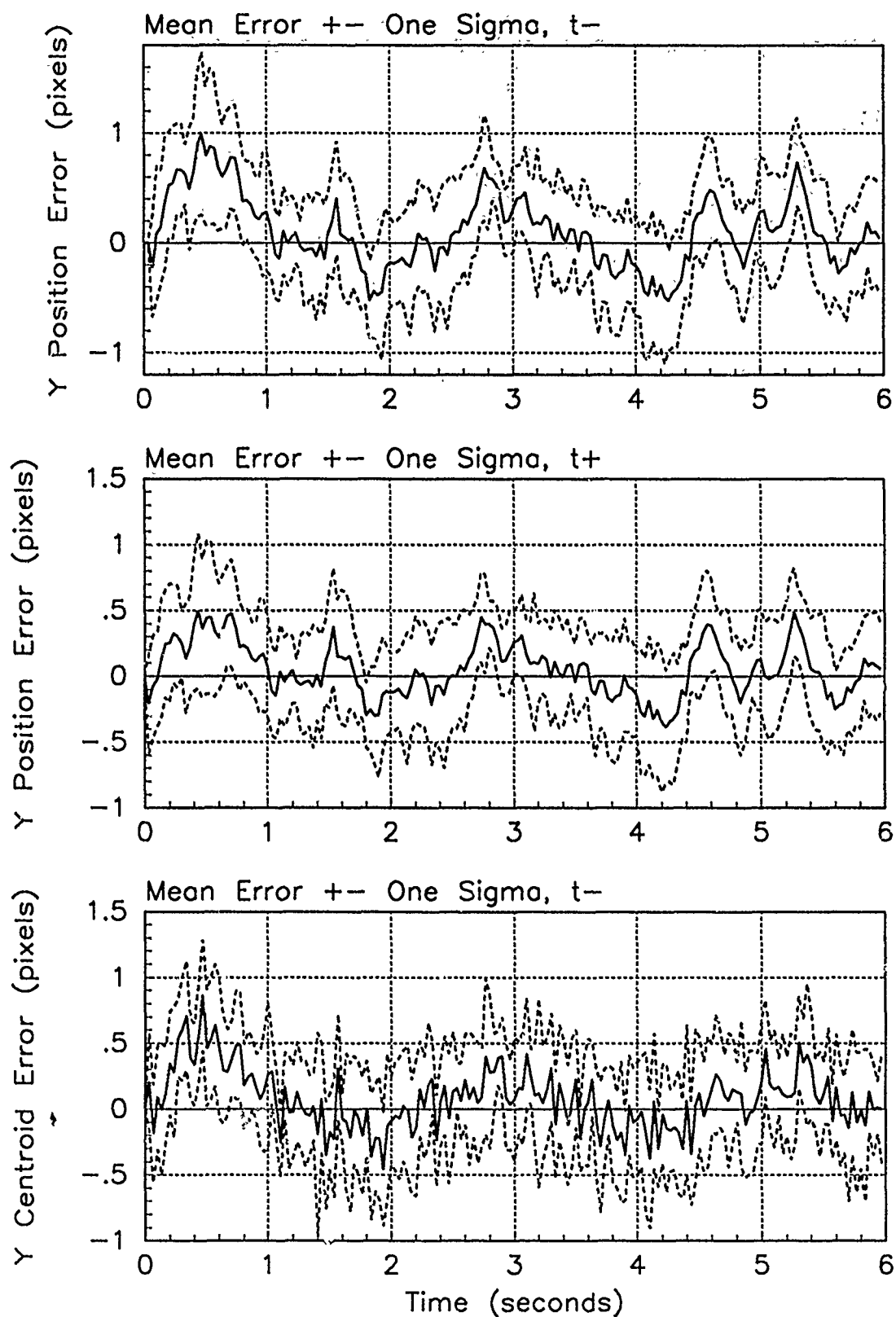


Figure D.45. Y-Error Plots; Notch MMAE-1R; PC is 4; Trajectory with $\omega = 2.8$

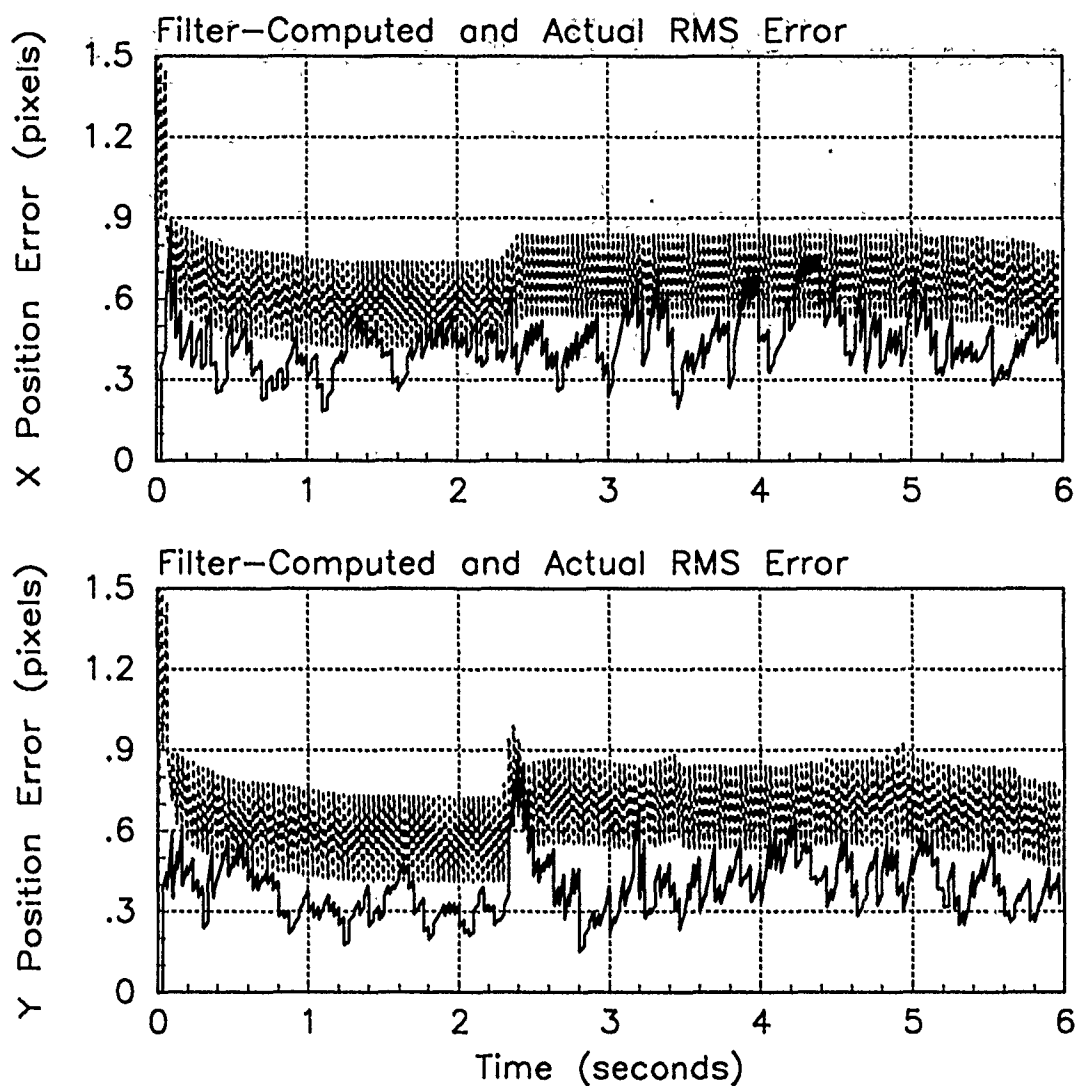


Figure D.46. RMS Error Plots; Notch MMAE-1R; PC is 1; Jinking Trajectory

Table D.16. Temporal Averages; Notch MMAE-1R; PC is 1; Jinking Trajectory.

Error in:	Mean	σ
$p_x(t_i^-)$	-0.020947	0.47031
$p_x(t_i^+)$	-0.013453	0.40945
$y_x(t_i^-)$	-0.0076075	0.40412
$p_y(t_i^-)$	0.13638	0.42032
$p_y(t_i^+)$	0.084965	0.35875
$y_y(t_i^-)$	0.10577	0.39181

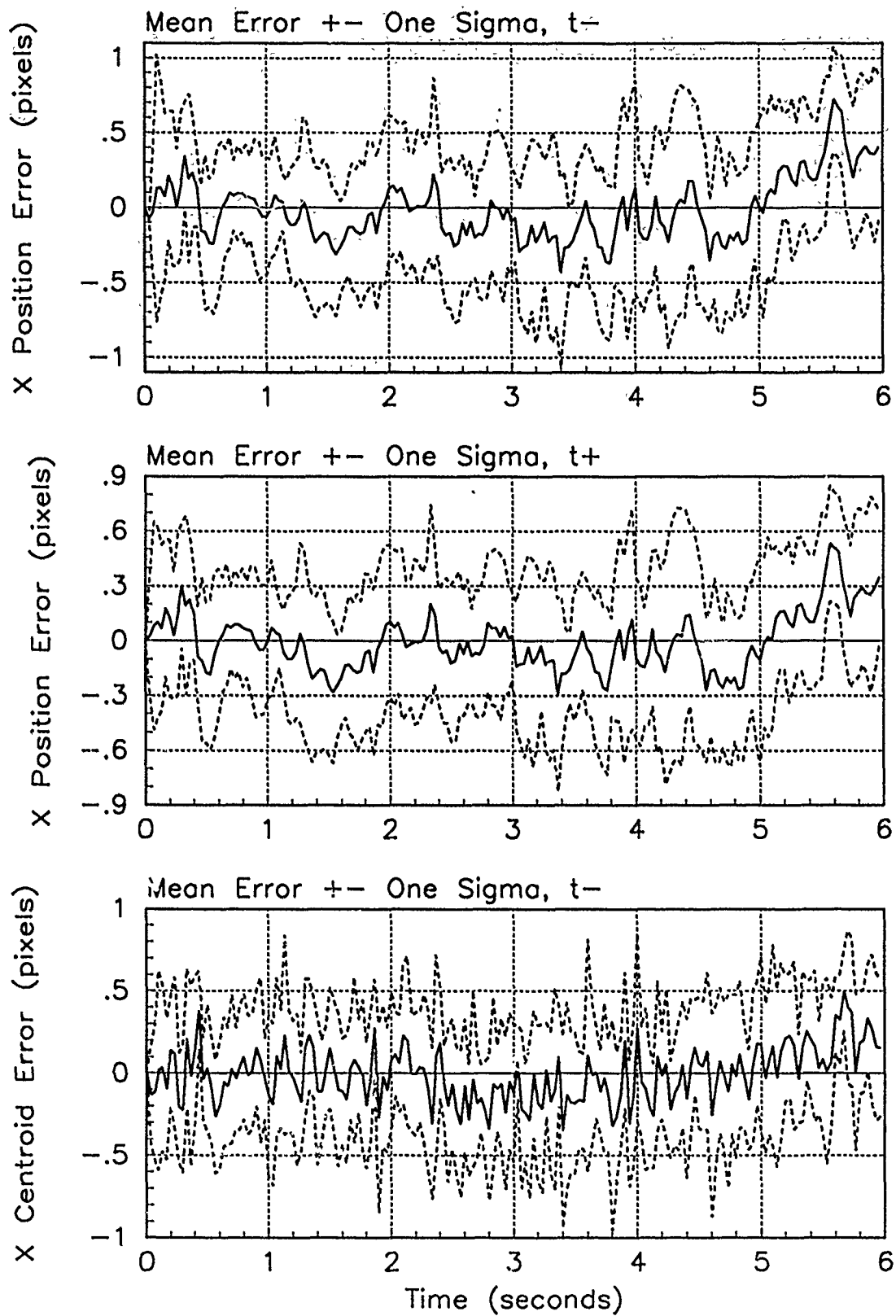


Figure D.47. X-Error Plots; Notch MMAE-1R; PC is 1; Jinking Trajectory

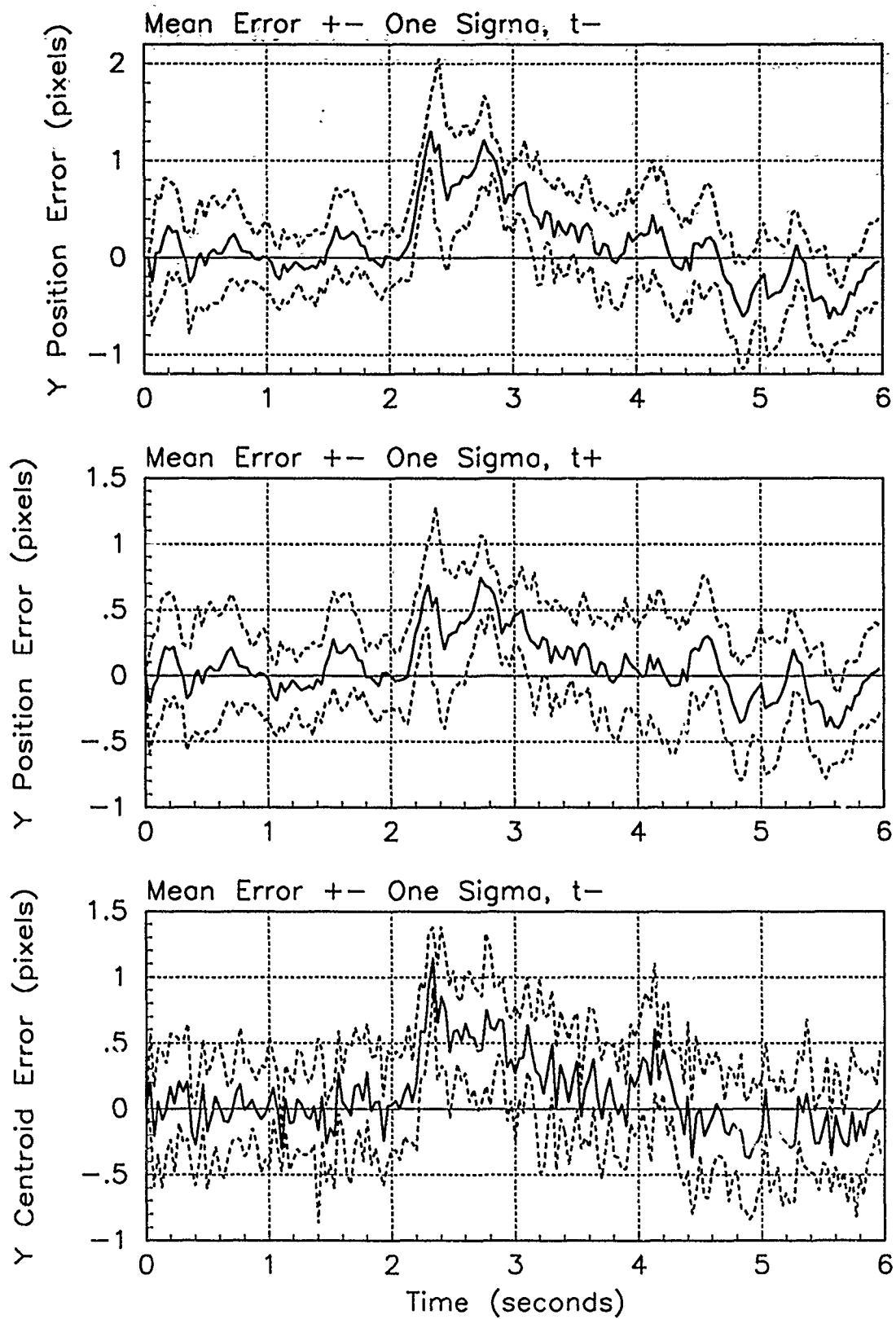


Figure D.48. Y-Error Plots; Notch MMAE-1R; PC is 1; Jinking Trajectory

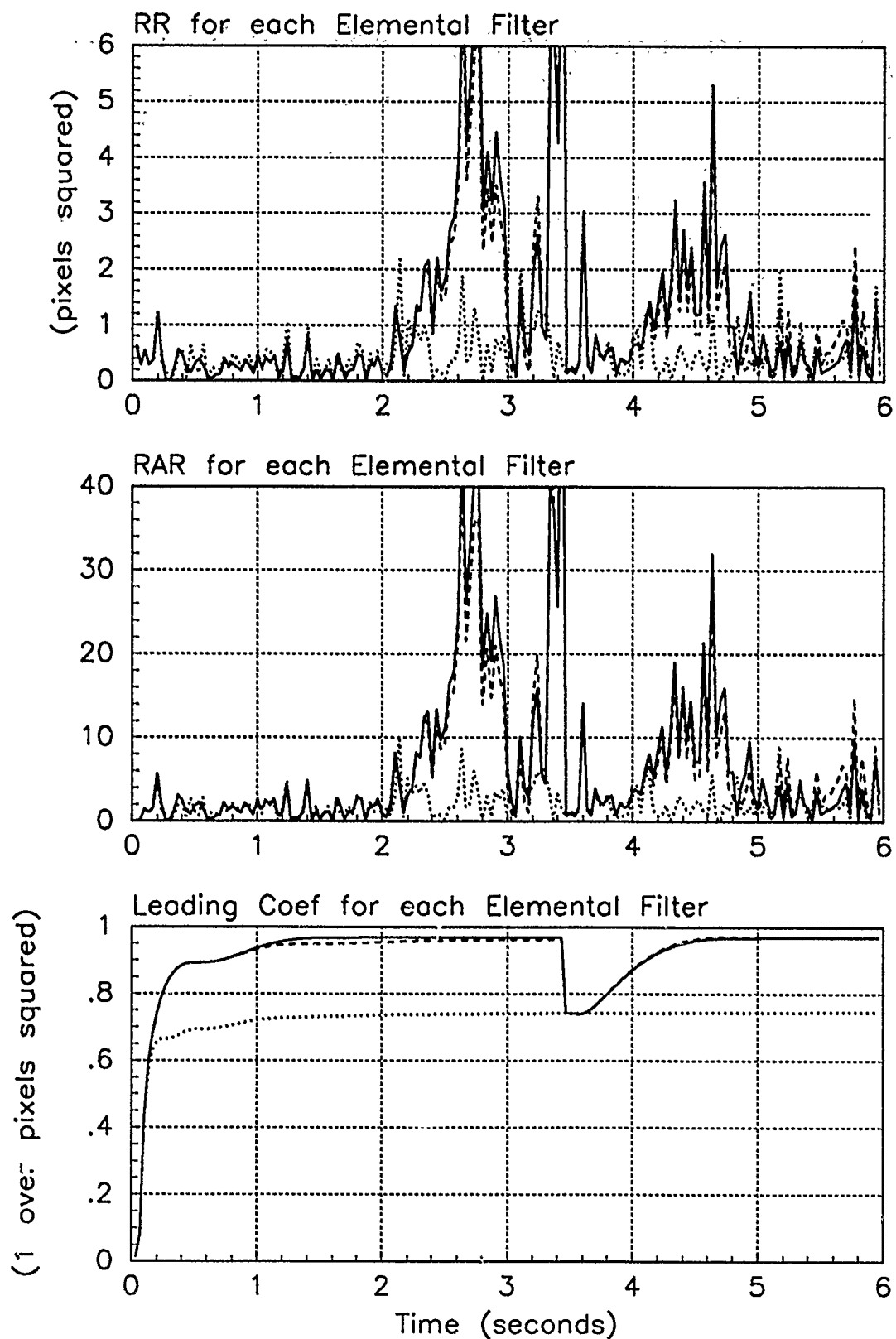


Figure D.49. Probability Calculation Plots; Notch MMAE-1R; PC is 1; Jinking Trajectory. Benign filter has solid line; intermediate filter has dashed line; harsh filter has dotted line.

Appendix E. *Error Plots for Notch MMAE-2*

This appendix contains the error plots for the MMAE with one elemental filter based on a first-order acceleration model and two elemental filters based on second-order acceleration models that are also referred to as notch filters. The intermediate filter model has $\omega = 1.32$ radians per second as discussed in Chapter V. The MMAE is referred to as the notch MMAE-2. All Monte Carlo studies were done with the MMAE tuned in the revised method.

The results for one Monte Carlo study typically consist of a set of three pages. The first page shows the RMS error plots for each of the x- and y-positions. The band is the dashed line for the filter-computed RMS error. The solid line is the actual RMS error calculated over the Monte Carlo study. Below these plots are two tables. The table on the left lists the temporal average of the position errors. This temporal average is from .5 seconds to the end of each of the 10 runs in the Monte Carlo study as described in Section 5.2. The table on the right is the list of the average $\mathbf{r}_k^T(t_i)\mathbf{r}_k(t_i)$ and $\mathbf{r}_k^T(t_i)\mathbf{A}_k^{-1}(t_i)\mathbf{r}_k(t_i)$ over the 10 runs for the entire run, not just the last 5.5 seconds. The lack of time notation (rather than the traditional overbar) in the table signifies the temporal average. The next page of each set shows the mean ± 1 standard deviation error plots for the x-position at time t_i^- and t_i^+ and the mean x-centroid position error at time t_i^- . The final page shows similar plots for the mean y-position errors. The solid line denotes the mean error while the dashed line is the mean $\pm \sigma$.

When the MMAE is tracking the target in a jinking maneuver, there is no table on the first page for the average $\mathbf{r}_k^T(t_i)\mathbf{r}_k(t_i)$ and $\mathbf{r}_k^T(t_i)\mathbf{A}_k^{-1}(t_i)\mathbf{r}_k(t_i)$ since each is expected to change greatly over the run due to the changing acceleration dynamics. Instead, the plots of the $\mathbf{r}_k^T(t_i)\mathbf{r}_k(t_i)$, $\mathbf{r}_k^T(t_i)\mathbf{A}_k^{-1}(t_i)\mathbf{r}_k(t_i)$, and leading coefficient needed in the hypothesis probability calculation are presented.

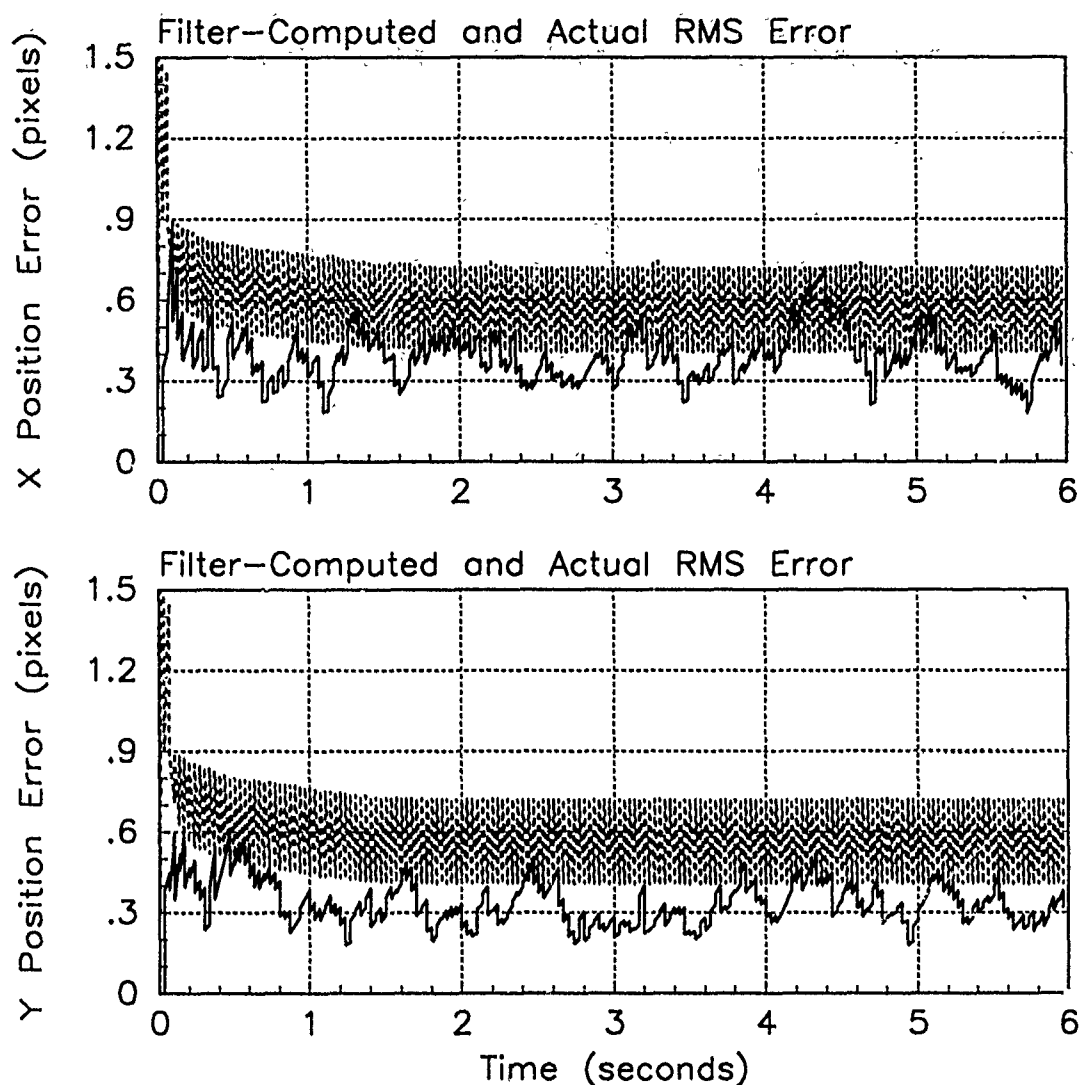


Figure E.1. RMS Error Plots; Notch MMAE-2R; PC is 1; Trajectory with $\omega = .01$

Table E.1. Temporal Averages and Residuals; Notch MMAE-2R; PC is 1; Trajectory with $\omega = .01$.

Error in:	Mean	σ
$p_x(t_i^-)$	0.16395	0.41076
$p_x(t_i^+)$	0.12649	0.37388
$y_x(t_i^-)$	0.10306	0.38144
$p_y(t_i^-)$	-0.0039394	0.34661
$p_y(t_i^+)$	-0.0025796	0.31421
$y_y(t_i^-)$	0.0020246	0.36641

Filter	$r_k^T r_k$	$r_k^T A_k^{-1} r_k$
Benign	0.31351	1.84793
Intermediate	0.33135	1.80755
Harsh	0.37906	1.72563

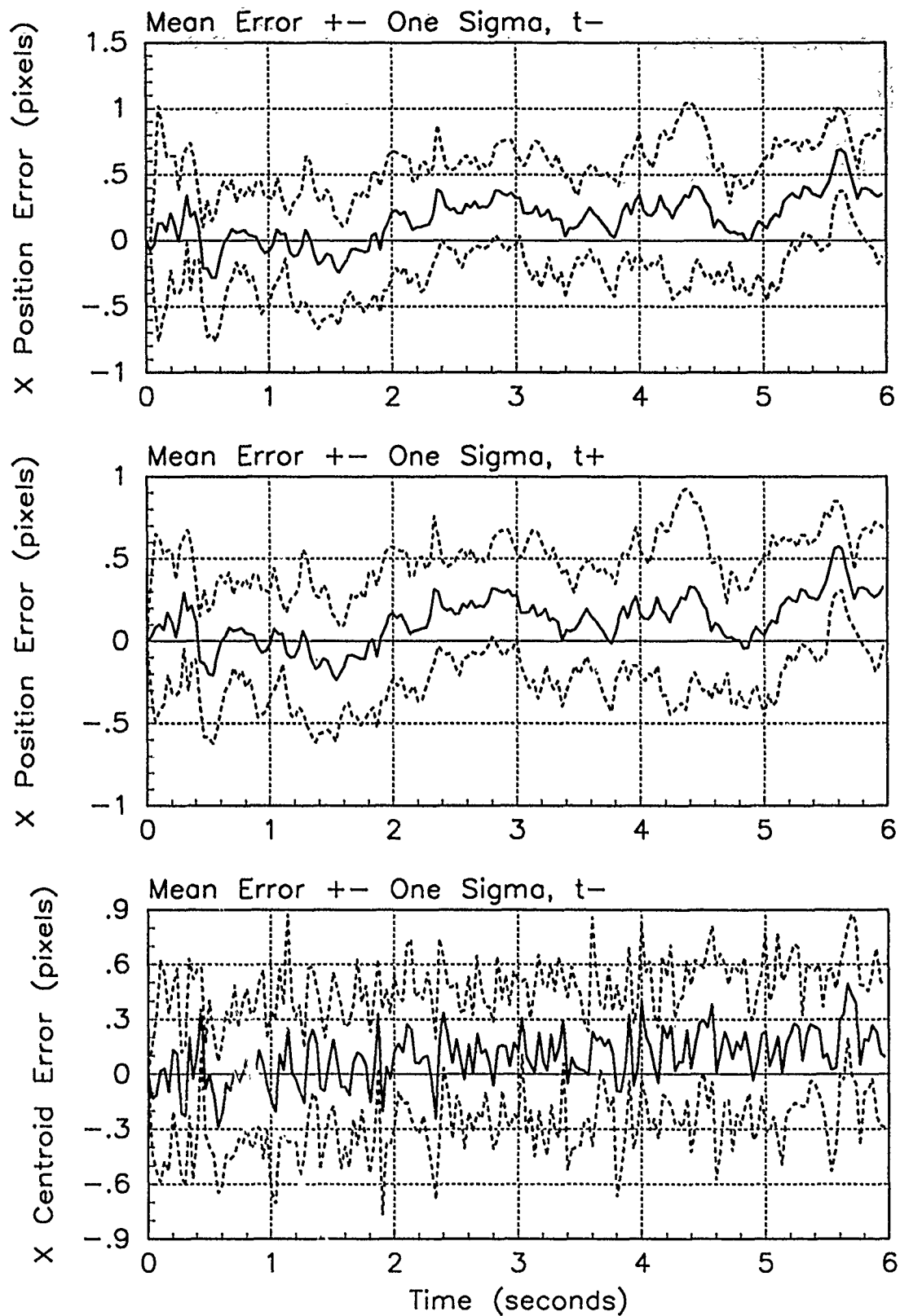


Figure E.2. X-Error Plots; Notch MMAE-2R; PC is 1; Trajectory with $\omega = .01$

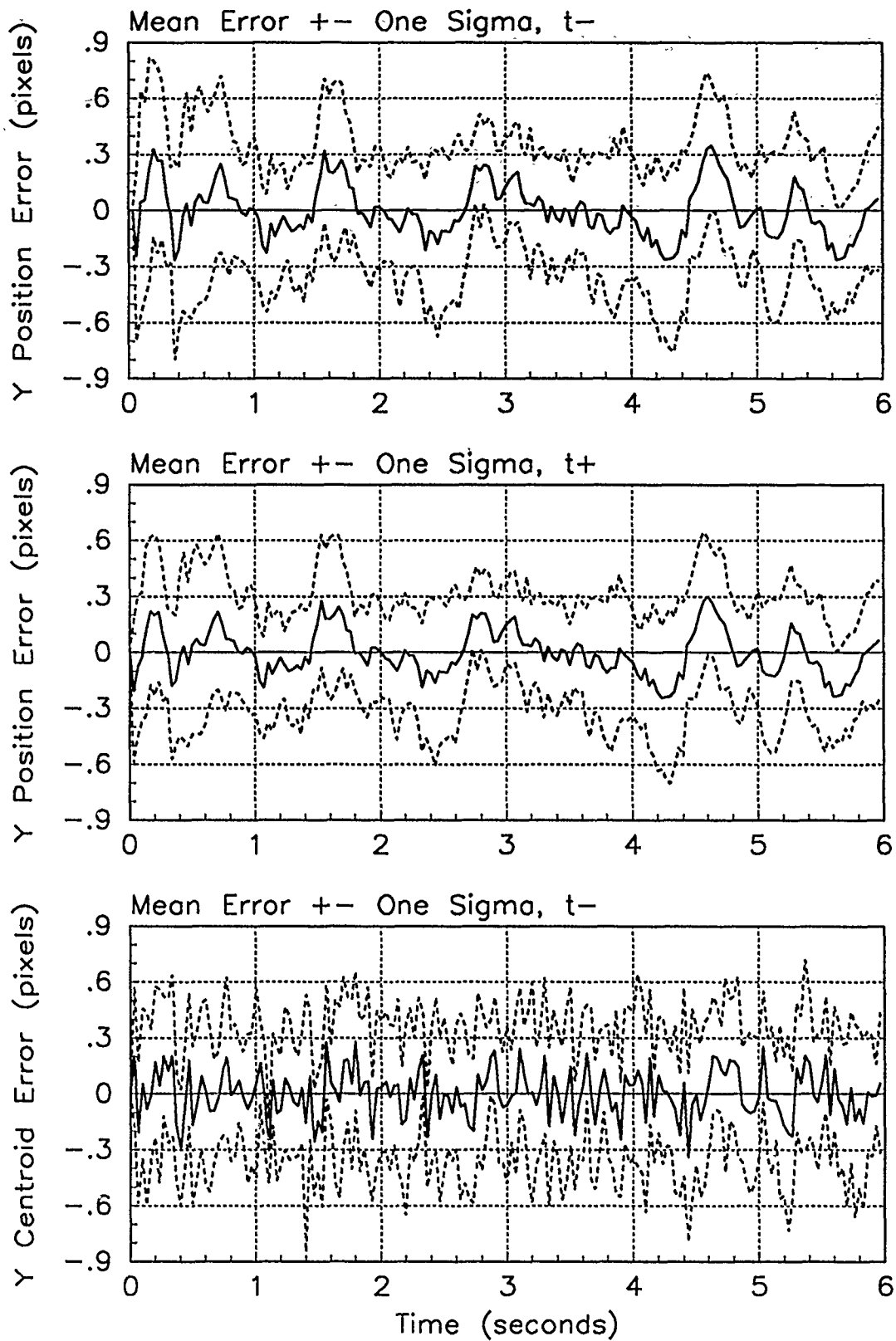


Figure E.3. Y-Error Plots; Notch MMAE-2R; PC is 1; Trajectory with $\omega = .01$

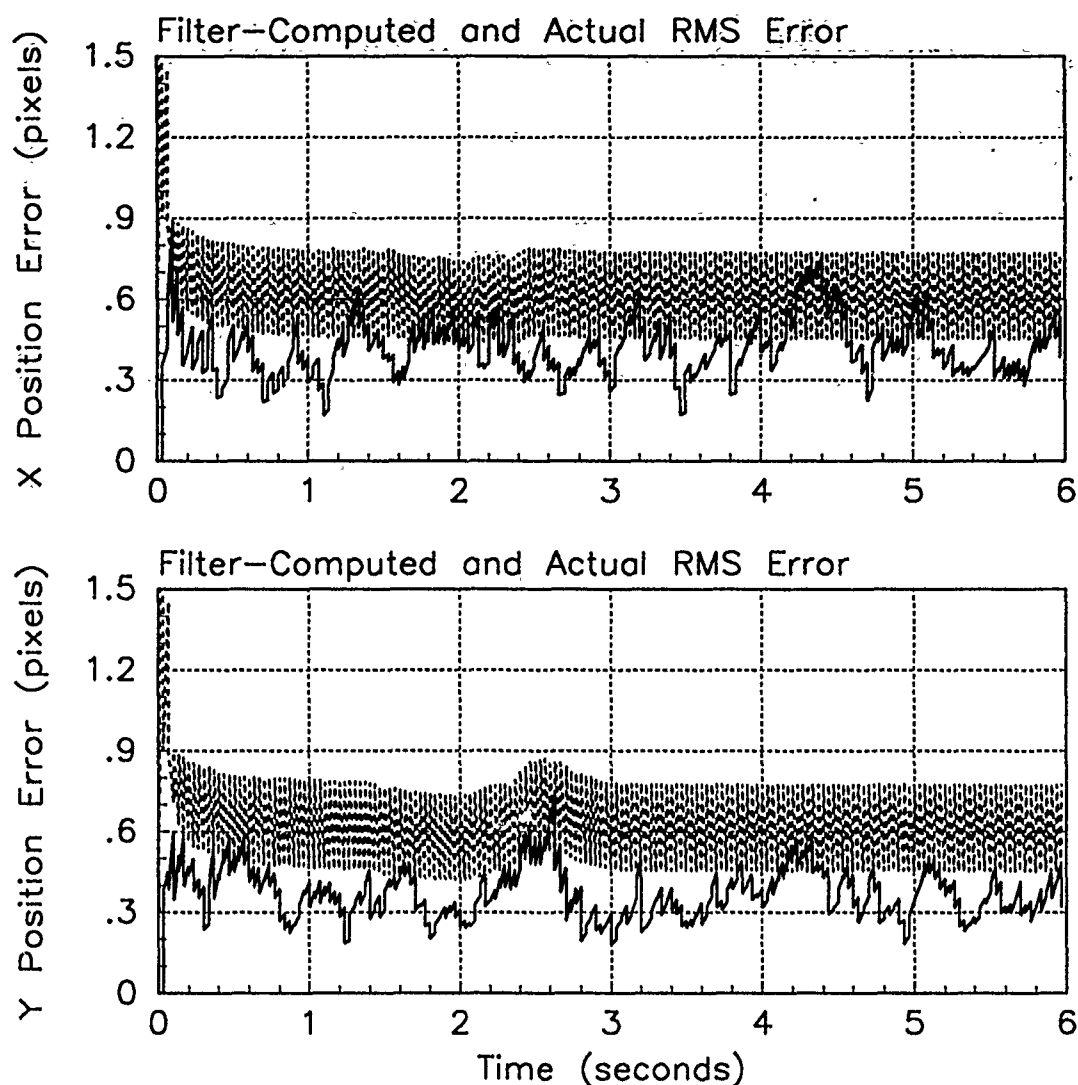


Figure E.4. RMS Error Plots; Notch MMAE-2R; PC is 1; Trajectory with $\omega = 1.32$

Table E.2. Temporal Averages and Residuals; Notch MMAE-2R; PC is 1; Trajectory with $\omega = 1.32$.

Error in:	Mean	σ
$p_x(t_i^-)$	-0.033154	0.44509
$p_x(t_i^+)$	-0.027812	0.39616
$y_x(t_i^-)$	-0.015701	0.39221
$p_y(t_i^-)$	-0.0082105	0.39073
$p_y(t_i^+)$	-0.013980	0.34328
$y_y(t_i^-)$	-0.015544	0.37448

Filter	$\mathbf{r}_k^T \mathbf{r}_k$	$\mathbf{r}_k^T \mathbf{A}_k^{-1} \mathbf{r}_k$
Benign	0.39640	2.34648
Intermediate	0.33310	1.81712
Harsh	0.39016	1.77704

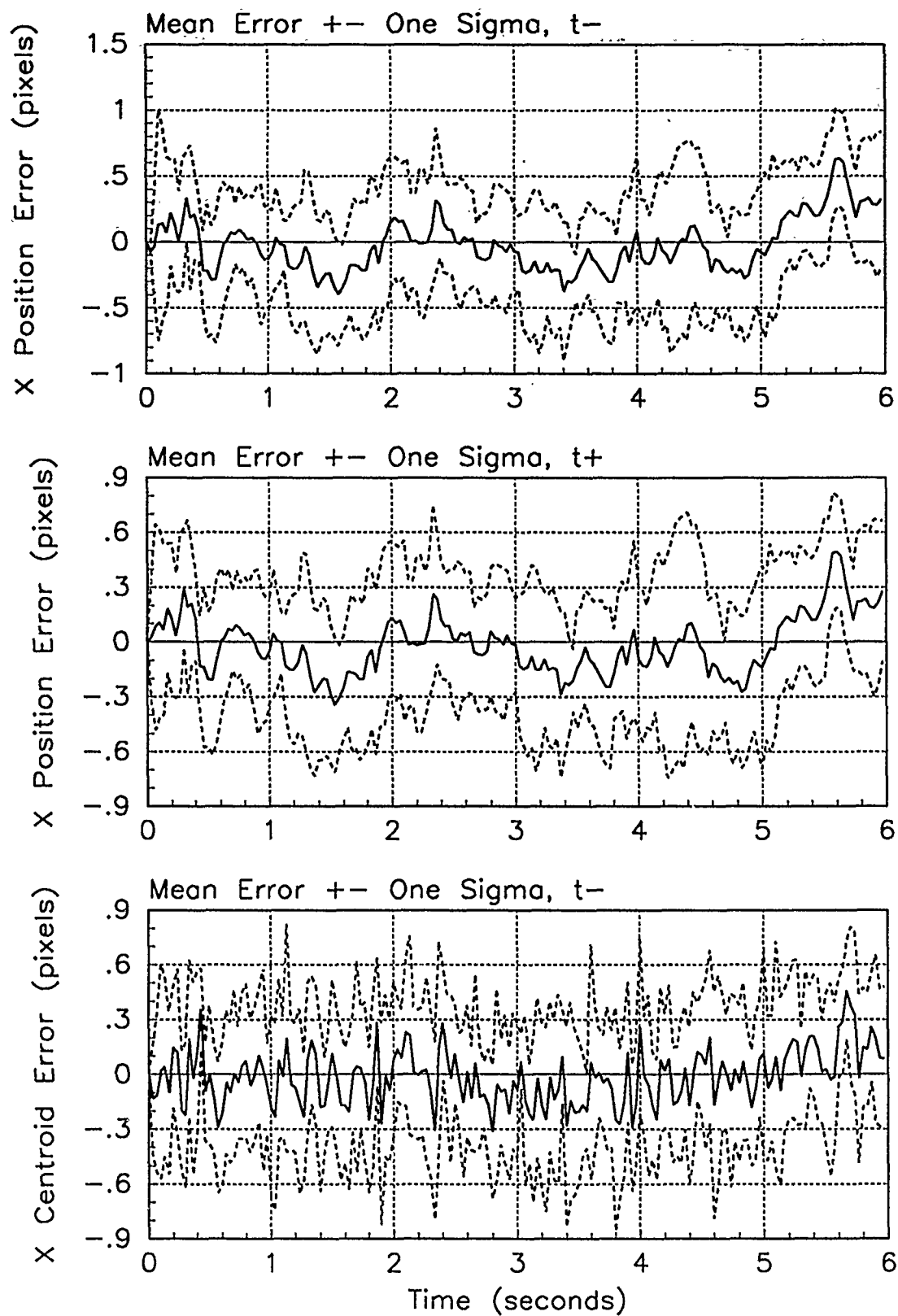


Figure E.5. X-Error Plots; Notch MMAE-2R; PC is 1; Trajectory with $\omega = 1.32$

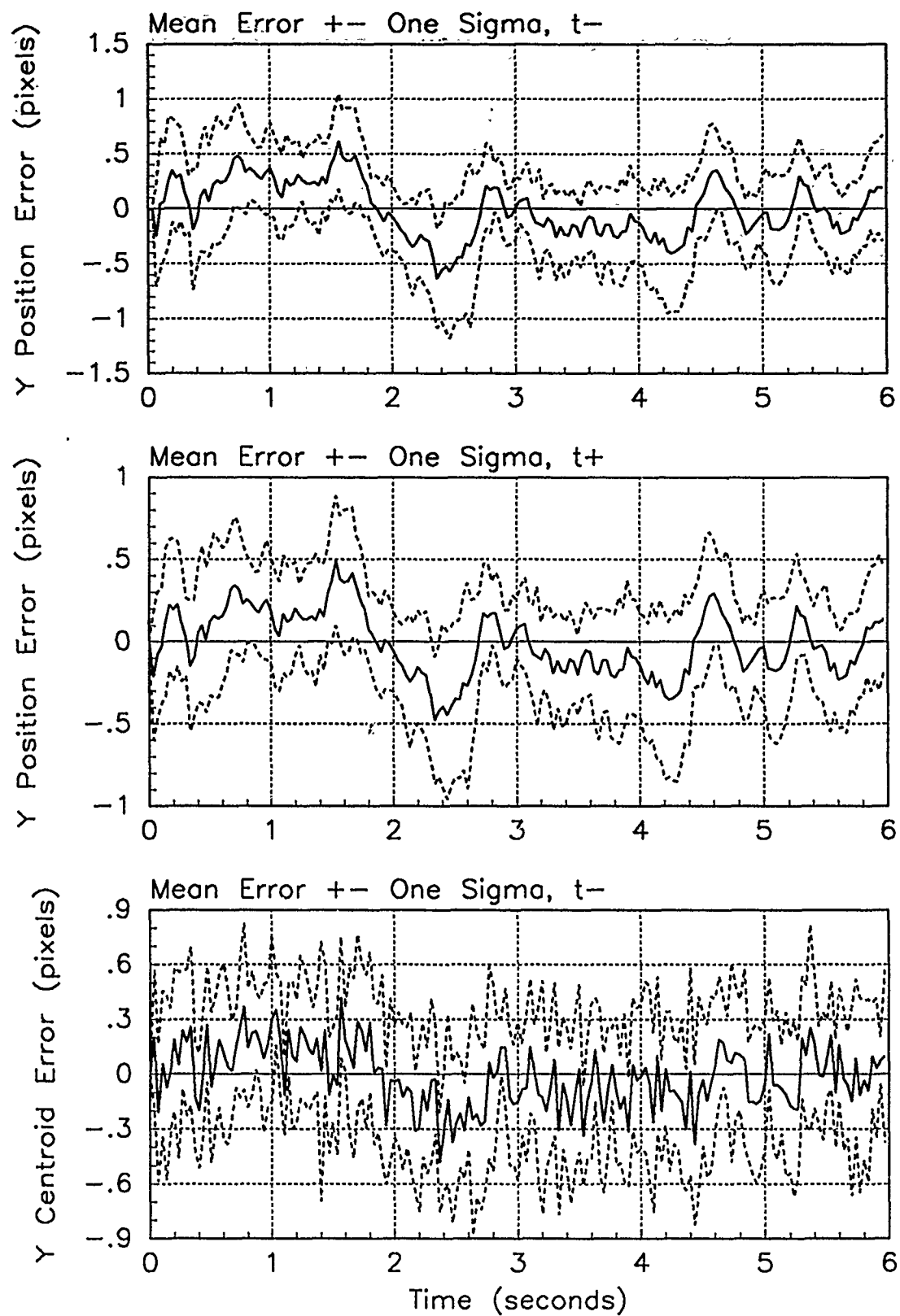


Figure E.6. Y-Error Plots; Notch MMAE-2R; PC is 1; Trajectory with $\omega = 1.32$

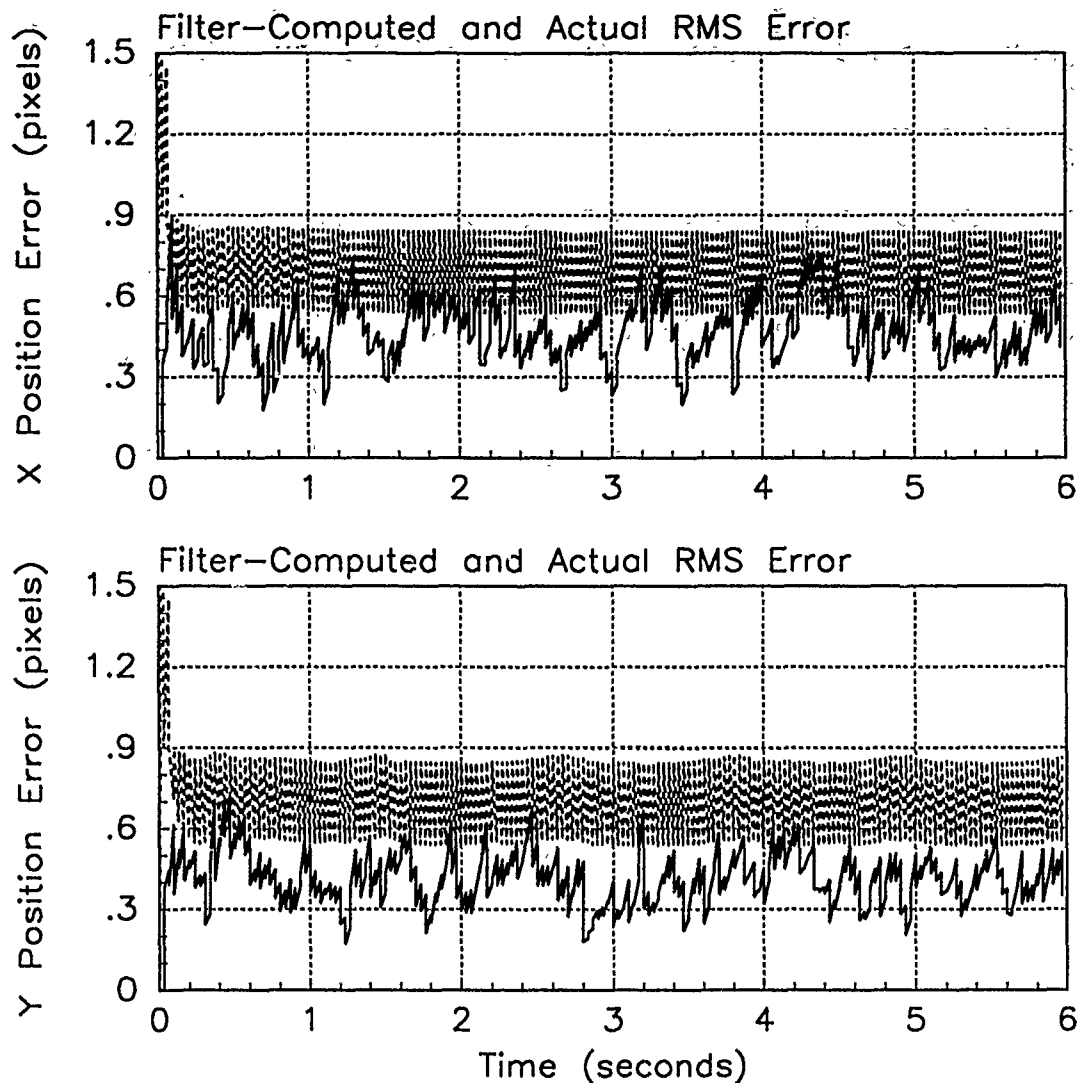


Figure E.7. RMS Error Plots; Notch MMAE-2R; PC is 1; Trajectory with $\omega = 2.8$

Table E.3. Temporal Averages and Residuals; Notch MMAE-2R; PC is 1; Trajectory with $\omega = 2.8$.

Error in:	Mean	σ
$p_x(t_i^-)$	-0.096333	0.51166
$p_x(t_i^+)$	-0.059868	0.43104
$y_x(t_i^-)$	-0.061052	0.41992
$p_y(t_i^-)$	0.066488	0.45012
$p_y(t_i^+)$	0.028088	0.37062
$y_y(t_i^-)$	0.046770	0.40278

Filter	$\mathbf{r}_k^T \mathbf{r}_k$	$\mathbf{r}_k^T \mathbf{A}_k^{-1} \mathbf{r}_k$
Benign	2.27674	13.30467
Intermediate	1.23253	6.79499
Harsh	0.40050	1.82004

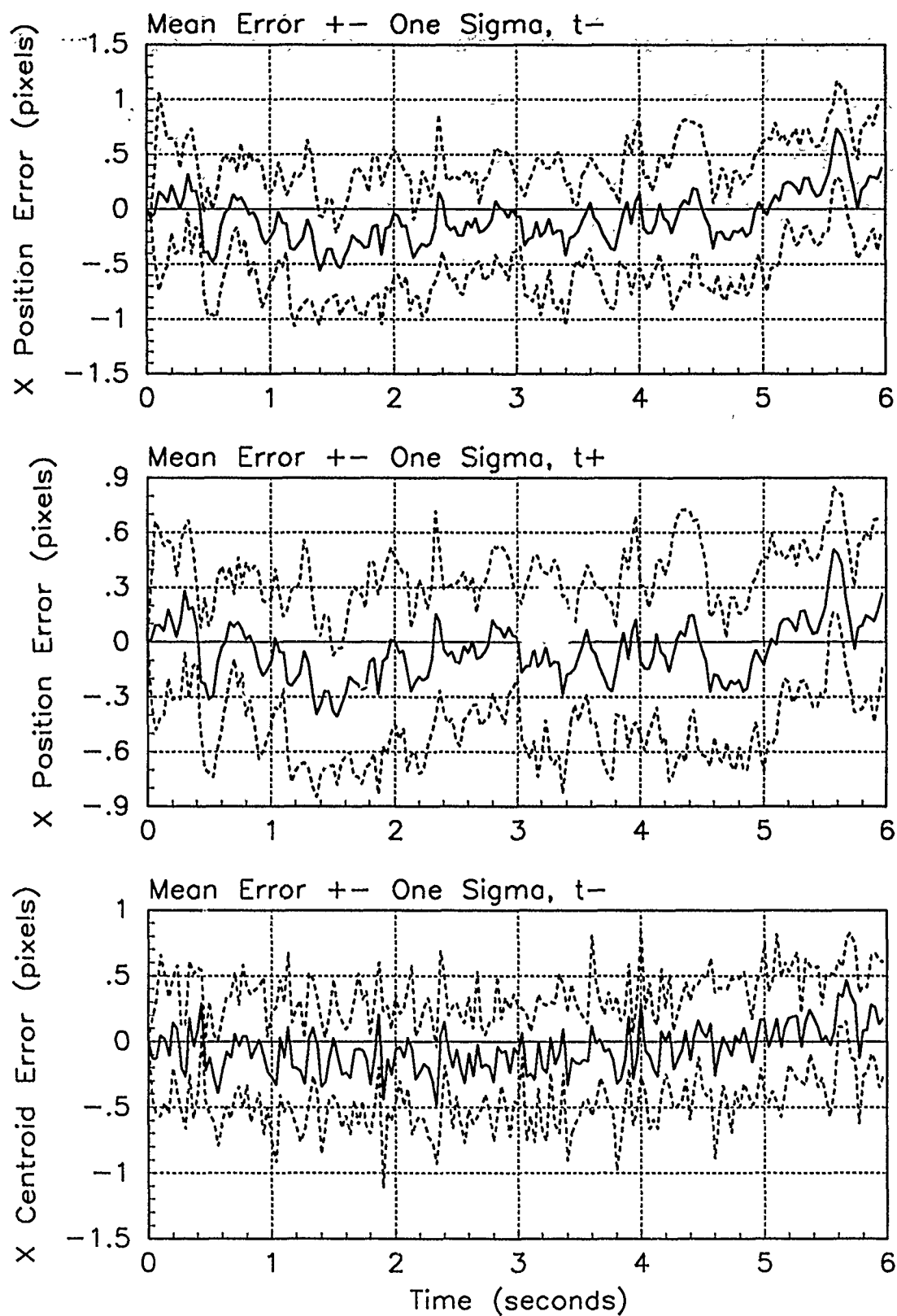


Figure E.8. X-Error Plots; Notch MMAE-2R; PC is 1; Trajectory with $\omega = 2.8$

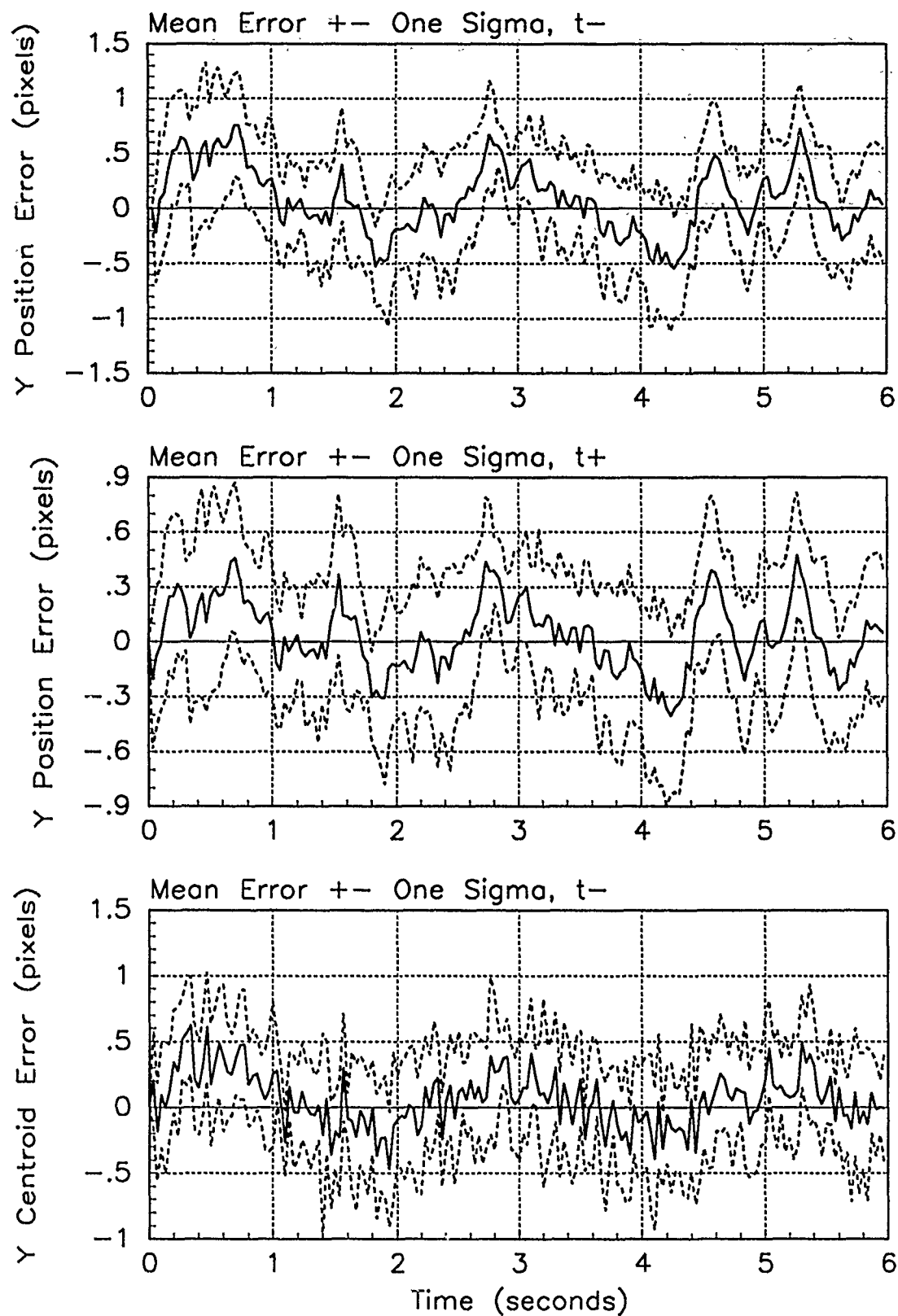


Figure E.9. Y-Error Plots; Notch MMAE-2R; PC is 1; Trajectory with $\omega = 2.8$;

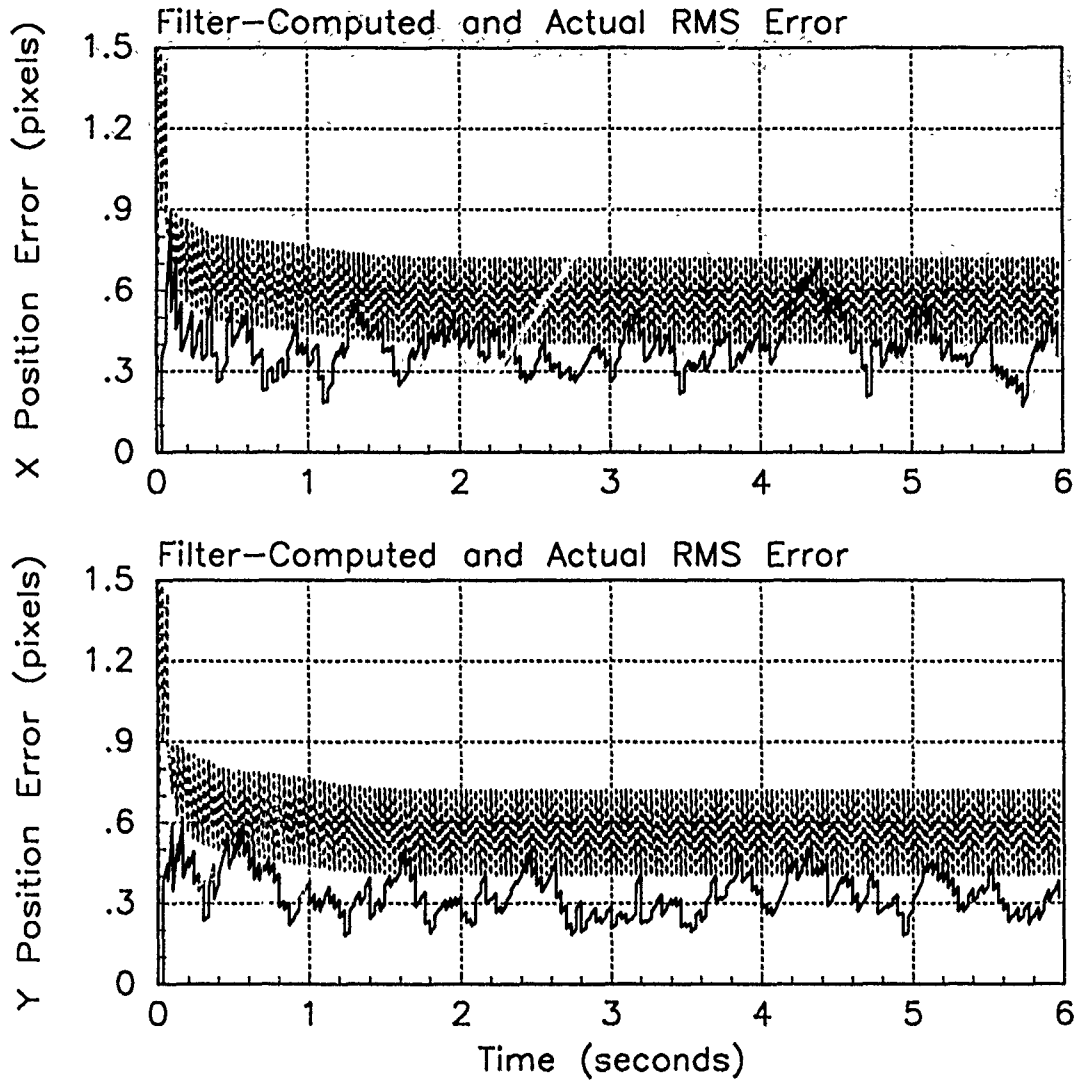


Figure E.10. RMS Error Plots; Notch MMAE-2R; PC is 2; Trajectory with $\omega = .01$

Table E.4. Temporal Averages and Residuals; Notch MMAE-2R; PC is 2; Trajectory with $\omega = .01$.

Error in:	Mean	σ
$p_x(t_i^-)$	0.16652	0.40800
$p_x(t_i^+)$	0.12716	0.37228
$y_x(t_i^-)$	0.10364	0.38029
$p_y(t_i^-)$	-0.0022974	0.34585
$p_y(t_i^+)$	-0.00076801	0.31391
$y_y(t_i^-)$	0.0037461	0.36747

Filter	$r_k^T r_k$	$r_k^T A_k^{-1} r_k$
Benign	0.31318	1.84589
Intermediate	0.33136	1.80754
Harsh	0.37947	1.72742

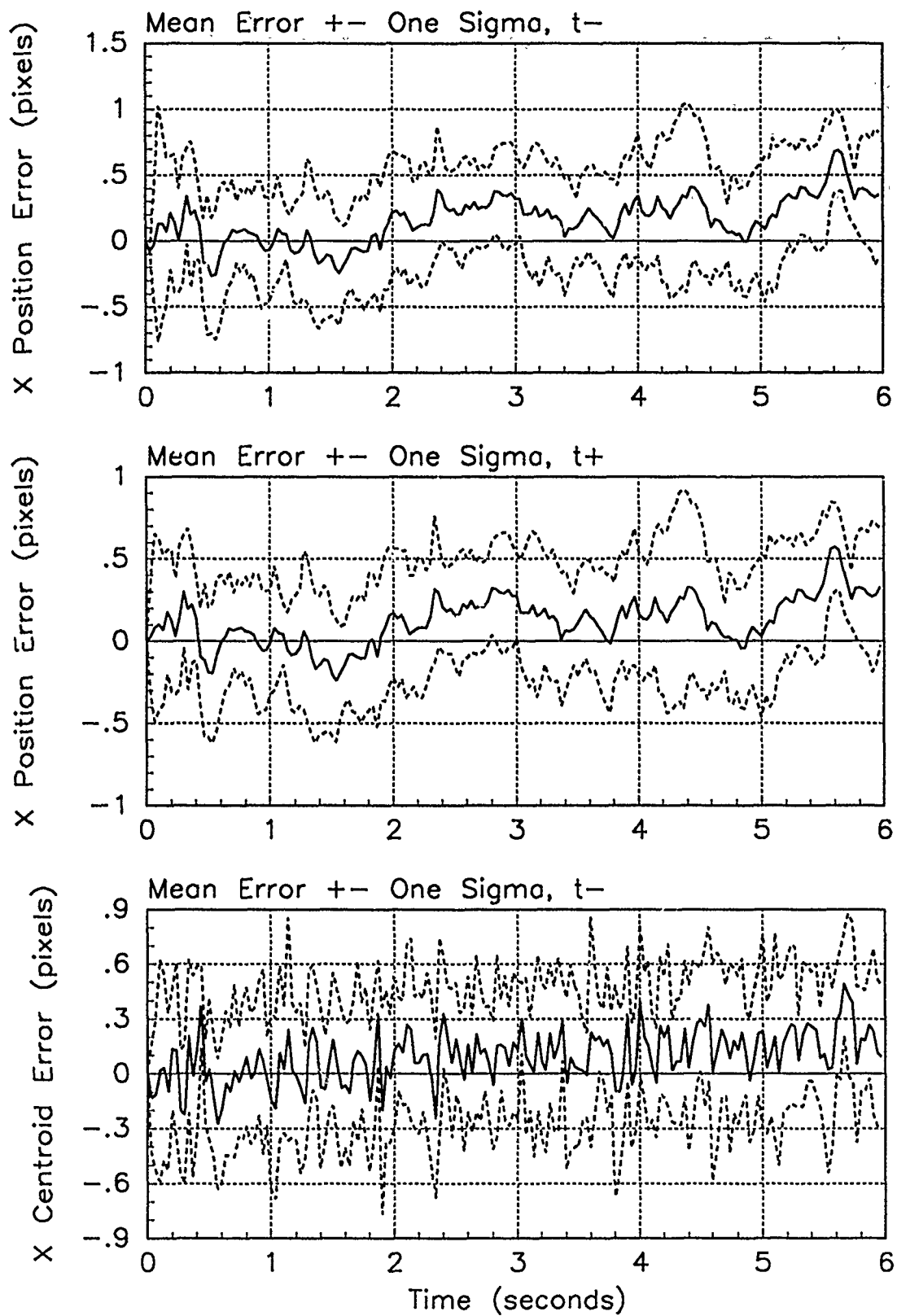


Figure E.11. X-Error Plots; Notch MMAE-2R; PC is 2; Trajectory with $\omega = .01$

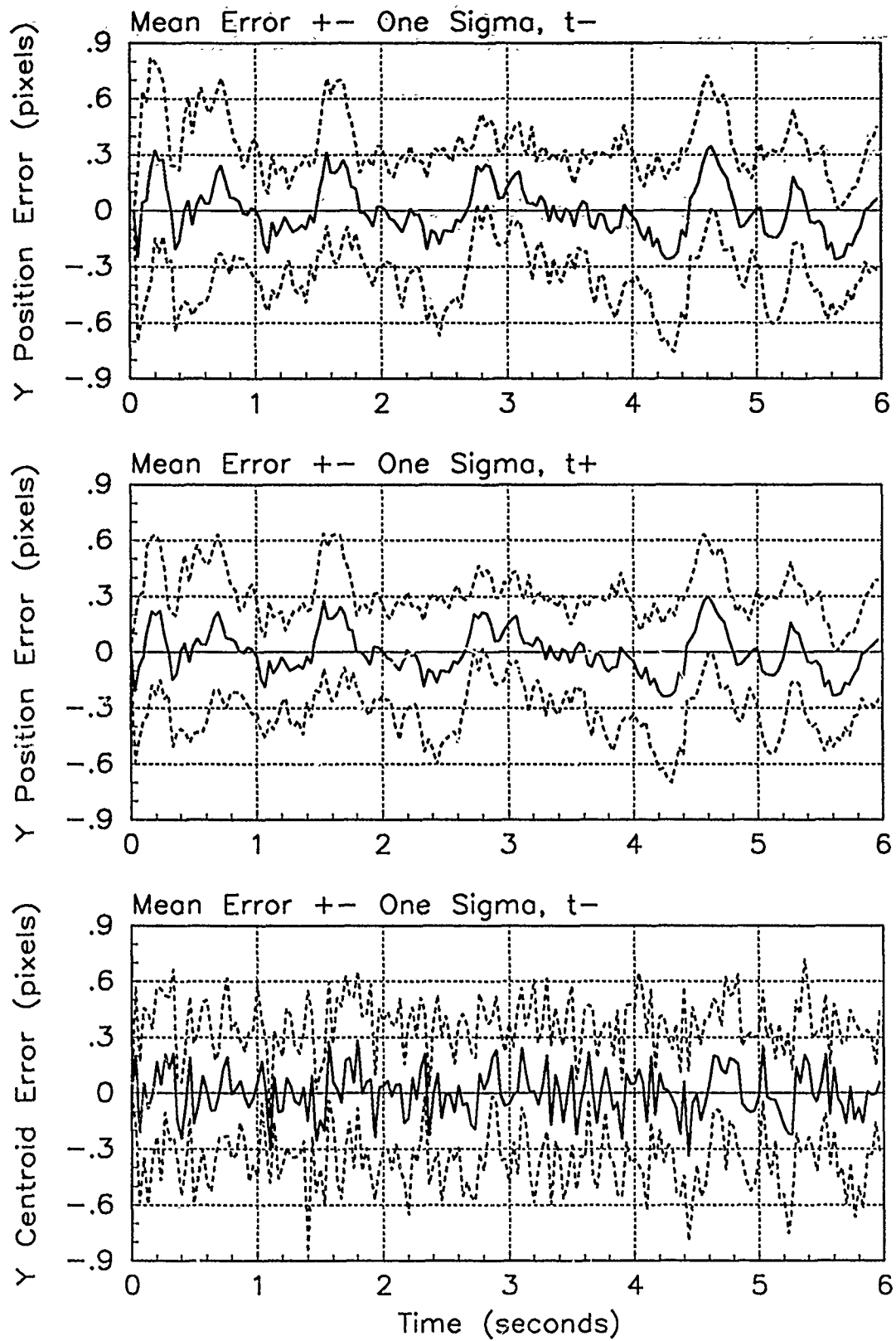


Figure E.12. Y-Error Plots; Notch MMAE-2R; PC is 2; Trajectory with $\omega = .01$

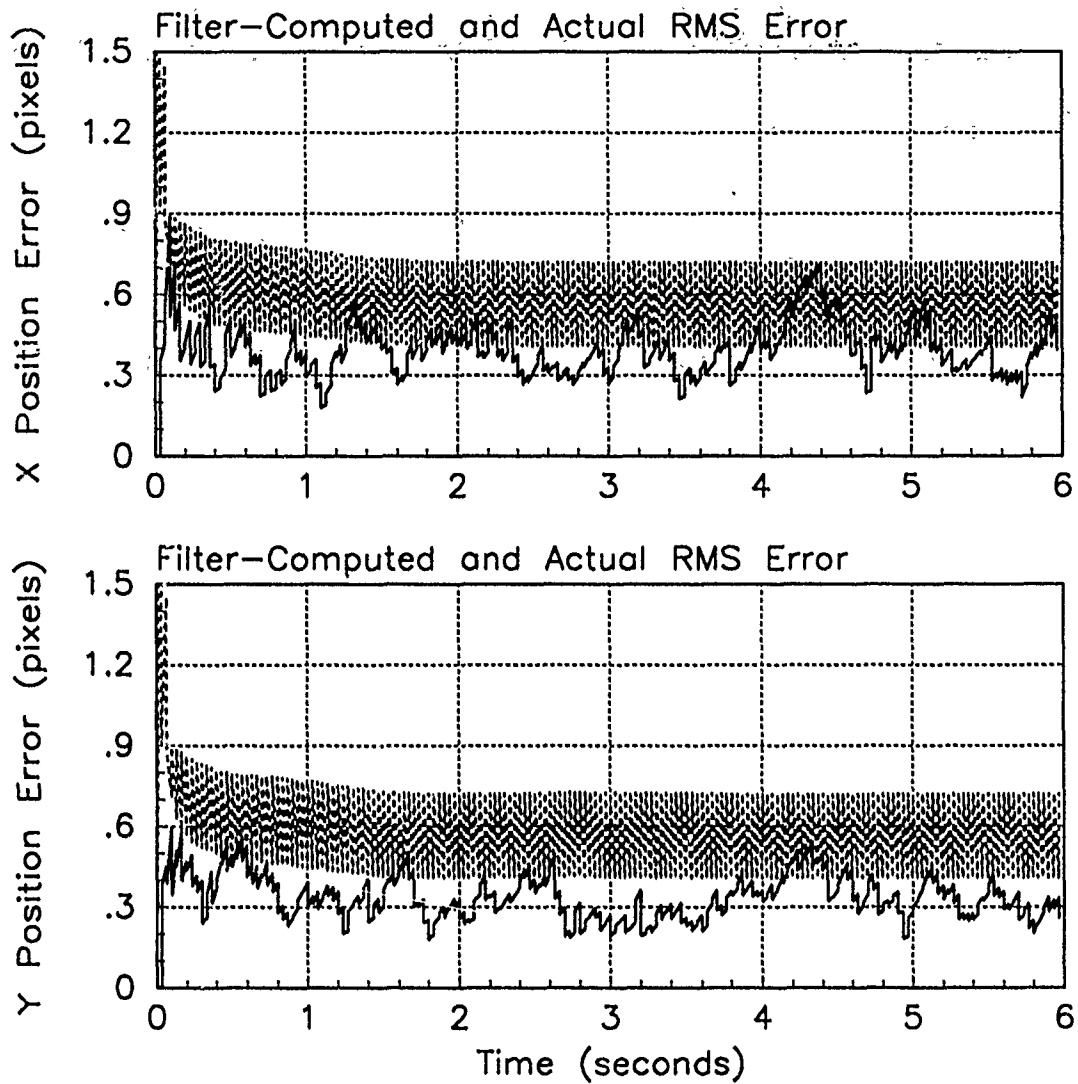


Figure E.13. RMS Error Plots; Notch MMAE-2R; PC is 2; Trajectory with $\omega = 1.32$

Table E.5. Temporal Averages and Residuals; Notch MMAE-2R; PC is 2; Trajectory with $\omega = 1.32$.

Error in:	Mean	σ
$p_x(t_i^-)$	0.16117	0.41127
$p_x(t_i^+)$	0.12256	0.37608
$y_x(t_i^-)$	0.099123	0.38065
$p_y(t_i^-)$	0.015718	0.34806
$p_y(t_i^+)$	0.00032987	0.31627
$y_y(t_i^-)$	0.0018954	0.36466

Filter	$r_k^T r_k$	$r_k^T A_k^{-1} r_k$
Benign	0.39225	2.32115
Intermediate	0.32824	1.78972
Harsh	0.38384	1.74748

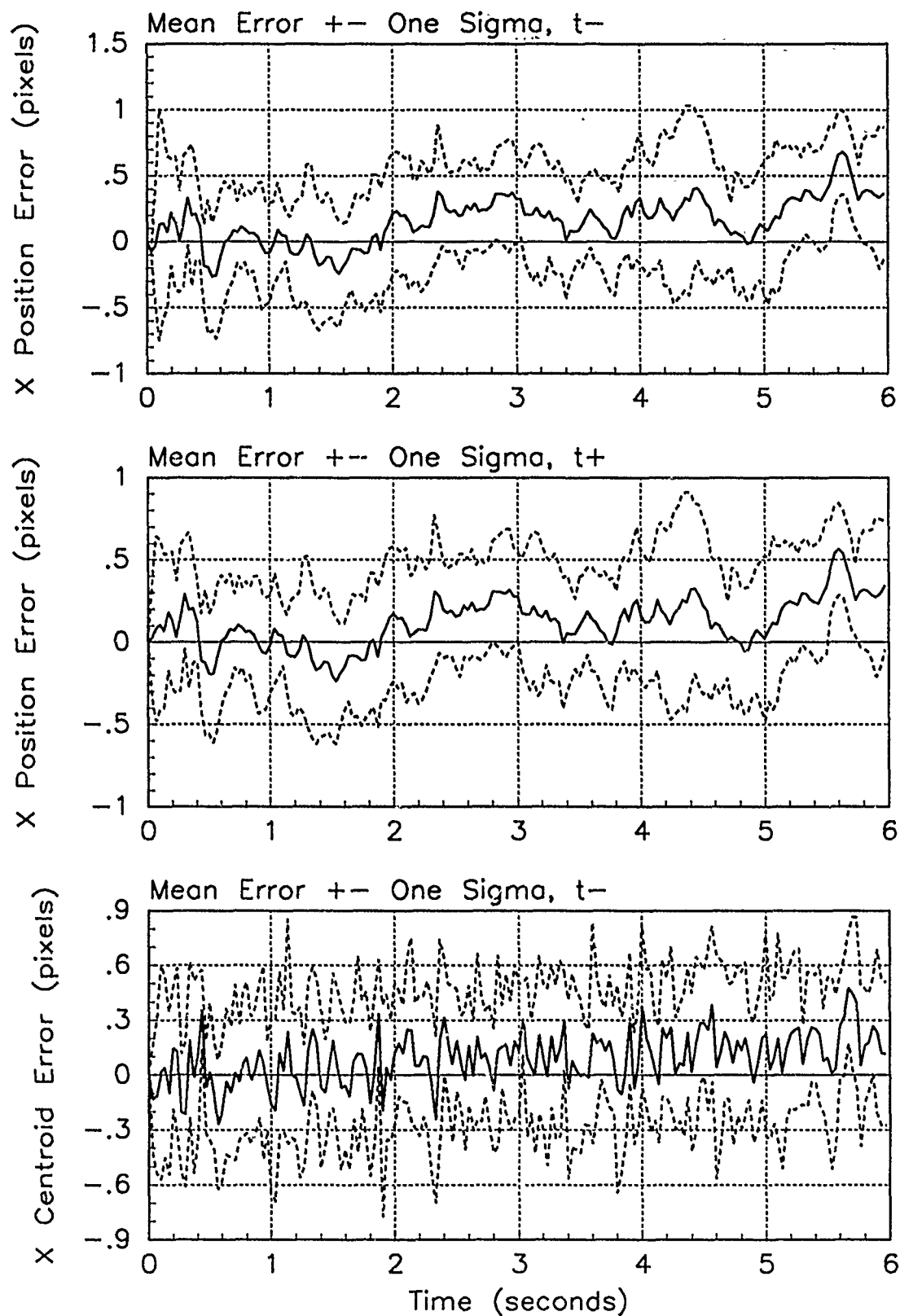


Figure E.14. X-Error Plots; Notch MMAE-2R; PC is 2; Trajectory with $\omega = 1.32$

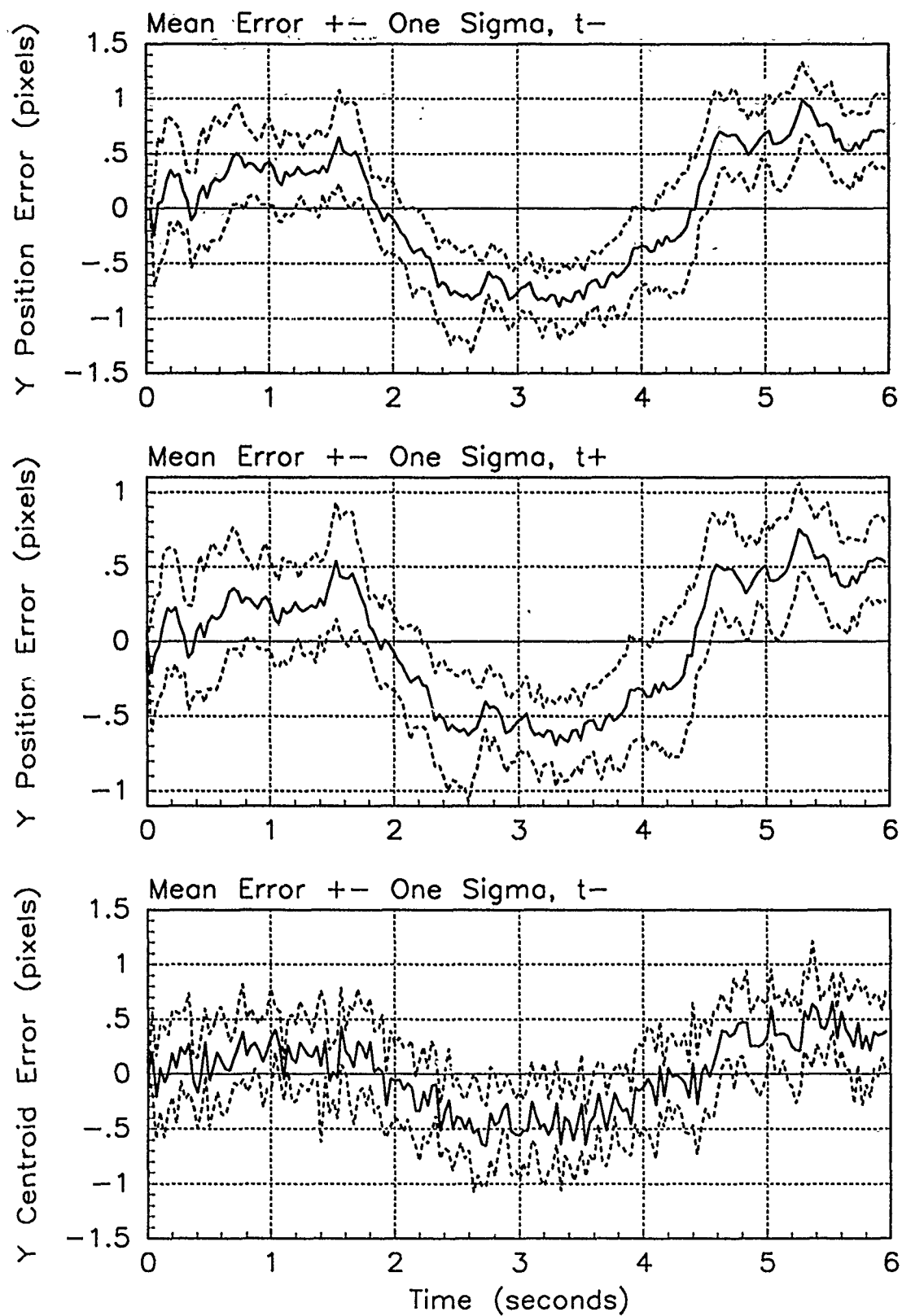


Figure E.15. Y-Error Plots; Notch MMAE-2R; PC is 2; Trajectory with $\omega = 1.32$

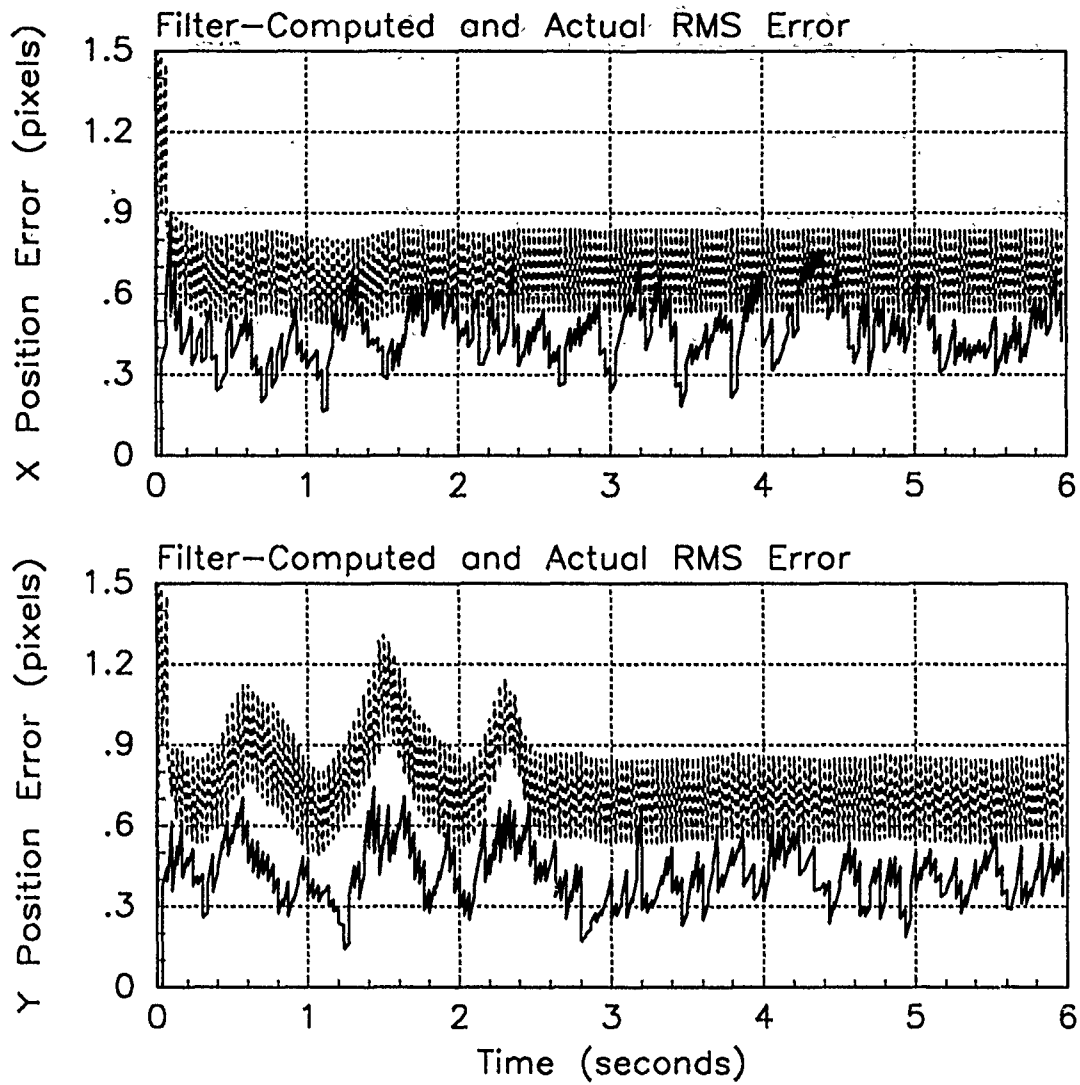


Figure E.16. RMS Error Plots; Notch MMAE-2R; PC is 2; Trajectory with $\omega = 2.8$

Table E.6. Temporal Averages and Residuals; Notch MMAE-2R; PC is 2; Trajectory with $\omega = 2.8$.

Error in:	Mean	σ
$p_x(t_i^-)$	-0.093410	0.49614
$p_x(t_i^+)$	-0.061646	0.42245
$y_x(t_i^-)$	-0.056087	0.41445
$p_y(t_i^-)$	0.059635	0.45977
$p_y(t_i^+)$	0.031220	0.37477
$y_y(t_i^-)$	0.040140	0.40561

Filter	$\mathbf{r}_k^T \mathbf{r}_k$	$\mathbf{r}_k^T \mathbf{A}_k^{-1} \mathbf{r}_k$
Benign	2.62346	15.41430
Intermediate	1.23224	6.79350
Harsh	0.40072	1.82109

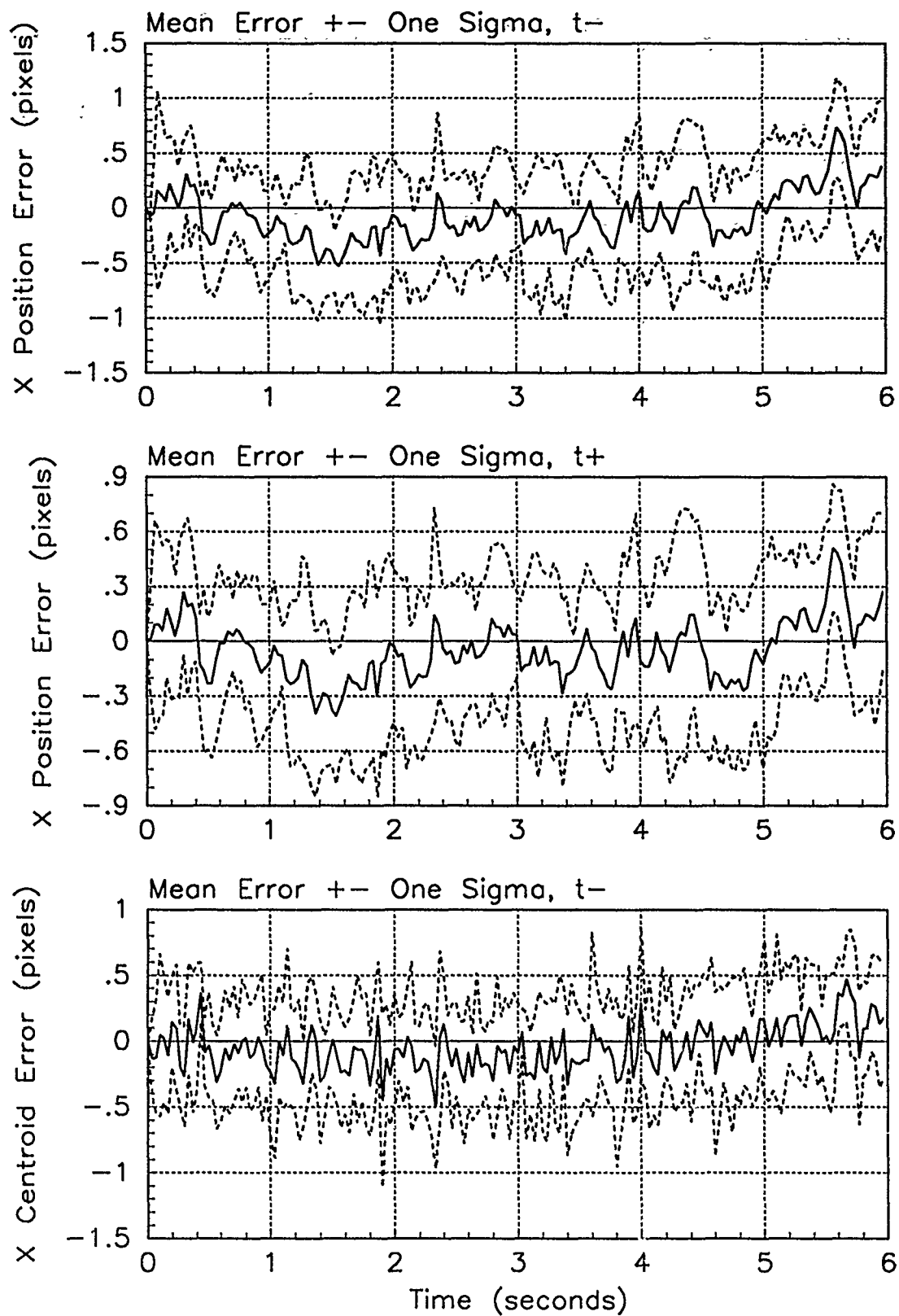


Figure E.17. X-Error Plots; Notch MMAE-2R; PC is 2; Trajectory with $\omega = 2.8$

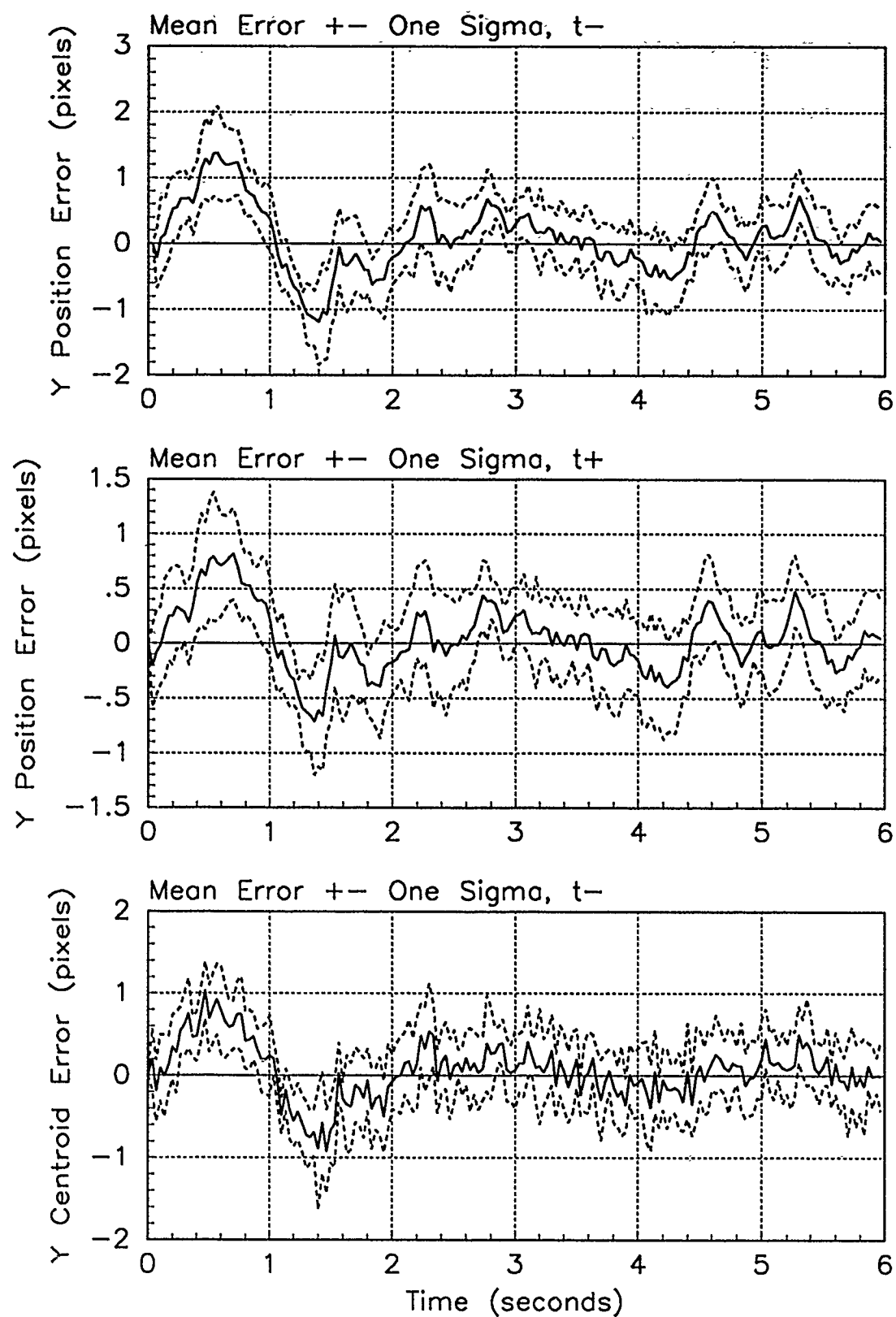


Figure E.18. Y-Error Plots; Notch MMAE-2R; PC is 2; Trajectory with $\omega = 2.8$

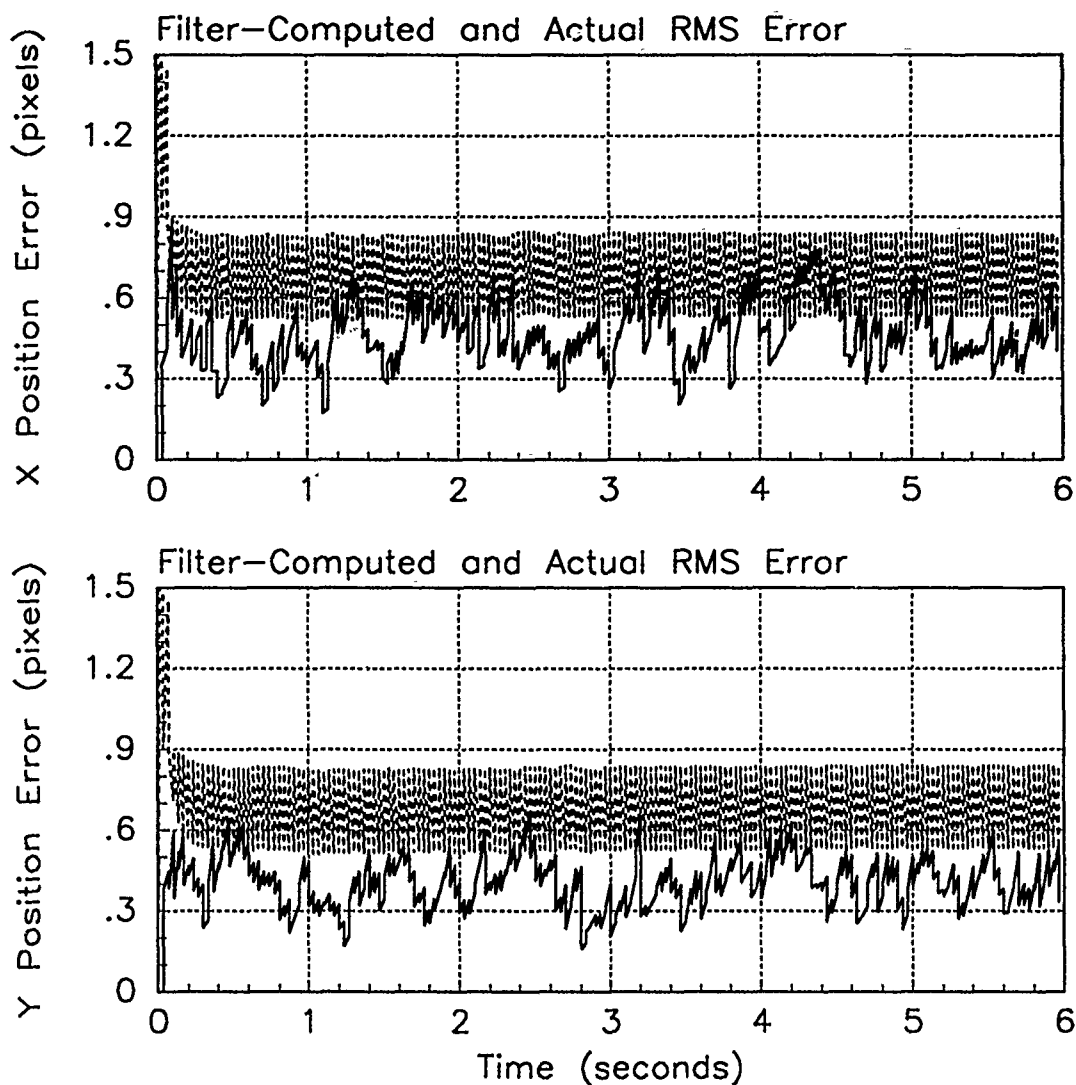


Figure E.19. RMS Error Plots; Notch MMAE-2R; PC is 3; Trajectory with $\omega = .01$

Table E.7. Temporal Averages and Residuals; Notch MMAE-2R; PC is 3; Trajectory with $\omega = .01$.

Error in:	Mean	σ
$p_x(t_i^-)$	-0.057365	0.50271
$p_x(t_i^+)$	-0.030515	0.42743
$y_x(t_i^-)$	-0.027730	0.41730
$p_y(t_i^-)$	-0.0052913	0.43981
$p_y(t_i^+)$	-0.0080775	0.36812
$y_y(t_i^-)$	-0.0028300	0.39639

Filter	$r_k^T r_k$	$r_k^T A_k^{-1} r_k$
Benign	0.31198	1.83872
Intermediate	0.33007	1.80050
Harsh	0.37765	1.71907

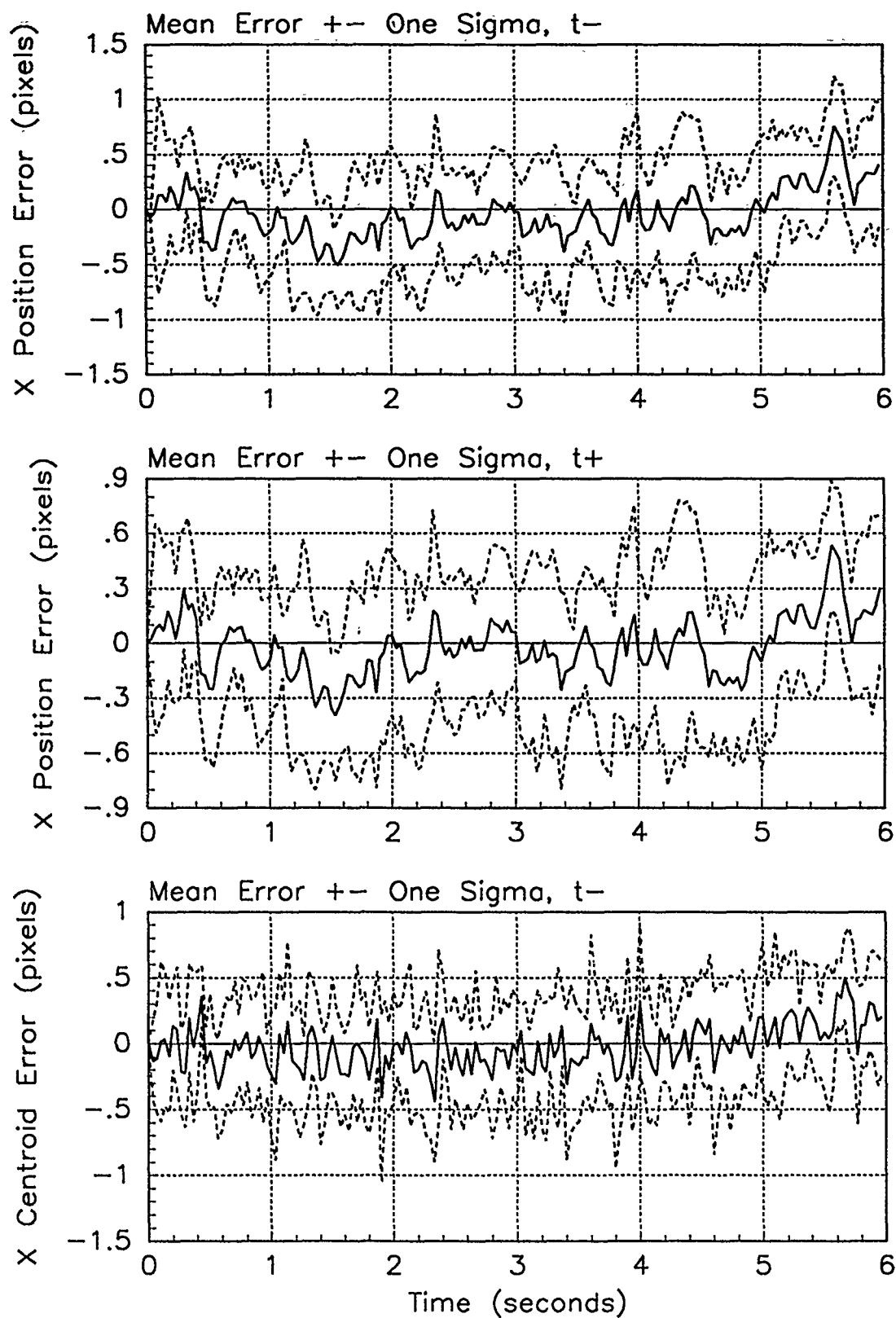


Figure E.20. X-Error Plots; Notch MMAE-2R; PC is 3; Trajectory with $\omega = .01$

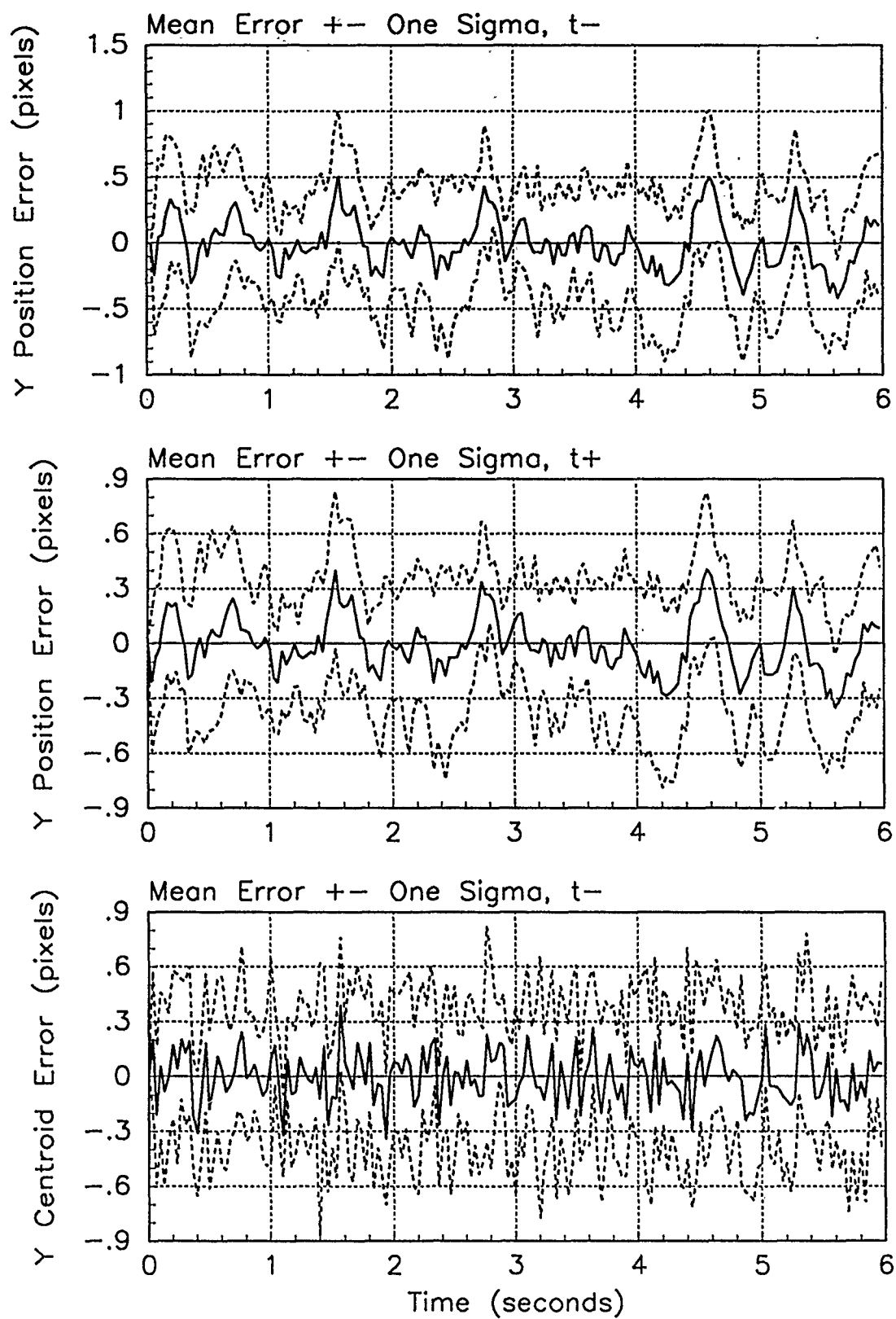


Figure E.21. Y-Error Plots; Notch MMAE-2R; PC is 3; Trajectory with $\omega = .01$

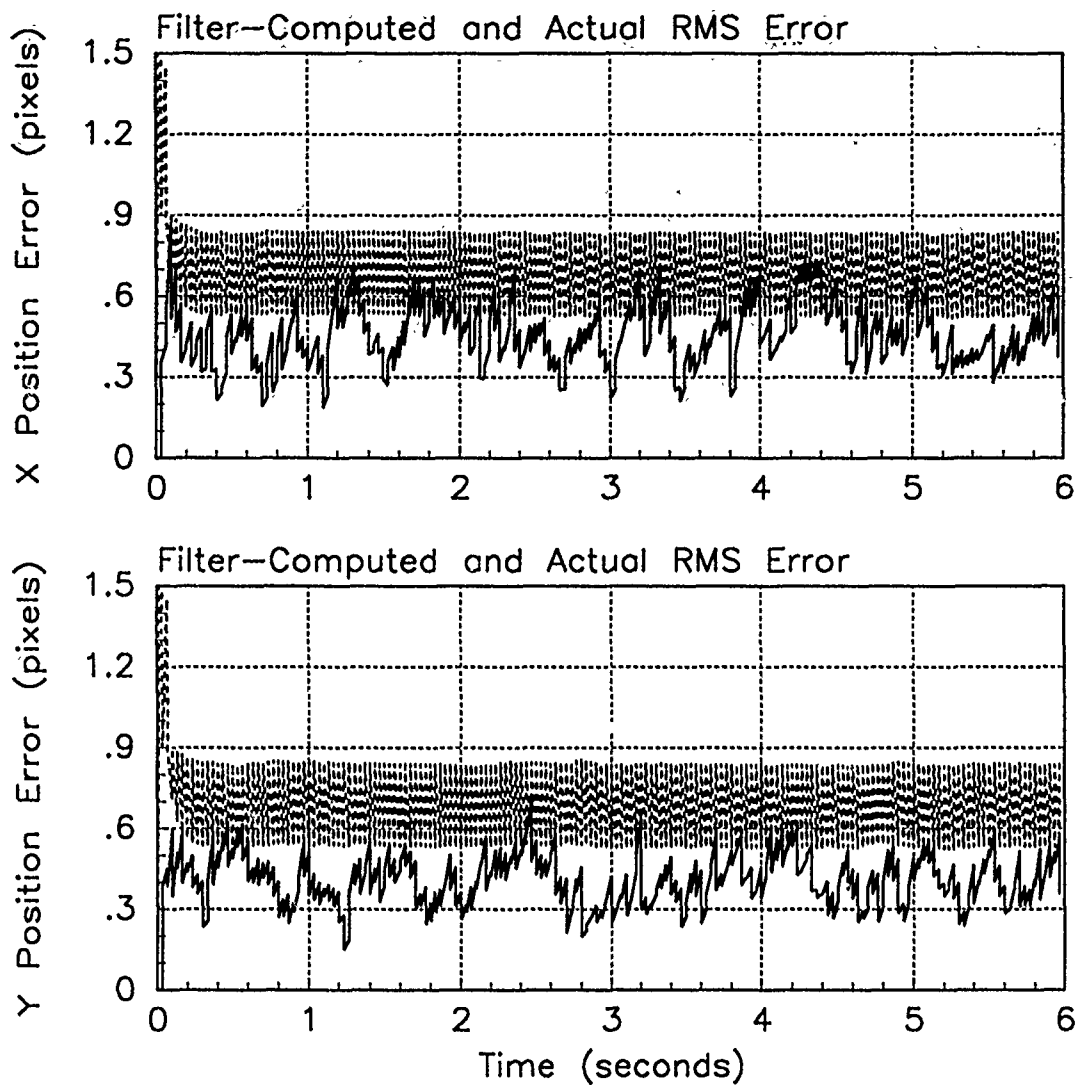


Figure E.22. RMS Error Plots; Notch MMAE-2R; PC is 3; Trajectory with $\omega = 1.32$

Table E.8. Temporal Averages and Residuals; Notch MMAE-2R; PC is 3; Trajectory with $\omega = 1.32$.

Error in:	Mean	σ
$p_x(t_i^-)$	-0.091315	0.49737
$p_x(t_i^+)$	-0.057604	0.42162
$y_x(t_i^-)$	-0.056153	0.41397
$p_y(t_i^-)$	0.0056087	0.44451
$p_y(t_i^+)$	-0.0092533	0.36878
$y_y(t_i^-)$	-0.00012055	0.40002

Filter	$r_k^T r_k$	$r_k^T A_k^{-1} r_k$
Benign	0.39661	2.34752
Intermediate	0.33319	1.81734
Harsh	0.38992	1.77566

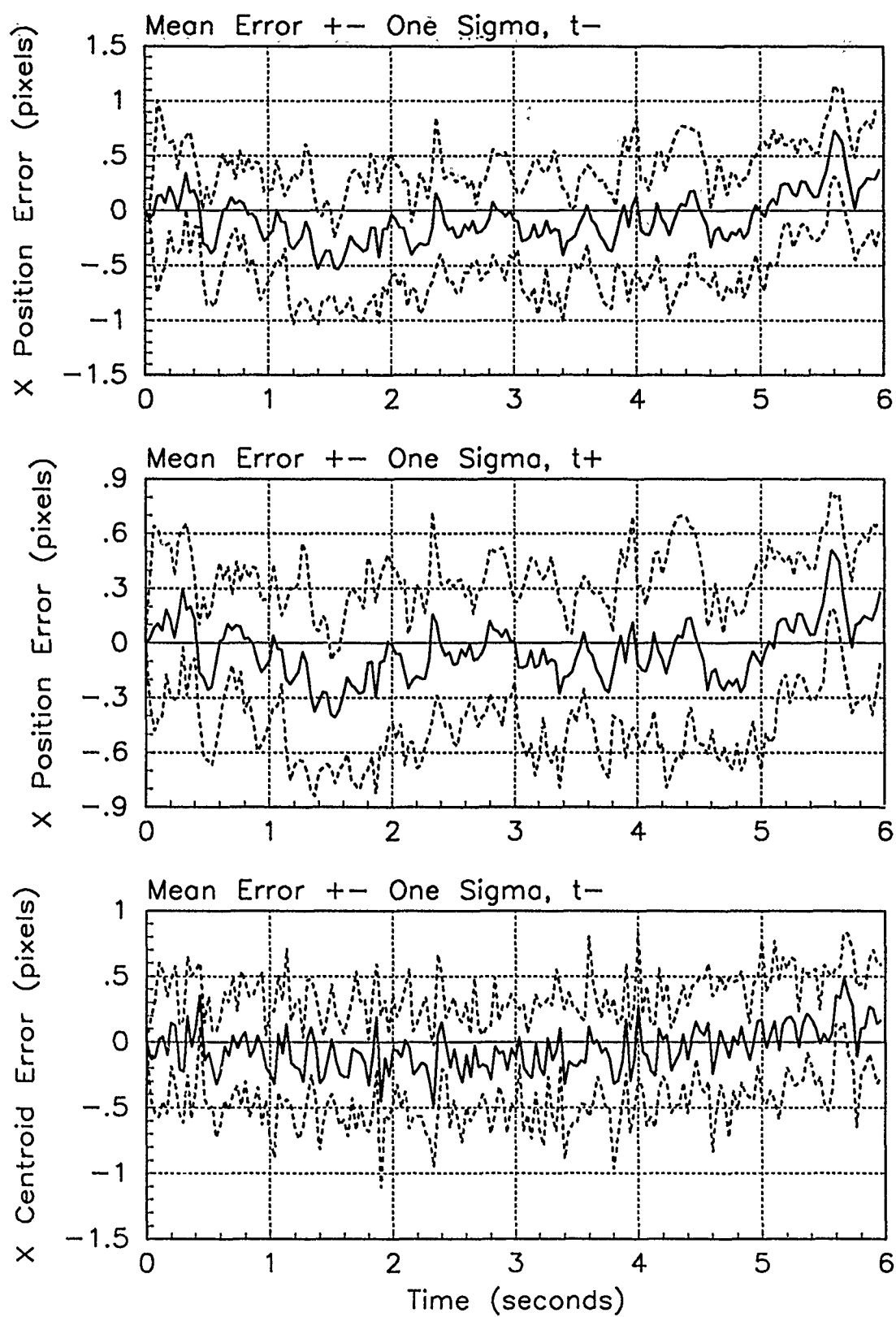


Figure E.23. X-Error Plots; Notch MMAE-2R; PC is 3; Trajectory with $\omega = 1.32$

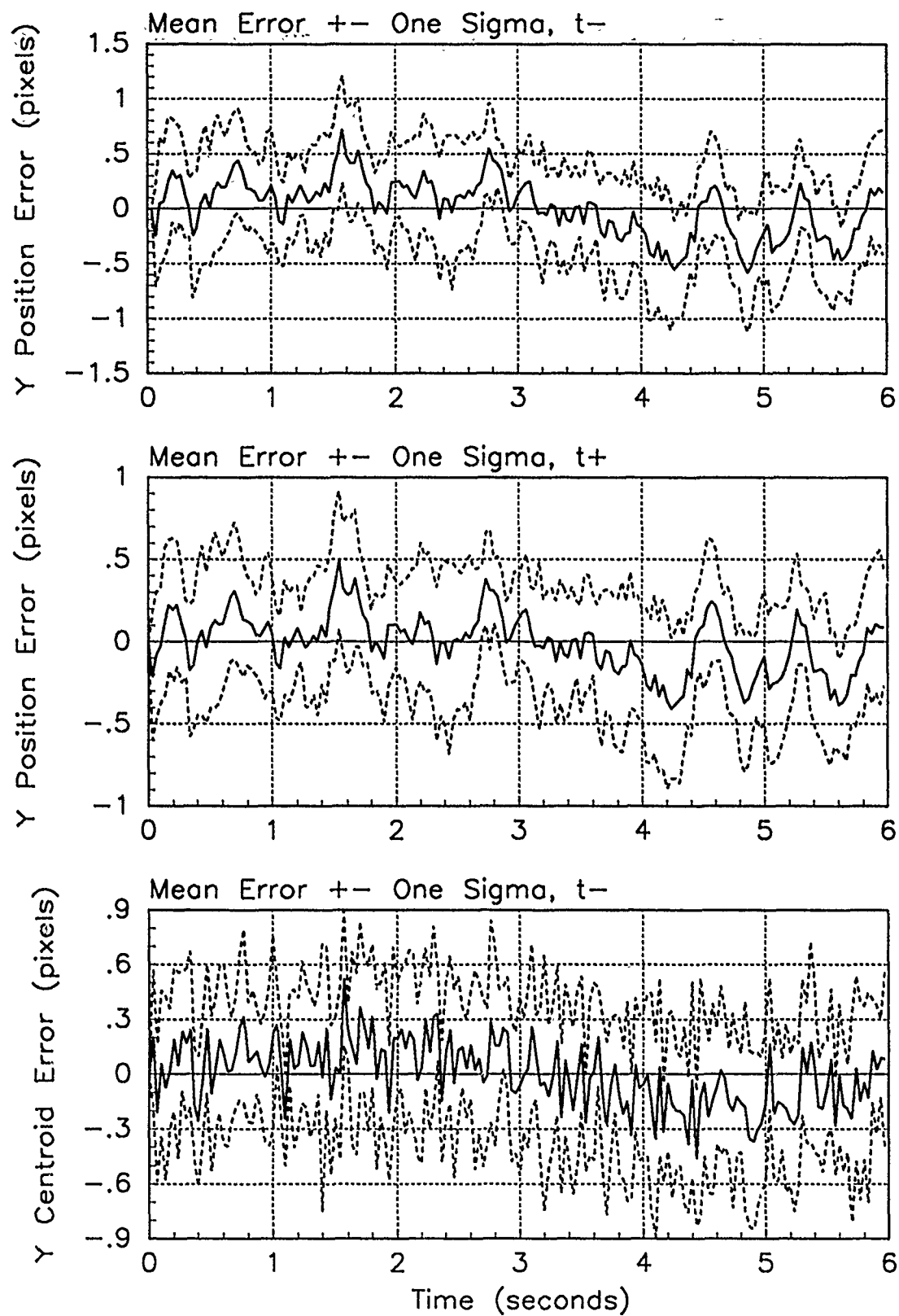


Figure E.24. Y-Error Plots; Notch MMAE-2R; PC is 3; Trajectory with $\omega = 1.32$

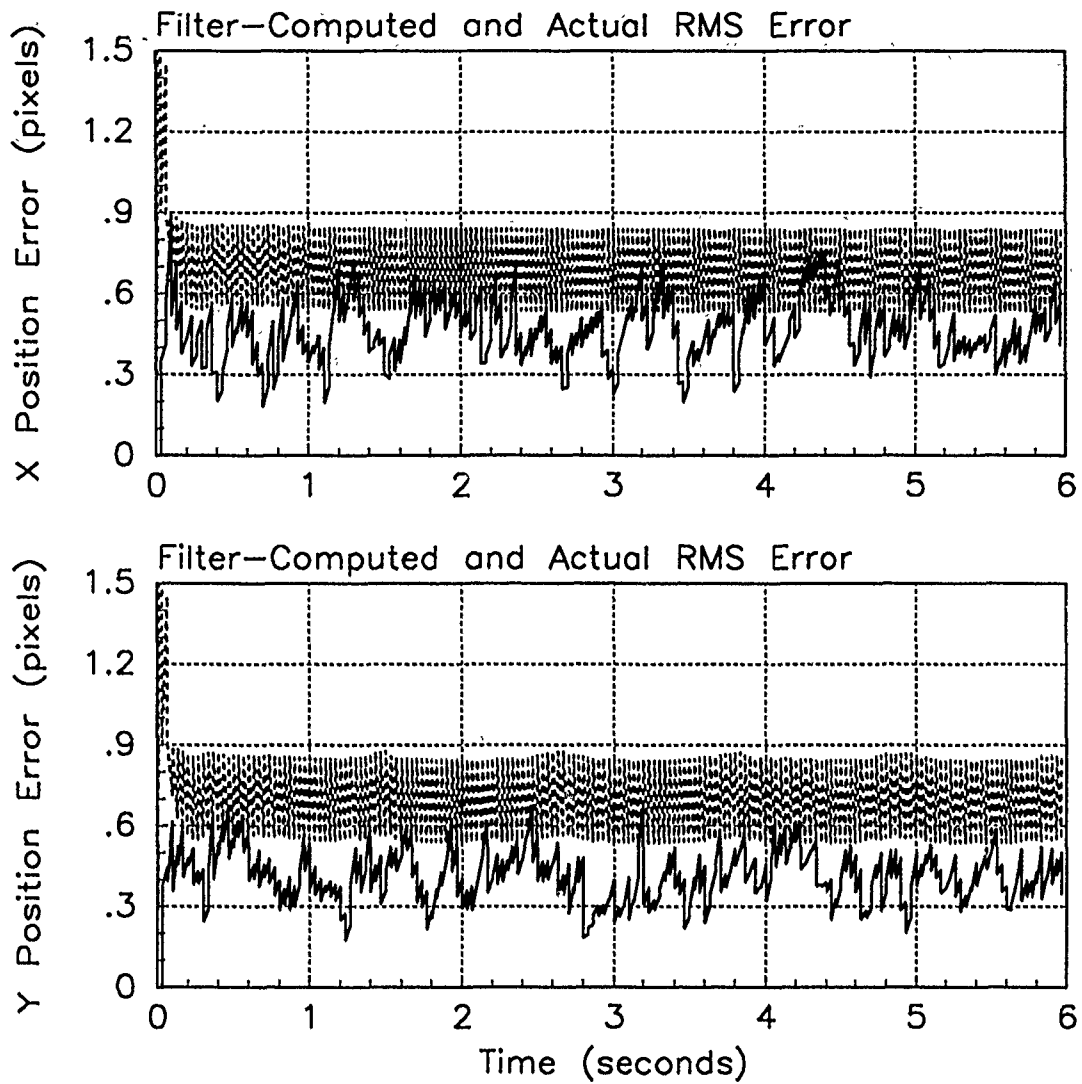


Figure E.25. RMS Error Plots; Notch MMAE-2R; PC is 3; Trajectory with $\omega = 2.8$

Table E.9. Temporal Averages and Residuals; Notch MMAE-2R; PC is 3; Trajectory with $\omega = 2.8$.

Error in:	Mean	σ
$p_x(t_i^-)$	-0.10444	0.51073
$p_x(t_i^+)$	-0.067960	0.42973
$y_x(t_i^-)$	-0.069137	0.41934
$p_y(t_i^-)$	0.064390	0.45039
$p_y(t_i^+)$	0.026317	0.37165
$y_y(t_i^-)$	0.044831	0.40208

Filter	$\mathbf{r}_k^T \mathbf{r}_k$	$\mathbf{r}_k^T \mathbf{A}_k^{-1} \mathbf{r}_k$
Benign	2.20156	12.84532
Intermediate	1.23268	6.79588
Harsh	0.40067	1.82089

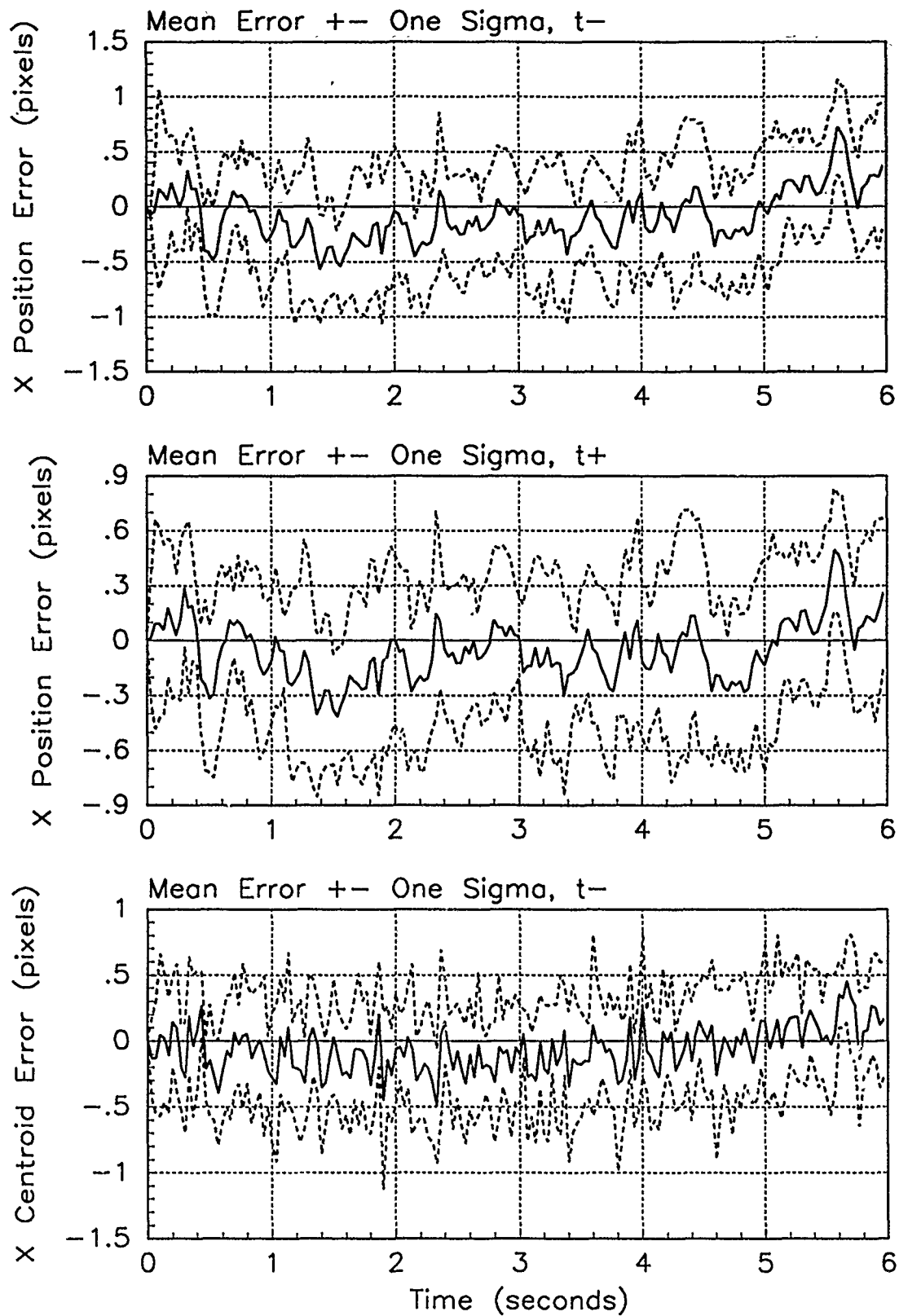


Figure E.26. X-Error Plots; Notch MMAE-2R; PC is 3; Trajectory with $\omega = 2.8$

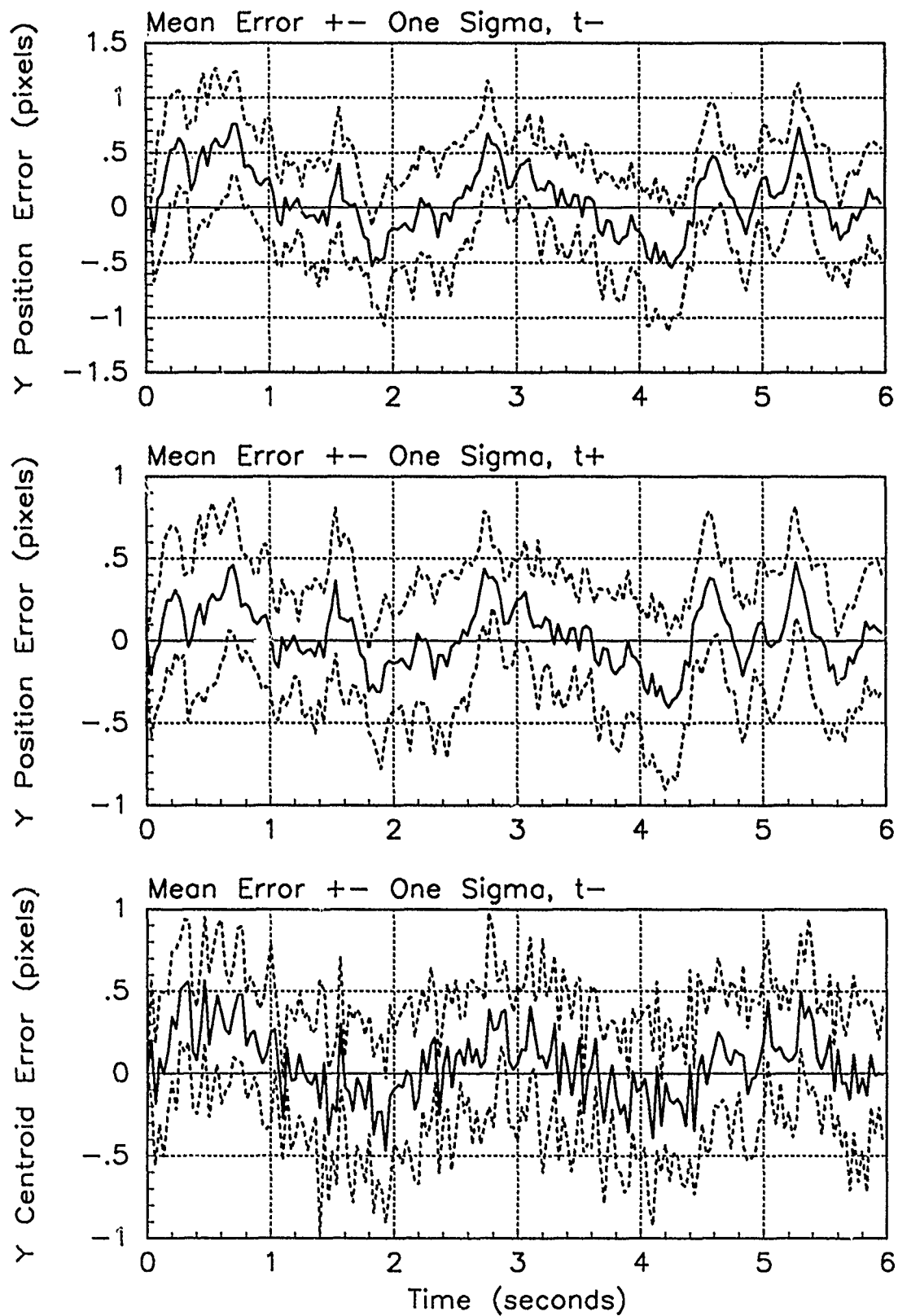


Figure E.27. Y-Error Plots; Notch MMAE-2R; PC is 3; Trajectory with $\omega = 2.8$

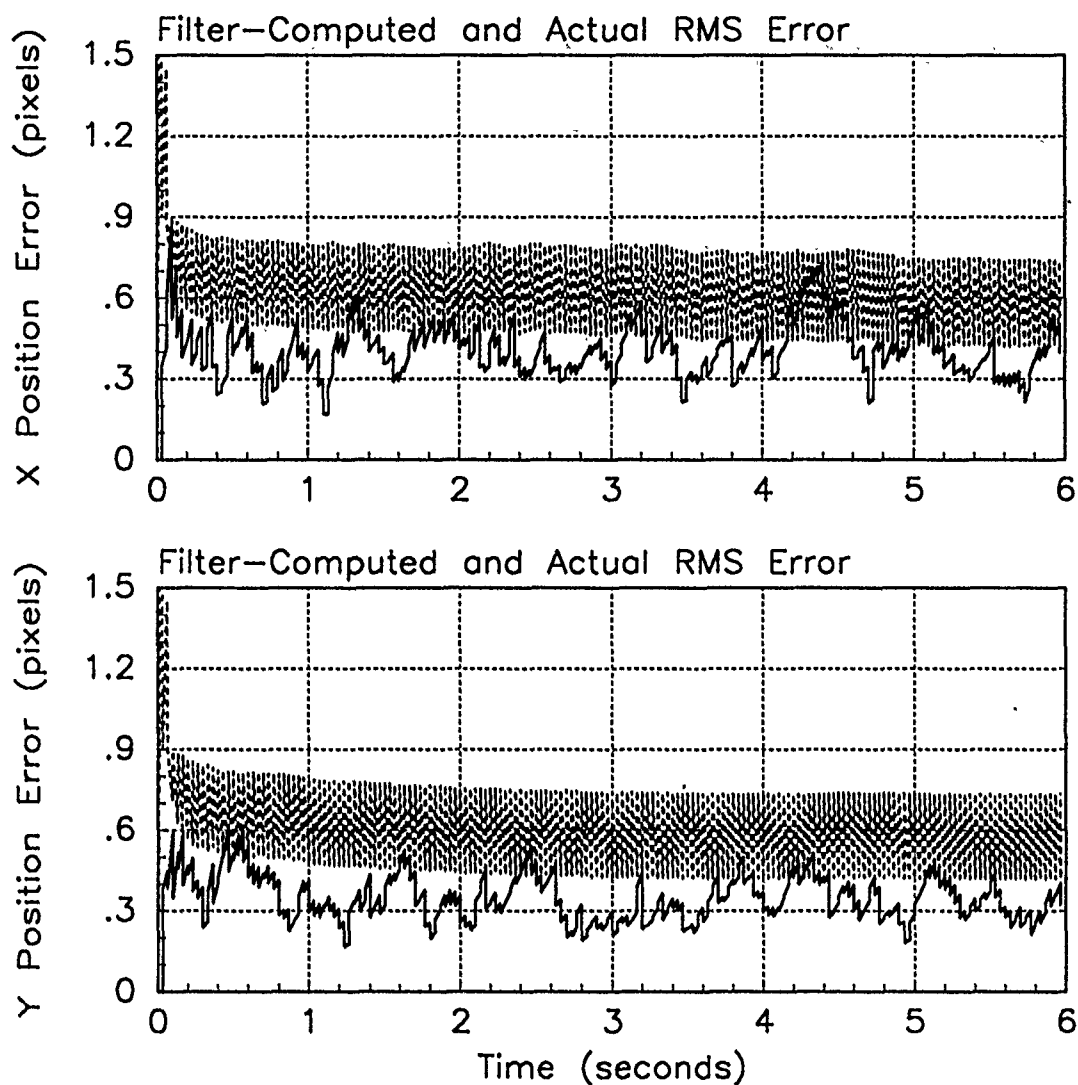


Figure E.28. RMS Error Plots; Notch MMAE-2R; PC is 4; Trajectory with $\omega = .01$

Table E.10. Temporal A and Residuals; Notch MMAE-2R; PC is 4; Trajectory with $\omega = .0$

Error in:	Mean	σ
$p_x(t_i^-)$	0.097821	0.42738
$p_x(t_i^+)$	0.081477	0.38664
$y_x(t_i^-)$	0.065413	0.38750
$p_y(t_i^-)$	0.0036758	0.36175
$p_y(t_i^+)$	0.0039819	0.32572
$y_y(t_i^-)$	0.0084724	0.37170

Filter	$r_k^T r_k$	$r_k^T A_k^{-1} r_k$
Benign	0.31476	1.85570
Intermediate	0.33195	1.81098
Harsh	0.38049	1.73231

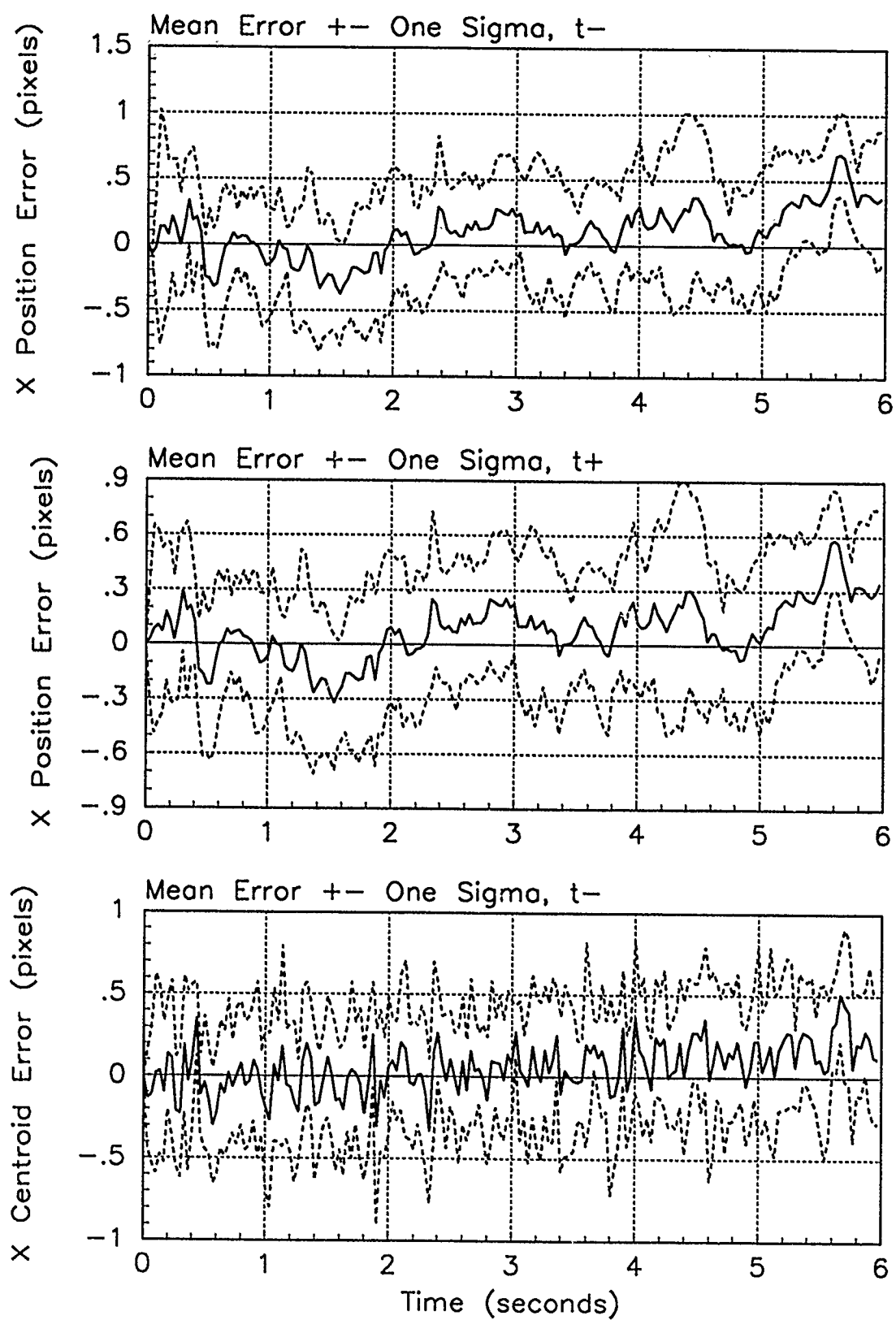


Figure E.29. X-Error Plots; Notch MMAE-2R; PC is 4; Trajectory with $\omega = .01$

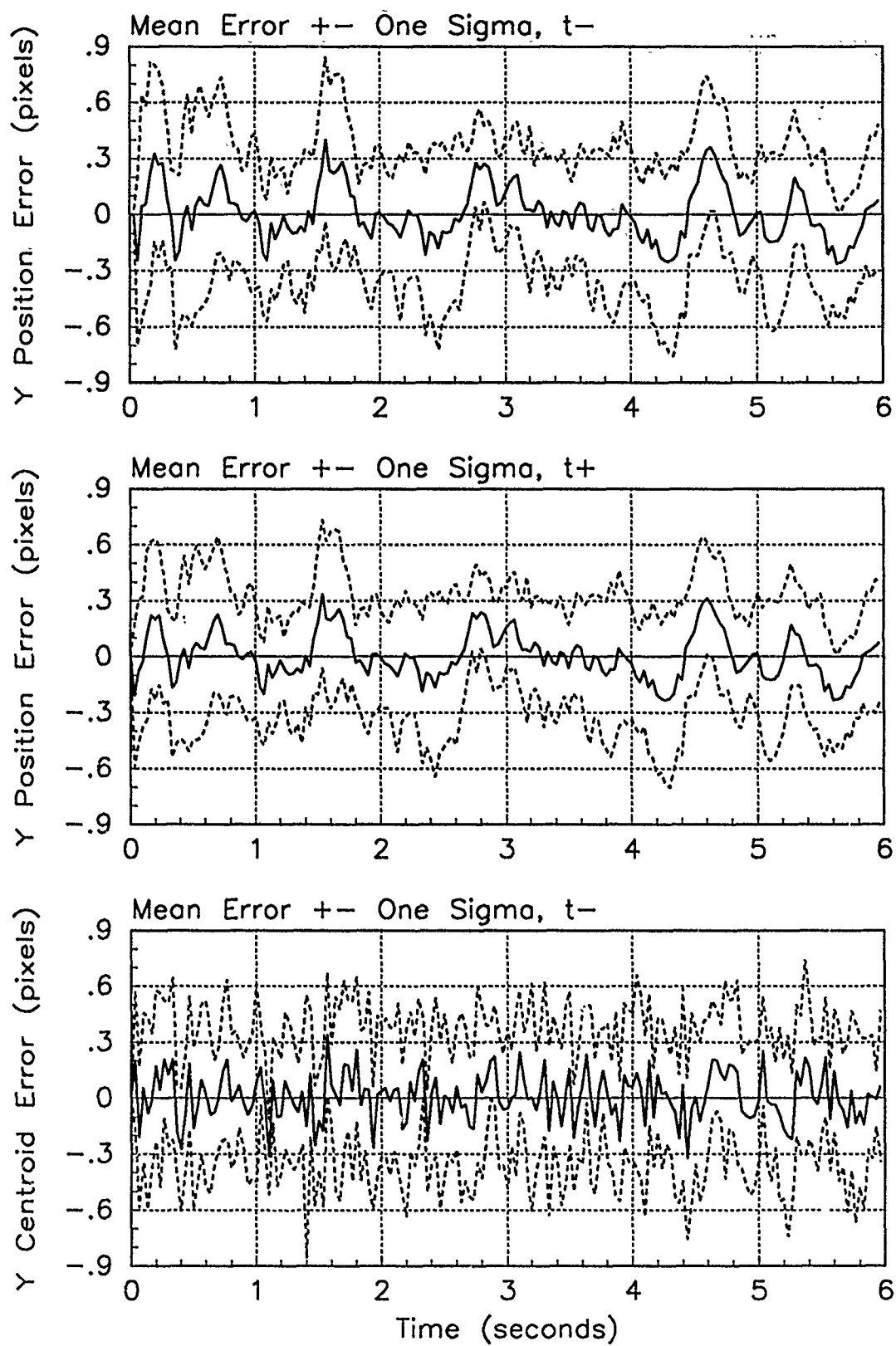


Figure E.30. Y-Error Plots; Notch MMAE-2R; PC is 4; Trajectory with $\omega = .01$

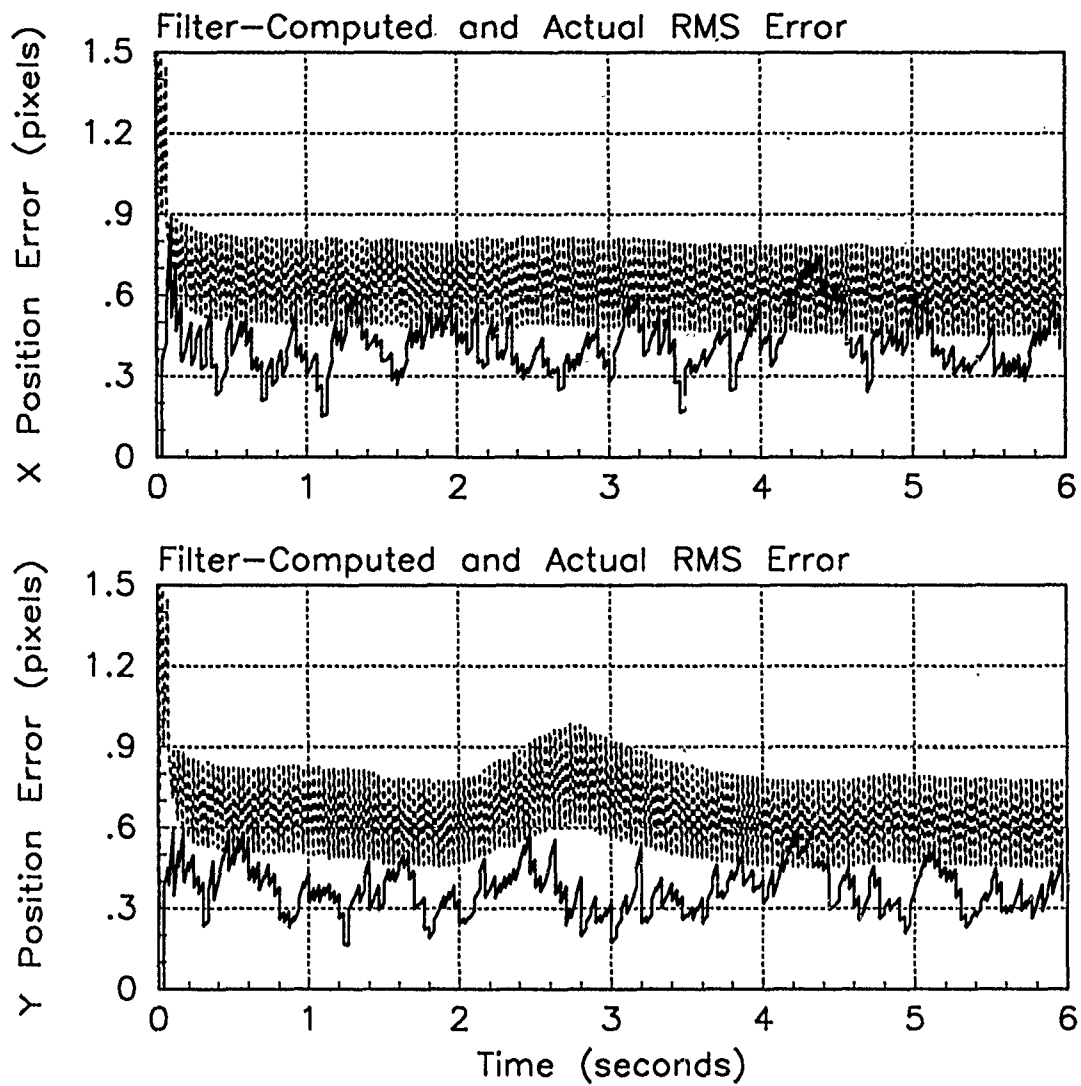


Figure E.31. RMS Error Plots; Notch MMAE-2R; PC is 4; Trajectory with $\omega = 1.32$

Table E.11. Temporal Averages and Residuals; Notch MMAE-2R; PC is 4; Trajectory with $\omega = 1.32$.

Error in:	Mean	σ
$p_x(t_i^-)$	-0.025702	0.44396
$p_x(t_i^+)$	-0.017072	0.39586
$y_x(t_i^-)$	-0.0097122	0.39111
$p_y(t_i^-)$	-0.014490	0.38864
$p_y(t_i^+)$	-0.022636	0.34311
$y_y(t_i^-)$	-0.014081	0.37820

Filter	$\mathbf{r}_k^T \mathbf{r}_k$	$\mathbf{r}_k^T \mathbf{A}_k^{-1} \mathbf{r}_k$
Benign	0.39773	2.35434
Intermediate	0.33460	1.82528
Harsh	0.39186	1.78481

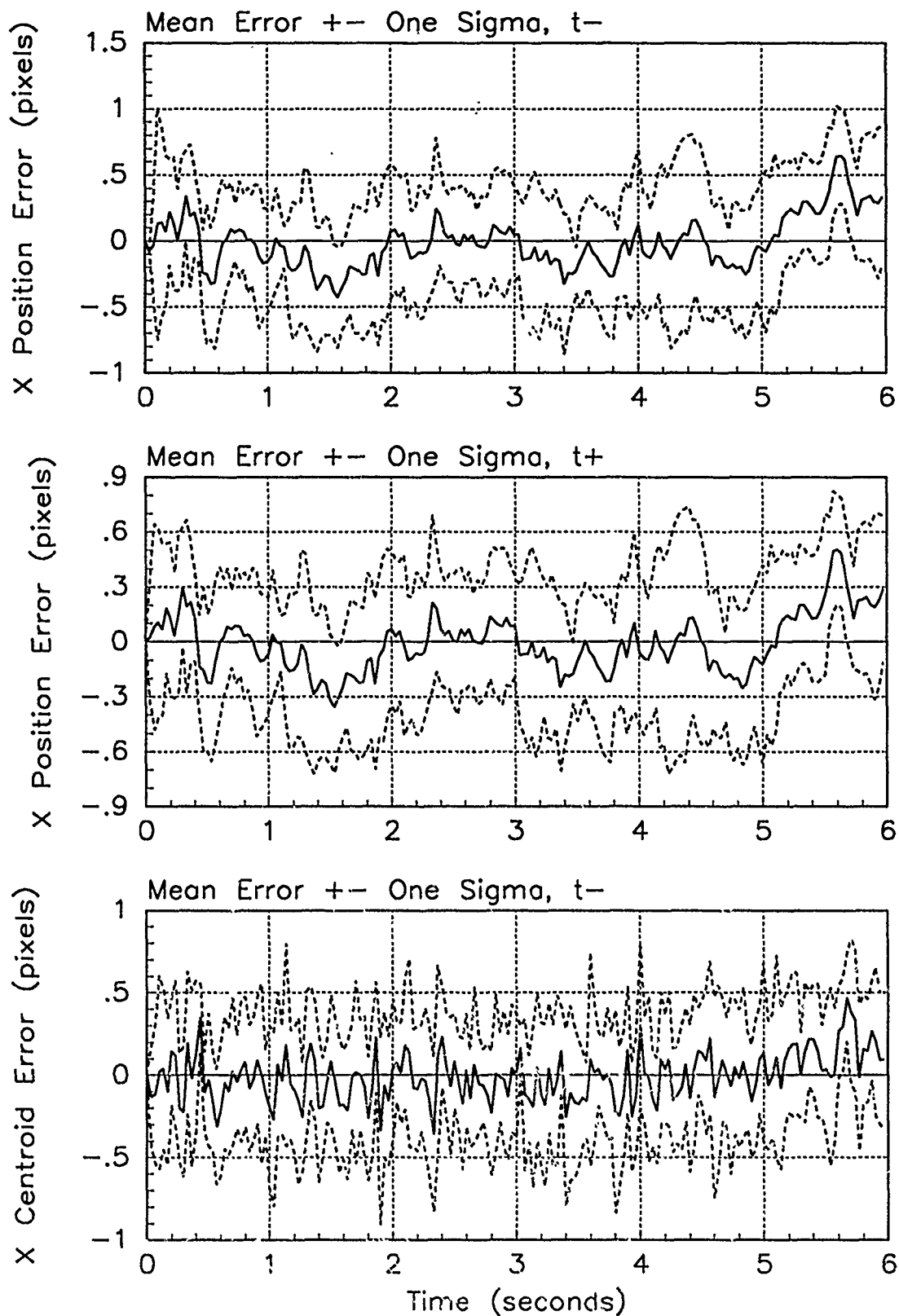


Figure E.32. X-Error Plots; Notch MMAE-2R; PC is 4; Trajectory with $\omega = 1.32$

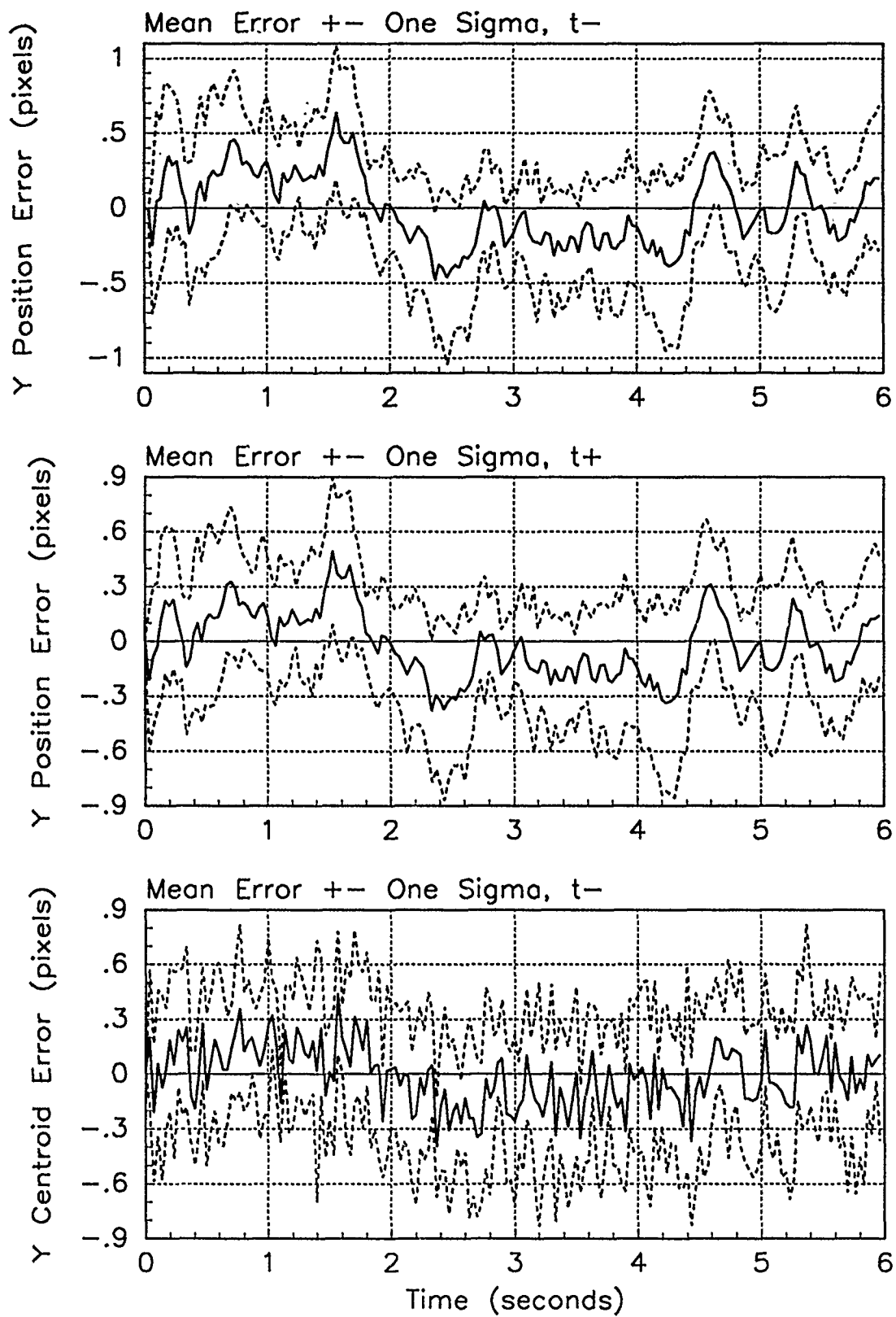


Figure E.33. Y-Error Plots; Notch MMAE-2R; PC is 4; Trajectory with $\omega = 1.32$

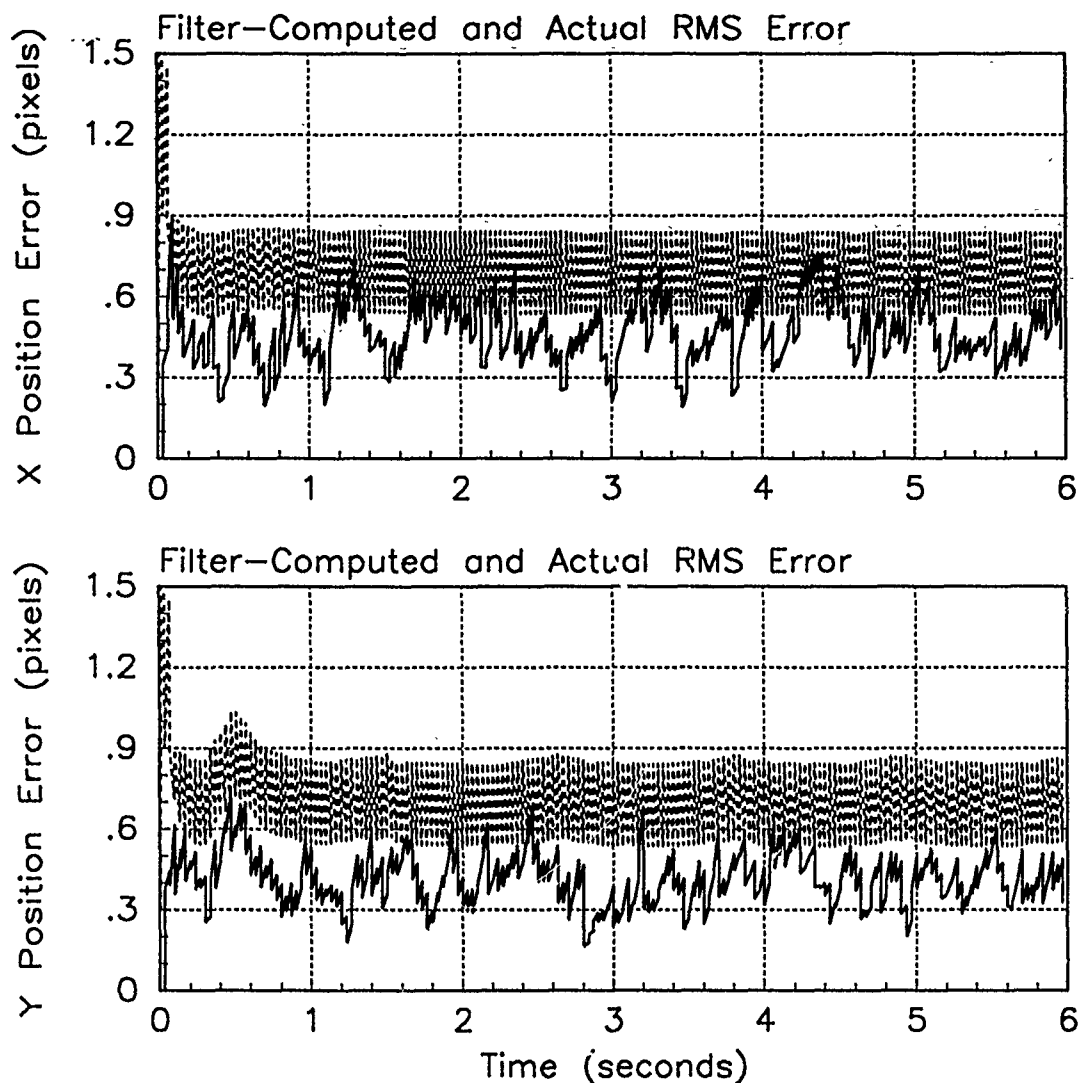


Figure E.34. RMS Error Plots; Notch MMAE-2R; PC is 4; Trajectory with $\omega = 2.8$

Table E.12. Temporal Averages and Residuals; Notch MMAE-2R; PC is 4; Trajectory with $\omega = 2.8$.

Error in:	Mean	σ
$p_x(t_i^-)$	-0.093356	0.50926
$p_x(t_i^+)$	-0.057692	0.42890
$y_x(t_i^-)$	-0.058363	0.41973
$p_y(t_i^-)$	0.085914	0.45259
$p_y(t_i^+)$	0.043384	0.37338
$y_y(t_i^-)$	0.062324	0.40152

Filter	$\mathbf{r}_k^T \mathbf{r}_k$	$\mathbf{r}_k^T \mathbf{A}_k^{-1} \mathbf{r}_k$
Benign	2.21312	12.91275
Intermediate	1.23460	6.80630
Harsh	0.40148	1.82447

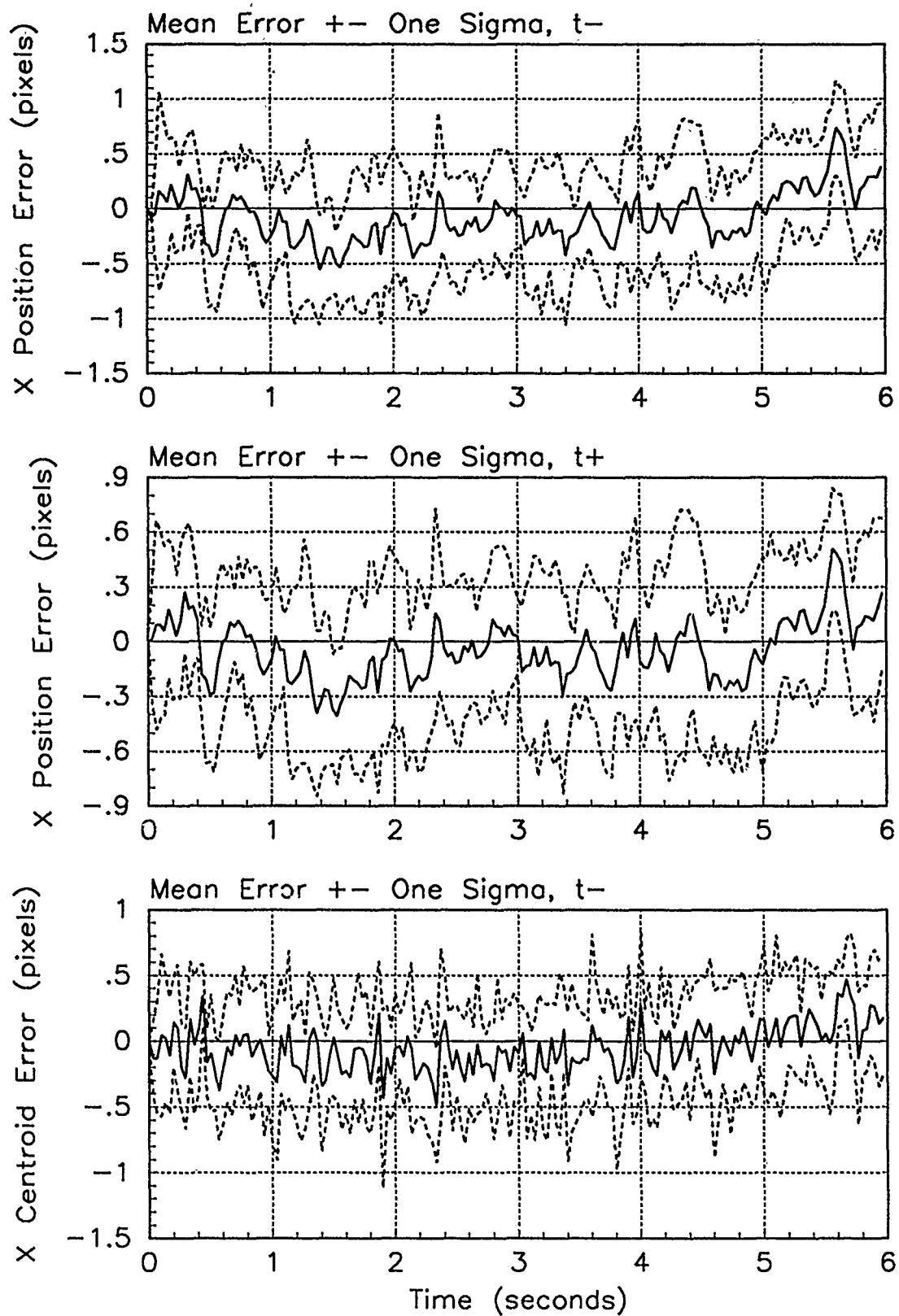


Figure E.35. X-Error Plots; Notch MMAE-2R; PC is 4; Trajectory with $\omega = 2.8$

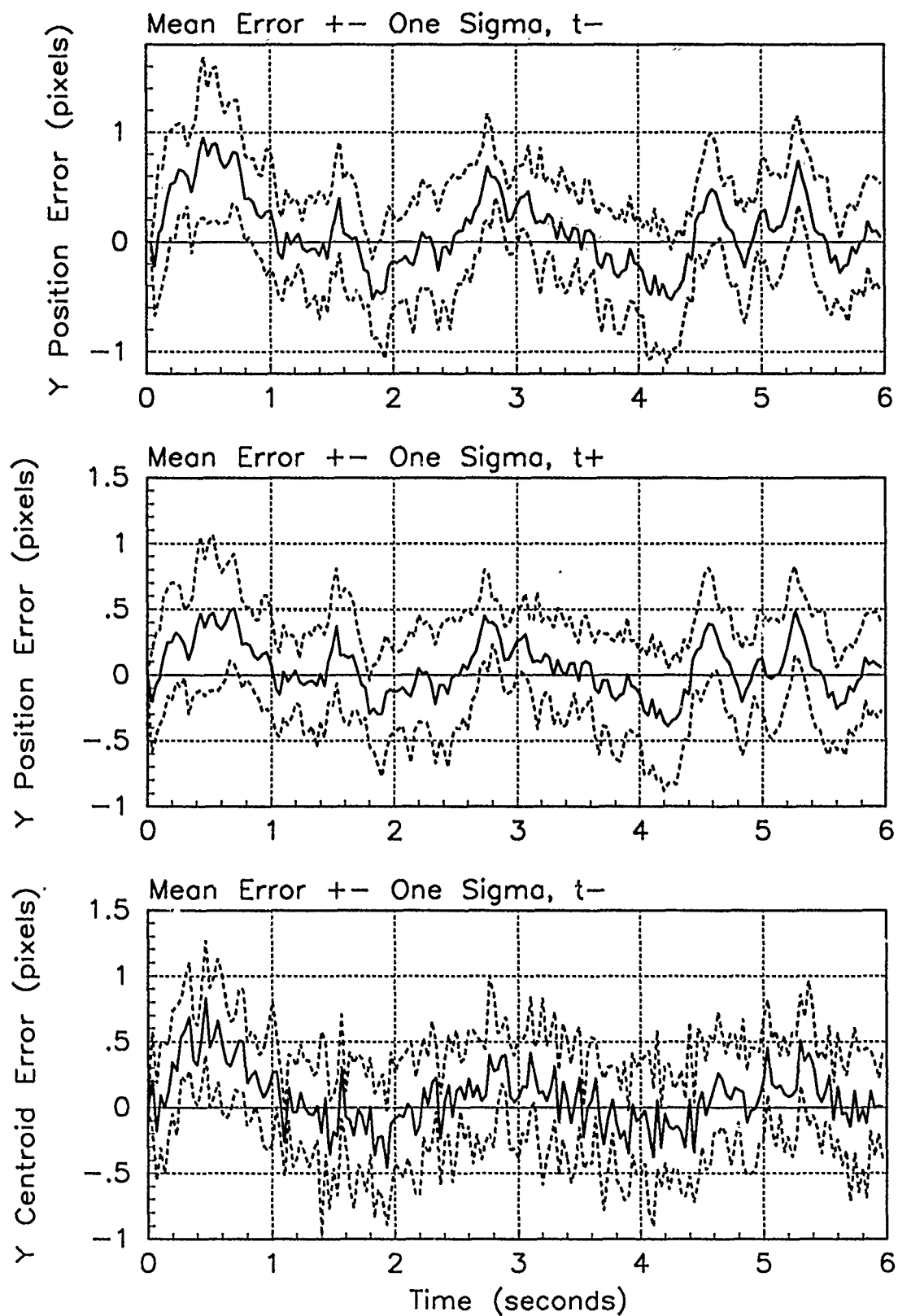


Figure E.36. Y-Error Plots; Notch MMAE-2R; PC is 4; Trajectory with $\omega = 2.8$

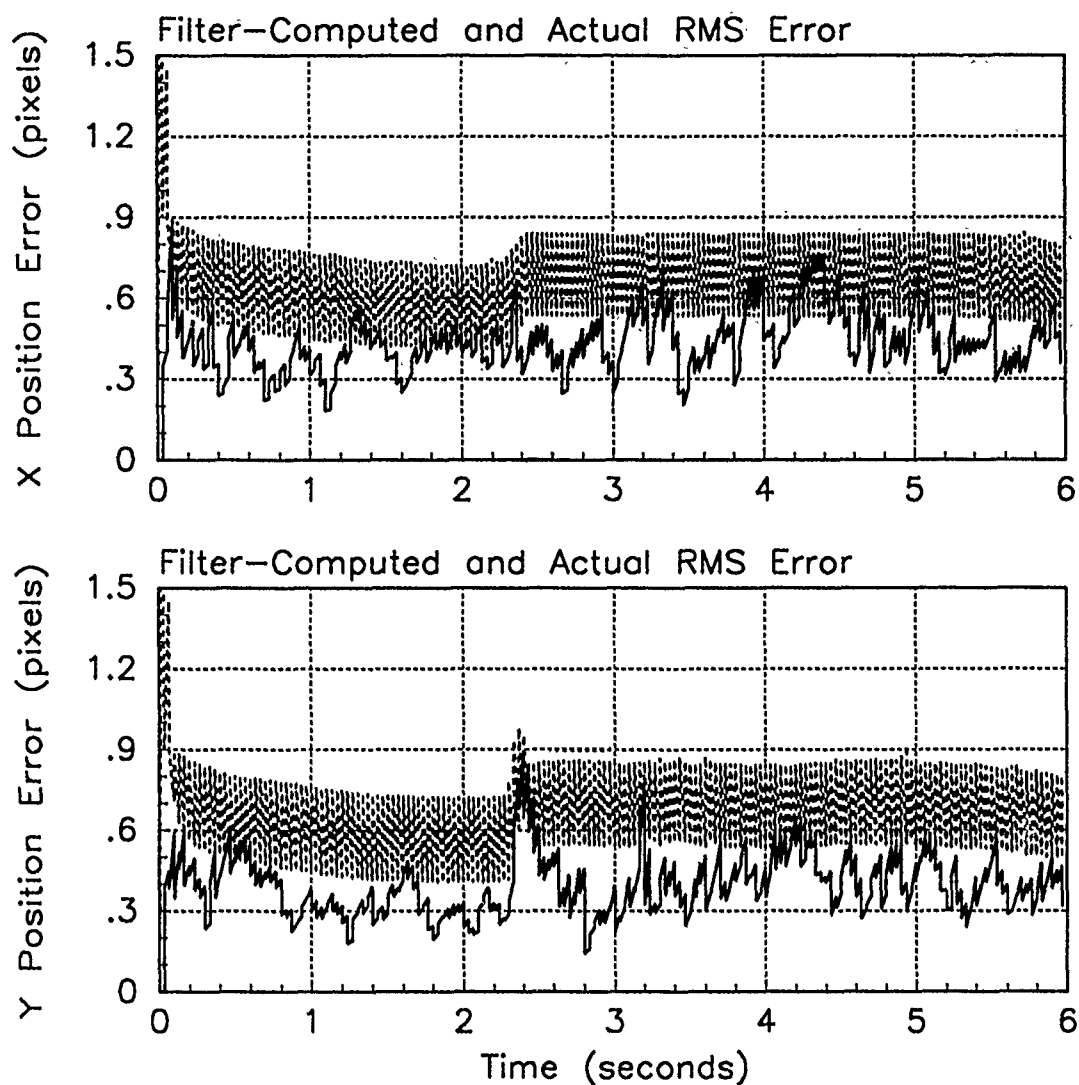


Figure E.37. RMS Error Plots; Notch MMAE-2R; PC is 1; Jinking Trajectory

Table E.13. Temporal Averages; Notch MMAE-2R; PC is 1; Jinking Trajectory.

Error in:	Mean	σ
$p_x(t_i^-)$	-0.0091597	0.47084
$p_x(t_i^+)$	-0.0045901	0.40771
$y_x(t_i^-)$	0.0013619	0.40565
$p_y(t_i^-)$	0.13653	0.42526
$p_y(t_i^+)$	0.087173	0.36126
$y_y(t_i^-)$	0.10617	0.39323

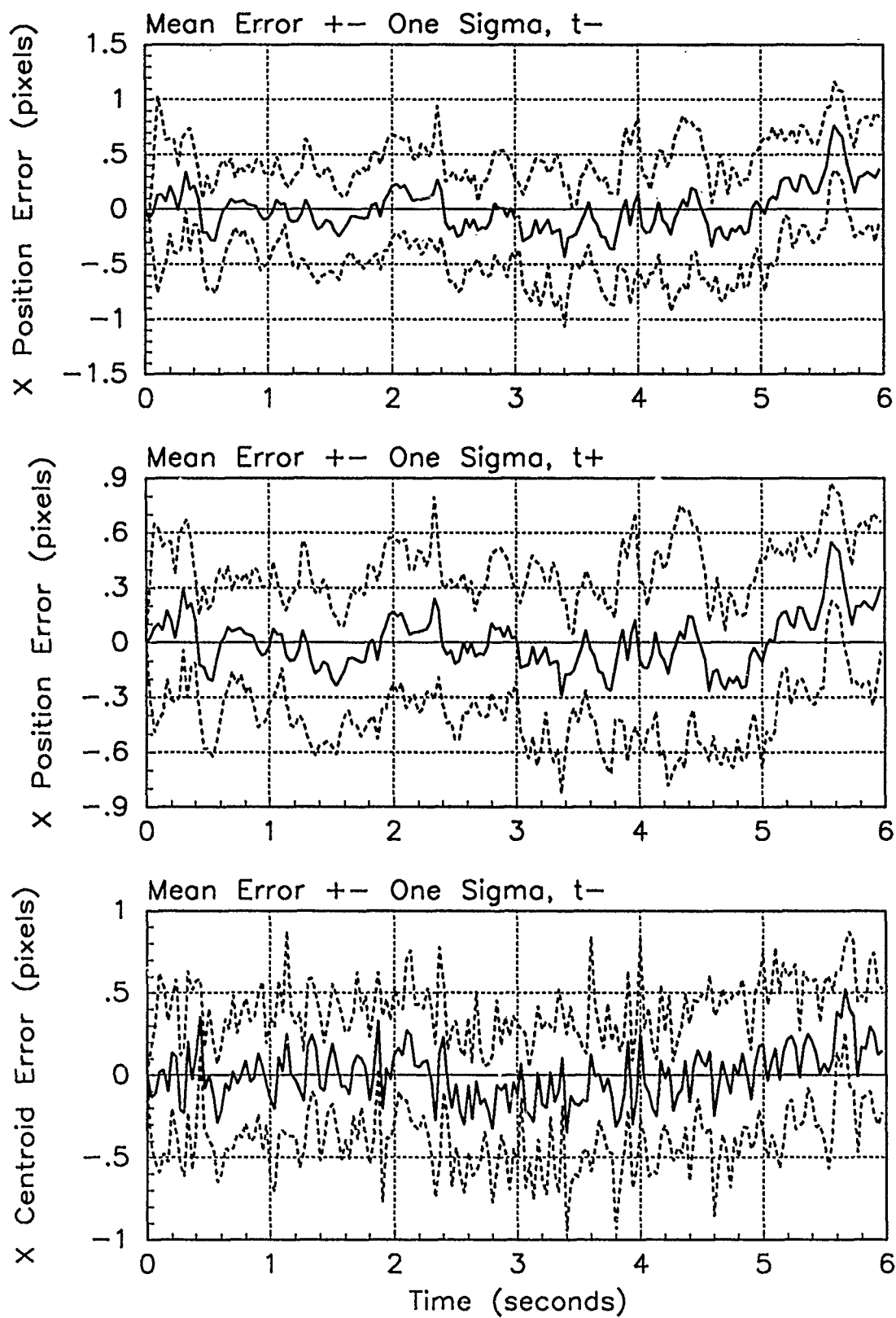


Figure E.38. X-Error Plots; Notch MMAE-2R; PC is 1; Jinking Trajectory

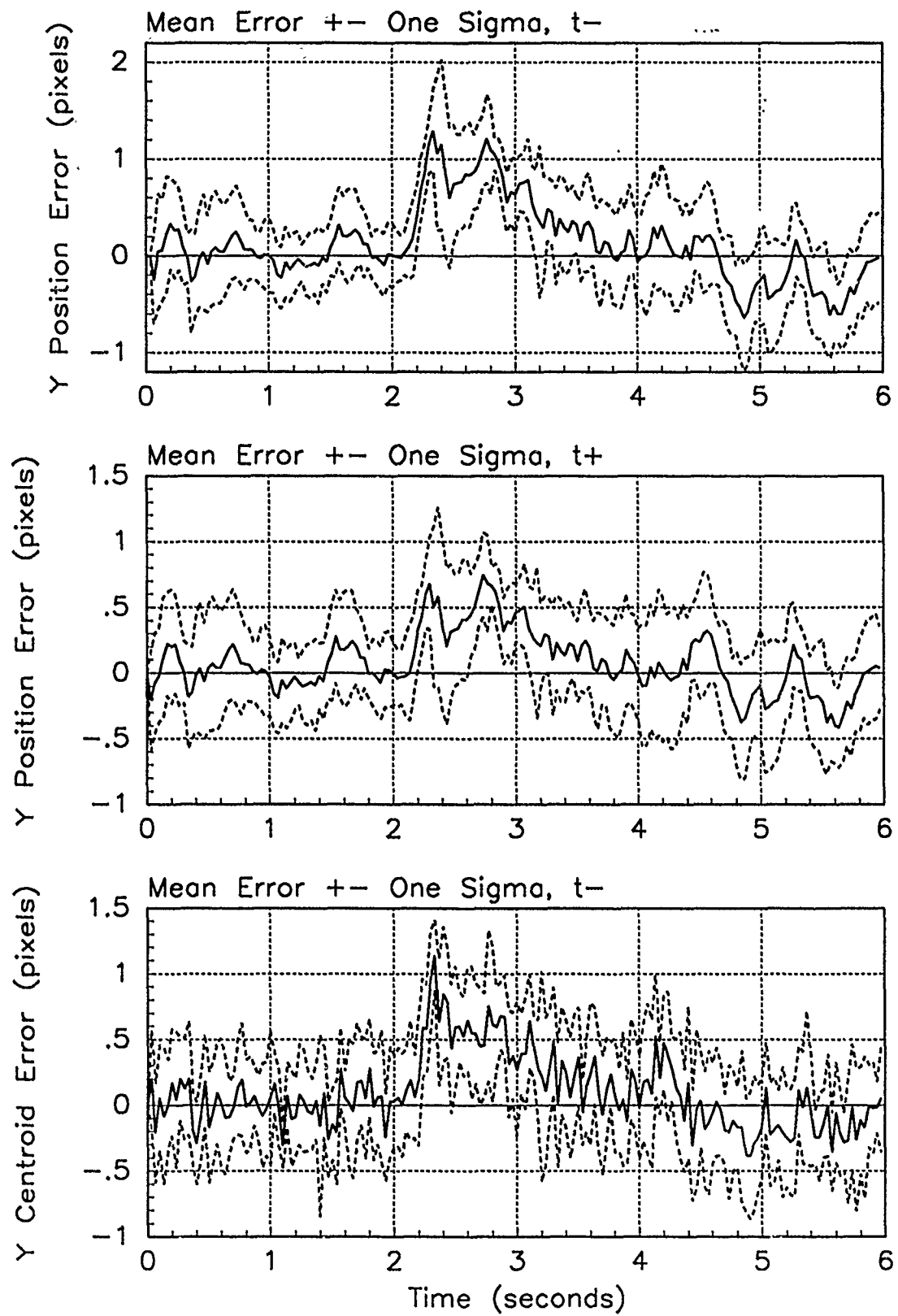


Figure E.39. Y-Error Plots; Notch MMAE-2R; PC is 1; Jinking Trajectory

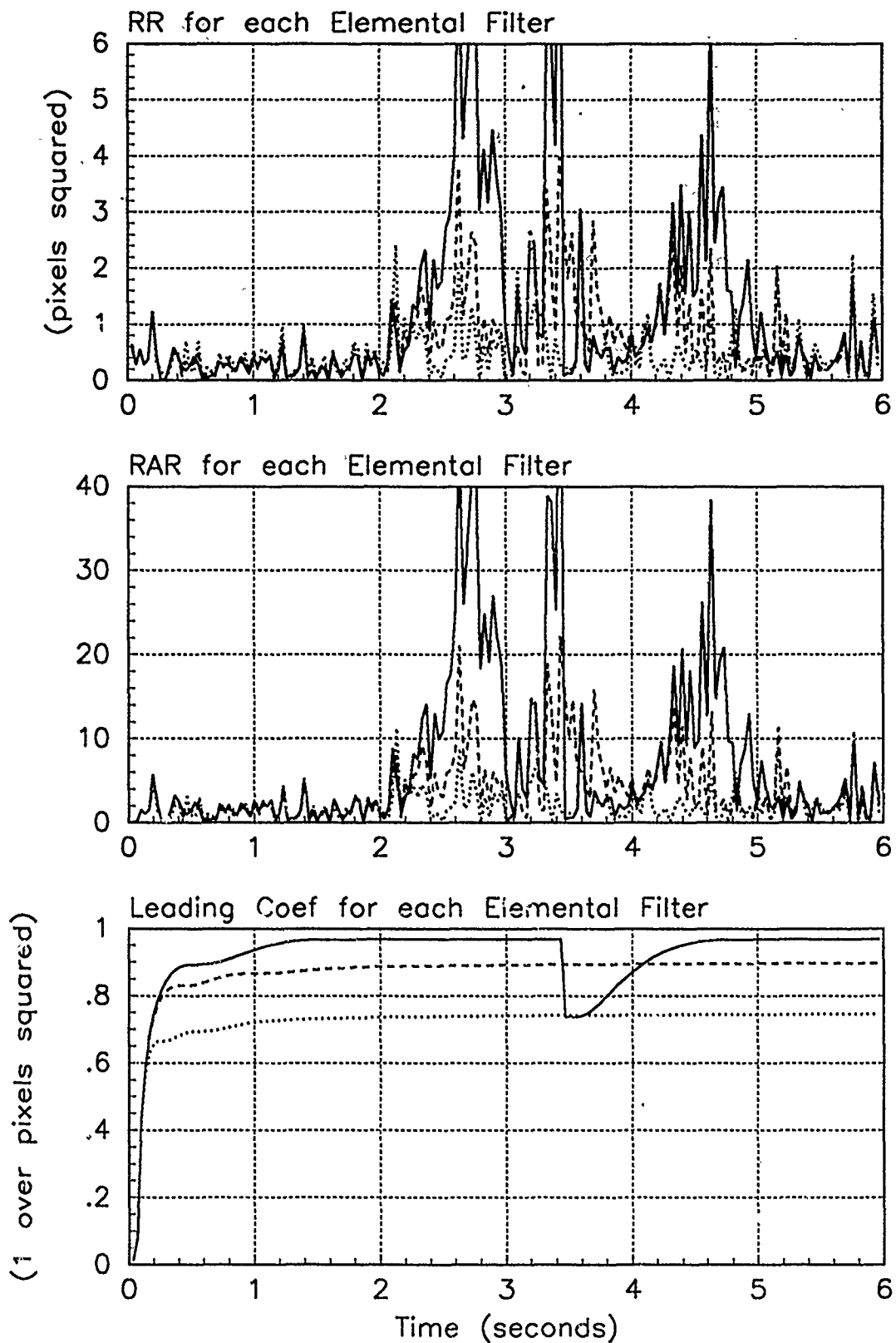


Figure E.40. Probability Calculation Plots; Notch MMAE-2R; PC is 1; Jinking Trajectory. Benign filter has solid line; intermediate filter has dashed line; harsh filter has dotted line.

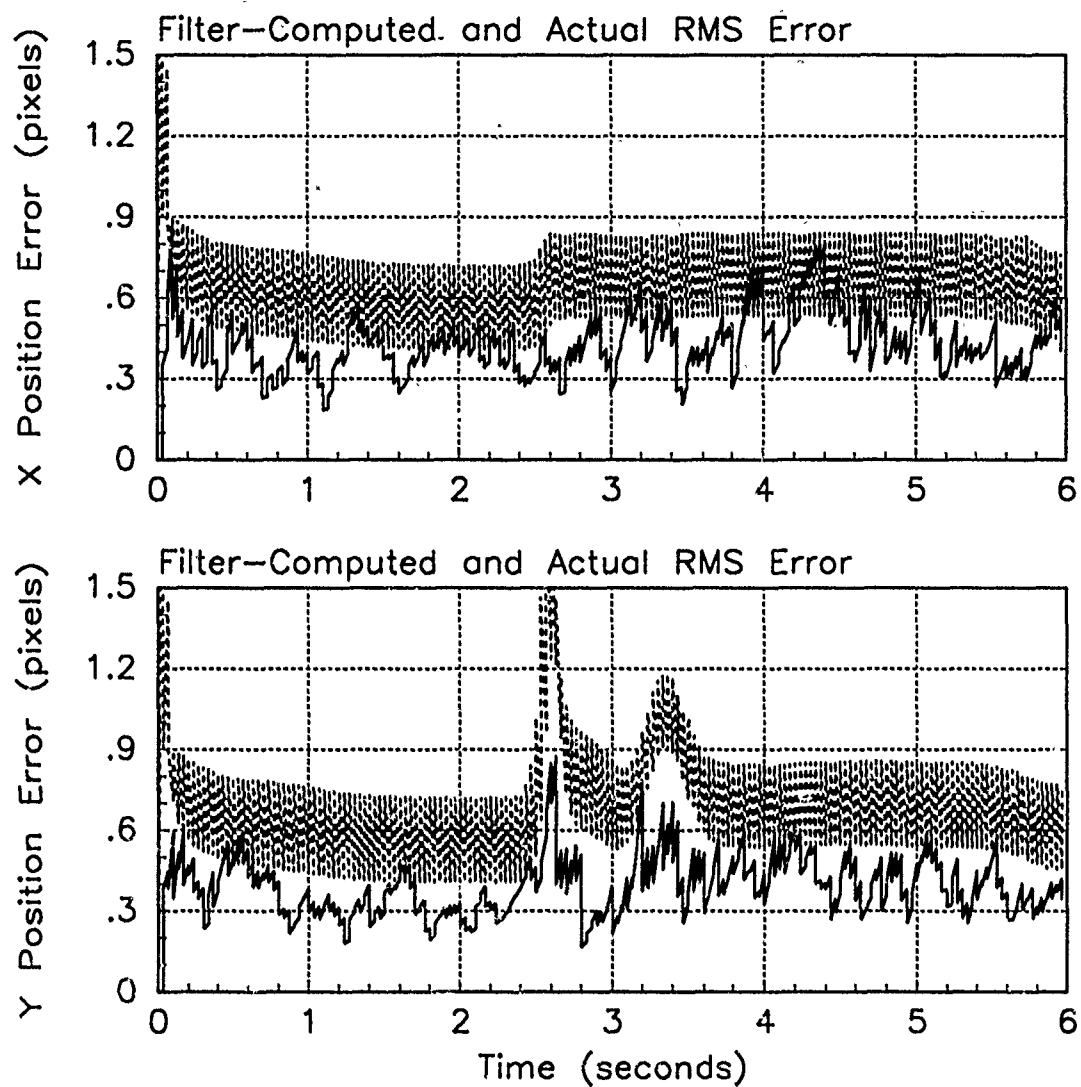


Figure E.41. RMS Error Plots; Notch MMAE-2R; PC is 2; Jinking Trajectory

Table E.14. Temporal Averages; Notch MMAE-2R; PC is 2; Jinking Trajectory.

Error in:	Mean	σ
$p_x(t_i^-)$	0.0092701	0.45886
$p_x(t_i^+)$	0.0066639	0.40148
$y_x(t_i^-)$	0.011071	0.40179
$p_y(t_i^-)$	0.19911	0.42516
$p_y(t_i^+)$	0.13660	0.35953
$y_y(t_i^-)$	0.13837	0.39503

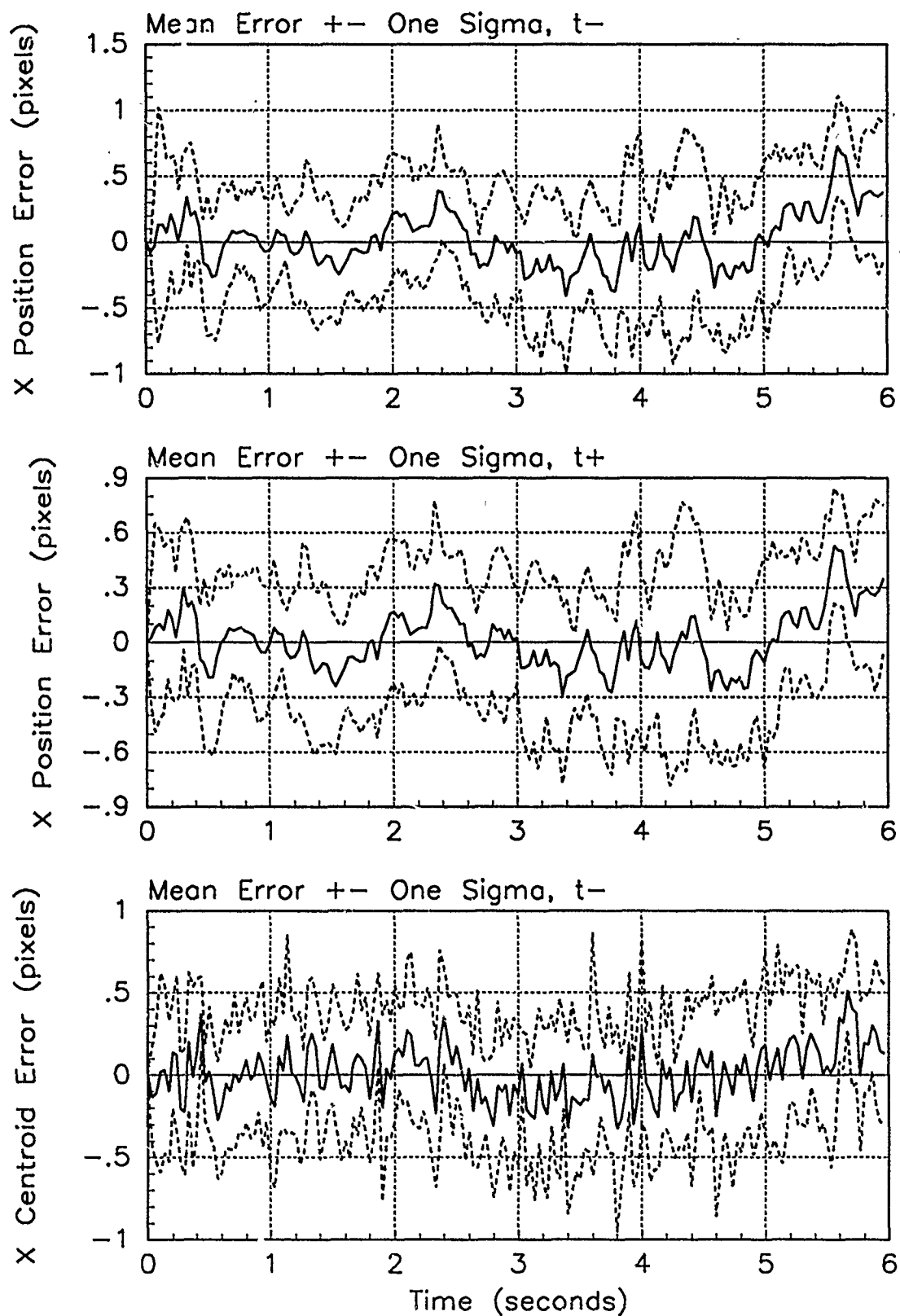


Figure E.42. X-Error Plots; Notch MMAE-2R; PC is 2; Jinking Trajectory

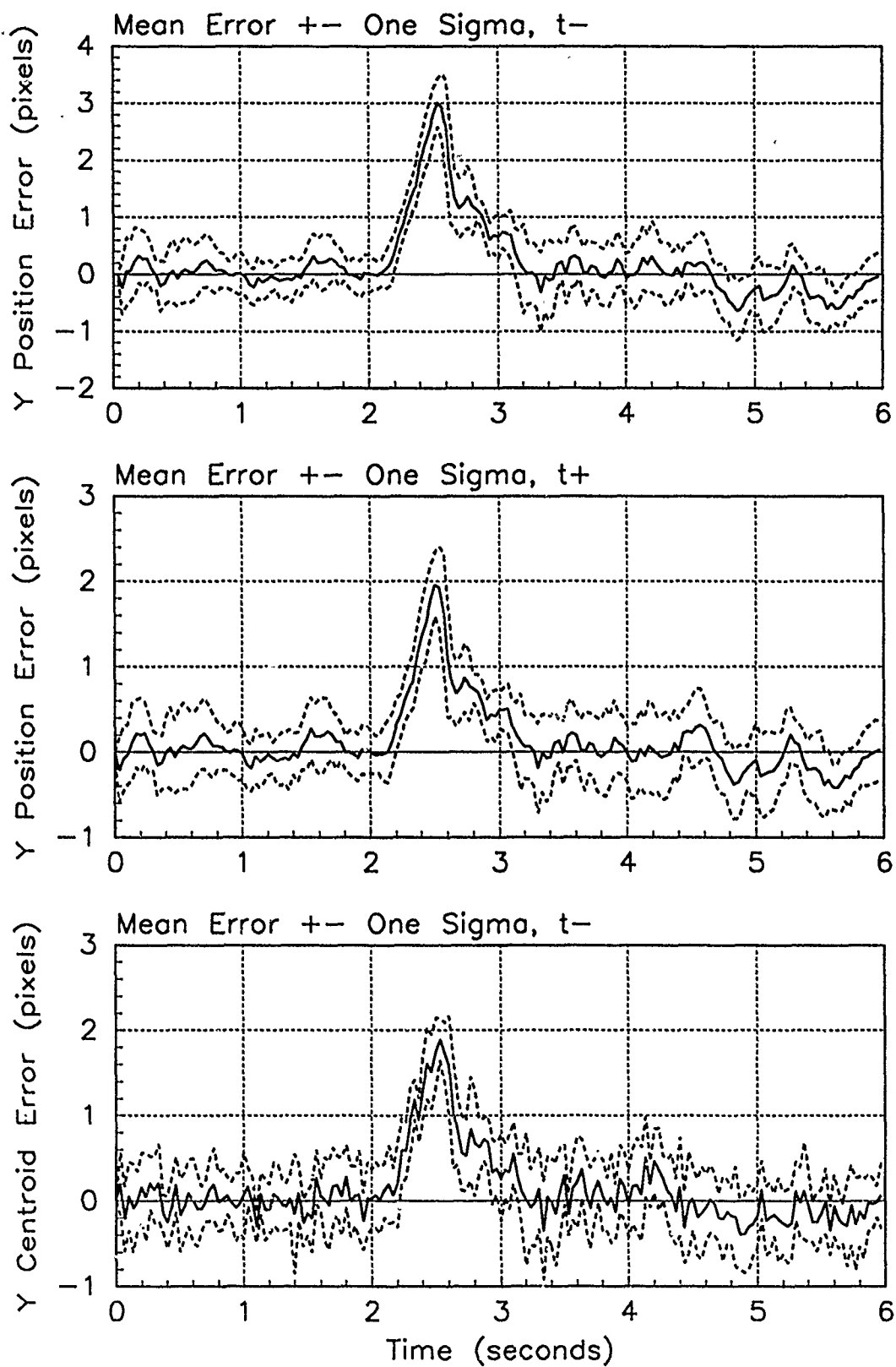


Figure E.43. Y-Error Plots; Notch MMAE-2R; PC is 2; Jinking Trajectory

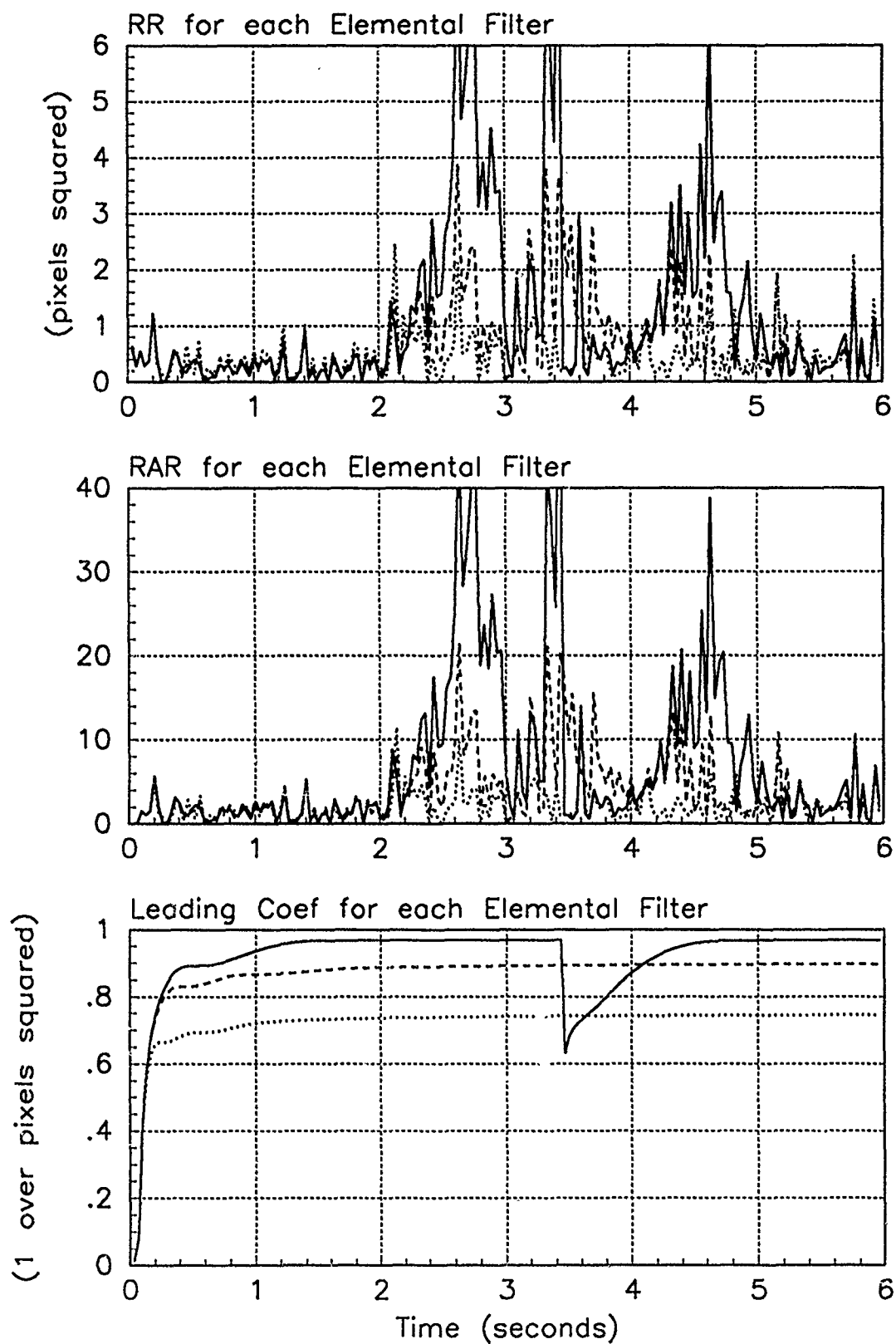


Figure E.44. Probability Calculation Plots; Notch MMAE-2R; PC is 2; Jinking Trajectory. Benign filter has solid line; intermediate filter has dashed line; harsh filter has dotted line.

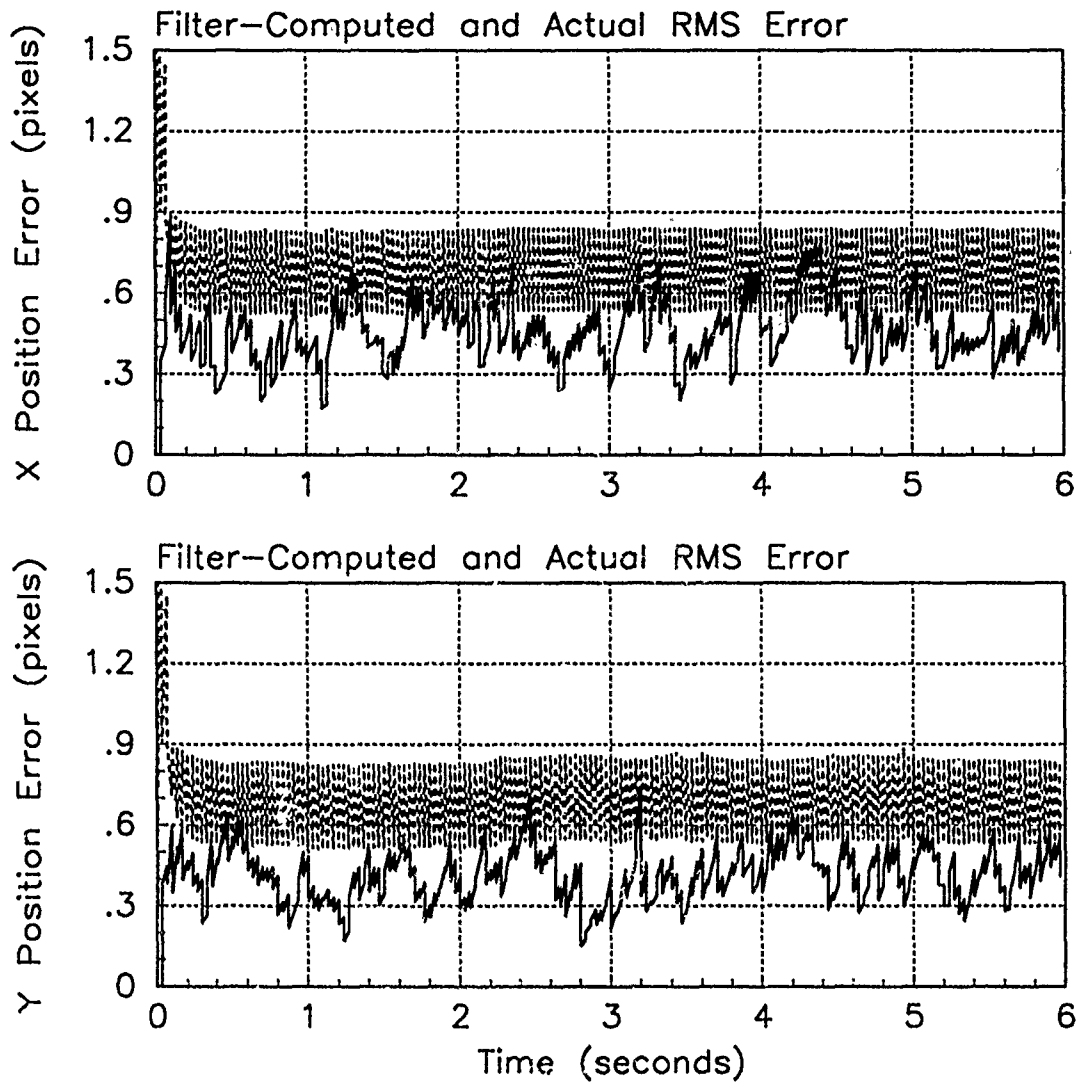


Figure E.45. RMS Error Plots; Notch MMAE-2R; PC is 3; Jinking Trajectory

Table E.15. Temporal Averages; Notch MMAE-2R; PC is 3; Jinking Trajectory.

Error in:	Mean	σ
$p_x(t_i^-)$	-0.070978	0.50184
$p_x(t_i^+)$	-0.041023	0.42579
$y_x(t_i^-)$	-0.038458	0.41694
$p_y(t_i^-)$	0.10343	0.45123
$p_y(t_i^+)$	0.060133	0.37858
$y_y(t_i^-)$	0.079114	0.40246

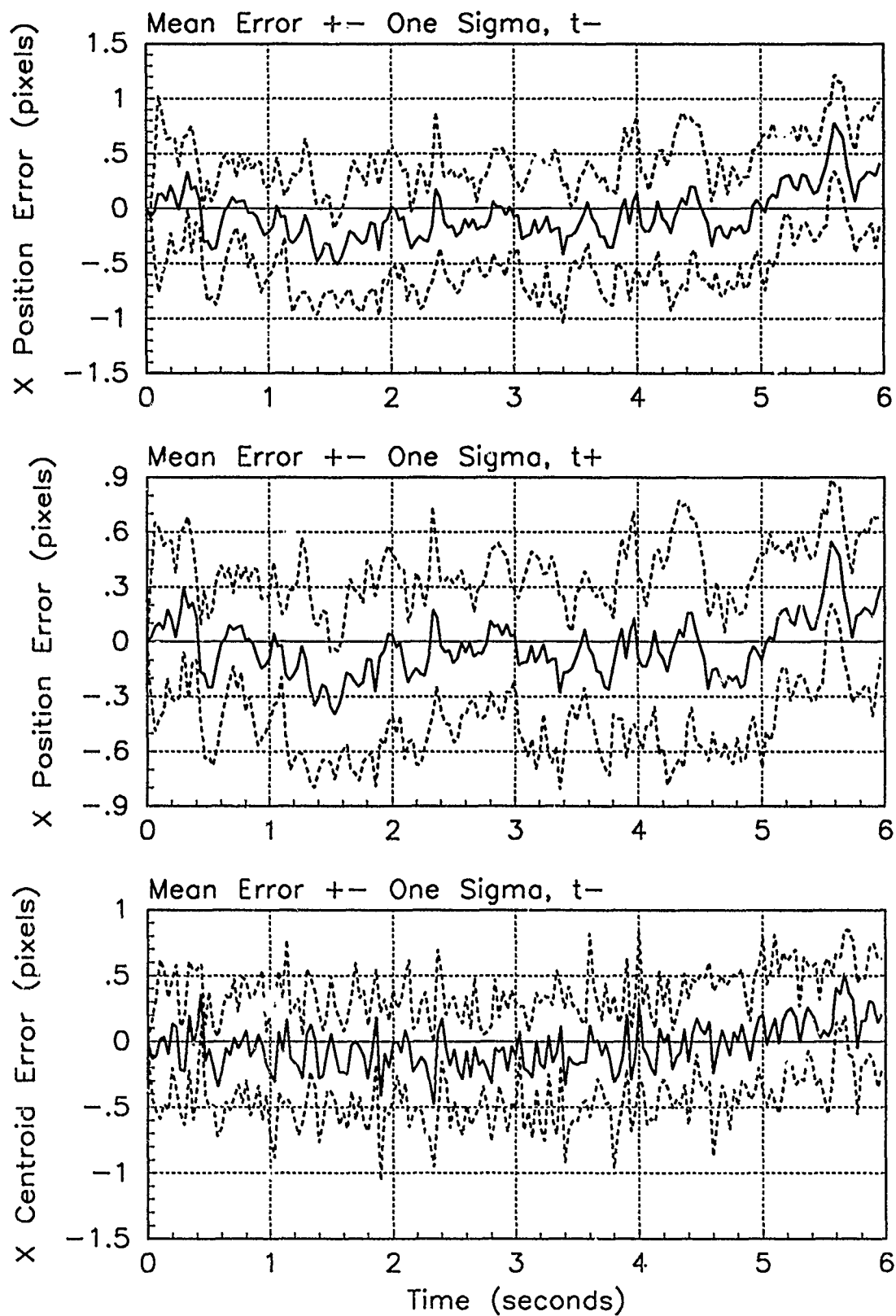


Figure E.46. X-Error Plots; Notch MMAE-2R; PC is 3; Jinking Trajectory

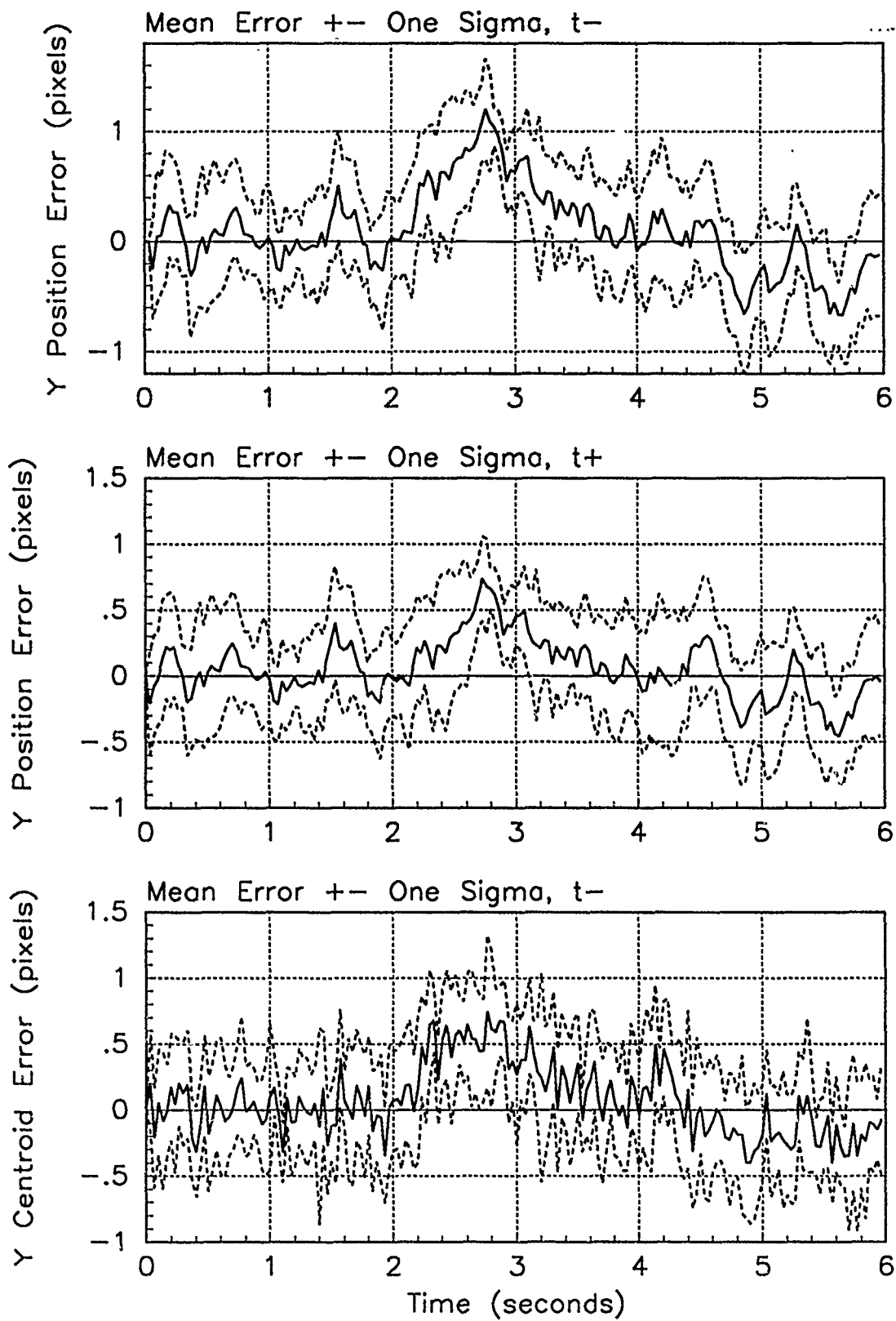


Figure E.47. Y-Error Plots; Notch MMAE-2R; PC is 3; Jinking Trajectory

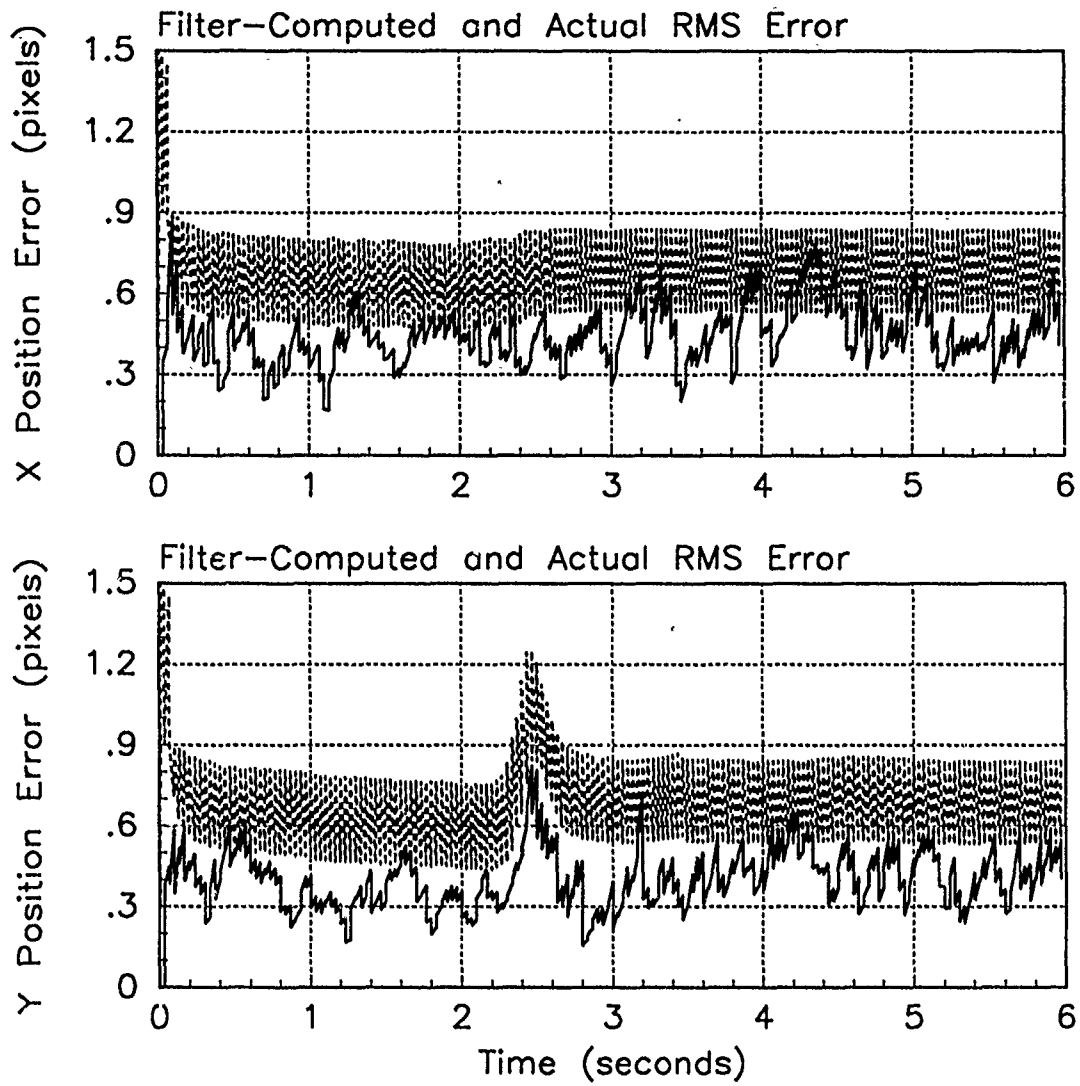


Figure E.49. RMS Error Plots; Notch MMAE-2R; PC is 4; Jinking 'Trajectory

Table E.16. Temporal Averages; Notch MMAE-2R; PC is 4; Jinking Trajectory.

Error in:	Mean	σ
$p_x(t_i^-)$	-0.037607	0.48179
$p_x(t_i^+)$	-0.024760	0.41634
$y_x(t_i^-)$	-0.015064	0.41064
$p_y(t_i^-)$	0.15135	0.43453
$p_y(t_i^+)$	0.095046	0.37039
$y_y(t_i^-)$	0.11017	0.39597

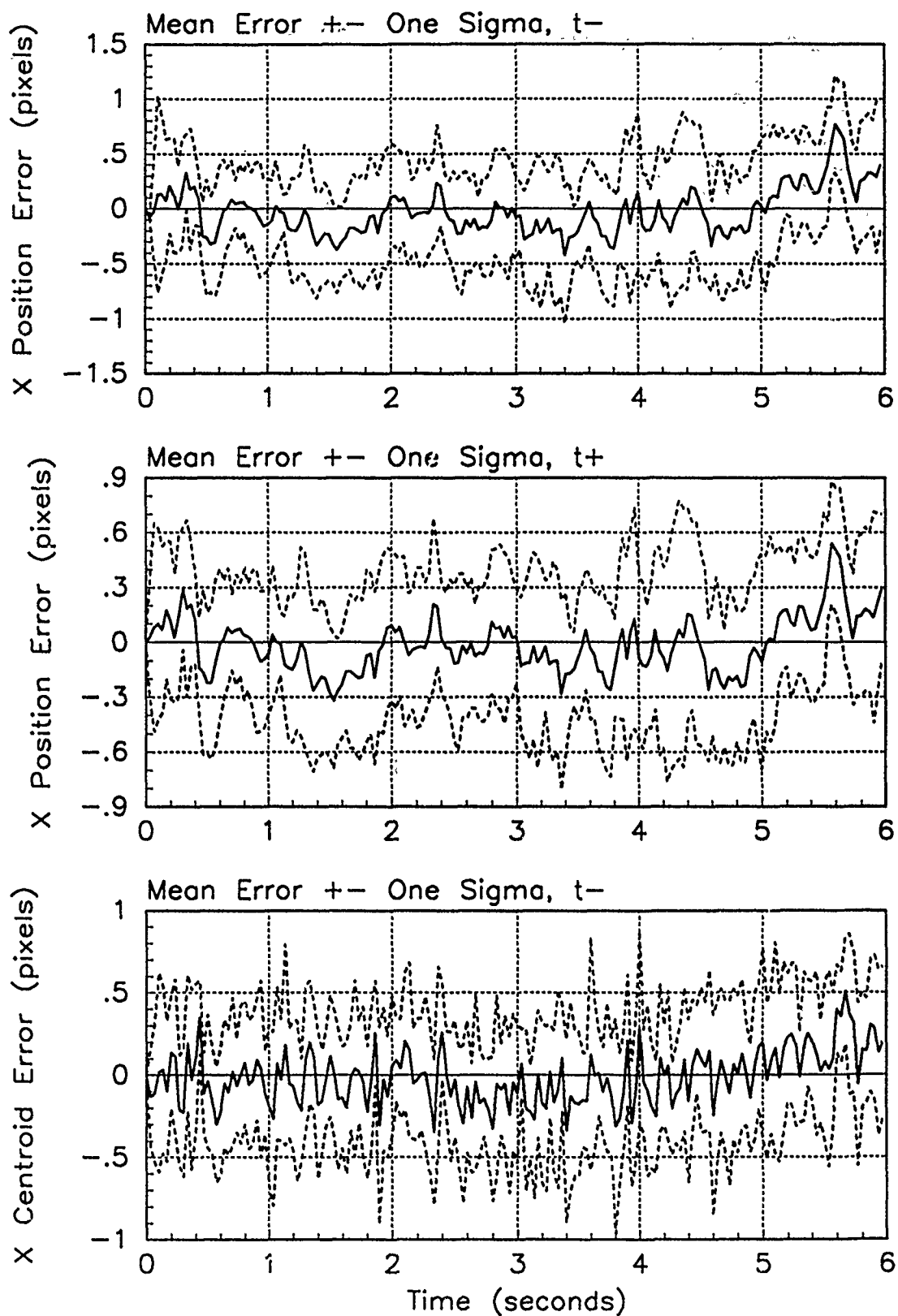


Figure E.50. X-Error Plots; Notch MMAE-2R; PC is 4; Jinking Trajectory

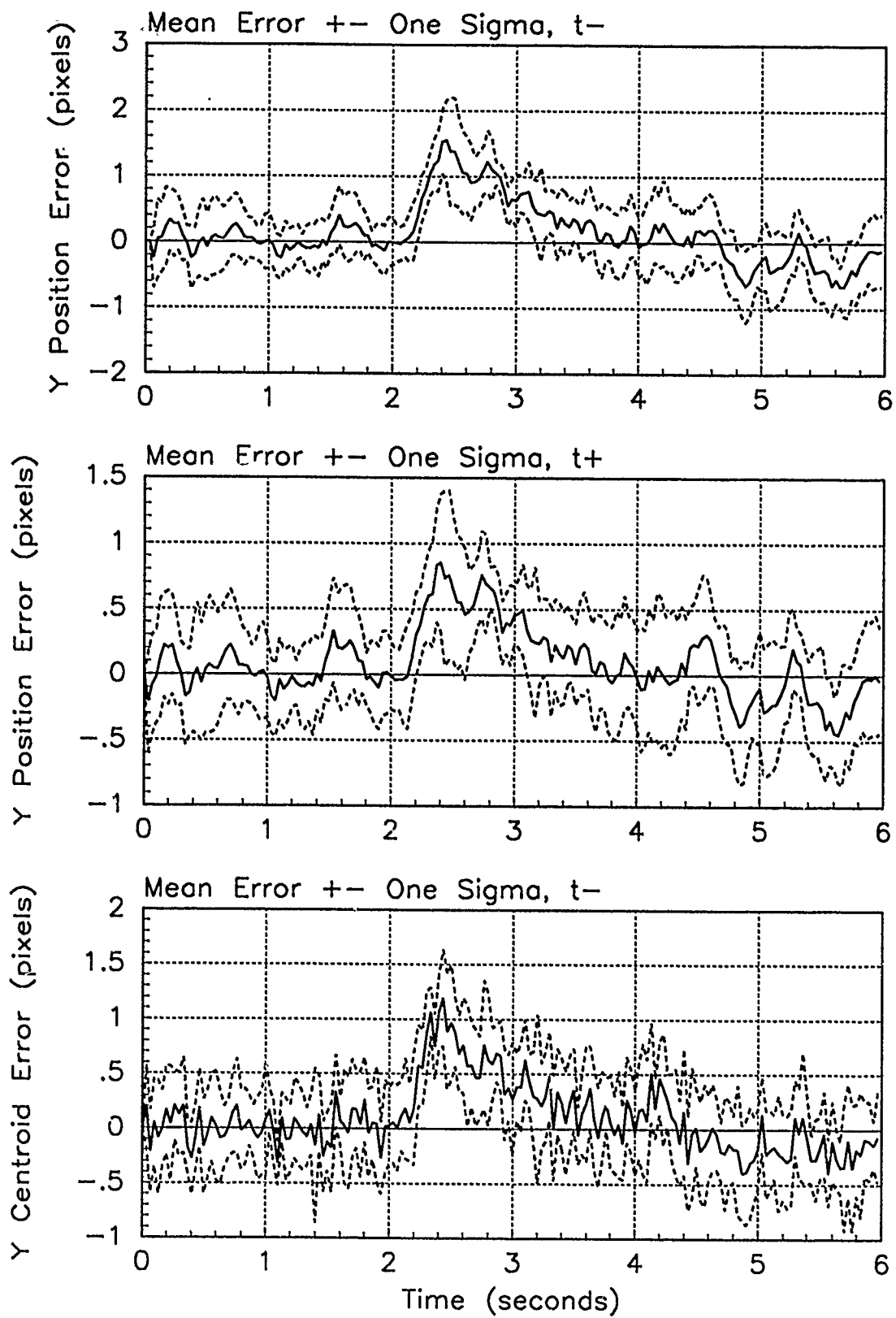


Figure E.51. Y-Error Plots; Notch MMAE-2R; PC is 4; Jinking Trajectory

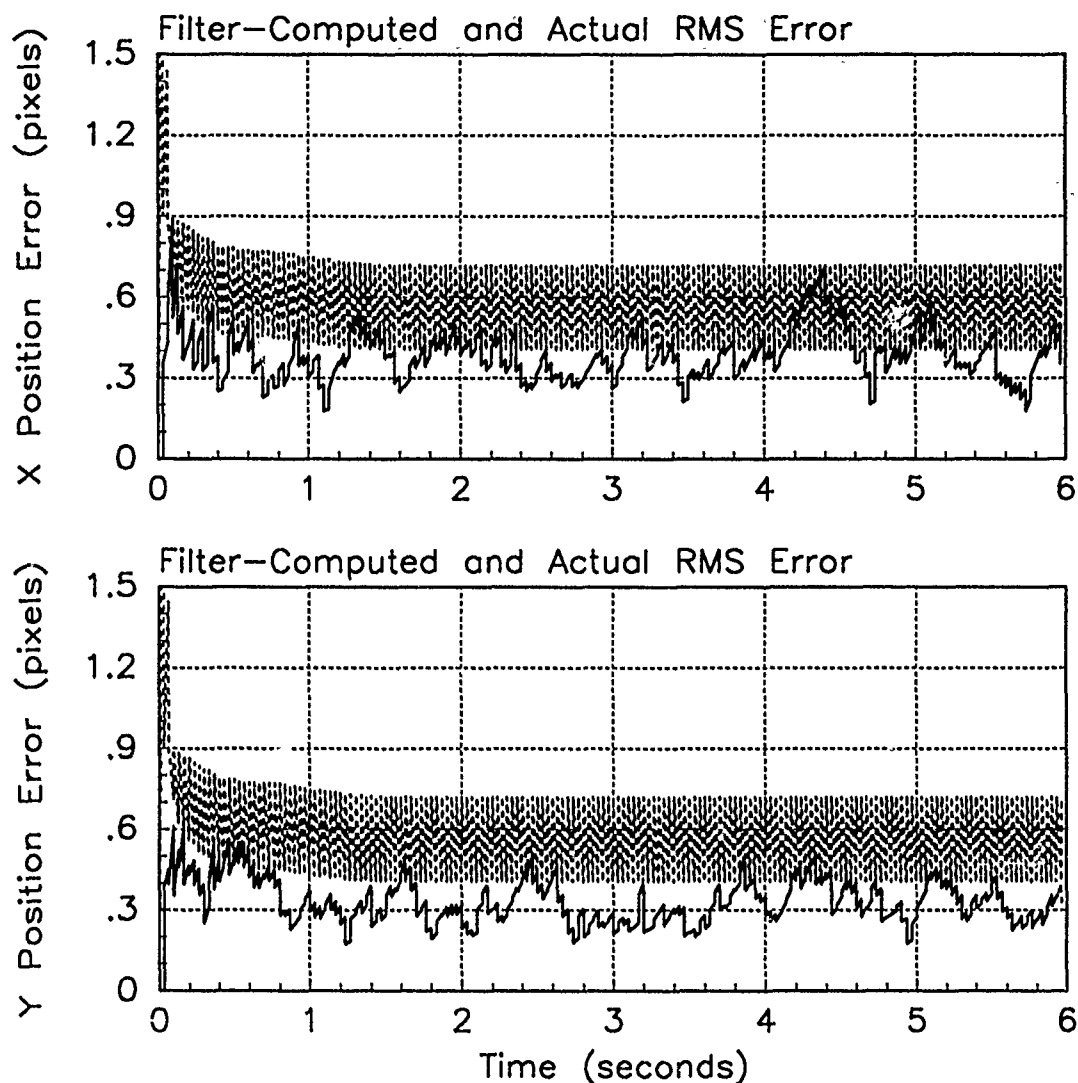


Figure E.53. RMS Error Plots; Notch MMAE-2RM; PC is 1; Trajectory with $\omega = .01$

Table E.17. Temporal Averages and Residuals; Notch MMAE-2RM; PC is 1; Trajectory with $\omega = .01$.

Error in:	Mean	σ
$p_x(t_i^-)$	0.15904	0.40347
$p_x(t_i^+)$	0.11759	0.36725
$y_x(t_i^-)$	0.094249	0.37923
$p_y(t_i^-)$	-0.011480	0.34310
$p_y(t_i^+)$	-0.0097946	0.31130
$y_y(t_i^-)$	-0.0053241	0.36629

Filter	$\mathbf{r}_k^T \mathbf{r}_k$	$\mathbf{r}_k^T \mathbf{A}_k^{-1} \mathbf{r}_k$
Benign	0.31242	1.84186
Intermediate	0.32972	1.79894
Harsh	0.37814	1.72173

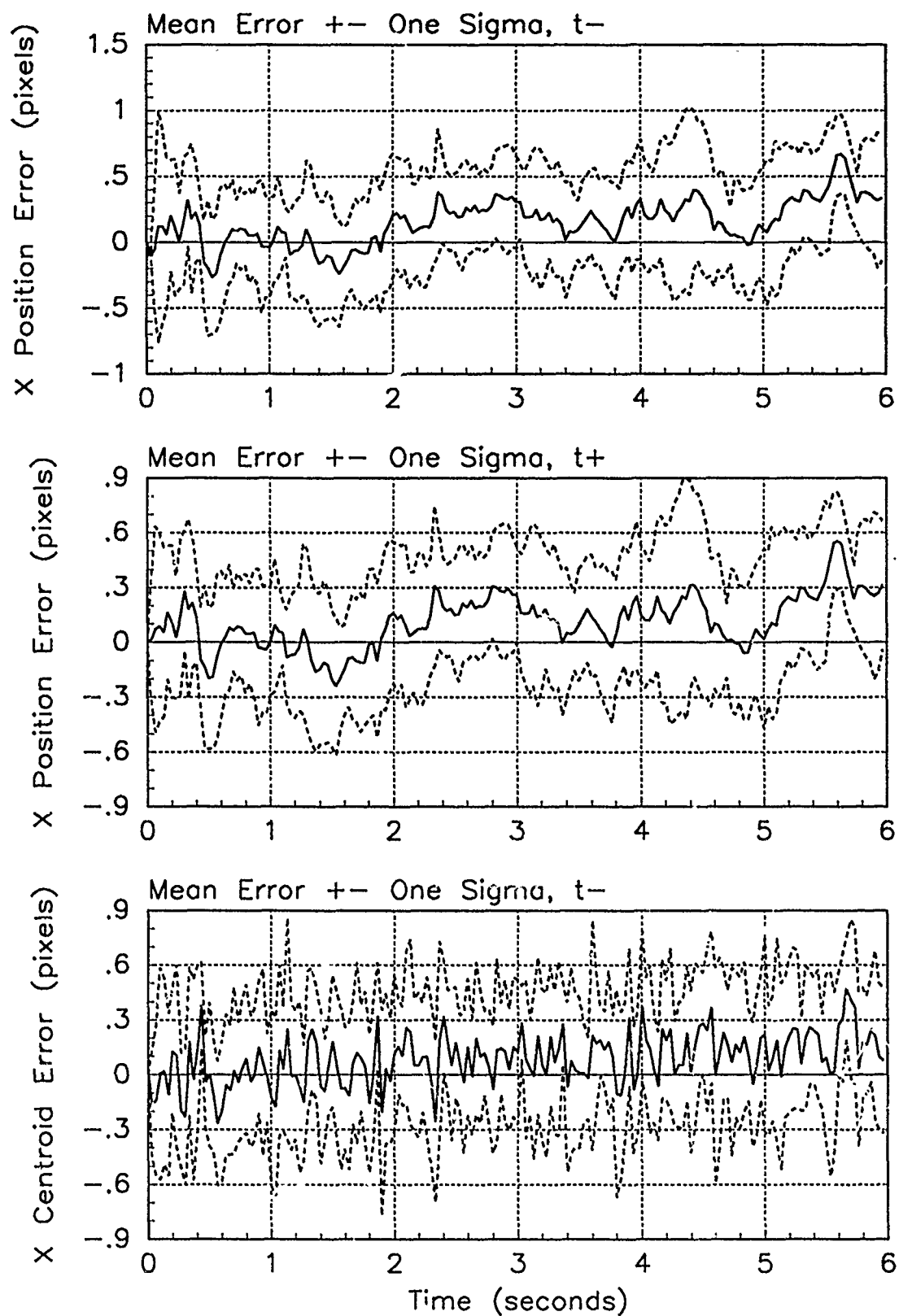


Figure E.54. X-Error Plots; Notch MMAE-2RM; PC is 1; Trajectory with $\omega = .01$

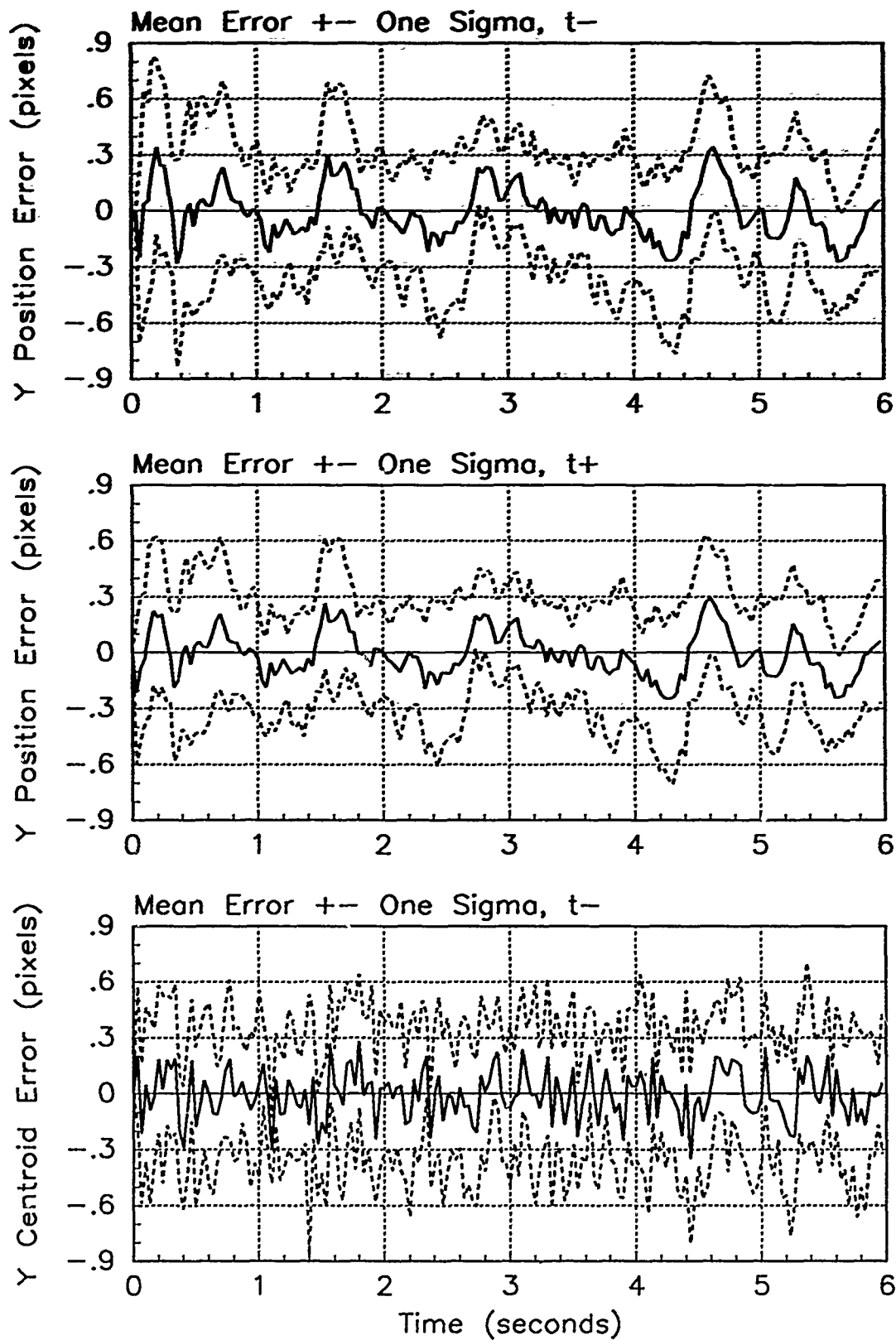


Figure E.55. Y-Error Plots; Notch MMAE 2RM; PC is 1; Trajectory with $\omega = .01$

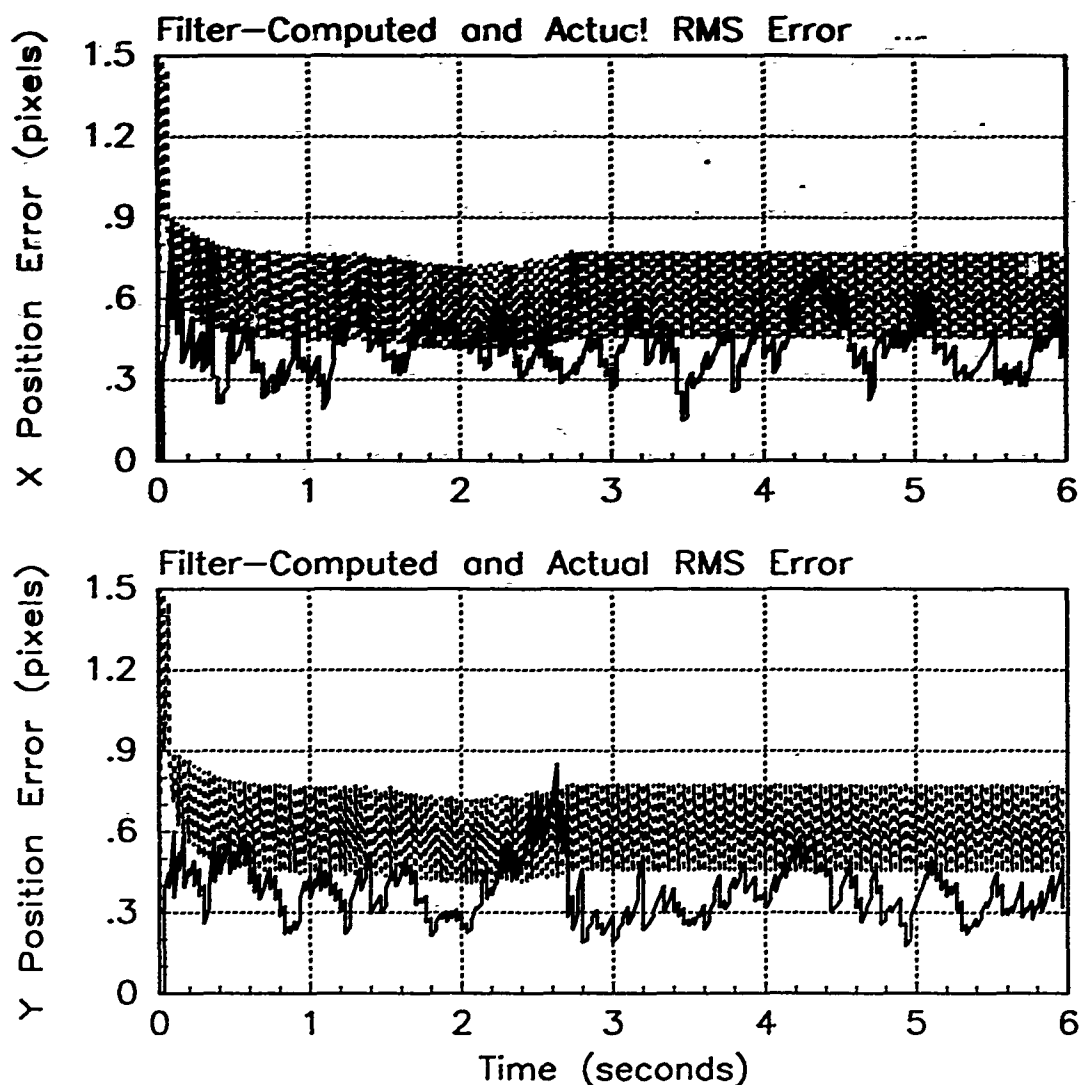


Figure E.56. RMS Error Plots; Notch MMAE-2RM; PC is 1; Trajectory with $\omega = 1.32$

Table E.18. Temporal Averages and Residuals; Notch MMAE-2RM; PC is 1; Trajectory with $\omega = 1.32$.

Error in:	Mean	σ
$p_x(t_i^-)$	-0.036431	0.44638
$p_x(t_i^+)$	-0.032749	0.39415
$y_x(t_i^-)$	-0.020003	0.39437
$p_y(t_i^-)$	-0.0066317	0.37211
$p_y(t_i^+)$	-0.011366	0.35045
$y_y(t_i^-)$	-0.013406	0.38162

Filter	$\mathbf{r}_k^T \mathbf{r}_k$	$\mathbf{r}_k^T \mathbf{A}_k^{-1} \mathbf{r}_k$
Benign	0.39511	2.33873
Intermediate	0.33222	1.81237
Harsh	0.38827	1.76856

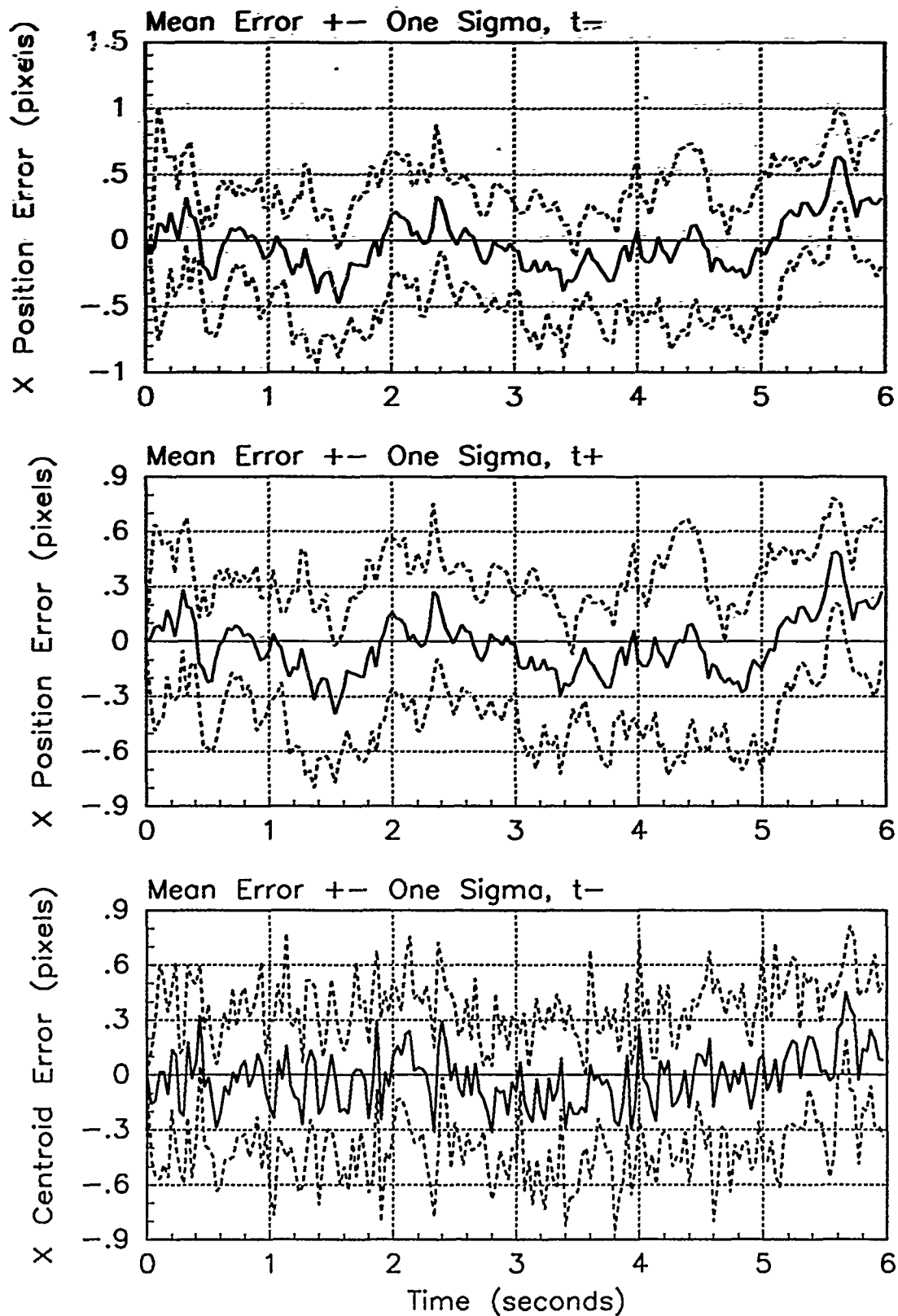


Figure E.57. X-Error Plots; Notch MMAE-2RM; PC is 1; Trajectory with $\omega = 1.32$

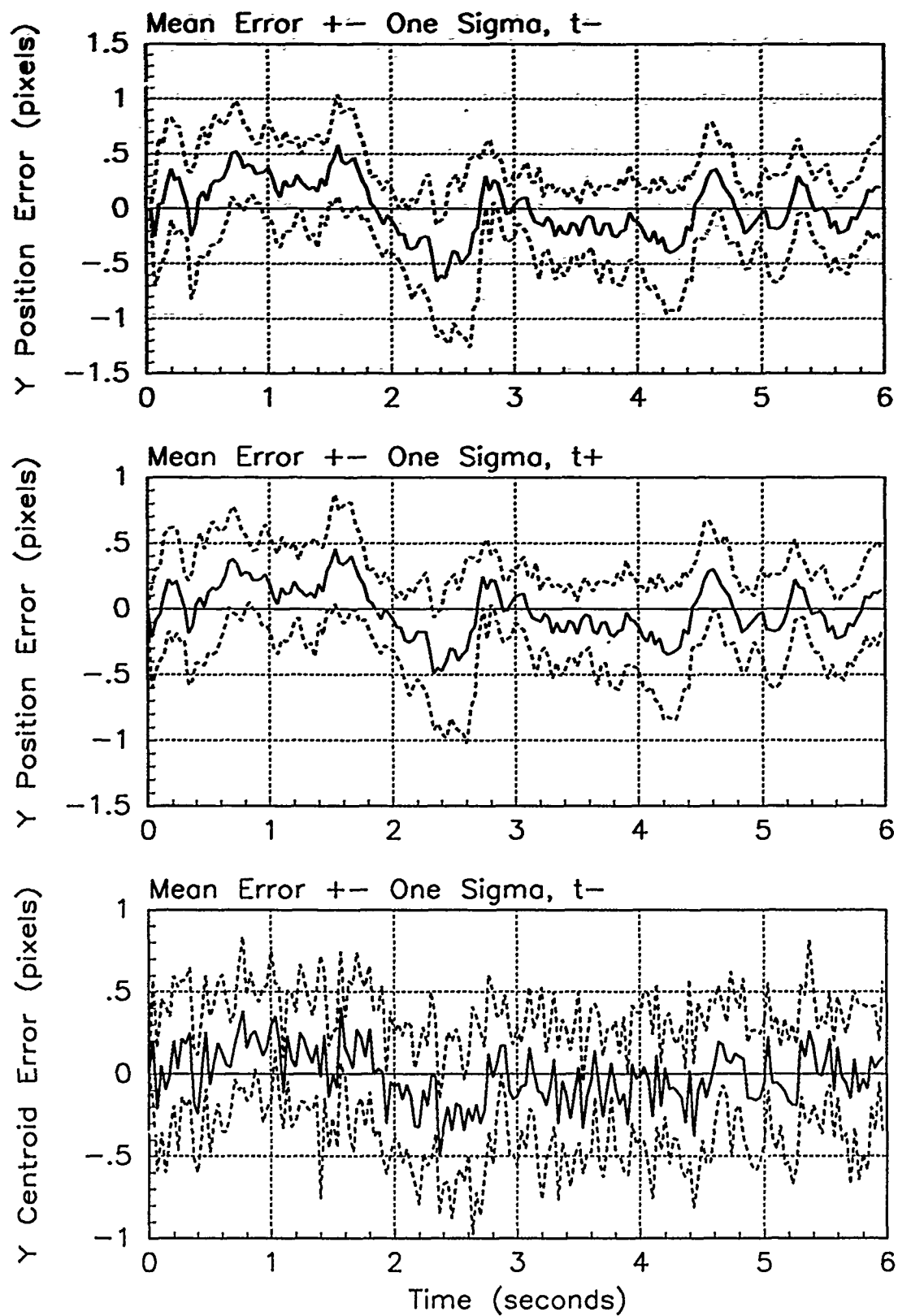


Figure E.58. Y-Error Plots; Notch MMAE-2RM; PC is 1; Trajectory with $\omega = 1.32$

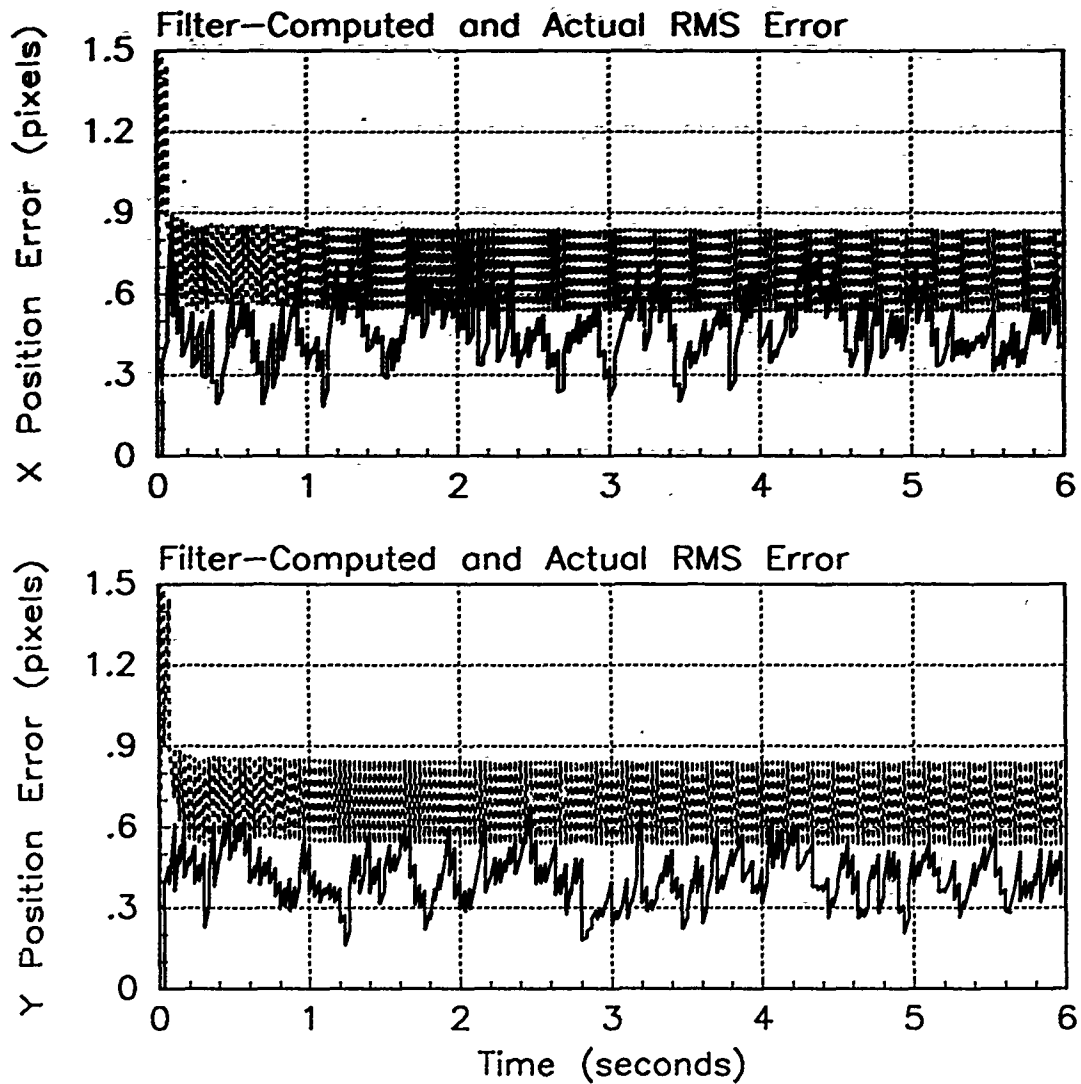


Figure E.59. RMS Error Plots; Notch MMAE-2RM; PC is 1; Trajectory with $\omega = 2.8$

Table E.19. Temporal Averages and Residuals; Notch MMAE-2RM; PC is 1; Trajectory with $\omega = 2.8$.

Error in:	Mean	σ
$p_x(t_i^-)$	-0.10278	0.50898
$p_x(t_i^+)$	-0.065960	0.42770
$y_x(t_i^-)$	-0.067352	0.41901
$p_y(t_i^-)$	0.048331	0.44956
$p_y(t_i^+)$	0.010367	0.37085
$y_y(t_i^-)$	0.028849	0.40185

Filter	$r_k^T r_k$	$r_k^T A_k^{-1} r_k$
Benign	2.15052	12.54454
Intermediate	1.23168	6.79064
Harsh	0.39981	1.81722

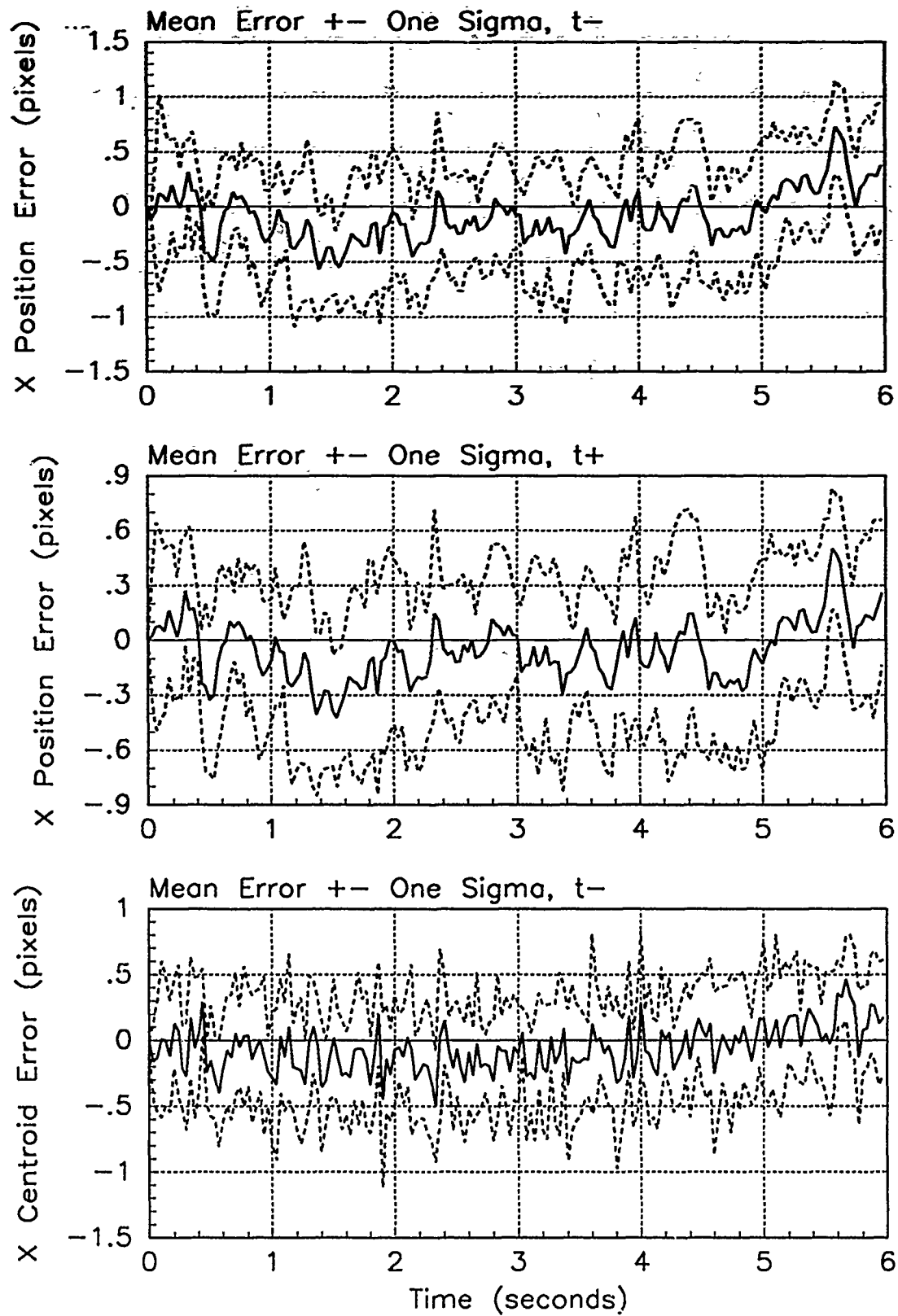


Figure E.60. X-Error Plots; Notch MMAE-2RM; PC is 1; Trajectory with $\omega = 2.8$

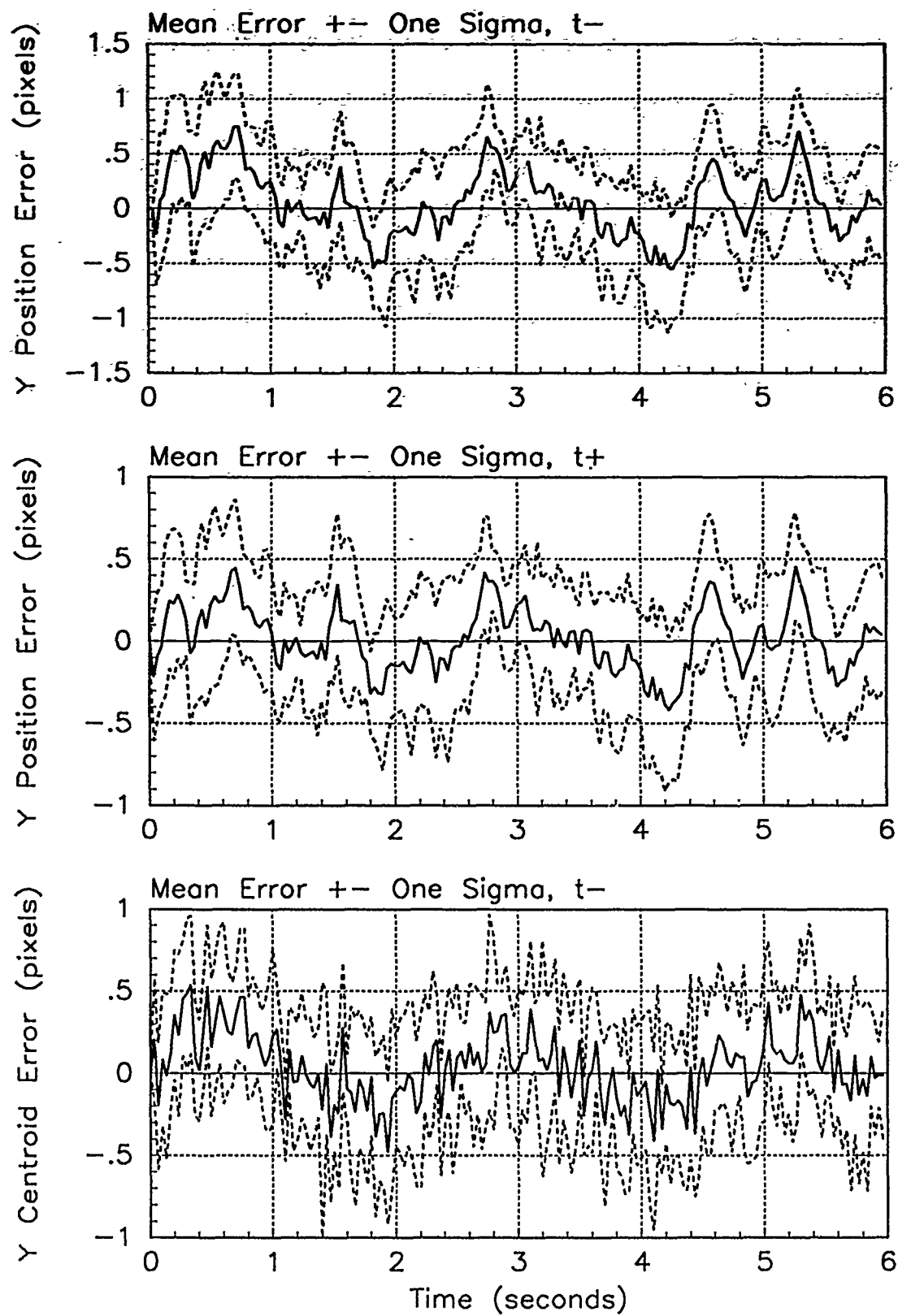


Figure E.61. Y-Error Plots; Notch MMAE-2RM; PC is 1; Trajectory with $\omega = 2.8$;

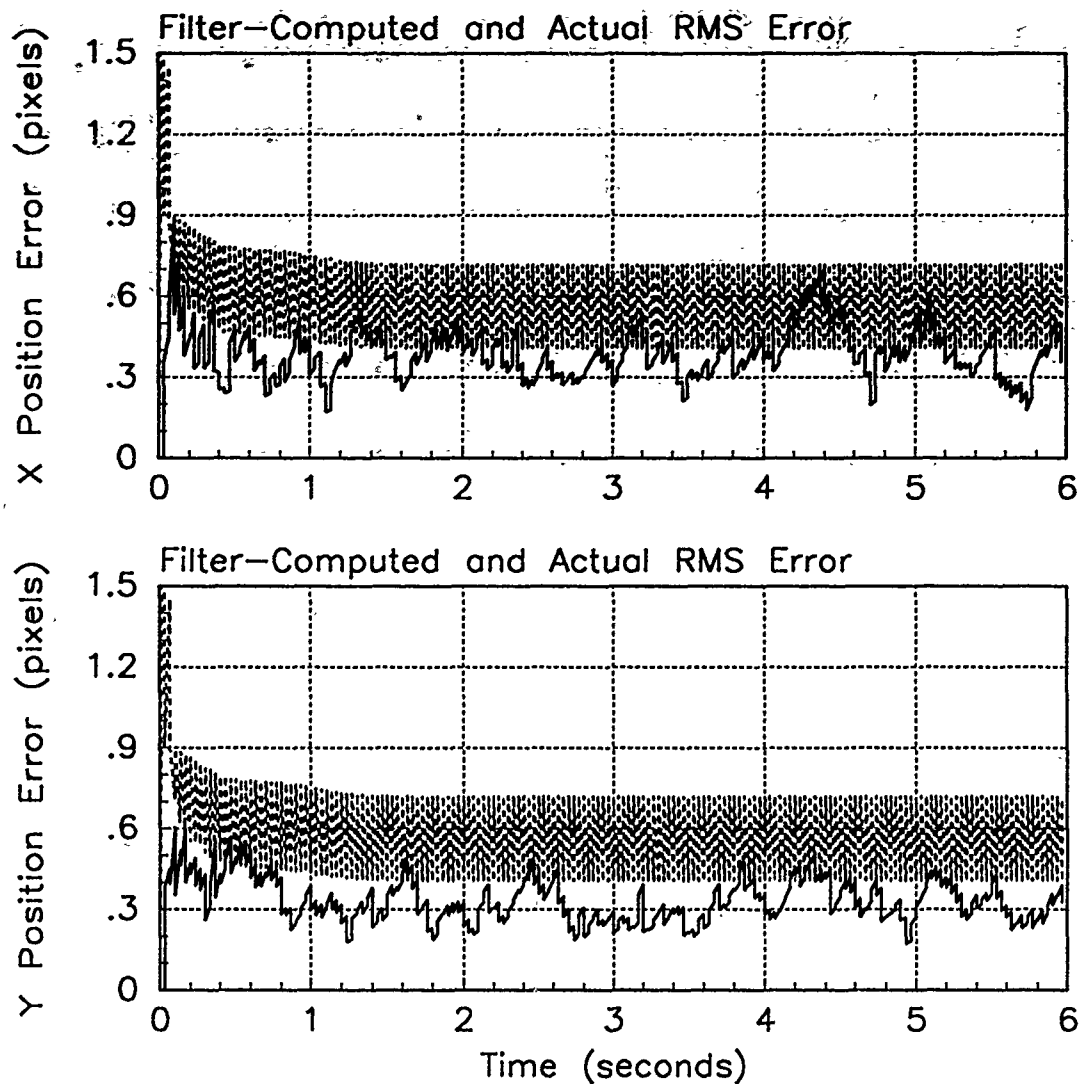


Figure E.62. RMS Error Plots; Notch MMAE-2RM; PC is 4; Trajectory with $\omega = .01$

Table E.20. Temporal Averages and Residuals; Notch MMAE-2RM; PC is 4; Trajectory with $\omega = .01$.

Error in:	Mean	σ
$p_x(t_i^-)$	0.15641	0.40369
$p_x(t_i^+)$	0.11529	0.36775
$y_x(t_i^-)$	0.091869	0.38077
$p_y(t_i^-)$	-0.0092784	0.34307
$p_y(t_i^+)$	-0.0075805	0.31108
$y_y(t_i^-)$	-0.0031090	0.36624

Filter	$r_k^T r_k$	$r_k^T A_k^{-1} r_k$
Benign	0.31317	1.84613
Intermediate	0.33002	1.80041
Harsh	0.37790	1.72046

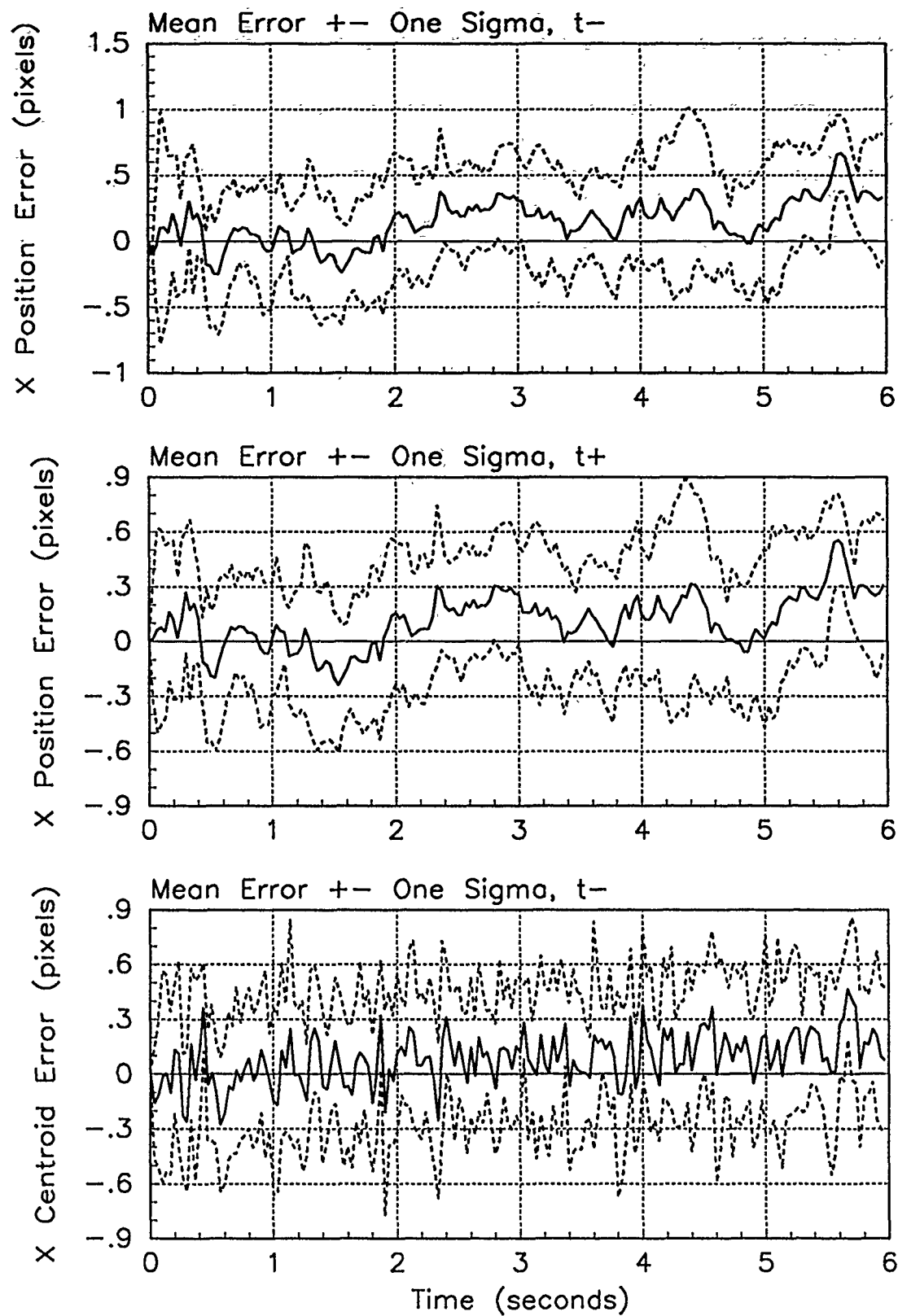


Figure E.63. X-Error Plots; Notch MMAE-2RM; PC is 4; Trajectory with $\omega = .01$

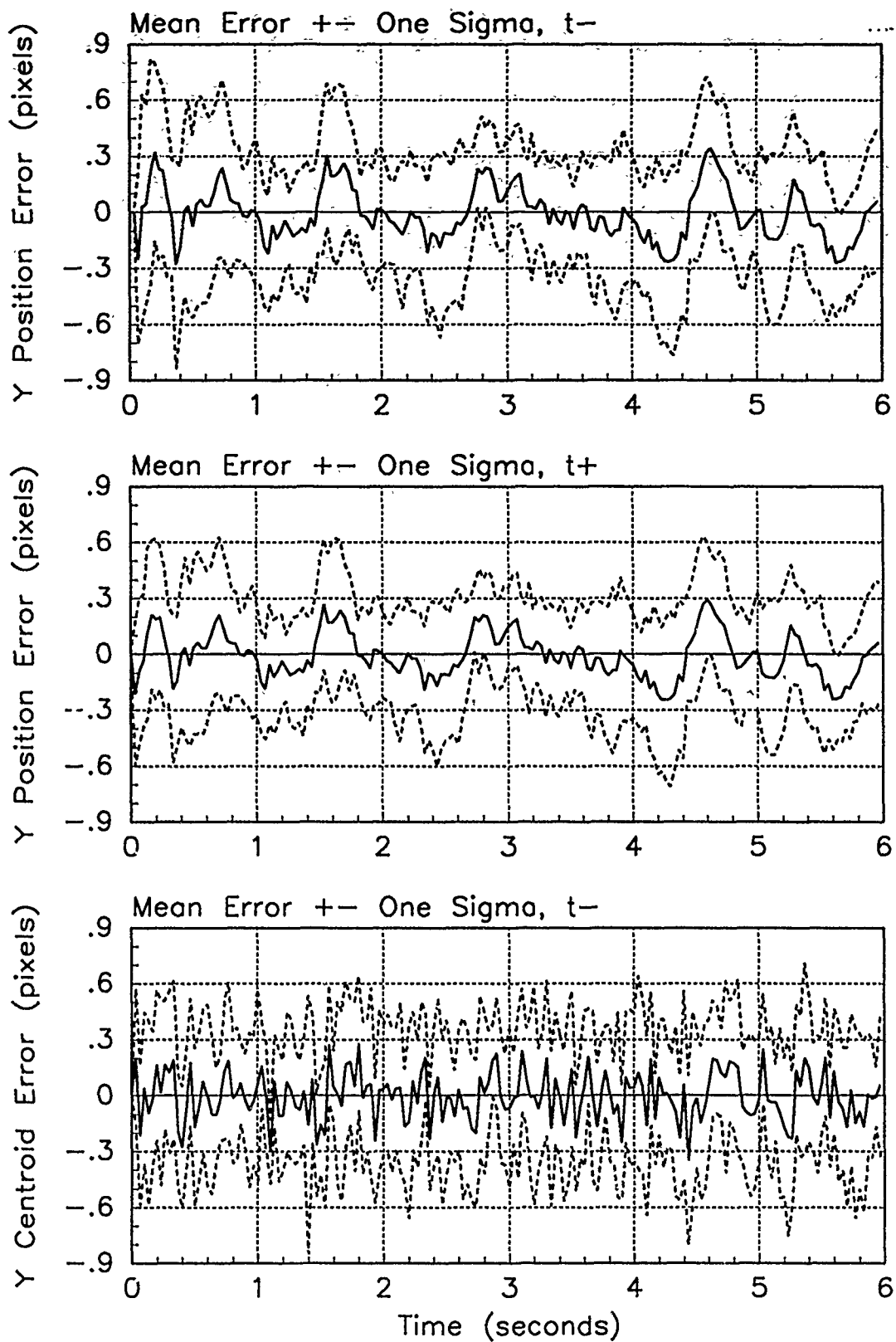


Figure E.64. Y-Error Plots; Notch MMAE-2RM; PC is 4; Trajectory with $\omega = .01$

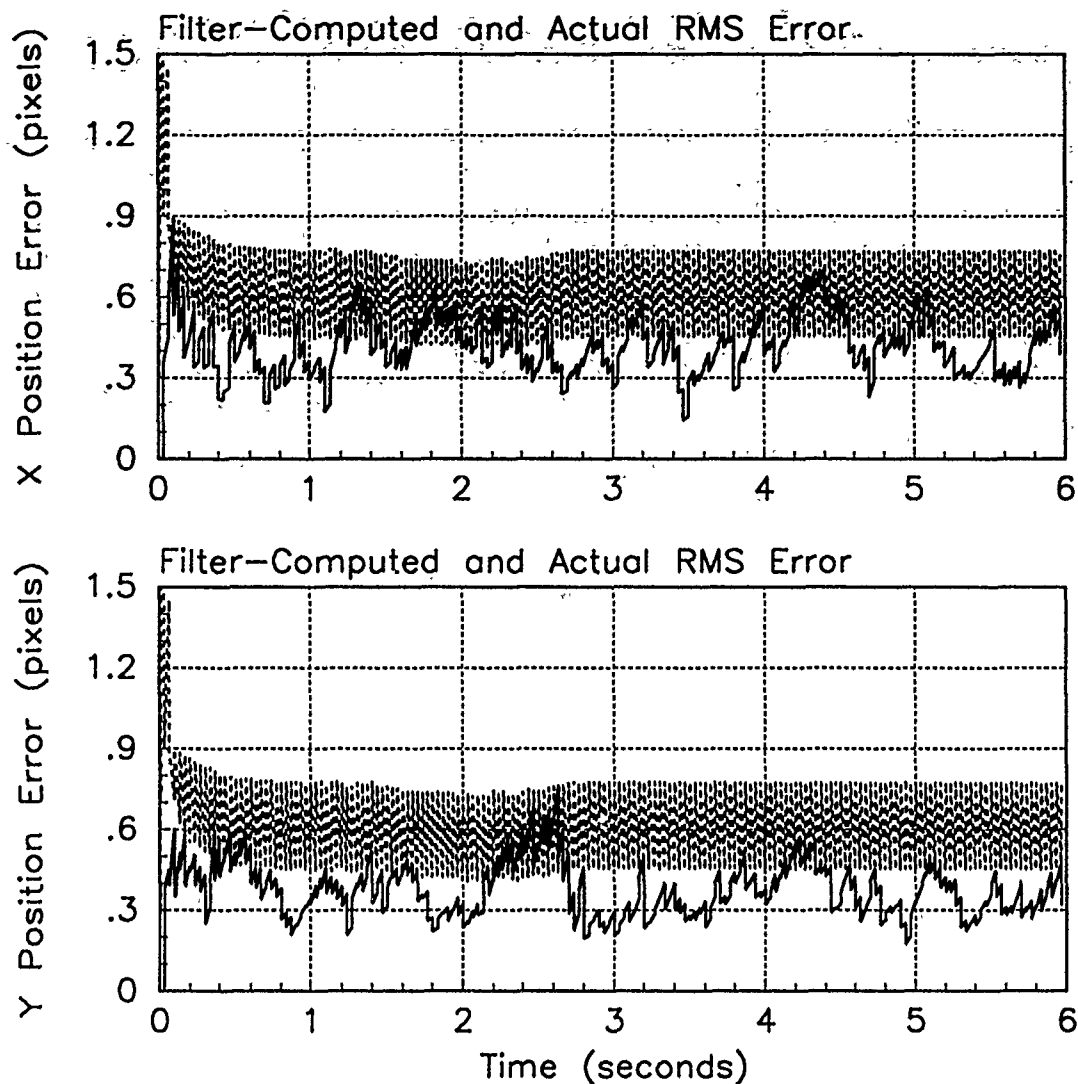


Figure E.65. RMS Error Plots; Notch MMAE-2RM; PC is 4; Trajectory with $\omega = 1.32$

Table E.21. Temporal Averages and Residuals; Notch MMAE-2RM; PC is 4; Trajectory with $\omega = 1.32$.

Error in:	Mean	σ
$p_x(t_i^-)$	-0.058428	0.44490
$p_x(t_i^+)$	-0.051705	0.39259
$y_x(t_i^-)$	-0.038729	0.39657
$p_y(t_i^-)$	0.0018327	0.39795
$p_y(t_i^+)$	-0.0046705	0.34698
$y_y(t_i^-)$	-0.0060652	0.38019

Filter	$\mathbf{r}_k^T \mathbf{r}_k$	$\mathbf{r}_k^T \mathbf{A}_k^{-1} \mathbf{r}_k$
Benign	0.39496	2.33781
Intermediate	0.33220	1.81221
Harsh	0.38849	1.76957

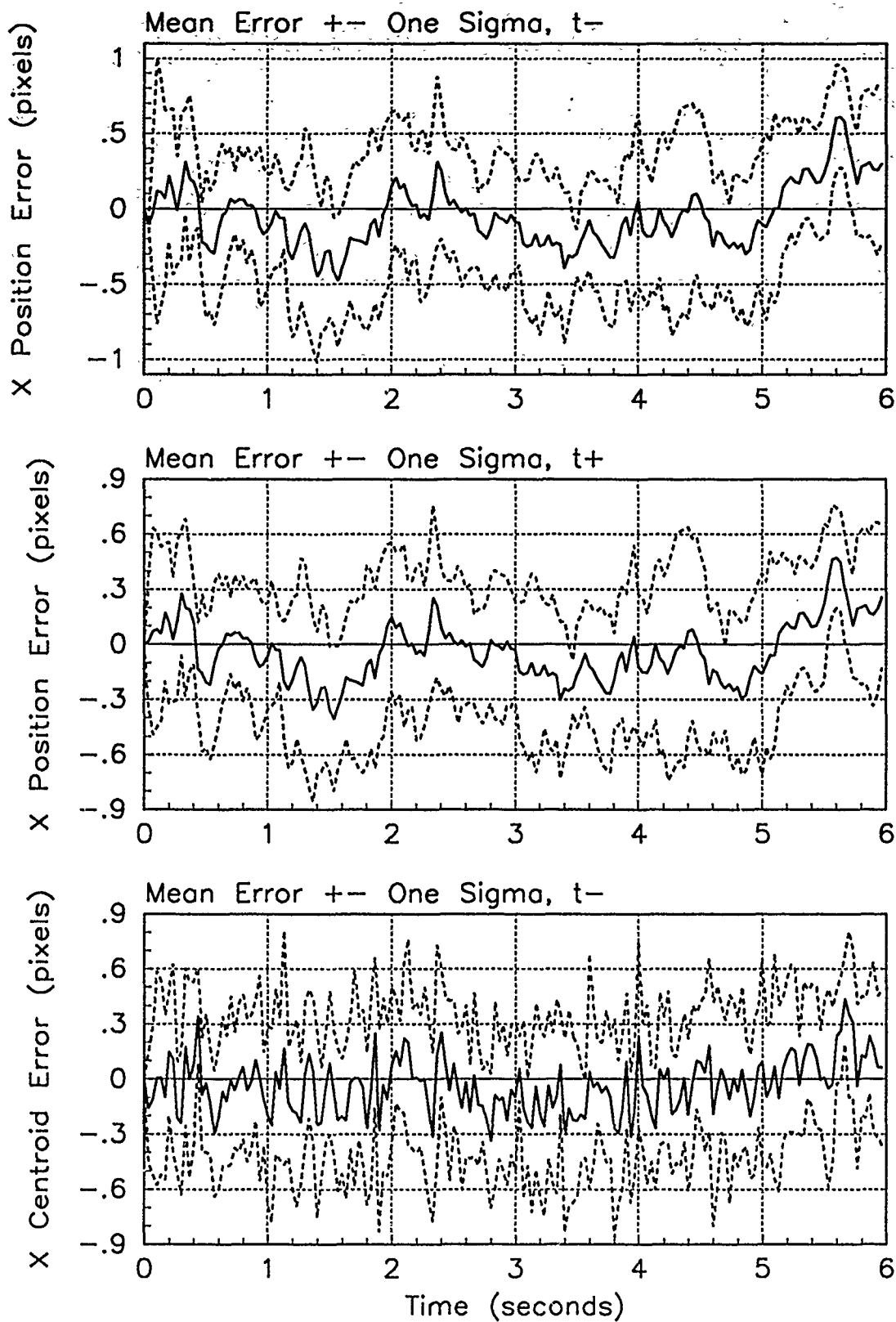


Figure E.66. X-Error Plots; Notch MMAE-2RM; PC is 4; Trajectory with $\omega = 1.32$

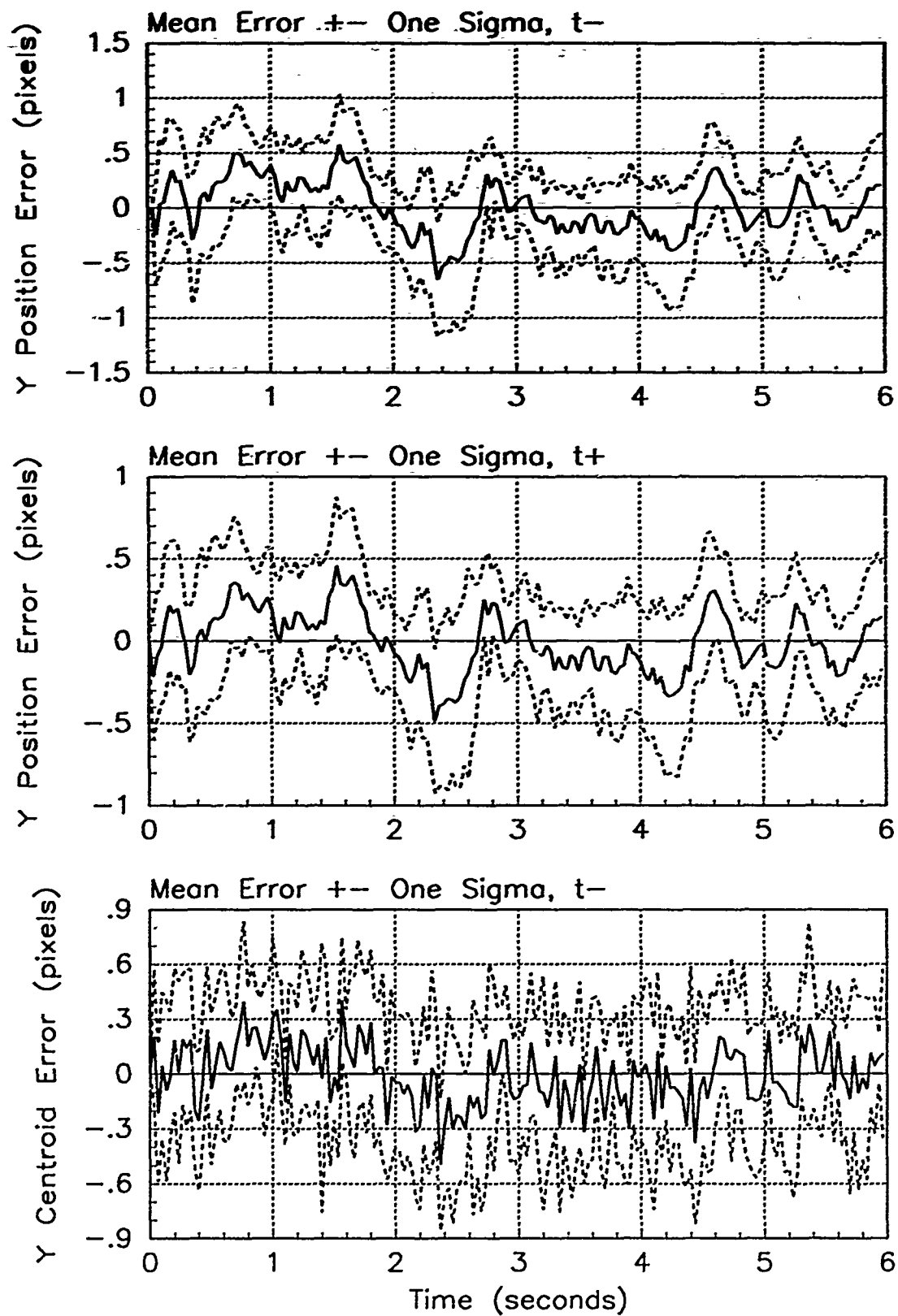


Figure E.67. Y-Error Plots; Notch MMAE-2RM; PC is 4; Trajectory with $\omega = 1.32$

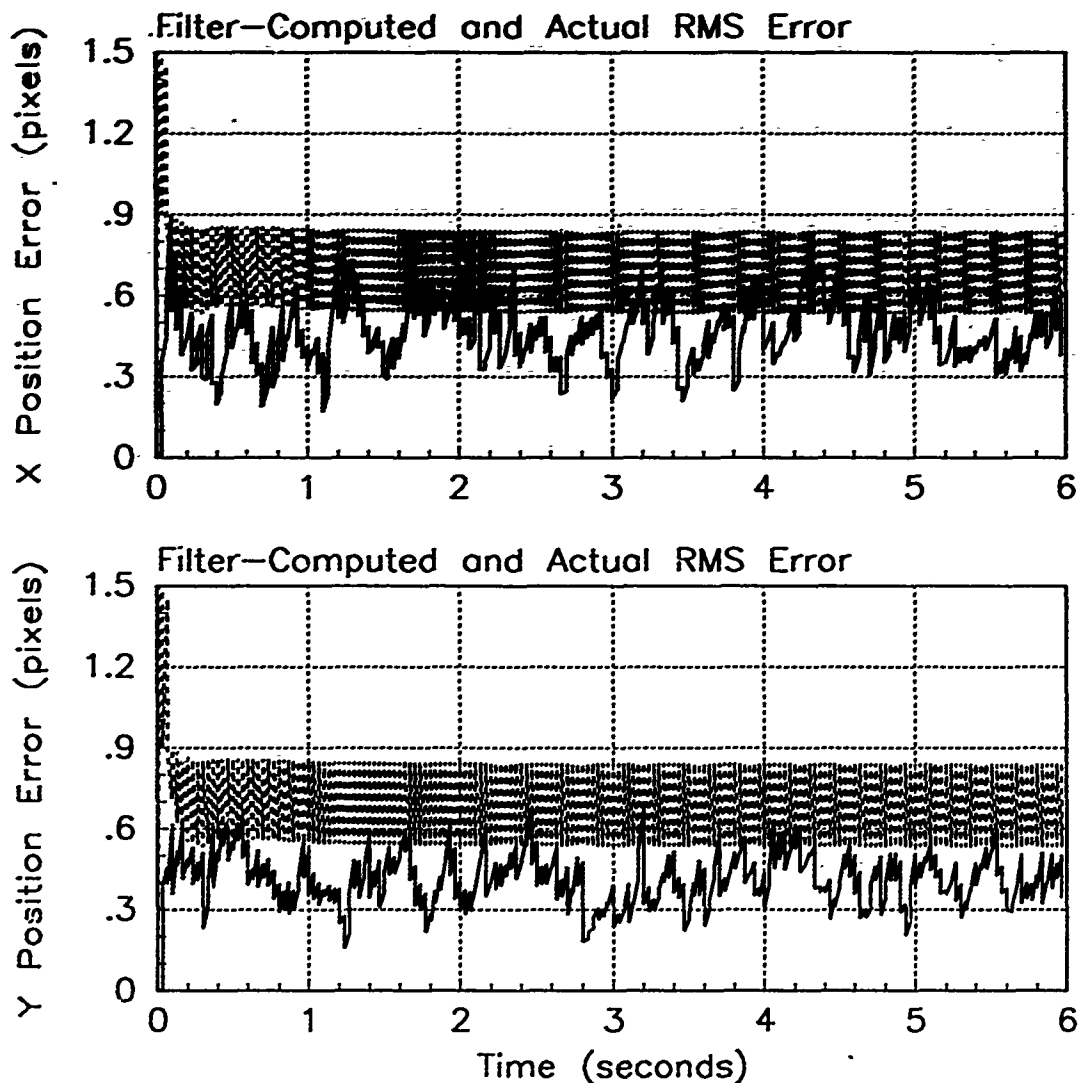


Figure E.68. RMS Error Plots; Notch MMAE-2RM; PC is 4; Trajectory with $\omega = 2.8$

Table E.22. Temporal Averages and Residuals; Notch MMAE-2RM; PC is 4; Trajectory with $\omega = 2.8$.

Error in:	Mean	σ
$p_x(t_i^-)$	-0.10655	0.50686
$p_x(t_i^+)$	-0.069795	0.42524
$y_x(t_i^-)$	-0.071117	0.41854
$p_y(t_i^-)$	0.054462	0.44973
$p_y(t_i^+)$	0.016408	0.37101
$y_y(t_i^-)$	0.034950	0.40231

Filter	$r_k^T r_k$	$r_k^T A_k^{-1} r_k$
Benign	2.15511	12.57190
Intermediate	1.23253	6.79541
Harsh	0.40027	1.81933

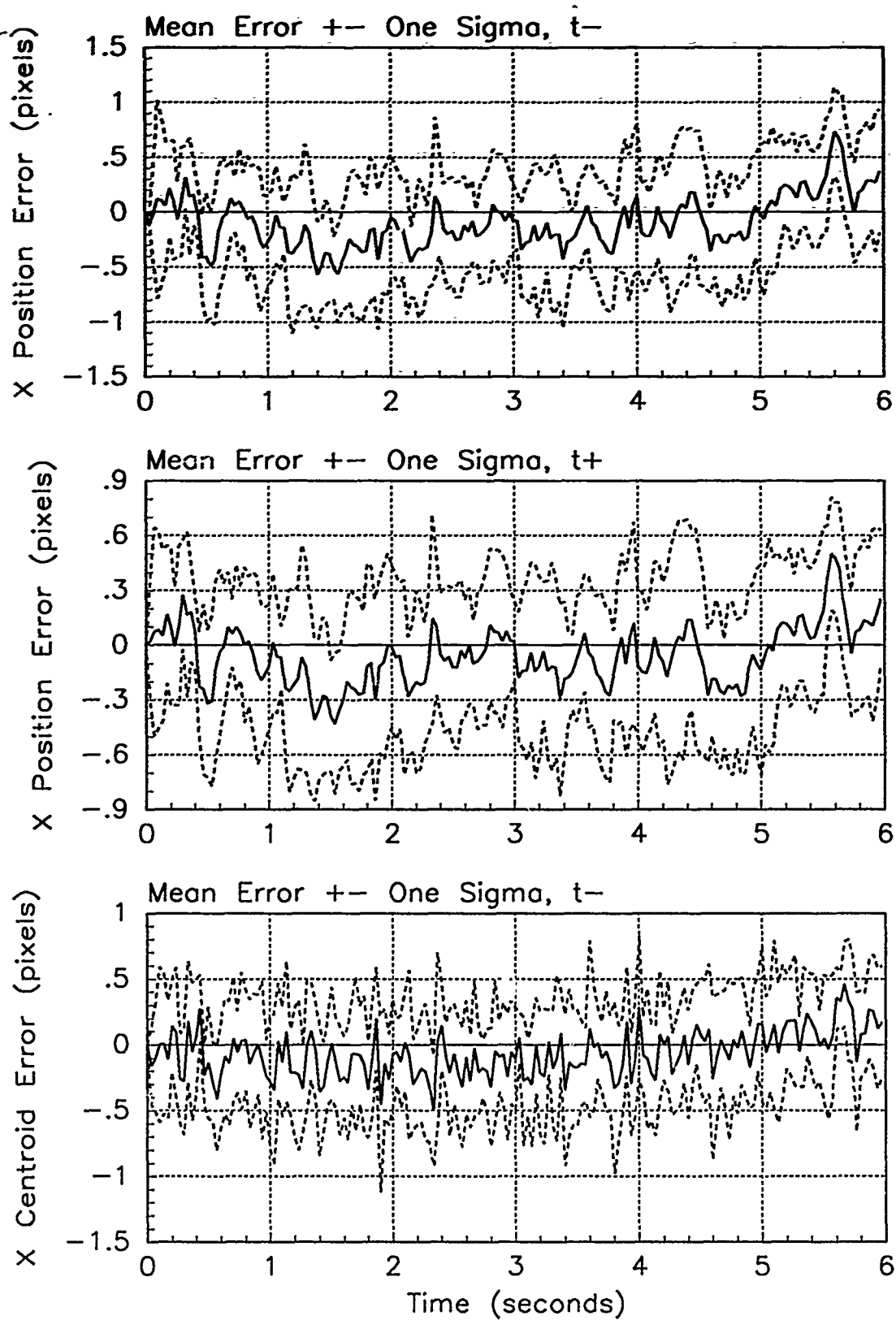


Figure E.69. X-Error Plots; Notch MMAE-2RM; PC is 4; Trajectory with $\omega = 2.8$

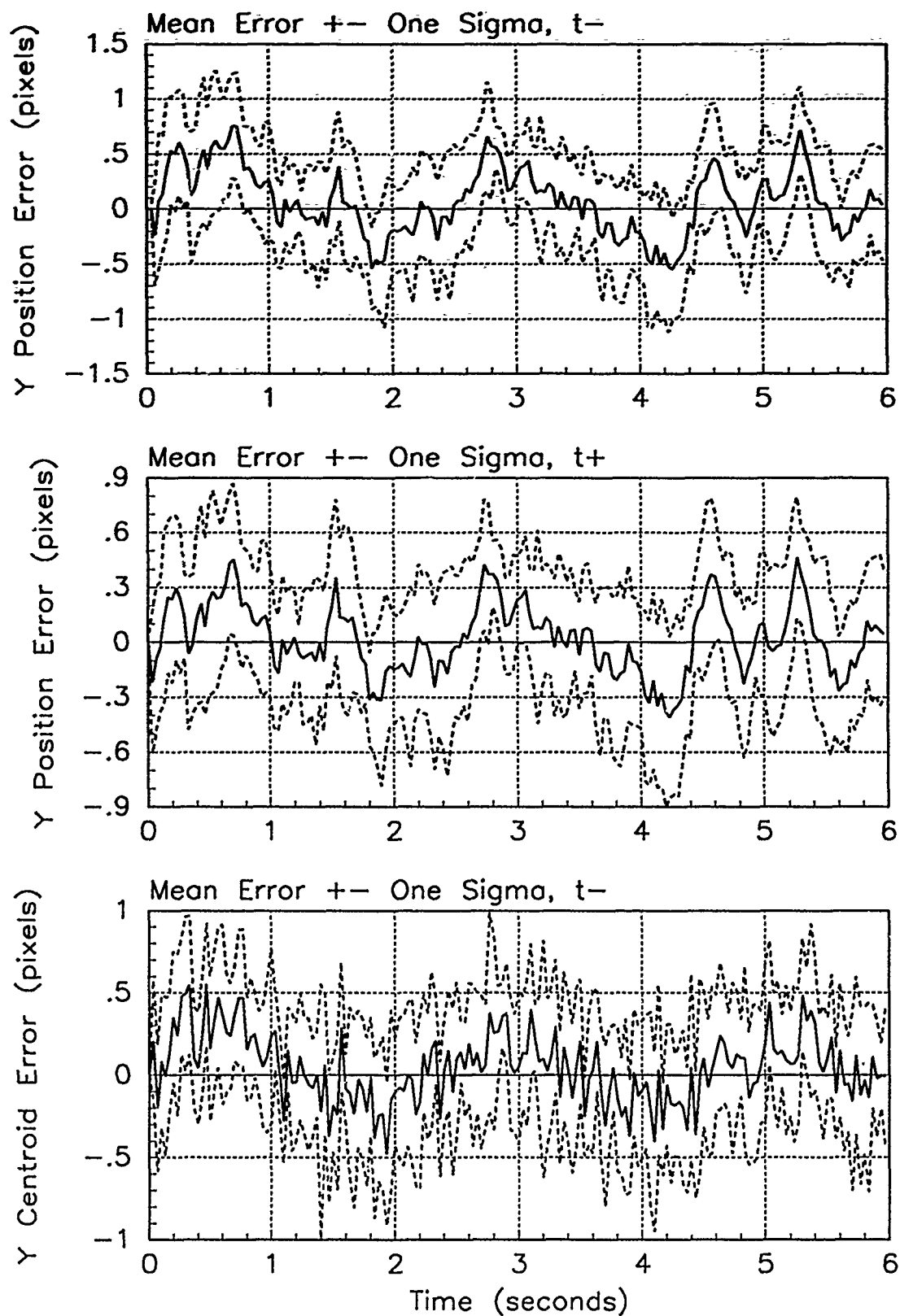


Figure E.70. Y-Error Plots; Notch MMAE-2RM; PC is 4; Trajectory with $\omega = 2.8$

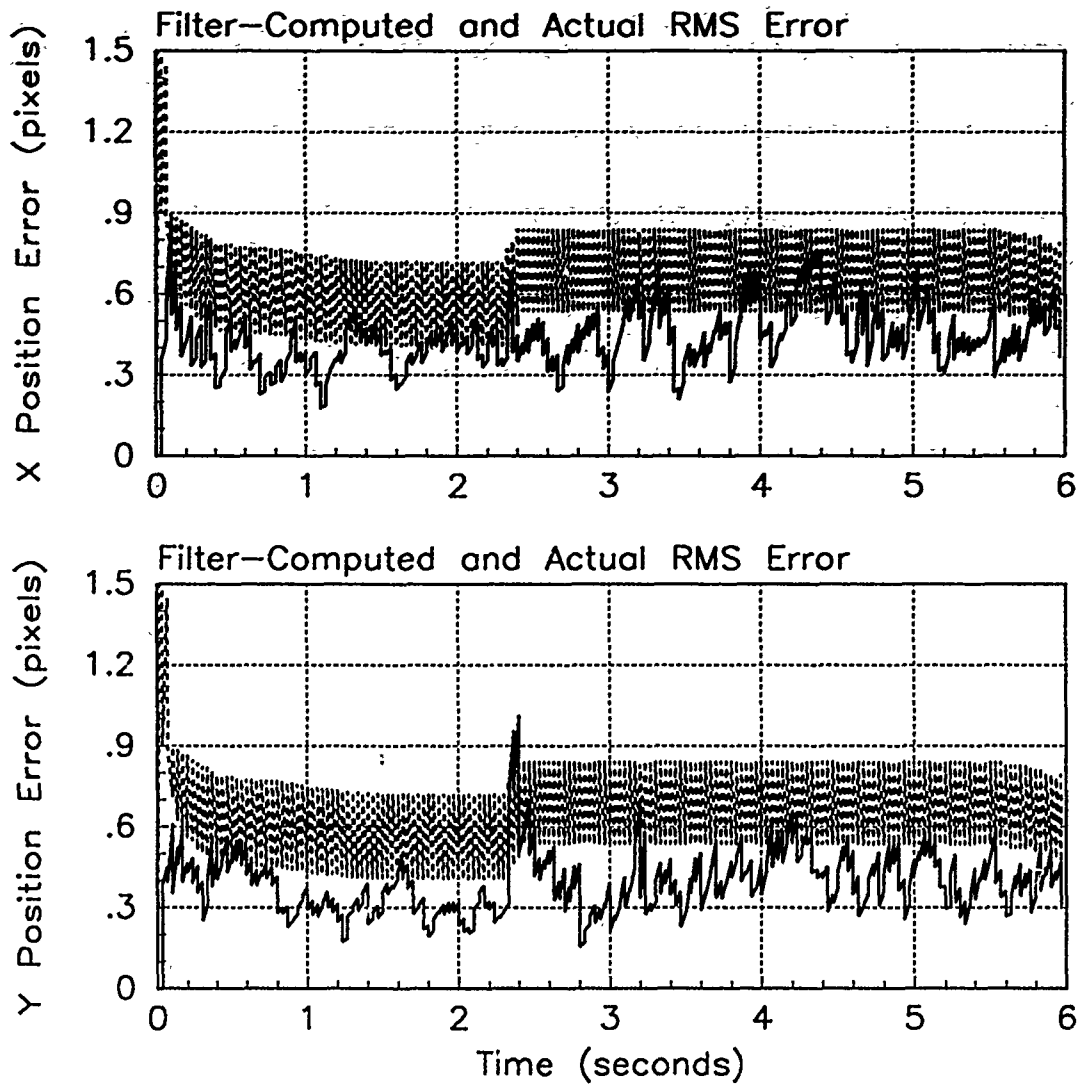


Figure E.71. RMS Error Plots; Notch MMAE-2RM; PC is 1; Jinking Trajectory

Table E.23. Temporal Averages; Notch MMAE-2RM; PC is 1; Jinking Trajectory.

Error in:	Mean	σ
$p_x(t_i^-)$	-0.013476	0.46916
$p_x(t_i^+)$	-0.013134	0.40511
$y_x(t_i^-)$	-0.0054122	0.40593
$p_y(t_i^-)$	0.12341	0.42130
$p_y(t_i^+)$	0.074803	0.35758
$y_y(t_i^-)$	0.093291	0.39254

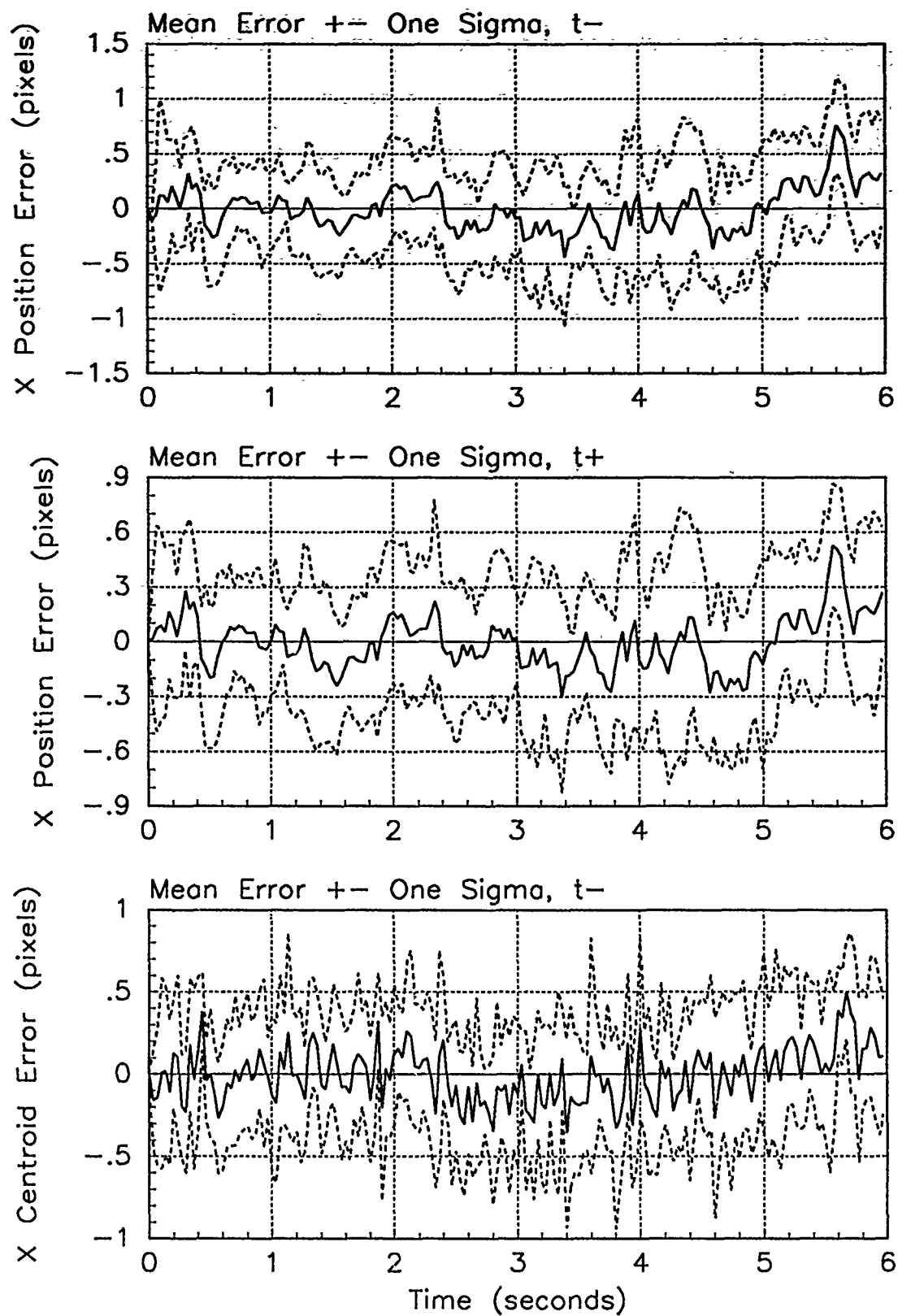


Figure E.72. X-Error Plots; Notch MMAE-2RM; PC is 1; Jinking Trajectory

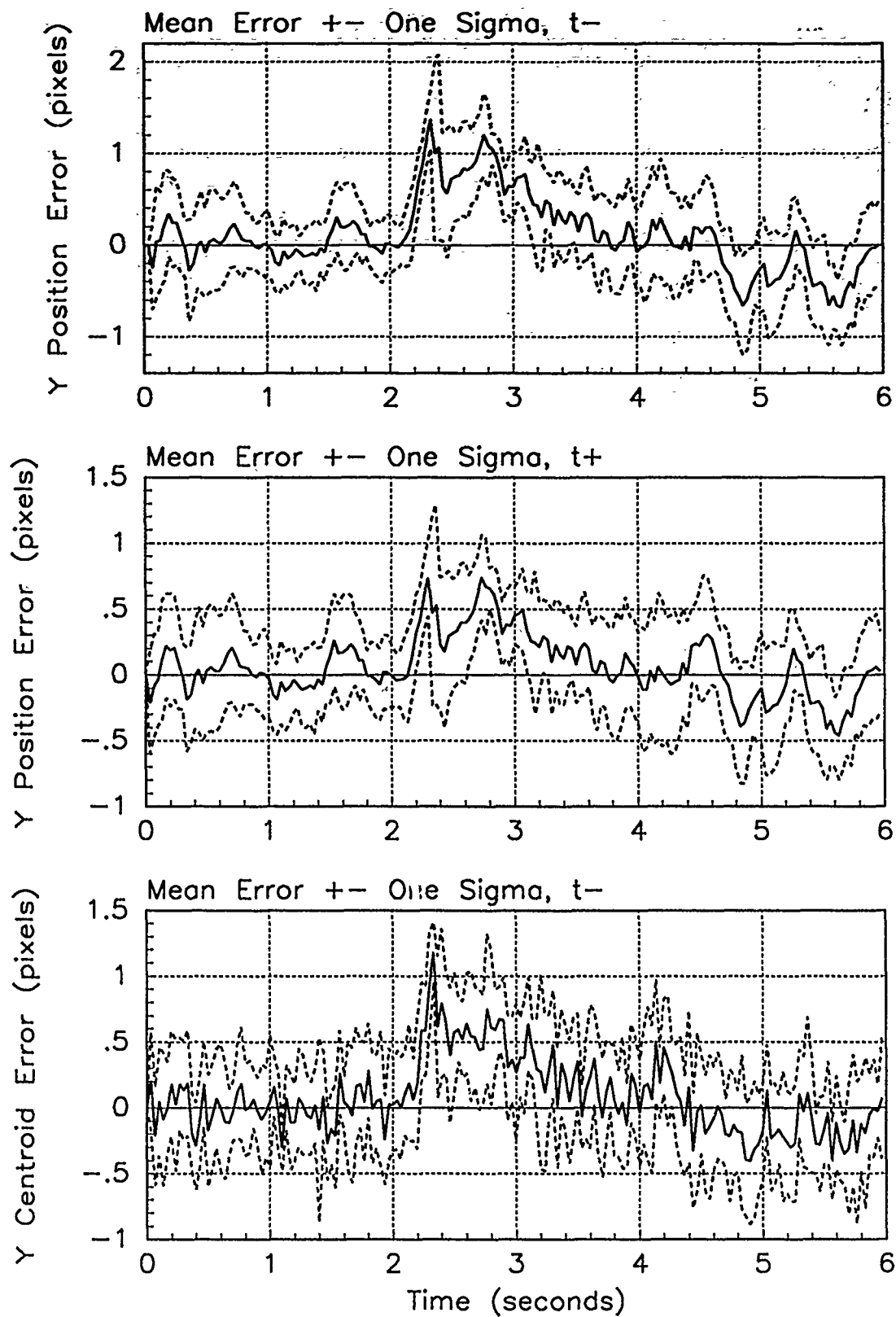


Figure E.73. Y-Error Plots; Notch MMAE-2RM; PC is 1; Jinking Trajectory

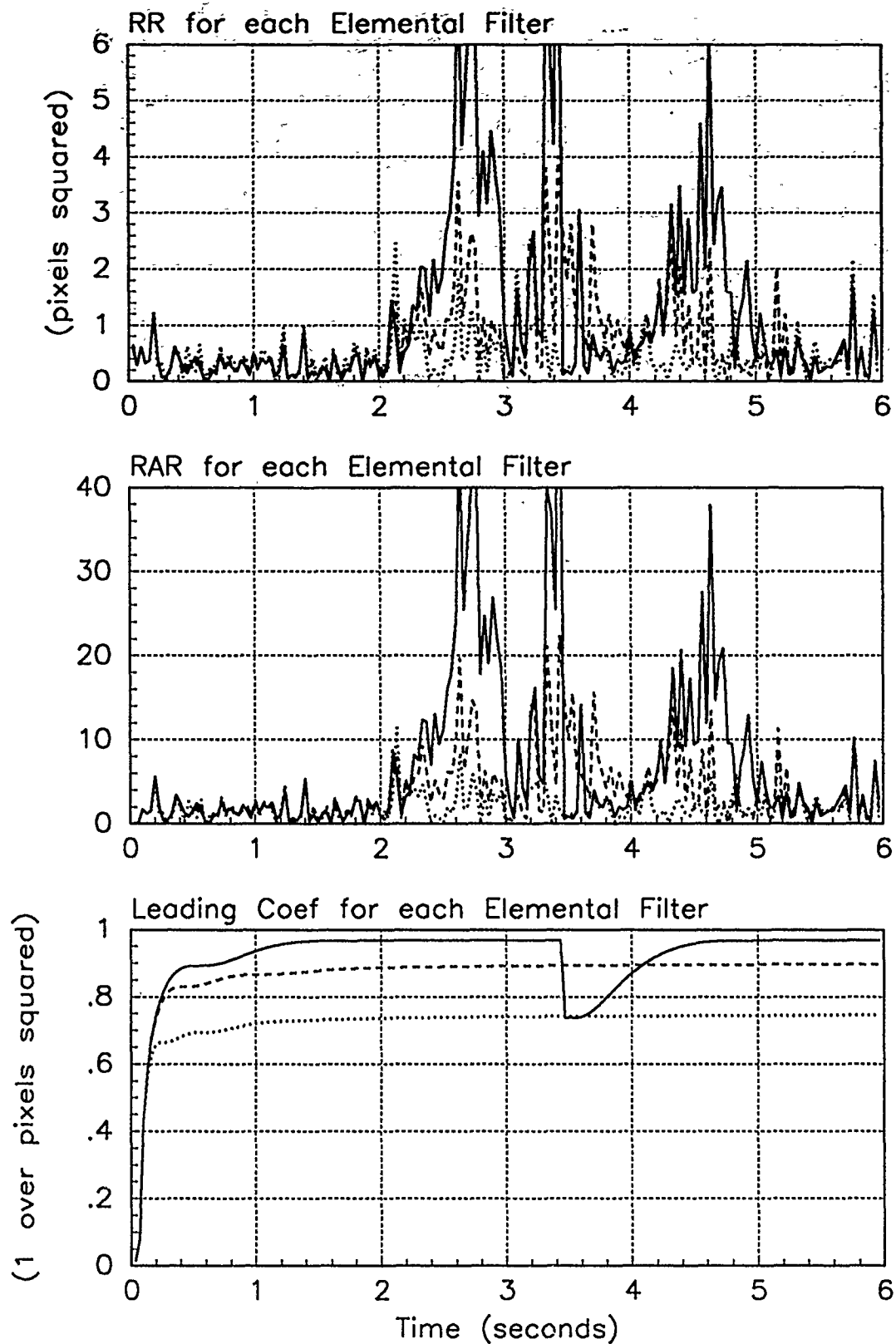


Figure E.74. Probability Calculation Plots; Notch MMAE-2RM; PC is 1; Jinking Trajectory. Benign filter has solid line; intermediate filter has dashed line; harsh filter has dotted line.

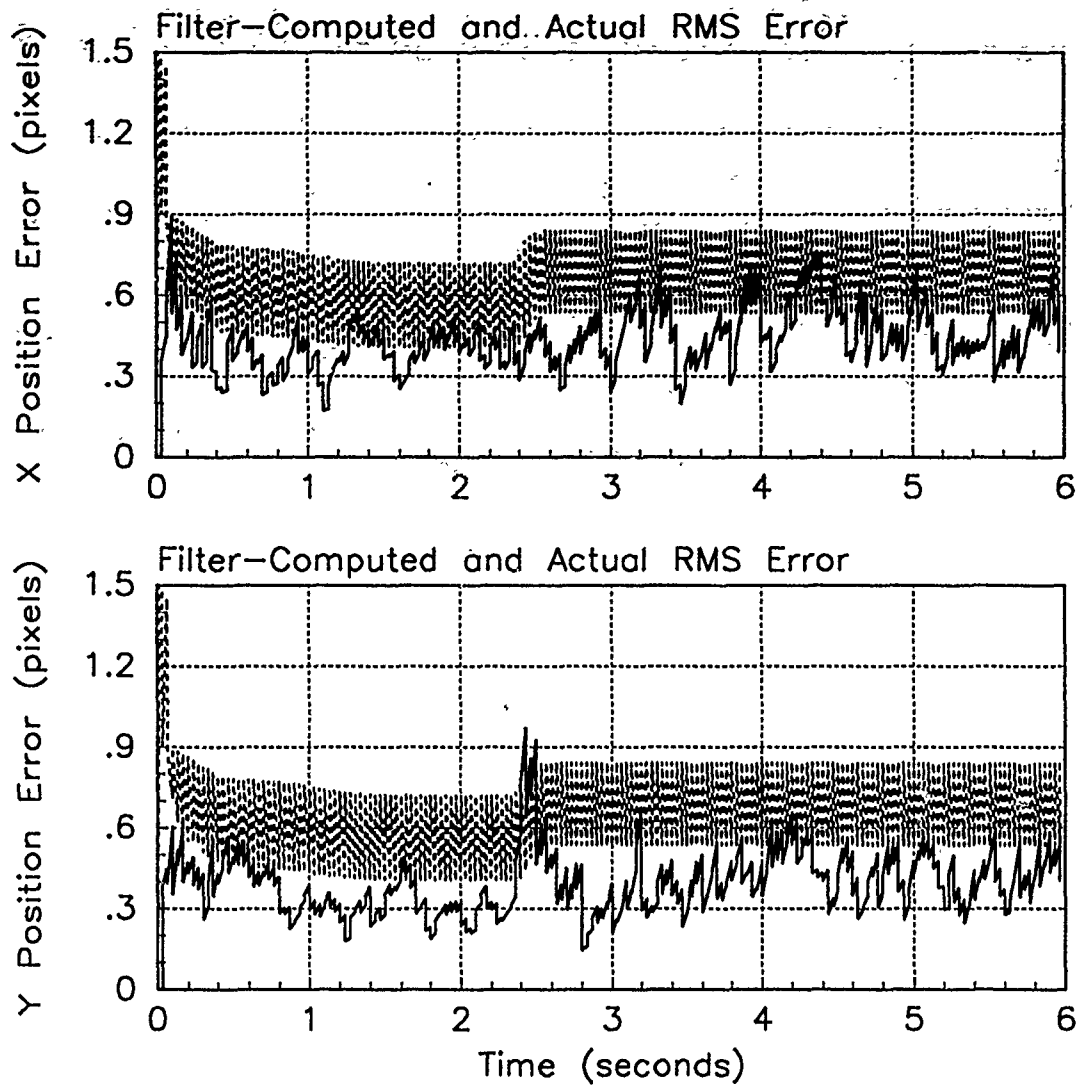


Figure E.75. RMS Error Plots; Notch MMAE-2RM; PC is 4; Jinking Trajectory

Table E.24. Temporal Averages; Notch MMAE-2RM; PC is 4; Jinking Trajectory.

Error in:	Mean	σ
$p_x(t_i^-)$	-0.016032	0.46839
$p_x(t_i^+)$	-0.017465	0.40464
$y_x(t_i^-)$	-0.0074021	0.40618
$p_y(t_i^-)$	0.14398	0.42371
$p_y(t_i^+)$	0.089285	0.36003
$y_y(t_i^-)$	0.10522	0.39282

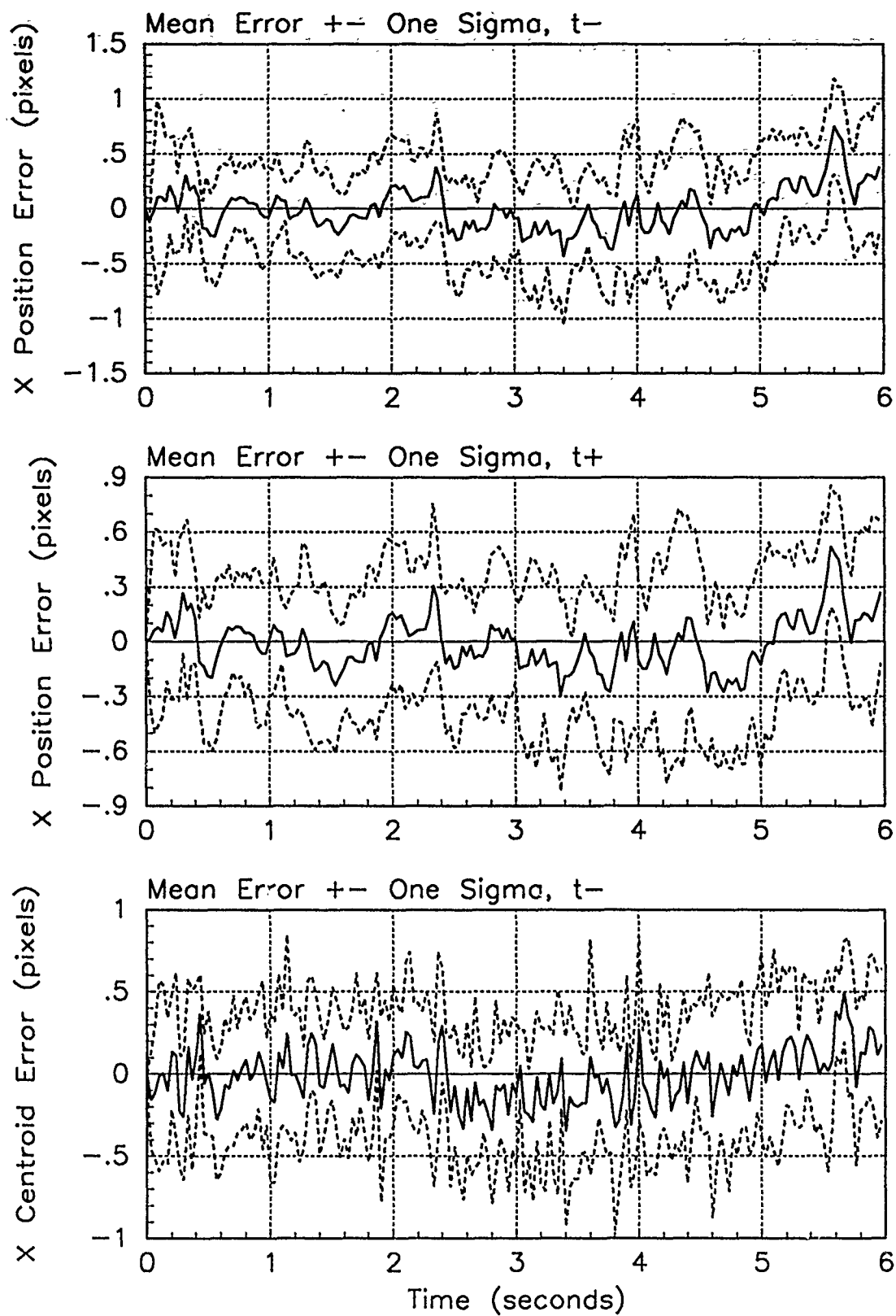


Figure E.76. X-Error Plots; Notch MMAE-2RM; PC is 4; Jinking Trajectory

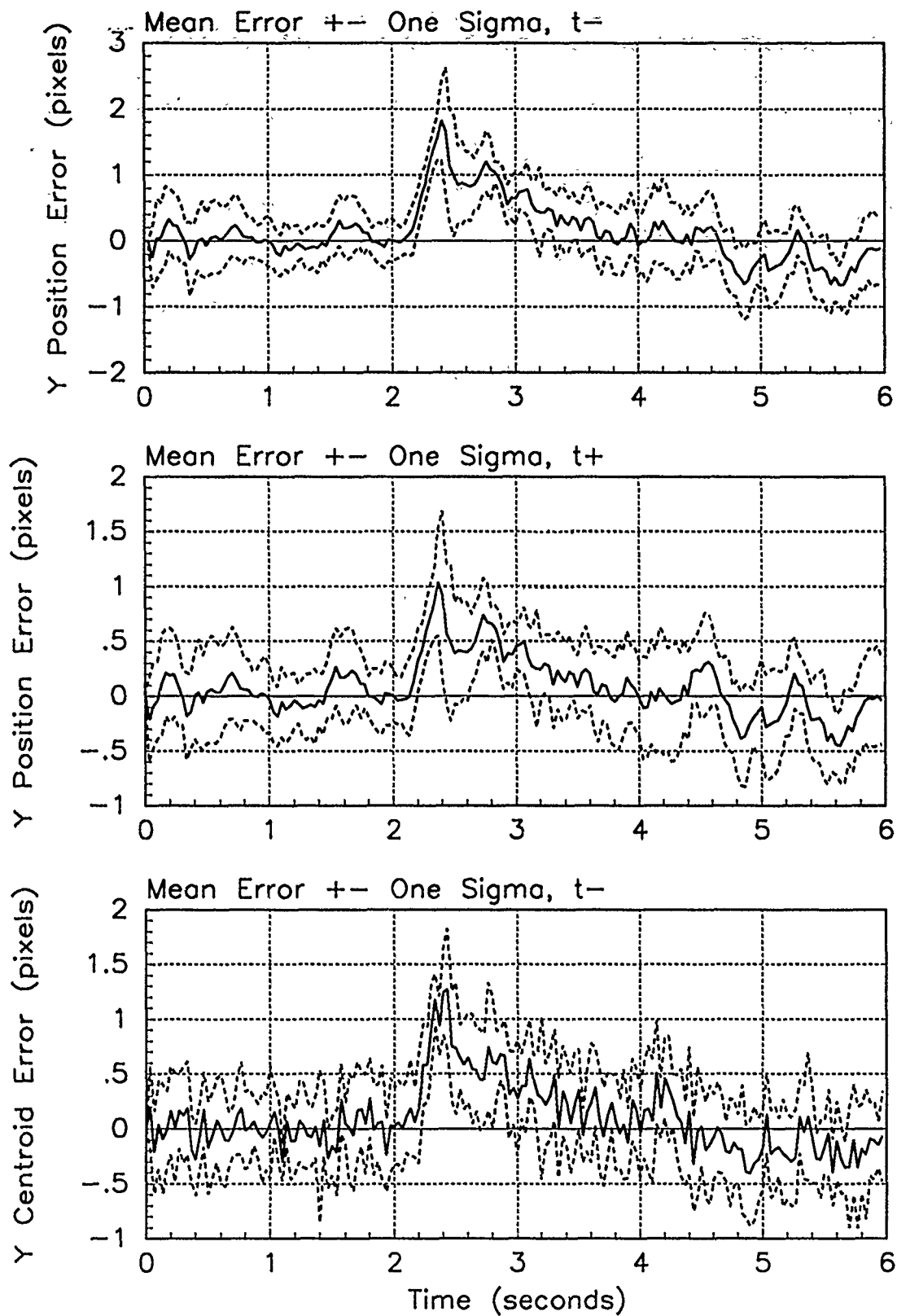


Figure E.77. Y-Error Plots; Notch MMAE-2RM; PC is 4; Jinking Trajectory

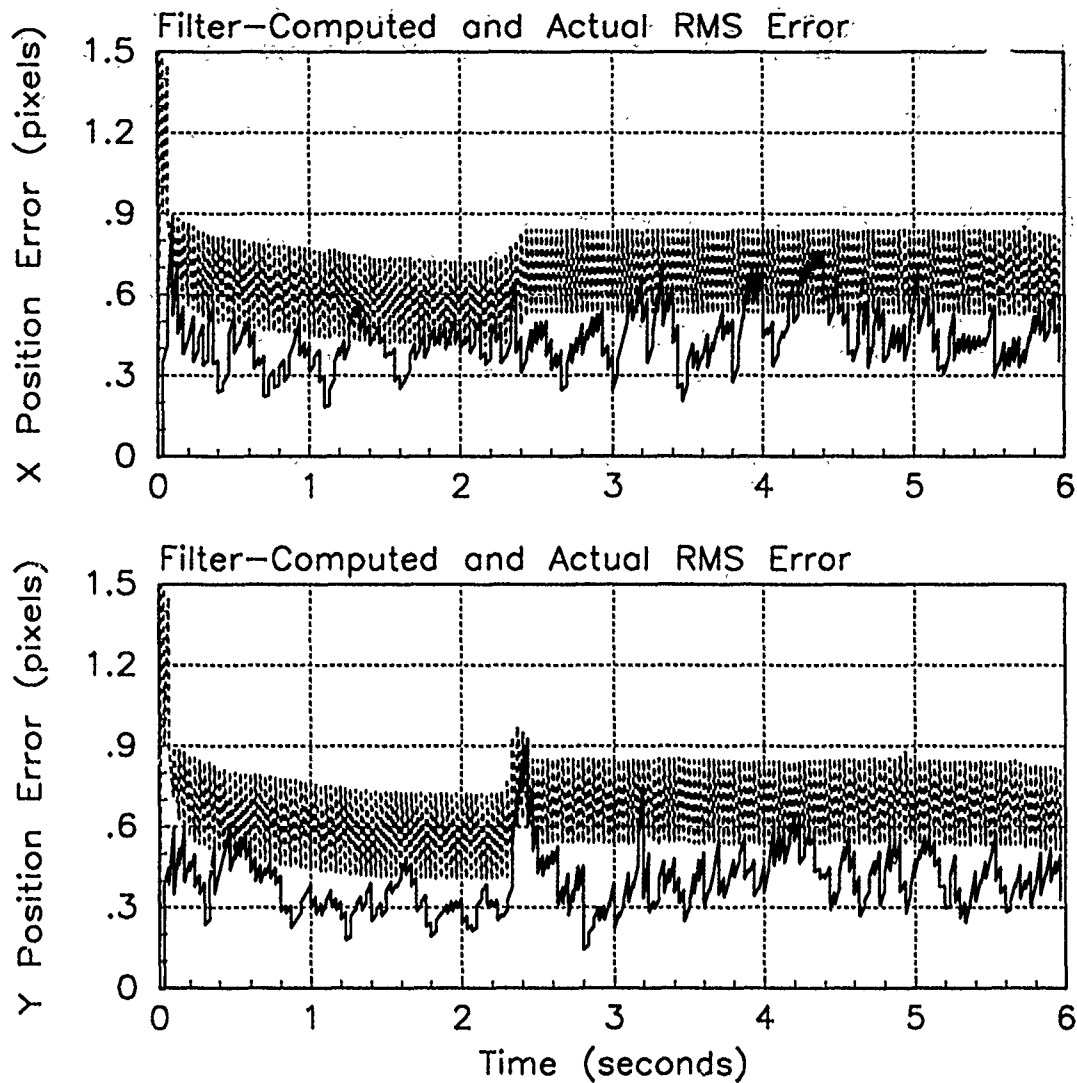


Figure E.79. RMS Error Plots; Notch MMAE-2R; PC is 1; LB is .0005; Jinking Trajectory

Table E.25. Temporal Averages; Notch MMAE-2R; PC is 1; LB is .0005; Jinking Trajectory.

Error in:	Mean	σ
$p_x(t_i^-)$	-0.013262	0.47240
$p_x(t_i^+)$	-0.0094648	0.40840
$y_x(t_i^-)$	-0.0021152	0.40683
$p_y(t_i^-)$	0.13289	0.42523
$p_y(t_i^+)$	0.083128	0.36120
$y_y(t_i^-)$	0.10133	0.39302

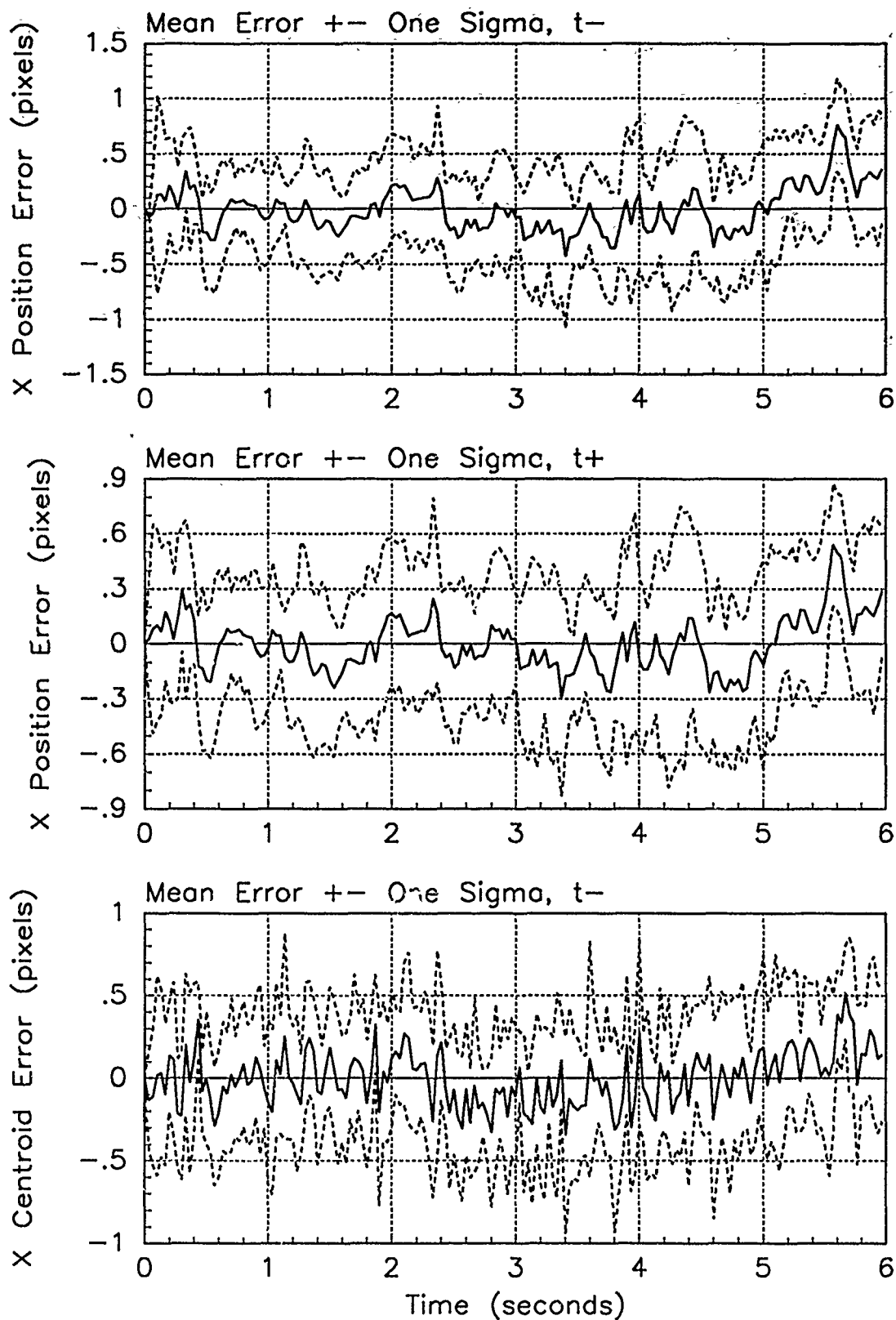


Figure E.80. X-Error Plots; Notch MMAE-2R; PC is 1; LB is .0005; Jinking Trajectory

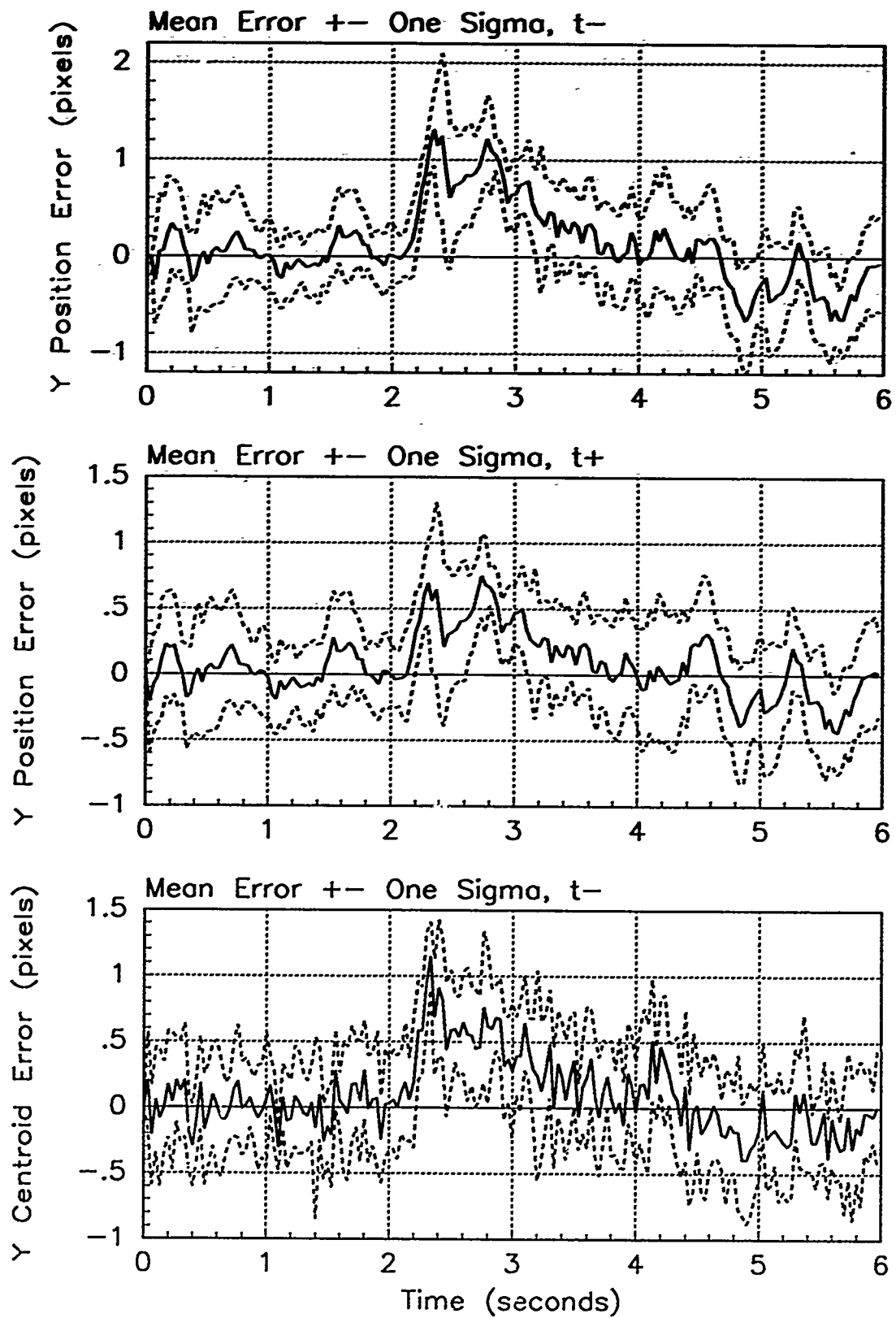


Figure E.81. Y-Error Plots; Notch MMAE-2R; PC is 1; LB is .0005; Jinking Trajectory

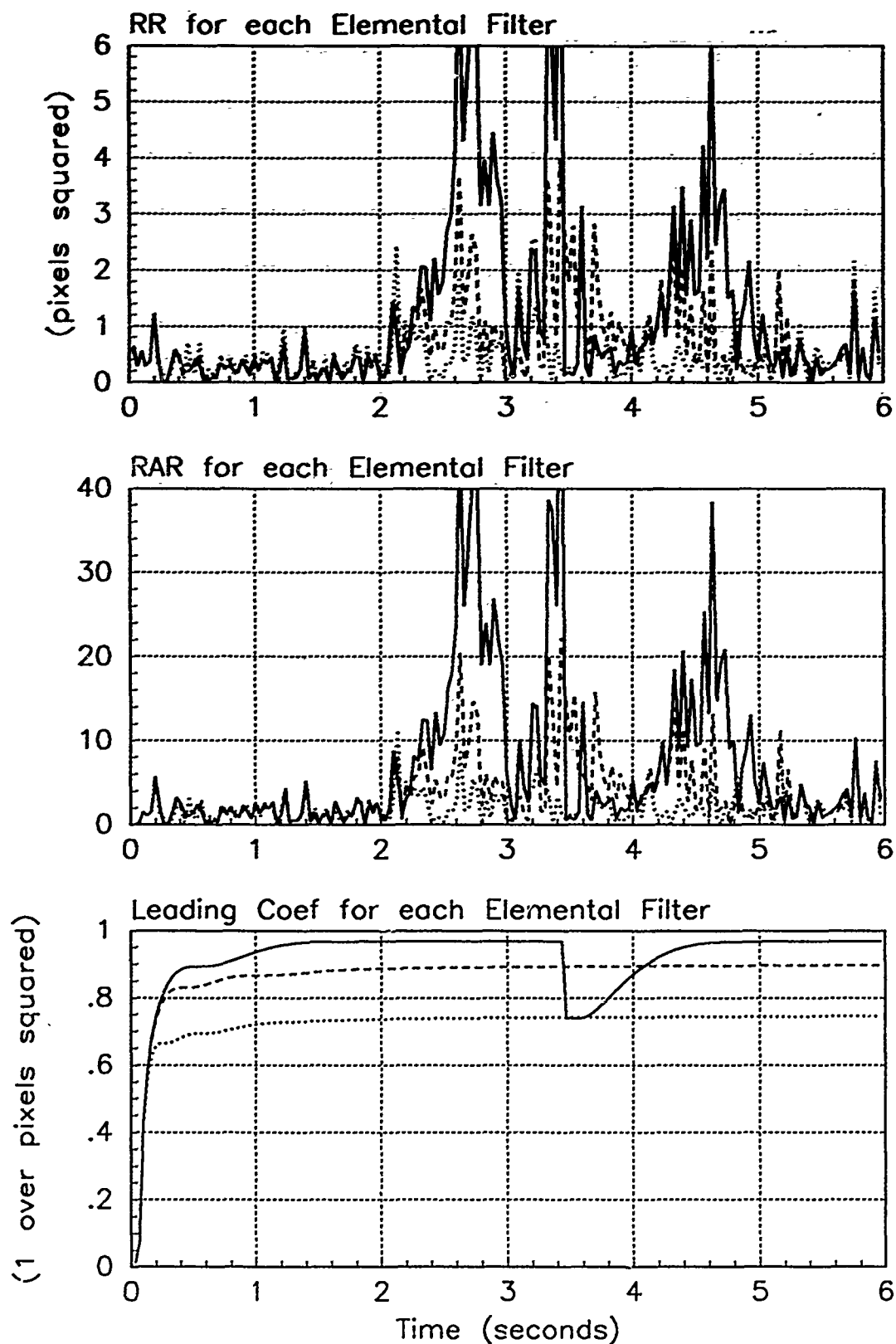


Figure E.82. Probability Calculation Plots; Notch MMAE-2R; PC is 1; LB is .0005; Jinking Trajectory. Benign filter has solid line; intermediate filter has dashed line; harsh filter has dotted line.

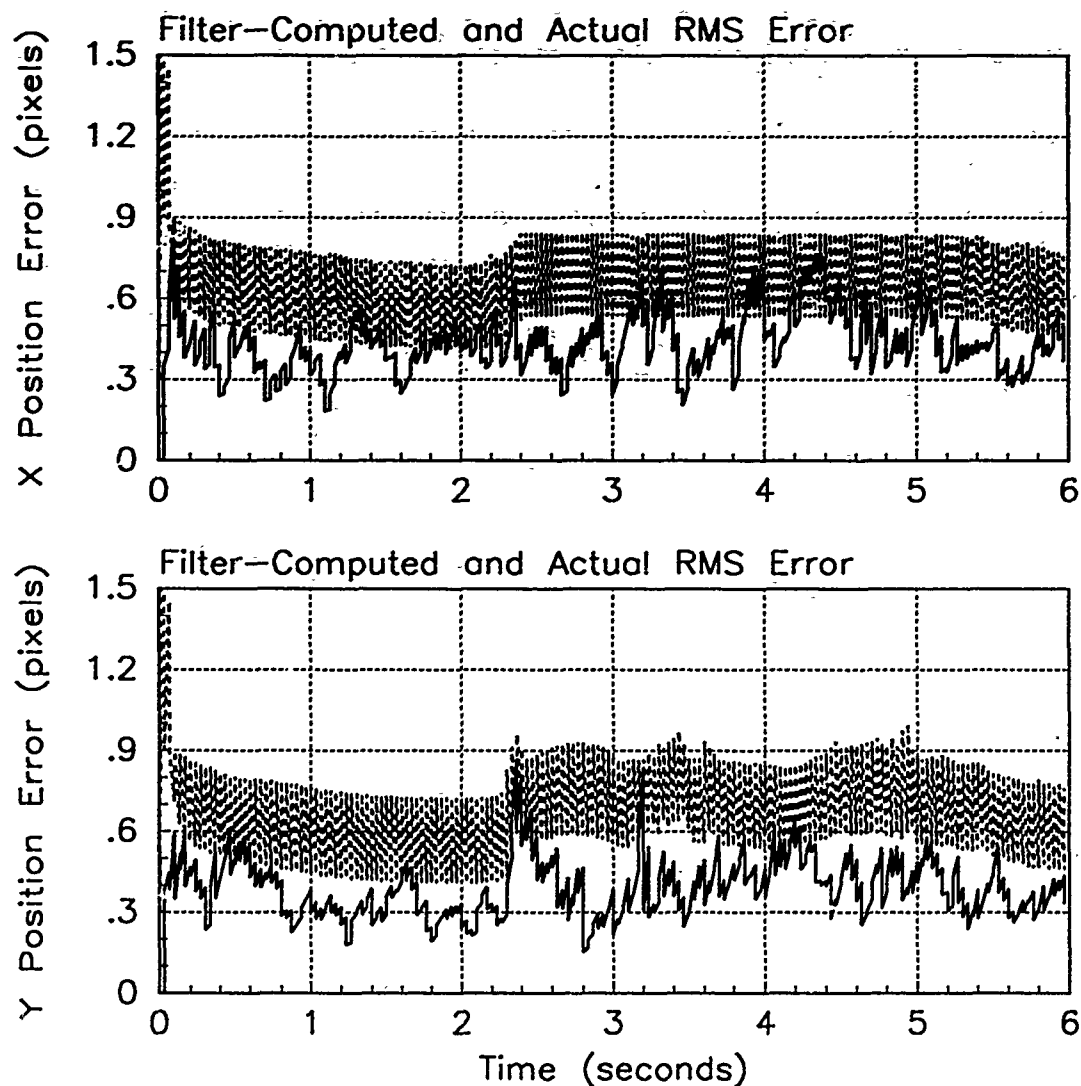


Figure E.83. RMS Error Plots; Notch MMAE-2R; PC is 1; LB is .005; Jinking Trajectory

Table E.26. Temporal Averages; Notch MMAE-2R; PC is 1; LB is .005; Jinking Trajectory.

Error in:	Mean	σ
$p_x(t_i^-)$	-0.0040466	0.46724
$p_x(t_i^+)$	0.0025857	0.40553
$y_x(t_i^-)$	0.0044920	0.40372
$p_y(t_i^-)$	0.13361	0.42075
$p_y(t_i^+)$	0.085555	0.35672
$y_y(t_i^-)$	0.10522	0.39225

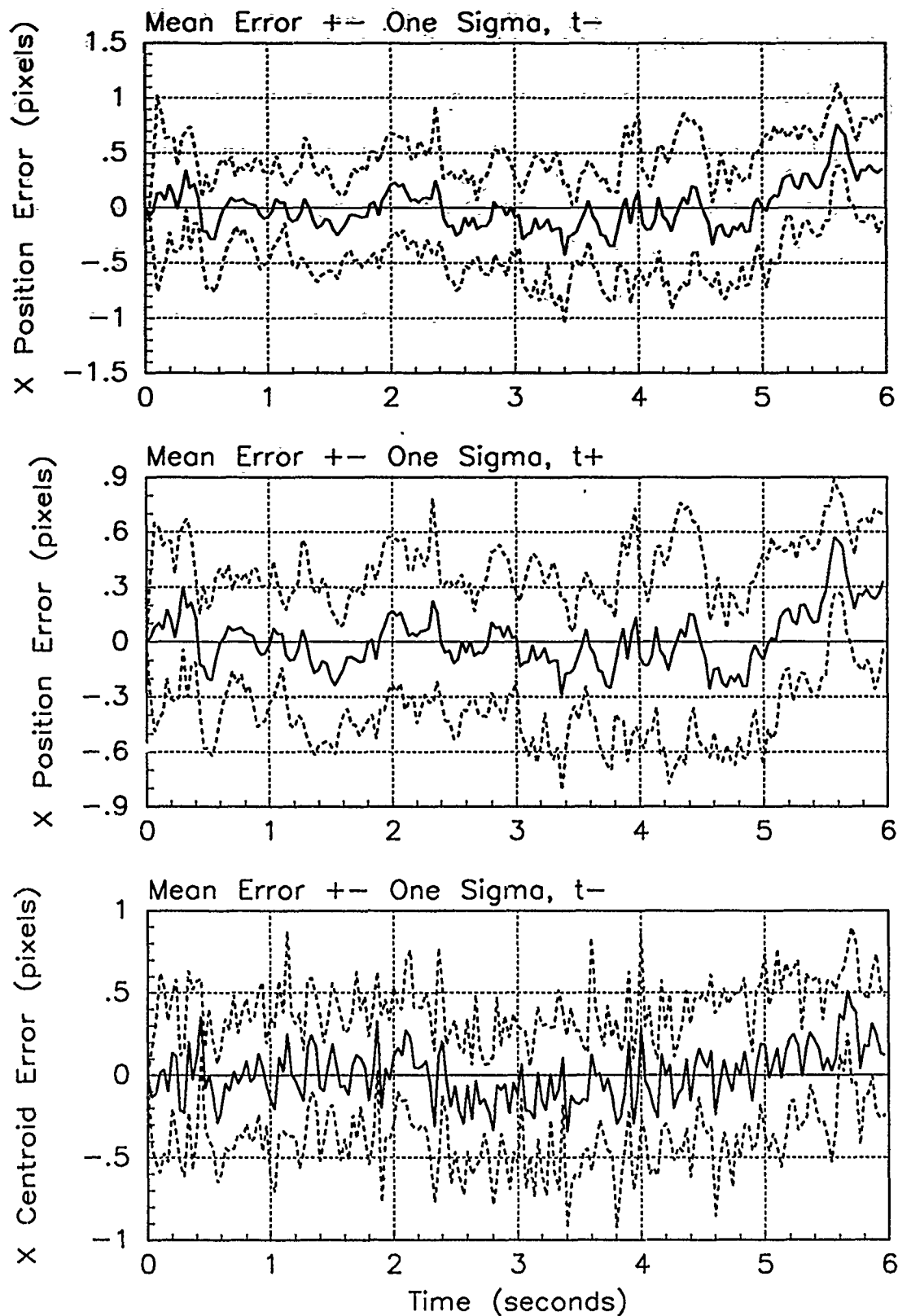


Figure E.84. X-Error Plots; Notch MMAE-2R; PC is 1; LB is .005; Jinking Trajectory

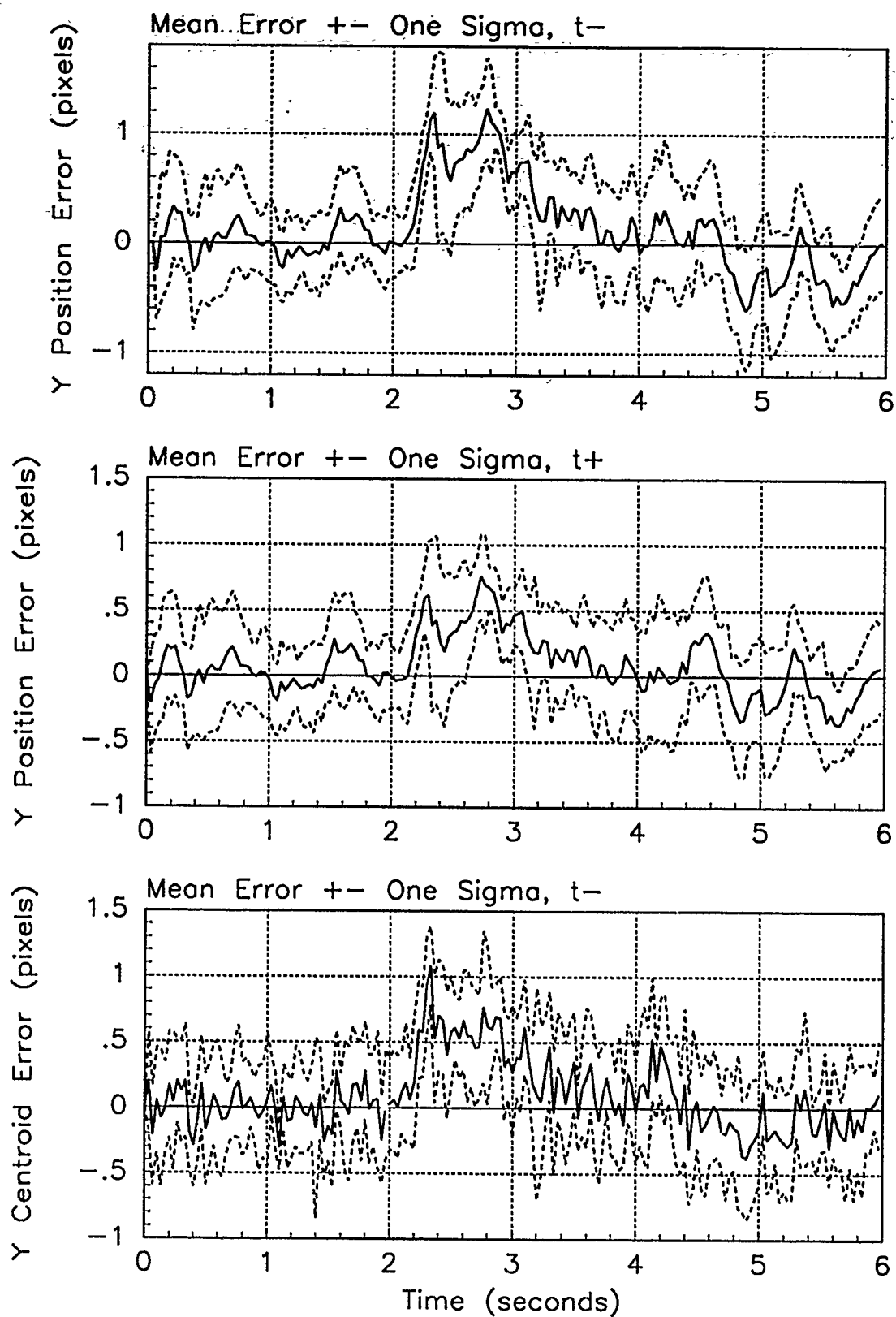


Figure E.85. Y-Error Plots; Notch MMAE-2R; PC is 1; LB is .005; Jinking Trajectory

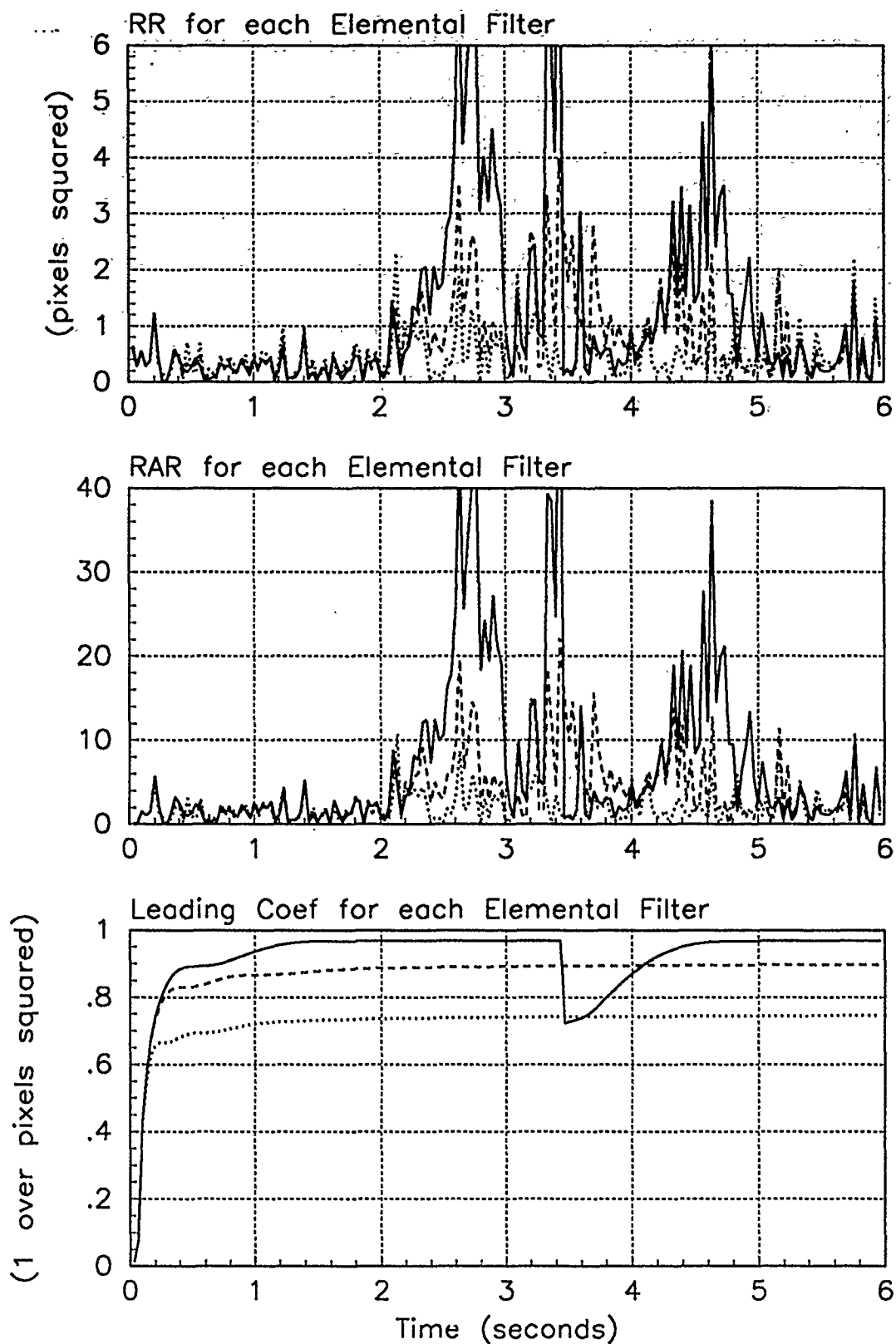


Figure E.86. Probability Calculation Plots; Notch MMAE-2R; PC is 1; LB is .005; Jinking Trajectory. Benign filter has solid line; intermediate filter has dashed line; harsh filter has dotted line.

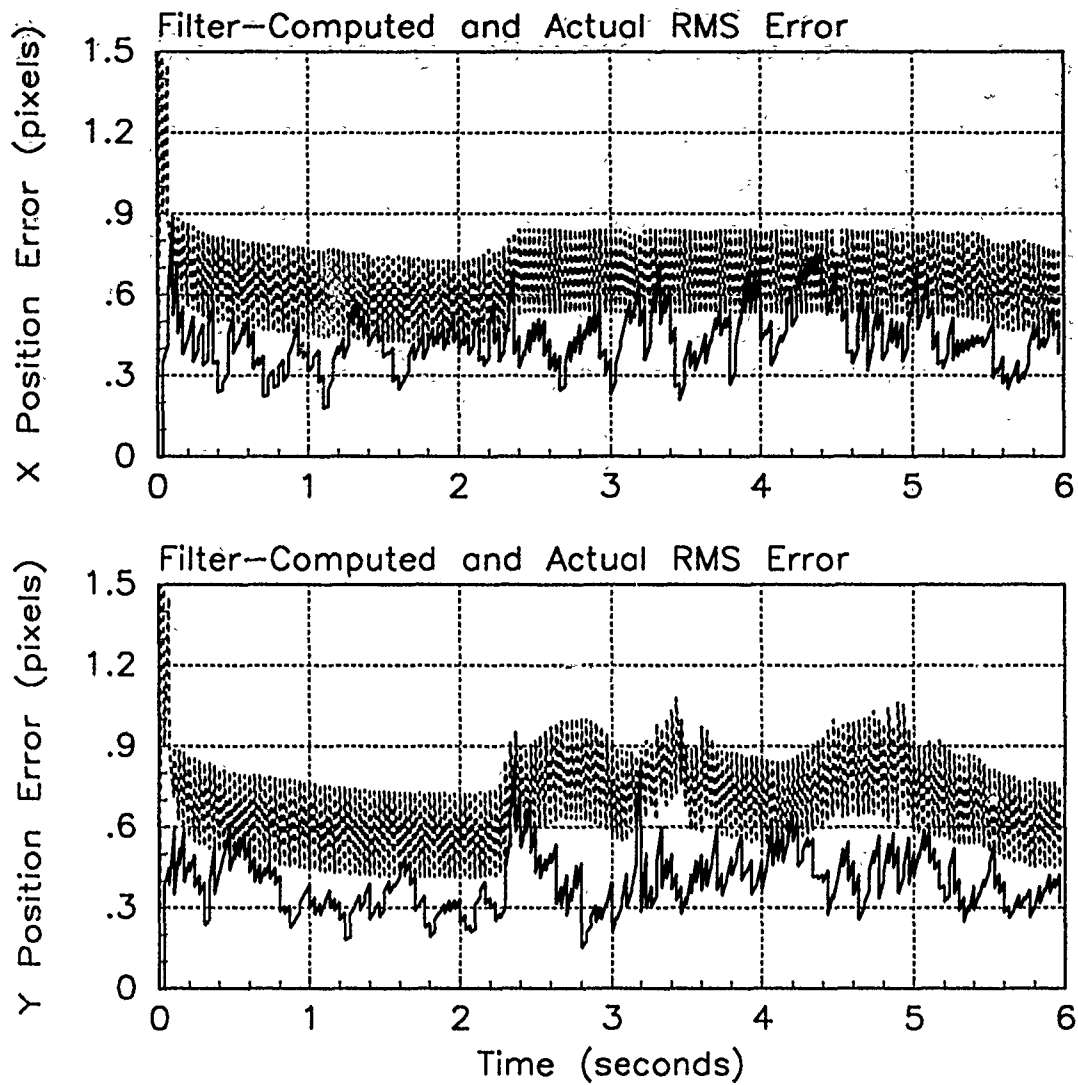


Figure E.87. RMS Error Plots; Notch MMAE-2R; PC is 1; LB is .01; Jinking Trajectory

Table E.27. Temporal Averages; Notch MMAE-2R; PC is 1; LB is .01; Jinking Trajectory.

Error in:	Mean	σ
$p_x(t_i^-)$	-0.0070001	0.46768
$p_x(t_i^+)$	0.00067360	0.40697
$y_x(t_i^-)$	0.0011930	0.40425
$p_y(t_i^-)$	0.12958	0.42494
$p_y(t_i^+)$	0.083140	0.36044
$y_y(t_i^-)$	0.10076	0.39329

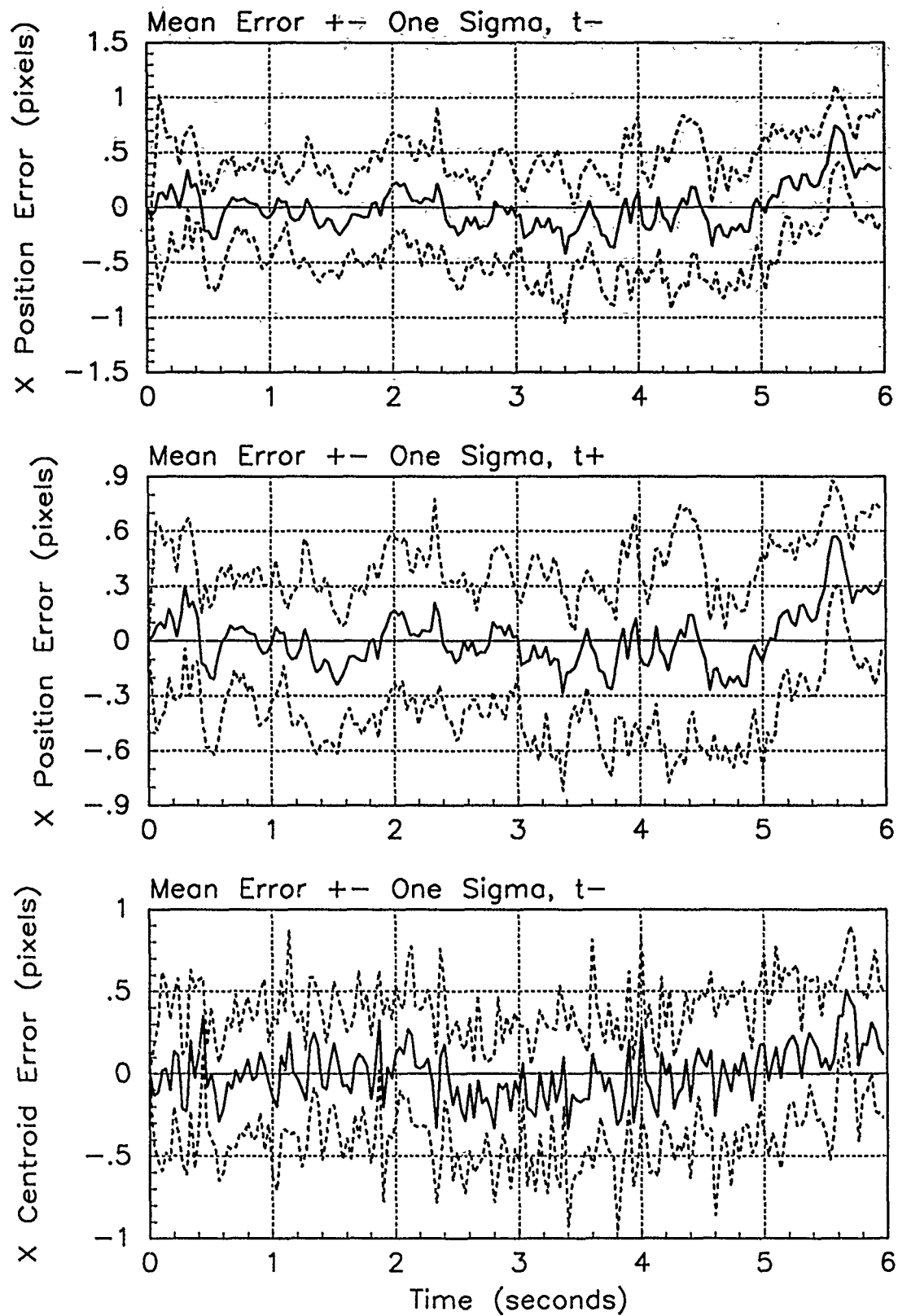


Figure E.88. X-Error Plots; Notch MMAE-2R; PC is 1; LB is .01; Jinking Trajectory

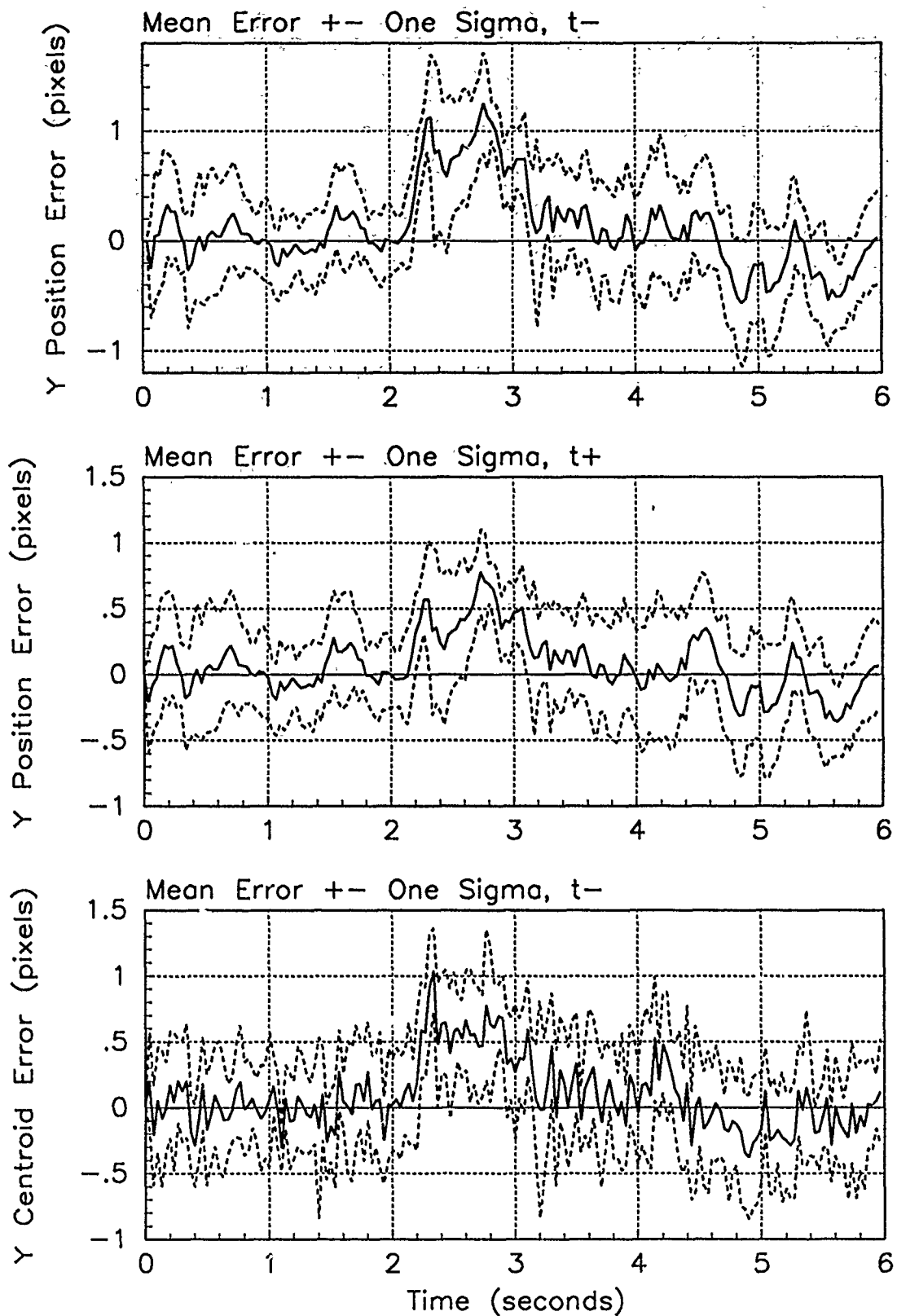


Figure E.89. Y-Error Plots; Notch MMAE-2R; PC is 1; LB is .01; Jinking Trajectory

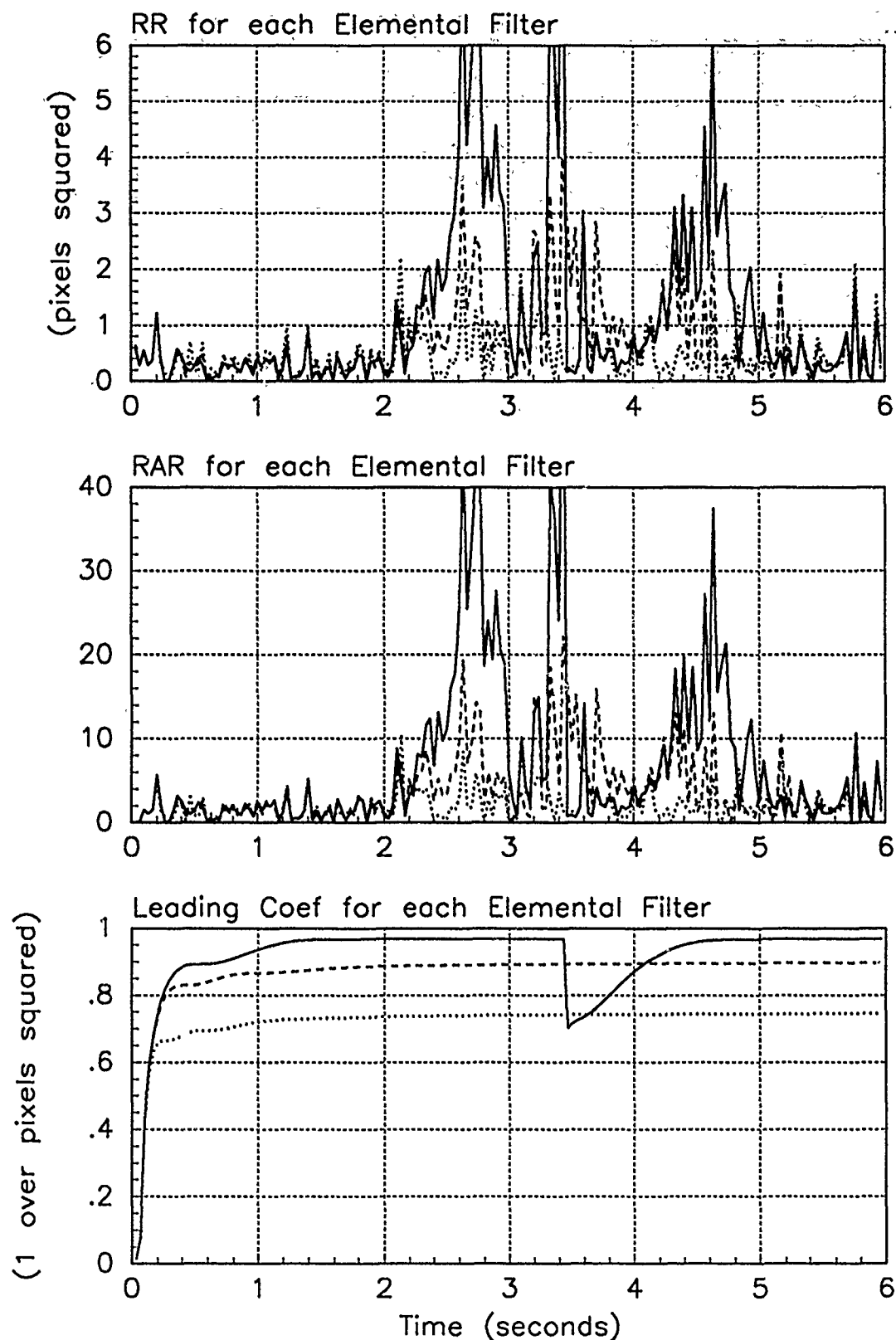


Figure E.90. Probability Calculation Plots; Notch MMAE-2R; PC is 1; LB is .01; Jinking Trajectory. Benign filter has solid line; intermediate filter has dashed line; harsh filter has dotted line.

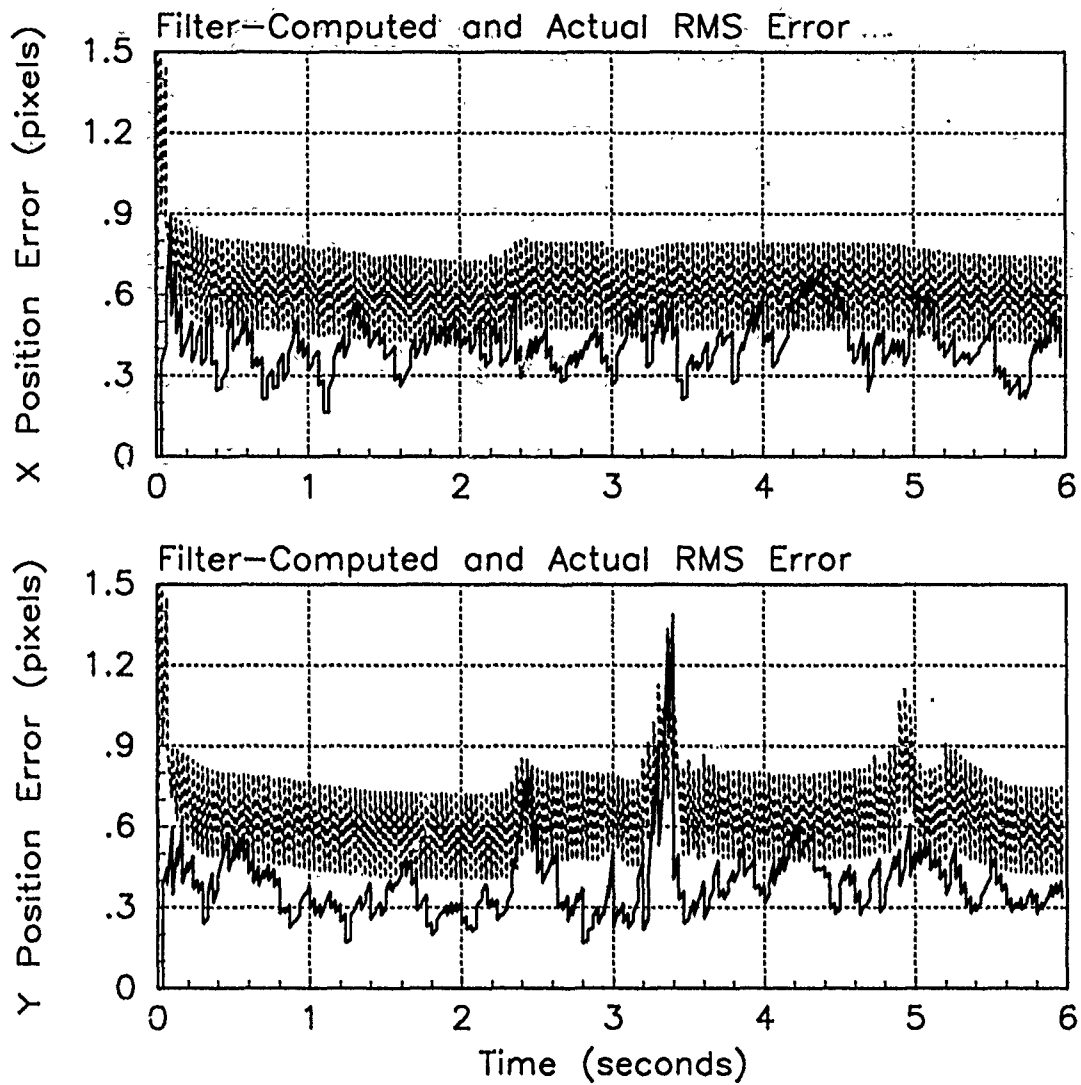


Figure E.91. RMS Error Plots; Notch MMAE-2FB; PC is 1; Jinking Trajectory

Table E.28. Temporal Averages; Notch MMAE-2FB; PC is 1; Jinking Trajectory.

Error in:	Mean	σ
$p_x(t_i^-)$	-0.067192	0.43698
$p_x(t_i^+)$	-0.044687	0.39109
$y_x(t_i^-)$	-0.033344	0.39124
$p_y(t_i^-)$	0.24085	0.41523
$p_y(t_i^+)$	0.19262	0.35910
$y_y(t_i^-)$	0.16781	0.39180

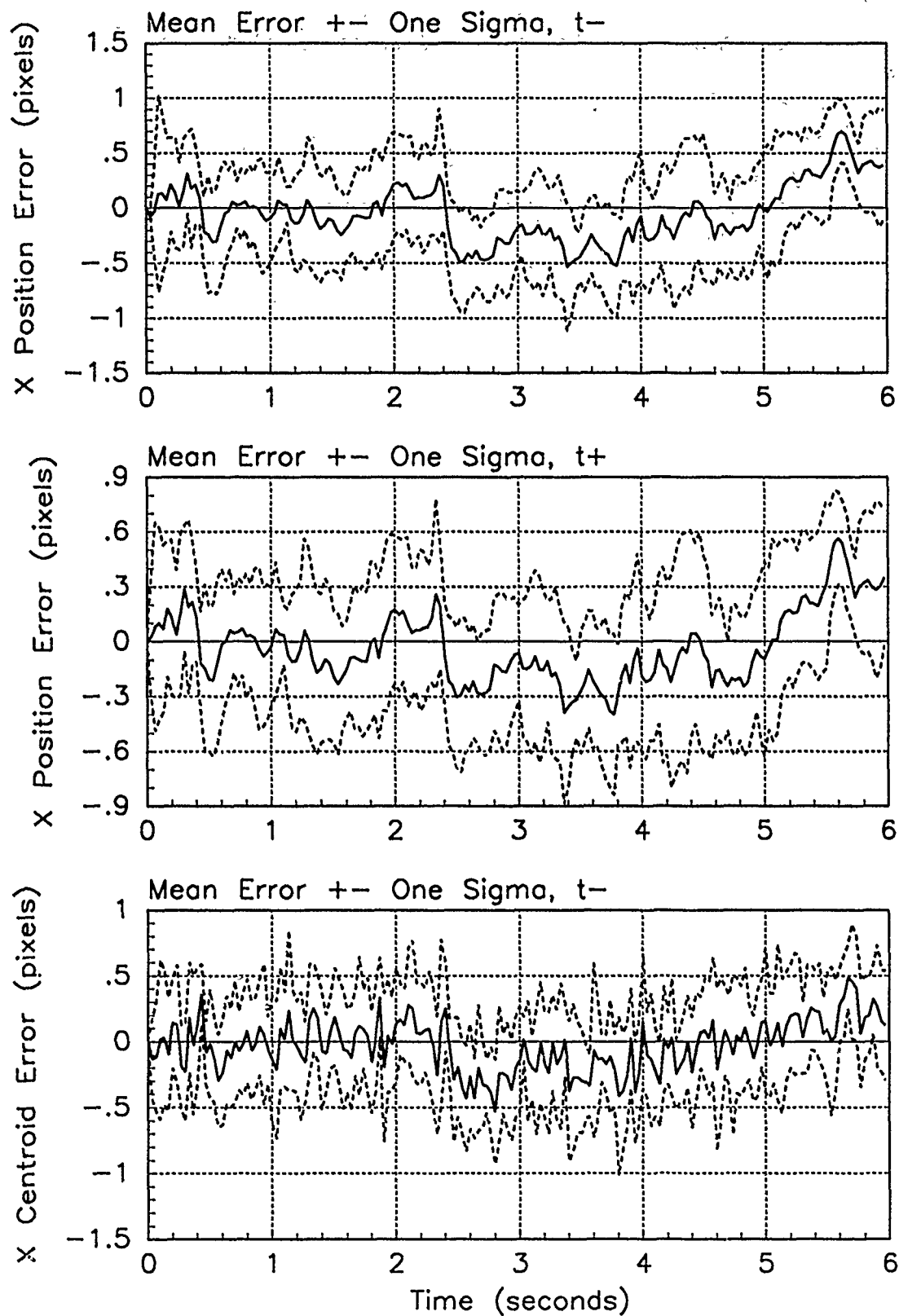


Figure E.92. X-Error Plots; Notch MMAE-2FB; PC is 1; Jinking Trajectory

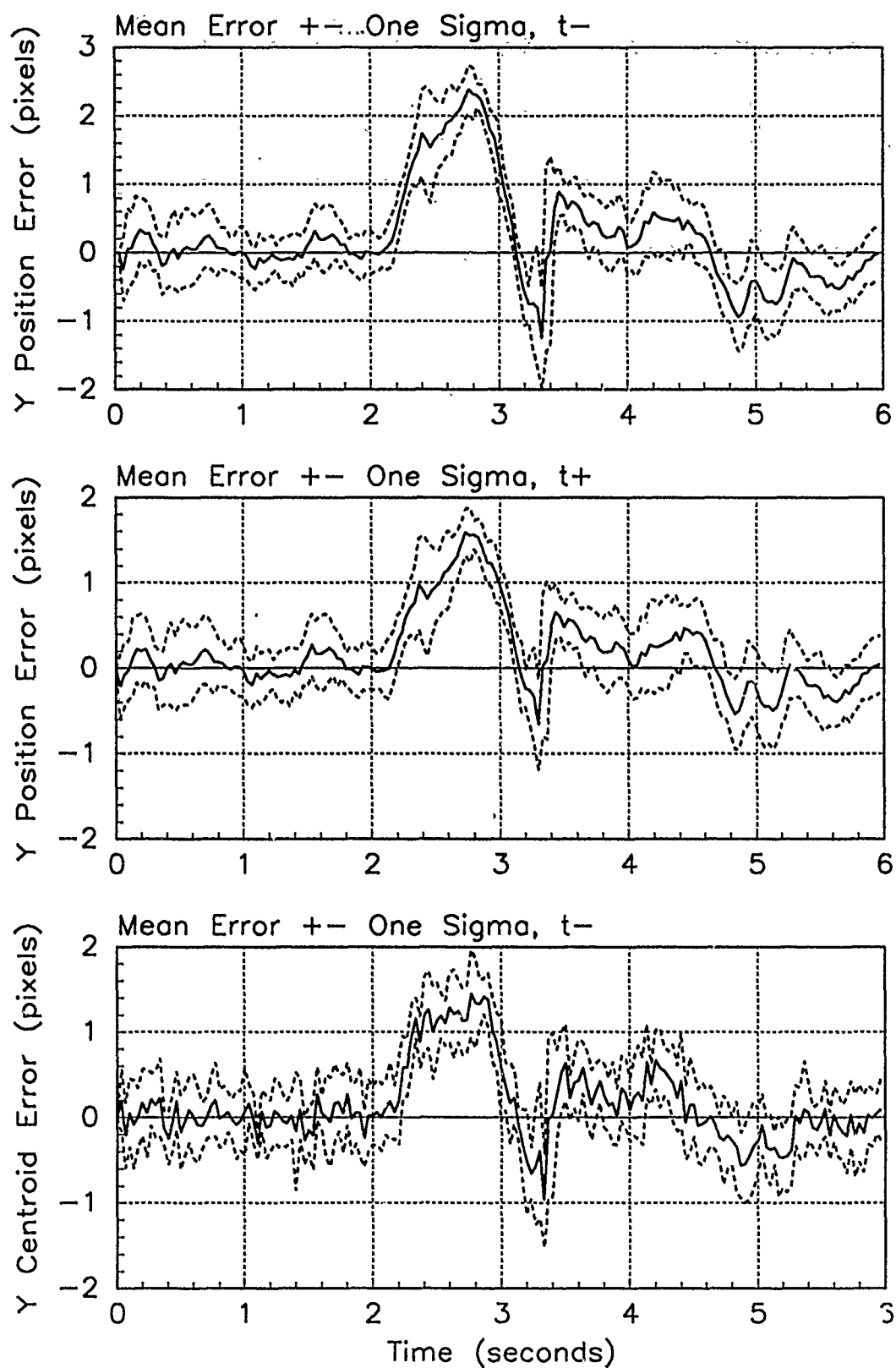


Figure E.93. Y-Error Plots; Notch MMAE-2FB; PC is 1; Jinking Trajectory

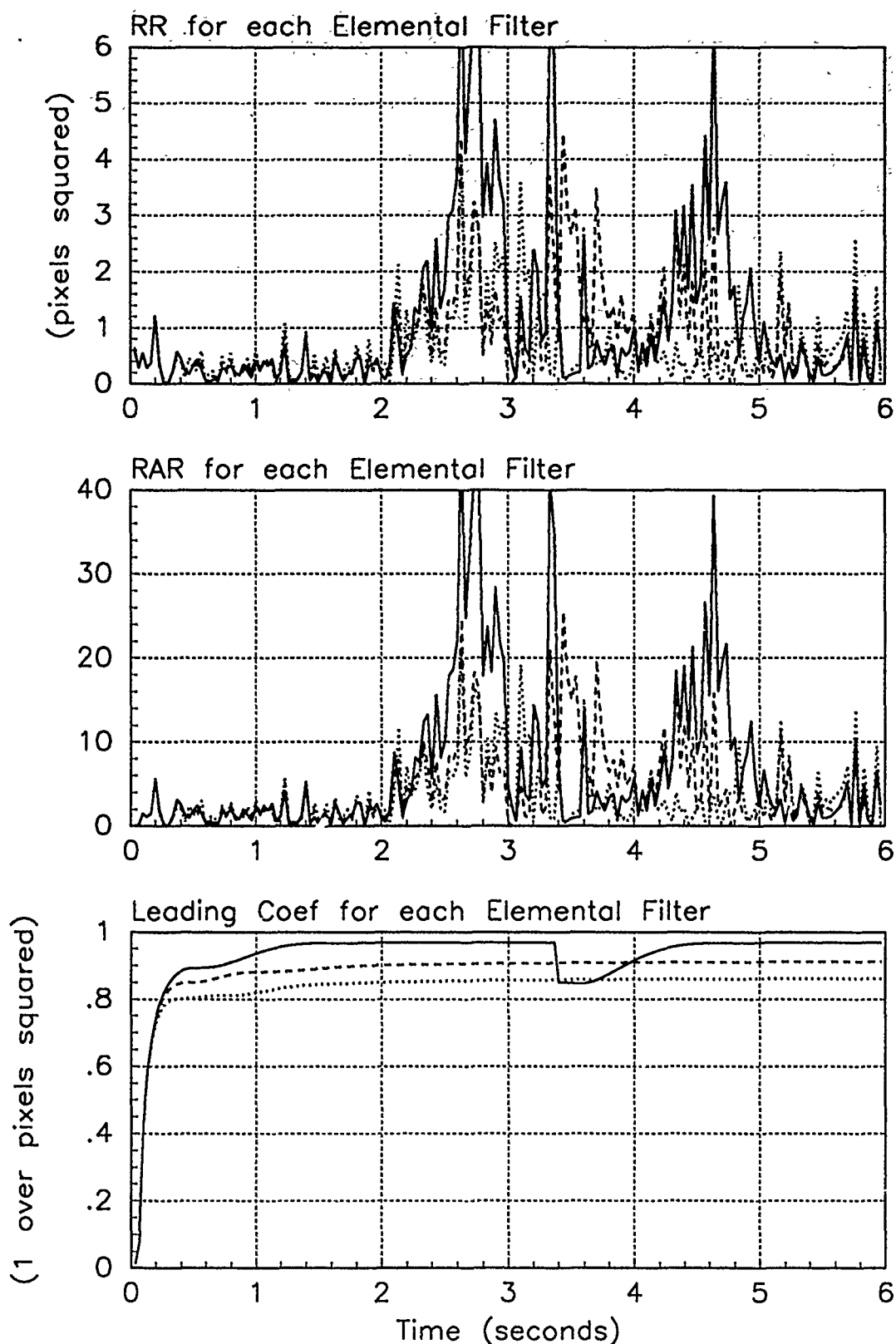


Figure E.94. Probability Calculation Plots; Notch MMAE-2FB; PC is 1; Jinking Trajectory. Benign filter has solid line; intermediate filter has dashed line; harsh filter has dotted line.

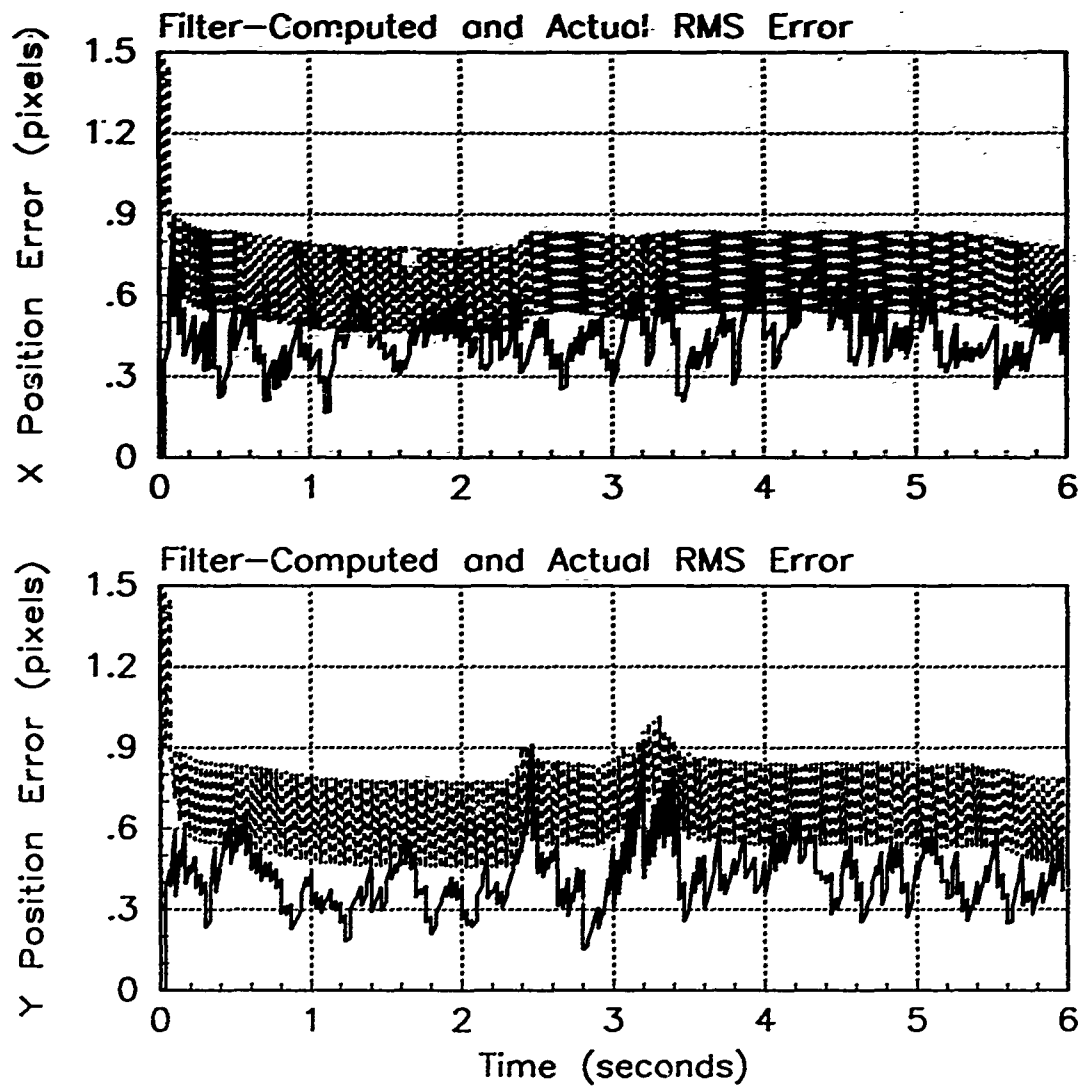


Figure E.95. RMS Error Plots; Notch MMAE-2FH; PC is 1; Jinking Trajectory

Table E.29. Temporal Averages; Notch MMAE-2FH; PC is 1; Jinking Trajectory.

Error in:	Mean	σ
$p_x(t_i^-)$	-0.022119	0.47749
$p_x(t_i^+)$	-0.014961	0.41091
$y_x(t_i^-)$	-0.0066979	0.40560
$p_y(t_i^-)$	0.088483	0.46066
$p_y(t_i^+)$	0.057249	0.38098
$y_y(t_i^-)$	0.066056	0.40906

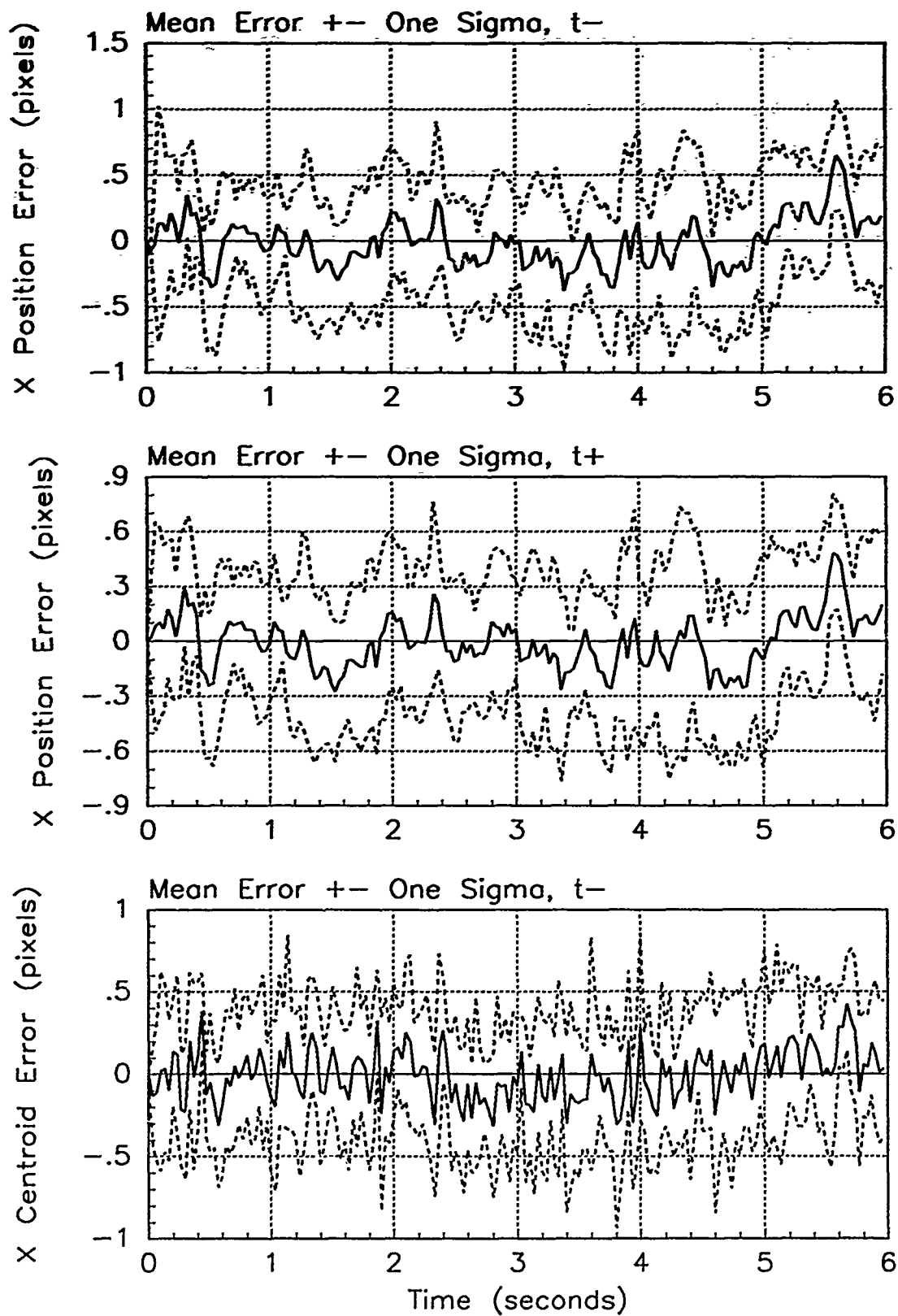


Figure E.96. X-Error Plots; Notch MMAE-2FH; PC is 1; Jinking Trajectory

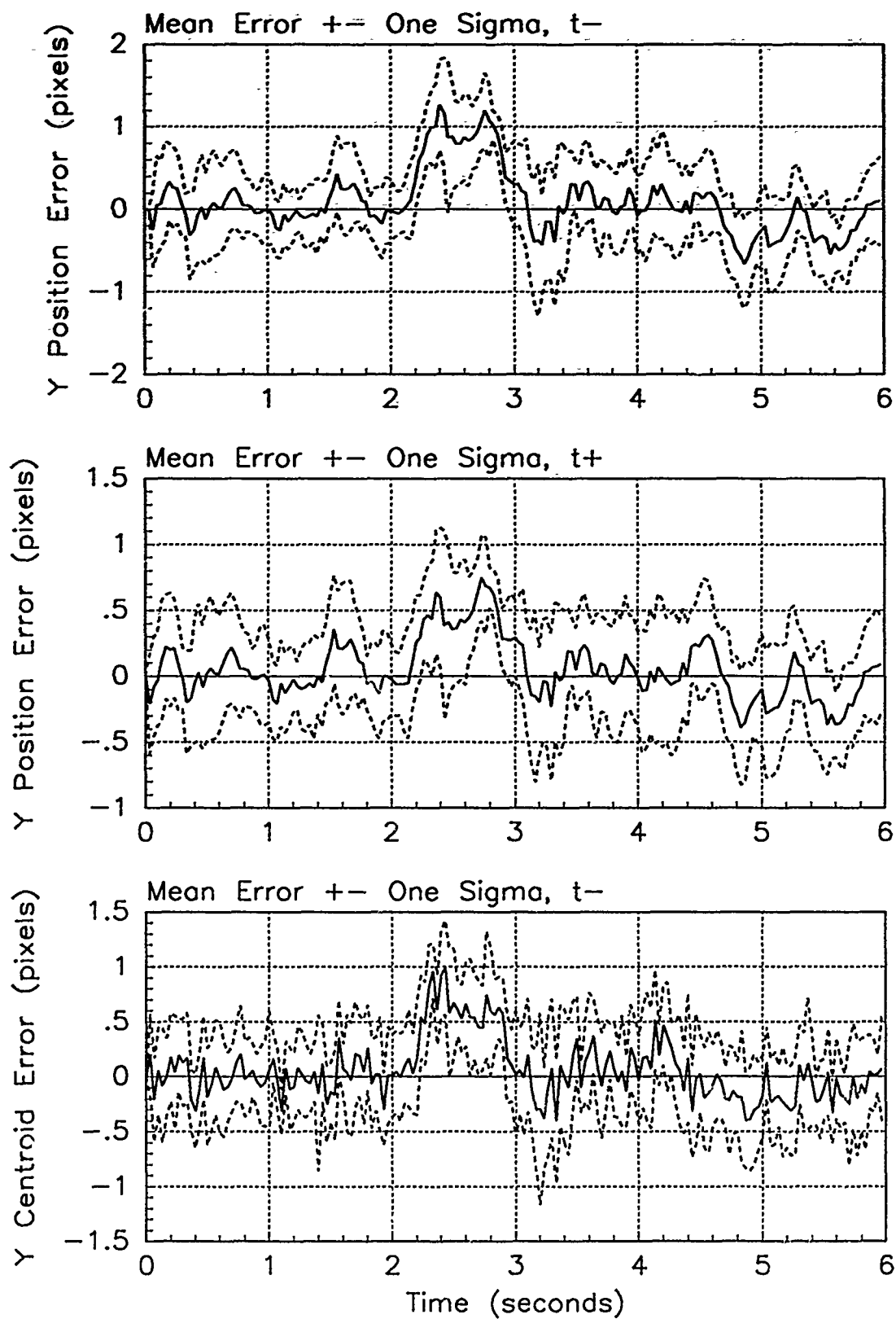


Figure E.97. Y-Error Plots; Notch MMAE-2FH; PC is 1; Jinking Trajectory

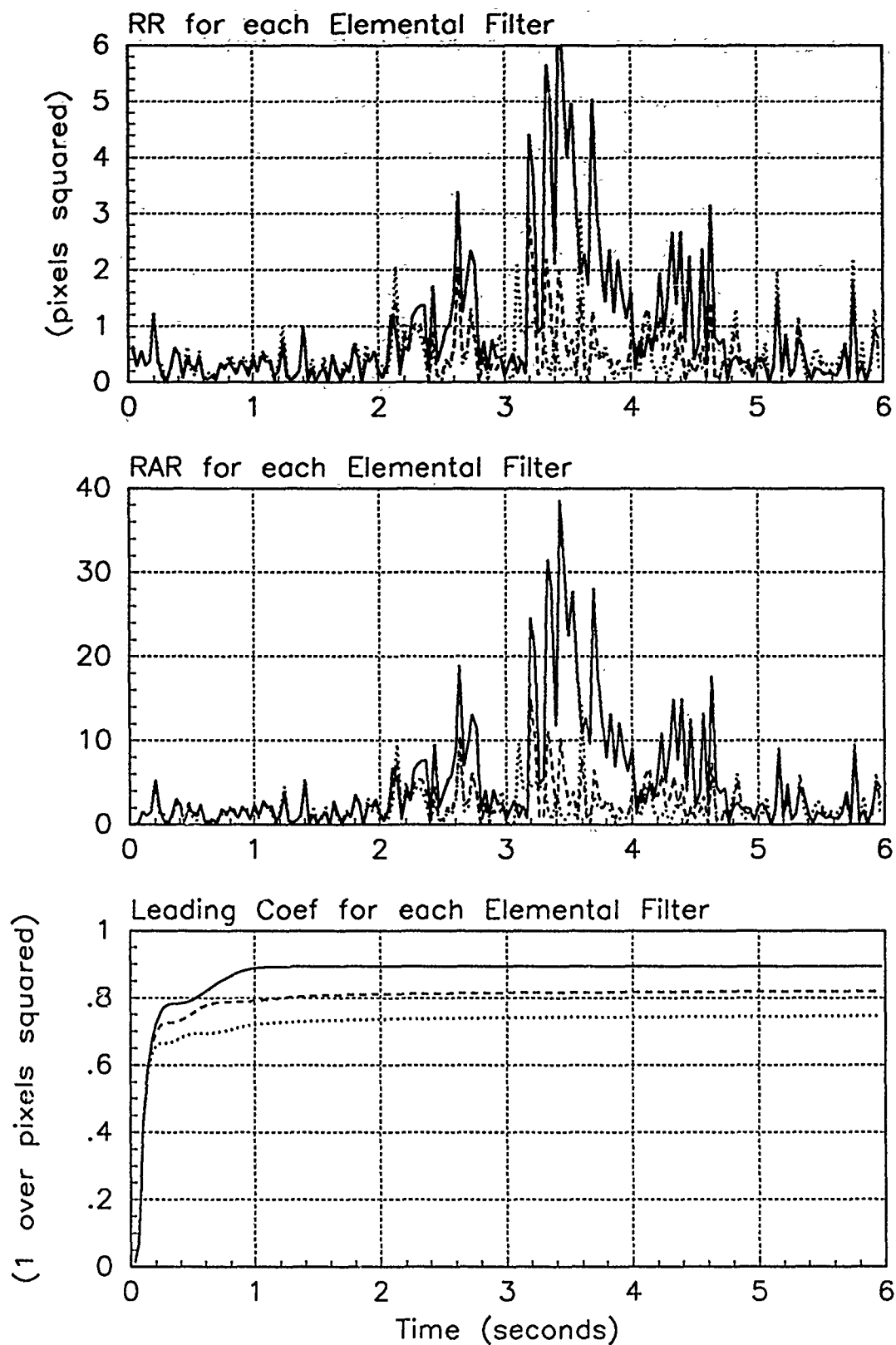


Figure E.98. Probability Calculation Plots; Notch MMAE-2FH; PC is 1; Jinking Trajectory. Benign filter has solid line; intermediate filter has dashed line; harsh filter has dotted line.

Appendix F. *Error Plots for First-Order MMAE*

This appendix shows the error plots for the MMAE with elemental filters *each* based on first-order acceleration models. The MMAE is referred to as the first-order MMAE. All Monte Carlo studies were done with the MMAE tuned in the revised method.

The results for one Monte Carlo study consists of a set of three pages. The first page shows the RMS error plots for each of the x- and y-positions. The band is the dashed line for the filter-computed RMS error. The solid line is the actual RMS error calculated over the Monte Carlo study. Below these plots are two tables. The table on the left lists the temporal average of the position errors. This temporal average is from .5 seconds to the end of each of the 10 runs in the Monte Carlo study as described in Section 5.2. The table on the right is the list of the average $\mathbf{r}_k^T(t_i)\mathbf{r}_k(t_i)$ and $\mathbf{r}_k^T(t_i)\mathbf{A}_k^{-1}(t_i)\mathbf{r}_k(t_i)$ over the 10 runs for the entire run, not just the last 5.5 seconds. The lack of time notation (rather than the traditional overbar) in the table signifies the temporal average. The next page of each set shows the mean ± 1 standard deviation error plots for the x-position at time t_i^- and t_i^+ and the mean x-centroid position error at time t_i^- . The final page shows similar plots for the mean y-position errors. The solid line denotes the mean error while the dashed line is the mean $\pm \sigma$.

When the MMAE is tracking the target in a jinking maneuver, there is no table on the first page for the average $\mathbf{r}_k^T(t_i)\mathbf{r}_k(t_i)$ and $\mathbf{r}_k^T(t_i)\mathbf{A}_k^{-1}(t_i)\mathbf{r}_k(t_i)$ since each is expected to change greatly over the run due to the changing acceleration dynamics. Instead, plots of the $\mathbf{r}_k^T(t_i)\mathbf{r}_k(t_i)$, $\mathbf{r}_k^T(t_i)\mathbf{A}_k^{-1}(t_i)\mathbf{r}_k(t_i)$, and leading coefficient needed in the hypothesis probability calculation are presented.

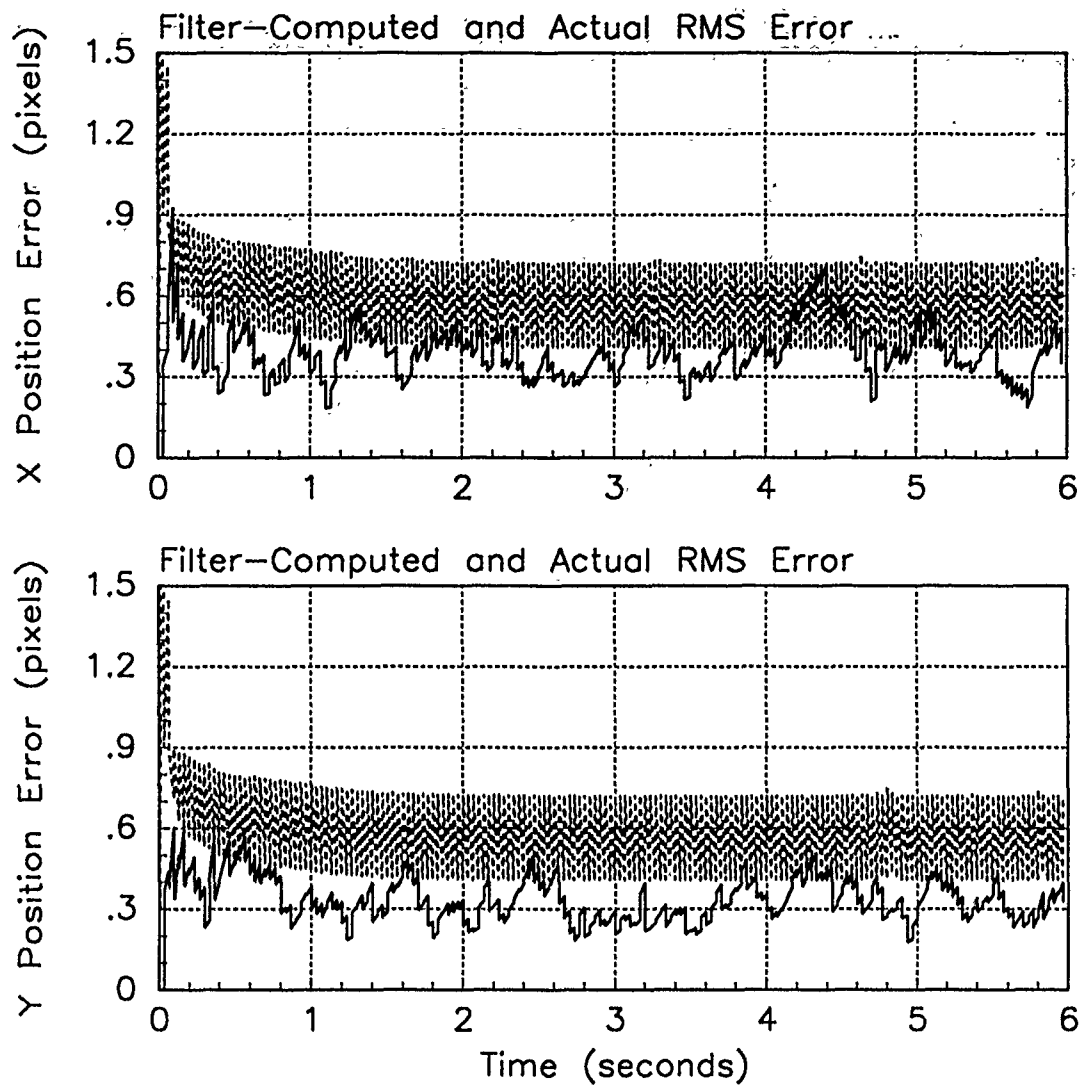


Figure F.1. RMS Error Plots; First-Order MMAE-R; PC is 1; Trajectory with $\omega = .01$

Table F.1. Temporal Averages and Residuals; First-Order MMAE-R; PC is 1; Trajectory with $\omega = .01$.

Error in:	Mean	σ
$p_x(t_i^-)$	0.15868	0.40832
$p_x(t_i^+)$	0.12117	0.37102
$y_x(t_i^-)$	0.098154	0.38119
$p_y(t_i^-)$	0.0051362	0.34680
$p_y(t_i^+)$	0.0064047	0.31464
$y_y(t_i^-)$	0.011017	0.36595

Filter	$\mathbf{r}_k^T \mathbf{r}_k$	$\mathbf{r}_k^T \mathbf{A}_k^{-1} \mathbf{r}_k$
Benign	0.31398	1.84920
Intermediate	0.33190	1.75898
Harsh	0.41606	1.55076

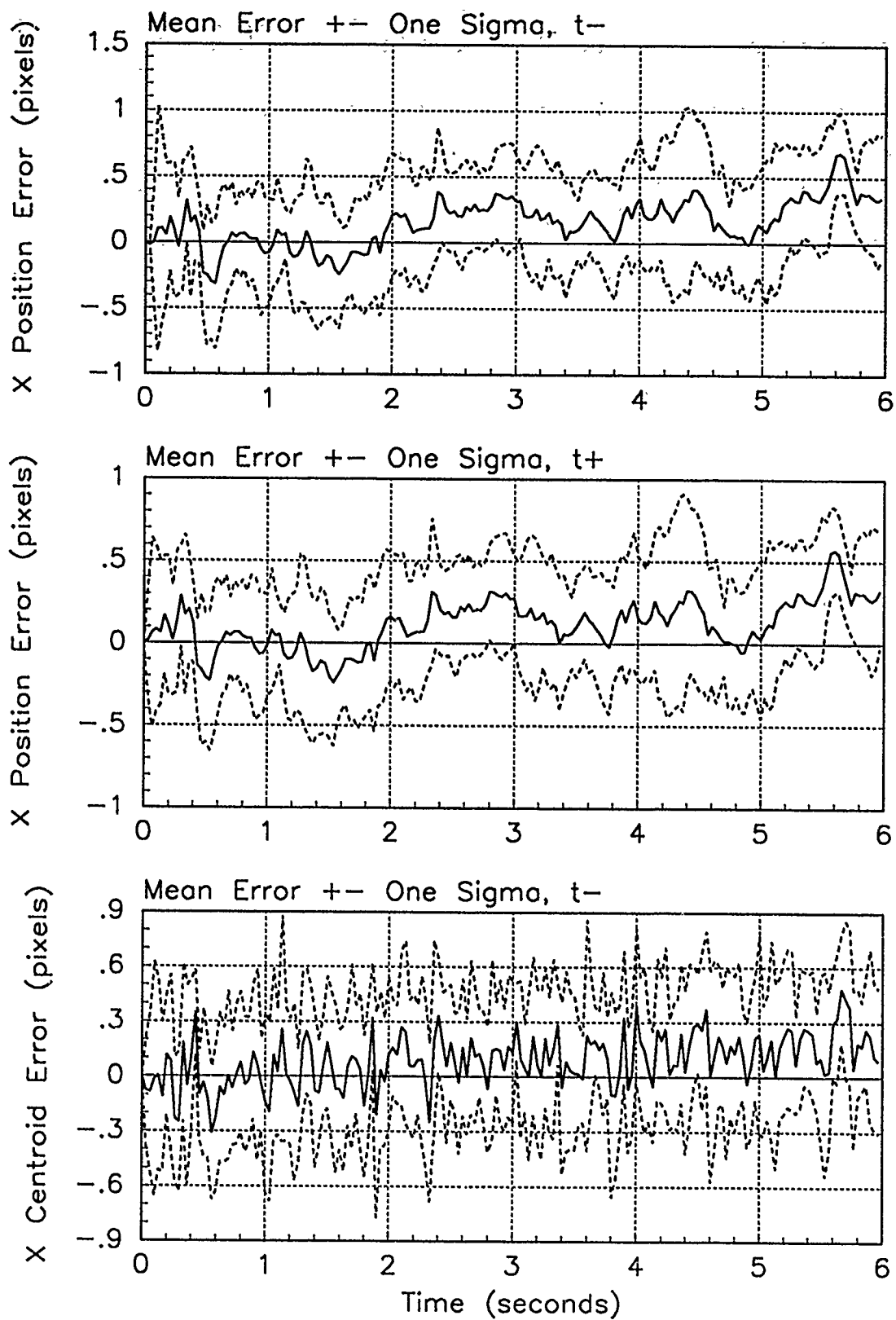


Figure F.2. X-Error Plots; First-Order MMAE-R; PC is 1; Trajectory with $\omega = .01$

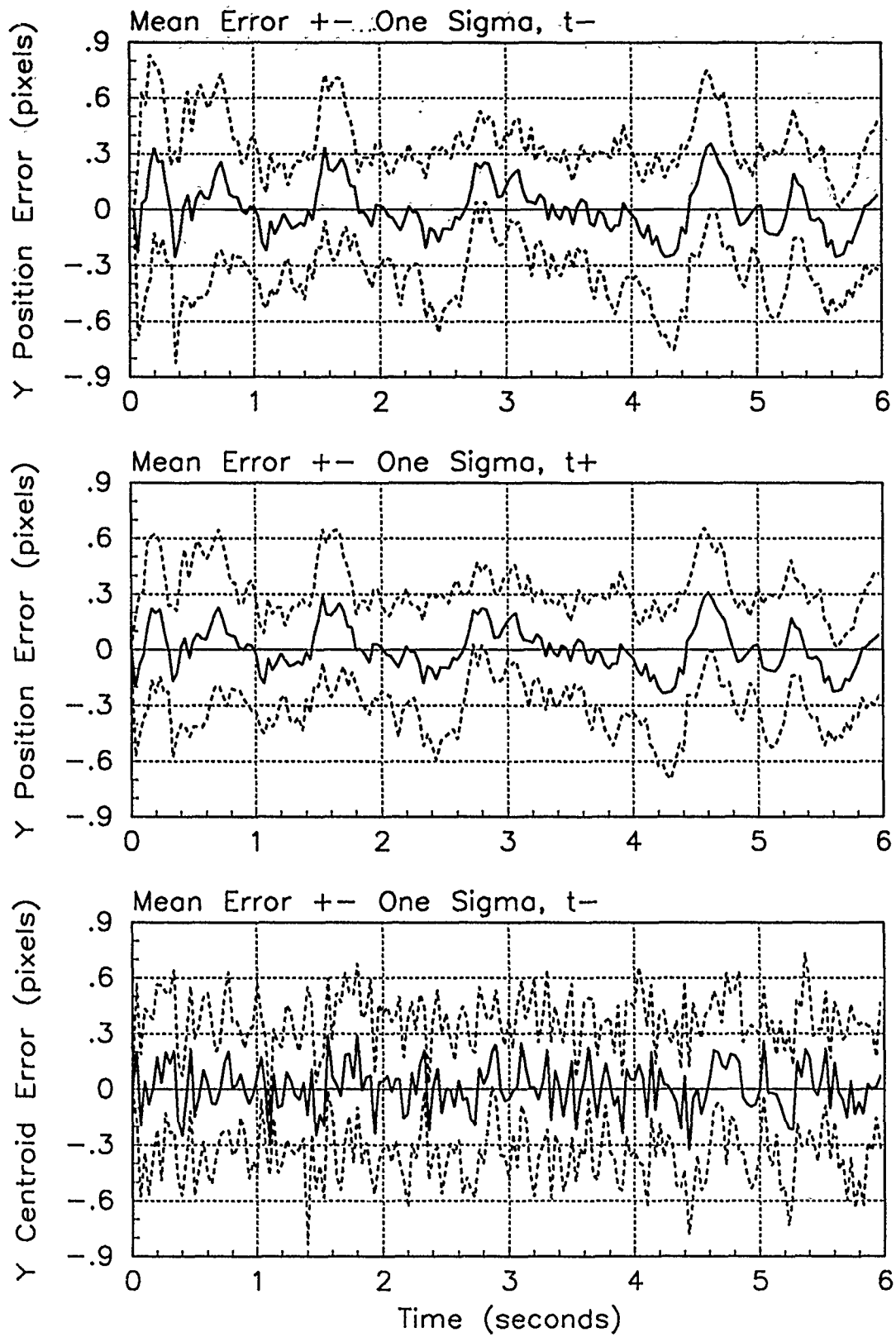


Figure F.3. Y-Error Plots; First-Order MMAE-R; PC is 1; Trajectory with $\omega = .01$

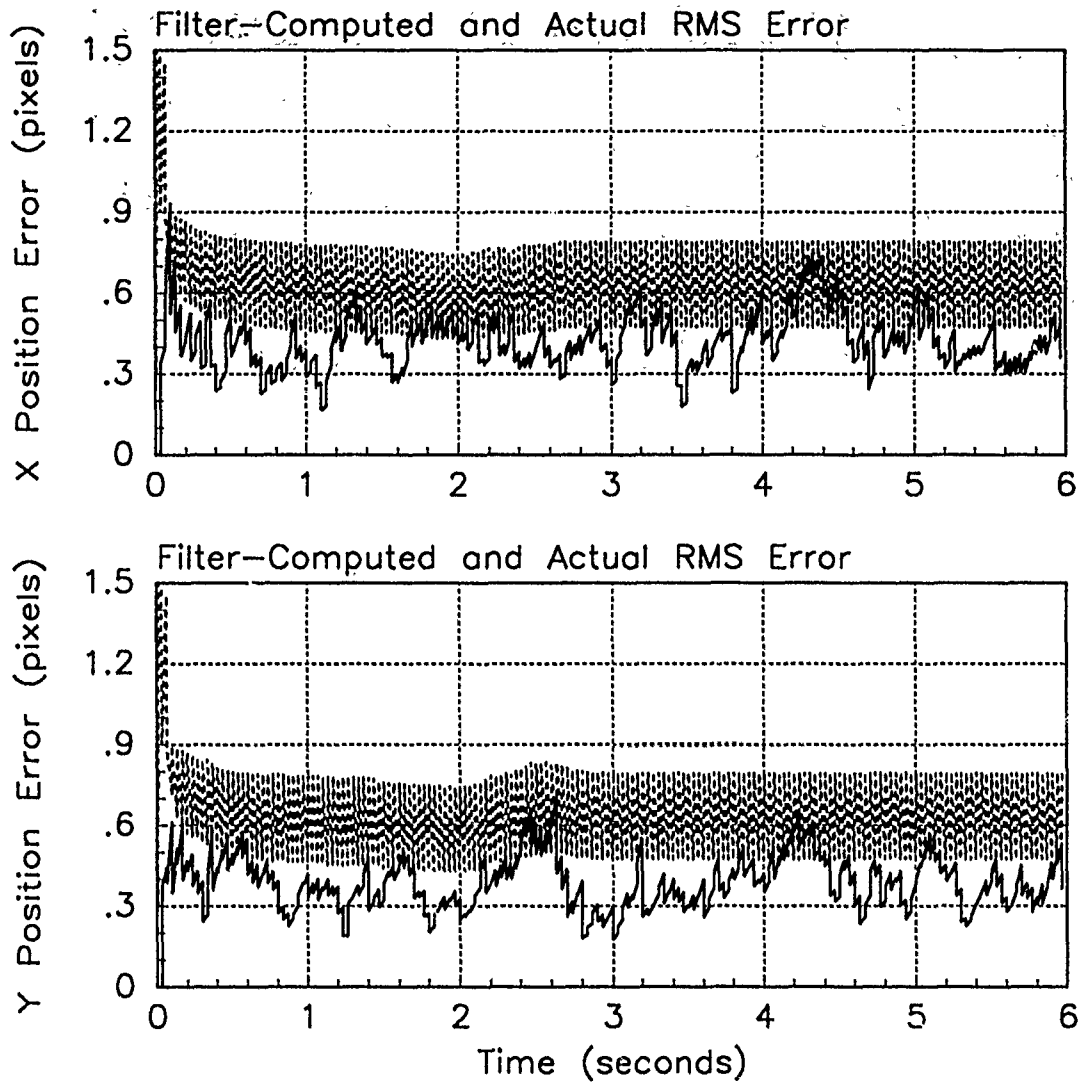


Figure F.4. RMS Error Plots; First-Order MMAE-R; PC is 1; Trajectory with $\omega = 1.32$

Table F.2. Temporal Averages and Residuals; First-Order MMAE-R; PC is 1; Trajectory with $\omega = 1.32$.

Error in:	Mean	σ
$p_x(t_i^-)$	0.057818	0.44716
$p_x(t_i^+)$	0.033986	0.39757
$y_x(t_i^-)$	0.042546	0.39483
$p_y(t_i^-)$	-0.0024213	0.40806
$p_y(t_i^+)$	-0.0070504	0.36088
$y_y(t_i^-)$	-0.0081275	0.38321

Filter	$r_k^T r_k$	$r_k^T A_k^{-1} r_k$
Benign	0.39482	2.33499
Intermediate	0.34213	1.81372
Harsh	0.40987	1.52774

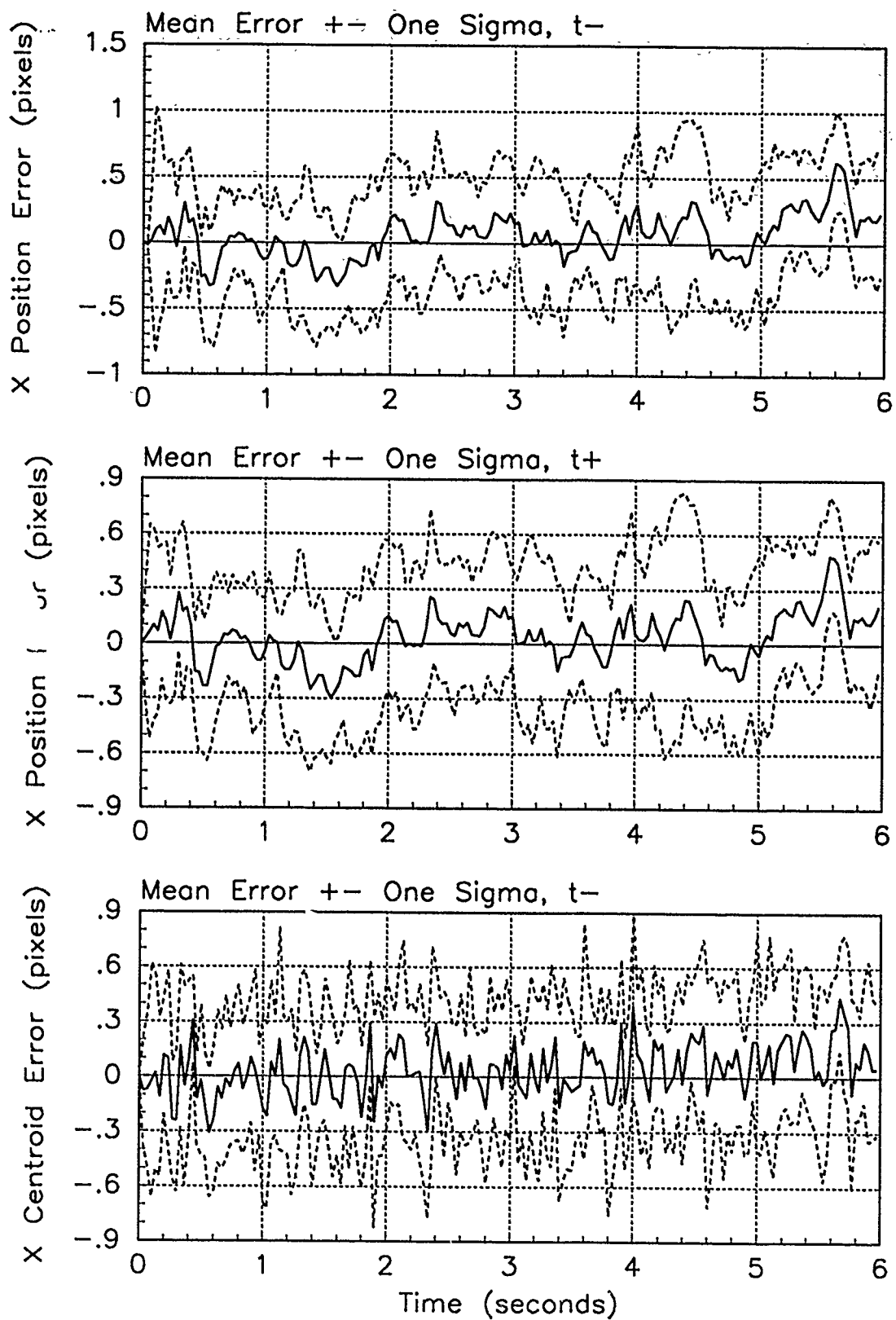


Figure F.5. X-Error Plots; First-Order MMAE-R; PC is 1; Trajectory with $\omega = 1.32$

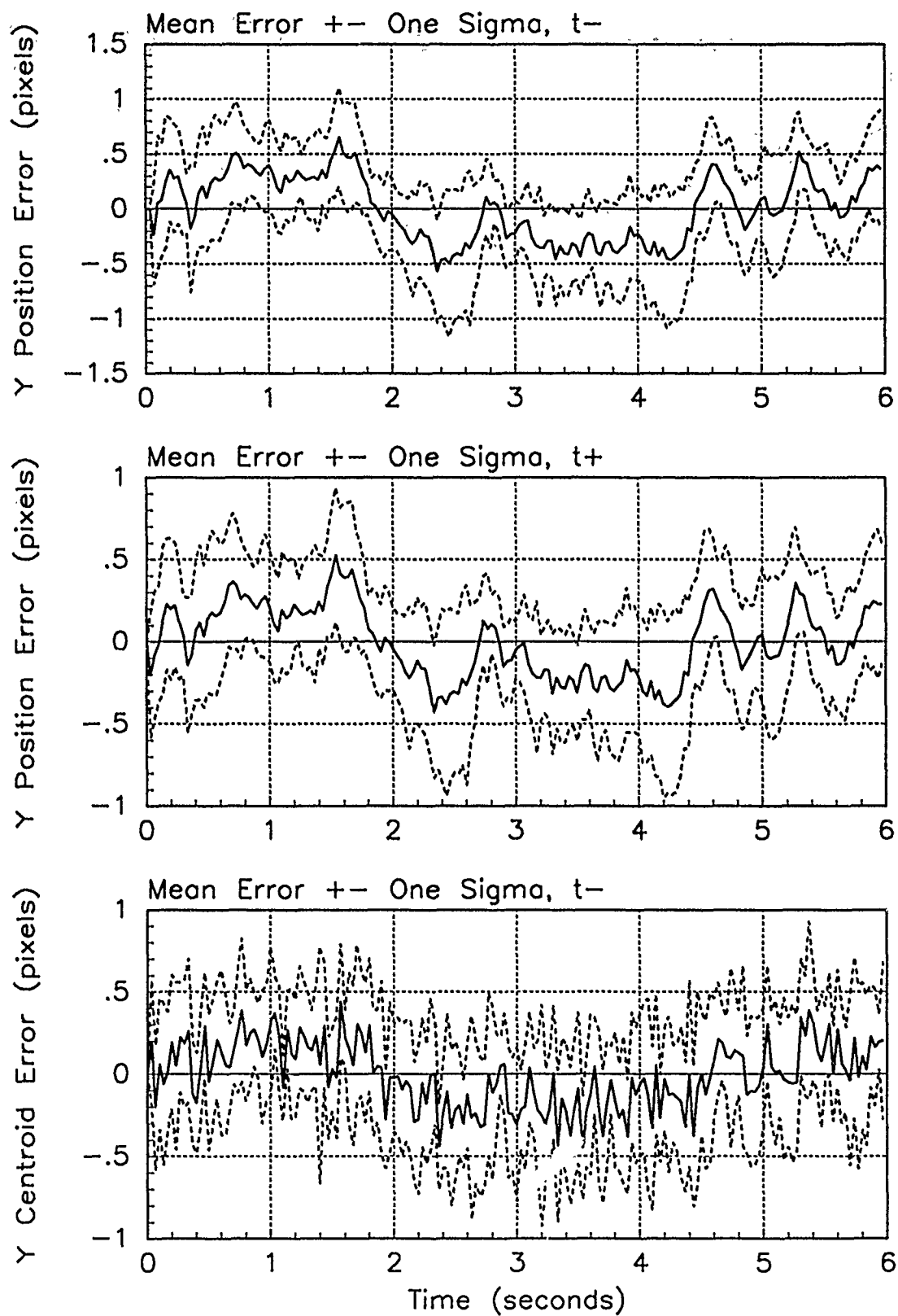


Figure F.6. Y-Error Plots; First-Order MMAE-R; PC is 1; Trajectory with $\omega = 1.32$

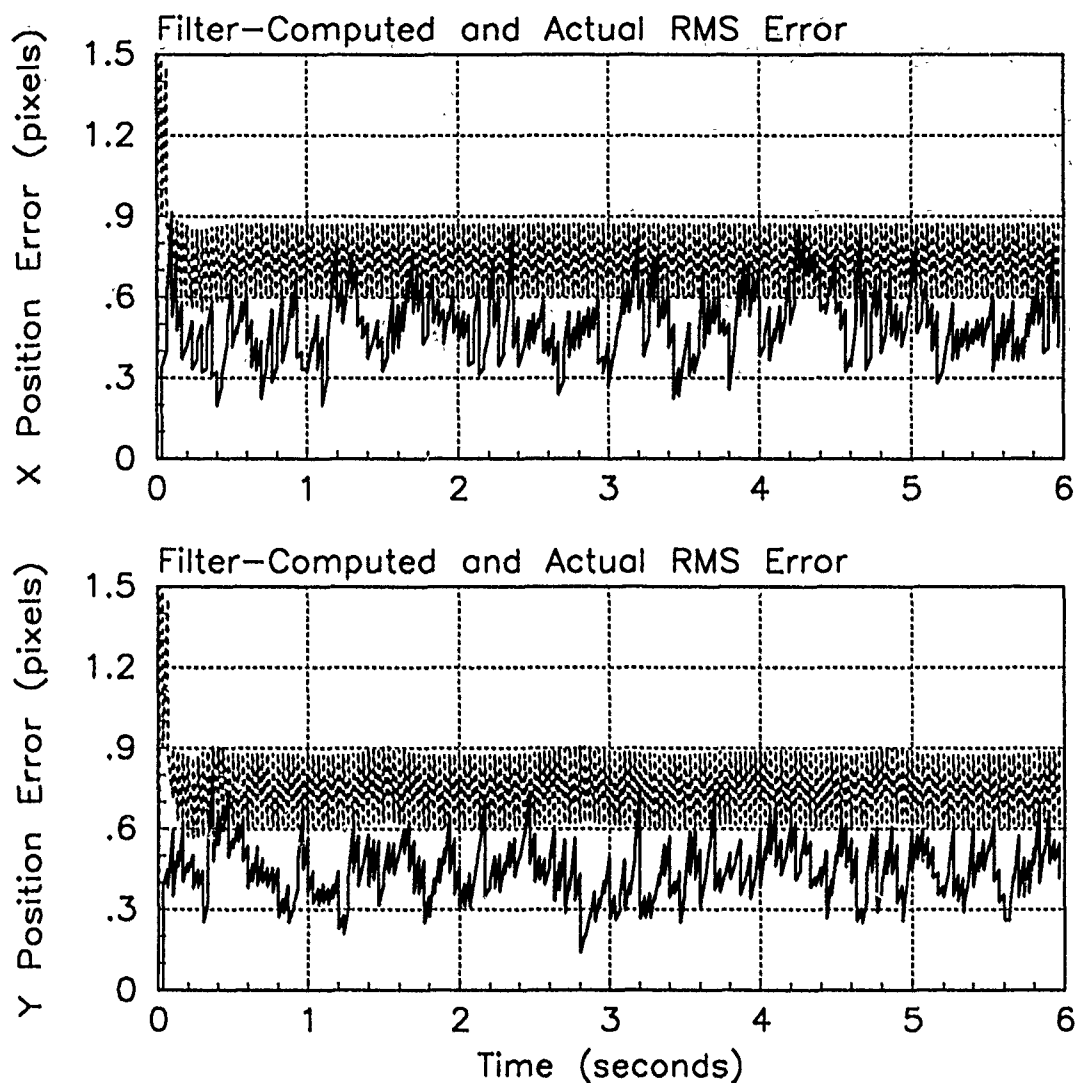


Figure F.7. RMS Error Plots; First-Order MMAE-R; PC is 1; Trajectory with $\omega = 2.8$

Table F.3. Temporal Averages and Residuals; First-Order MMAE-R; PC is 1; Trajectory with $\omega = 2.8$.

Error in:	Mean	σ
$p_x(t_i^-)$	-0.022937	0.55944
$p_x(t_i^+)$	-0.024402	0.44596
$y_x(t_i^-)$	-0.010097	0.44613
$p_y(t_i^-)$	0.012936	0.49776
$p_y(t_i^+)$	-0.0026746	0.38626
$y_y(t_i^-)$	0.0082901	0.42864

Filter	$\mathbf{r}_k^T \mathbf{r}_k$	$\mathbf{r}_k^T \mathbf{A}_k^{-1} \mathbf{r}_k$
Benign	2.69663	15.72584
Intermediate	0.98172	5.23861
Harsh	0.46939	1.75040

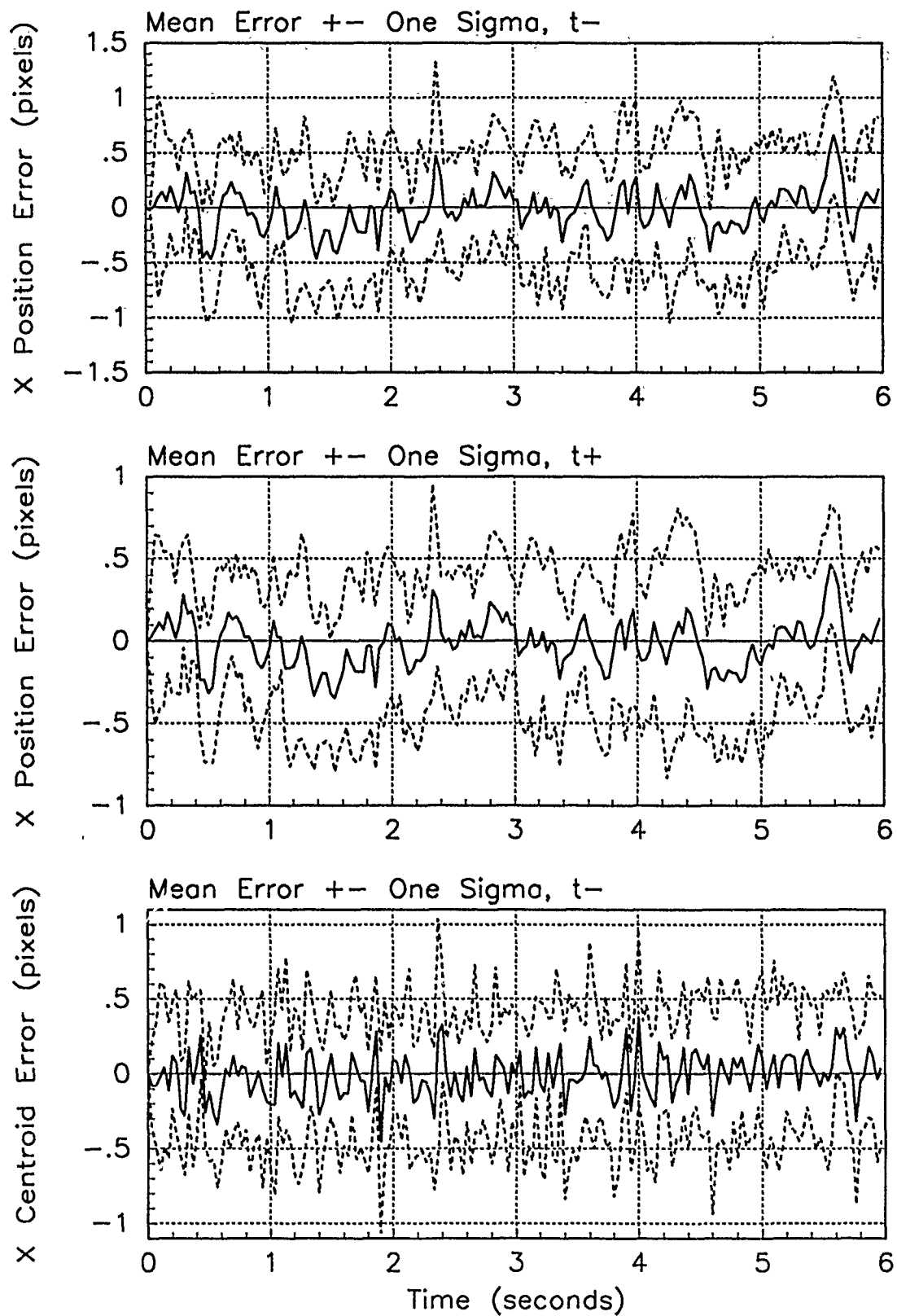


Figure F.8. X-Error Plots; First-Order MMAE-R; PC is 1; Trajectory with $\omega = 2.8$

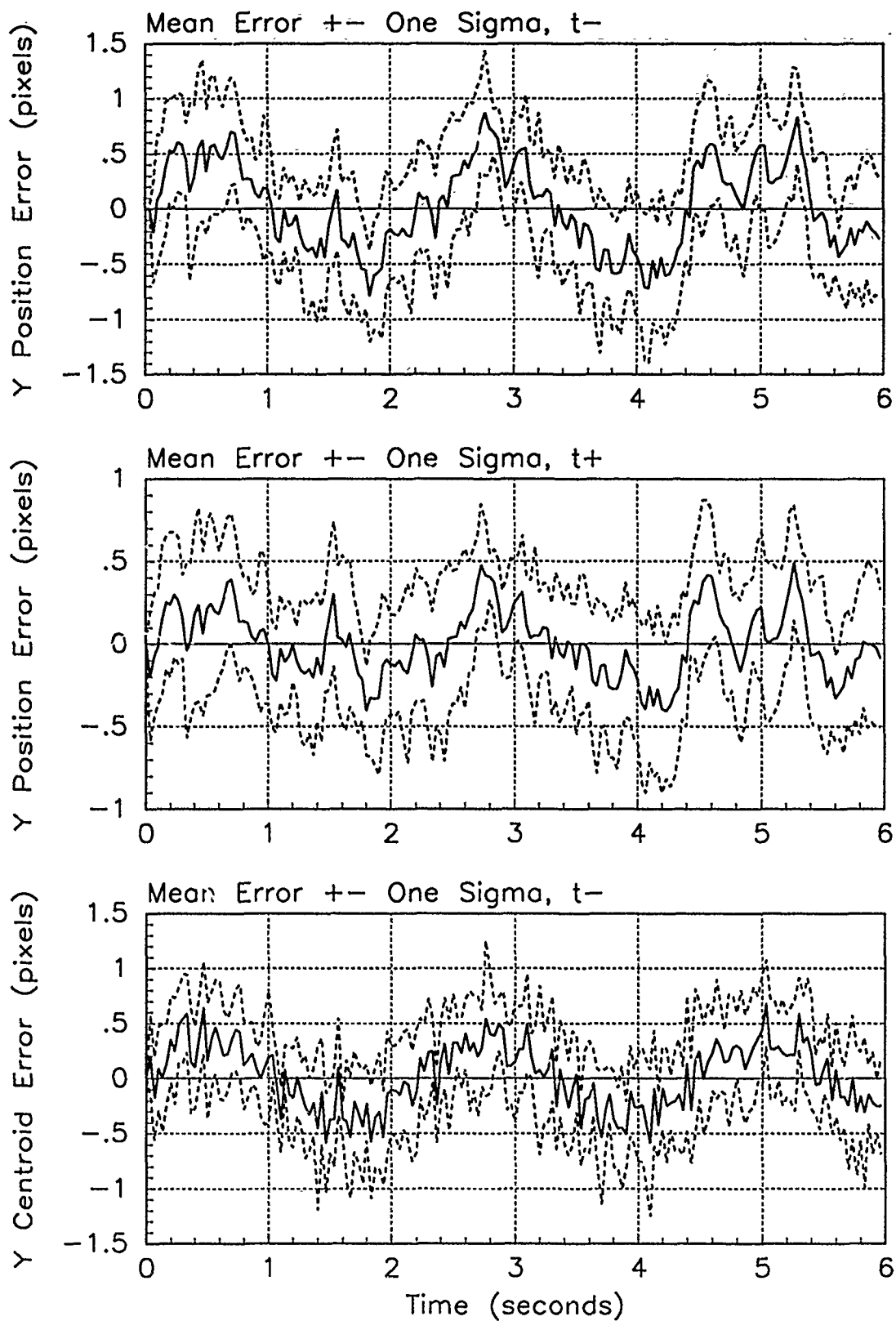


Figure F.9. Y-Error Plots; First-Order MMAE-R; PC is 1; Trajectory with $\omega = 2.8$

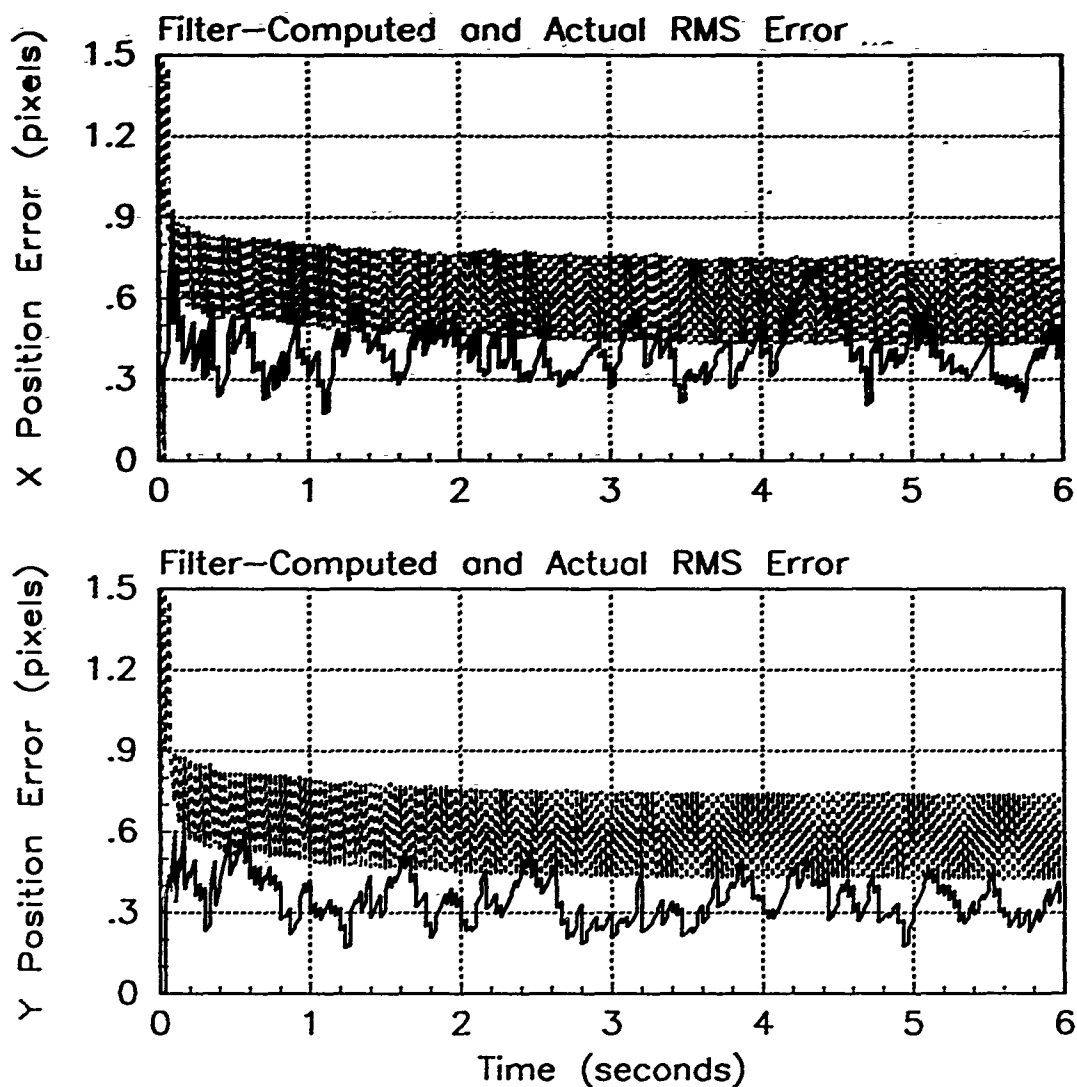


Figure F.10. RMS Error Plots; First-Order MMAE-R; PC is 4; Trajectory with $\omega = .01$

Table F.4. Temporal Averages and Residuals; First-Order MMAE-R; PC is 4; Trajectory with $\omega = .01$.

Error in:	Mean	σ
$p_x(t_i^-)$	0.11442	0.42164
$p_x(t_i^+)$	0.085762	0.38103
$y_x(t_i^-)$	0.070765	0.38486
$p_y(t_i^-)$	0.0025993	0.36127
$p_y(t_i^+)$	0.0034330	0.32493
$y_y(t_i^-)$	0.0078587	0.37027

Filter	$r_k^T r_k$	$r_k^T A_k^{-1} r_k$
Benign	0.31523	1.85689
Intermediate	0.33312	1.76567
Harsh	0.41874	1.56092

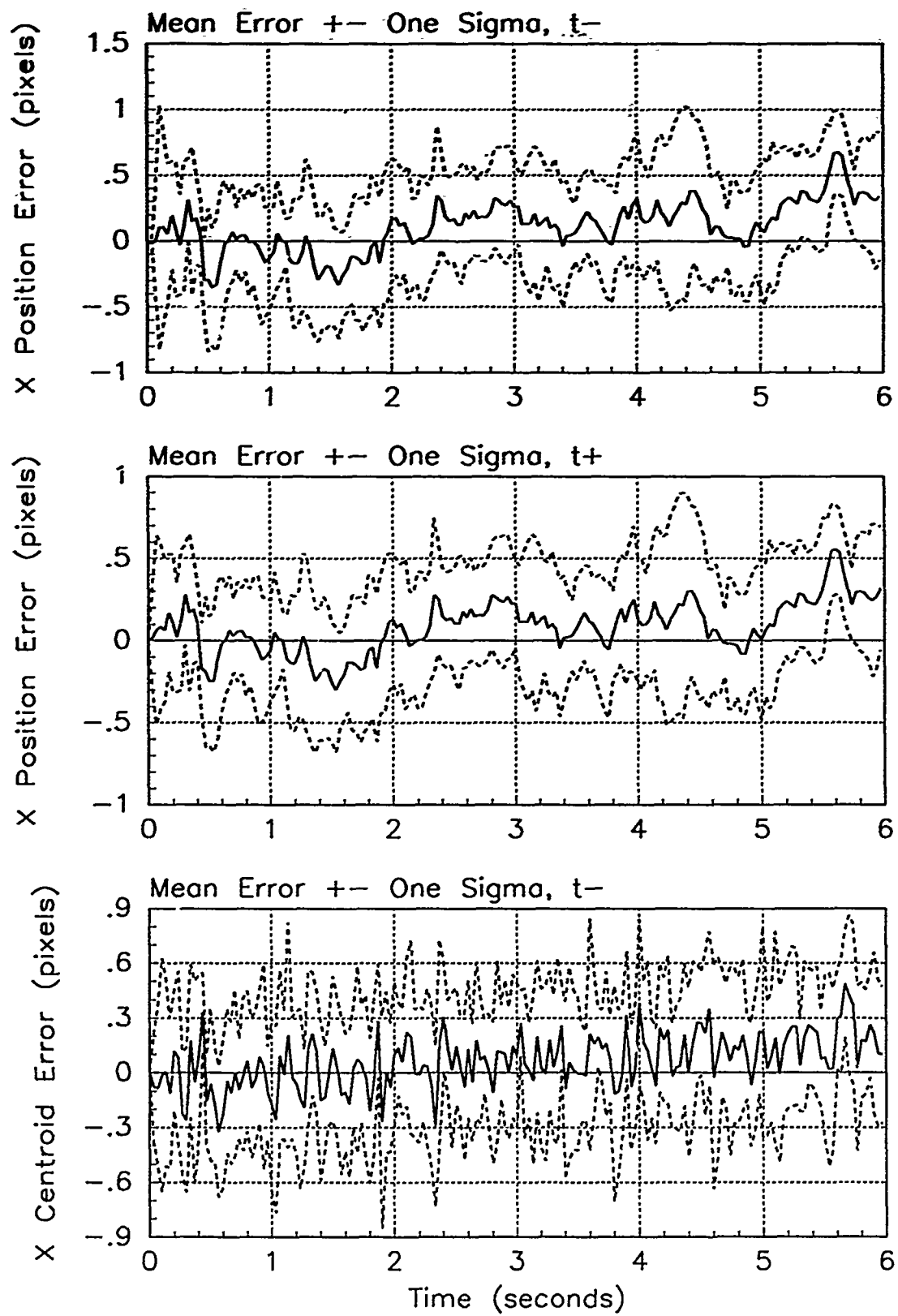


Figure F.11. X-Error Plots; First-Order MMAE-R; PC is 4; Trajectory with $\omega = .01$

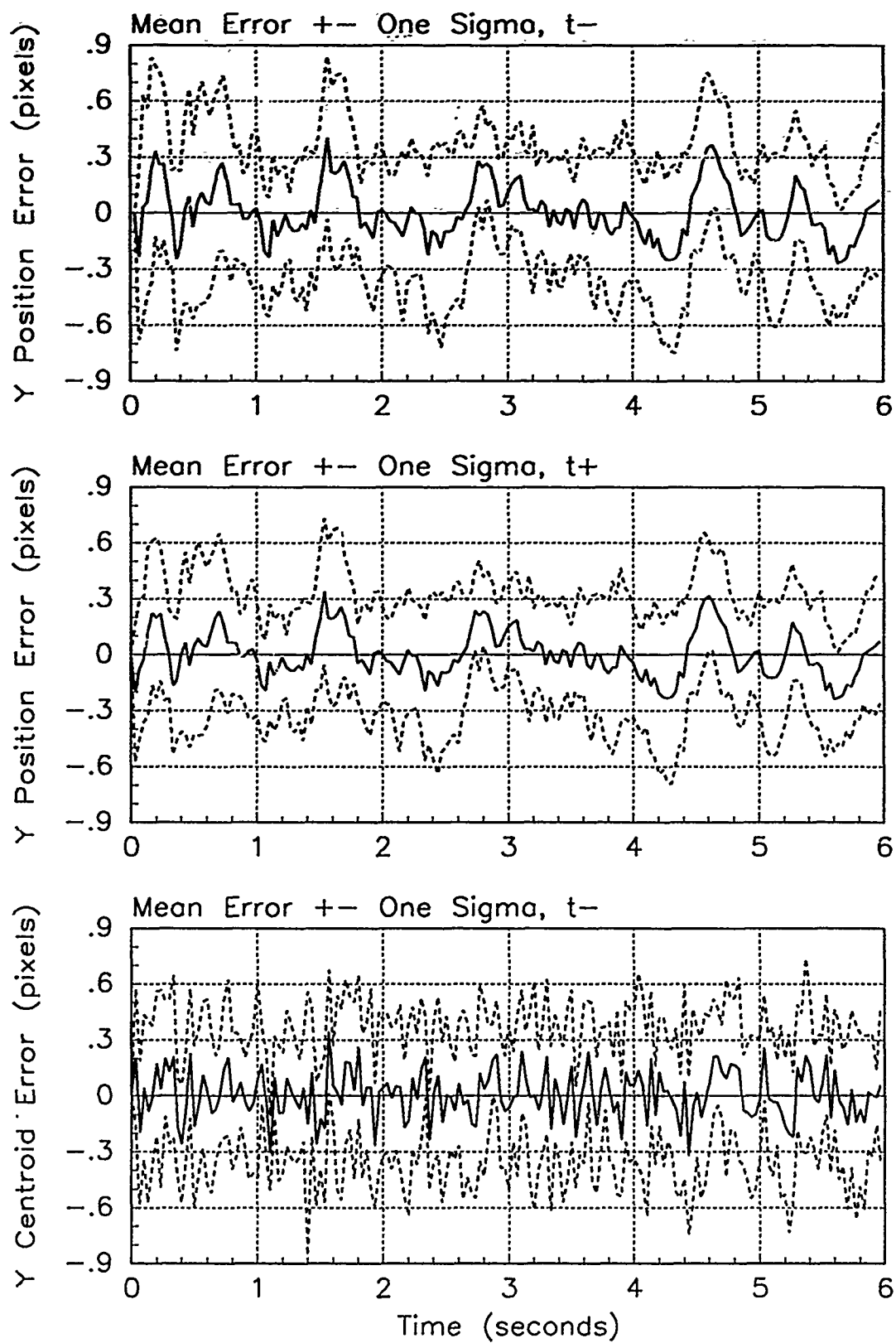


Figure F.12. Y-Error Plots; First-Order MMAE-R; PC is 4; Trajectory with $\omega = .01$

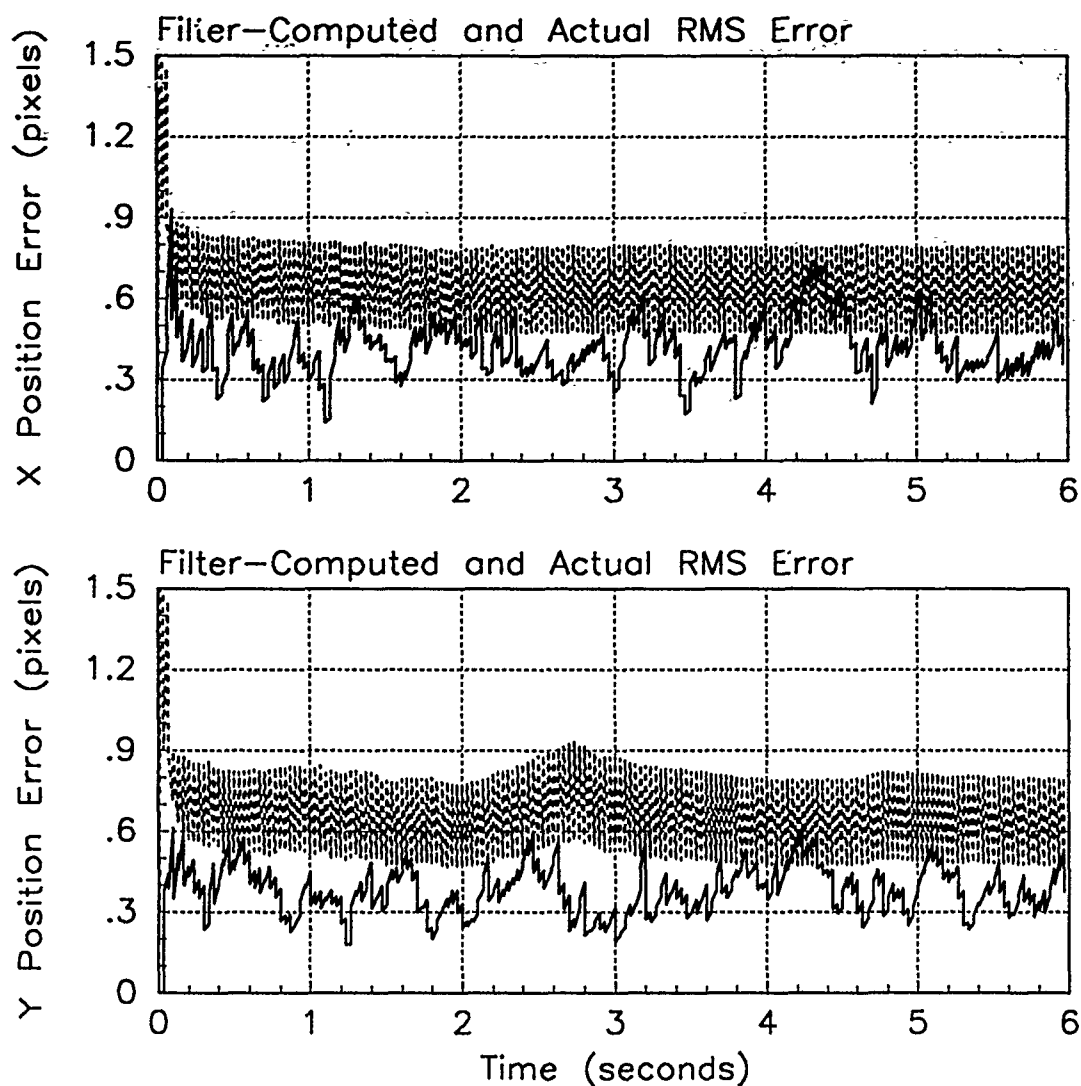


Figure F.13. RMS Error Plots; First-Order MMAE-R; PC is 4; Trajectory with $\omega = 1.32$

Table F.5. Temporal Averages and Residuals; First-Order MMAE-R; PC is 4; Trajectory with $\omega = 1.32$.

Error in:	Mean	σ
$p_x(t_i^-)$	0.062867	0.44319
$p_x(t_i^+)$	0.040271	0.39356
$y_x(t_i^-)$	0.045719	0.39182
$p_y(t_i^-)$	-0.025904	0.40133
$p_y(t_i^+)$	-0.029409	0.35530
$y_y(t_i^-)$	-0.021276	0.38006

Filter	$\mathbf{r}_k^T \mathbf{r}_k$	$\mathbf{r}_k^T \mathbf{A}_k^{-1} \mathbf{r}_k$
Benign	0.39518	2.33718
Intermediate	0.34223	1.81435
Harsh	0.40940	1.52597

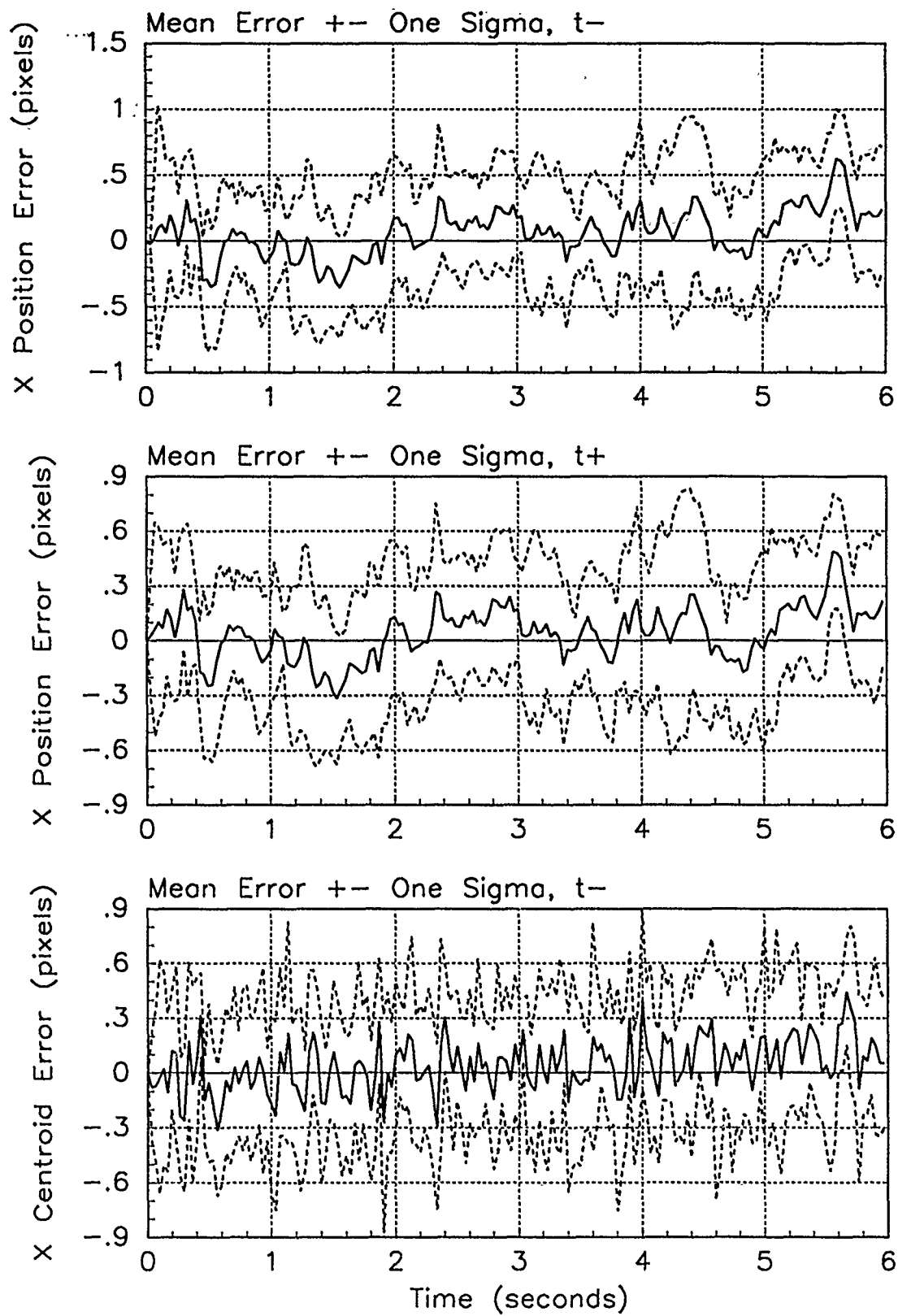


Figure F.14. X-Error Plots; First-Order MMAE-R; PC is 4; Trajectory with $\omega = 1.32$

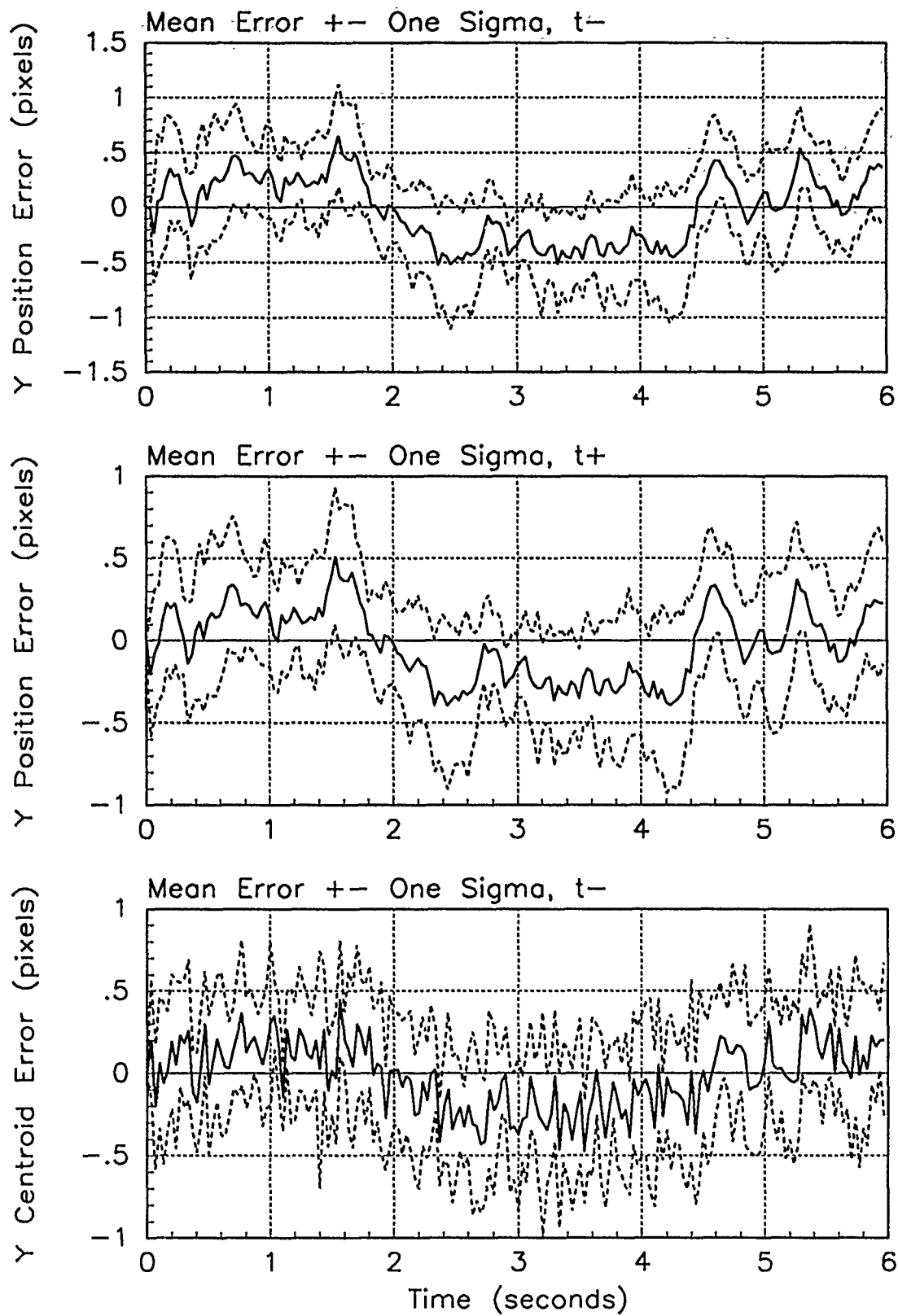


Figure F.15. Y-Error Plots; First-Order MMAE-R; PC is 4; Trajectory with $\omega = 1.32$

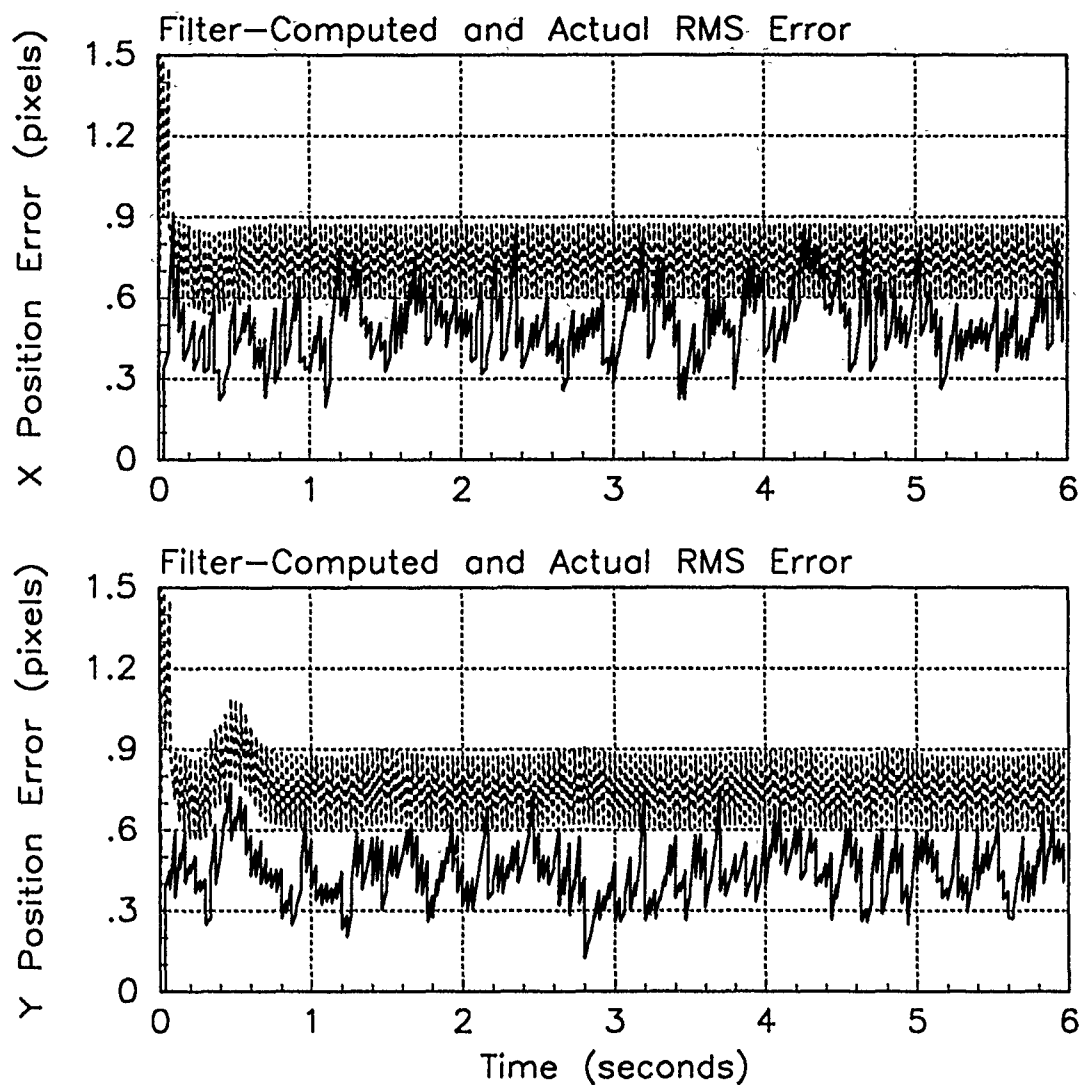


Figure F.16. RMS Error Plots; First-Order MMAE-R; PC is 4; Trajectory with $\omega = 2.8$

Table F.6. Temporal Averages and Residuals; First-Order MMAE-R; PC is 4; Trajectory with $\omega = 2.8$.

Error in:	Mean	σ
$p_x(t_i^-)$	-0.015750	0.55956
$p_x(t_i^+)$	-0.017707	0.44688
$y_x(t_i^-)$	-0.0030663	0.44580
$p_y(t_i^-)$	0.027256	0.50058
$p_y(t_i^+)$	0.0073189	0.38922
$y_y(t_i^-)$	0.018990	0.42867

Filter	$\mathbf{r}_k^T \mathbf{r}_k$	$\mathbf{r}_k^T \mathbf{A}_k^{-1} \mathbf{r}_k$
Benign	2.67626	15.60465
Intermediate	0.98082	5.23367
Harsh	0.46882	1.74825

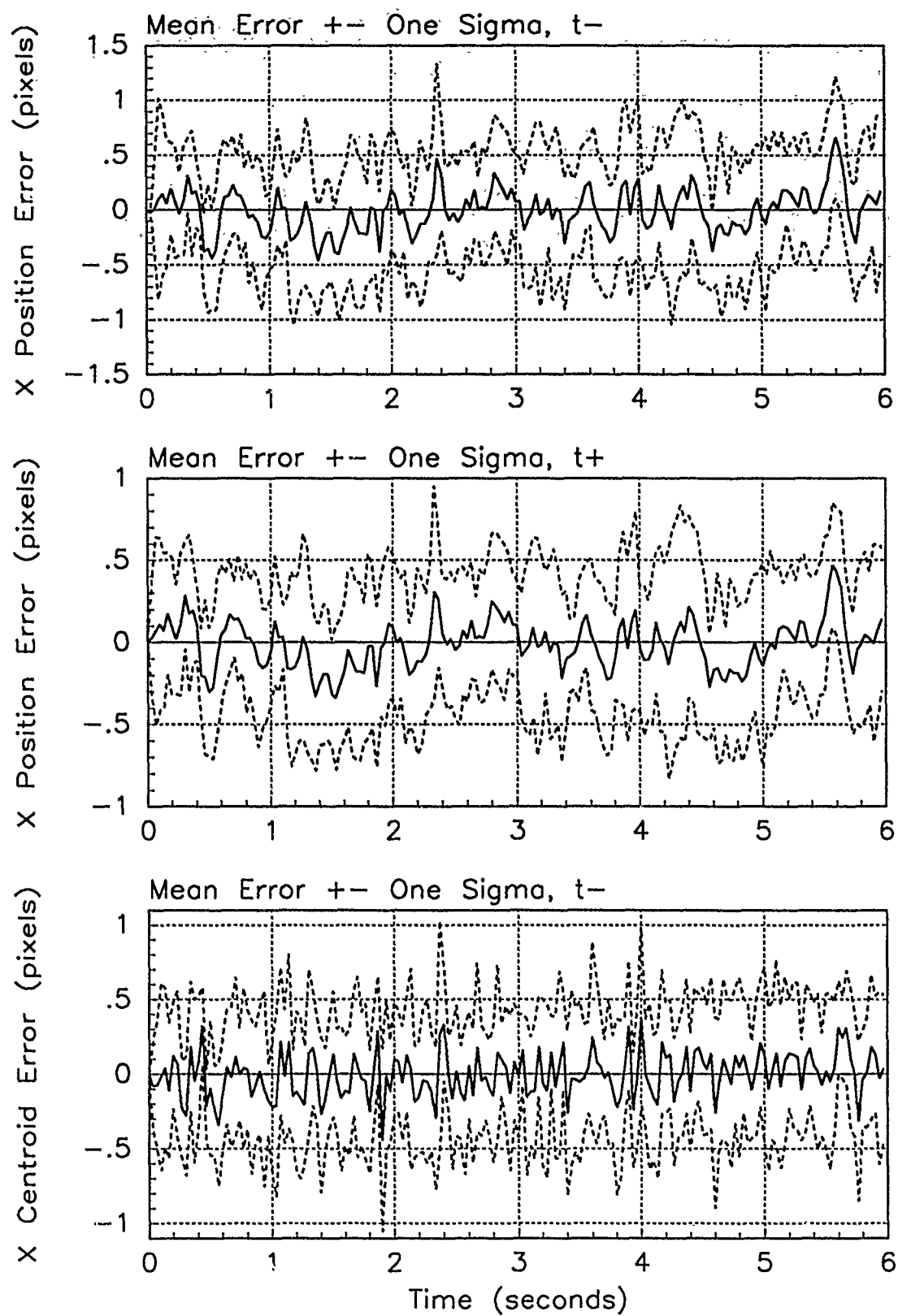


Figure F.17. X-Error Plots; First-Order MMAE-R; PC is 4; Trajectory with $\omega = 2.8$

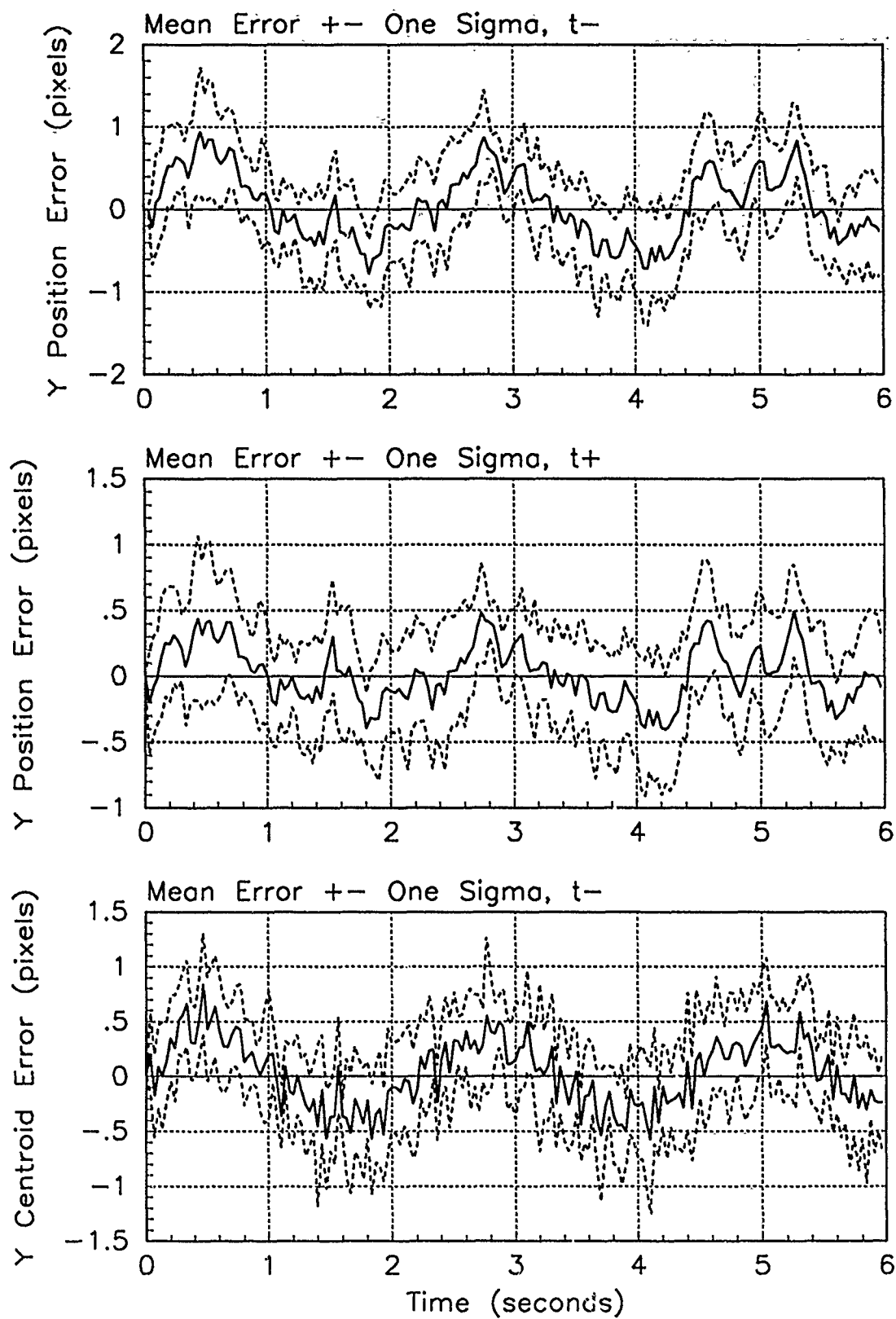


Figure F.18. Y-Error Plots; First-Order MMAE-R; PC is 4; Trajectory with $\omega = 2.8$

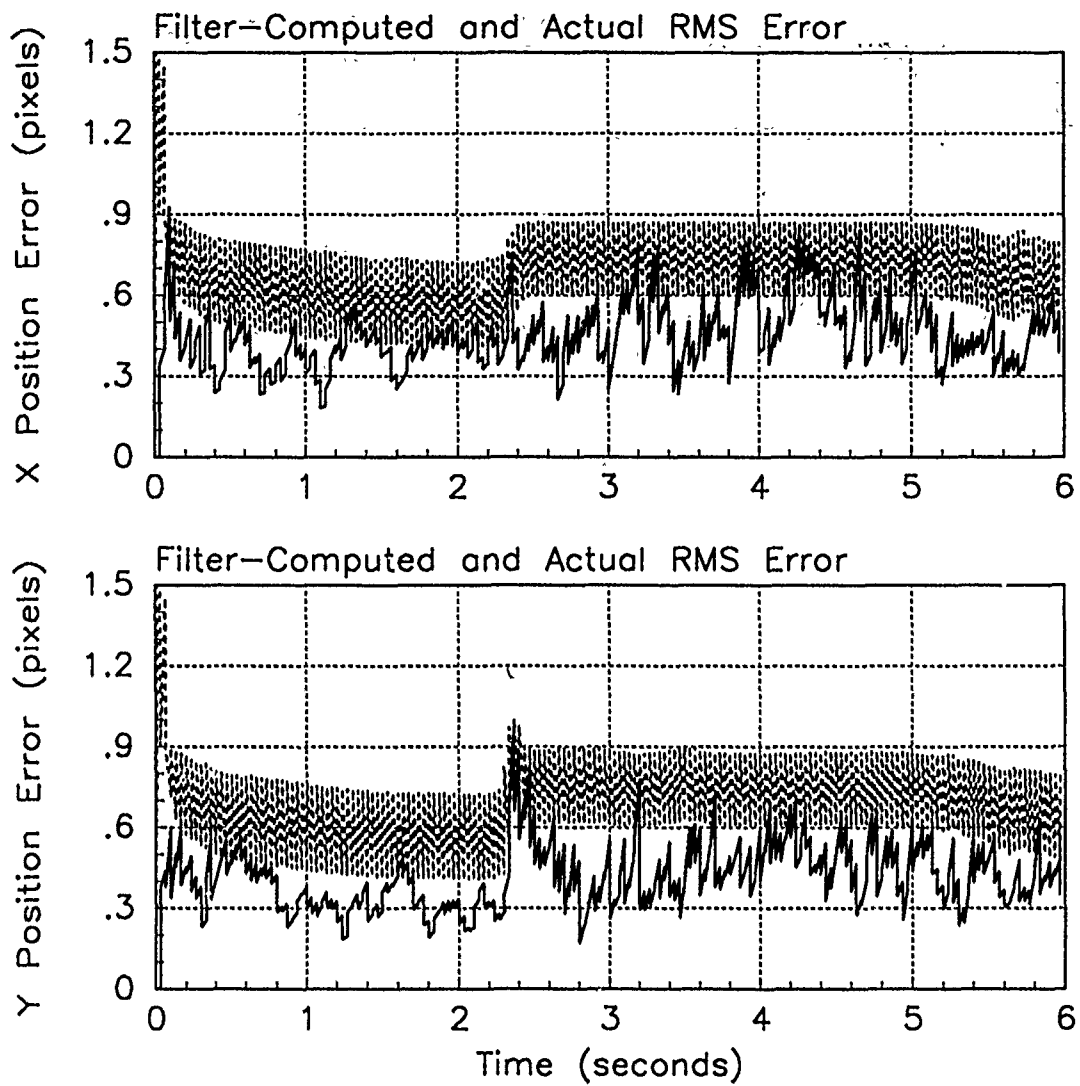


Figure F.19. RMS Error Plots; First-Order MMAE-R; PC is 1; Jinking Trajectory

Table F.7. Temporal Averages and Residuals; First-Order MMAE-R; PC is 1; Jinking Trajectory.

Error in:	Mean	σ
$p_x(t_i^-)$	0.034563	0.49723
$p_x(t_i^+)$	0.018161	0.41243
$y_x(t_i^-)$	0.031366	0.41929
$p_y(t_i^-)$	0.024590	0.45909
$p_y(t_i^+)$	0.017355	0.37569
$y_y(t_i^-)$	0.020847	0.40925

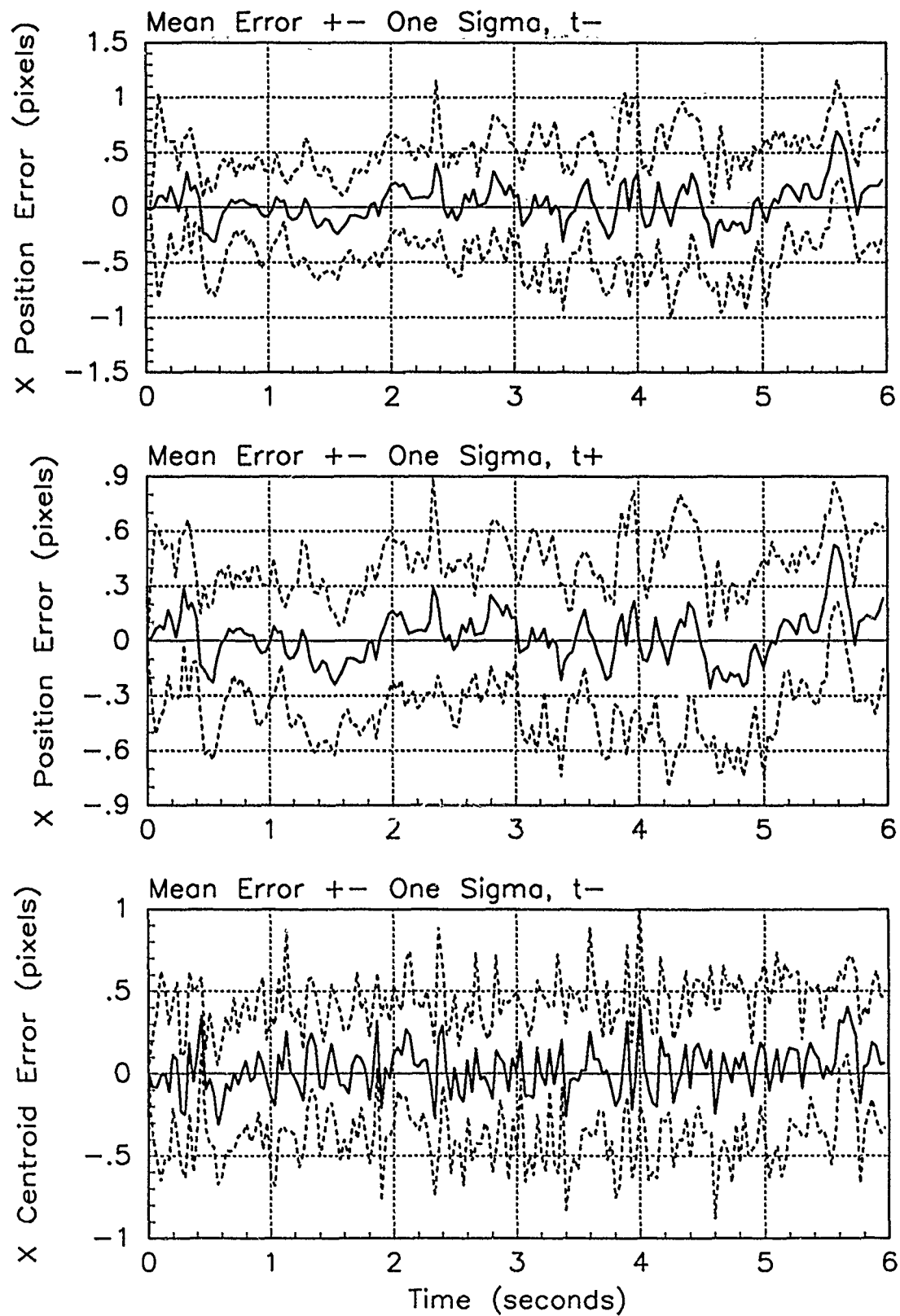


Figure F.20. X-Error Plots; First-Order MMAE-R; PC is 1; Jinking Trajectory

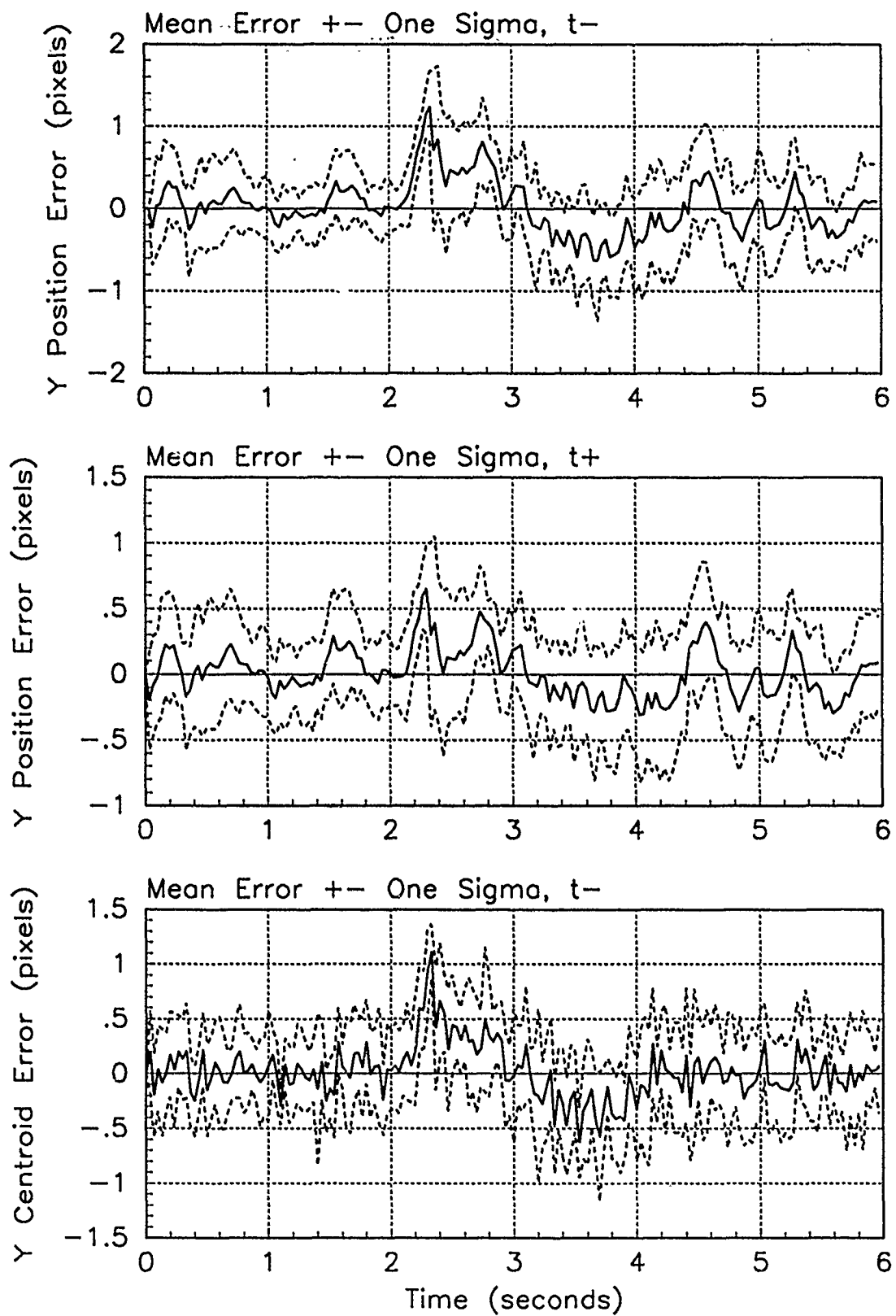


Figure F.21. Y-Error Plots; First-Order MMAE-R; PC is 1; Jinking Trajectory

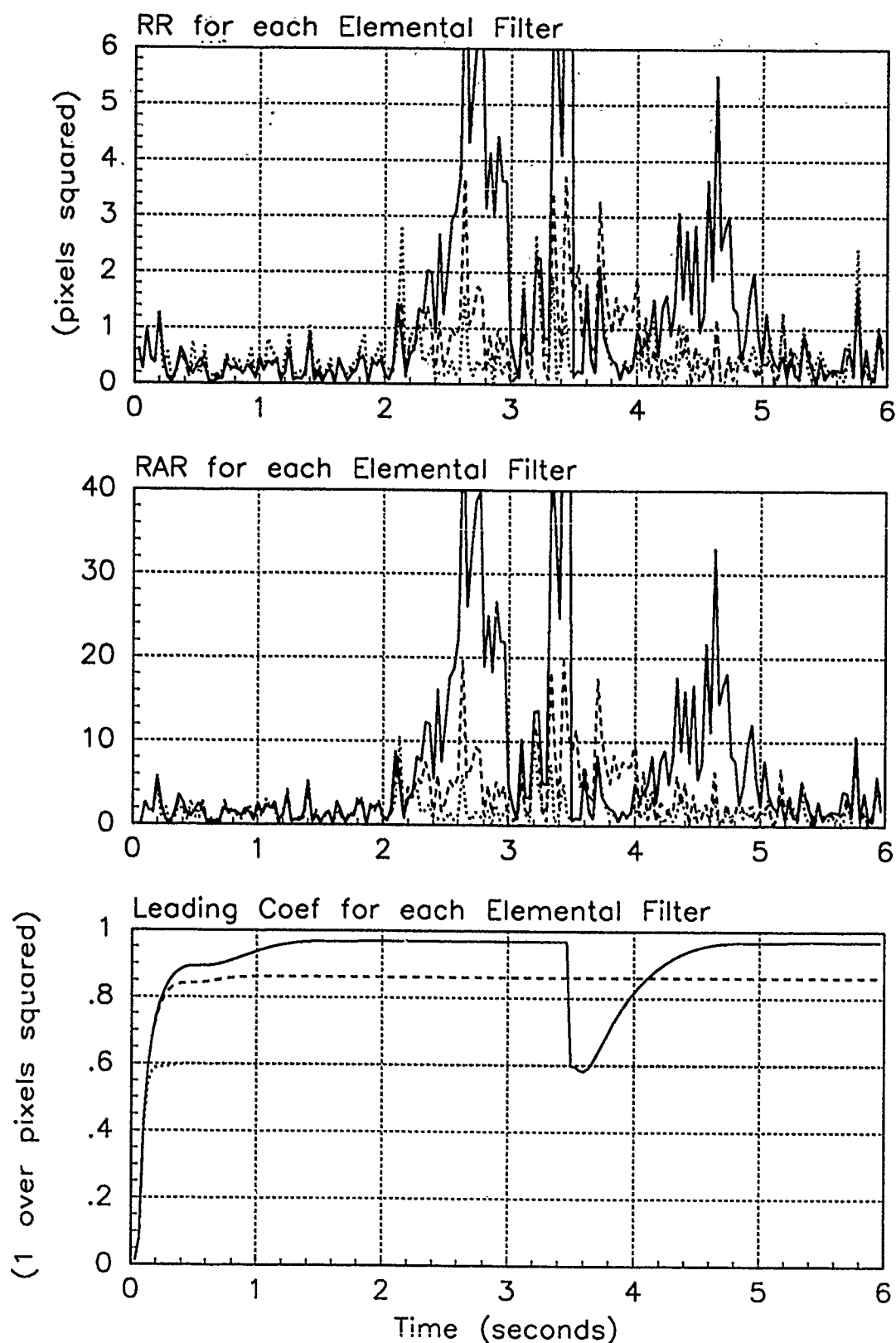


Figure F.22. Probability Calculation Plots; First-Order MMAE-R; PC is 1; Jinking Trajectory. Benign filter has solid line; intermediate filter has dashed line; harsh filter has dotted line.

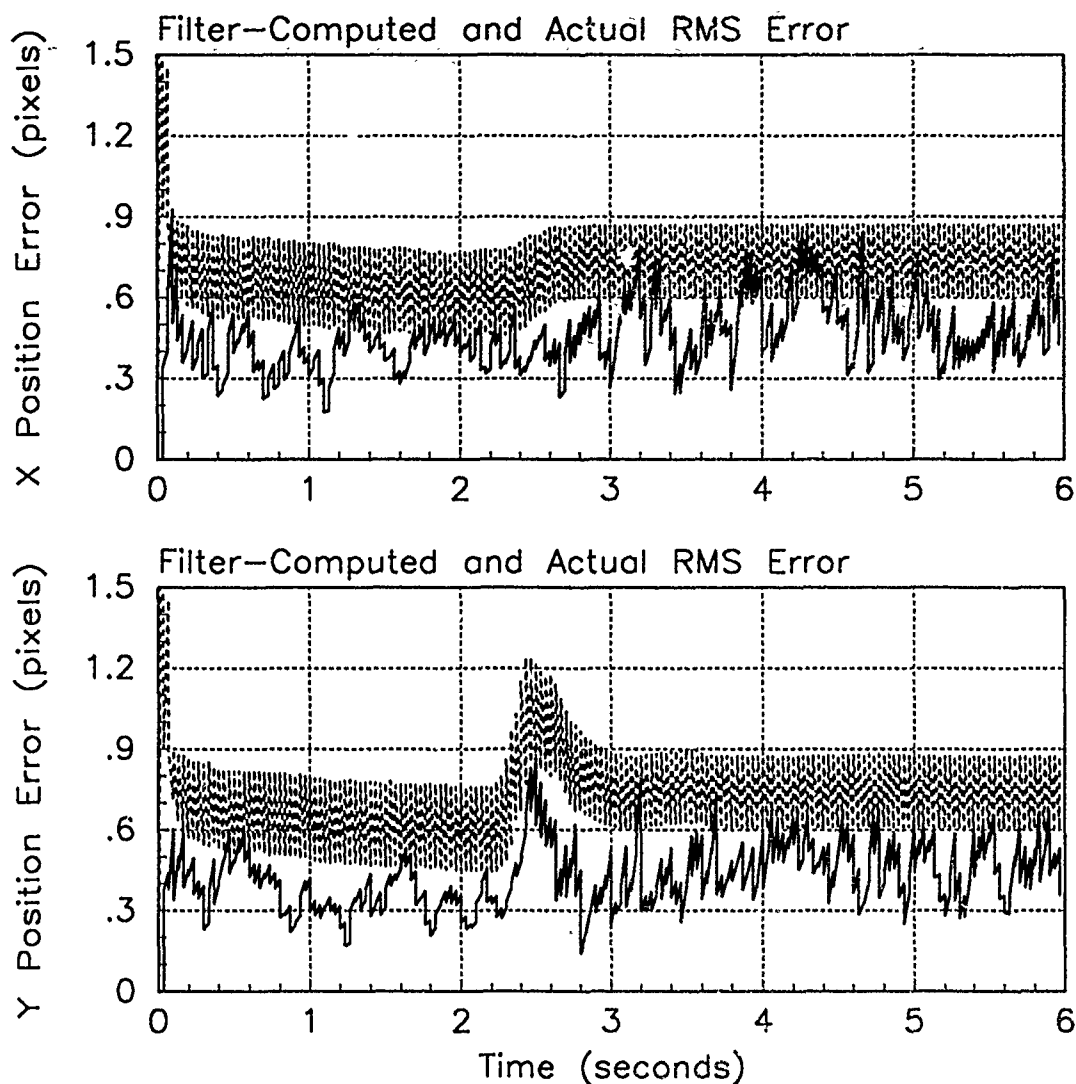


Figure F.23. RMS Error Plots; First-Order MMAE-R; PC is 4; Jinking Trajectory

Table F.8. Temporal Averages and Residuals; First-Order MMAE-R; PC is 4; Jinking Trajectory.

Error in:	Mean	σ
$p_x(t_i^-)$	0.0029189	0.50868
$p_x(t_i^+)$	-0.0065459	0.42018
$y_x(t_i^-)$	0.012048	0.42481
$p_y(t_i^-)$	0.062903	0.47264
$p_y(t_i^+)$	0.041699	0.38468
$y_y(t_i^-)$	0.040567	0.41512

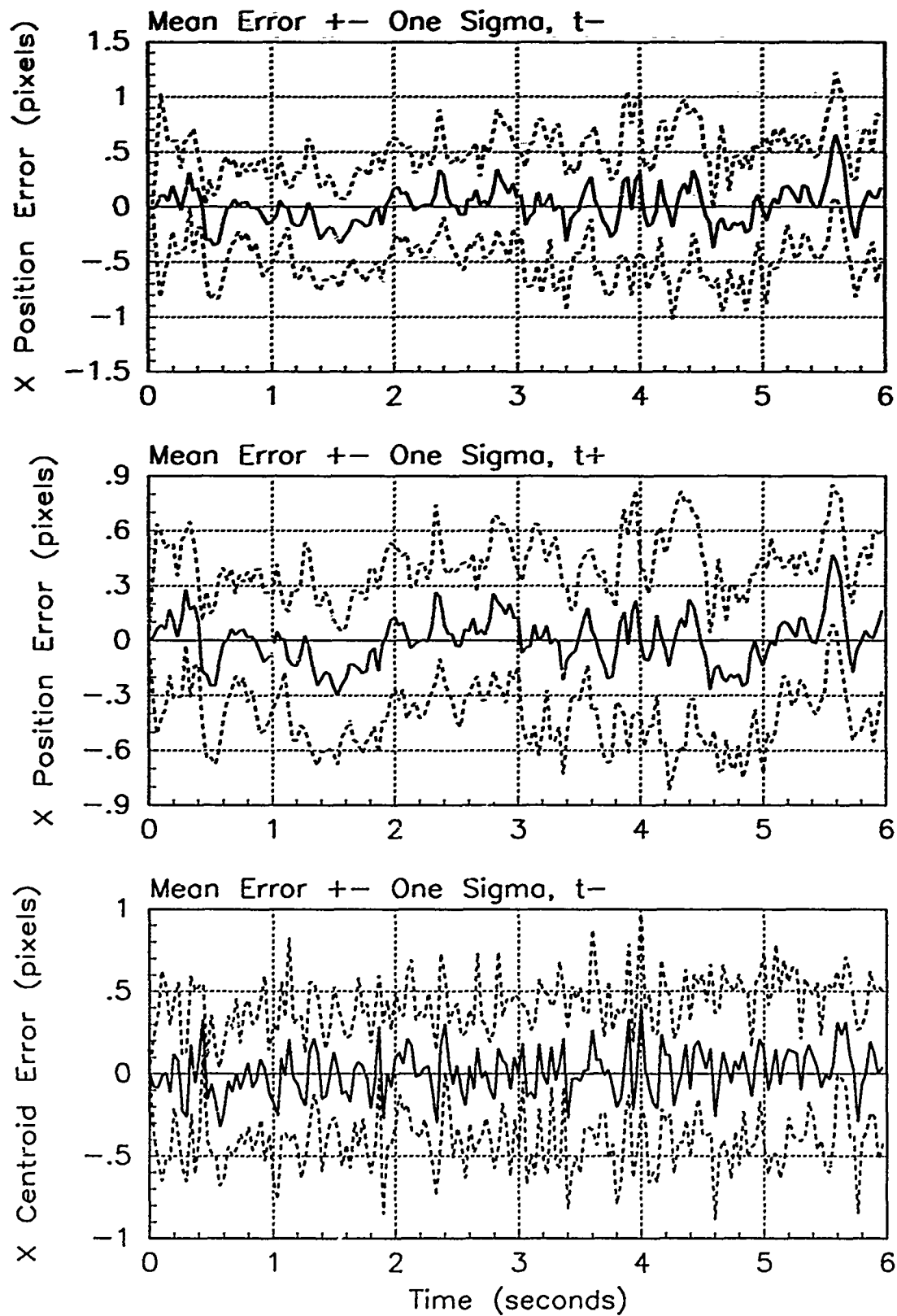


Figure F.24. X-Error Plots; First-Order MMAE-R; PC is 4; Jinking Trajectory

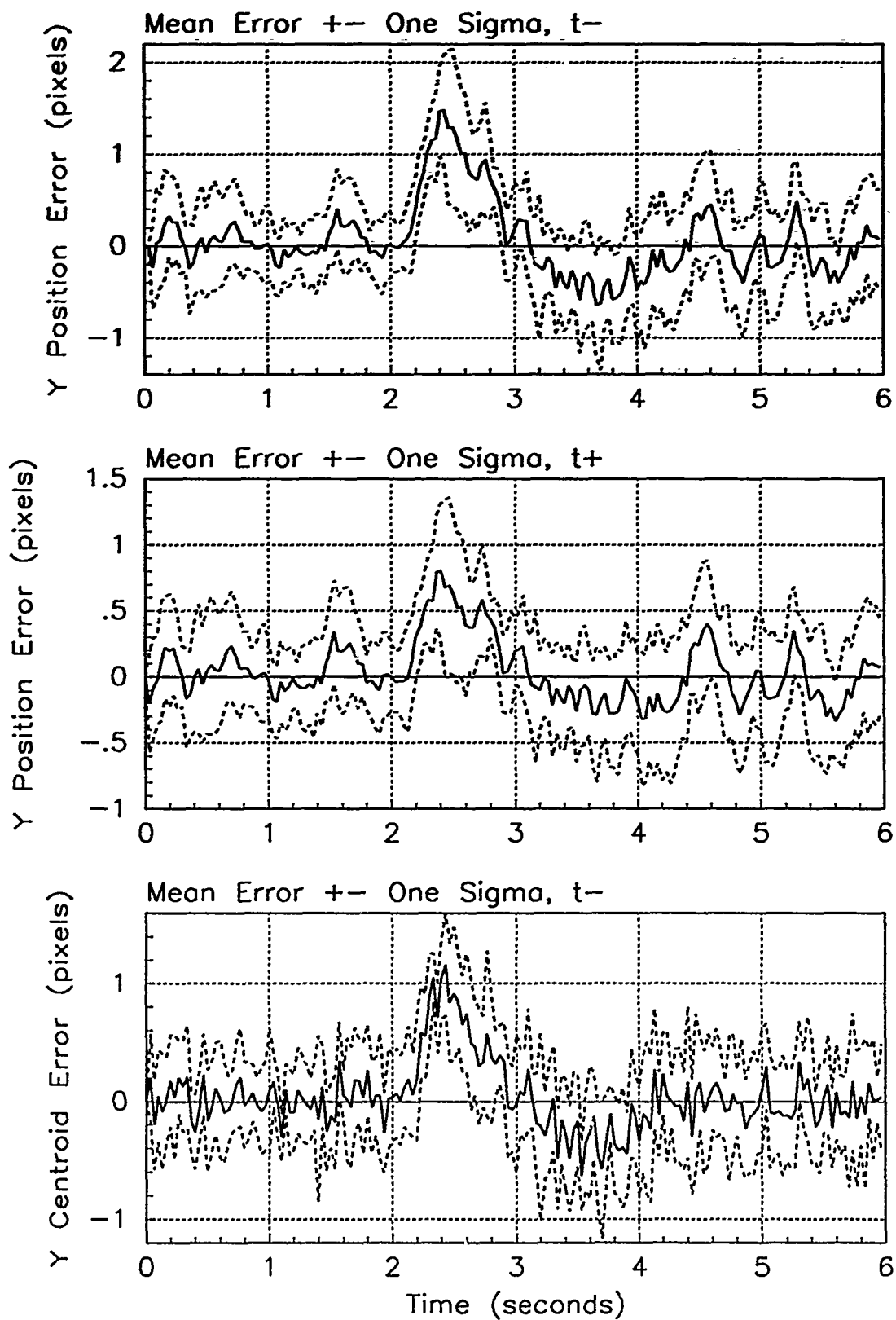


Figure F.25. Y-Error Plots; First-Order MMAE-R; PC is 4; Jinking Trajectory

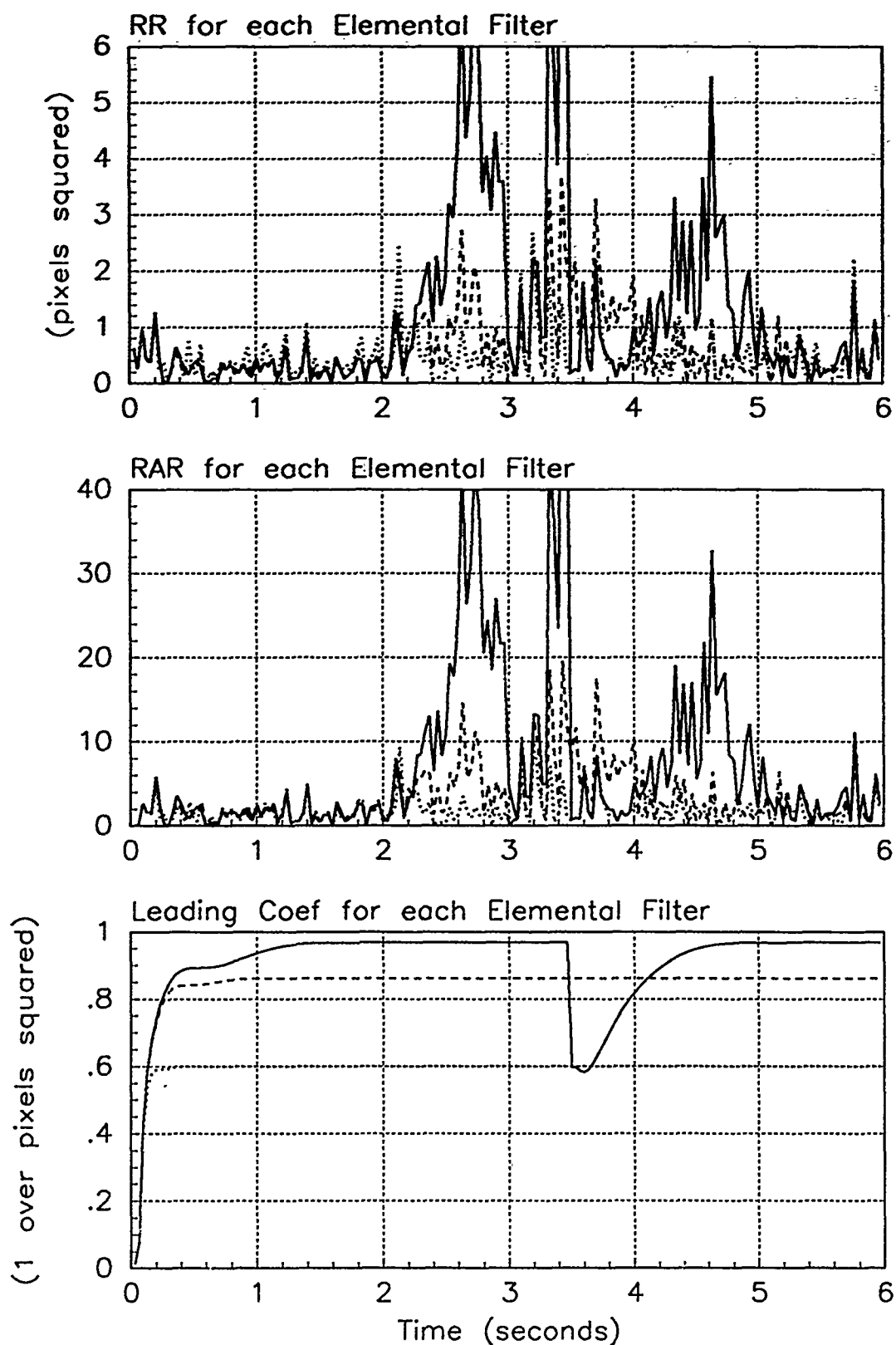


Figure F.26. Probability Calculation Plots; First-Order MMAE-R; PC is 4; Jinking Trajectory. Benign filter has solid line; intermediate filter has dashed line; harsh filter has dotted line.

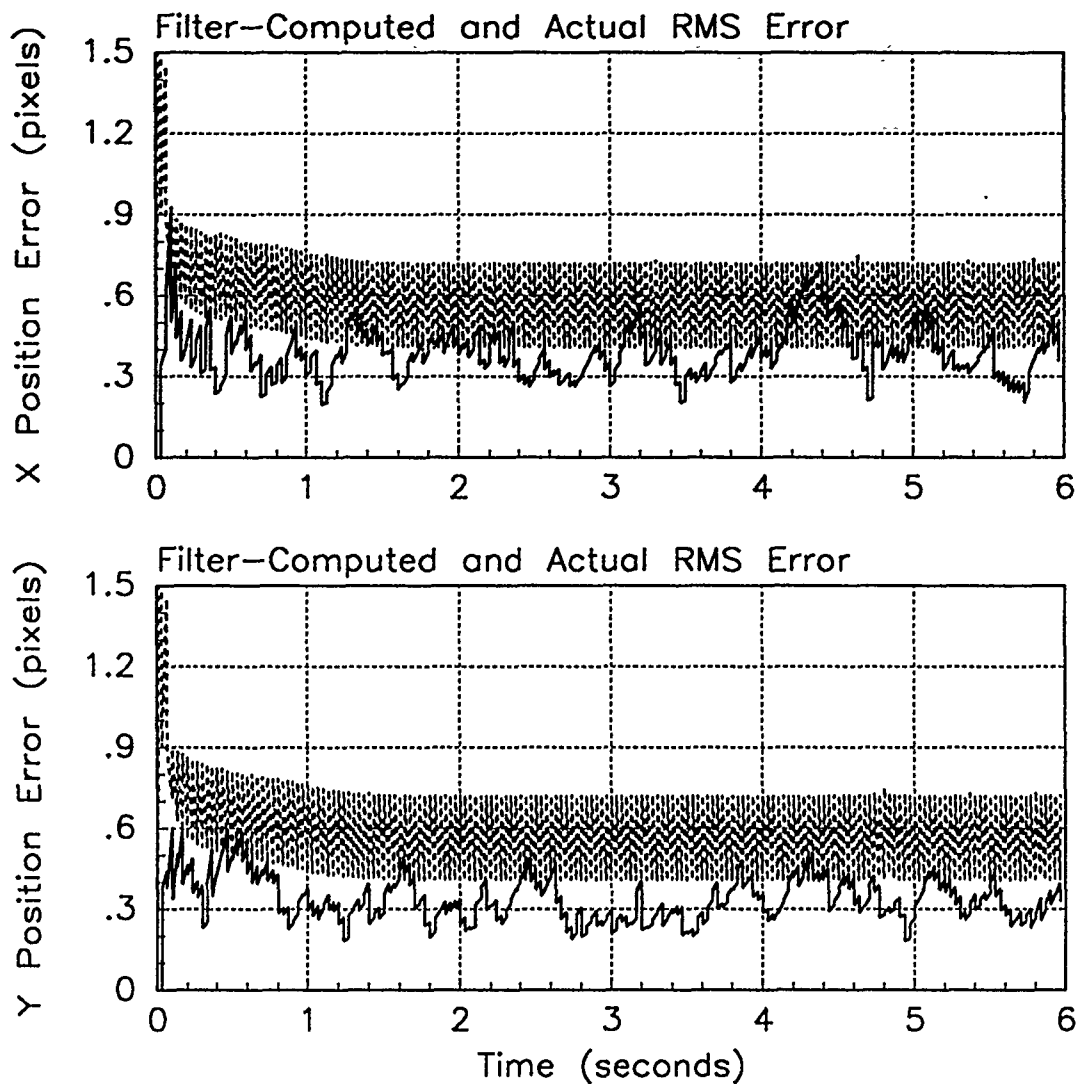


Figure F.27. RMS Error Plots; First-Order MMAE-FB; PC is 1; Trajectory with $\omega = .01$

Table F.9. Temporal Averages and Residuals; First-Order MMAE-FB; PC is 1; Trajectory with $\omega = .01$.

Error in:	Mean	σ
$p_x(t_i^-)$	0.16528	0.40632
$p_x(t_i^+)$	0.12577	0.36997
$y_x(t_i^-)$	0.10202	0.37950
$p_y(t_i^-)$	-0.0030356	0.34764
$p_y(t_i^+)$	-0.0016989	0.31555
$y_y(t_i^-)$	0.0029201	0.36677

Filter	$\mathbf{r}_k^T \mathbf{r}_k$	$\mathbf{r}_k^T \mathbf{A}_k^{-1} \mathbf{r}_k$
Benign	0.31415	1.85020
Intermediate	0.35000	1.70701
Harsh	0.38647	1.60664

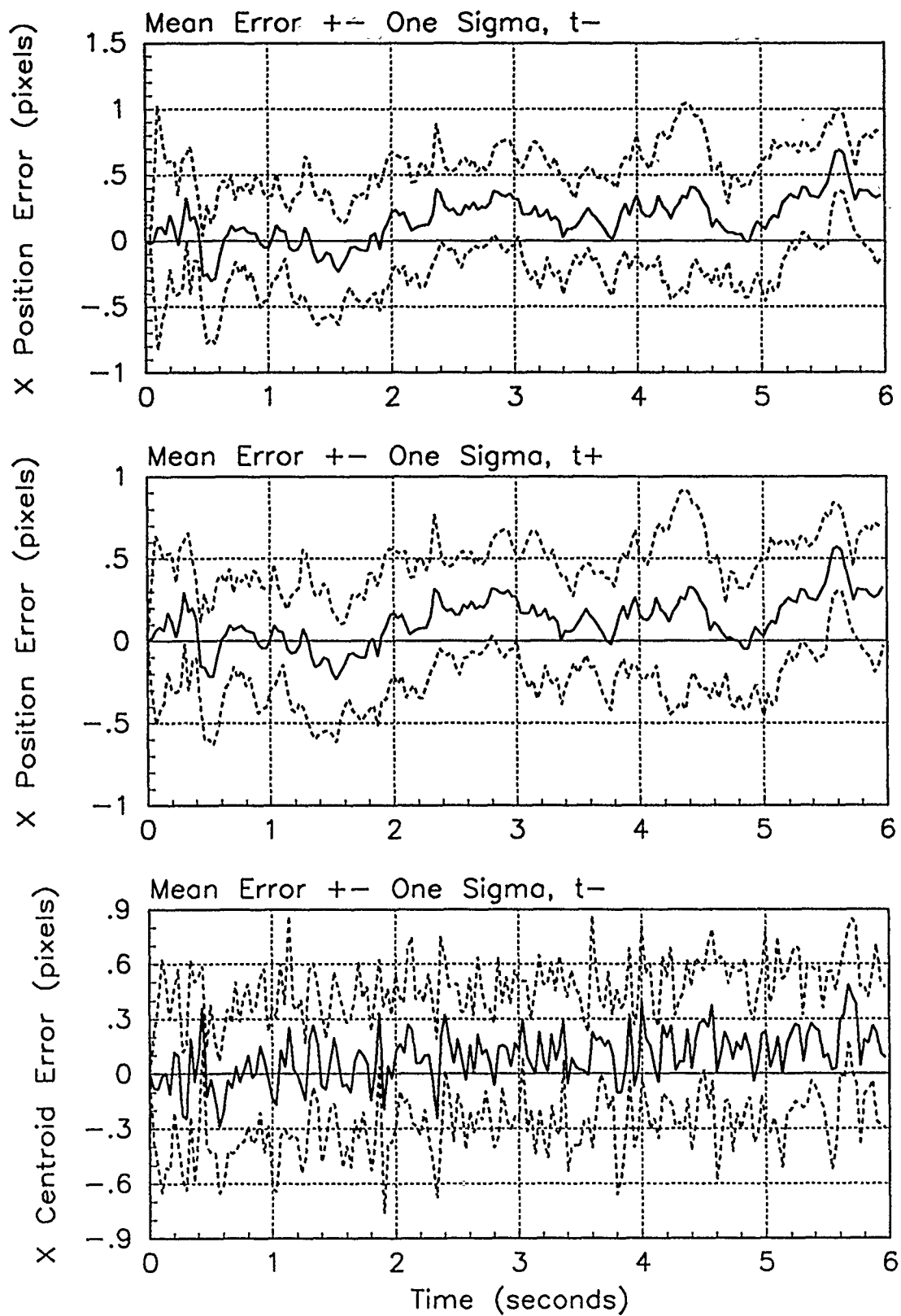


Figure F.28. X-Error Plots; First-Order MMAE-FB; PC is 1; Trajectory with $\omega = .01$

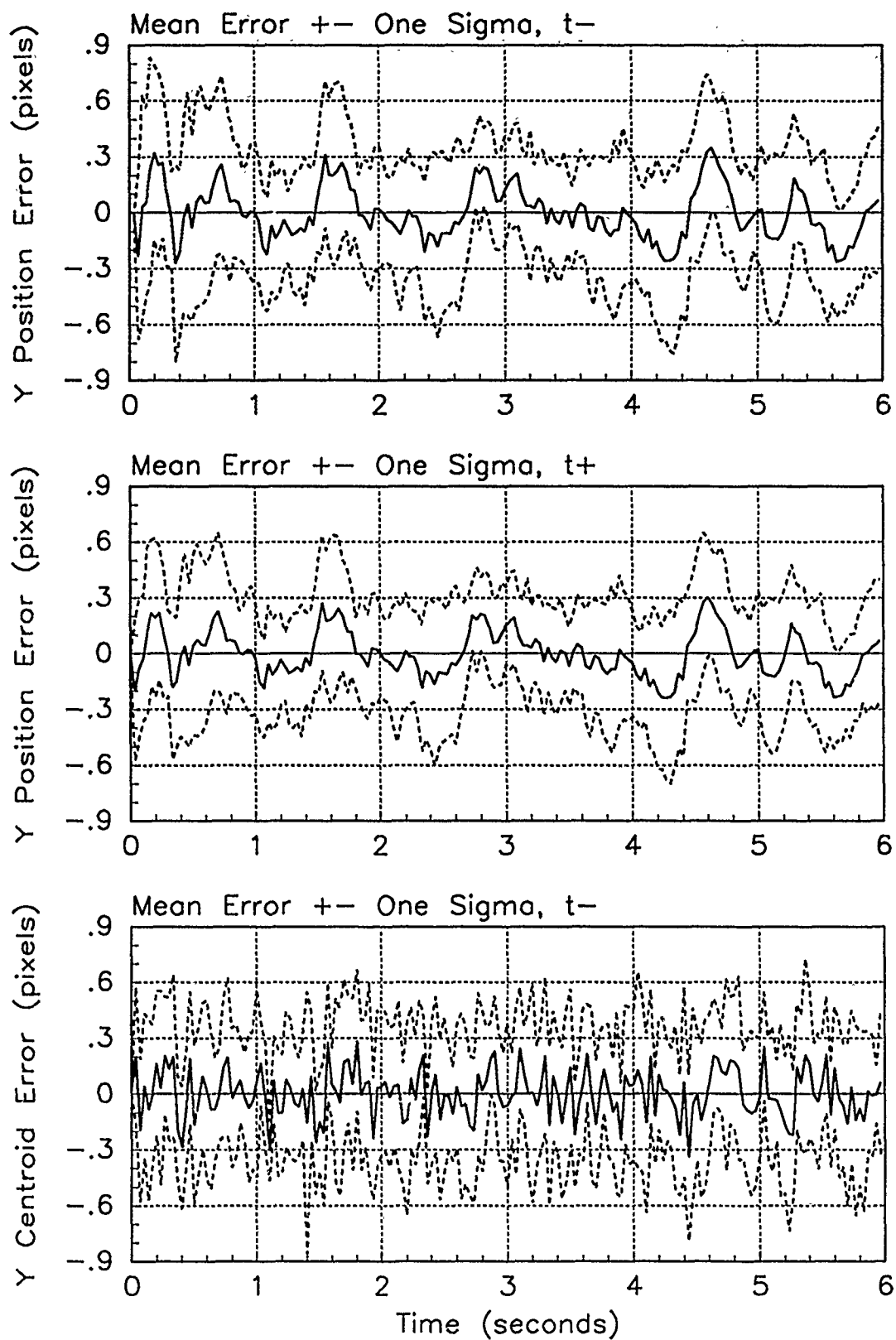


Figure F.29. Y-Error Plots; First-Order MMAE-FB; PC is 1; Trajectory with $\omega = .01$

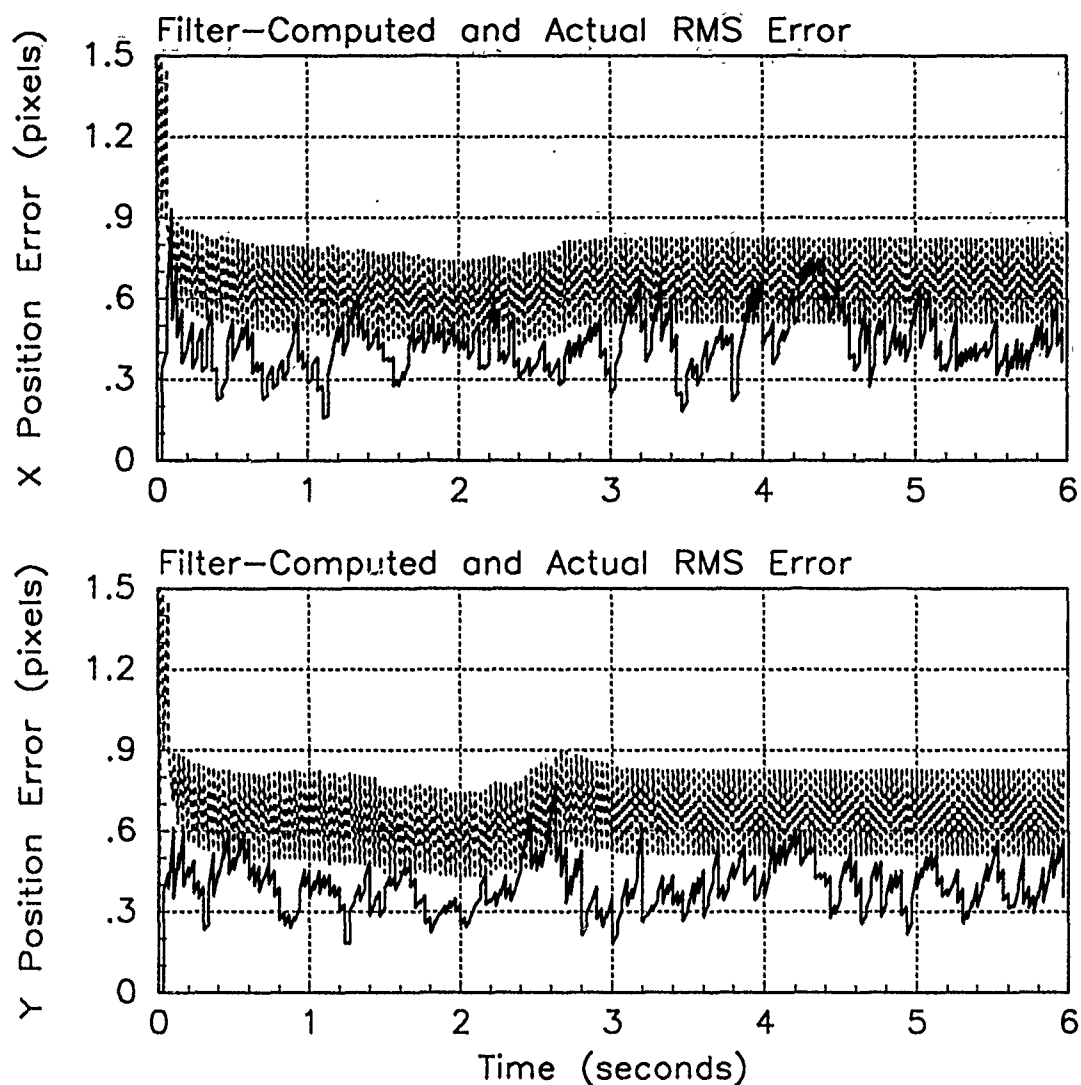


Figure F.30. RMS Error Plots; First-Order MMAE-FB; PC is 1; Trajectory with $\omega = 1.32$

Table F.10. Temporal Averages and Residuals; First-Order MMAE-FB; PC is 1; Trajectory with $\omega = 1.32$.

Error in:	Mean	σ
$p_x(t_i^-)$	0.045651	0.46321
$p_x(t_i^+)$	0.026013	0.40486
$y_x(t_i^-)$	0.037215	0.40084
$p_y(t_i^-)$	-0.021472	0.42602
$p_y(t_i^+)$	-0.022343	0.36528
$y_y(t_i^-)$	-0.022785	0.38598

Filter	$\mathbf{r}_k^T \mathbf{r}_k$	$\mathbf{r}_k^T \mathbf{A}_k^{-1} \mathbf{r}_k$
Benign	0.39558	2.33950
Intermediate	0.34910	1.70255
Harsh	0.38397	1.59621

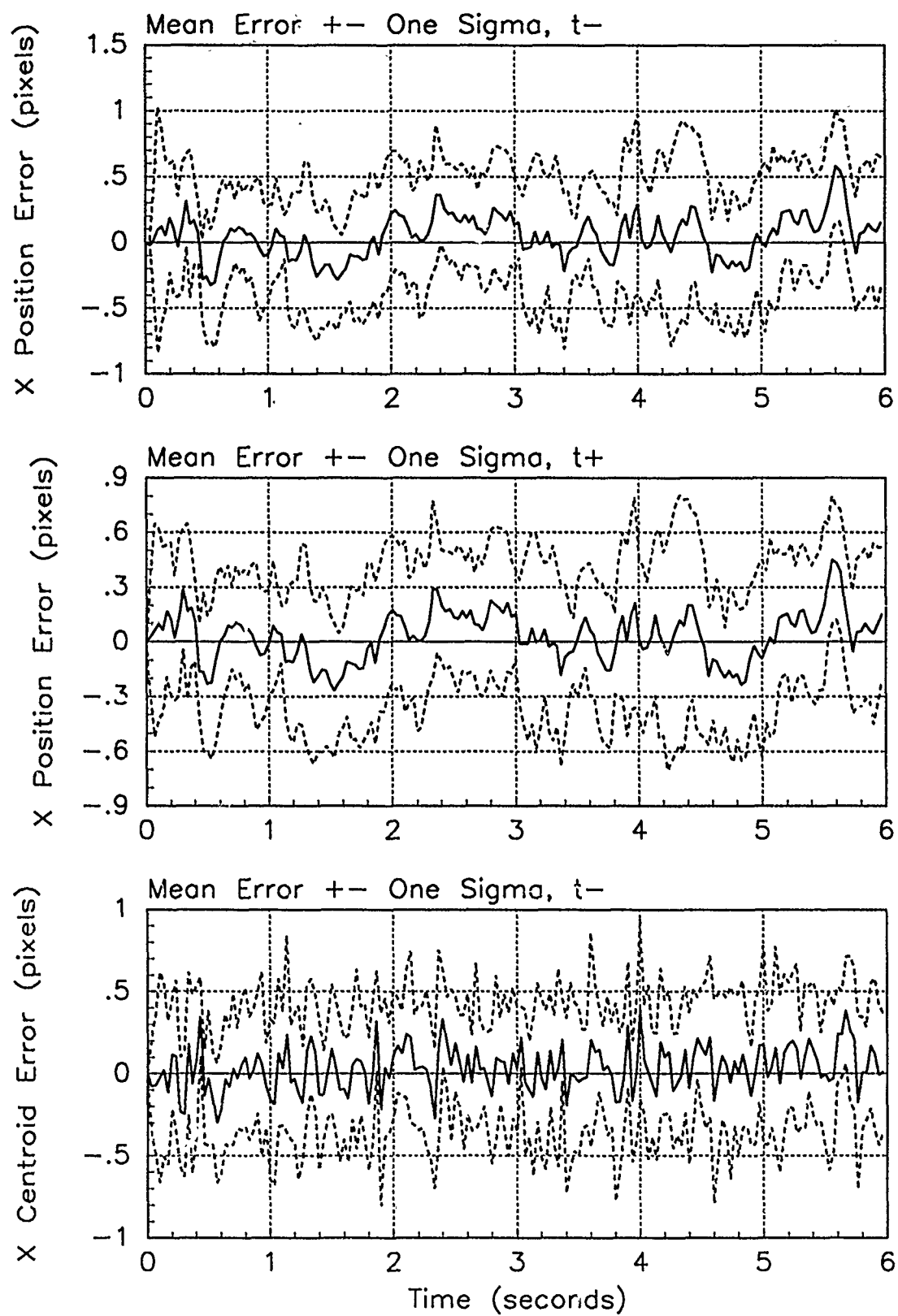


Figure F.31. X-Error Plots; First-Order MMAE-FB; PC is 1; Trajectory with $\omega = 1.32$

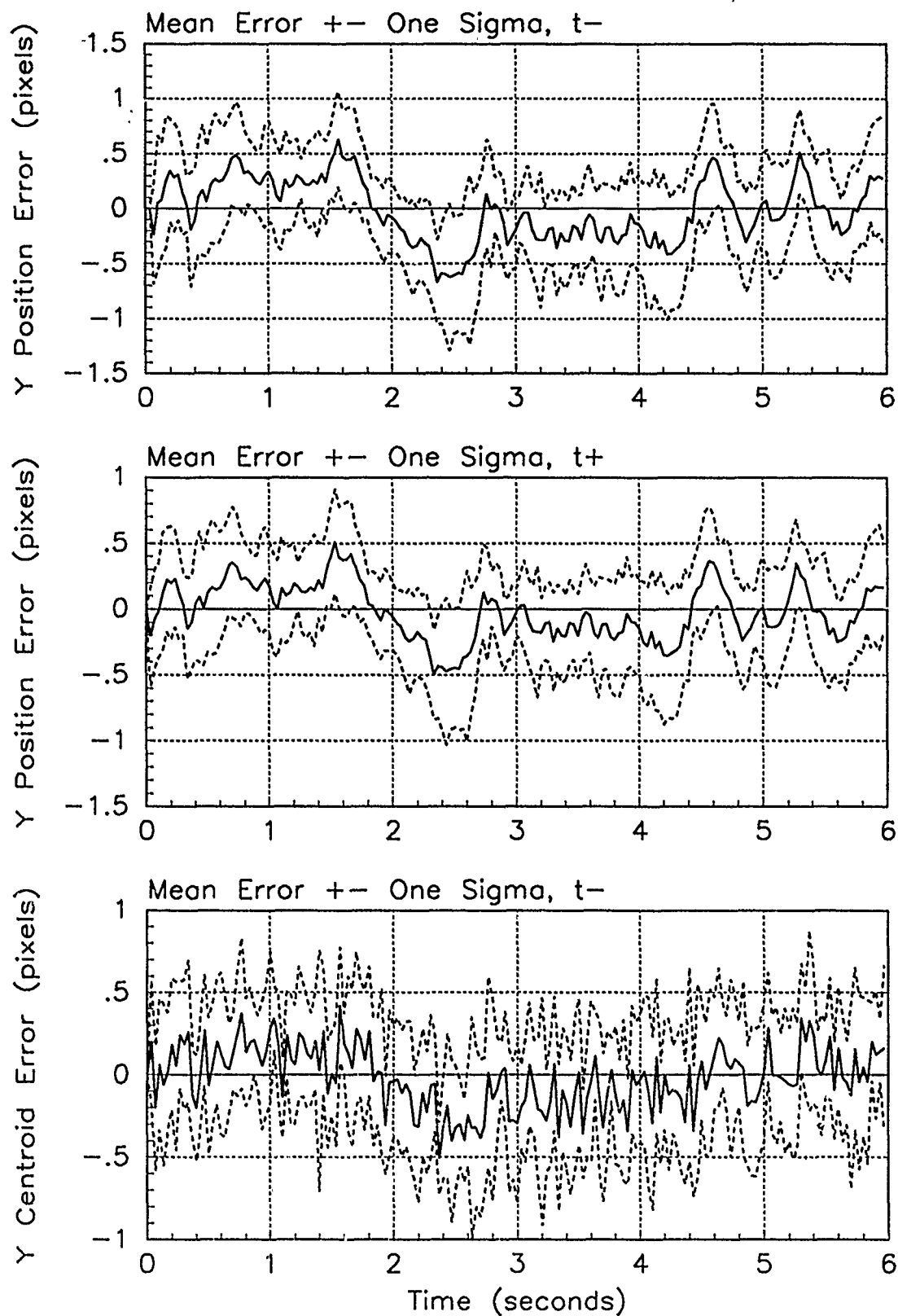


Figure F.32. Y-Error Plots; First-Order MMAE-FB; PC is 1; Trajectory with $\omega = 1.32$

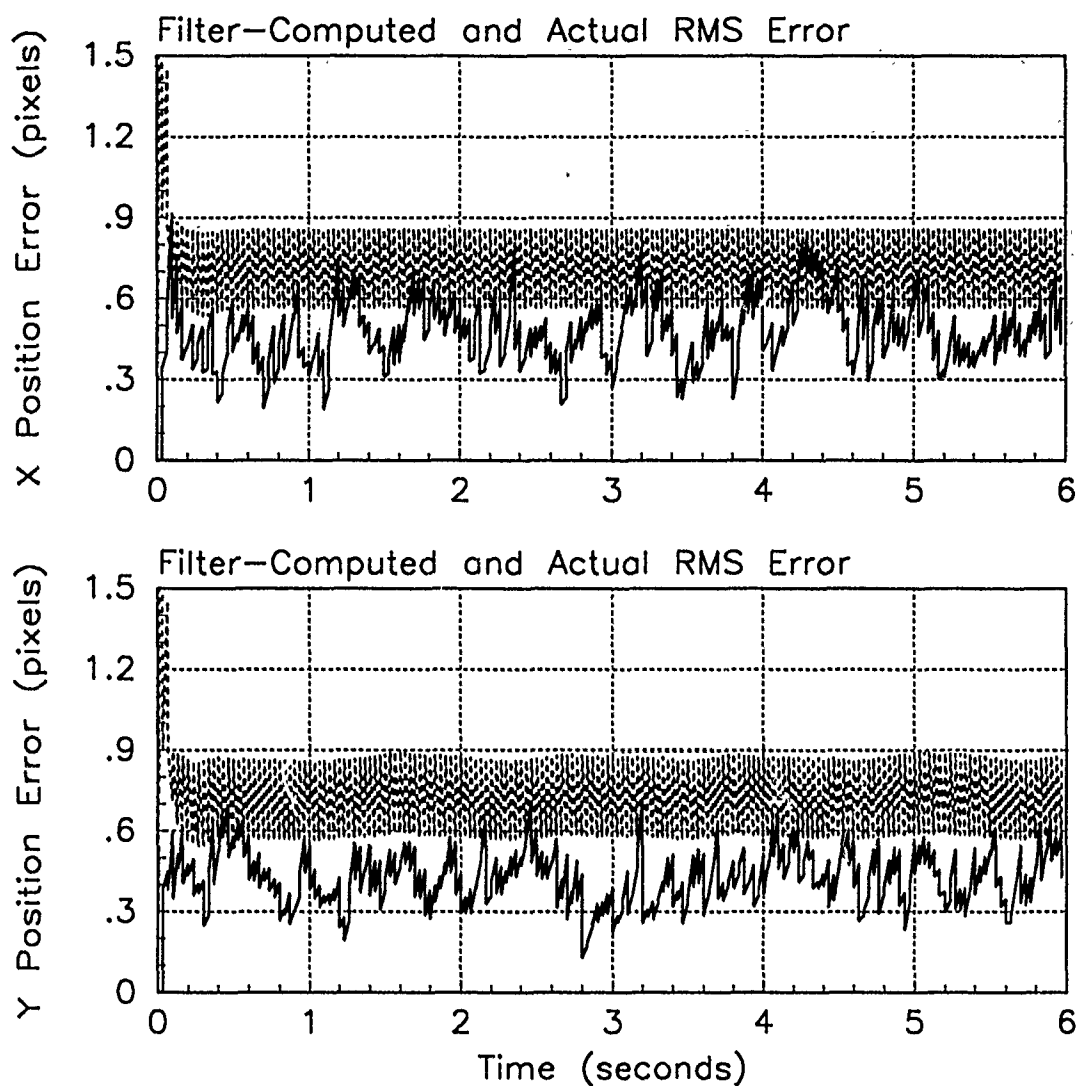


Figure F.33. RMS Error Plots; First-Order MMAE-FB; PC is 1; Trajectory with $\omega = 2.8$

Table F.11. Temporal Averages and Residuals; First-Order MMAE-FB; PC is 1; Trajectory with $\omega = 2.8$.

Error in:	Mean	σ
$p_x(t_i^-)$	-0.0063046	0.52794
$p_x(t_i^+)$	-0.0086904	0.43546
$y_x(t_i^-)$	0.0060853	0.43040
$p_y(t_i^-)$	0.056067	0.46951
$p_y(t_i^+)$	0.035263	0.37882
$y_y(t_i^-)$	0.045077	0.41084

Filter	$\mathbf{r}_k^T \mathbf{r}_k$	$\mathbf{r}_k^T \mathbf{A}_k^{-1} \mathbf{r}_k$
Benign	3.91350	23.24718
Intermediate	0.58717	2.87271
Harsh	0.48816	2.03137

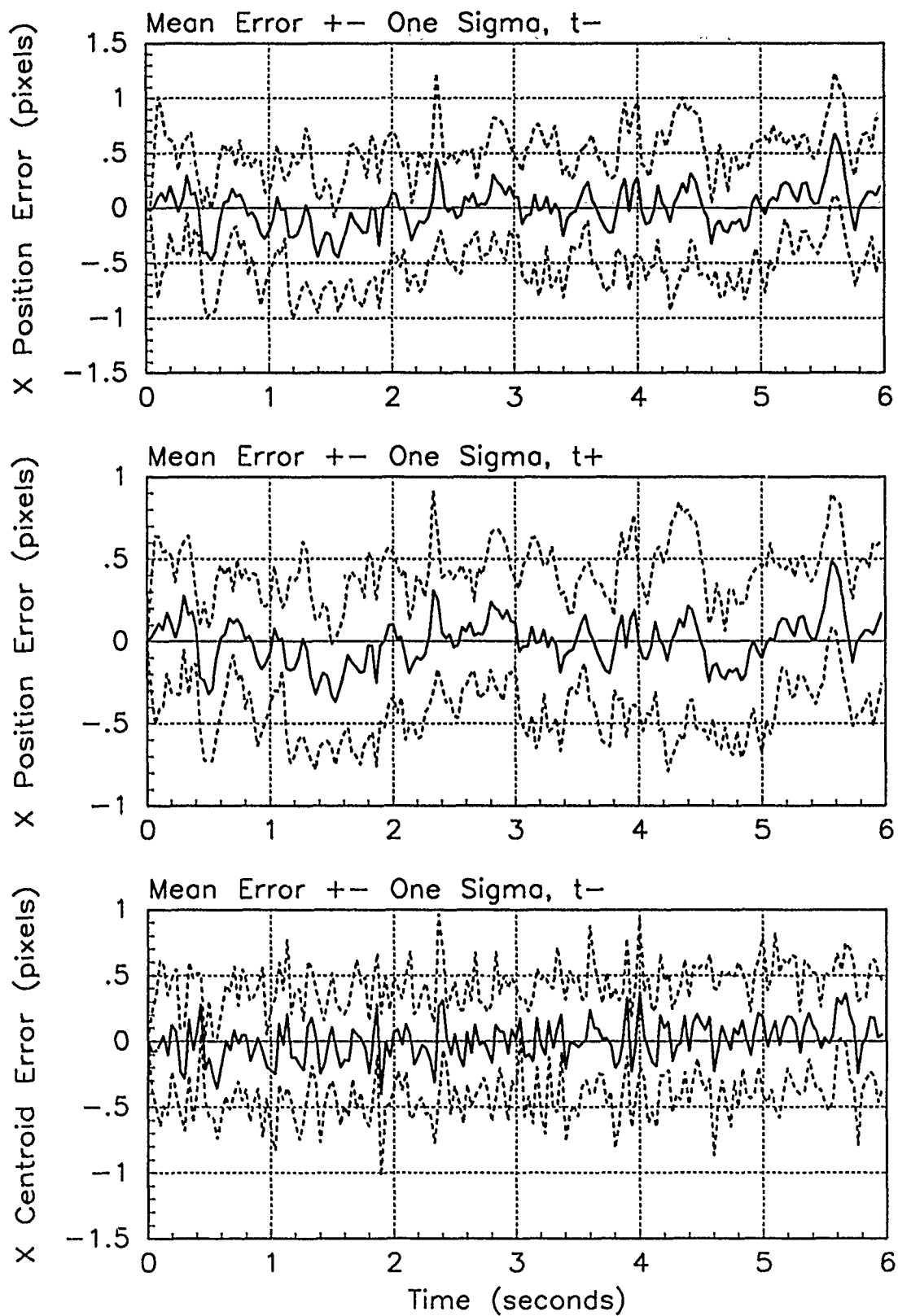


Figure F.34. X-Error Plots; First-Order MMAE-FB; PC is 1; Trajectory with $\omega = 2.8$

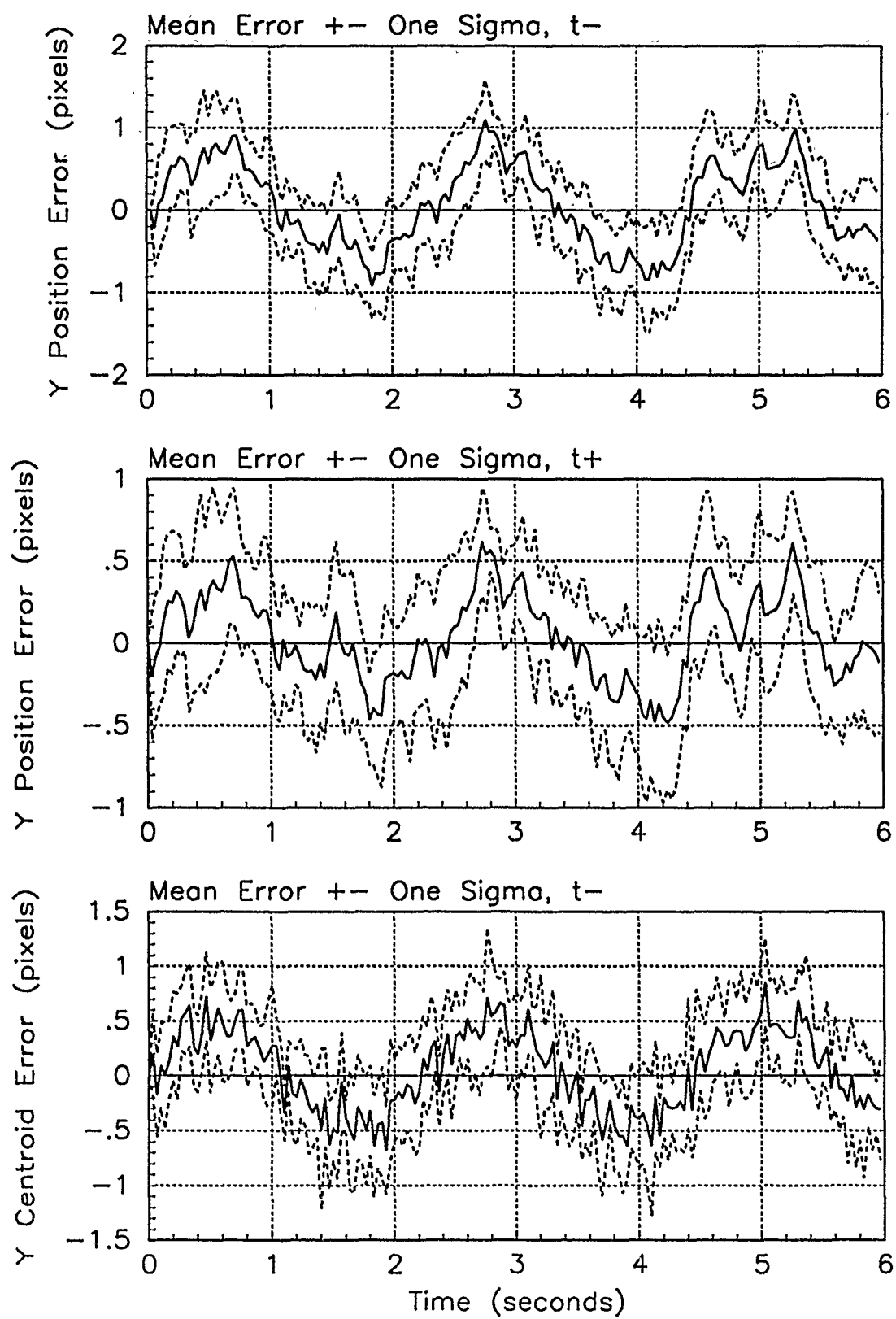


Figure F.35. Y-Error Plots; First-Order MMAE-FB; PC is 1; Trajectory with $\omega = 2.8$

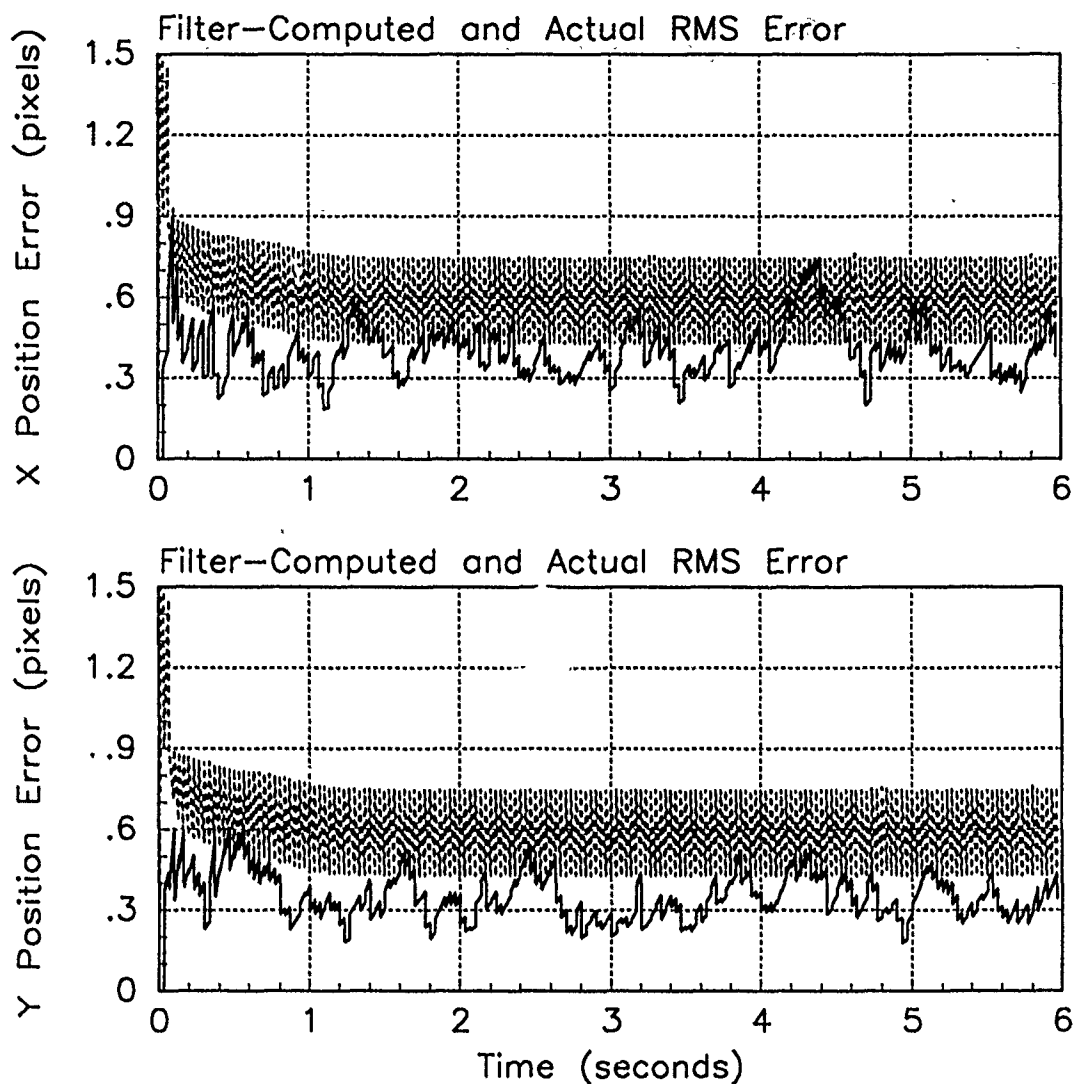


Figure F.36. RMS Error Plots; First-Order MMAE-FH; PC is 1; Trajectory with $\omega = .01$

Table F.12. Temporal Averages and Residuals; First-Order MMAE-FH; PC is 1; Trajectory with $\omega = .01$.

Error in:	Mean	σ
$p_x(t_i^-)$	0.11580	0.42424
$p_x(t_i^+)$	0.085036	0.38211
$y_x(t_i^-)$	0.078042	0.38214
$p_y(t_i^-)$	-0.0028899	0.36568
$p_y(t_i^+)$	-0.0017195	0.32779
$y_y(t_i^-)$	0.0027658	0.37086

Filter	$\mathbf{r}_k^T \mathbf{r}_k$	$\mathbf{r}_k^T \mathbf{A}_k^{-1} \mathbf{r}_k$
Benign	0.31612	1.80449
Intermediate	0.36594	1.67018
Harsh	0.41545	1.54853

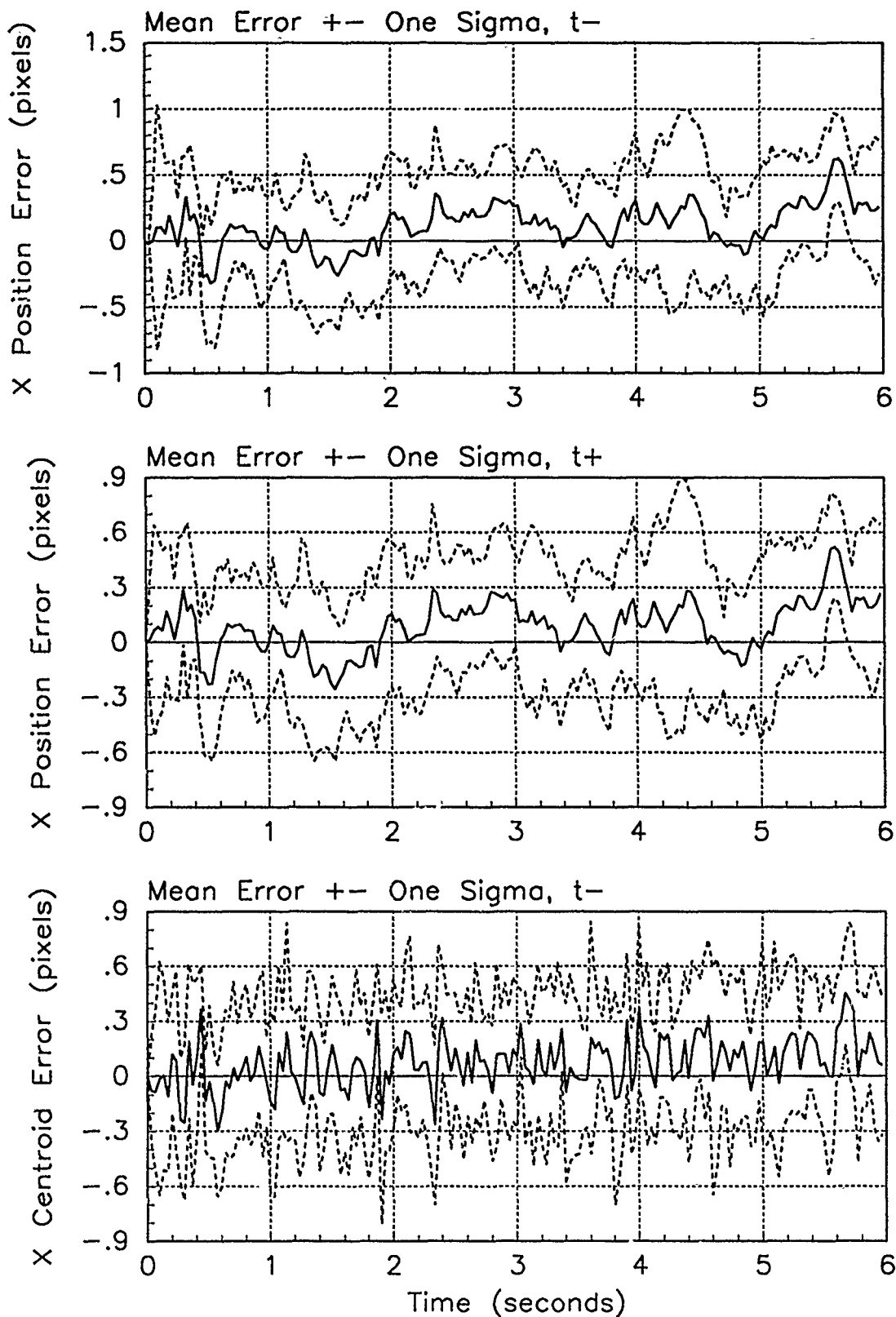


Figure F.37. X-Error Plots; First-Order MMAE-FH; PC is 1; Trajectory with $\omega = .01$

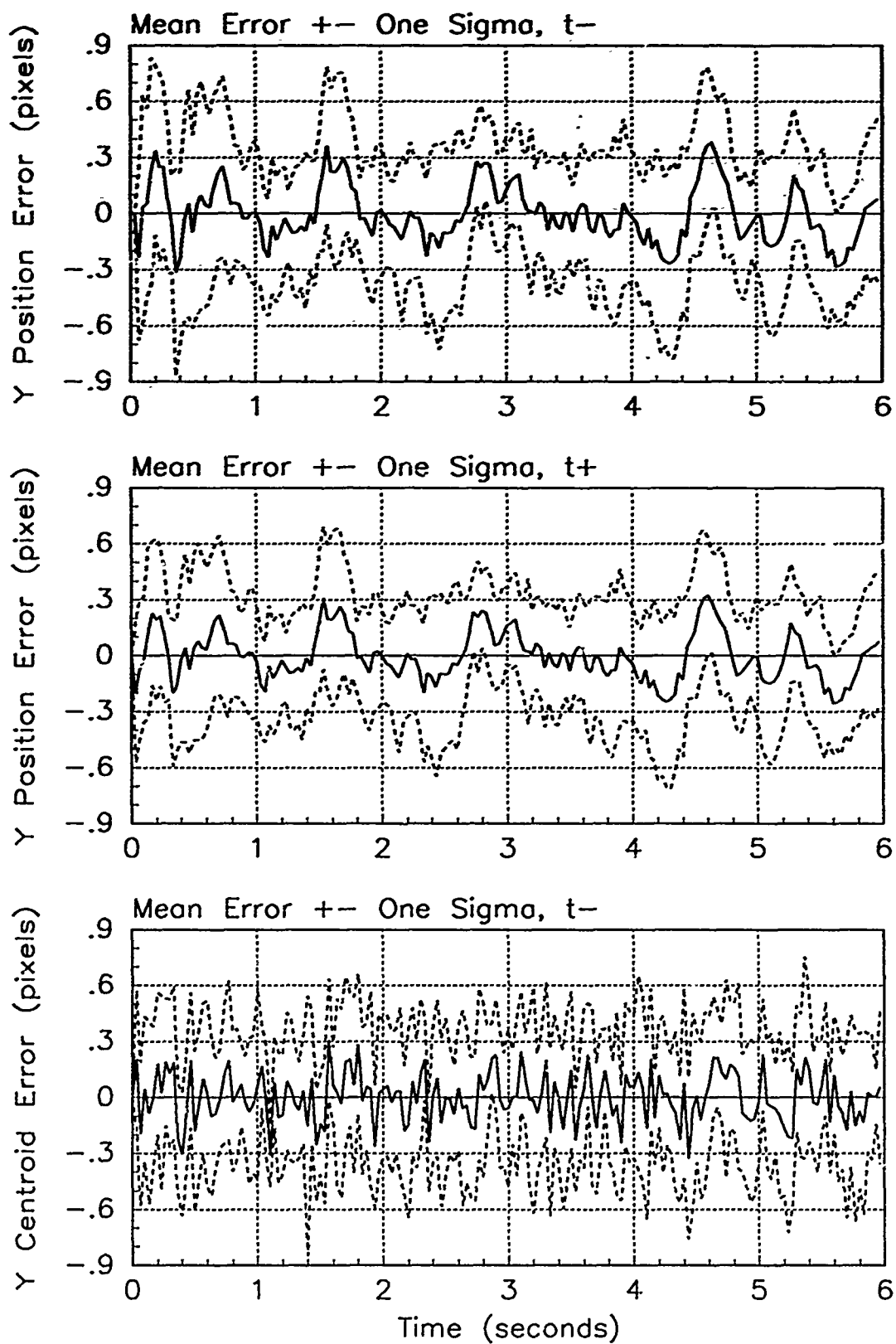


Figure F.38. Y-Error Plots; First-Order MMAE-FH; PC is 1; Trajectory with $\omega = .01$

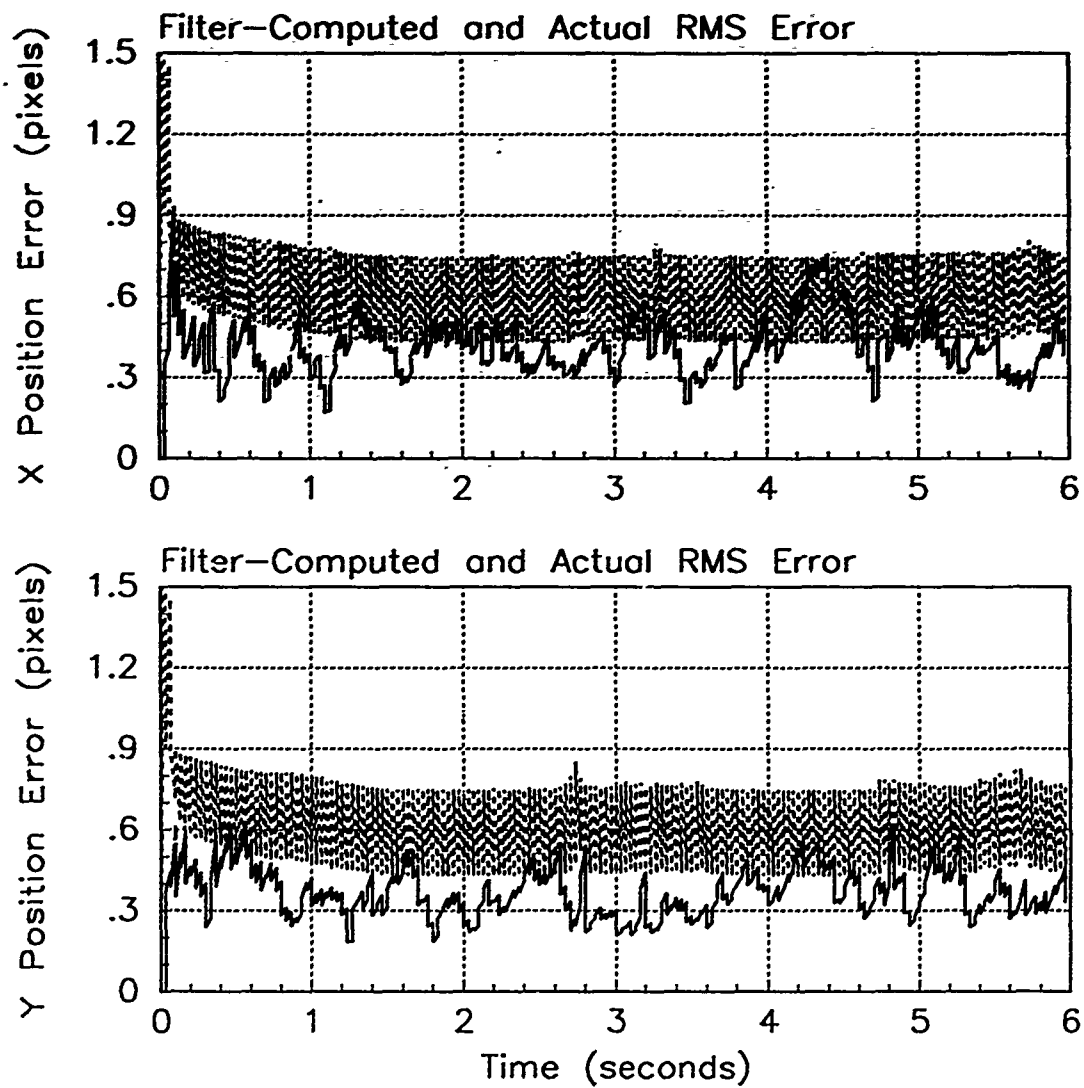


Figure F.39. RMS Error Plots; First-Order MMAE-FH; PC is 1; Trajectory with $\omega = 1.32$

Table F.13. Temporal Averages and Residuals; First-Order MMAE-FH; PC is 1; Trajectory with $\omega = 1.32$.

Error in:	Mean	σ
$p_x(t_i^-)$	0.088745	0.43603
$p_x(t_i^+)$	0.059248	0.39308
$y_x(t_i^-)$	0.053840	0.38965
$p_y(t_i^-)$	-0.0088055	0.38312
$p_y(t_i^+)$	-0.019678	0.34112
$y_y(t_i^-)$	-0.014389	0.37312

Filter	$r_k^T r_k$	$r_k^T A_k^{-1} r_k$
Benign	0.35077	2.00592
Intermediate	0.35858	1.63629
Harsh	0.40562	1.51172

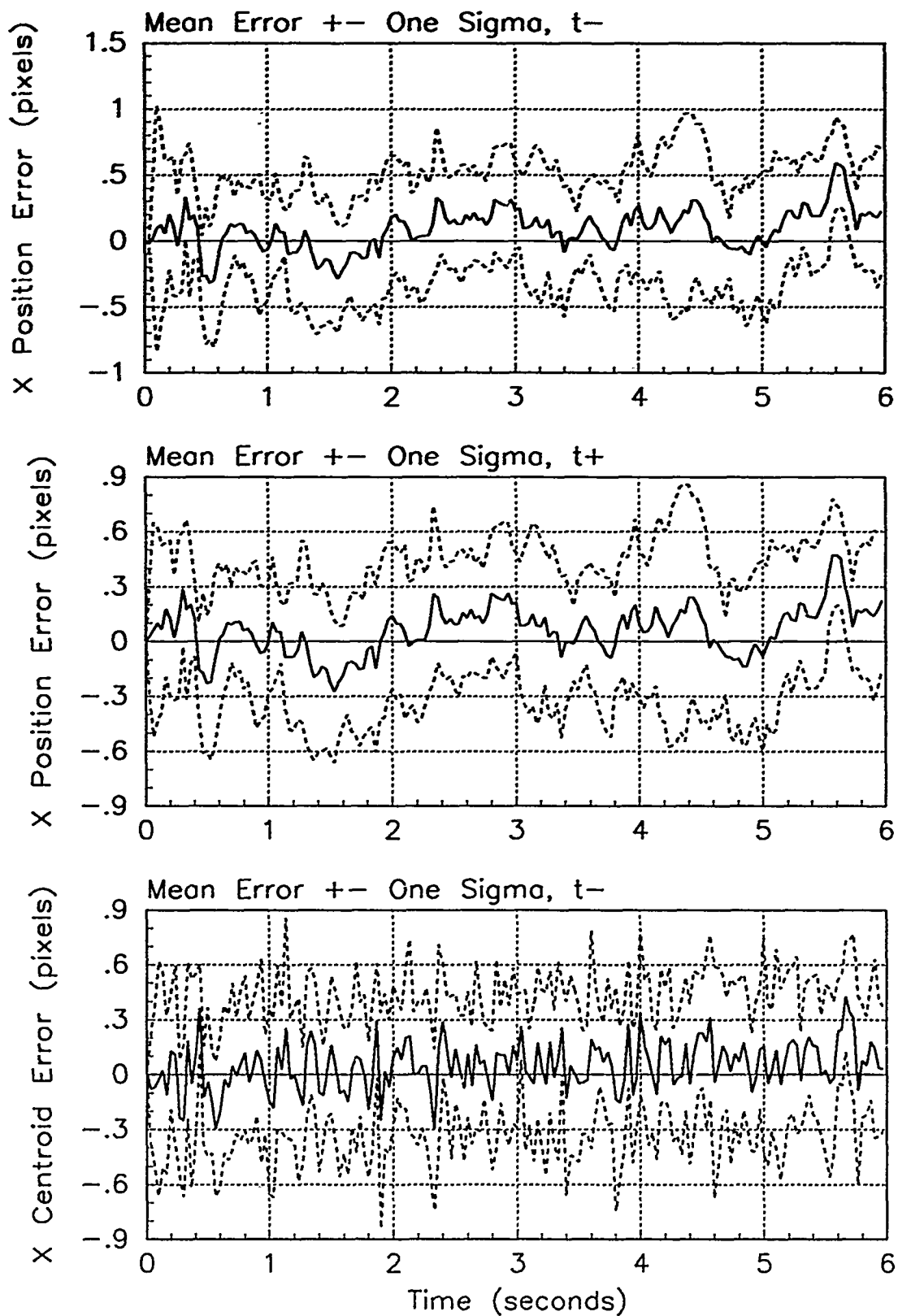


Figure F.40. X-Error Plots; First-Order MMAE-FH; PC is 1; Trajectory with $\omega = 1.32$

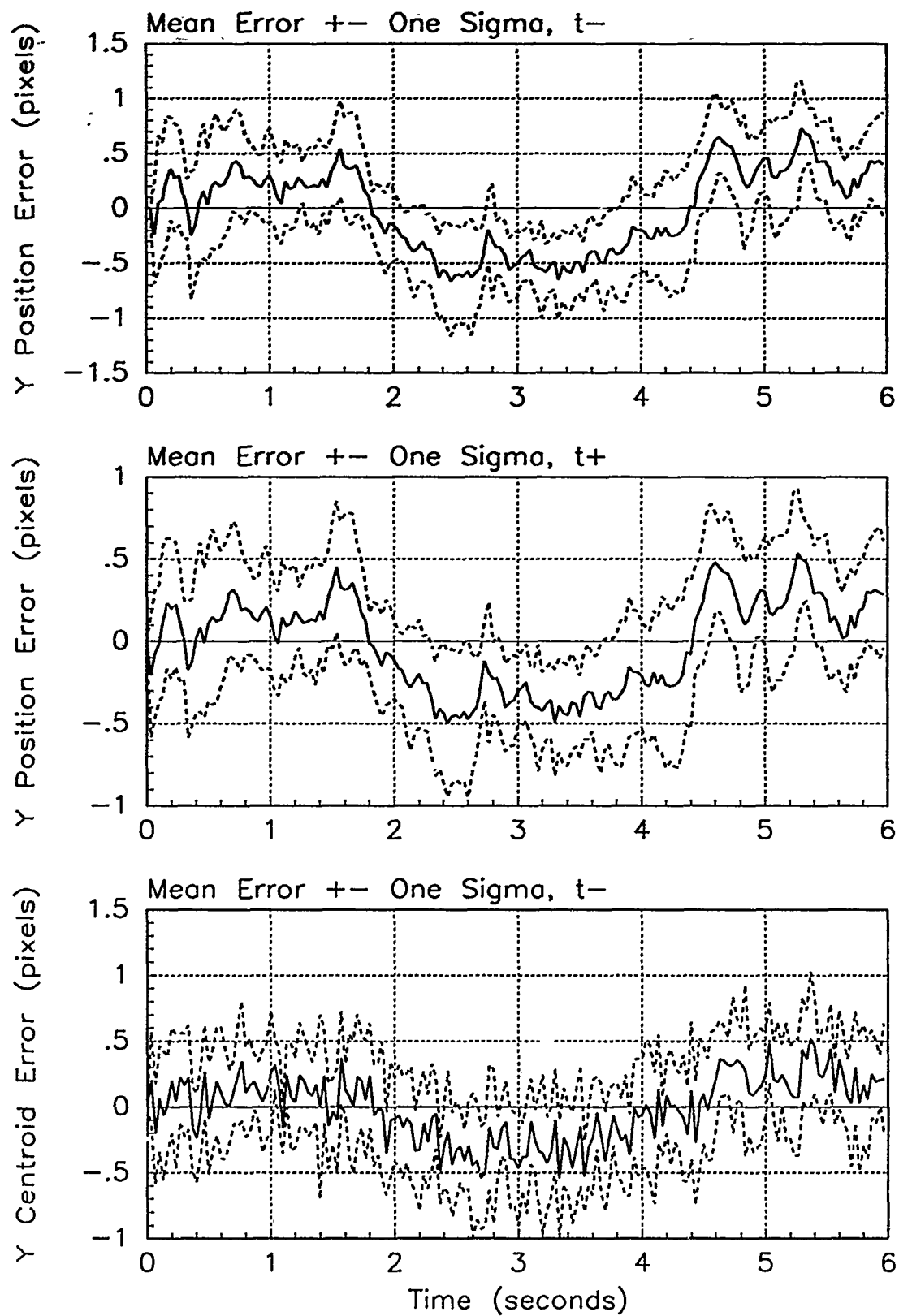


Figure F.41. Y-Error Plots; First-Order MMAE-FII; PC is 1; Trajectory with $\omega = 1.32$

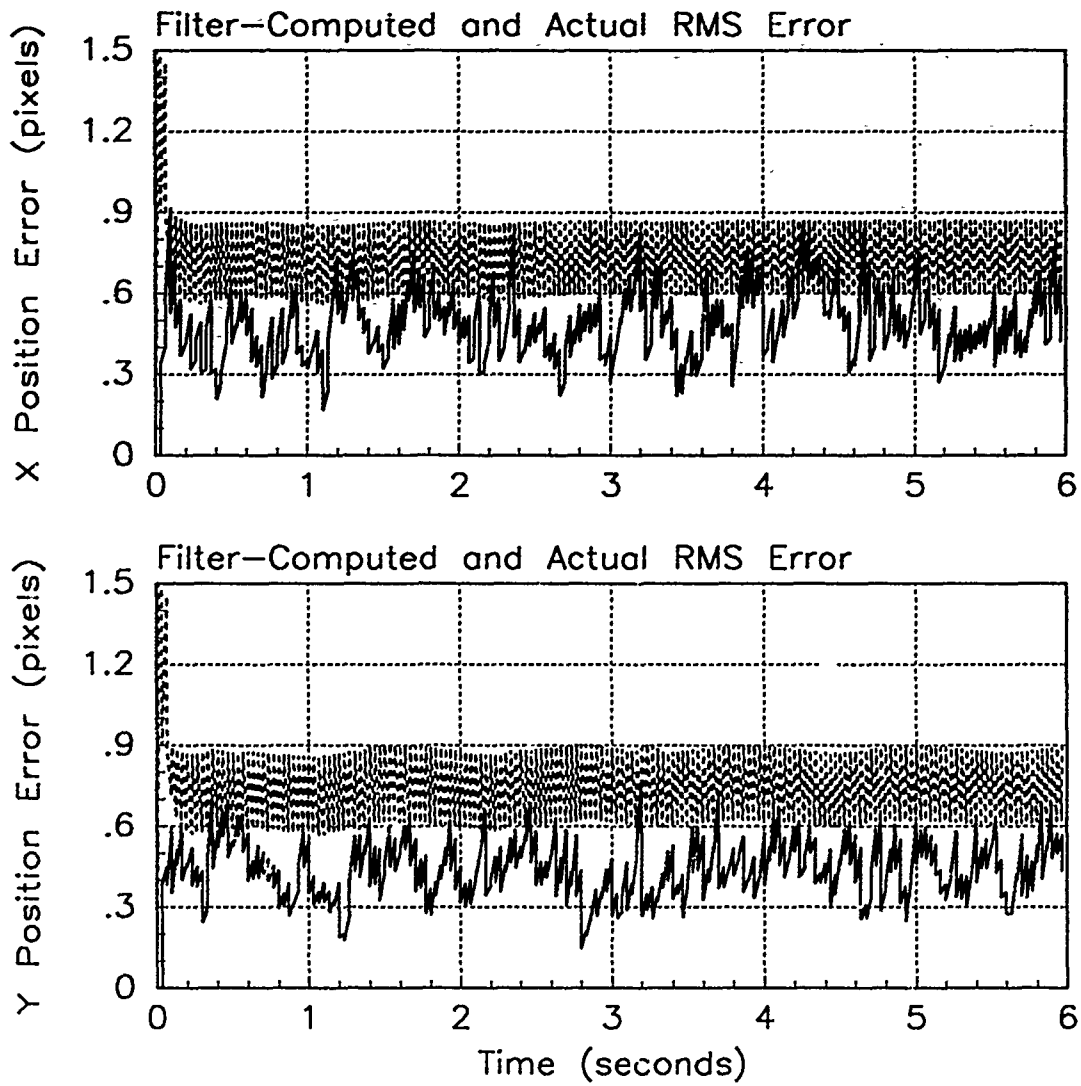


Figure F.42. RMS Error Plots; First-Order MMAE-FH; PC is 1; Trajectory with $\omega = 2.8$

Table F.14. Temporal Averages and Residuals; First-Order MMAE-FH; PC is 1; Trajectory with $\omega = 2.8$.

Error in:	Mean	σ
$p_x(t_i^-)$	-0.018740	0.54556
$p_x(t_i^+)$	-0.021292	0.43676
$y_x(t_i^-)$	-0.0058123	0.44014
$p_y(t_i^-)$	-0.015370	0.49408
$p_y(t_i^+)$	-0.025484	0.38544
$y_y(t_i^-)$	-0.018680	0.42806

Filter	$r_k^T r_k$	$r_k^T A_k^{-1} r_k$
Benign	3.62457	21.09311
Intermediate	0.48645	2.22368
Harsh	0.46795	1.74499

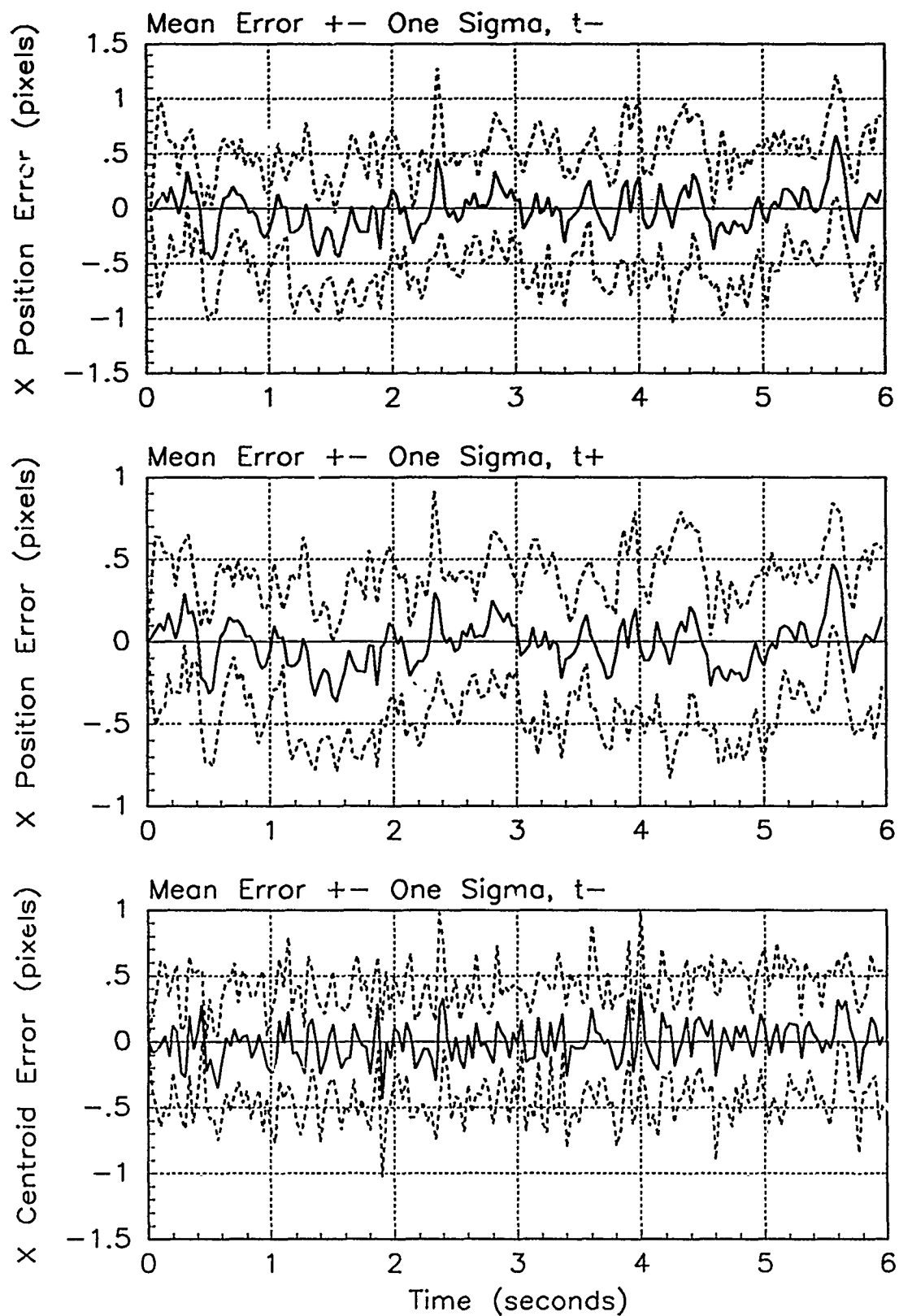


Figure F.43. X-Error Plots; First-Order MMAE-FH; PC is 1; Trajectory with $\omega = 2.8$

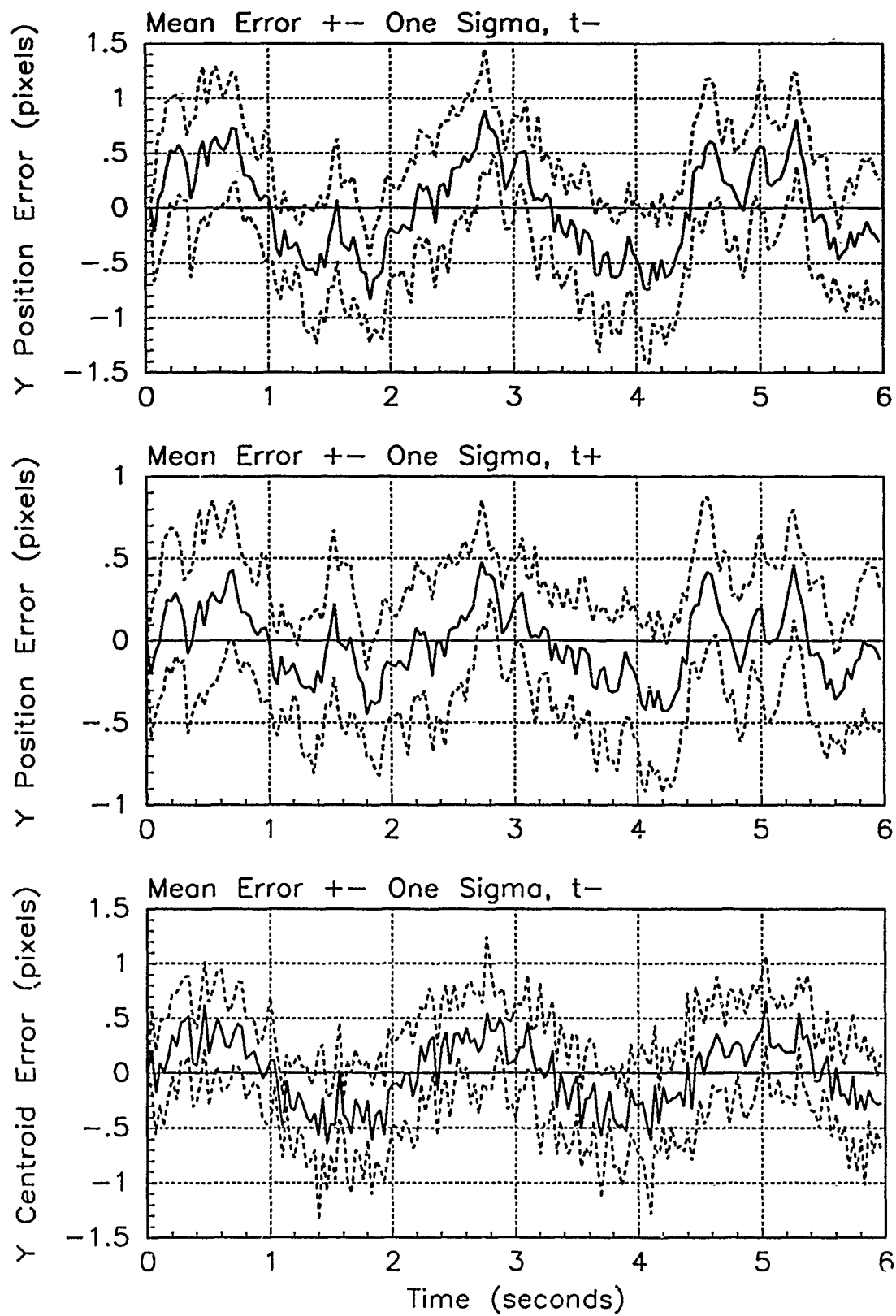


Figure F.44. Y-Error Plots; First-Order MMAE-FH; PC is 1; Trajectory with $\omega = 2.8$

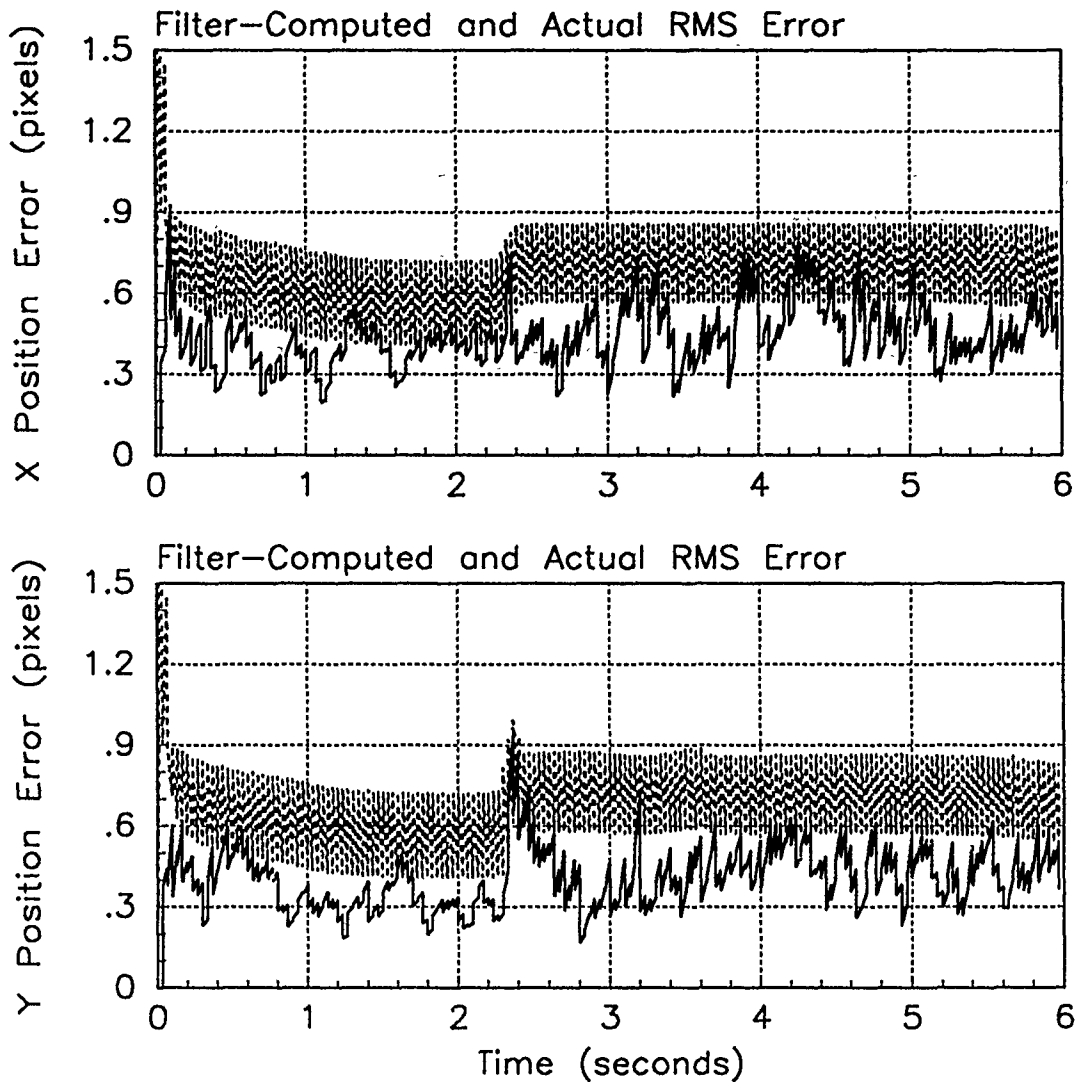


Figure F.45. RMS Error Plots; First-Order MMAE-FB; PC is 1; Jinking Trajectory

Table F.15. Temporal Averages and Residuals; First-Order MMAE-FB; PC is 1; Jinking Trajectory.

Error in:	Mean	σ
$p_x(t_i^-)$	0.042970	0.48133
$p_x(t_i^+)$	0.022726	0.40679
$y_x(t_i^-)$	0.038922	0.41157
$p_y(t_i^-)$	0.0090056	0.44386
$p_y(t_i^+)$	0.0037421	0.37020
$y_y(t_i^-)$	0.0056431	0.40119

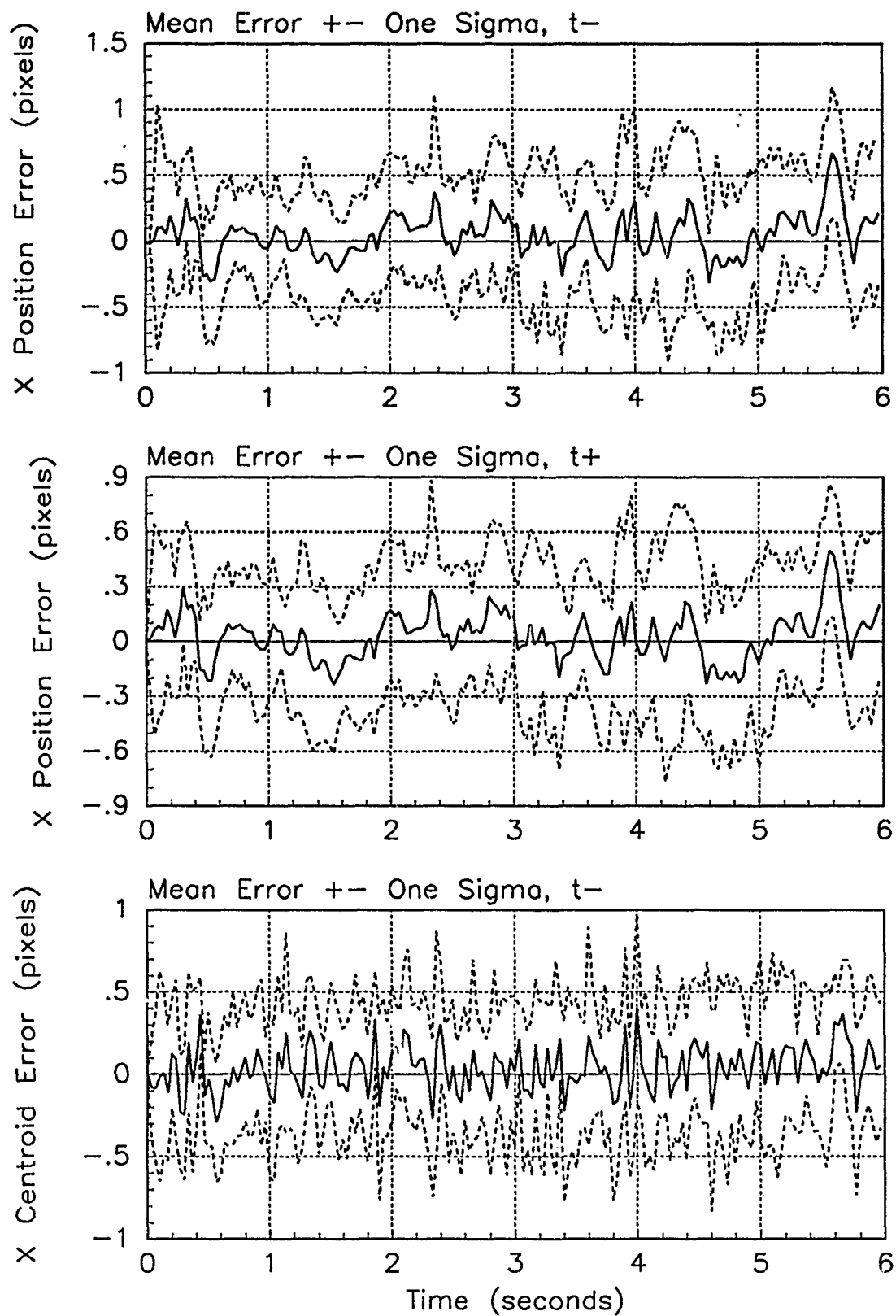


Figure F.46. X-Error Plots; First-Order MMAE-FB; PC is 1; Jinking Trajectory

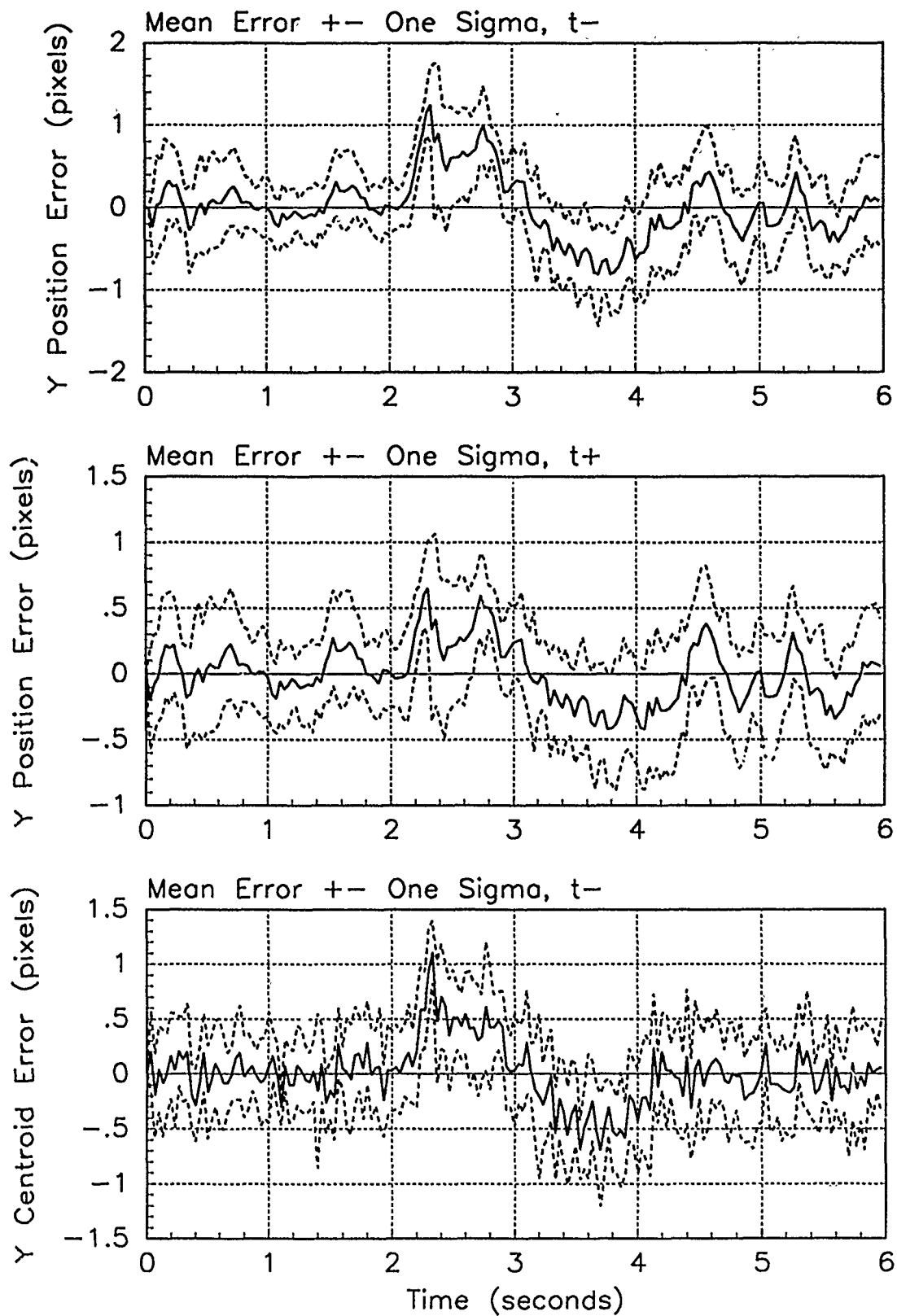


Figure F.47. Y-Error Plots; First-Order MMAE-FB; PC is 1; Jinking Trajectory

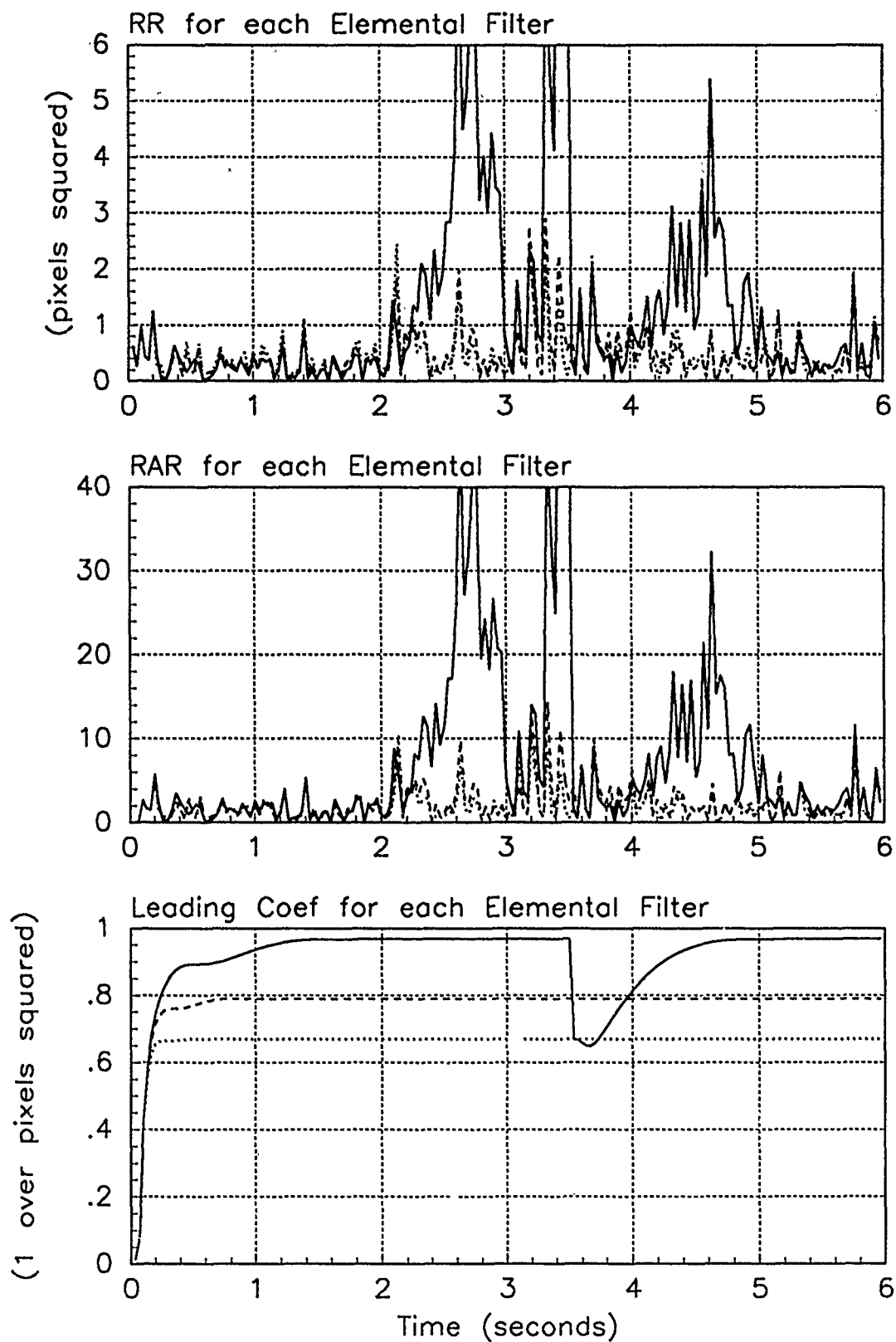


Figure F.48. Probability Calculation Plots; First-Order MMAE-FB; PC is 1; Jinking Trajectory. Benign filter has solid line; intermediate filter has dashed line; harsh filter has dotted line.

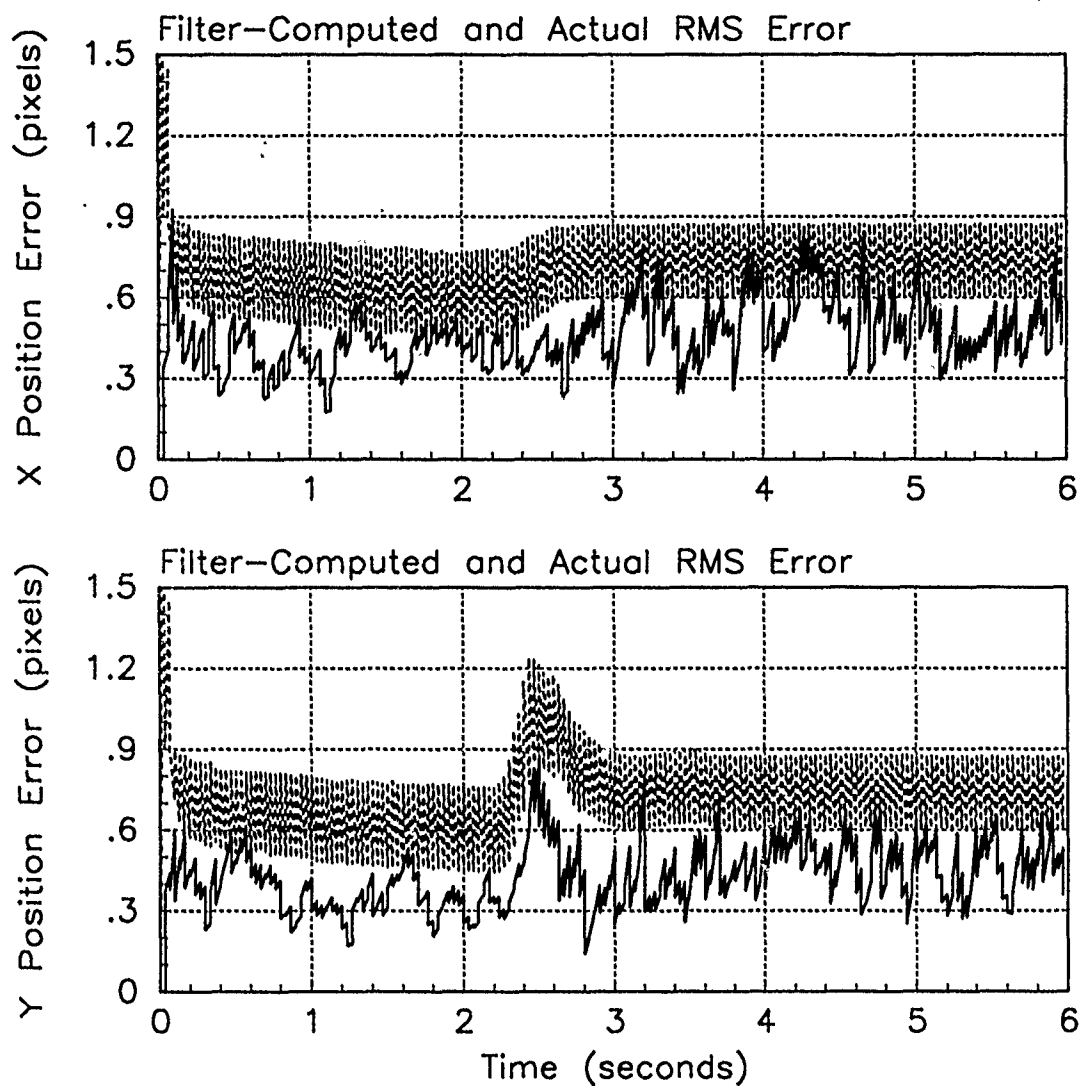


Figure F.49. RMS Error Plots; First-Order MMAE-FH; PC is 1; Jinking Trajectory

Table F.16. Temporal Averages and Residuals; First-Order MMAE-FH; PC is 1; Jinking Trajectory.

Error in:	Mean	σ
$p_x(t_i^-)$	0.0029189	0.50868
$p_x(t_i^+)$	-0.0065459	0.42018
$y_x(t_i^-)$	0.012048	0.42481
$p_y(t_i^-)$	0.062903	0.47264
$p_y(t_i^+)$	0.041699	0.38468
$y_y(t_i^-)$	0.040567	0.41512

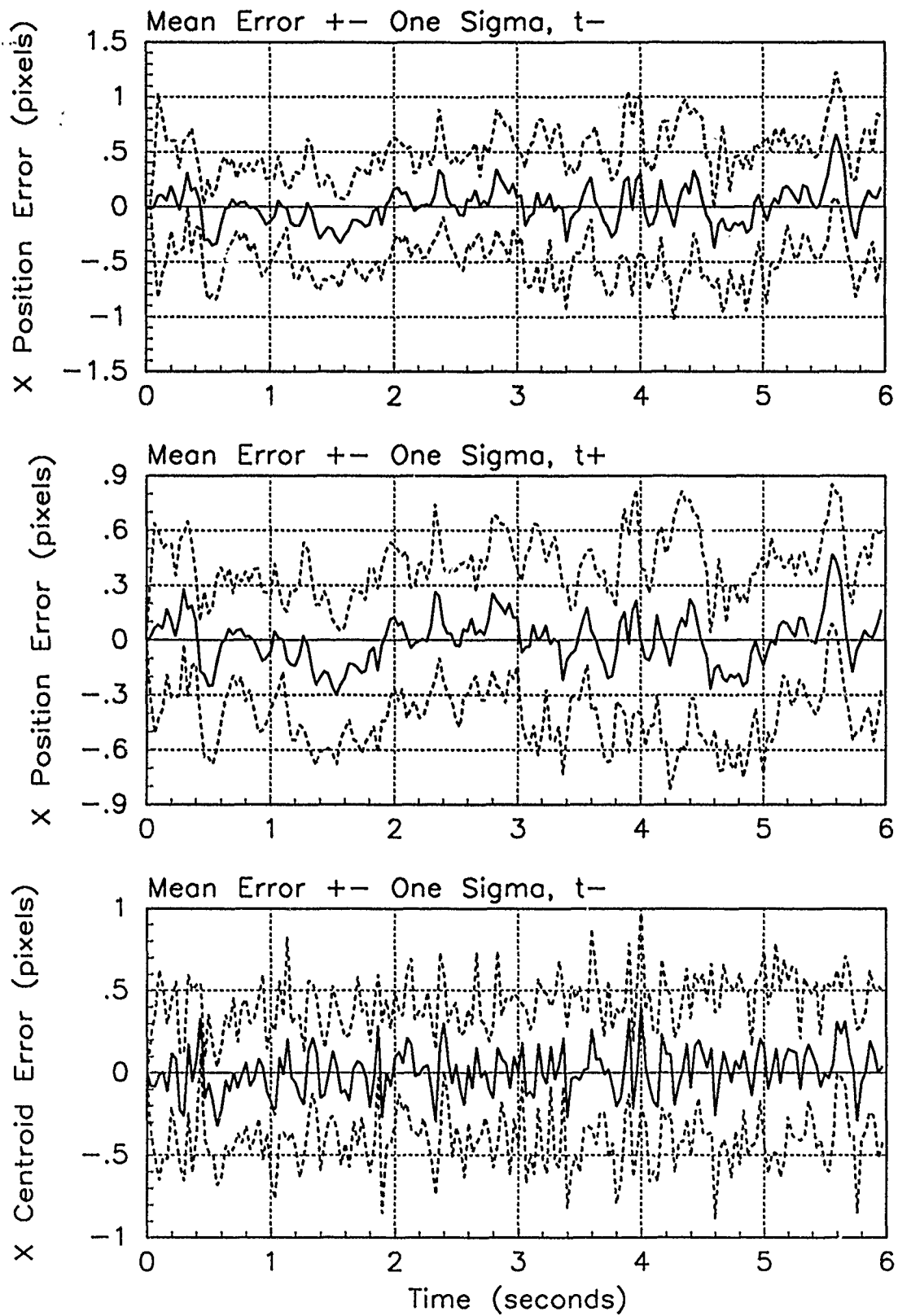


Figure F.50. X-Error Plots; First-Order MMAE-FH; PC is 1; Jinking Trajectory

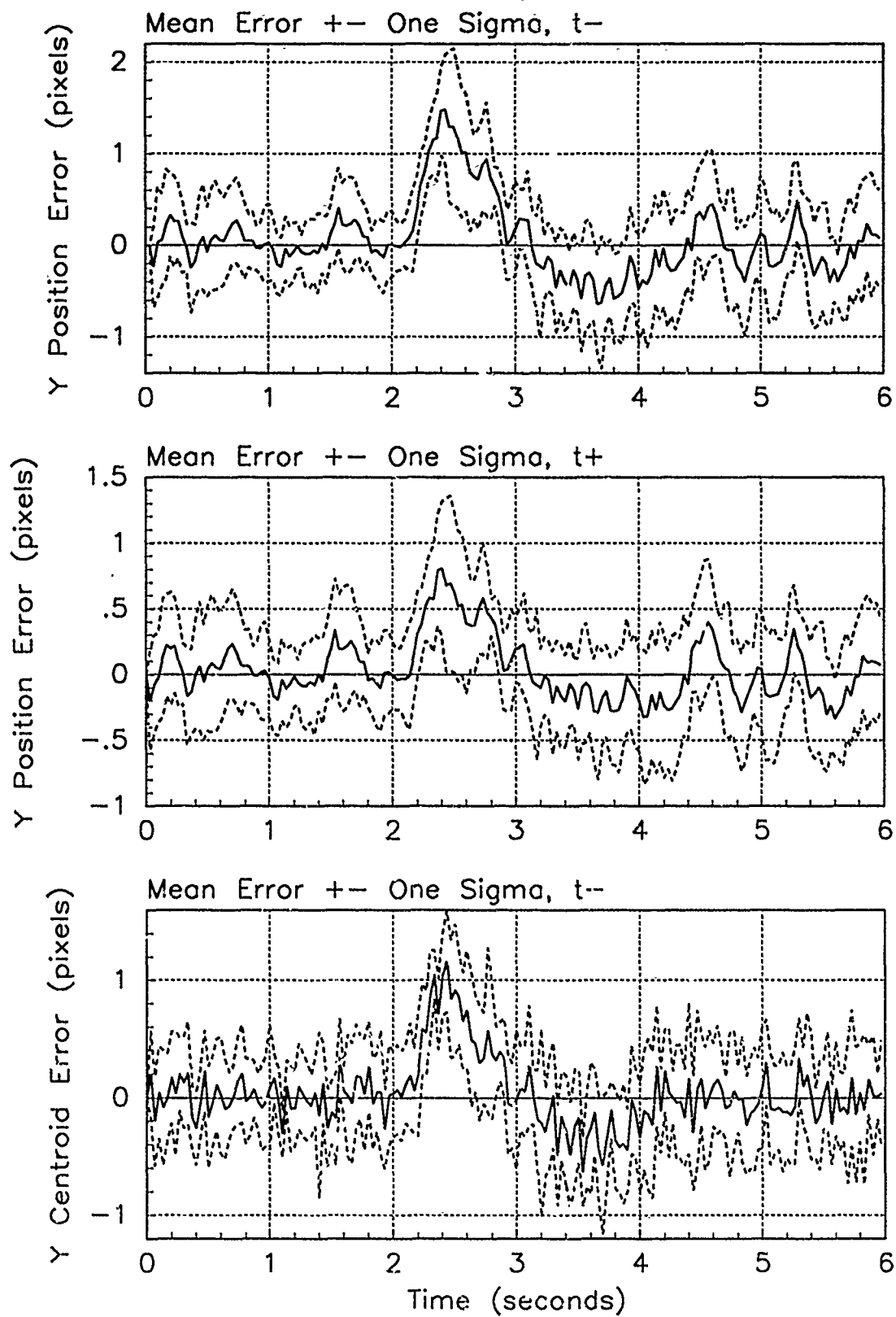


Figure F.51. Y-Error Plots; First-Order MMAE-FH; PC is 1; Jinking Trajectory

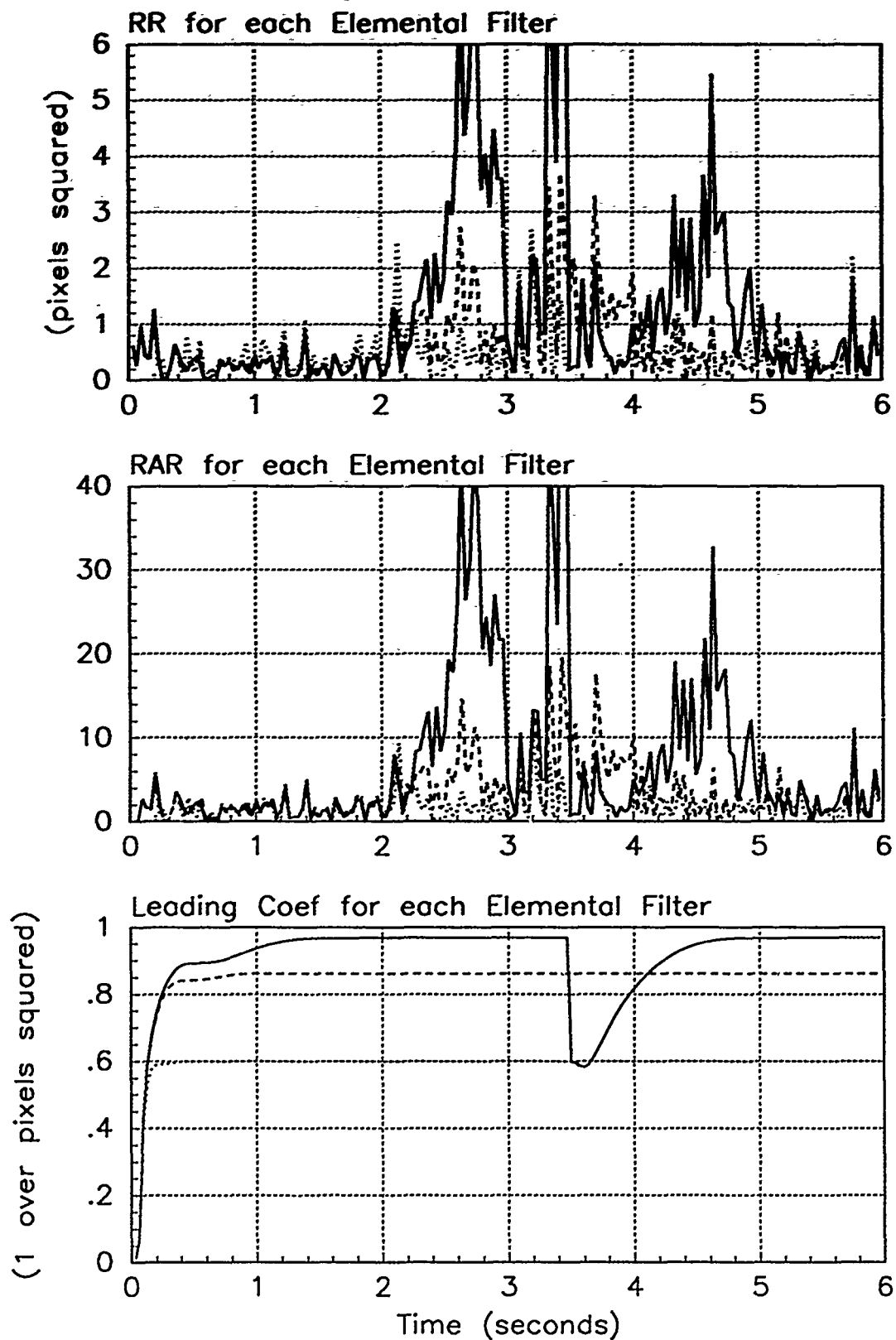


Figure F.52. Probability Calculation Plots; First-Order MMAE-FH; PC is 1; Jinking Trajectory. Benign filter has solid line; intermediate filter has dashed line; harsh filter has dotted line.

Bibliography

1. Flynn, P. M. *Alternative Dynamics Models and Multiple Model Filtering for a Short Range Tracker*. MS thesis, AFIT/GE/ENG/81D, School of Engineering, Air Force Institute of Technology (AU), Wright-Patterson AFB OH, December 1981.
2. Integrated Systems Incorporated. *Matrixx*. Matrix Analysis Package Version 7.0. Santa Clara, CA 95054-1215, October 1988.
3. Jensen, Robert L. and Douglas A. Harnly. *An Adaptive Distributed-Measurement Extended Kalman Filter for a Short Range Tracker*. MS thesis, AFIT/GA/EE/79-1, School of Engineering, Air Force Institute of Technology (AU), Wright-Patterson AFB OH, December 1979.
4. Kozemchak, Mark R. *Enhanced Image Tracking: Analysis of Two Acceleration Models in Tracking Multiple Hot-Spot Images*. MS thesis, AFIT/GE/ENG/82D, School of Engineering, Air Force Institute of Technology (AU), Wright-Patterson AFB OH, December 1982.
5. Leeney, T. A. *A Multiple Model Adaptive Tracking Algorithm Against Airborne Targets*. MS thesis, AFIT/GE/ENG/87D-37, School of Engineering, Air Force Institute of Technology (AU), Wright-Patterson AFB OH, December 1987.
6. Loving, Phyllis A. *Bayesian vs. MAP Multiple Model Adaptive Estimation for Field of View Expansion in Tracking Airborne Targets*. MS thesis, AFIT/GE/ENG/85M, School of Engineering, Air Force Institute of Technology (AU), Wright-Patterson AFB OH, March 1985.
7. Maybeck, Peter S. *Stochastic Models, Estimation, and Control, Volume I*. New York: Academic Press, 1979.
8. Maybeck, Peter S. *Stochastic Models, Estimation, and control, Volume II*. New York: Academic Press, 1982.
9. Maybeck, Peter S. and Richard D. Stevens. "Reconfigurable Flight Control via Multiple Model Adaptive Control Methods," *Proceedings of the IEEE Conference on Decision and Control*, page 3351 (December 1990).
10. Maybeck, Peter S., Professor. Personal interviews. AFIT, Wright-Patterson AFB OH, January and February 1991.
11. Mercier, D. E. *An Extended Kalman Filter for Use in a Shared Aperture Medium Range Tracker*. MS thesis, AFIT/GE/ENG/78D-3, School of Engineering, Air Force Institute of Technology (AU), Wright-Patterson AFB OH, December 1978.
12. Millner, P. P. *Enhanced Tracking of Airborne Targets Using a Correlator/Kalman Filter*. MS thesis, AFIT/GA/EE/82M, School of Engineering, Air Force Institute of Technology (AU), Wright-Patterson AFB OH, March 1982.
13. Muravez, Randall Joseph. *Multiple Model Adaptive Estimation and Prediction with the Harmonically Balanced Kalman Filter Bank*. MS thesis, California State Polytechnic University, Pomona, Pomona, CA, 1989.

14. Netzer, Allan S. *Characteristics of Bayesian Multiple Model Adaptive Estimation for Tracking Airborne Targets*. MS thesis, AFIT/GAE/ENG/85D-2, School of Engineering, Air Force Institute of Technology (AU), Wright-Patterson AFB OH, December 1985.
15. Norton, John E. *Multiple Model Adaptive Tracking of Airborne Targets*. MS thesis, AFIT/GA/ENG/88D-2, School of Engineering, Air Force Institute of Technology (AU), Wright-Patterson AFB OH, December 1988.
16. Rogers, Steven K. *Advanced Tracking of Airborne Targets Using Forward Looking Infrared Measurements*. MS thesis, AFIT/GE/ENG/81D, School of Engineering, Air Force Institute of Technology (AU), Wright-Patterson AFB OH, December 1981.
17. Singletery, J. *Adaptive Laser Pointing and Tracking Problem*. MS thesis, AFIT/GEO/EE/80D-12, School of Engineering, Air Force Institute of Technology (AU), Wright-Patterson AFB OH, December 1980.
18. Stevens, Richard D. *Characterization of a Reconfigurable Multiple Model Adaptive Controller using a STOL F-15 Model*. MS thesis, AFIT/GE/ENG/89D, School of Engineering, Air Force Institute of Technology (AU), Wright-Patterson AFB OH, December 1989.
19. Suizu, Robert I. *Advanced Tracking of Airborne Targets Using Multiple Model Adaptive Filtering Techniques for Adaptive Field of View Expansion*. MS thesis, AFIT/GE/ENG/83D, School of Engineering, Air Force Institute of Technology (AU), Wright-Patterson AFB OH, December 1983.
20. Tobin, David M. *A Multiple Model Adaptive Tracking Algorithm for a High Energy Laser Weapon System*. MS thesis, AFIT/GE/ENG/86D-37, School of Engineering, Air Force Institute of Technology (AU), Wright-Patterson AFB OH, December 1986.